

Reductive Samarium
Catalysis Enabled By A
Thermochemical Roadmap

Thesis by
Emily A. Boyd

In Partial Fulfillment of the Requirements for
the degree of
Doctor of Philosophy

The Caltech logo, featuring the word "Caltech" in a bold, orange, sans-serif font.

CALIFORNIA INSTITUTE OF TECHNOLOGY
Pasadena, California

2025
(Defended 13 May, 2025)

© 2025

Emily A. Boyd
ORCID: 0000-0003-0150-5396

ACKNOWLEDGEMENTS

My Ph.D. has been shaped by the combination of my Grandpa Bob's catch-all advice—"when there's a fork in the road, take it"—and a long list of good influences. My high school chemistry and physics teacher, Mr. Smith, taught me to love problem simplification and introduced me to my first Hess cycle. I am very proud of my Marmaton Valley High School education in general, which may not have included AP classes, but did stretch me out of my smart-kid comfort zone to develop skills (public speaking, collaboration, and ability to handle failure) that have served me well in my Ph.D. In particular I want to thank my teachers—Julie Tholen, Elysa Buss, and Maria Gunselman—and my first collaborator, Payton Wilson.

At the University of Kansas, through sheer luck I stumbled into undergraduate research in the lab of Professor James Blakemore, who has continued to provide excellent advice and support throughout my Ph.D. That first summer was a truly pivotal experience in which I learned just how fun it is to sit around waiting for solvent to pump down and listen to extremely smart, passionate people talk about chemistry. I had incredible mentors and friends in the Blakemore group: Davide Lionetti, Keaton Prather, Julie Hopkins-Leseberg, and Will Moore, to name a few.

James' and Davide's guidance were instrumental in the series of fortuitous events that led to the opportunity to join the lab of Professor Jonas Peters at Caltech. Since then, Jonas has instilled a great number of valuable lessons that I assume will echo in my brain for the foreseeable future: to pursue problems I find interesting, to design experiments with the cake (and eating it) in mind, to value constructive criticism, and to tell a good story. Likely most importantly, I am privileged to have existed for my whole time at Caltech with the reassuring knowledge that Jonas is acting in my best interests.

I'm very grateful to Christian Johansen for welcoming me graciously onto his project three years ago. Since that crazed sprint of a summer, I've benefited so much from continuing to share ideas as we followed our own threads (that, to our shock, eventually found a way to intersect). Working with Christian has had a profound positive impact on my basic thought processes, and I appreciate his inclination to amplify quieter voices, both in group meeting and karaoke.

The postdocs I've overlapped with in the Peters group have been extremely influential. I am very fortunate that Lucie Nurdin started in the lab at a time when I really needed a role model; she taught me not to fear vacuum pumps and to strive to be a better person, not just scientist. I'm grateful to John Ovian for asking exceptionally good questions (especially at KML) and helping me work through chemistry, professional, and life problems over many long lunches. I'm fortunate to have been able to work with Hoimin Jung as a very patient, talented collaborator. Pablo Garrido-Barros taught me electrochemistry and optimism, and Joe Derosa, figure-making and persistence.

As senior graduate students when I started in the group, Matt Chalkley and Dirk Schild kindly answered many of my naïve questions. Nick Watkins' friendly competitiveness and gregarious nature eased my transition to Caltech. Enric Adillon and Sasha Alabugin continue to hold the Peters group to a high intellectual standard. Madeline Hicks' tenacity and scientific rigor are unparalleled. I enjoyed many wide-ranging chats with Catherine Romero, and I'm very grateful to her and Mengdi Li for making our office bay fun. I consider the opportunity to mentor someone as talented as Drew Tarnopol a privilege, and award him MVP of our Jeopardoscopy team. Alex Pavelic is one of the warmest chemists and glovebox companions I've known. Seungju Kang's fearlessness going after tricky intermediates is inspiring. I've likely learned more from mentoring Luke Zhou and Bao Nguyen than they have from me, and I'm very excited to see what they do next.

I am extremely grateful for Professor Sarah Reisman's advice and encouragement both as one of my committee members and as part of the collaboration that underlies all of the work in this thesis. Dave Charboneau from Sarah's group and Skyler Ware from Professor Kim See's group were steadfast collaborators in the early days, when from all of our angles it was unclear if anything would ever come of our efforts. I especially want to thank Chung Shin for his hard work on the zinc-driven samarium catalysis.

I want to thank my committee members, Professor Theo Agapie and Professor Greg Fu, for all of their guidance. Their questions have pushed me to analyze my data more deeply and select problems with more care, and I appreciate their support in figuring out my next steps. Caltech is a special environment for research, in large part due to the brilliant staff who keep the place running. I'm particularly grateful to Paul Oyala and Nate Hart, not only for their EPR and glass-blowing expertise, but also for being high-quality trivia

team members. I also want to thank Julianne Just, without whom I would probably still be struggling to get my props exam scheduled.

I'm lucky to have a tight support system outside of Caltech. My friends—Sarah Zajonz, Emma Pryor-Piazza, Skylar Pryor-Piazza, and Shaylyn Hubbell—endlessly amaze me with their accomplishments and compassion. Clara has a preternatural ability to sense when I need a three-hour sister chat. My dad reminds me to watch the Royals, which got me through a lot of long afternoons on our Covid shift schedule. My mom has listened patiently to so much more than her fair share of samarium angst, and I do not take her unconditional support for granted. Zach Wood is inextricable from my chemistry journey, and I would not have gotten to this point without his partnership.

Finally, my great-aunt Ruth planted the image of an eccentric but fiercely intellectual female academic, out-pontificating all the men over red wine and wild rice soup in big red glasses, leather pants, and chunky boots, in my childhood brain. Matching her sheer force of personality and will is an unrealistic goal, but I will keep trying to take up space.

ABSTRACT

Samarium diiodide is a versatile single-electron reductant. Its reactivity is modulated by recruitment of a wide range of additives to its large coordination sphere. Binding of strong Lewis bases produces more potent Sm(II) reductants, while polar protic donors promote net proton-coupled electron transfer to a variety of unsaturated substrates including intermediates of molybdenum-catalyzed nitrogen reduction. However, samarium(II) reagents are used (super)stoichiometrically in all but a few select cases because mild, tunable methods for selective reduction of oxidized samarium(III) products back to the active samarium(II) state were unavailable at the outset of the following studies. Chapter 1 frames the challenge of catalytic samarium turnover in the context of nitrogen fixation. Proton-coupled electron transfer and inner-sphere electron transfer are introduced as two potential catalytic roles for samarium(II), and a strategy for proton-coupled reduction of problematic samarium(III)-alkoxide intermediates to achieve turnover is outlined. Chapter 2 describes a well-defined model system used to construct extended quantitative thermochemical cycles mapping proton transfer, electron transfer, and ligand association at samarium. The samarium(II) complex binds a secondary amide to generate a remarkably potent net hydrogen atom donor. In Chapter 2, this driving force is leveraged in iron-catalyzed nitrogen reduction; the strongly reducing, weakly acidic nature of the samarium reagent leads to selective generation of hydrazine over ammonia (99:1). In Chapter 3, the benchmarked samarium(III)-alkoxide protonolysis thermodynamics inform selection of Brønsted acids that can be coupled with a mild reductant (zinc powder or an applied electrochemical potential) to achieve catalytic samarium turnover in reductive coupling of ketones and acrylates to form γ -lactones. Photodriven methods for this samarium-catalyzed transformation are reported in Chapter 5. Finally, in Chapter 6, the hypothesis that samarium(II) might serve as an inner-sphere reductant in nitrogen reduction with transition metal catalysts guides design of conditions for tandem samarium/molybdenum catalysis in electrocatalytic nitrogen reduction to ammonia with the lowest driving force and highest Faradaic efficiency (82%) reported to date for a nonaqueous system at atmospheric pressure.

PUBLISHED CONTENT AND CONTRIBUTIONS

Boyd, E.A.; Peters, J. C. *J. Am. Chem. Soc.* **2022**, *144*, 21337. doi: 10.1021/jacs.2c09580.

E.A.B. designed and performed all experiments. E.A.B. and J.C.P. wrote the manuscript.

Boyd, E.A.; Peters, J. C. *J. Am. Chem. Soc.* **2023**, *145*, 14784. doi: 10.1021/jacs.3c03352.

E.A.B. designed and performed all experiments. E.A.B. and J.C.P. wrote the manuscript.

Boyd, E.A.,[†] Shin, C.,[†] Charboneau, D. J.; Peters, J. C.; Reisman, S.E. *Science* **2024**, *385*, 847. doi: 10.1126/science.adp5777.

[†]Authors contributed equally and are listed alphabetically.

E.A.B. developed the protonolysis strategy and performed all electroanalytical studies and electrocatalysis optimization. E.A.B. helped to write the manuscript.

Johansen, C. M.;[†] Boyd, E.A.,[†] Tarnopol, D.E.; Peters, J. C. *J. Am. Chem. Soc.* **2024**, *146*, 25456. doi: 10.1021/jacs.4c10053.

[†]Authors contributed equally.

E.A.B. contributed to the development of conditions for Sm^{II} photogeneration and catalysis and performed all electroanalytical studies. E.A.B. helped to write the manuscript.

Boyd, E.A.; Jung, H.; Peters, J. C. *J. Am. Chem. Soc.* **2025**, *147*, 4695. doi: 10.1021/jacs.4c14845.

E.A.B. designed and performed all experiments involving the pyridine-anchored molybdenum catalyt. E.A.B., H.J., and J.C.P. wrote the manuscript.

TABLE OF CONTENTS

Chapter 1. Introduction	1
1.1 Opening Remarks	1
1.2 Kinetic Challenges in N ₂ R	2
1.3 Sm ^{II} Reduction Potentials	7
1.4 Sm ^{II} as a Proton-Coupled Reductant	10
1.3 Sm ^{II} as an Inner-Sphere Reductant	15
References.....	18
Chapter 2. Sm(II)-mediated proton-coupled electron transfer: quantifying very weak N–H and O–H homolytic bond strengths and factors controlling them ...	28
2.1 Introduction	28
2.2 Results and Discussion.....	32
2.2.1 Redox Chemistry of Sm ^{II}	32
2.2.1 PCET Reactivity of Sm ^{II}	34
2.2.3 Electrochemical PCET with [Sm ^{III} –PH] ⁺	37
2.2.4 Thermochemical Estimates	39
2.2.5 Origins of Bond-Weakening	45
2.2.6 Implications for SmI ₂ -based PCET Reagents	48
2.2.7 Considerations for Sm-mediated Electrocatalysis	48
2.3 Conclusions	54
References.....	55
Chapter 3. Highly selective Fe-catalyzed nitrogen fixation to hydrazine enabled by Sm(II) reagents with tailored redox potential and p<i>K</i>_a	62
3.1 Introduction	62
3.2 Results.....	67
3.3 Discussion.....	81
3.4 Conclusions	86
References.....	88
Chapter 4. Reductive samarium (electro)catalysis enabled by samarium(III)-alkoxide protonolysis	96
4.1 Introduction	96
4.2 Development of Mild Turnover Conditions for Reductive SmI ₂ Catalysis	100
4.3 Demonstration of Electrocatalysis	106
4.4 Thermochemistry and Outlook	115
References.....	121

Chapter 5. Photodriven Sm(III)-to-Sm(II) reduction for catalytic applications	
.....	126
5.1 Introduction	126
5.2 Photoreduction of Sm ^{III} Species.....	129
5.3 Proof-of-Concept Photodriven Sm Catalysis	135
References.....	140
Chapter 6. Samarium as a catalytic electron-transfer mediator in electrocatalytic nitrogen reduction to ammonia.....	147
6.1 Introduction	147
6.2 Results and Discussion.....	150
References.....	165
Appendix A. Supplementary Information for Chapter 2.....	172
Appendix B. Supplementary Information for Chapter 3.....	244
Appendix C. Supplementary Information for Chapter 4.....	269
Appendix D. Supplementary Information for Chapter 5.....	296
Appendix E. Supplementary Information for Chapter 6.....	339

LIST OF FIGURES

1.1: Catalytic N ₂ R with PNP ₃ MoBr ₃ with chemical, electrochemical, and photochemical driving force	5
1.2: Aqueous and nonaqueous Ln ^{III/II} reduction potentials.	8
1.3: PCET to M–N _x H _y	11
1.4: Turnover pathways for Sm ^{II} –EH as a PCET catalyst.....	13
1.5: ISET mechanism with SmI ₂	17
2.1: Quantification of coordination-induced bond weakening at Sm ^{II}	31
2.2: Chemical and electrochemical conversion between Sm ^{II} and [Sm ^{III}]PF ₆	34
2.3: Reactivity of Sm ^{II} –PH and Sm ^{II} –MeOH with <i>trans</i> -stilbene to generate Sm ^{III} –P and Sm ^{III} –OMe	35
2.4: Solid-state structures of Sm ^{III} –P and Sm ^{III} –OMe.....	36
2.5: CVs of [Sm ^{III}]PF ₆ in the presence of combinations of PH, PMe, and/or DPE	38
2.6: Summary of thermochemical cycles and equations with PH.....	41
2.7: CV titration of [Sm ^{III} –NCMe]PF ₆ with PH in CH ₃ CN	42
2.8: Equilibria relevant to p <i>K</i> _a determinations.....	43
2.9: Summary of thermochemical cycles and equations with MeOH	44
2.10: (A) CV titration of the Sm ^{III} –ketyl adduct Sm ^{III} –OCPh ₂ · with benzophenone and plot of E _{1/2} as a function of benzophenone concentration (B) Thermochemical cycle used to determine Δ <i>G</i> ^o _{Sm(III)–E} for Sm ^{III} –OCPh ₂ ·	50
2.11. Steps demonstrated in a hypothetical Sm-mediated electrocatalytic PCET cycle.	53
3.1: Distal, alternating, and hybrid mechanisms of N ₂ R	63
3.2: Selectivity of catalytic N ₂ R with Fe dependent on reagent thermodynamics	66
3.3: (A) Fe-catalyzed reduction of N ₂ with Sm ^{II} –PH. (B) ¹ H NMR spectrum of Sm ^{III} –P as the byproduct of catalysis (C) ¹⁵ N{ ¹ H} NMR spectrum of ¹⁵ NH ₂ ¹⁵ NH ₃ Cl and ¹⁵ NH ₄ Cl obtained following acidic workup of the reaction under ¹⁵ N ₂	68

3.4: Relative reduction potentials of $\text{FeN}_2^{0/-}$, FeNNMe_2^- , and Sm^{II} reagents in toluene	72
3.5: Mössbauer and CW EPR spectra of the standard catalytic reaction mixture (toluene, 1 mM $^{57}\text{FeN}_2$, 32 equiv PH, 40 equiv Sm^{II}) freeze quenched after stirring at $-78\text{ }^\circ\text{C}$ for the indicated time.	75
3.6: Displacement of $[\text{FeN}_2]^-$ from $[\text{Sm}^{\text{III}}]^+$ by PMe evidenced by (A) CW X-band EPR spectra (B) IR spectra	77
3.7: Possible pathways activated by $[\text{Sm}^{\text{III}}]^+$ coordination to FeN_2^-	79
3.8: Products of reaction of FeNNMe_2 with 3 equiv Sm^{II} -PH.....	80
3.9: Proposed role of FeNNH_2 as selectivity branchpoint in Fe -catalyzed N_2R to NH_3 vs NH_3	84
3.10: Relationship between reduction potential and N_2H_4 vs NH_3 yield upon protonation of a series of tungsten hydrazido(2-) complexes.....	86
4.1: Utility of stoichiometric Sm^{II} reductants in diverse applications	96
4.2: Targeted Sm^{II} -catalyzed cycle for ketyl-olefin coupling	98
4.3: (A) Representative Sm catalysis precedents. (B) Inverse relationship between Sm^{III} -ligand affinity and reduction potential. (C) Sm-catalyzed reductive cross-coupling of ketones and acrylates.....	99
4.4: Conversion of $\text{Sm}(\text{O}^i\text{Pr})_3$ to SmI_3 with LutHNTf ₂ and LiI.	101
4.5: Reaction optimization and control experiments conducted at 0.05 mmol scale	103
4.6: Substrate scope of Sm-catalyzed reactions with Zn^0	105
4.7: Diastereoselectivity of intramolecular Sm catalysis with <i>E</i> - and <i>Z</i> - 1ab . 106	
4.8: CVs of $\text{Sm}(\text{OTf})_3$ and MgI_2 after the addition of either substrates 1a or 1m , 2 , the combination of ketone and acrylate substrates, and the acid LutHNTf ₂ overlaid with the CVs of the substrates, acid, and MgI_2 in the absence of Sm.	108
4.9: CVs of $\text{Sm}(\text{OTf})_3$ and $^n\text{Bu}_4\text{NI}$ after the addition of the substrates 1a and 2 followed by titration of $\text{Mg}(\text{NTf}_2)_2$	110
4.10: CVs of $\text{Sm}(\text{OTf})_3$, $^n\text{Bu}_4\text{NI}$, and acetophenone (B) Plots of $E_{p,c}$ vs $\log([\mathbf{1m}])$	112

4.11: Left: CVs of Sm(OTf) ₃ , ⁿ Bu ₄ NI, and 1a or 2 . Right: experimental $i_{p,a}/i_{p,c}$ values at varying scan rates at each substrate concentration plotted vs log(λ) using m and k_C values that result in a good fit with the simulated working curve.	114
4.12: CPE conditions	115
4.13: Thermochemical cycle describing Sm ^{III} –OR protonolysis and CVs demonstrating reversibility of Sm(O ^{<i>i</i>} Pr) ₃ protonolysis and iodide substitution with ColHNTf ₂ and LiI	116
4.14: CVs demonstrating the sensitivity of net protonolysis and iodide substitution of Sm(O ^{<i>i</i>} Pr) ₃ to the acid p <i>K</i> _a and availability of iodide.....	117
4.15: Product distribution of Sm-catalyzed reductive cross-coupling of acetophenone and ^t Bu-acrylate as a function of dielectric strength and acid p <i>K</i> _a	118
4.16: CVs demonstrating the sensitivity of net protonolysis and ligand substitution of Sm(O ^{<i>i</i>} Pr) ₃ to the identity of the substituting ligand.....	119
5.1: Generalized Sm ^{III/II} catalytic cycle.....	127
5.2: Antenna strategy for photodriven Ln ^{II} catalysis.....	128
5.3: Activation of HEH ₂ toward photoreduction by Gd ^{III} or Sm ^{III}	129
5.4: UV–vis spectra following photoreduction of SmI ₃ and SmI ₂ (O ^{<i>i</i>} Pr)(L) _{<i>n</i>} by HEH ₂ to form SmI ₂	130
5.5: CVs of Sm(O ^{<i>i</i>} Pr) ₃ in the presence of iodide and proton sources.....	131
5.6: UV-vis spectra following photoreductions of Sm ^{III} species with [Ir]PF ₆ photocatalyst and rationale for photoinduced net PCET from HEH ₂ to [Sm ^{III} –OR] species	132
5.7: (A) Sm ^{II} species generated in the presence of various ligands by a photoredox approach. (B) UV–vis spectra following photogeneration of SmBr ₂ and Sm(HMPA) ₄ ²⁺	134
5.8: Proposed mechanism of Sm cross-coupling under Ir-free conditions	139
6.1: (A) Li-mediated <i>e</i> N ₂ R. (B) Low-overpotential <i>e</i> N ₂ R with well-defined homogeneous catalysts. (C) Mo-catalyzed N ₂ R using stoichiometric SmI ₂ as the reductant. (D) Tandem Sm/Mo-catalyzed <i>e</i> N ₂ R.....	148

6.2: CVs of (A) the cathode solution following exhaustive electrolysis of SmI ₃ with PNP ₃ MoBr ₃ at -1.45 V; (B) SmI ₃ , PNP ₃ MoBr ₃ , and PNP ₃ Mo(N)I; (C) the reaction mixture of SmI ₂ and PNP ₃ MoBr ₃ ; (D) SmI ₃ following addition of ⁿ Bu ₄ NBr.	154
6.3: (A) CVs of the cathode solution under the standard electrocatalytic conditions with PNP ₃ MoBr ₃ recorded after passage of 0-1.3 C; inset: NH ₃ production as a function of charge passed. (B) CVs of the cathode solution before and after exhaustive electrolysis	156
6.4: CVs of (A) PNP ₃ Mo(N)I following addition of 0.5 equiv I ₂ and (B) in situ-generated [PNP ₃ Mo ^V (N)I] ⁺ in the presence of increasing [ⁿ Hep ₄ NI]	158
6.5: CVs of in situ-generated [PNP ₃ Mo ^V (N)I] ⁺ following successive addition of (A) LutHNTf ₂ and Lut or (B) PicHNTf ₂ and Pic; (C) 64 mM PicHNTf ₂ at varying scan rates; and (D) Square scheme describing PT and ET steps at the PNP ₃ Mo ^{V/IV} (N)I redox couple	160
6.6: Plots of Mo ^{V/IV} E _{1/2} as a function of the [baseH ⁺]:[base] ratio	162
6.7: CV of PNP ₃ Mo(N)I in the presence of LutHNTf ₂ overlaid with the LutHNTf ₂ background	163
6.8: Proposed role of Sm ^{III/II} redox in mediation of selective Mo-catalyzed N ₂ R.	164
6.9: Comparison of the overpotential, Faradaic efficiency, and yield rate of the Sm- and Mo-mediated eN ₂ R reported here with representative nonaqueous eN ₂ R systems from the literature	165
A1. ¹ H NMR of [Sm ^{III}]PF ₆ in CD ₃ CN (400 MHz)	179
A2. ³¹ P NMR of [Sm ^{III}]PF ₆ in CD ₃ CN (162 MHz)	179
A3. ¹⁹ F NMR of [Sm ^{III}]PF ₆ in CD ₃ CN (376 MHz).	180
A4. ¹ H NMR of Sm ^{III} -P in C ₆ D ₆ (400 MHz).....	180
A5. ¹³ C{ ¹ H} NMR of Sm ^{III} -P in C ₆ D ₆ (126 MHz)	181
A6. ¹ H NMR of Sm ^{III} -OMe in C ₆ D ₆ (400 MHz).....	181
A7. ¹³ C{ ¹ H} NMR of Sm ^{III} -OMe in C ₆ D ₆ (126 MHz)	182
A8. ¹ H NMR in C ₆ D ₆ (400 MHz, r.t.) following the reaction of Sm ^{II} with 1 equiv. PH	184

A9. ^1H NMR in C_6D_6 (400 MHz, r.t.) following the reaction of Sm^{II} with 1 equiv. MeOH	185
A10. ^1H NMR in CDCl_3 (400 MHz, r.t.) showing organic products of the reaction of Sm^{II} - PH with 0.5 equiv. <i>trans</i> -stilbene.....	187
A11. ^1H NMR in CDCl_3 (400 MHz, r.t.) showing organic products of the reaction of Sm^{II} - PH with 0.5 equiv. tetraphenylethylene.....	187
A12. ^1H NMR in CDCl_3 (400 MHz, r.t.) showing organic products of the reaction of Sm^{II} - PH with 0.5 equiv. 1,1-diphenylethylene.....	188
A13. ^1H NMR in C_6D_6 (400 MHz, r.t.) showing products of the reaction of Sm^{II} -MeOH with 0.5 equiv. <i>trans</i> -stilbene.....	189
A14. ^1H NMR in C_6D_6 (400 MHz, r.t.) showing products of the reaction of Sm^{II} -MeOH with 0.5 equiv. 1,1-diphenylethylene.....	190
A15. ^1H NMR in C_6D_6 (400 MHz, r.t.) showing products of the reaction of Sm^{II} -MeOH with 0.5 equiv. 1,1,2,2-tetraphenylethylene.....	191
A16. ^1H NMR in CD_3CN (400 MHz, r.t.) of $[\text{Sm}^{\text{III}}]\text{PF}_6$ in the presence of 1 equiv. DBU	192
A17. ^1H NMR in CD_3CN (400 MHz, r.t.) of $[\text{Sm}^{\text{III}}]\text{PF}_6$ in the presence of 3 equiv. PMe	192
A18. ^1H NMR in CD_3CN (400 MHz, r.t.) of $[\text{Sm}^{\text{III}}]\text{PF}_6$ in the presence of 3 equiv. PMe and 2 equiv. DBU.....	193
A19. ^1H NMR in CD_3CN (400 MHz, r.t.) of $[\text{Sm}^{\text{III}}]\text{PF}_6$ in the presence of 7.5 equiv. $^i\text{Pr}_2\text{NH}$	193
A20. ^1H NMR in CD_3CN (400 MHz, r.t.) of $[\text{Sm}^{\text{III}}]\text{PF}_6$ in the presence of 5 equiv. quinuclidine.....	194
A21. ^1H DOSY in C_6D_6 (400 MHz, r.t., $\delta = 4.0$ ms, $\Delta = 150$ ms) of Sm^{II} -PH..	196
A22. ^1H DOSY in C_6D_6 (400 MHz, r.t., $\delta = 4.0$ ms, $\Delta = 150$ ms) of Sm^{III} -P....	196
A23. ^1H DOSY in C_6D_6 (400 MHz, r.t., $\delta = 4.0$ ms, $\Delta = 150$ ms) of Sm^{II} -MeOH	197

A24. ^1H DOSY in C_6D_6 (400 MHz, r.t., $\delta = 4.0$ ms, $\Delta = 150$ ms) of $\text{Sm}^{\text{III}}\text{-OMe}$	197
A25. Points used to estimate $r_{\text{H}(\text{theo})}$ for $\text{Sm}^{\text{III}}\text{-P}$	198
A26. Points used to estimate $r_{\text{H}(\text{theo})}$ for $\text{Sm}^{\text{III}}\text{-OMe}$	198
A27. CVs of 1 mM Sm^{II} in DME (0.2 M $^n\text{Bu}_4\text{NPF}_6$) on glassy carbon with variable scan rate.....	200
A28. CVs of 1 mM $[\text{Sm}^{\text{III}}]\text{PF}_6$ in DME (0.2 M $^n\text{Bu}_4\text{NPF}_6$) on glassy carbon with variable scan rate.....	201
A29. CVs of 1 mM $[\text{Sm}^{\text{III}}]\text{PF}_6$ in CH_3CN (0.1 M $^n\text{Bu}_4\text{NPF}_6$) on glassy carbon with variable scan rate.....	202
A30. CV in DME (0.2 M $^n\text{Bu}_4\text{NPF}_6$) on glassy carbon of 1 mM benzophenone	202
A31. CVs in DME (0.2 M $^n\text{Bu}_4\text{NPF}_6$) on glassy carbon of 1 mM $[\text{Sm}^{\text{III}}]\text{PF}_6$ with 1-10 mM benzophenone	203
A32. CVs in DME (0.2 M $^n\text{Bu}_4\text{NPF}_6$) on glassy carbon of 1 mM $[\text{Sm}^{\text{III}}]\text{PF}_6$ with 30 equiv. PH and 80 equiv. DPE at varying scan rate	205
A33. Plots to determine k_{PCET}	206
A34. ^1H NMR in CD_3CN (400 MHz, r.t.) of DBU	223
A35. ^1H NMR in CD_3CN (400 MHz, r.t.) of $[\text{DBUH}]\text{PF}_6$	223
A36. ^1H NMR in CD_3CN (400 MHz, r.t.) of $^i\text{Pr}_2\text{NH}$	224
A37. ^1H NMR in CD_3CN (400 MHz, r.t.) of $[\text{}^i\text{Pr}_2\text{NH}]\text{PF}_6$	224
A38. ^1H NMR in CD_3CN (400 MHz, r.t.) of quin.....	225
A39. ^1H NMR in CD_3CN (400 MHz, r.t.) of $[\text{quinH}]\text{PF}_6$	225
A40. Superimposed ^1H NMR in CD_3CN (400 MHz, r.t.) of $[\text{Sm}^{\text{III}}\text{-NCMe}]\text{PF}_6$ in the presence of 3 equiv and 4 equiv PH.....	226
A41. Aliphatic region of ^1H NMR of $\text{Sm}^{\text{III}}\text{-P}$ in CD_3CN (400 MHz)	227
A42. ^1H NMR of $\text{Sm}^{\text{III}}\text{-OMe}$ in CD_3CN (400 MHz).	227
A43. ^1H NMR in CD_3CN (400 MHz, r.t.) of a set of titration experiments of $[\text{Sm}^{\text{III}}\text{-NCMe}]\text{PF}_6$ with PH.....	228
A44. ^1H NMR in CD_3CN (400 MHz, r.t.) of a second set of titration experiments of $[\text{Sm}^{\text{III}}\text{-NCMe}]\text{PF}_6$ with PH.....	229

A45. ^1H NMR in CD_3CN (400 MHz, r.t.) of a third set of titration experiments of $[\text{Sm}^{\text{III}}\text{-NCMe}]\text{PF}_6$ with PH.....	230
A46. ^1H NMR in CD_3CN (400 MHz, r.t.) of titration experiments of $[\text{Sm}^{\text{III}}\text{-PH}]\text{PF}_6$ with DBU	231
A47. ^1H NMR in CD_3CN (400 MHz, r.t.) of a second set of titration experiments of $[\text{Sm}^{\text{III}}\text{-PH}]\text{PF}_6$ with DBU.....	232
A48. ^1H NMR in CD_3CN (400 MHz, r.t.) of a third set of titration experiments of $[\text{Sm}^{\text{III}}\text{-PH}]\text{PF}_6$ with DBU.....	233
A49. ^1H NMR in CD_3CN (400 MHz, r.t.) of a set of titration experiments of $[\text{Sm}^{\text{III}}\text{-NCMe}]\text{PF}_6$ and MeOH with $^i\text{Pr}_2\text{NH}$	234
A50. ^1H NMR in CD_3CN (400 MHz, r.t.) of a set of titration experiments of $[\text{Sm}^{\text{III}}\text{-NCMe}]\text{PF}_6$ and MeOH with quin.....	235
A51. ^1H NMR in CD_3CN (400 MHz, r.t.) of a second set of titration experiments of $[\text{Sm}^{\text{III}}\text{-NCMe}]\text{PF}_6$ and MeOH	236
B1. ^1H NMR (CD_3CN , 400 MHz) spectra of $[\text{Sm}^{\text{III}}]\text{PF}_6$ with varying amounts of CF_3PH	251
B2. ^1H NMR (CD_3CN , 400 MHz) spectra of $[\text{Sm}^{\text{III}}\text{-CF}_3\text{PH}]\text{PF}_6$ with varying amounts of $^i\text{Pr}_2\text{NH}$	253
B3. ^1H NMR (CD_3OD , 400 MHz) spectrum of $\text{Me}_2\text{NNH}_3\text{Cl}$ and $\text{Me}_2\text{NH}_2\text{Cl}$	254
B4. ^1H NMR (CD_3OD , 400 MHz) spectrum of $\text{Me}_2\text{NNH}_3\text{Cl}$ and $\text{Me}_2\text{NH}_2\text{Cl}$ generated from the reaction of $\text{P}_3^{\text{B}}\text{FeNNMe}_2$, Sm^{II} (3 equiv), and PH (3 equiv) in toluene at -78°C	255
B5. CW X-band EPR spectrum (toluene, 77K) following the reaction of FeN_2 (2 mM) with 10 equiv $\text{SmI}_2(\text{THF})_2$ and 20 equiv HMPA.....	258
B6. CW X-band EPR spectrum (toluene, 77K) following the reaction of FeN_2 (2 mM) with 10 equiv $\text{SmI}_2(\text{THF})_2$ and 40 equiv HMPA.....	259
B7. CW EPR spectrum (2-MeTHF, 77K) following the reaction of FeN_2 (2 mM) with 1 equiv Sm^{II}	260
B8. CW EPR spectrum (2-MeTHF, 77K) following the reaction of FeN_2Me_2 (2 mM) with 1 equiv Sm^{II}	261

B9: Full IR spectra of the reaction of FeN_2 with 3 equiv Sm^{II} and n equiv PMe	263
B10: CV of FeN_2 (1 mM) in DME (0.2 M $^n\text{Bu}_4\text{NPF}_6$) in a window showing the $\text{FeN}_2^{-/2-}$ couple at -3.1 V vs $\text{Fc}^{+/0}$	264
C1: Photograph of the two-compartment cell employed in CPE experiments....	277
C2: CPE of 1a under the standard conditions	281
C3: CPE of 1m under the standard conditions	281
C4: CV of 1a	282
C5: CV of phenyl acrylate	283
C6: CV of LutHNTf_2	283
C7: CV of 1a and MgI_2	284
C8: CV of 2 and MgI_2	284
C9: CV of 1a , 2 , and LutHNTf_2	285
C10: Representative simulations overlaid with experimental CVs of $\text{Sm}(\text{OTf})_3$ and $^n\text{Bu}_4\text{NI}$ (25 equiv) in 2-MeTHF containing 0.2 M BMPyNTf_2	286
C11: Representative simulation of an EC wave with $k_0 = 0.0075 \text{ cm s}^{-1}$, $k_{\text{obs}} = 0.05 \text{ s}^{-1}$, and $\nu = 50 \text{ mV s}^{-1}$	287
C12: Experimental $i_{\text{p,a}}/i_{\text{p,c}}$ values collected from CVs at varying scan rates of $\text{Sm}(\text{OTf})_3$, $^n\text{Bu}_4\text{NI}$, and the aliphatic ketone 1a plotted vs $\log(\lambda)$ using k_{C} values that provide the best fit with the simulated working curve	288
C13: Experimental $i_{\text{p,a}}/i_{\text{p,c}}$ values collected from CVs at varying scan rates of $\text{Sm}(\text{OTf})_3$, $^n\text{Bu}_4\text{NI}$, and phenyl acrylate 2 plotted vs $\log(\lambda)$ using k_{C} values that provide the best fit with the simulated working curve	288
C14: CV of $\text{Sm}(\text{O}^i\text{Pr})_3$	289
C15: CV of $\text{Sm}(\text{O}^i\text{Pr})_3$, 15 , and LiBr overlaid with the CV of 15	289
C16: CV of $\text{Sm}(\text{O}^i\text{Pr})_3$, LiI , and 14 , in THF or 2-MeTHF	290
C17: Dimerization study of aliphatic ketone and phenyl acrylate under standard conditions	292
D1: Typical setup for catalytic experiments.	300

D2: ^1H NMR (400 MHz, CDCl_3) of a typical crude reaction mixture reacting 1a with phenyl acrylate to produce 3a by method B	301
D3: Comparison of ^1H NMR of typical reaction spectra with authentic lactone product	302
D4: ^1H NMR (400 MHz, CDCl_3) of a typical crude reaction mixture reacting 1b with phenyl acrylate to produce 3b by method B	303
D5: ^1H NMR (400 MHz, CDCl_3) of a typical crude reaction mixture reacting 1m with phenyl acrylate to produce 3m by method A.....	304
D6: ^1H NMR (400 MHz, CDCl_3) of a typical crude reaction mixture reacting 1aa with phenyl acrylate to produce 3aa and 4aa by method A	305
D7: ^1H NMR (400 MHz, CDCl_3) of a typical crude reaction mixture reacting 1m with <i>tert</i> -butyl acrylate to produce 5m by method A	306
D8: UV-vis traces following the reaction of SmI_2 + ketone 1a + acrylate 2 ; HEH_2 + 1a + 2 ; and SmI_2 + HEH_2 + 1a + 2 in 2-MeTHF	308
D9: UV-vis traces following the reaction of SmI_2 + 1a + 2 ; phenH_2 + 1a + 2 ; and SmI_2 + 1a + 2 + phenH_2 in 2-MeTHF	309
D10: UV-vis traces of $\text{Sm}(\text{O}^i\text{Pr})_3$, $^n\text{Hep}_4\text{NI}$, and HNTf_2 ; HEH_2 ; and $\text{Sm}(\text{O}^i\text{Pr})_3$, $^n\text{Hep}_4\text{NI}$, HNTf_2 , and HEH_2 in THF	310
D11: UV-vis traces of $\text{Sm}(\text{O}^i\text{Pr})_3$, $^n\text{Hep}_4\text{NI}$, LutHNTf_2 ; phenH_2 ; and $\text{Sm}(\text{O}^i\text{Pr})_3$, $^n\text{Hep}_4\text{NI}$, LutHNTf_2 , and phenH_2 in THF.....	311
D12: UV-vis traces of $\text{Sm}(\text{O}^i\text{Pr})_3$, $^n\text{Hep}_4\text{NI}$, LutHNTf_2 ; HEH_2 ; and $\text{Sm}(\text{O}^i\text{Pr})_3$, $^n\text{Hep}_4\text{NI}$, LutHNTf_2 , and HEH_2 in THF	312
D13: Titration of $\text{Sm}(\text{OTf})_3$ into a solution of HEH_2 in THF	312
D14: Attempted photogeneration of SmI_2 from a THF solution of SmI_3 and HEH_2	314
D15: Attempted photogeneration of SmI_2 from a THF solution of $\text{Sm}(\text{O}^i\text{Pr})_3$, $^n\text{Hep}_4\text{NI}$, and HEH_2	315
D16: Photogeneration of SmI_2 from a THF solution of SmI_3 and HEH_2 with $[\text{Ir}]\text{PF}_6$ in the absence of base	316
D17: Photogeneration of SmI_2 in the presence of ethylene glycol from a THF solution of SmI_3 , HEH_2 , and pyridine with $[\text{Ir}]\text{PF}_6$	317

D18: Photogeneration of SmI ₂ in the presence of MeO((CH ₂) ₂ O) ₃ H from a THF solution of SmI ₃ , HEH ₂ , and pyridine with [Ir]PF ₆	318
D19: Photogeneration and decay of SmI ₂ from THF solution of SmI ₃ , L*, [Ir]PF ₆ , and HEH ₂	319
D20: Attempted photogeneration of SmBr ₂ from a THF solution of SmI ₃ , ⁿ Bu ₄ NBr, HEH ₂ , and Lut	320
D21: Attempted photogeneration of Sm(HMPA) ₄ ²⁺ from a THF solution of SmI ₃ , HMPA, HEH ₂ , and Lut.....	321
D22: Attempted photogeneration of SmBr ₂ from a THF solution of SmI ₃ , ⁿ Bu ₄ NBr, [Ir(ppy) ₂ (dtbbpy)]PF ₆ , and Et ₃ N.....	322
D23: Attempted photogeneration of Sm(HMPA) ₄ ²⁺ from a THF solution of SmI ₃ , HMPA, [Ir(ppy) ₂ (dtbbpy)]PF ₆ , and Et ₃ N.....	323
D24: Attempted photogeneration of Sm(BINAPO) ₂ from a THF solution of SmI ₃ , BINAPO, [Ir(ppy) ₂ (dtbbpy)]PF ₆ , and Et ₃ N.....	324
D25: Photogeneration of SmBr ₂ from THF solution of SmI ₃ , ⁿ Bu ₄ NBr, 3DPA2FBN, AcrH ₂ , and Et ₃ N	325
D26: Photogeneration of SmI ₂ (HMPA) ₄ from THF solution of SmI ₃ , HMPA, 3DPA2FBN, AcrH ₂ , and Et ₃ N.....	326
D27: Photogeneration of Sm(BINAPO) ₂ from THF solution of SmI ₃ , BINAPO, 3DPA2FBN, AcrH ₂ , and Et ₃ N	327
D28: CVs of SmI ₃ in the presence of 0-40 mM ⁿ Hep ₄ NI	329
D29: CV of [Ir]PF ₆	329
D30: CV of 3DPA2FBN	330
D31: CV of SmI ₂ and ⁿ Hep ₄ NI	330
D32: CV of SmI ₃ , ⁿ Hep ₄ NI, and ethylene glycol	331
D33: CV of SmI ₂ , ⁿ Hep ₄ NI, and MeO((CH ₂) ₂ O) ₃ H.....	331
D34: CV of SmI ₂ , ⁿ Hep ₄ NI, and 3-aza-3-benzyl-1(R),5,(R)-dihydroxy-1,5-diphenylpentane	332
D35: CV of SmI ₃ and ⁿ Bu ₄ NBr.....	333
D36: CV of SmI ₂ , ⁿ Hep ₄ NI, and BINAPO	333
D37: CV of SmI ₂ and HMPA	334

D38: An alternative scheme for second net H ⁺ delivery in catalytic ketone-acrylate coupling reaction	335
D39: Proposed scheme for catalytic ketone-acrylate coupling reaction with [Ir] ⁺	336
E1: Two-compartment cell used for CPE experiments.....	343
E2: ¹ H NMR (<i>d</i> ₆ -DMSO, 400 MHz) spectrum of the basic, volatile products of <i>e</i> N ₂ R under the standard conditions	346
E3: ¹ H NMR (<i>d</i> ₆ -DMSO, 400 MHz) spectrum of the basic, volatile products of <i>e</i> N ₂ R under (A) the standard conditions; (B) the standard conditions in the absence of Sm; and (C) the standard conditions in the absence of Mo.	347
E4: ¹ H NMR (<i>d</i> ₆ -DMSO, 400 MHz) spectrum of the basic, volatile products of <i>e</i> N ₂ R under ¹⁴ N ₂ or ¹⁵ N ₂	348
E5: ¹ H NMR (<i>d</i> ₆ -DMSO, 400 MHz) spectrum of the basic, volatile products of <i>e</i> N ₂ R under ¹⁵ N ₂ stopped after passage of 2.2 or 8.0 C	349
E6: CPE under the standard <i>e</i> N ₂ R conditions and plot of the total yield of NH ₃ vs charge passed	350
E7: ¹ H NMR (CDCl ₃ , 400 MHz) spectrum of the organic species extracted from the anode compartment following passage of 10.8 C of charge under the standard <i>e</i> N ₂ R conditions	351
E8: CPE under the standard <i>e</i> N ₂ R conditions in the absence of PNPMoBr ₃ 352	
E9: CV of SmI ₃ following the addition of 1 equiv H ₂ O an CPE under the standard <i>e</i> N ₂ R conditions in the presence of 1 equiv H ₂ O per Sm.....	352
E10: CPE under the standard <i>e</i> N ₂ R conditions using PNPMo(N)I (0.46 mM) and SmI ₃ as catalysts at Sm loadings of 3.7 mM and 0.46 mM	353
E11: CV of the cathode solution after passage of 7.0 C using PNPMoNI (0.46 mM) and SmI ₃ (0.46 mM) as catalysts.....	354
E12: UV-Vis spectra for the Griess analysis of a 0.1 M KOH solution exposed to the atmosphere of the ¹⁴ N ₂ -filled glovebox.....	356
E13: UV-Vis spectra for the Griess analysis of a 0.1 M KOH solution exposed to ¹⁵ N ₂	357

E14: UV-Vis spectra for the Griess analysis of a 0.1 M solution of ${}^n\text{Bu}_4\text{NNTf}_2$ in THF	358
E15: Scan rate-normalized CVs of in situ-generated $[\text{PNPMo}^{\text{V}}(\text{N})\text{I}]^+$ in the presence of LutHNTf ₂ at 25-300 mV s ⁻¹	359
E16: CVs of in situ-generated $[\text{PNPMo}^{\text{V}}(\text{N})\text{I}]^+$ in the presence of LutHNTf ₂ following addition of ${}^n\text{Hep}_4\text{NI}$	360

LIST OF TABLES

3.1: Summary of Fe-catalyzed N ₂ R data with Sm ^{II} -based reductants	69
5.1: Photodriven Sm-catalyzed coupling of ketones and phenyl acrylate to form lactone products.	137
6.1: Summary of electrocatalytic N ₂ R data mediated by Mo and Sm.	151
A1: DOSY measured diffusion coefficients, <i>D</i> , and estimated hydrodynamic radii, <i>r</i> _H , of the Sm complexes.	195
A2: Crystallographic data for complexes Sm ^{III} -P and Sm ^{III} -OMe.	199
A3: ¹ H NMR shifts of pure compounds used in the <i>K</i> _{assoc} determination for [Sm ^{III} -PH]PF ₆ in CD ₃ CN.	211
A4: ¹ H NMR data for the Sm complex during three separate titration experiments of [Sm ^{III} -NCMe]PF ₆ in 0.7 mL CD ₃ CN with aliquots of 250 mM PH.	211
A5: ¹ H NMR shifts of pure compounds used in the p <i>K</i> _a determination for [Sm ^{III} -PH]PF ₆ in CD ₃ CN	212
A6: ¹ H NMR data for the Sm complex during a titration of [Sm ^{III} -PH]PF ₆ with DBU.	212
A7: ¹ H NMR data for the amidine/amidinium during a titration of [Sm ^{III} -PH]PF ₆ with DBU.	213
A8: Equilibrium constants derived from data in Table A6 and Table A7	213
A9: ¹ H NMR data for the Sm complex during a second titration of [Sm ^{III} -PH]PF ₆ with DBU.	214
A10: ¹ H NMR data for the amidine/amidinium during a second titration of [Sm ^{III} -PH]PF ₆ with DBU.	214
A11: Equilibrium constants derived from data in Table A9 and Table A10.	214
A12: ¹ H NMR data for the Sm complex during a third titration of [Sm ^{III} -PH]PF ₆ with DBU.	215
A13: ¹ H NMR data for the amidine/amidinium during a third titration of [Sm ^{III} -PH]PF ₆ with DBU.	215

A14: Equilibrium constants derived from data in Table A12 and Table A13.....	216
A15: Final equilibrium constants from Table A8, A11, and A14.....	217
A16: ^1H NMR shifts of pure compounds used in the $\text{p}K_{\text{a,eff}}$ determination for $[\text{Sm}^{\text{III}}\text{-NCMe}]\text{PF}_6$ and MeOH in CD_3CN	217
A17: ^1H NMR data for the Sm complex during a titration of $[\text{Sm}^{\text{III}}\text{-NCMe}]\text{PF}_6$ and MeOH with $^i\text{Pr}_2\text{NH}_2$	218
^1H NMR data for the amine/ammonium during a titration of $[\text{Sm}^{\text{III}}\text{-NCMe}]\text{PF}_6$ and MeOH with $^i\text{Pr}_2\text{NH}_2$	218
A19: Equilibrium constants derived from data in Table A17 and Table A18.....	219
A20: ^1H NMR data for the Sm complex during a titration of $[\text{Sm}^{\text{III}}\text{-NCMe}]\text{PF}_6$ and MeOH with quin.	219
A21: ^1H NMR data for the amine/ammonium during a titration of $[\text{Sm}^{\text{III}}\text{-NCMe}]\text{PF}_6$ and MeOH with quin.....	220
A22: Equilibrium constants derived from data in Table A20 and Table A21.....	220
A23: ^1H NMR data for the Sm complex during a second titration of $[\text{Sm}^{\text{III}}\text{-NCMe}]\text{PF}_6$ and MeOH with quin.	221
A24: ^1H NMR data for the amine/ammonium during a second titration of $[\text{Sm}^{\text{III}}\text{-NCMe}]\text{PF}_6$ and MeOH with quin.....	221
A25: Equilibrium constants derived from data in Table A23 and Table A24.....	222
A26: Final equilibrium constants from Table A19, A22, and A25.....	222
B1. Catalysis with variable acid (0.5 μmol FeN_2 , toluene, -78°C , 12 h).....	265
C1: Selected electrode screening data toward optimized CPE conditions. ...	278
C2: Selected additive screening data toward optimized CPE conditions.	279
C3: Control experiments probing role of electrochemically-driven $\text{Sm}^{\text{III/II}}$ redox in CPE.	280
C4: Product distribution with 2-MeTHF as a solvent.....	293
C4: Product distribution with THF as a solvent.....	293

C4: Product distribution with MeCN as a solvent.....	294
C4: Product distribution with DME as a solvent.....	294
D1: Yields for cross- vs homocoupled products in selected aryl ketone cross-coupling reactions.	307
E1: Individual eN_2R experiments under the standard conditions.	346
E2: Results of electrolysis under the standard conditions under 1 atm argon instead of N_2	349
E3: Estimation of overpotential $\Delta\Delta G_{f(NH_3)}$ for representative eN_2R systems	364

NOMENCLATURE

BAr^F4⁻. Tetrakis(3,5-bis(trifluoromethyl)phenyl)borate

BDFE. Bond-dissociation free energy

BMPip. 1-butyl-1-methylpiperidinium

BMPy. 1-butyl-1-methylpyrrolidinium

BPh₄⁻. Tetraphenylborate

bpy. 2,2'-bipyridine

C_G. Thermodynamic constant accounting for the free energy of forming H[•] from H⁺ and e⁻

Col. 2,4,6-trimethylpyridinium

Cp. Cyclopentadienyl

Cp*. Decamethylcyclopentadienyl

CPE. Controlled-potential electrolysis

CPET. Concerted proton-electron transfer

CV. Cyclic voltammetry

CW. Continuous wave

δ. Isomer shift

ΔE_q. Quadrupole splitting

ΔΔG_f. Excess energy relative to the free energy of formation

ΔG_f. Gibbs free energy of formation

DBU. 1,8-diazabicyclo[5.4.0]undec-7-ene

DME. Dimethoxyethane

DOSY. Diffusion-ordered spectroscopy

DPE. 1,1-diphenylethylene

E° . Standard reduction potential

$E_{1/2}$. Midpoint potential

E_{app} . Applied potential

EH. Lewis-basic ligand containing a Brønsted acidic proton

eN_2R . Electrochemical nitrogen reduction.

$E_{p,c}$. Peak anodic potential

$E_{p,c}$. Peak cathodic potential

EPR. Electron paramagnetic resonance

ET. Electron transfer

F.E. Faradaic efficiency

F. Faraday's constant

$Fc^{+/0}$. Reversible ferrocenium/ferrocene couple.

g_n . Nuclear g-value

η . Overpotential

HEH₂. Hantzsch ester

HER. Dihydrogen evolution reaction

HMPA. Hexamethylphosphoramide

IR. Infrared

ISSET. Inner-sphere electron transfer

LiN₂R. Lithium-mediated N₂R.

Ln. Lanthanide

Lut. 2,6-dimethylpyridinium

MeCN. Acetonitrile

ν . Scan rate

ν_{AA} . A–A stretching frequency

N_{α} . Nitrogen atom proximal to the metal in metal–N₂ complexes.

N_{β} . Nitrogen atom proximal to the metal in metal–N₂ complexes.

N₂R. Dinitrogen reduction to NH₃ or N₂H₄

NMR. Nuclear magnetic resonance

NTf₂⁻. *Bis*-trifluoromethylsulfonimide

OSET. Outer-sphere electron transfer

OTf⁻. Trifluoromethylsulfonate

PCET. Proton-coupled electron transfer

PF₆⁻. Hexafluorophosphate

PH. 2-pyrrolidinone

Pic. 2-methylpyridine

PMe. *N*-methyl-2-pyrrolidinone

PNP. 2,6-*bis*(di-*tert*-butylphosphinomethyl)pyridine

ppy. 2-phenylpyridine

PT. Proton transfer

R. Ideal gas constant

SHE. Standard hydrogen electrode

T. Temperature

THF. Tetrahydrofuran

TON. Turnover number

TOF. Turnover frequency

UV-vis. UV-visible

INTRODUCTION

1.1 Opening Remarks

This thesis describes development and select applications of mild conditions for reductive samarium (Sm) catalysis. This work stems from the rich chemistry of samarium(II) iodide (SmI_2) as a stoichiometric single-electron reductant. Kagan and coworkers reported straightforward synthesis of solvated SmI_2 in tetrahydrofuran (THF) from Sm metal and 1,2-diiodoethane in 1977 and subsequently catalogued its reductive activation of a suite of organic functional groups.¹ Since this introduction, the applications of SmI_2 for functional group manipulation and C–C bond-forming reactions in organic synthesis have been characterized by high chemo- and stereoselectivity which can be tuned empirically using various additives.²

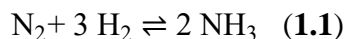
The primary drawback of Sm(II) chemistry is that it almost always requires a stoichiometric amount of Sm, limiting application in large-scale settings. Because each Sm(II) center provides only one electron, multiple equivalents of SmI_2 are necessary for multielectron transformations. Moreover, additives (e.g., carcinogenic hexamethylphosphoramide, chiral ligands in enantioselective transformations) must also be employed (super)stoichiometrically.²⁻⁴ Use of Sm in catalytic quantities coupled to a less valuable terminal reductant would facilitate scale-up of Sm(II)-mediated transformations.

While organic synthesis is the practical application of Sm catalysis, my contributions to the following chapters were motivated by the hypothesis that Sm co-electrocatalysis would enable selective conversion of dinitrogen (N_2) to ammonia (NH_3) driven by

electricity at a low overpotential. This outcome, which is ultimately demonstrated in² Chapter 6, was not feasible using the few examples of conditions for net-reductive Sm catalysis that were available at the outset of my thesis research. I will use this space to highlight the attributes of Sm that guided this hypothesis and how, in turn, approaching Sm catalysis development with the specific requirements of N₂ reduction (N₂R) in mind led to fundamental and practical advances over prior art.

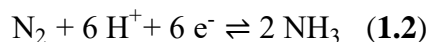
1.2 Kinetic challenges in N₂R

The free energy of formation (ΔG_f) of NH₃ from N₂ and H₂ is $-4.3 \text{ kcal mol}^{-1}$ (eqn 1.1; all thermodynamic values provided in MeCN at 298 K unless otherwise noted).⁵ NH₃ is produced on massive industrial scale by this balanced reaction over iron-based heterogeneous catalysts in the Haber-Bosch process, which is estimated to sustain half of the current global population.⁶ However, high temperatures are necessary to overcome the kinetic barrier to eqn 1.1, resulting in a slightly uphill standard reaction free energy. High pressures of N₂ and H₂ are therefore employed to drive the reaction to products.



In nature, N₂R to NH₃ is carried out by the iron-molybdenum cofactor (FeMoco) of nitrogenase enzymes in nitrogen-fixing bacteria through combination of N₂ with proton (H⁺) and electron (e⁻) equivalents (eqn 1.2). Again, this transformation has favorable thermodynamics: the standard potential of N₂/NH₄⁺ interconversion (defined at pH 0) is +0.275 V vs the standard hydrogen electrode (SHE).⁷ However, 16 equivalents of ATP (adenosine triphosphate) are expended per molecule of N₂ that is reduced. Additionally, while theoretically only 6 reducing equivalents are necessary to reduce one N₂, 8 reducing

equivalents are consumed per turnover under most conditions, with loss of the additional³ $2\text{H}^+ / 2\text{e}^-$ as H_2 .



Both primary routes to NH_3 as the bioavailable form of nitrogen require significant excess energy input beyond the thermodynamic minimum (in the form of fossil fuel combustion in the Haber-Bosch process, or ATP hydrolysis in biological N_2R ; corresponding to roughly 120 and 60 kcal mol⁻¹ of NH_3 produced, respectively).^{8,9} Moreover, nature, after billions of years of catalyst optimization, is still operating at only 75% yield. This situation casts the opportunity for improving catalytic N_2R methods using H^+ and e^- equivalents as a formidable challenge (or, on a cynical day, as a fool's errand). Nevertheless, the following criteria (and associated figures of merit) should all carry weight in evaluation of N_2R systems:

- i)* high yield (Faradaic efficiency (F.E.) for electrocatalytic processes)
- ii)* high NH_3 yield rate (catalyst turnover frequency, TOF)
- iii)* high catalyst stability (catalyst turnover number, TON)
- iv)* H_2 or H_2O as terminal H^+/e^- source
- v)* low excess driving force provided by a renewable energy source (light or electricity)

We generally prefer to use $\Delta\Delta G_f$ to quantify driving force for criterion *v*,¹⁰ which references the thermodynamic driving force of a given terminal H^+/e^- source to H_2 . To do so, the effective bond dissociation free energy (BDFE_{eff}) describing the thermodynamics of the net loss of a hydrogen atom (H^\bullet) from an acid/reductant pair (eqn 1.3, which combines the reduction potential of the e^- source E° , the $\text{p}K_s$ of the H^+ source, and the

solvent-dependent constant C_G)⁵ is compared to the H–H BDFE of H₂ (eqn 1.4).⁴ Development of N₂R catalysts that operate at low driving force is important not only from an energy efficiency standpoint, but also because background combination of 2H⁺/2e⁻ to release H₂ (the hydrogen evolution reaction, HER) is less competitive at low $\Delta\Delta G_f$, facilitating higher NH₃ yield.

$$\text{BDFE}_{\text{eff}} = 23.06(E^\circ) + 1.37(\text{p}K_a) + C_G \quad (\mathbf{1.3})$$

$$\Delta\Delta G_f(\text{NH}_3) = 3 \left(\frac{1}{2}(\text{BDFE}_{\text{H}_2}) - \text{BDFE}_{\text{eff}} \right) \quad (\mathbf{1.4})$$

While none of the alternative N₂R systems developed over the last century surpass the Haber-Bosch process by all figures of merit, proof-of-concept studies expose strategies for targeting individual criteria. Lithium-mediated N₂R (LiN₂R) systems successfully harness electrochemical driving force to cleave N₂ at ambient temperature and pressure, via reduction of Li⁺ to Li⁰ followed by Li₃N formation.¹¹ This process has been coupled to anodic water-derived H₂ oxidation, and a F.E. > 99% was achieved at somewhat elevated pressure (20 bar).^{12–14} However, the strongly cathodic applied potential (E_{app}) required to form Li⁰ as a discrete intermediate (≤ -3.7 V) imposes a theoretical limit on $\Delta\Delta G_f$ as ≥ 65 kcal mol⁻¹ (assuming ≤ 40 as a reasonable maximum $\text{p}K_a$ value for the buffer system used to shuttle H⁺ harvested at the anode to protonate Li₃N at the cathode).

By contrast, N₂R with well-defined transition metal coordination complexes as catalysts can operate at much lower driving force.^{10,15} Schrock's first demonstration of catalytic N₂R at ambient temperature and pressure at a single molybdenum site employed 2,6-lutidinium (LutH⁺, $\text{p}K_a$ 9.5 in THF)¹⁶ as the proton source and decamethylchromocene ($E^\circ(\text{Cr}^{\text{III/II}}) -1.47$ V in THF)¹⁷ as a mild reductant, corresponding to an excess driving force of only 32 kcal mol⁻¹ of NH₃.¹⁸ Nishibayashi's Mo-based catalysts supported by pincer

ligands (e.g., PNP, Figure 1.1) can be driven by similarly weak reductant/acid⁵ combinations.¹⁹ Ligand design and conditions optimization has resulted in impressive improvements to catalyst rate, stability, and yield.^{20,21} However, these and related systems¹⁰ are limited by criteria *iv* and *v*, because the driving force and reducing equivalents are provided by stoichiometric chemical reagents.

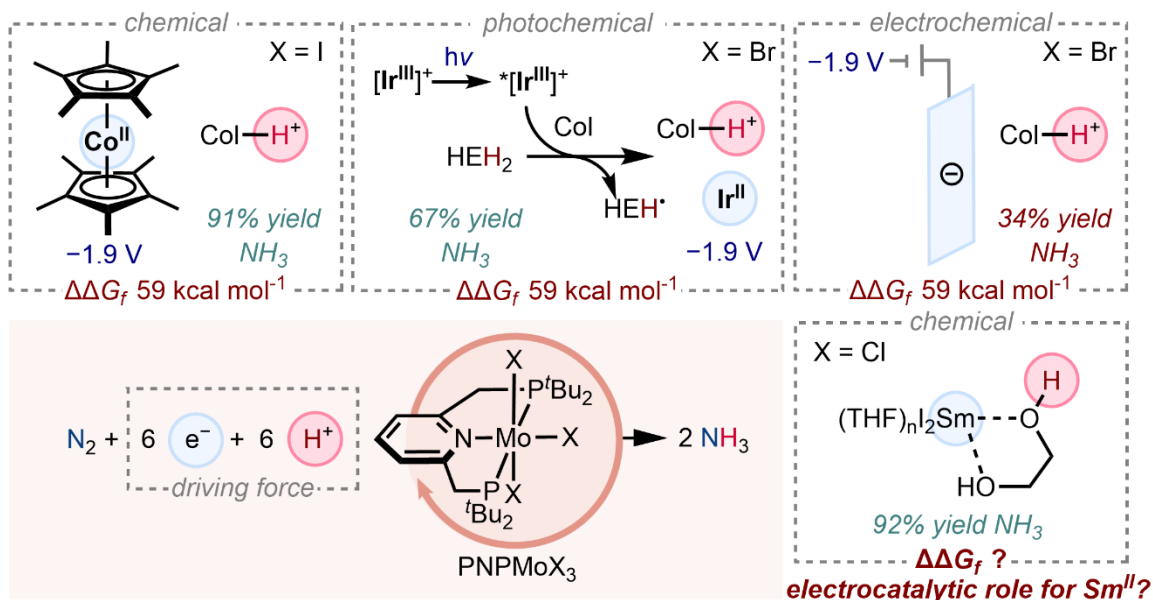


Figure 1.1: Catalytic N₂R with PNPMoBr₃ with chemical, electrochemical, and photochemical driving force.^{21–24}

Recent efforts have therefore focused on interfacing molecular N₂R catalysts with photochemical^{22,25,26} and electrochemical^{23,27–31} sources of driving force. We established blue light-driven transfer hydrogenation of N₂ by 3 equivalents of Hantzsch ester (HEH₂) in up to 67% yield using PNPMoBr₃ as precatalyst.²² In the dark, this transformation would be nearly thermoneutral ($\Delta\Delta G_f$ 1.7 kcal mol⁻¹), and so while HEH₂ serves as the terminal H⁺/e⁻ source, light provides the input energy needed to drive the reaction at an appreciable rate. We propose that e⁻ and H⁺ equivalents harvested from HEH₂ are delivered to MoN_xH_y intermediates by the Ir^{II} state of a photoredox catalyst with $E^\circ(\text{Ir}^{\text{III/II}})$ ca. -1.9 V (e.g.,

[Ir(ppy)₂(dtbbpy)]⁺) and the acid component of a 2,4,6-collidinium/collidine⁶ (ColH⁺/Col, p*K*_a 10.4) buffer system, respectively (Figure 1.1). It is useful to note that these thermodynamic values for H⁺/e⁻ transfer mimic those of the chemical acid/reductant system used previously for N₂R with PNPMoBr₃ (ColHOTf and decamethylcobaltocene (Cp*₂Co), *E*^o(Co^{III/II}) -1.91 V; Figure 1.1), corresponding to ΔΔ*G*_{*f*} 59 kcal mol⁻¹.³²

Meanwhile, our group established *e*N₂R with [PNPMo] catalysts by two different strategies. One operates essentially by swapping Cp*₂Co for an applied electrochemical potential of -1.9 V with ColH⁺ as the bulk proton source (Figure 1.1).²³ The other uses an aniline-appended cobaltocene mediator to colocalize H⁺ and e⁻ equivalents sourced from tosic acid monohydrate (TsOH•H₂O) and an electrode polarized at -1.25 V, respectively, for delivery to MoN_{*x*}H_{*y*} via proton-coupled electron transfer (PCET).³⁰ However, both systems were limited to a F.E. of 34%. In the former system, this is likely due to competitive background electroreduction of ColH⁺ at the strongly cathodic applied potential; this is hard to avoid at the relatively harsh driving force of ΔΔ*G*_{*f*} 59 kcal mol⁻¹. While the latter system operates at milder driving force (ΔΔ*G*_{*f*} 47 kcal mol⁻¹), the strongly acidic, weakly reducing PCET mediator may not be well-matched to [PNPMo], which typically operates under moderately acidic conditions.

In considering alternative strategies to translate the high N₂R activity of pincer Mo catalysts to electrochemical conditions, Nishibayashi and coworkers' reports of Mo-catalyzed N₂R to NH₃ with exceptionally high yield (> 90%) using SmI₂ as the reductant and H₂O or ethylene glycol as the proton source provided inspiration and raised many interesting questions (Figure 1.1).^{24,33} What is the driving force ΔΔ*G*_{*f*} of these conditions, in which the reduction potential and p*K*_a are ill-defined? Why is this cocktail so selective

for NH₃ over dihydrogen (H₂)? Can the Sm^{III} byproducts be converted back to the active⁷ Sm^{II} state electrochemically at a modest applied potential? If so, what tandem catalytic role might Sm^{II} play? The following sections provide background to address each of these questions.

1.3 Sm^{II} Reduction Potentials

Like the rest of the lanthanide (Ln) series, samarium prefers the +3 oxidation state, in which its 5 valence electrons lie in 4*f* orbitals buried in the inert gas core. However, the divalent state lies in an energetic sweet spot for use as a reducing agent. The other classically redox-active lanthanides, Eu²⁺ and Yb²⁺, are stabilized by half- and fully-filled 4*f* shells ([Xe]4*f*⁷ and [Xe]4*f*¹⁴, respectively). Because Sm²⁺ is one electron removed from a half-filled valence shell ([Xe]4*f*⁶), it is more reactive toward weak oxidants than is Eu or Yb.³⁴ Approaching the half-filled configuration, however, lends Sm²⁺ stability relative to the remaining Ln²⁺ series, and Sm(II) species are thus more readily synthetically accessed.

This trend is quantified by the standard reduction potentials (E°) for Ln^{3+/2+} given in the table in Figure 1.2.^{35,36} It is important to note that these values are derived for the aqueous metal ions (i.e., Ln(OH₂)_{*n*}^{3+/2+}) using thermochemical cycles. Direct experimental measurement of $E^\circ(\text{Ln}^{3+/2+})$ using electrochemical techniques is complicated in part by the fact that the lanthanide ions tend to interact with many supporting electrolytes;³⁶ for example, the first value for $E^\circ(\text{Eu}^{3+/2+})$ determined electrochemically (−0.43 V vs SHE) was an overestimate due to favorable coordination of formate ion present in excess to Eu³⁺.³⁷ Evaluation in more “innocent” electrolytes (e.g., perchlorate) provided the accepted standard value of −0.35 V.³⁸

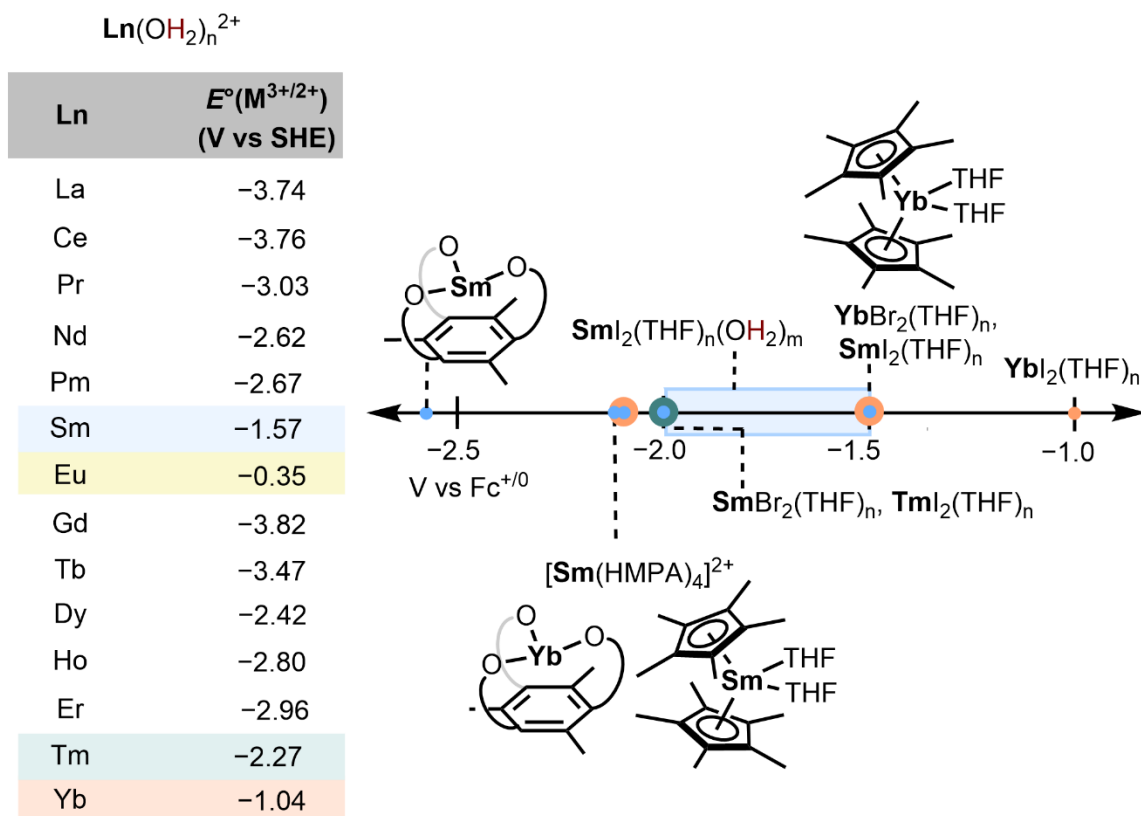


Figure 1.2: Aqueous (left)³⁶ and nonaqueous (right)^{39–43} $\text{Ln}^{\text{III/II}}$ reduction potentials.

This issue is magnified in the organic solvents typical of synthetic application of Sm(II) which do not support a high degree of ionization to “free” solvated ions (i.e., $\text{Sm}(\text{THF})_n^{3+/2+}$).⁴⁴ As a result, the rigorous answer to the question, “what is the reduction potential of SmI_2 in THF?” is nuanced, but desirable to understand the reactivity of SmI_2 in catalytic N_2R . Skrydstrup and coworkers extracted the formal potential describing interconversion of $\text{SmI}_2(\text{THF})_n$ and a short-lived $\text{SmI}_2(\text{THF})_n^+$ species as -1.41 V (all nonaqueous potentials are referenced to ferrocenium/ferrocene).⁴¹ This redox process is distinct from the standard potential for interconversion of $\text{SmI}_3(\text{THF})_n$ and $\text{SmI}_2(\text{THF})_n$, which is coupled to I^- loss. We have measured $E^\circ(\text{SmI}_3/[\text{SmI}_2 + \text{I}^-])$ as -1.58 V in THF with tetrabutylammonium *bis*-triflimide ($^n\text{Bu}_4\text{NNTf}_2$) as supporting electrolyte (see

Appendix D4).⁴⁵ The reducing power of $\text{SmI}_2(\text{THF})_n$ is best quantified by the former⁹ potential, while the latter is a better estimate of the driving force needed to reduce SmI_3 to SmI_2 . Both values are of use when considering catalytic cycles containing both electron transfer (ET) from SmI_2 to target substrates and catalyst turnover by reduction of SmI_3 with a terminal reductant.

Changes in the reactivity of SmI_2 as a function of different Lewis basic additives are typically ascribed to coordination of the additive to Sm^{II} to produce a stronger reductant.^{46–}
⁵⁰ Again, uncertainties in speciation arising from a large coordination sphere of kinetically labile monodentate ligands necessitate extremely thorough studies to rigorously quantify the reducing power of discrete $[\text{Sm}^{\text{II}}]$ complexes.⁴⁰ The conditions employed to collect electrochemical data (solvent and supporting electrolyte) as well as methods of analysis in the primary literature must be considered on a case-by-case basis to evaluate whether the reported potentials depicted in Figure 1.2 are applicable to specific situations. For example, the effect of H_2O coordination on the $\text{Sm}^{\text{III/II}}$ reduction potential of $\text{SmI}_2(\text{THF})_n$ should be factored into the driving force for Mo-catalyzed N_2R . While standard potentials cannot be extracted from the electrochemistry of SmI_2 with H_2O reported by Flowers and coworkers due to loss of reversibility, the observed potential of Sm^{II} oxidation shifts negative by 570 mV in the presence of a sufficient excess of H_2O to saturate the Sm coordination sphere (>500 equiv).^{42,48} This shift provides an approximate upper bound on the reducing power of $[\text{SmI}_n(\text{OH}_2)_m]\text{I}_{2-n}$ as $E^\circ(\text{Sm}^{\text{III/II}}) < -1.98 \text{ V}$.⁴¹ However, only one equivalent of H_2O per Sm is used in the N_2R catalysis, and so the most strongly reducing Sm^{II} species available under these conditions is likely not the aquo complex. An intermediate, presumably less

reducing mixed-ligand adduct with the average formulation $\text{SmI}_2(\text{THF})_n\text{OH}_2$ must be¹⁰ competent for reduction of MoN_xH_y .

Within this uncertainty, there were two limiting interpretations with respect to the possibility of tandem Sm catalysis in Mo-mediated N_2R . First, it is feasible that the reduction potential of $\text{SmI}_2(\text{THF})_n\text{OH}_2$ is coincidentally close to -1.9 V, and thus mimics all the other reducing agents with this driving force for outer-sphere ET (OSET). In this limit, Sm^{II} would be unlikely to provide a major catalytic enhancement over an electrode held at -1.9 V. Second, though, it is equally feasible that the reduction potential of $\text{SmI}_2(\text{THF})_n\text{OH}_2$ is significantly positive of -1.9 V. In this scenario, the Sm^{II} reagent might be accessing a mechanism in N_2R distinct from OSET. Indeed, in the organic literature, ISET and PCET mechanisms for $\text{SmI}_2\cdot\text{H}_2\text{O}$ reductions are well established. Given this precedent, we hypothesized that Sm^{II} catalysis based on one of these mechanisms would facilitate selective, low-overpotential N_2R with a suitable transition metal cocatalyst. For the interested reader, the next two sections aim to summarize the evolution of more specific forms of this hypothesis over the course of my thesis work.

1.4 Sm^{II} as a Proton-Coupled Reductant

This thesis uses the currently accepted definition for PCET as any reaction involving the transfer of both proton(s) and electron(s),⁵ while “concerted proton-electron transfer” (CPET) refers to a reaction in which a proton and an electron originating from different molecular orbitals are transferred in a single concerted step (i.e., the diagonal path in Figure 1.3). A reductive PCET catalyst colocalizes H^+/e^- equivalents in a single molecule or association complex and decreases the barrier of their transfer from a terminal acid and reductant to a substrate.^{51,52}

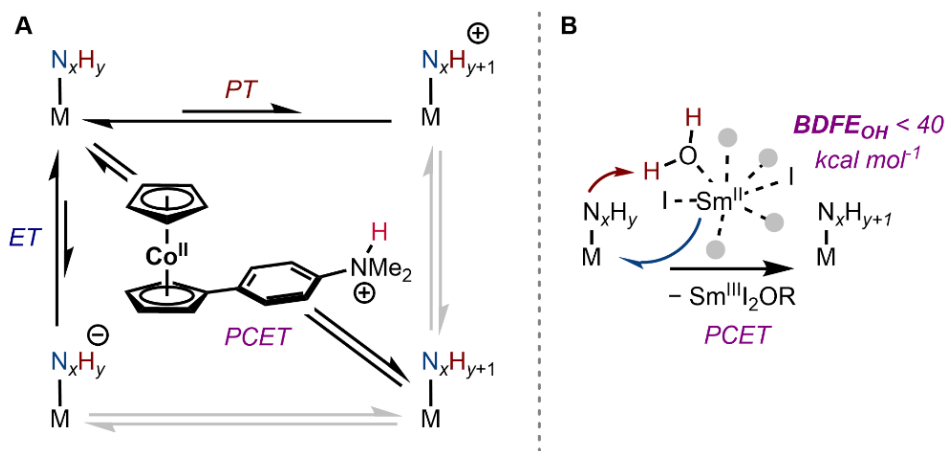


Figure 1.3: PCET to $M-N_xH_y$ from (A) an aniline-appended cobaltocene PCET catalyst or (B) $SmI_2 \cdot H_2O$.

We initially focused on development of Sm as a reductive PCET catalyst in N_2R . Some historical context is useful to explain this starting point. Our group had recently shown that protonation of Cp^*Co yields the ring-protonated species $[Cp^*Co(Cp^*H)]^+$, and proposed that PCET from the resulting weak C–H bond (bond dissociation free energy (BDFE_{C–H}) < 29 kcal mol⁻¹) enhances the rate of N–H bond formation in N_2R catalyzed by iron complexes.^{29,53,54} However, HER from $[Cp^*Co(Cp^*H)]^+$ by subsequent ET/PT steps is facile,⁵⁵ limiting the extent to which this PCET catalyst platform can improve the overall selectivity for N_2R over HER.²⁹ This led to design of aniline-appended cobaltocene as a poor HER catalyst but effective PCET catalyst,⁵¹ including application to tandem electrocatalytic N_2R at low overpotential.³⁰

Around the same time, studies from the groups of Flowers and Mayer provided evidence for PCET from $SmI_2 \cdot H_2O$ in reduction of unsaturated hydrocarbons, aliphatic esters, and enamines.^{56–58} Estimates for the O–H BDFE of an ill-defined $[Sm(THF)_mI_n(OH_2)_p]I_{2-n}$ species ranged from 40 kcal mol⁻¹ to as low as 26 kcal mol⁻¹. The exceptionally low latter value, derived by Kolmar et al for $Sm(OH_2)_n^{2+}$ in water,⁵⁸ provided

a rationalization for successful reductions of metal-nitride species by SmI_2 in the¹² presence of 1-10 equiv of H_2O in THF to release NH_3 via initial downhill PCET, when initial OSET would be uphill by as much as 1 V.^{33,59}

Against this backdrop, we envisioned the cycle for Sm^{II} -electrocatalyzed PCET in Figure 1.4. The Sm^{II} -EH state (where EH is H_2O , an alcohol, or a secondary amide) could transfer $1\text{H}^+/1\text{e}^-$ to a substrate (e.g., $\text{M}-\text{N}_x\text{H}_y$) with a kinetic enhancement over the same net transformation via stepwise ETPT from the electrode/exogeneous acid. Faster PCET catalysis would be favored by a high affinity of EH for Sm^{II} .^{60,61} Sm^{II} -EH adducts are curiously stable with respect to HER,^{58,62} possibly because they do not readily undergo further reduction and protonation to access a kinetically facile monometallic HER mechanism. We therefore anticipated that Sm-mediated HER would not pose a problem.

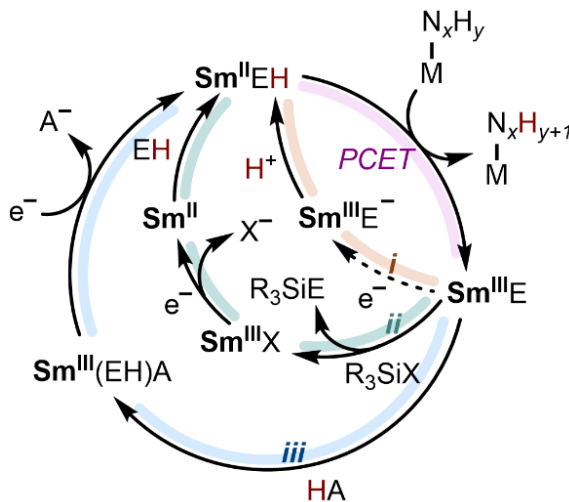


Figure 1.4: Turnover pathways for Sm^{II} -EH as a PCET catalyst.

The key challenge in this proposed cycle was turnover of Sm^{III} -E back to Sm^{II} -EH. Direct reduction of Sm^{III} -E is very difficult due to the strongly donating anionic oxygen donor ligand (pathway *i*). Previous strategies for Sm catalysis used halosilanes to cleave alkoxides (OR^-) from Sm^{III} -OR as silyl ethers and generate a reducible SmX_3 intermediate

(X = halide, pathway *ii*).⁶³⁻⁶⁷ However, to operate at the SmI₃/SmI₂ redox couple, an¹³ iodosilane or silyl triflate must be used,⁶³ neither of which would be compatible with excess EH. While a less reactive chlorosilane would be less prone to hydrolysis, Sm has a higher affinity for chloride than iodide and thus SmCl₃ would be the dominant Sm^{III} species after a few turnovers. Reduction to SmCl₂ would then require a much more negative applied potential (ca. -2.0 V), which ran counter to our goal of decreasing the overpotential of *e*N₂R.

We therefore focused on pathway *iii*, which hinged on identification of a terminal Brønsted acid (HA) that could protonate Sm^{III}-E to access an easily reduced [Sm^{III}-EH]A state. We knew that we would want to use the weakest possible acid, both to minimize $\Delta\Delta G_f$ in *e*N₂R applications and to avoid competing electrode-mediated HER at the potential necessary to generate the Sm^{II} state. However, the effect of coordination of strongly oxophilic Sm^{III} on the nonaqueous acidity of polar protic ligands had not been quantitatively studied. Additionally, candidates for the conjugate base A⁻ would have to be selected carefully to avoid competitive binding (and an associated cathodic shift to $E(\text{Sm}^{\text{III/II}})$) following PT.

At this stage, the lack of robust thermodynamic information describing each of the steps in the targeted cycle prompted us to develop a well-defined model system to thermochemically benchmark ET, PT, and ligand association processes underlying Sm^{II}-mediated PCET (Chapter 2).⁶⁸ The key finding of this study was that the pK_a of [Sm^{III}-O(R)H]⁺ is relatively unaffected by the supporting ligand environment in comparison to the highly sensitive Sm^{III/II} reduction potential. According to eqn 1.3, it follows that PCET reagents based on SmI₂ ($E^\circ(\text{Sm}^{\text{III/II}}) - 1.41 \text{ V}$) and a given EH are likely to have appreciably

higher BDFEs than the corresponding benchmarked adduct with the well-defined Sm^{II} ¹⁴ complex ($< 28 \text{ kcal mol}^{-1}$), which has $E^\circ(\text{Sm}^{\text{III/II}}) -2.43 \text{ V}$. Because a higher BDFE corresponds to lower driving force for N_2R (eqn 1.4), this conclusion is consistent with our subsequent observation that the well-defined, low-BDFE Sm^{II} complexes outperformed SmI_2 -based PCET reagents in Fe-catalyzed N_2R (Chapter 3),⁶⁹ as the Fe catalyst generally requires higher driving force than Mo-based catalysts.¹⁵

The benchmarking study also pointed to mild Brønsted acids as a means of cleaving alkoxides from problematic $\text{Sm}^{\text{III}}\text{-OR}$ intermediates that are generated as the byproduct of many other reduction reactions of SmI_2 other than PCET. In collaboration with the Reisman group, this strategy was applied to SmI_2 -catalyzed ketone-acrylate coupling to form γ -lactones (Chapter 4).⁷⁰ Lutidinium *bis*-triflimide (LutHNTf_2) and either Zn^0 or an applied electrochemical potential of -1.55 V carry out $\text{Sm}^{\text{III}}\text{-OR}$ protonolysis and reduction to regenerate SmI_2 (pathway *iii*). This nearly thermoneutral turnover by net PCET is mild relative to the previous catalytic SmI_2 system using Me_3SiOTf as terminal oxophile, likely facilitating a comparatively broad substrate scope.⁶³

Despite this progress, the cycle in Figure 1.4 for Sm^{II} as a PCET catalyst remains elusive. However, a number of observations collected over the course of these studies, as well as a deepened appreciation for the mechanisms of SmI_2 reduction reactions in organic synthesis, caused us to question whether PCET was the only possible explanation for the unusual activity of SmI_2 in catalytic N_2R . Specifically, we examined the alternative hypothesis that SmI_2 could serve as an ISET catalyst in reduction of MN_xH_y intermediates.

1.5 Sm^{II} as an Inner-Sphere Reductant

A Sm^{III/II} reduction potential of ca. -1.5 V does not square with the observed high reactivity of SmI₂ toward very weakly oxidizing functional groups in the absence of proton sources. For example, ET from SmI₂ to benzophenone ($E^\circ(\text{Ph}_2\text{CO}^{0/-}) = -2.30$ V in THF) is uphill by 890 mV. Nevertheless, SmI₂ reacts reversibly with Ph₂CO to generate the corresponding ketyl radical. Hoz and coworkers measured the equilibrium constant for this reaction and concluded that strongly favorable coordination of Ph₂CO^{•-} to SmI₂(THF)_{*n*}⁺ must supply the missing 20 kcal mol⁻¹ of thermodynamic driving force.⁷¹

Moreover, Skrydstrup and coworkers found that the rate of reduction of acetophenone by SmI₂ is 9 orders of magnitude faster than the predicted rate of a 25.6 kcal mol⁻¹ uphill OSET process from Marcus theory.⁴¹ Ketone reduction is therefore proposed to occur by an ISET mechanism in which coordination of the ketone to SmI₂ induces ET via buildup of a favorable Sm^{δ+}-O^{δ-} interaction in the transition state. Subsequent examination of the ET mechanisms of various oxidants (aromatic and alkyl ketones, alkyl halides) with various Sm^{II} reductants (SmBr₂, SmCl₂, SmI₂/HMPA adducts) by the groups of Flowers and Skrydstrup revealed that in virtually all cases, ISET enhancements should be invoked to explain the observed reaction rates,^{40,46,47} notably including the reduction of ketones and aldehydes by SmI₂•H₂O.⁵⁷

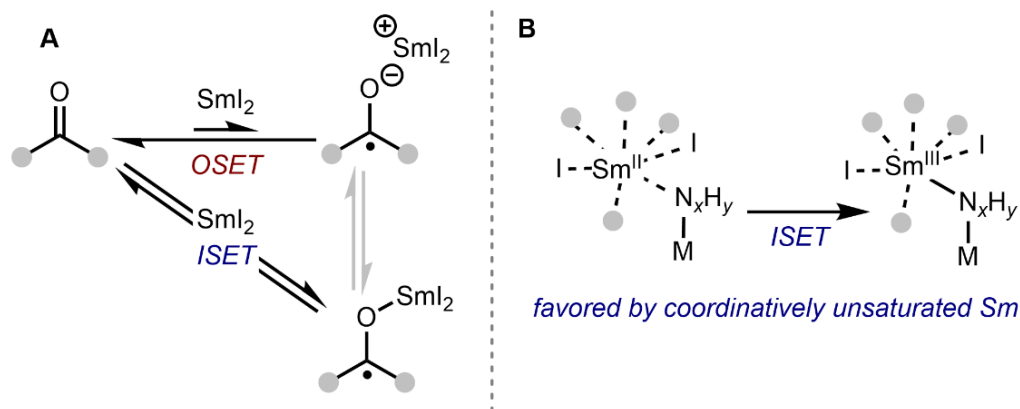


Figure 1.5: ISET mechanism with SmI_2 illustrated for (A) carbonyl reduction and (B) M-catalyzed N_2R .

Both Sm^{III} and Sm^{II} are azaphilic,⁷² suggesting that reduction of $\text{M}-\text{N}_x\text{H}_y$ intermediates by Sm^{II} species would likely occur by ISET. Indeed, in seminal work by Evans and coworkers, reversible binding of N_2 to the organometallic Sm^{II} complex Cp^*_2Sm in noncoordinating solvent is accompanied by ET to form a N_2^{2-} unit coordinated to the resulting Sm^{III} centers in $(\text{Cp}^*_2\text{Sm})_2(\mu\text{-}\eta^1\text{-}\eta^1\text{-N}_2)$.⁷³ The $\text{Sm}^{\text{III/II}}$ reduction potential of $\text{Cp}^*_2\text{Sm}(\text{THF})_2$ is only -2.12 V,³⁹ and so a strong $\text{Sm}^{\delta+}\text{-N}^{\delta-}$ interaction must drive this ISET process. In Chapter 3, we observe favorable association between $[\text{Sm}^{\text{III}}]^+$ and $[\text{Fe}]\text{N}_2^-$ intermediates in Fe-catalyzed N_2R ,⁶⁹ suggestive of ISET in the reduction of $[\text{Fe}]\text{N}_2$ by the Sm^{II} complex.

Building on studies of SmI_2 as an ISET catalyst for reductive ketone-acrylate coupling (Chapters 4 and 5),^{45,63,70} we began formulating *a priori* design rules for SmI_2 ISET catalysis in N_2R . OH-based proton sources (and associated alkoxide or hydroxide poisons) can be omitted entirely. The Sm coordination sphere should be left as coordinatively unsaturated as possible to maximize affinity for $\text{M}-\text{N}_x\text{H}_y$. The proton source should be noncoordinating and capable of protonating the least basic $\text{M}-\text{N}_x\text{H}_y$ intermediate. Based on

these strategies, in Chapter 6 we ultimately report eN_2R cocatalyzed by $PNPMoBr_3$ and $SmI_3(THF)_n$ with 82% F.E. and $\Delta\Delta G_f$ 39 kcal mol⁻¹.⁷⁴

REFERENCES

- (1) Girard, P.; Namy, J. L.; Kagan, H. B. Divalent lanthanide derivatives in organic synthesis. 1. Mild preparation of samarium iodide and ytterbium iodide and their use as reducing or coupling agents. *J. Am. Chem. Soc.* **1980**, *102* (8), 2693–2698.
- (2) Szostak, M.; Fazakerley, N. J.; Parmar, D.; Procter, D. J. Cross-coupling reactions using samarium(II) iodide. *Chem. Rev.* **2014**, *114* (11), 5959–6039.
- (3) Otsubo, K.; Inanaga, J.; Yamaguchi, M. SmI₂-induced highly regioselective reduction of α,β -epoxy esters and γ,δ -epoxy- α,β -unsaturated esters. An efficient route to optically active β -hydroxy and δ -hydroxy esters. *Tetrahedron Lett.* **1987**, *28* (38), 4437–4440.
- (4) Kern, N.; Plesniak, M. P.; McDouall, J. J. W.; Procter, D. J. Enantioselective cyclizations and cyclization cascades of samarium ketyl radicals. *Nat. Chem.* **2017**, *9* (12), 1198–1204.
- (5) Agarwal, R. G.; Coste, S. C.; Groff, B. D.; Heuer, A. M.; Noh, H.; Parada, G. A.; Wise, C. F.; Nichols, E. M.; Warren, J. J.; Mayer, J. M. Free energies of proton-coupled electron transfer reagents and their applications. *Chem. Rev.* **2022**, *122* (1), 1–49.
- (6) Smil, V. *Enriching the Earth: Fritz Haber, Carl Bosch, and the Transformation of World Food Production*; MIT Press: Cambridge, MA, USA, 2000.
- (7) Lindley, B. M.; Appel, A. M.; Krogh-Jespersen, K.; Mayer, J. M.; Miller, A. J. M. Evaluating the thermodynamics of electrocatalytic N₂ reduction in acetonitrile. *ACS Energy Lett.* **2016**, *1* (4), 698–704.

- (8) Erfani, N.; Baharudin, L.; Watson, M. Recent advances and intensifications in Haber-Bosch ammonia synthesis process. *Chem. Eng. Process. - Process Intensif.* **2024**, *204*, 109962.
- (9) van der Ham, C. J. M.; Koper, M. T. M.; Hetterscheid, D. G. H. Challenges in reduction of dinitrogen by proton and electron transfer. *Chem. Soc. Rev.* **2014**, *43* (15), 5183–5191.
- (10) Chalkley, M. J.; Drover, M. W.; Peters, J. C. Catalytic N₂-to-NH₃ (or -N₂H₄) conversion by well-defined molecular coordination complexes. *Chem. Rev.* **2020**, *120* (12), 5582–5636.
- (11) Tsuneto, A.; Kudo, A.; Sakata, T. Efficient electrochemical reduction of N₂ to NH₃ catalyzed by lithium. *Chem. Lett.* **1993**, *22* (5), 851–854.
- (12) Du, H.-L.; Chatti, M.; Hodgetts, R. Y.; Cherepanov, P. V.; Nguyen, C. K.; Matuszek, K.; MacFarlane, D. R.; Simonov, A. N. Electroreduction of nitrogen with almost 100% current-to-ammonia efficiency. *Nature* **2022**, *609* (7928), 722–727.
- (13) Suryanto, B. H. R.; Matuszek, K.; Choi, J.; Hodgetts, R. Y.; Du, H.-L.; Bakker, J. M.; Kang, C. S. M.; Cherepanov, P. V.; Simonov, A. N.; MacFarlane, D. R. Nitrogen reduction to ammonia at high efficiency and rates based on a phosphonium proton shuttle. *Science* **2021**, *372* (6547), 1187–1191.
- (14) Lazouski, N.; Chung, M.; Williams, K.; Gala, M. L.; Manthiram, K. Non-aqueous gas diffusion electrodes for rapid ammonia synthesis from nitrogen and water-splitting-derived hydrogen. *Nat. Catal.* **2020**, *3* (5), 463–469.
- (15) Chalkley, M. J.; Peters, J. C. Relating N–H bond strengths to the overpotential for catalytic nitrogen fixation. *Eur. J. Inorg. Chem.* **2020**, *2020* (15–16), 1353–1357.

- (16) Garrido, G.; Koort, E.; Ràfols, C.; Bosch, E.; Rodima, T.; Leito, I.; Rosés, M.²⁰ Acid–base equilibria in nonpolar media. Absolute pK_a scale of bases in tetrahydrofuran. *J. Org. Chem.* **2006**, *71* (24), 9062–9067.
- (17) Johansen, C. M.; Peters, J. C. Catalytic reduction of cyanide to ammonia and methane at a mononuclear Fe site. *J. Am. Chem. Soc.* **2024**, *146* (8), 5343–5354.
- (18) Yandulov, D. V.; Schrock, R. R. Catalytic reduction of dinitrogen to ammonia at a single molybdenum center. *Science* **2003**, *301* (5629), 76–78.
- (19) Arashiba, K.; Miyake, Y.; Nishibayashi, Y. A molybdenum complex bearing PNP-type pincer ligands leads to the catalytic reduction of dinitrogen into ammonia. *Nat. Chem.* **2011**, *3* (2), 120–125.
- (20) Ashida, Y.; Mizushima, T.; Arashiba, K.; Egi, A.; Tanaka, H.; Yoshizawa, K.; Nishibayashi, Y. Catalytic production of ammonia from dinitrogen employing molybdenum complexes bearing N-heterocyclic carbene-based PCP-type pincer ligands. *Nat. Synth.* **2023**, 1–10.
- (21) Arashiba, K.; Eizawa, A.; Tanaka, H.; Nakajima, K.; Yoshizawa, K.; Nishibayashi, Y. Catalytic nitrogen fixation via direct cleavage of nitrogen–nitrogen triple bond of molecular dinitrogen under ambient reaction conditions. *Bull. Chem. Soc. Jpn.* **2017**, *90* (10), 1111–1118.
- (22) Johansen, C. M.; Boyd, E. A.; Peters, J. C. Catalytic transfer hydrogenation of N_2 to NH_3 via a photoredox catalysis strategy. *Sci. Adv.* **2022**, *8* (43), eade3510.
- (23) Ibrahim, A. F.; Garrido-Barros, P.; Peters, J. C. Electrocatalytic nitrogen reduction on a molybdenum complex bearing a PNP pincer ligand. *ACS Catal.* **2023**, *13* (1), 72–78.

- (24) Ashida, Y.; Arashiba, K.; Tanaka, H.; Egi, A.; Nakajima, K.; Yoshizawa, K.;²¹ Nishibayashi, Y. Molybdenum-catalyzed ammonia formation using simple monodentate and bidentate phosphines as auxiliary ligands. *Inorg. Chem.* **2019**, *58* (14), 8927–8932.
- (25) Ashida, Y.; Onozuka, Y.; Arashiba, K.; Konomi, A.; Tanaka, H.; Kuriyama, S.; Yamazaki, Y.; Yoshizawa, K.; Nishibayashi, Y. Catalytic nitrogen fixation using visible light energy. *Nat. Commun.* **2022**, *13* (1), 7263.
- (26) Kim, J.; Panetti, G. B.; Kaul, N.; Kim, S.; Chirik, P. J. Photodriven ammonia synthesis from N₂ and H₂: Recycling of a molecular molybdenum nitride. *J. Am. Chem. Soc.* **2025**, *147* (10), 8215–8226.
- (27) Pickett, C. J.; Talarmin, J. Electrosynthesis of ammonia. *Nature* **1985**, *317* (6038), 652–653.
- (28) Del Castillo, T. J.; Thompson, N. B.; Peters, J. C. A synthetic single-site Fe nitrogenase: high turnover, freeze-quench ⁵⁷Fe Mössbauer data, and a hydride resting state. *J. Am. Chem. Soc.* **2016**, *138* (16), 5341–5350.
- (29) Chalkley, M. J.; Del Castillo, T. J.; Matson, B. D.; Peters, J. C. Fe-mediated nitrogen fixation with a metallocene mediator: exploring pK_a effects and demonstrating electrocatalysis. *J. Am. Chem. Soc.* **2018**, *140* (19), 6122–6129.
- (30) Garrido-Barros, P.; Derosa, J.; Chalkley, M. J.; Peters, J. C. Tandem electrocatalytic N₂ fixation via proton-coupled electron transfer. *Nature* **2022**, *609* (7925), 71–76.
- (31) Bruch, Q. J.; Malakar, S.; Goldman, A. S.; Miller, A. J. M. Mechanisms of electrochemical N₂ splitting by a molybdenum pincer complex. *Inorg. Chem.* **2022**, *61* (4), 2307–2318.

- (32) Connelly, N. G.; Geiger, W. E. Chemical redox agents for organometallic²² chemistry. *Chem. Rev.* **1996**, *96* (2), 877–910.
- (33) Ashida, Y.; Arashiba, K.; Nakajima, K.; Nishibayashi, Y. Molybdenum-catalysed ammonia production with samarium diiodide and alcohols or water. *Nature* **2019**, *568* (7753), 536–540.
- (34) Szostak, M.; Procter, D. J. Beyond samarium diiodide: vistas in reductive chemistry mediated by lanthanides(II). *Angew. Chem. Int. Ed.* **2012**, *51* (37), 9238–9256.
- (35) Johnson, D. A. Relative stabilities of dipositive and tripositive lanthanoid ions in aqueous solution. *J. Chem. Soc. Dalton Trans.* **1974**, No. 16, 1671–1675.
- (36) Morss, L. R. Thermochemical properties of yttrium, lanthanum, and the lanthanide elements and ions. *Chem. Rev.* **1976**, *76* (6), 827–841.
- (37) McCoy, H. N. Contribution to the chemistry of europium. *J. Am. Chem. Soc.* **1936**, *58* (9), 1577–1580.
- (38) Anderson, L. B.; Macero, D. J. The formal reduction potential of the europium(III)-europium(II) system. *J. Phys. Chem.* **1963**, *67* (9), 1942–1942.
- (39) Veauthier, J. M.; Schelter, E. J.; Carlson, C. N.; Scott, B. L.; Re, R. E. D.; Thompson, J. D.; Kiplinger, J. L.; Morris, D. E.; John, K. D. Direct comparison of the magnetic and electronic properties of samarocene and ytterbocene terpyridine complexes. *Inorg. Chem.* **2008**, *47* (13), 5841–5849.
- (40) Enemærke, R. J.; Hertz, T.; Skrydstrup, T.; Daasbjerg, K. Evidence for ionic samarium(II) species in THF/HMPA solution and investigation of their electron-donating properties. *Chem. – Eur. J.* **2000**, *6* (20), 3747–3754.

- (41) Enemærke, R. J.; Daasbjerg, K.; Skrydstrup, T. Is samarium diiodide an inner- or outer-sphere electron donating agent? *Chem. Commun.* **1999**, 0 (4), 343–344.
- (42) Prasad, E.; Flowers, R. A. Mechanistic impact of water addition to SmI₂: consequences in the ground and transition state. *J. Am. Chem. Soc.* **2005**, 127 (51), 18093–18099.
- (43) Halter, D. P.; Palumbo, C. T.; Ziller, J. W.; Gembicky, M.; Rheingold, A. L.; Evans, W. J.; Meyer, K. Electrocatalytic H₂O reduction with f-elements: mechanistic insight and overpotential tuning in a series of lanthanide complexes. *J. Am. Chem. Soc.* **2018**, 140 (7), 2587–2594.
- (44) Yamamoto, A.; Liu, X.; Arashiba, K.; Konomi, A.; Tanaka, H.; Yoshizawa, K.; Nishibayashi, Y.; Yoshida, H. Coordination structure of samarium diiodide in a tetrahydrofuran–water mixture. *Inorg. Chem.* **2023**, 62 (14), 5348–5356.
- (45) Johansen, C. M.; Boyd, E. A.; Tarnopol, D. E.; Peters, J. C. Photodriven Sm(III)-to-Sm(II) reduction for catalytic applications. *J. Am. Chem. Soc.* **2024**, 146 (37), 25456–25461.
- (46) Fuchs, J. R.; Mitchell, M. L.; Shabangi, M.; Flowers, R. A. The effect of lithium bromide and lithium chloride on the reactivity of SmI₂ in THF. *Tetrahedron Lett.* **1997**, 38 (47), 8157–8158.
- (47) Prasad, E.; Flowers, R. A. Reduction of ketones and alkyl iodides by SmI₂ and Sm(II)-HMPA complexes. Rate and mechanistic studies. *J. Am. Chem. Soc.* **2002**, 124 (24), 6895–6899.

- (48) Shabangi, M.; Flowers, R. A. Electrochemical investigation of the reducing power of SmI₂ in THF and the effect of HMPA cosolvent. *Tetrahedron Lett.* **1997**, *38* (7), 1137–1140.
- (49) Shabangi, M.; Sealy, J. M.; Fuchs, J. R.; Flowers, R. A. The effect of cosolvent on the reducing power of SmI₂ in tetrahydrofuran. *Tetrahedron Lett.* **1998**, *39* (25), 4429–4432.
- (50) Szostak, M.; Spain, M.; Procter, D. J. Determination of the effective redox potentials of SmI₂, SmBr₂, SmCl₂, and their complexes with water by reduction of aromatic hydrocarbons. Reduction of anthracene and stilbene by samarium(II) iodide–water complex. *J. Org. Chem.* **2014**, *79* (6), 2522–2537.
- (51) Chalkley, M. J.; Garrido-Barros, P.; Peters, J. C. A molecular mediator for reductive concerted proton–electron transfers via electrocatalysis. *Science* **2020**, *369* (6505), 850–854.
- (52) Dey, S.; Masero, F.; Brack, E.; Fontecave, M.; Mougel, V. Electrocatalytic metal hydride generation using CPET mediators. *Nature* **2022**, *607* (7919), 499–506.
- (53) Chalkley, M. J.; Del Castillo, T. J.; Matson, B. D.; Roddy, J. P.; Peters, J. C. Catalytic N₂-to-NH₃ conversion by Fe at lower driving force: A proposed role for metallocene-mediated PCET. *ACS Cent. Sci.* **2017**, *3* (3), 217–223.
- (54) Chalkley, M. J.; Oyala, P. H.; Peters, J. C. Cp* noninnocence leads to a remarkably weak C–H bond via metallocene protonation. *J. Am. Chem. Soc.* **2019**, *141* (11), 4721–4729.
- (55) Koelle, U.; Infelta, P. P.; Graetzel, M. Kinetics and mechanism of the reduction of protons to hydrogen by cobaltocene. *Inorg. Chem.* **1988**, *27* (5), 879–883.

- (56) Chciuk, T. V.; Flowers, R. A. Proton-coupled electron transfer in the reduction of²⁵ arenes by SmI₂–water complexes. *J. Am. Chem. Soc.* **2015**, *137* (35), 11526–11531.
- (57) Chciuk, T. V.; Anderson, W. R.; Flowers, R. A. Proton-coupled electron transfer in the reduction of carbonyls by samarium diiodide–water complexes. *J. Am. Chem. Soc.* **2016**, *138* (28), 8738–8741.
- (58) Kolmar, S. S.; Mayer, J. M. SmI₂(H₂O)_n reduction of electron rich enamines by proton-coupled electron transfer. *J. Am. Chem. Soc.* **2017**, *139* (31), 10687–10692.
- (59) Bruch, Q. J.; Connor, G. P.; Chen, C.-H.; Holland, P. L.; Mayer, J. M.; Hasanayn, F.; Miller, A. J. M. Dinitrogen reduction to ammonium at rhenium utilizing light and proton-coupled electron transfer. *J. Am. Chem. Soc.* **2019**, *141* (51), 20198–20208.
- (60) Chciuk, T. V.; Li, A. M.; Vazquez-Lopez, A.; Anderson, W. R.; Flowers, R. A. Secondary amides as hydrogen atom transfer promoters for reactions of samarium diiodide. *Org. Lett.* **2017**, *19* (1), 290–293.
- (61) Boekell, N. G.; Bartulovich, C. O.; Maity, S.; Flowers, R. A. I. Accessing unusual reactivity through chelation-promoted bond weakening. *Inorg. Chem.* **2023**, *62* (12), 5040–5045.
- (62) Boekell, N. G.; Flowers, R. A. Coordination-induced bond weakening. *Chem. Rev.* **2022**, *122* (16), 13447–13477.
- (63) Corey, E. J.; Zheng, G. Z. Catalytic reactions of samarium (II) iodide. *Tetrahedron Lett.* **1997**, *38* (12), 2045–2048.
- (64) Nomura, R.; Matsuno, T.; Endo, T. Samarium iodide-catalyzed pinacol coupling of carbonyl compounds. *J. Am. Chem. Soc.* **1996**, *118* (46), 11666–11667.

- (65) Aspinall, H. C.; Greeves, N.; Valla, C. Samarium diiodide-catalyzed²⁶ diastereoselective pinacol couplings. *Org. Lett.* **2005**, *7* (10), 1919–1922.
- (66) Maity, S.; Flowers, R. A. Mechanistic study and development of catalytic reactions of Sm(II). *J. Am. Chem. Soc.* **2019**, *141* (7), 3207–3216.
- (67) Sun, L.; Sahloul, K.; Mellah, M. Use of electrochemistry to provide efficient SmI₂ catalytic system for coupling reactions. *ACS Catal.* **2013**, *3* (11), 2568–2573.
- (68) Boyd, E. A.; Peters, J. C. Sm(II)-mediated proton-coupled electron transfer: quantifying very weak N–H and O–H homolytic bond strengths and factors controlling them. *J. Am. Chem. Soc.* **2022**, *144* (46), 21337–21346.
- (69) Boyd, E. A.; Peters, J. C. Highly selective Fe-catalyzed nitrogen fixation to hydrazine enabled by Sm(II) reagents with tailored redox potential and pK_a. *J. Am. Chem. Soc.* **2023**, *145* (27), 14784–14792.
- (70) Boyd, E. A.; Shin, C.; Charboneau, D. J.; Peters, J. C.; Reisman, S. E. Reductive samarium (electro)catalysis enabled by Sm^{III}-alkoxide protonolysis. *Science* **2024**, *385* (6711), 847–853.
- (71) Farran, H.; Hoz, S. Quantifying the electrostatic driving force behind SmI₂ reductions. *Org. Lett.* **2008**, *10* (21), 4875–4877.
- (72) Maity, S.; Flowers, R. A.; Hoz, S. Aza versus oxophilicity of SmI₂: A break of a paradigm. *Chem. – Eur. J.* **2017**, *23* (67), 17070–17077.
- (73) Evans, W. J.; Ulibarri, T. A.; Ziller, J. W. Isolation and x-ray crystal structure of the first dinitrogen complex of an f-element metal, [(C₅Me₅)₂Sm]₂N₂. *J. Am. Chem. Soc.* **1988**, *110* (20), 6877–6879.

- (74) Boyd, E. A.; Jung, H.; Peters, J. C. Samarium as a Catalytic Electron-Transfer²⁷
Mediator in Electrocatalytic Nitrogen Reduction to Ammonia. *J. Am. Chem. Soc.*
2025, *147* (6), 4695–4700.

SM(II)-MEDIATED PROTON-COUPLED ELECTRON TRANSFER: QUANTIFYING VERY WEAK N–H AND O–H HOMOLYTIC BOND STRENGTHS AND FACTORS CONTROLLING THEM

Reproduced with permission from Boyd, E.A.; Peters, J. C. *J. Am. Chem. Soc.* **2022**, *144*, 21337. doi: 10.1021/jacs.2c09580

2.1 Introduction

Samarium(II) diiodide (SmI_2) is one of the most versatile and selective single-electron reductants currently available.^{1,2} The lability of ligands at the lanthanide center allows for facile variation of the reductant strength and steric profile of Sm(II) by in situ reaction of $\text{SmI}_2(\text{THF})_n$ with various additives.^{3–5} Additionally, the pronounced oxophilicity of samarium (and the lanthanides in general) affords SmI_2 a strong thermodynamic bias for reactions that form $\text{Sm}^{\text{III}}\text{–O}$ bonds.⁶ The combination of these characteristics has resulted in the emergence of SmI_2 /alcohol adducts as reductive proton-coupled electron transfer (PCET) reagents.

As illustrated in Figure 2.1A, the coordination of water (as well as alcohols, secondary amides, or ammonia, generally defined as EH) to SmI_2 yields $[\text{Sm}^{\text{II}}\text{–EH}]$ species capable of PCET (sometimes designated concerted proton-electron transfer (CPET)) to substrates for which initial electron transfer (ET) would be highly endergonic.^{7–13} Contrasting other strong reductive PCET reagents, and critical to their efficacy, $[\text{Sm}^{\text{II}}\text{–EH}]$ adducts are curiously stable with respect to the hydrogen evolution reaction (HER).⁸

While the reported PCET reaction profiles of $\text{Sm}^{\text{II}}\text{–EH}$ reagents indicate that coordination to Sm^{II} results in highly significant O– or N–H bond weakening in EH, the ill-defined speciation of $[\text{Sm}^{\text{II}}\text{–EH}]$ has hampered precise quantitation of this effect. For

example, the O–H bond dissociation free energy (BDFE_{O–H}) of the aqueous Sm²⁺ ion,²⁹ which can be formulated as Sm(H₂O)_n²⁺, has been most recently estimated as 26 kcal mol⁻¹ by Kolmar and Mayer. However, the degree to which this value can be extended to widely used organic solvents (e.g., in THF, where [SmI_{2–n}(THF)_m(H₂O)_p]ⁿ⁺ species will dominate) is unclear; BDFEs typically vary substantially among different complexes of a metal ion.¹⁴ Mayer’s 2017 study indeed underscores this dilemma, pointing to the uncertainty in speciation and the insolubility of Sm(III) products as limits on a more precise thermodynamic evaluation of the BDFE_{O–H} for Sm(II) in water/THF mixtures.⁸ Knowledge of such values is key to reliable benchmarking of PCET reagent strengths,¹⁴ estimation of chemical overpotentials,¹⁵ and evaluation of available mechanistic pathways.¹⁶

The BDFE_{O–H} of SmI₂(H₂O)_n(THF)_m has been alternatively constrained as less than or equal to the first BDFE_{C–H} formed in substrates which it can successfully reduce, such as anthracene (~39 kcal mol⁻¹) or an enamine (~31 kcal mol⁻¹, see Figure 2.1A).^{7,8,10,11,17} While a reasonable starting point, the possibility of an uphill initial PCET step cannot be discounted. The driving force for hydrogenation of an alkene substrate is defined by the *average* of the first and second BDFE_{C–H} formed in the reduced substrate, as illustrated in Figure 2.1A. Therefore, reduction of anthracene to dihydroanthracene, for example, only allows reliable bracketing of the BDFE_{O–H} of SmI₂(H₂O)_n(THF)_m to ≤ 54.2 kcal mol⁻¹ solely based on this thermodynamic argument.^{18,19}

An upper bound value can instead be estimated analytically based on a kinetic evaluation of PCET from SmI₂(H₂O)_n(THF)_m to an enamine substrate with BDFE_{C–H,1} = 31 kcal mol⁻¹.⁸ A hydrogenation mechanism composed of an initial CPET step (*k*₁) followed by irreversible consumption of the radical intermediate by a second equivalent of

Sm(II) (k_2) is shown in Figure 2.1A. Based on deuterium labeling studies, which indicate³⁰ that the initial PCET step is irreversible under the reaction conditions,⁸ and by constraining k_2 to values below the diffusion-controlled limit ($\sim 10^9 \text{ M}^{-1} \text{ s}^{-1}$), an upper limit on k_{-1} is estimated to satisfy $k_2[\text{Sm}^{\text{II}}\text{-OH}_2] \gg k_{-1}[\text{Sm}^{\text{III}}\text{-OH}]$ at the lowest $[\text{Sm}^{\text{II}}\text{-OH}_2]$ obtained during the reaction.²⁰ Combined with an approximate k_1 based on the reported timescale of this conversion,^{8,20} we suggest that a reliably deduced conservative upper bound for the $\text{BDFE}_{\text{O-H}}$ of $\text{SmI}_2(\text{H}_2\text{O})_n(\text{THF})_m$ is $42 \pm 1 \text{ kcal mol}^{-1}$. Relatedly, using pyrrolidinone (abbreviated herein as PH) instead of H_2O as the $\text{Sm}^{\text{II}}\text{-EH}$ reagent in the reduction of phenanthrene, we estimate a similar upper bound for the $\text{BDFE}_{\text{N-H}}$ in $\text{SmI}_2(\text{PH})_n(\text{THF})_m$ as $41 \pm 1 \text{ kcal mol}^{-1}$.¹⁰ A detailed discussion of these estimates is provided in the Supporting Information.

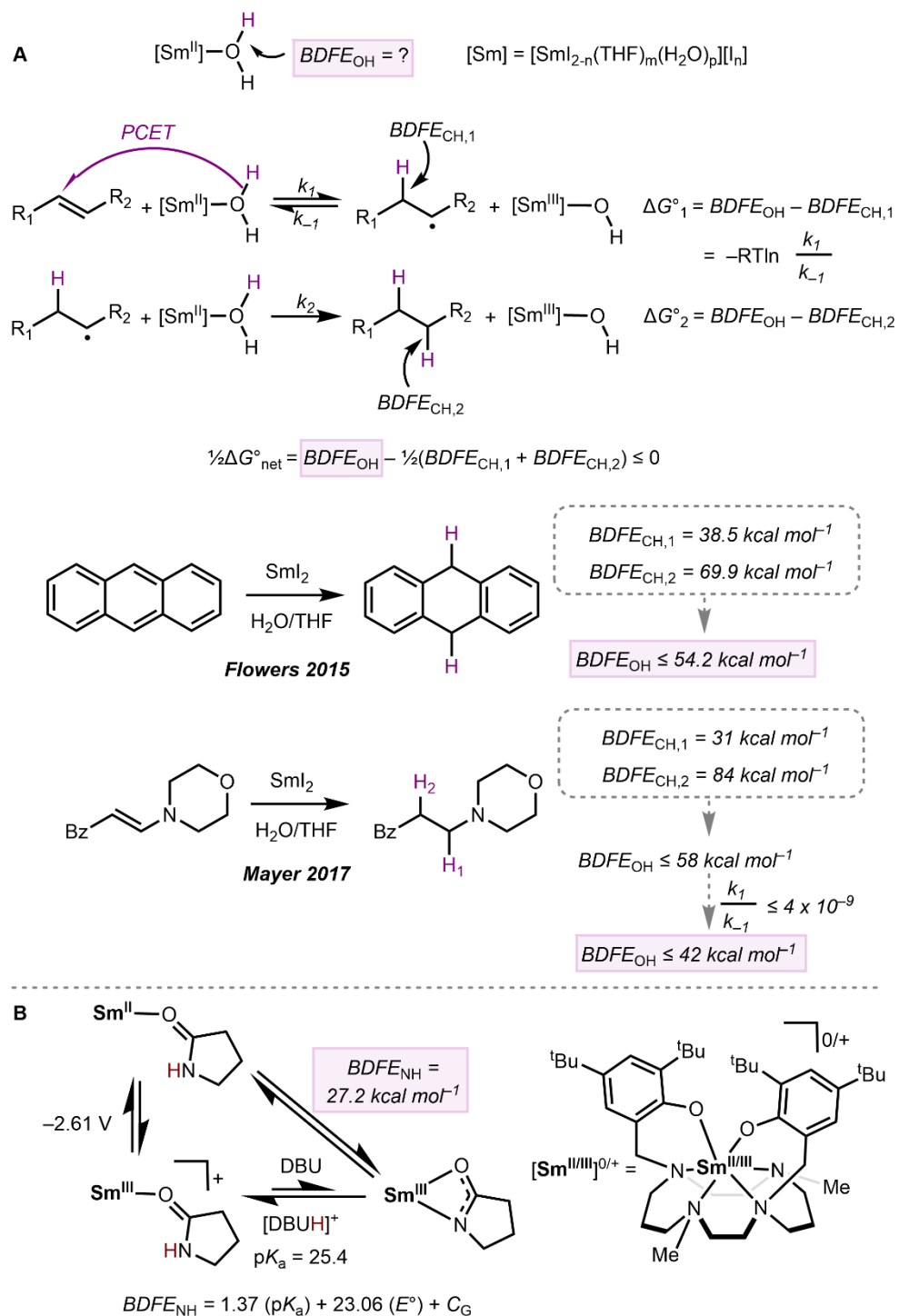


Figure 2.1: Quantification of coordination-induced bond weakening at Sm^{II} .^{7,8}

While these upper bound estimates are fully consistent with strong EH activation on binding to $Sm(II)$, as yet it is not, from available data at least, possible to discern how close

they truly are to the 26 kcal mol⁻¹ estimate most recently provided. Given the broad and³² growing utility of Sm^{II}-EH reagents, and the associated importance of correlating their BDFE_{E-H} values with their reactivity profiles,²¹⁻²³ a more quantitative evaluation of Sm^{II}-induced bond weakening is desirable.

To address this challenge, we study a [Sm^{II}-EH] subunit within the bulky, strongly chelating supporting ligand (^tBu₂ArOH)₂Me₂cyclam (1,8-bis(2-hydroxy-3,5-di-*tert*-butylbenzyl)-4,11-dimethyl-1,4,8,11-tetraazacyclotetradecane) reported by Maria et al. (Figure 2.1B).^{24,25} As we show, well-behaved electrochemistry and speciation for this system enables reliable determination of very low BDFE_{X-H} values (< 28 kcal mol⁻¹) for two kinetically stable [Sm^{II}-EH] adducts, and we provide evidence and associated arguments to suggest that these values are likely appreciably lower than those for SmI₂ in THF in the presence of related proton donors. The present model system hence provides a robust benchmark for considering Sm^{II}-EH BDFEs more broadly. Additionally, the chemistry described points to the future possibility of using such systems to drive electrocatalytic reductions with Sm via PCET processes.

2.2 Results and Discussion

2.2.1 Redox Chemistry of Sm^{II}

Electrochemical reduction of Sm^{III} to Sm^{II} has not been widely explored. For SmI₃ in particular, cases in which it has been demonstrated have required nontraditional electrodes (e.g., Sm metal) and electrolytes (e.g., ionic liquids).^{26,27} However, several Sm^{III} complexes supported by bulky multidentate ligands exhibit reversible electrochemical reduction under more typical conditions.^{28,29} Cyclic voltammetry (CV) experiments were therefore

undertaken to evaluate the facility of $\text{Sm}^{\text{III/II}}$ redox cycling with the³³ $(^{\text{tBu}}\text{ArO})_2\text{Me}_2\text{cyclam}$ ligand (Figure 2.2).

Oxidation of the $((^{\text{tBu}}\text{ArO})_2\text{Me}_2\text{cyclam})\text{Sm}^{\text{II}}$ complex **Sm^{II}** with one equivalent of thallium hexafluorophosphate yields a pale yellow species with heteronuclear NMR signatures consistent with its assignment as cationic $[\text{Sm}^{\text{III}}]\text{PF}_6$ (Figure 2.2), a PF_6^- analogue of the known salt $[\text{Sm}^{\text{III}}]\text{BPh}_4$.²⁵ The CV of $[\text{Sm}^{\text{III}}]\text{PF}_6$ in DME (0.2 M $^{\text{nBu}}\text{NPF}_6$) on a glassy carbon electrode reveals a reversible 1e^- reduction at -2.43 V vs $\text{Fc}^{+/0}$ (Figure 2.2, blue trace) assigned as the $\text{Sm}^{\text{III/II}}$ couple. **Sm^{II}** exhibits a nearly identical couple at -2.45 V vs $\text{Fc}^{+/0}$ (Figure 2.2, green trace), supporting assignment of this wave to a $\text{Sm}^{\text{III/II}}$ redox process. Both **Sm^{II}** and $[\text{Sm}^{\text{III}}]\text{PF}_6$ display peak-to-peak separations smaller than that of the $\text{Fc}^{+/0}$ wave under the same conditions, indicative of facile heterogeneous ET kinetics. The reduction potential of cationic $[\text{Sm}^{\text{III}}]\text{PF}_6$ is 170 mV positive of the neutral *tris*-aryloxy Sm^{III} complex reported by Meyer and co-workers.²⁸

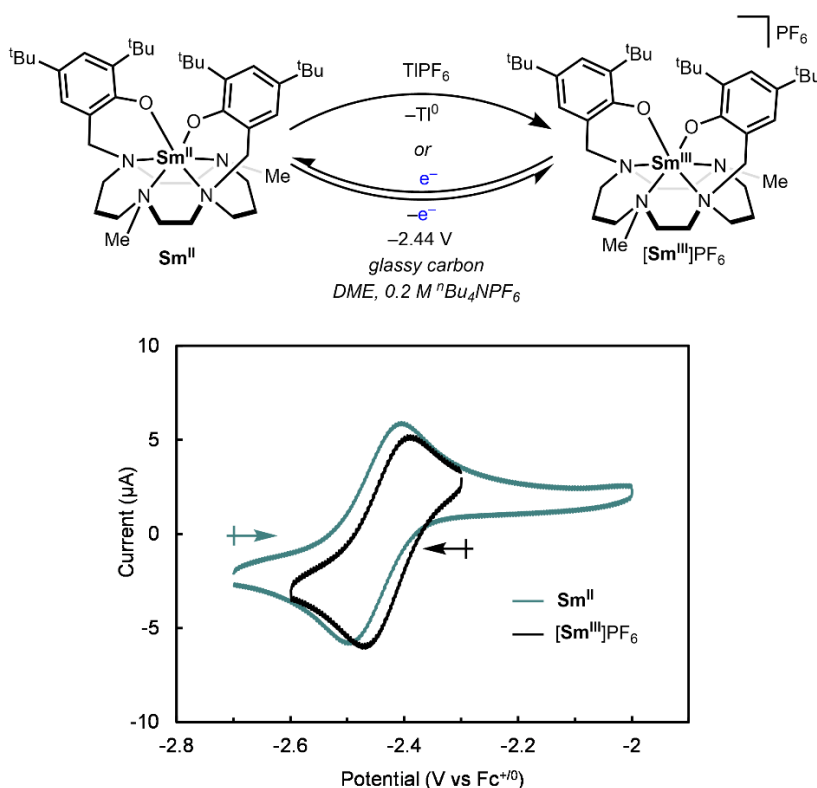


Figure 2.2: Chemical and electrochemical conversion between Sm^{II} and $[\text{Sm}^{\text{III}}]\text{PF}_6$. CVs of Sm^{II} (green, 1 mM) and $[\text{Sm}^{\text{III}}]\text{PF}_6$ (blue, 1 mM) were recorded at 100 mV s^{-1} in DME containing 0.2 M $n\text{Bu}_4\text{NPF}_6$ with a glassy carbon working electrode, platinum wire counter, and a $\text{Ag}^{+/0}$ pseudoreference electrode.

2.2.2 PCET Reactivity of Sm^{II}

To evaluate the ability of Sm^{II} to mimic the PCET reactivity observed with SmI_2 , we explored its behavior in the presence of protic ligands. The addition of one equivalent of 2-pyrrolidinone (PH) to Sm^{II} in benzene results in a color change from brown to green, consistent with the coordination of PH to Sm^{II} to generate a $\text{Sm}^{\text{II}}\text{-PH}$ species.²⁵ The solution fades to colorless over the course of ca. 3 days, producing H_2 and the oxidized, deprotonated Sm^{III} -pyrrolidinonate complex $\text{Sm}^{\text{III}}\text{-P}$ in moderate yield (see Appendix A3.3).

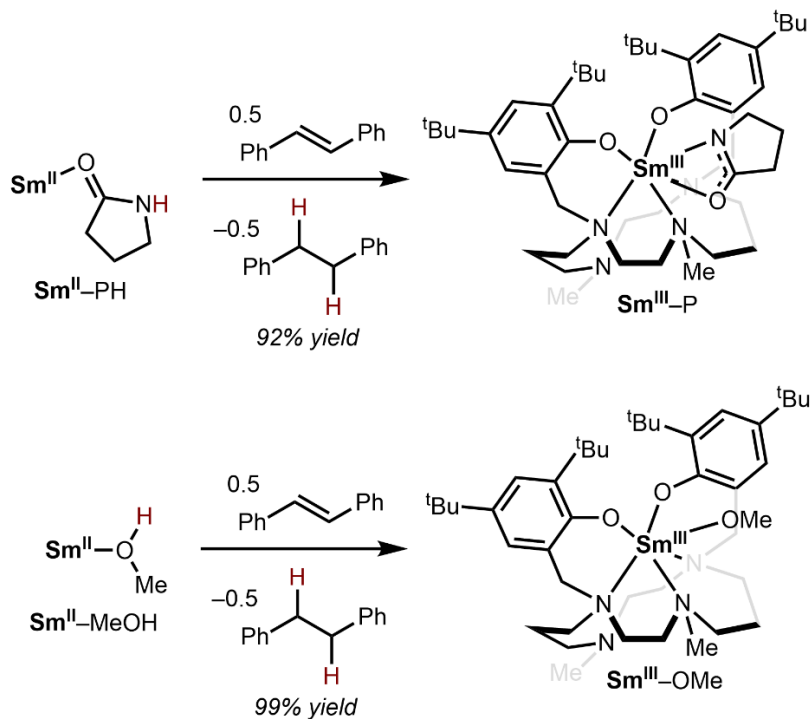


Figure 2.3: Reactivity of $\text{Sm}^{\text{II}}\text{-PH}$ and $\text{Sm}^{\text{II}}\text{-MeOH}$ with *trans*-stilbene to generate $\text{Sm}^{\text{III}}\text{-P}$ and $\text{Sm}^{\text{III}}\text{-OMe}$.

Alternatively, $\text{Sm}^{\text{II}}\text{-PH}$ reacts instantaneously with 0.5 equivalents of the styrenyl substrates *trans*-stilbene, 1,1-diphenylethylene (DPE), and tetraphenylethylene to generate hydrogenated products in 83–92% yields (see Figure 2.3 and Appendix A). Complex $\text{Sm}^{\text{III}}\text{-P}$, the product of net H^{\bullet} release, was isolated as a colorless solid from the reaction of $\text{Sm}^{\text{II}}\text{-PH}$ with excess styrene. Its solid-state crystal structure (Figure 2.4) reveals a seven-coordinate Sm^{III} center in which the pyrrrolidinone ligand binds κ^2 and one of the cyclam amine groups is dissociated. Similar flexibility of this ligand has been observed in its complexes of Yb.²⁴ Diffusion ordered spectroscopy (DOSY) suggests that $\text{Sm}^{\text{III}}\text{-P}$ remains monomeric in the solution phase (Appendix A3.5).

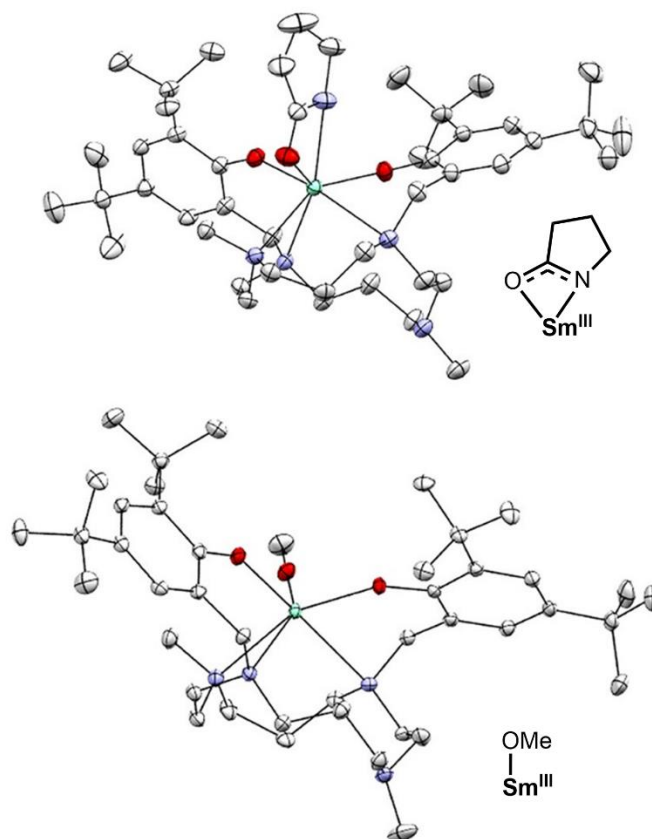


Figure 2.4: Solid-state structures of $\text{Sm}^{\text{III}}\text{-P}$ and $\text{Sm}^{\text{III}}\text{-OMe}$ with thermal ellipsoids set at 50% probability. Hydrogen atoms and co-crystallized solvents are omitted for clarity.

Replacing PH with MeOH results in analogous reactivity. In benzene, the green Sm^{II} -MeOH adduct evolves H_2 over the course of ca. 3 days. Alternatively, it can be intercepted by the styrenyl substrates *trans*-stilbene, DPE, and tetraphenylethylene to yield hydrogenated products in high conversion (see Appendix A3.3). In all cases, the colorless $\text{Sm}^{\text{III}}\text{-OMe}$ complex $\text{Sm}^{\text{III}}\text{-OMe}$ is obtained (Figure 2.4). Single crystals of $\text{Sm}^{\text{III}}\text{-OMe}$ were obtained from the reaction of $\text{Sm}^{\text{II}}\text{-MeOH}$ with *trans*-stilbene. In the solid state, $\text{Sm}^{\text{III}}\text{-OMe}$ is six-coordinate with one of the cyclam amine donors dissociated as in its pyrrolidinonate analogue $\text{Sm}^{\text{III}}\text{-P}$.

2.2.3 Electrochemical PCET with $[\text{Sm}^{\text{III}}\text{-PH}]^+$

The well-behaved electrochemistry of $[\text{Sm}^{\text{III}}]\text{PF}_6$ is conserved upon coordination of PH. Addition of up to 30 equivalents of PH causes the $\text{Sm}^{\text{III/II}}$ couple of $[\text{Sm}^{\text{III}}]\text{PF}_6$ to shift cathodically, but the wave remains reversible (red trace in Figure 2.5). This response suggests that PH coordinates to the Sm^{III} center of $[\text{Sm}^{\text{III}}]\text{PF}_6$ to form a more electron-rich $[\text{Sm}^{\text{III}}\text{-PH}]^+$ adduct that is reduced to $\text{Sm}^{\text{II}}\text{-PH}$ at -2.58 V vs $\text{Fc}^{+/0}$. The reversibility of the wave is consistent with the observed kinetic stability of $\text{Sm}^{\text{II}}\text{-PH}$. Similar behavior is observed with the aprotic N-methylpyrrolidinone (PMe) analogue of PH, and a reversible $\text{Sm}^{\text{III/II}}$ couple for the $[\text{Sm}^{\text{III}}\text{-PMe}]^+$ adduct is assigned at -2.61 V vs $\text{Fc}^{+/0}$ (yellow trace).

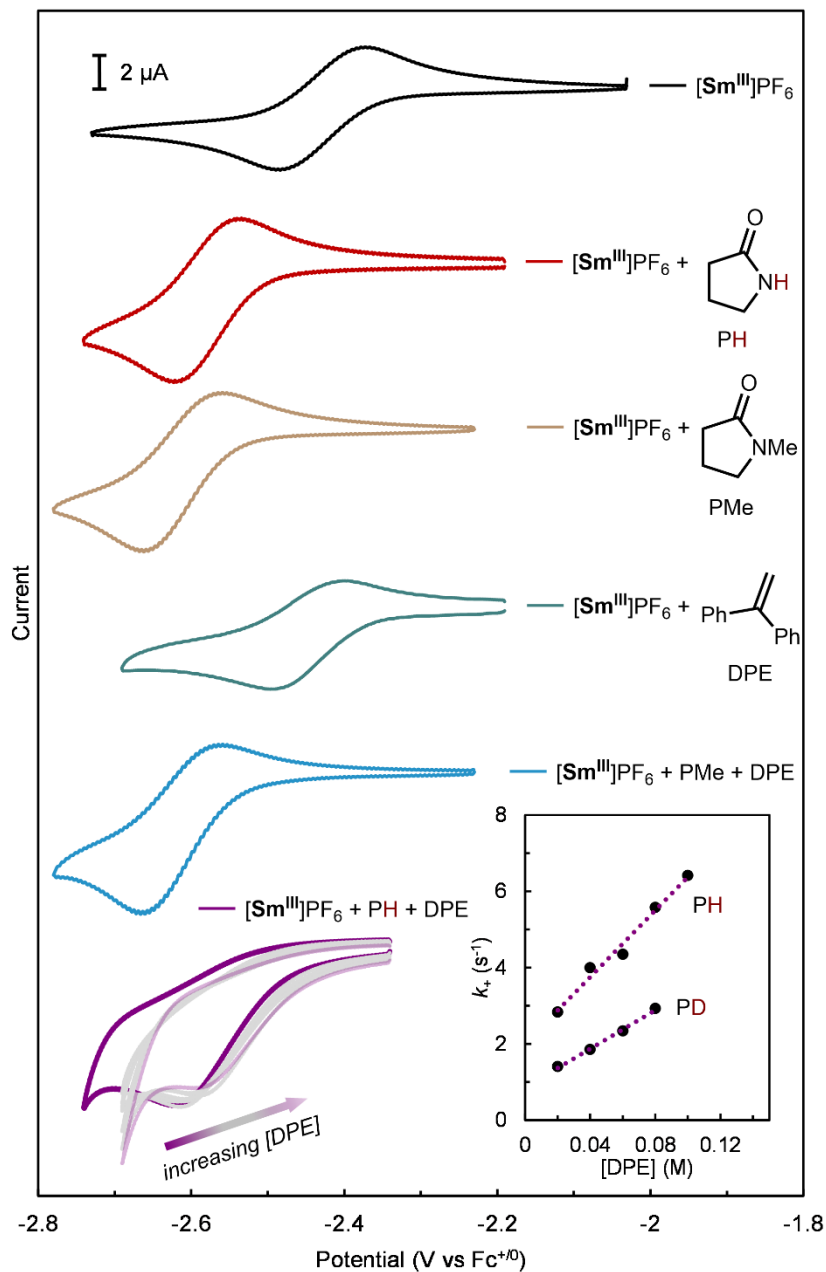


Figure 2.5: CVs of $[\text{Sm}^{\text{III}}]\text{PF}_6$ (1 mM) in the presence of combinations of PH (30 mM), PMe (30 mM), and/or DPE. The concentration of DPE is 20 mM in the blue trace and ranges from 20 to 160 mM in the purple traces. CVs were recorded at 100 mV s^{-1} in DME containing $0.2 \text{ M } n\text{-Bu}_4\text{NPF}_6$ with a glassy carbon working electrode, platinum wire counter, and $\text{Ag}^{+/0}$ pseudoreference electrode. The inset shows the plots used to extract the KIE for the reaction of Sm^{II} -PH with DPE.

39
Addition of DPE to $[\text{Sm}^{\text{III}}]\text{PF}_6$ or to $[\text{Sm}^{\text{III}}\text{-PMe}]^+$ does not significantly perturb their respective $\text{Sm}^{\text{III/II}}$ couples (blue and green traces), indicating that neither Sm^{II} nor the more reducing $\text{Sm}^{\text{II}}\text{-PMe}$ reacts irreversibly with DPE on the CV timescale. However, addition of 20 equivalents of DPE to $[\text{Sm}^{\text{III}}\text{-PH}]^+$ (purple trace) results in loss of reversibility in the $\text{Sm}^{\text{III/II}}$ couple. These data show that the presence of an N–H (instead of N–Me) bond in the electrochemically generated $\text{Sm}^{\text{II}}\text{-PH}$ adduct facilitates its reaction with DPE.

Analysis of the evolution of the cathodic peak potential $E_{p,c}$ with the scan rate enables extraction of the observed rate constant k_+ for the reaction of $\text{Sm}^{\text{II}}\text{-PH}$ with DPE under pseudo-first-order conditions (see Appendix A5.1).³⁰ The observed rate constant k_+ increases linearly with increasing concentration of DPE (Figure 2.5 inset). The proton-coupled reduction of DPE by $\text{Sm}^{\text{II}}\text{-PH}$ is therefore first order in the substrate with a rate constant of $44 \text{ M}^{-1} \text{ s}^{-1}$. Repeating this measurement with 2-pyrrolidinone-*d*₁ gives a $k_{\text{H}}/k_{\text{D}}$ ratio of 2.3. This kinetic isotope effect is similar to the value of 2.1 reported for PCET from $\text{SmI}_2/\text{H}_2\text{O}$ to anthracene that has been assigned as concerted.⁷ We note that a stepwise mechanism in the present case, comprising an uphill initial ET step followed by fast PT, cannot be discounted because of the very negative reduction potential of $\text{Sm}^{\text{II}}\text{-PH}$.

2.2.4 Thermochemical Estimates

The reactivities of $\text{Sm}^{\text{II}}\text{-PH}$ and $\text{Sm}^{\text{II}}\text{-MeOH}$ are suggestive of coordination-induced bond weakening akin to that observed with SmI_2 and alcohol or amide ligands.^{7–10} As discussed above, ill-defined SmI_2 /alcohol mixtures are not conducive to quantitative measurements of coordination-induced bond weakening at Sm^{II} owing, for example, to ill-defined speciation and solubility issues. The comparatively tractable system $\text{Sm}^{\text{II}}\text{-PH}$ provides a platform to directly interrogate this issue. Accordingly, the $\text{BDFE}_{\text{N-H}}$ of $\text{Sm}^{\text{II}}\text{-$

PH was determined using the thermochemical cycle highlighted in purple in Figure 2.6,⁴⁰ which requires determination of the Sm^{III/II} reduction potential and the pK_a of [Sm^{III}-PH]⁺.

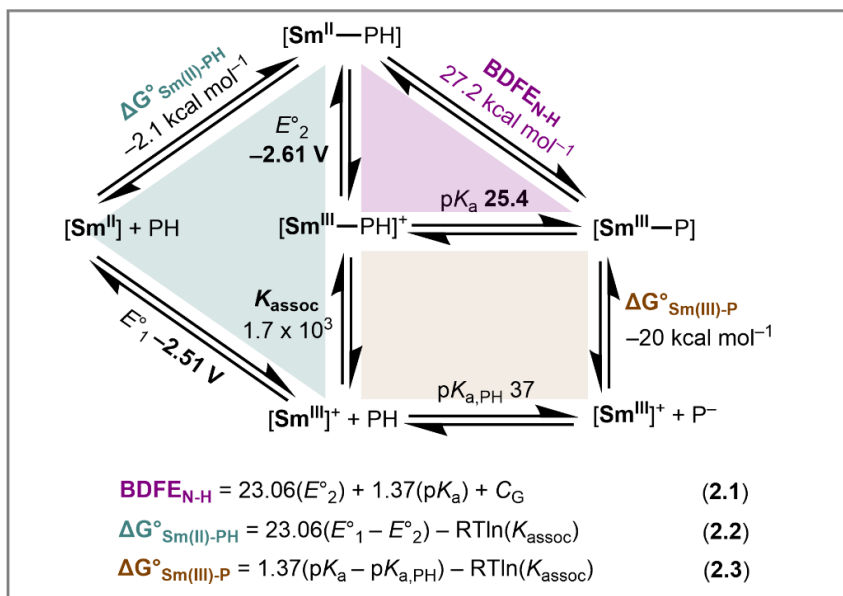


Figure 2.6: Summary of thermochemical cycles and equations with PH as the proton source.

We have collected all thermochemical data in acetonitrile because of the availability⁴¹ of reliable thermodynamic parameters and pK_a scales in this solvent.^{14,31} The crystal structure of $[\text{Sm}^{\text{III}}]\text{BPh}_4$ obtained from an MeCN solution contains bound MeCN, and NMR data are consistent with MeCN coordination in the solution phase to form a $[\text{Sm}^{\text{III}}\text{-NCMe}]^+$ adduct.²⁵ The CV of $[\text{Sm}^{\text{III}}\text{-NCMe}]\text{PF}_6$ in MeCN (0.1M $n\text{Bu}_4\text{NPF}_6$) is reversible with $E_{1/2}(\text{Sm}^{\text{III/II}}) = -2.51$ V vs $\text{Fc}^{+/0}$ (Figure 2.7, blue trace). Titration of $[\text{Sm}^{\text{III}}\text{-NCMe}]\text{PF}_6$ with PH results in a negative shift in the cathodic wave, consistent with the displacement of MeCN by the more strongly donating amide. The CV profile remains unchanged past 15 equiv PH, suggesting that all of $[\text{Sm}^{\text{III}}]\text{PF}_6$ is ligated by PH at this concentration. Increasing the concentration of PH also results in some loss of reversibility which may be attributed to the reduction of acetonitrile solvent by $\text{Sm}^{\text{II}}\text{-PH}$.³² However, there is a slight anodic return wave which becomes more pronounced at faster scan rates. This feature was used to estimate the $E_{1/2}(\text{Sm}^{\text{III/II}})$ of $[\text{Sm}^{\text{III}}\text{-PH}]^+$ as -2.61 V vs $\text{Fc}^{+/0}$ in MeCN.

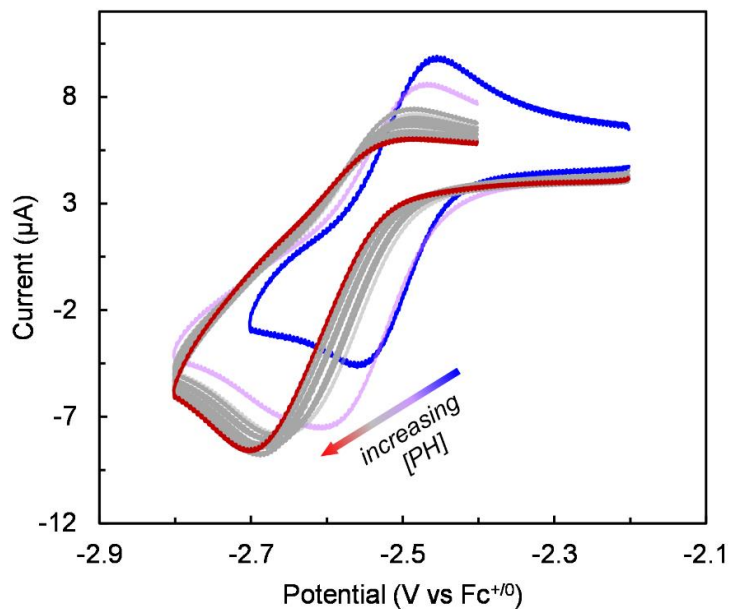


Figure 2.7: CV titration of the Sm^{III} cation [**Sm^{III}-NCMe**]PF₆ (1 mM, blue trace) with PH (1–15 equiv) at 100 mV s⁻¹ in CH₃CN containing 0.1 M *t*Bu₄NPF₆ with a glassy carbon working electrode, platinum wire counter, and Ag⁺⁰ pseudoreference electrode.

The p*K*_a of [**Sm^{III}-PH**]⁺ was measured using ¹H NMR spectroscopic titration measurements. Addition of three equivalents PH to [**Sm^{III}-NCMe**]PF₆ in CD₃CN generates [**Sm^{III}-PH**]⁺ in situ (see Appendix A6). The equilibrium binding constant for the formation of [**Sm^{III}-PH**]⁺ was determined to be $(1.7 \pm 0.7) \times 10^3$ (eqn 2.4 in Figure 2.8). [**Sm^{III}-PH**]⁺ establishes a rapid proton-transfer equilibrium with the base 1,8-diazabicyclo[5.4.0]undec-7-ene (DBU) to form **Sm^{III}-P** and [DBUH]⁺ (p*K*_a = 24.3 in CH₃CN³¹; Figure 2.8, eqn 2.5). Analysis of the chemical shifts of the equilibrium mixture (Appendix A6) yields the desired p*K*_a of [**Sm^{III}-PH**]⁺ as 25.4 ± 0.2 . Control reactions between DBU and [**Sm^{III}-NCMe**]PF₆ or a mixture of [**Sm^{III}-NCMe**]PF₆ and P*Me* revealed no interaction between these reagents in the absence of an acidic proton, ruling out DBU coordination as a competitive pathway.

With these data, along with the value of C_G in CH_3CN ($52.6 \text{ kcal mol}^{-1}$),¹⁴ the⁴³ experimental $\text{BDFE}_{\text{N-H}}$ of $\text{Sm}^{\text{II}}\text{-PH}$ is determined from eqn 2.1 in Figure 2.6 to be $27.2 \pm 0.3 \text{ kcal mol}^{-1}$.

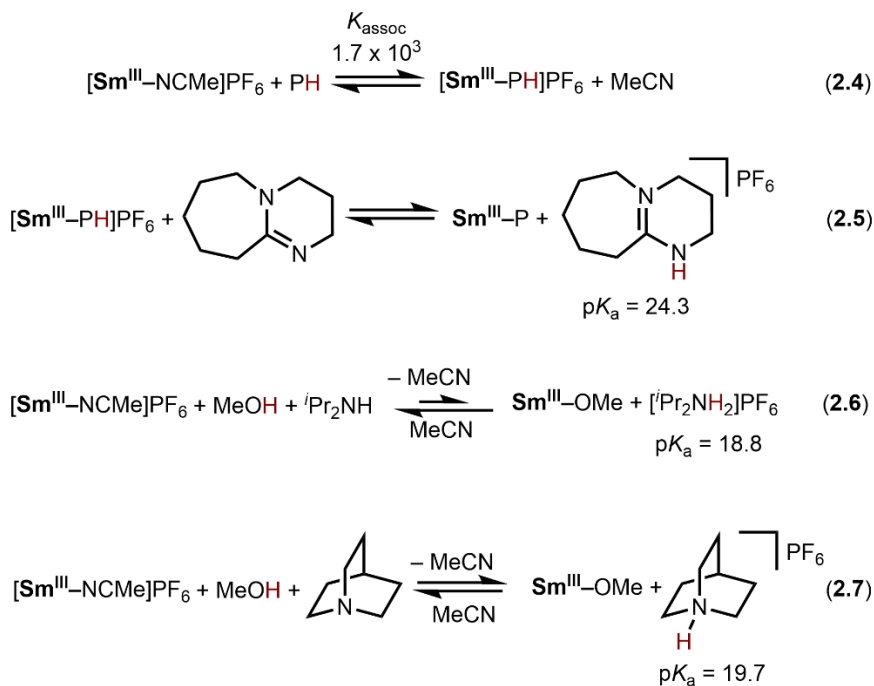


Figure 2.8: Equilibria relevant to $\text{p}K_{\text{a}}$ determinations.

The $\text{BDFE}_{\text{O-H}}$ of $\text{Sm}^{\text{II}}\text{-MeOH}$ could not be determined with eqn 2.1 because a $\text{Sm}^{\text{III/II}}$ couple could not be definitively assigned for $[\text{Sm}^{\text{II}}\text{-MeOH}]^+$. To reliably estimate $\text{BDFE}_{\text{O-H}}$ for the MeOH adduct of Sm^{II} , we employed the alternative thermodynamic cycle highlighted in purple in Figure 2.9 and represented by eqn 2.9. In CD_3CN , binding of MeOH to $[\text{Sm}^{\text{II}}\text{-NCMe}]\text{PF}_6$ is negligible. The effective $\text{p}K_{\text{a}}$ of $[\text{Sm}^{\text{II}}\text{-NCMe}]\text{PF}_6$ in the presence of MeOH ($\text{p}K_{\text{a,eff}}$) was therefore determined by titration measurements. Addition of diisopropylamine ($\text{p}K_{\text{a}} = 18.8$ in CH_3CN)³¹ or quinuclidine ($\text{p}K_{\text{a}} = 19.7$ in CH_3CN) to a mixture of $[\text{Sm}^{\text{III}}]\text{PF}_6$ and MeOH results in ^1H NMR shifts attributed to the proton-transfer equilibria in eqns 2.6 and 2.7 shown in Figure 2.8. The desired $\text{p}K_{\text{a,eff}}$ value for the

combination of $[\text{Sm}^{\text{III}}\text{-NCMe}]\text{PF}_6$ and MeOH can be extracted from either reaction as 19.9 ± 0.2 (see Appendix A6). As with DBU, neither amine interacts with $[\text{Sm}^{\text{III}}\text{-NCMe}]\text{PF}_6$ in the absence of MeOH.

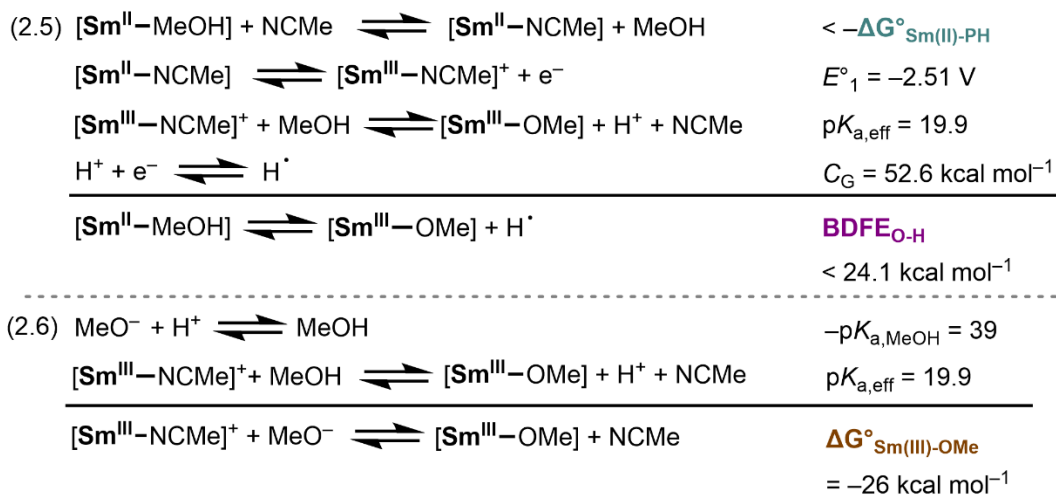
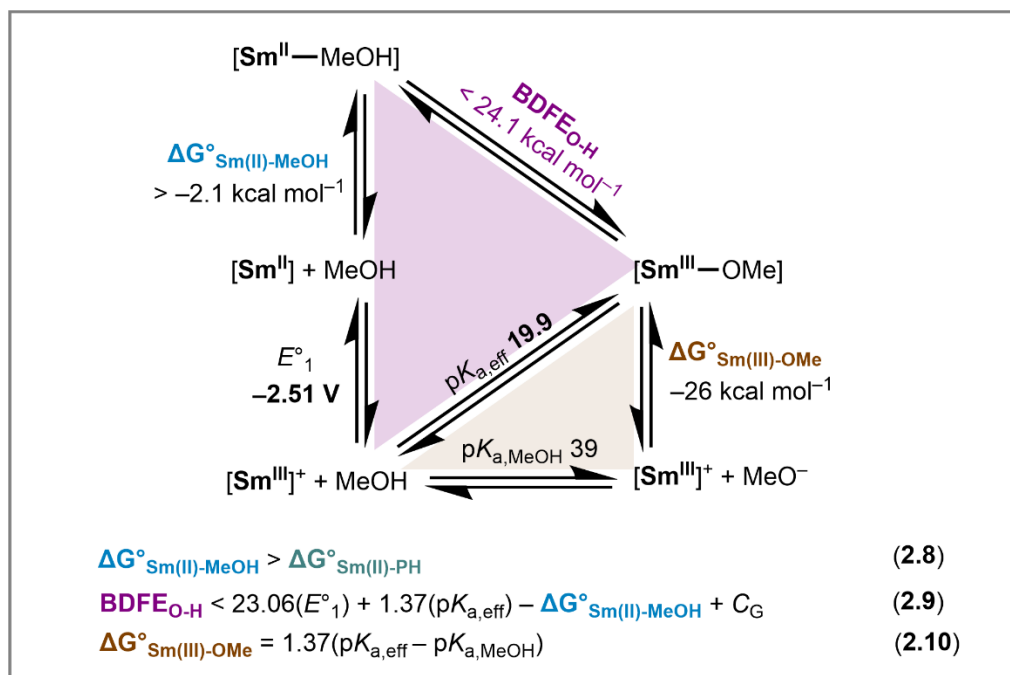


Figure 2.9: Summary of thermochemical cycles and equations with MeOH as the proton source.

The binding affinity of MeOH to Sm^{II} ($\Delta G^\circ_{\text{Sm(II)-MeOH}}$) is bracketed by cross-reference to the cycle highlighted in green in Figure 2.6 for the affinity of PH to Sm^{II} ($\Delta G^\circ_{\text{Sm(II)-PH}}$;

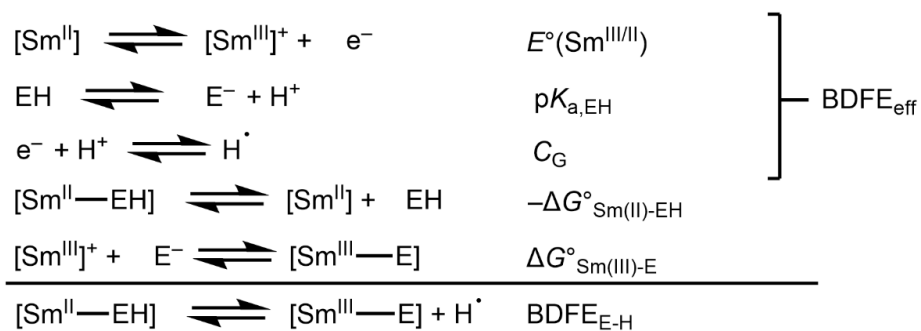
eqn 2.2). Because MeOH has a lower affinity for Sm(II) compared to PH, $\Delta G^\circ_{\text{Sm(II)-MeOH}}$ must be more positive (i.e., $\Delta G^\circ_{\text{Sm(II)-MeOH}} > -2.1 \text{ kcal mol}^{-1}$; eqn 2.8). A reliable upper limit of $\leq 24.1 \text{ kcal mol}^{-1}$ is therefore determined for the BDFE_{O-H} of **Sm^{II}**-MeOH.

2.2.5 Origins of Bond Weakening

Coordination of PH or MeOH to **Sm^{II}** yields two of the strongest reductive PCET reagents whose BDFE values have been systematically characterized.^{14,33,34} The N-H bond in **Sm^{II}**-PH is weakened by ca. 69 kcal mol^{-1} from that of free PH,¹⁰ which for comparison is 13 kcal mol^{-1} more weakened than the N-H bonds in a $\text{Mo}^{\text{I}}\text{-NH}_3$ complex previously described by Chirik and co-workers as a fascinating example of dramatic coordination-induced bond weakening.^{35,36} Similarly, O-H bond weakening in **Sm^{II}**-MeOH is more pronounced than that in $\text{Cp}_2\text{Ti}(\text{OH}_2)$ complexes by at least $\sim 10 \text{ kcal mol}^{-1}$.^{14,37,38} The magnitude of the BDFE_{N-H} of **Sm^{II}**-PH is also 10 kcal mol^{-1} weaker than the N-H bond we have measured for N,N-dimethylanilinium-appended cobaltocene, which contained the weakest experimentally determined BDFE_{N-H} that had been reported to date.³⁹

It is instructive to next consider the origins of the dramatic bond weakening determined herein. First, we note that the bulk of the difference in BDFE_{N-H} between free pyrrolidinone and **Sm^{II}**-PH is independent of coordination. Bond weakening can be regarded as an increased capacity to give up H^\bullet , or equivalently, a proton and an electron. For example, homolytic cleavage of the N-H bond in PH is thermodynamically equivalent to deprotonation to form pyrrolidinonate, followed by oxidation. Coupling deprotonation of PH to facile oxidation of any strong reductant such as **Sm^{II}** is thermodynamically much more favorable. This is formalized by defining the “effective” BDFE, BDFE_{eff}, which describes the net removal of H^\bullet from a noninteracting combination of reductant and acid

(eqn 2.11). The $BDFE_{\text{eff}}$ of the $\text{Sm}^{\text{II}}/\text{EH}$ combinations explored here can be determined⁴⁶ by the insertion of the reduction potential of $[\text{Sm}^{\text{III}}\text{-NCMe}]\text{PF}_6$ (-2.51 V) and the pK_a of PH (estimated as 37 in CH_3CN)^{40,41} or MeOH (~ 39)⁴² into eqn 2.11 to yield values of 45 and 48 kcal mol^{-1} for $\text{Sm}^{\text{II}}/\text{PH}$ and $\text{Sm}^{\text{II}}/\text{MeOH}$, respectively. These values represent bond weakening of ~ 50 kcal mol^{-1} compared to free PH and MeOH. The same values could be obtained with PH or MeOH and any reductant with $E^\circ \approx -2.5$ V.



$$BDFE_{\text{eff}} = 23.06(E^\circ(\text{Sm}^{\text{III/II}})) + 1.37(pK_{a,\text{EH}}) + C_G \quad (2.11)$$

$$BDFE_{\text{E-H}} = BDFE_{\text{eff}} - \Delta G^\circ_{\text{Sm(II)-EH}} + \Delta G^\circ_{\text{Sm(III)-E}} \quad (2.12)$$

$$\Delta BDFE = BDFE_{\text{eff}} - BDFE_{\text{E-H}} = \Delta G^\circ_{\text{Sm(III)-E}} - \Delta G^\circ_{\text{Sm(II)-EH}} \quad (2.13)$$

However, unlike some PCET reagents composed of synthetically linked but electronically decoupled ET and PT mediators,^{39,43} there is a significant difference between the $BDFE_{\text{eff}}$ and $BDFE_{\text{X-H}}$ values for $\text{Sm}^{\text{II}}/\text{PH}$ and $\text{Sm}^{\text{II}}/\text{MeOH}$. As laid out in eqns 2.11-2.13, the difference, $\Delta BDFE$, can be decomposed into the binding energy of EH to $\text{Sm}(\text{II})$ ($\Delta G^\circ_{\text{Sm(II)-EH}}$) and the affinity of E^- for $\text{Sm}(\text{III})^+$ ($\Delta G^\circ_{\text{Sm(III)-E}}$). A larger $\Delta BDFE$ is obtained with a *weaker* $\text{Sm}^{\text{II}}\text{-EH}$ association (more positive $\Delta G^\circ_{\text{Sm(II)-EH}}$) and a *stronger* $\text{Sm}^{\text{III}}\text{-E}$ interaction (more negative $\Delta G^\circ_{\text{Sm(III)-E}}$).

Because $\Delta G^\circ_{\text{Sm(II)-EH}}$ is estimated to be close to thermoneutral for the systems described here (-2.1 kcal mol^{-1} and > -2.1 kcal mol^{-1} for PH and MeOH binding to Sm^{II} , respectively), the $\text{Sm}^{\text{III}}\text{-E}$ interactions dominate the $\Delta BDFE$. $\Delta G^\circ_{\text{Sm(III)-E}}$ values were

determined using the orange-highlighted thermodynamic cycles and eqns 2.3 and 2.10⁴⁷ in Figures 2.6 and 2.9 as $-20 \text{ kcal mol}^{-1}$ for **Sm^{III}-P** and $-26 \text{ kcal mol}^{-1}$ for **Sm^{III}-OMe**. The stronger affinity of OMe^- for **Sm^{III}** results in the slightly lower $\text{BDFE}_{\text{O-H}}$ of **Sm^{II}-MeOH**, despite the **Sm^{II}/MeOH** pair having the higher BDFE_{eff} because of the somewhat weaker acidity of MeOH compared to PH. Rational modulation of the BDFE of $[\text{Sm}^{\text{II}}\text{-EH}]$ species based on the $\text{p}K_{\text{a}}$ of free EH is therefore not straightforward, as the **Sm^{III}** binding affinities of different E^- anions are not readily predictable.

An alternative strategy for BDFE weakening that emerges from eqn 2.12 is to decrease the affinity of EH for **Sm^{II}**. This conclusion is somewhat counterintuitive; indeed, while MeOH has a lower affinity for **SmI₂** in THF than H_2O , **SmI₂** is more prone to PCET reactivity in the presence of H_2O than MeOH despite the likely similarity in $\Delta G^\circ_{\text{Sm(III)-E}}$ for methoxide and hydroxide. We attribute this discrepancy to two possible origins: first, if EH is such a poor donor ligand that a $[\text{Sm}^{\text{II}}\text{-EH}]$ complex forms only in a very low equilibrium concentration, PCET (which typically requires pre-association of at least two components of the reaction) cannot occur at appreciable rates. Second, EH with lower affinity for **Sm^{II}** typically produces a less pronounced cathodic shift in **Sm^{III/II}** reduction potential.⁴ This effect is likely to counteract a more positive $\Delta G^\circ_{\text{Sm(II)-EH}}$ in eqns 2.11 and 2.12 (vide infra), resulting in a smaller degree of net bond weakening, further illustrating the complex interdependence of parameters that determine the $\text{BDFE}_{\text{X-H}}$ of $[\text{Sm}^{\text{II}}\text{-EH}]$ reagents.

2.2.6 Implications for **SmI₂-Based PCET Reagents**

Because the saturated coordination sphere of $[\text{Sm}^{\text{II}}\text{-PH}]$ is unlikely to vary between THF and MeCN solvents, the $\text{BDFE}_{\text{N-H}}$ of **Sm^{II}-PH** is expected to be very similar in these two solvents.¹⁴ This assumption enables comparison of the $\text{BDFE}_{\text{N-H}}$ of **Sm^{II}-PH**

determined here as $27.2 \text{ kcal mol}^{-1}$ to the reported $\text{BDFE}_{\text{N-H}}$ of the PH adduct of SmI_2 ⁴⁸ in THF ($\text{SmI}_2(\text{THF})_n(\text{PH})_m$, $25.3 \text{ kcal mol}^{-1}$),¹⁰ suggesting that the $\text{BDFE}_{\text{X-H}}$ of $[\text{Sm}^{\text{II}}-\text{EH}]$ species is nearly invariable with the coordination sphere of Sm^{II} . However, as laid out in the introduction, the known PCET reactivity of $\text{SmI}_2(\text{THF})_n(\text{PH})_m$ could still be accessed with a $\text{BDFE}_{\text{N-H}}$ as high as 41 kcal mol^{-1} , leading to the inverse conclusion that $[\text{Sm}^{\text{II}}-\text{EH}]$ BDFE 's are highly sensitive to supporting ligands. In this section, we reason that the latter conclusion is more likely.

The oxidation of SmI_2 shifts negative by up to 0.77 V in THF with the addition of excess PMe .⁴ As shown in Figure 2.5, PMe and PH coordination have similar effects on the $\text{Sm}^{\text{III/II}}$ reduction potential of $[\text{Sm}^{\text{III}}]\text{PF}_6$. The $\text{Sm}^{\text{III/II}}$ reduction potential of $\text{SmI}_2(\text{THF})_n(\text{PH})_m$ can therefore be approximated as $\sim -2.2 \text{ V vs Fc}^{+/0}$,⁴⁴ 0.4 V positive of that of $\text{Sm}^{\text{II}}-\text{PH}$ ($-2.58 \text{ V vs Fc}^{+/0}$ in DME). The relationship between $\text{BDFE}_{\text{X-H}}$ and E° varies dramatically across different classes of metal-bound ligands. For example, for a series of $[\text{Cu}^{\text{II}}-\text{OH}_2]$ complexes with varied electron donating/withdrawing properties in the supporting ligand backbone, a 0.38 V increase in E° is offset by a decrease in $\text{p}K_{\text{a}}$ such that the $\text{BDFE}_{\text{O-H}}$ of the aquo ligand increases by only 3 kcal mol^{-1} .⁴⁵ By contrast, the $\text{BDFE}_{\text{N-H}}$ of a Ru^{II} -bound imidazole fragment increases by almost 18 kcal mol^{-1} with the incorporation of electron-withdrawing groups in the ancillary ligands that shift E° positive by 0.93 V but have virtually no effect on the $\text{p}K_{\text{a}}$.⁴⁶

We posit that the $\text{p}K_{\text{a}}$ of a $[\text{Sm}^{\text{III}}-\text{EH}]^+$ complex is unlikely to depend strongly on the supporting ligands (consequently, $\text{BDFE}_{\text{X-H}}$ should most strongly correlate with $E^\circ(\text{Sm}^{\text{III/II}})$). For a given EH , the $\text{p}K_{\text{a}}$ of $[\text{Sm}^{\text{III}}-\text{EH}]^+$ is dictated by the binding energy of EH to $\text{Sm}(\text{III})^+$ ($\Delta G^\circ_{\text{Sm}(\text{III})-\text{EH}}$) and the affinity of E^- for $\text{Sm}(\text{III})^+$ ($\Delta G^\circ_{\text{Sm}(\text{III})-\text{E}}$) (e.g., eqn

2.3). When the former becomes more favorable, the pK_a increases. It seems unlikely that⁴⁹ a Sm(III)^+ complex with a bulky, strongly chelating ligand (e.g., $[\text{Sm}^{\text{III}}]\text{PF}_6$) would have a higher affinity for EH than a complex with more labile monodentate ligands (e.g., $\text{SmI}_2(\text{THF})_n(\text{PH})_m$), so the predominant mechanism by which increasing E° could be counterbalanced by decreasing pK_a correlates with the variation of $\Delta G^\circ_{\text{Sm(III)-E}}$.

Farran and Hoz measured the strength of $\Delta G^\circ_{\text{Sm(III)-E}}$ between $[\text{SmI}_2(\text{THF})_n]^+$ and the benzophenone ketyl radical anion ($\text{Ph}_2\text{CO}^{\cdot-}$) as $-19 \text{ kcal mol}^{-1}$ based on inner-sphere ET equilibria.⁶ We therefore sought to access this value with $[\text{Sm}^{\text{III}}]^+$ in order to make a direct comparison of $\Delta G^\circ_{\text{Sm(III)-E}}$ values for the same Sm^{III} -alkoxide fragment in these dramatically different coordination spheres.

Reduction of benzophenone by Sm^{II} is downhill even in the absence of additional driving force from alkoxide binding ($\Delta E^\circ = 150 \text{ mV}$ in DME). Accordingly, the addition of 1 equiv of benzophenone to 1 mM Sm^{II} in DME containing 0.2 M $n\text{Bu}_4\text{NPF}_6$ results in an immediate color change from dark green to dark purple. The open circuit potential of the solution shifts from -2.5 to -1.7 V vs $\text{Fc}^{+/0}$. Sweeping positive from open circuit reveals an irreversible anodic wave with $E_{p,a} = -1.62 \text{ V}$ vs $\text{Fc}^{+/0}$ (Figure 2.10A, red trace). The same wave is present in the CV of 1 mM $[\text{Sm}^{\text{III}}]\text{PF}_6$ with 1 equiv of benzophenone (Figure A31). In both systems, the anodic wave shifts positive and gains reversibility with increasing benzophenone concentration. Beyond 10 mM benzophenone, the shift in $E_{1/2}$ is linear with $\log([\text{benzophenone}])$ with a slope of 60.8 mV/dec (Figure 2.10A).

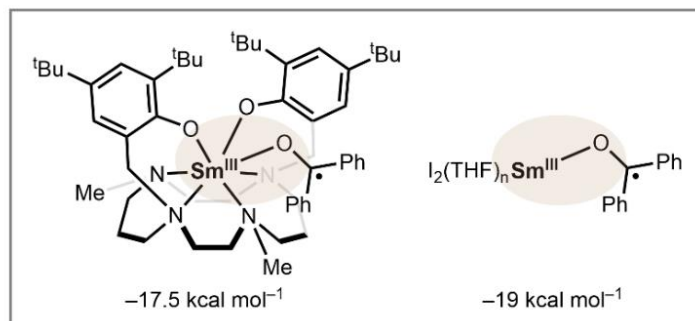
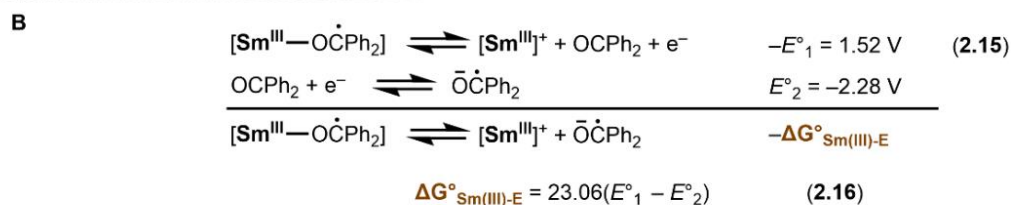
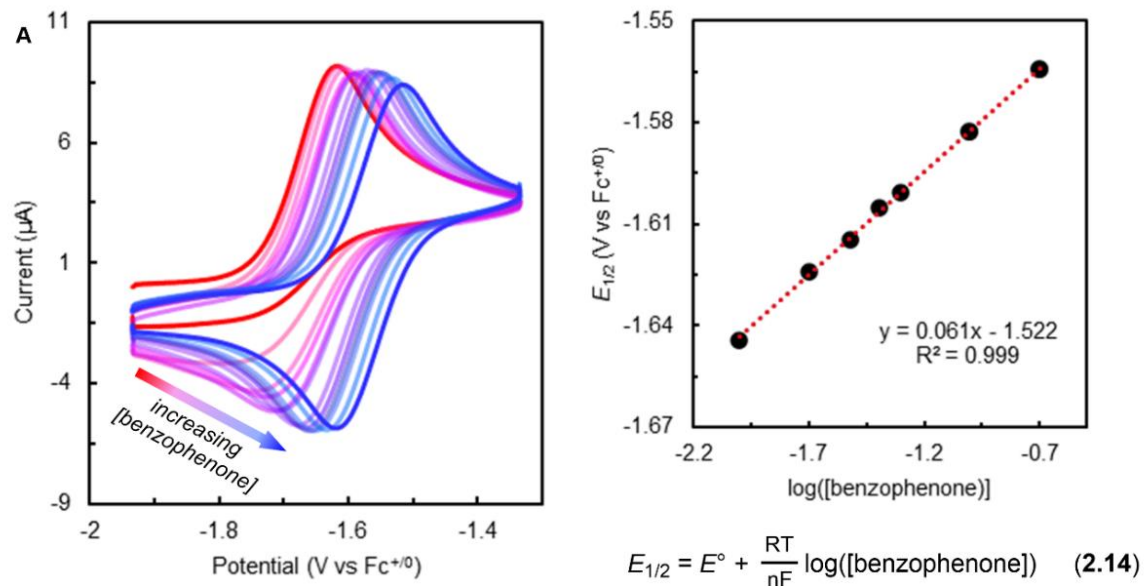


Figure 2.10: (A) CV titration of the Sm^{III} -ketyl adduct $\text{Sm}^{\text{III}}\text{-OCPh}_2^{\bullet}$ (1 mM) with benzophenone (1–200 equiv) and plot of $E_{1/2}$ as a function of benzophenone concentration fitting eqn 2.14. CVs are recorded at 100 mV s^{-1} in DME containing $0.2 \text{ M } ^n\text{Bu}_4\text{NPF}_6$ with a glassy carbon working electrode, platinum wire counter, and $\text{Ag}^{+/0}$ pseudoreference electrode. (B) Thermochemical cycle used to determine $\Delta G^\circ_{\text{Sm(III)-E}}$ for $\text{Sm}^{\text{III}}\text{-OCPh}_2^{\bullet}$ and comparison with $\Delta G^\circ_{\text{Sm(III)-E}}$ reported for the analogous SmI_2 -based species,⁶ which we represent for simplicity as $\text{I}_2(\text{THF})_n\text{Sm-OCPh}_2^{\bullet}$.

These data are consistent with the assignment of the new anodic feature to the⁵¹ oxidation of a $\text{Sm}^{\text{III}}\text{-OCPh}_2^{\bullet}$ species ($\text{Sm}^{\text{III}}\text{-OCPh}_2^{\bullet}$) generated in situ from the reaction of Sm^{II} and benzophenone (Figure 2.10B, eqn 2.15). The oxidation is coupled to benzophenone dissociation. At high [benzophenone], the reverse process becomes fast, giving rise to the return cathodic wave corresponding to benzophenone coordination and reduction. In this concentration regime, the system can be approximated as Nernstian and is described by eqn 2.14.

The intercept of the plot of $\log([\text{benzophenone}])$ vs $E_{1/2}$ provides E° for the net equilibrium process as -1.52 V vs $\text{Fc}^{+/0}$. Using the Hess cycle in Figure 2.10B and eqn 2.16, the summation of this reaction with the reduction of benzophenone (-2.28 V vs $\text{Fc}^{+/0}$ in DME with 0.2 M $n\text{Bu}_4\text{NPF}_6$ on glassy carbon, Figure A30) predicts $\Delta G^{\circ}_{\text{Sm(III)-E}}$ for $\text{Sm}^{\text{III}}\text{-OCPh}_2^{\bullet}$ as -17.5 kcal mol⁻¹. The Sm^{III} -alkoxide interaction strengths in $\text{Sm}^{\text{III}}\text{-OCPh}_2^{\bullet}$ and the analogous SmI_2 -based species, formulated for simplicity as $\text{I}_2(\text{THF})_n\text{Sm-OCPh}_2^{\bullet}$, are therefore of very similar magnitude, despite the 1 V difference in the reduction potential of the Sm^{II} reagents. Furthermore, while the simplified representation of $\text{I}_2(\text{THF})_n\text{Sm-OCPh}_2^{\bullet}$ does not account for any rapid dimerization or ligand scrambling equilibria that might occur at this state, these processes (if they exist) are contained in the reported $\Delta G^{\circ}_{\text{Sm(III)-E}}$ value, leading to a possible overestimation of the interaction strength (more negative $\Delta G^{\circ}_{\text{Sm(III)-E}}$). Because the much less labile coordination sphere of Sm^{II} makes it less prone to such stabilizing equilibria, the $\Delta G^{\circ}_{\text{Sm(III)-E}}$ for the two $[\text{Sm}^{\text{III}}\text{-OCPh}_2^{\bullet}]$ species may be even more comparable.

Based on this comparison, we extrapolate that P^- should have a similar affinity for $[\text{Sm}^{\text{III}}]^+$ and $[\text{SmI}_2(\text{THF})_n(\text{PH})_{m-1}]^+$, implying that the difference in reduction potentials

between $\text{Sm}^{\text{II}}\text{-PH}$ and $\text{SmI}_2(\text{THF})_n(\text{PH})_m$ is unlikely to be canceled out by an opposite⁵² difference in $\text{p}K_{\text{a}}$. This conclusion is consistent with evidence suggesting that SmBr_2 , a substantially stronger reductant than SmI_2 , induces greater O–H bond weakening in THF/ H_2O mixtures.⁴⁷ As a result, we suspect that the $\text{BDFE}_{\text{N-H}}$ of $\text{SmI}_2(\text{THF})_n(\text{PH})_m$ is closer to 35 than 25 kcalmol^{-1} . Importantly, this analysis does not account for additional driving force for the loss of H^\bullet from $\text{SmI}_2(\text{THF})_n(\text{PH})_m$ gained from oligomerization or precipitation. However, it does motivate further development of $[\text{Sm}^{\text{II}}\text{-EH}]$ -based PCET reagents whose $\text{BDFE}_{\text{X-H}}$ values can be tuned by E° .

2.2.7 Considerations for Sm-Mediated Electrocatalysis

Despite the versatile role Sm-mediated reductions serve in synthesis, such systems to date have overwhelmingly required the use of stoichiometric equivalents of Sm. The thermochemical studies presented above traverse the hypothetical steps needed to electrochemically regenerate $[\text{Sm}^{\text{II}}\text{-EH}]$ from $[\text{Sm}^{\text{III}}\text{-E}]$ (Figure 2.11). PCET from $\text{Sm}^{\text{II}}\text{-PH}$ (step 1) generates $\text{Sm}^{\text{III}}\text{-P}$, which is monomeric and soluble in organic solvents, unlike the multimeric $[\text{Sm}^{\text{III}}\text{-E}]$ products obtained from SmI_2/EH in the absence of a bulky supporting ligand.¹⁵ $\text{Sm}^{\text{III}}\text{-P}$ can be reversibly protonated by $[\text{DBUH}]^+$ in MeCN to generate $[\text{Sm}^{\text{III}}\text{-PH}]^+$ (step 2). This demonstration of selective proton transfer to $\text{Sm}^{\text{III}}\text{-alkoxides}$ is of particular note, as the cleavage of strong f-element-oxygen bonds has been cited as the primary barrier to many possible catalytic transformations.⁴⁸ Finally, the chelating ligand supports reversible electrochemical reduction back to the Sm^{II} state $\text{Sm}^{\text{II}}\text{-PH}$ (step 3).

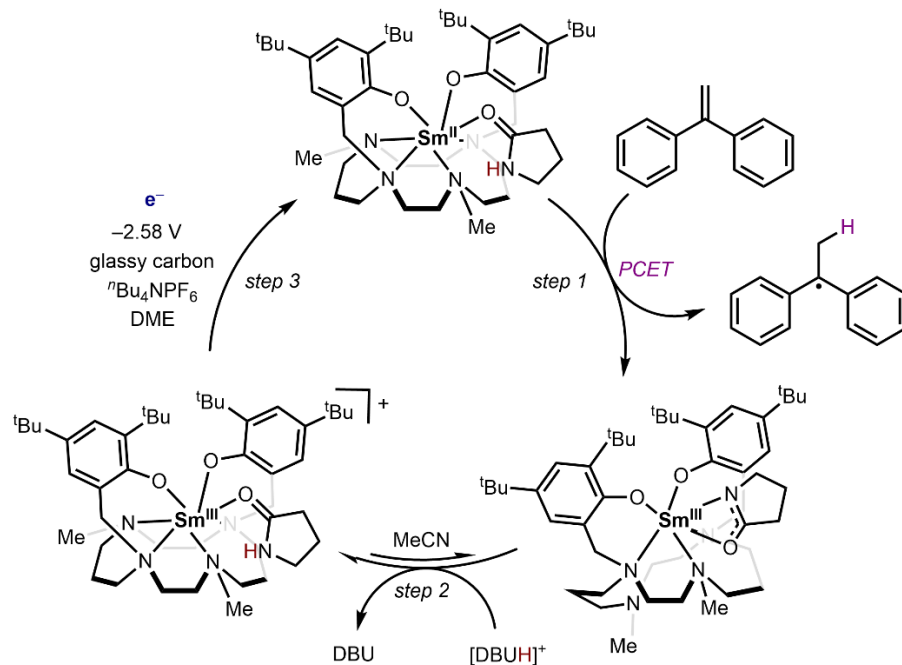


Figure 2.11. Steps demonstrated in a hypothetical Sm-mediated electrocatalytic PCET cycle.

Attempts to integrate the individual steps in Figure 2.11 into a one-pot electrocatalytic reaction have thus far been unsuccessful because of rapid electrode-mediated HER with the acids used in the protonation step ([DBUH]⁺, alkylammoniums) at the negative potentials required to access the relevant Sm^{III/II} couples. Identification of an electrode/acid combination with slow electrode-mediated HER kinetics (while retaining rapid Sm^{III/II} heterogeneous electron transfer kinetics) is hence desirable toward realizing Figure 2.11. However, we note that the generation of species with $BDFE_{X-H} < 28 \text{ kcal mol}^{-1}$ by successive protonation and electrochemical reduction steps necessitates holding the electrode at a $> 1 \text{ V}$ overpotential relative to the thermodynamic HER potential of the required acid. Few acids circumvent electrode-mediated HER at such high overpotentials.⁴⁹ Therefore, tuning the $BDFE_{X-H}$ of the [Sm^{II}-EH] species to somewhat higher values (> 30

kcal mol⁻¹) may be prudent to expand the acid and electrode combinations that could⁵⁴ serve to regenerate the PCET donor without substantial background HER.³⁹

2.3 Conclusions

To close, the ((^tBu²ArO)₂Me₂cyclam)Sm^{II} complex **Sm^{II}** binds 2-pyrrolidinone or MeOH to generate remarkably strong sources of H[•]. The well-defined nature of these complexes, as well as their oxidized and deprotonated congeners, enables direct measurement of thermodynamic parameters necessary to reliably estimate their BDFE_{X-H} values as 27.2 kcal mol⁻¹ and < 24.1 kcal mol⁻¹, and we provide evidence and arguments to suggest that these values are likely appreciably weaker than those derived from SmI₂ in THF in the presence of related proton donors. Nevertheless, these complexes cement the view that Sm^{II} coordination induces the most significant bond weakening reported to date. The origins of this effect lie in the reductant strength of Sm^{II} and in the very strong Sm^{III}-alkoxide (or -pyrrolidinonate) interactions in the net PCET products. While Sm^{III/II} redox potentials vary dramatically with the donor strength of ancillary ligands, we demonstrate that predominantly ionic Sm^{III}-alkoxide bond strengths are relatively insensitive to the makeup of the inner coordination sphere, pointing to strategies for rationally tuning [Sm^{II}-EH] BDFE values via E° . The detailed thermochemical description of electron, proton, and hydrogen atom transfer at samarium presented in this chapter serves as the foundation for development of samarium-mediated (electro)catalysis with applications to organic synthesis and small-molecule reduction described in the following chapters.

REFERENCES

- (1) Girard, P.; Namy, J. L.; Kagan, H. B. Divalent lanthanide derivatives in organic synthesis. 1. Mild preparation of samarium iodide and ytterbium iodide and their use as reducing or coupling agents. *J. Am. Chem. Soc.* **1980**, *102* (8), 2693–2698.
- (2) Szostak, M.; Fazakerley, N. J.; Parmar, D.; Procter, D. J. Cross-coupling reactions using samarium(II) iodide. *Chem. Rev.* **2014**, *114* (11), 5959–6039.
- (3) Szostak, M.; Procter, D. J. Beyond samarium diiodide: vistas in reductive chemistry mediated by lanthanides(II). *Angew. Chem. Int. Ed.* **2012**, *51* (37), 9238–9256.
- (4) Shabangi, M.; Sealy, J. M.; Fuchs, J. R.; Flowers, R. A. The effect of cosolvent on the reducing power of SmI₂ in tetrahydrofuran. *Tetrahedron Lett.* **1998**, *39* (25), 4429–4432.
- (5) Shabangi, M.; Flowers, R. A. Electrochemical investigation of the reducing power of SmI₂ in THF and the effect of HMPA cosolvent. *Tetrahedron Lett.* **1997**, *38* (7), 1137–1140.
- (6) Farran, H.; Hoz, S. Quantifying the electrostatic driving force behind SmI₂ reductions. *Org. Lett.* **2008**, *10* (21), 4875–4877.
- (7) Chciuk, T. V.; Flowers, R. A. Proton-coupled electron transfer in the reduction of arenes by SmI₂–water complexes. *J. Am. Chem. Soc.* **2015**, *137* (35), 11526–11531.
- (8) Kolmar, S. S.; Mayer, J. M. SmI₂(H₂O)_n reduction of electron rich enamines by proton-coupled electron transfer. *J. Am. Chem. Soc.* **2017**, *139* (31), 10687–10692.

- (9) Chciuk, T. V.; Anderson, W. R.; Flowers, R. A. Proton-coupled electron transfer in the reduction of carbonyls by samarium diiodide–water complexes. *J. Am. Chem. Soc.* **2016**, *138* (28), 8738–8741.
- (10) Chciuk, T. V.; Li, A. M.; Vazquez-Lopez, A.; Anderson, W. R.; Flowers, R. A. Secondary amides as hydrogen atom transfer promoters for reactions of samarium diiodide. *Org. Lett.* **2017**, *19* (1), 290–293.
- (11) Ramírez-Solís, A.; Boekell, N. G.; León-Pimentel, C. I.; Saint-Martin, H.; Bartulovich, C. O.; Flowers, R. A. Ammonia solvation vs aqueous solvation of samarium diiodide. A theoretical and experimental approach to understanding bond activation upon coordination to Sm(II). *J. Org. Chem.* **2022**, *87* (3), 1689–1697.
- (12) Bartulovich, C. O.; Flowers, R. A. Coordination-induced O–H bond weakening in Sm(II)-water complexes. *Dalton Trans.* **2019**, *48* (43), 16142–16147.
- (13) Boekell, N. G.; Flowers, R. A. Coordination-induced bond weakening. *Chem. Rev.* **2022**, *122* (16), 13447–13477.
- (14) Agarwal, R. G.; Coste, S. C.; Groff, B. D.; Heuer, A. M.; Noh, H.; Parada, G. A.; Wise, C. F.; Nichols, E. M.; Warren, J. J.; Mayer, J. M. Free energies of proton-coupled electron transfer reagents and their applications. *Chem. Rev.* **2022**, *122* (1), 1–49.
- (15) Ashida, Y.; Arashiba, K.; Nakajima, K.; Nishibayashi, Y. Molybdenum-catalysed ammonia production with samarium diiodide and alcohols or water. *Nature* **2019**, *568* (7753), 536–540.
- (16) Ashida, Y.; Arashiba, K.; Tanaka, H.; Egi, A.; Nakajima, K.; Yoshizawa, K.; Nishibayashi, Y. Molybdenum-catalyzed ammonia formation using simple

- monodentate and bidentate phosphines as auxiliary ligands. *Inorg. Chem.* **2019**, 58⁵⁷ (14), 8927–8932.
- (17) BDFE_{C-H} values for anthracene and the enamine determined by subtracting the entropy of H[•] solvation ($TS^\circ(\text{H}^\bullet)_{\text{solv}} = 6.4 \text{ kcal mol}^{-1}$) from reported BDE values according to ref. 14.
- (18) Stein, S. E.; Brown, R. L. Prediction of carbon-hydrogen bond dissociation energies for polycyclic aromatic hydrocarbons of arbitrary size. *J. Am. Chem. Soc.* **1991**, 113 (3), 787–793.
- (19) Luo, Y.-R. *Comprehensive Handbook of Chemical Bond Energies*; Taylor and Francis Group, LLC: Boca Raton, FL, 2007.
- (20) Mayer and coworkers report that the reaction of a 0.024 M solution of the enamine substrate with 0.072 M SmI₂ and 3.6 M H₂O is complete in 600 s. Because SmI₂ is used in excess, the minimum concentration of [Sm^{II}-OH₂] is estimated as 0.024 M (after all substrate has been consumed). The average reaction velocity is $4 \times 10^{-5} \text{ M s}^{-1}$. Assuming a first order dependence on Sm(II) and substrate, the rate constant k_1 is estimated as $2 \times 10^{-2} \text{ M}^{-1} \text{ s}^{-1}$. The Supporting Information contains an estimate of k_1 for this reaction from a more rigorous integrated rate law expression, but the ultimate bracketed BDFE is relatively insensitive to this estimate.
- (21) Chalkley, M. J.; Peters, J. C. Relating N–H bond strengths to the overpotential for catalytic nitrogen fixation. *Eur. J. Inorg. Chem.* **2020**, 2020 (15–16), 1353–1357.
- (22) Tarantino, K. T.; Liu, P.; Knowles, R. R. Catalytic ketyl-olefin cyclizations enabled by proton-coupled electron transfer. *J. Am. Chem. Soc.* **2013**, 135 (27), 10022–10025.

- (23) Park, Y.; Kim, S.; Tian, L.; Zhong, H.; Scholes, G. D.; Chirik, P. J. Visible light⁵⁸ enables catalytic formation of weak chemical bonds with molecular hydrogen. *Nat. Chem.* **2021**, *13* (10), 969–976.
- (24) Maria, L.; Santos, I. C.; Alves, L. G.; Marçalo, J.; Martins, A. M. Rare earth metal complexes anchored on a new dianionic bis(phenolate)dimethylaminocyclam ligand. *J. Organomet. Chem.* **2013**, *728*, 57–67.
- (25) Maria, L.; Soares, M.; C. Santos, I.; R. Sousa, V.; Mora, E.; Marçalo, J.; V. Luzyanin, K. A novel samarium(II) complex bearing a dianionic bis(phenolate)cyclam ligand: synthesis, structure and electron-transfer reactions. *Dalton Trans.* **2016**, *45* (9), 3778–3790.
- (26) Sun, L.; Sahloul, K.; Mellah, M. Use of electrochemistry to provide efficient SmI₂ catalytic system for coupling reactions. *ACS Catal.* **2013**, *3* (11), 2568–2573.
- (27) Arashiba, K.; Kanega, R.; Himeda, Y.; Nishibayashi, Y. Electrochemical reduction of samarium triiodide into samarium diiodide. *Chem. Lett.* **2020**, *49* (10), 1171–1173.
- (28) Halter, D. P.; Palumbo, C. T.; Ziller, J. W.; Gembicky, M.; Rheingold, A. L.; Evans, W. J.; Meyer, K. Electrocatalytic H₂O reduction with f-elements: mechanistic insight and overpotential tuning in a series of lanthanide complexes. *J. Am. Chem. Soc.* **2018**, *140* (7), 2587–2594.
- (29) Veauthier, J. M.; Schelter, E. J.; Carlson, C. N.; Scott, B. L.; Re, R. E. D.; Thompson, J. D.; Kiplinger, J. L.; Morris, D. E.; John, K. D. Direct comparison of the magnetic and electronic properties of samarocene and ytterbocene terpyridine complexes. *Inorg. Chem.* **2008**, *47* (13), 5841–5849.

- (30) Savéant, J.-M. *Elements of Molecular and Biomolecular Electrochemistry*; John Wiley & Sons, Inc: Hoboken, New Jersey, 2006.
- (31) Tshepelevitsh, S.; Kütt, A.; Lõkov, M.; Kaljurand, I.; Saame, J.; Heering, A.; Plieger, P. G.; Vianello, R.; Leito, I. On the basicity of organic bases in different media. *Eur. J. Org. Chem.* **2019**, 2019 (40), 6735–6748.
- (32) Prasad, E.; Flowers, R. A. Mechanistic impact of water addition to SmI₂: consequences in the ground and transition state. *J. Am. Chem. Soc.* **2005**, 127 (51), 18093–18099.
- (33) Chalkley, M. J.; Oyala, P. H.; Peters, J. C. Cp* noninnocence leads to a remarkably weak C–H bond via metallocene protonation. *J. Am. Chem. Soc.* **2019**, 141 (11), 4721–4729.
- (34) Schild, D. J.; Drover, M. W.; Oyala, P. H.; Peters, J. C. Generating potent C–H PCET donors: ligand-induced Fe-to-ring proton migration from a Cp*Fe^{III}–H complex demonstrates a promising strategy. *J. Am. Chem. Soc.* **2020**, 142 (44), 18963–18970.
- (35) Bezdek, M. J.; Guo, S.; Chirik, P. J. Coordination-induced weakening of ammonia, water, and hydrazine X–H bonds in a molybdenum complex. *Science* **2016**, 354 (6313), 730–733.
- (36) The literature BDFE_{X-H} values originally determined using the Bordwell equation have been adjusted here by the recently reported correction to the C_G value in acetonitrile (ref. 14).
- (37) Cuerva, J. M.; Campaña, A. G.; Justicia, J.; Rosales, A.; Oller-López, J. L.; Robles, R.; Cárdenas, D. J.; Buñuel, E.; Oltra, J. E. Water: the ideal hydrogen-atom source in

free-radical chemistry mediated by Ti^{III} and other single-electron-transfer metals.

Angew. Chem. Int. Ed. **2006**, *45* (33), 5522–5526.

- (38) This value is based on the gas-phase $\text{BDFE}_{\text{O-H}}$ of MeOH reported as $96.4 \text{ kcal mol}^{-1}$ (ref 14).
- (39) Chalkley, M. J.; Garrido-Barros, P.; Peters, J. C. A molecular mediator for reductive concerted proton-electron transfers via electrocatalysis. *Science* **2020**, *369* (6505), 850–854.
- (40) The pK_a of PH was estimated in MeCN using the solvent conversion equations developed by Leito et al (ref 39) and the pK_a of PH in DMSO: Bordwell, F. G. Equilibrium acidities in dimethyl sulfoxide solution. *Acc. Chem. Res.* 1988, *21* (12), 456–463.
- (41) Kütt, A.; Tshepelevitsh, S.; Saame, J.; Lõkov, M.; Kaljurand, I.; Selberg, S.; Leito, I. Strengths of acids in acetonitrile. *Eur. J. Org. Chem.* **2021**, *2021* (9), 1407–1419.
- (42) Felton, G. A. N.; Vannucci, A. K.; Okumura, N.; Lockett, L. T.; Evans, D. H.; Glass, R. S.; Lichtenberger, D. L. Hydrogen generation from weak acids: electrochemical and computational studies in the $[(\eta^5\text{-C}_5\text{H}_5)\text{Fe}(\text{CO})_2]_2$ system. *Organometallics* **2008**, *27* (18), 4671–4679.
- (43) Manner, V. W.; Mayer, J. M. Concerted proton–electron transfer in a ruthenium terpyridyl-benzoate system with a large separation between the redox and basic sites. *J. Am. Chem. Soc.* **2009**, *131* (29), 9874–9875.
- (44) Enemærke, R. J.; Hertz, T.; Skrydstrup, T.; Daasbjerg, K. Evidence for ionic samarium(II) species in THF/HMPA solution and investigation of their electron-donating properties. *Chem. – Eur. J.* **2000**, *6* (20), 3747–3754.

- (45) Dhar, D.; Yee, G. M.; Spaeth, A. D.; Boyce, D. W.; Zhang, H.; Dereli, B.; Cramer,⁶¹ C. J.; Tolman, W. B. Perturbing the copper(III)–hydroxide unit through ligand structural variation. *J. Am. Chem. Soc.* **2016**, *138* (1), 356–368.
- (46) Wu, A.; Masland, J.; Swartz, R. D.; Kaminsky, W.; Mayer, J. M. Synthesis and characterization of ruthenium bis(β -diketonato) pyridine-imidazole complexes for hydrogen atom transfer. *Inorg. Chem.* **2007**, *46* (26), 11190–11201.
- (47) Ramírez-Solís, A.; Bartulovich, C. O.; Chciuk, T. V.; Hernández-Cobos, J.; Saint-Martin, H.; Maron, L.; Anderson, W. R.; Li, A. M.; Flowers, R. A. Experimental and theoretical studies on the implications of halide-dependent aqueous solvation of Sm(II). *J. Am. Chem. Soc.* **2018**, *140* (48), 16731–16739.
- (48) Wedal, J. C.; Evans, W. J. A rare-earth metal retrospective to stimulate all fields. *J. Am. Chem. Soc.* **2021**, *143* (44), 18354–18367.
- (49) McCarthy, B. D.; Martin, D. J.; Rountree, E. S.; Ullman, A. C.; Dempsey, J. L. Electrochemical reduction of Brønsted acids by glassy carbon in acetonitrile—implications for electrocatalytic hydrogen evolution. *Inorg. Chem.* **2014**, *53* (16), 8350–8361.

HIGHLY SELECTIVE FE-CATALYZED NITROGEN FIXATION TO HYDRAZINE ENABLED BY SM(II) REAGENTS WITH TAILORED REDOX POTENTIAL AND PKA

Reproduced in part with permission from Boyd, E.A.; Peters, J. C. *J. Am. Chem. Soc.* 2023, 145, 14784. doi: [10.1021/jacs.3c03352](https://doi.org/10.1021/jacs.3c03352)

3.1 Introduction

The field of molecular N₂ reduction (N₂R) catalysis has proliferated in the decades following Chatt's early discovery that transition metals (e.g., Mo/W) could facilitate the reductive protonation of coordinated N₂.^{1,2} Schrock's 2003 report of a mechanistically well-defined synthetic Mo catalyst for N₂-to-NH₃ conversion invigorated interest.³ New Mo catalysts,⁴ catalysts featuring other metals (e.g., Fe),⁵ and the development of varied reaction conditions combined with the low-temperature characterization of highly reactive M-N_xH_y species, alongside studies of their independent reactivity patterns, have significantly broadened our understanding of factors that underpin N₂R by synthetic coordination complexes.² Figure 3.1 summarizes the distal, alternating, and "hybrid" mechanisms that have been widely considered for N₂R to NH₃ and/or hydrazine (N₂H₄).⁶⁻

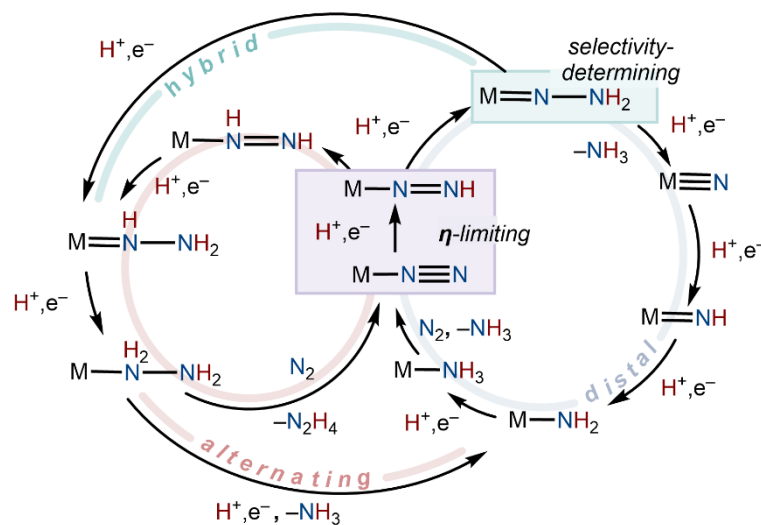


Figure 3.1: Distal, alternating, and hybrid mechanisms of N₂R.

These advances notwithstanding, the catalytic $4\text{H}^+/4\text{e}^-$ reduction of N₂ to N₂H₄ remains underdeveloped by comparison with N₂-to-NH₃ conversion. In previous work, Shilov and co-workers reported a variety of group V and VI metal salts acting as catalysts for N₂R under high pressure and strongly reducing, alkaline conditions, with impressive turnover numbers, electron efficiency, and selectivity for N₂H₄,^{9,10} however, the ill-defined nature of these systems limited mechanistic understanding. Relatedly, while the vanadium-dependent nitrogenase enzyme produces some N₂H₄, the origin of this selectivity is unknown.¹¹ Even among well-defined N₂R catalysts that show moderate to high N₂H₄ selectivity,^{12–15} present understanding of factors that favor N₂H₄ over NH₃ is limited.¹⁶ With NH₃ and N₂H₄ emerging as prospective zero-carbon fuel alternatives in light of the energetic and infrastructural challenges associated with compression, storage, and transfer of hydrogen fuel,^{17–19} delineating factors that dictate N₂H₄ versus NH₃ catalytic selectivity is of considerable interest.

A key metric in fuel synthesis is overpotential (η) or the excess energy input (in the form of chemical reagents, applied electrochemical potential, photochemical irradiation, or

temperature and pressure) beyond the thermodynamic standard-state potential of a⁶⁴ reaction required to achieve an appreciable reaction rate. Eqns 3.1–4 define the overpotential for generation of NH₃, N₂H₄, or their protonated forms as a function of the applied potential (E_{app}) and the acid strength ($\text{p}K_a$) of a reaction system in acetonitrile at room temperature.²⁰ Despite significant progress in catalyst and conditions development,^{2,21–23} N₂-to-NH₃ reduction systems still suffer from high η . As N₂H₄ is produced industrially via the oxidation of NH₃,²⁴ the overpotential for its generation is in turn gated by the efficiency of NH₃ synthesis. Based on the N₂R reaction mechanisms laid out in Figure 3.1, tailoring systems to favor direct N₂-to-N₂H₄ conversion represents a promising strategy for decreasing the overpotential of hydrazine synthesis, necessitating studies to control N₂R product selectivity.

$$\eta_{\text{NH}_3} = +0.04 - 0.059(\text{p}K_a) - E_{\text{appl}} \quad (3.1)$$

$$\eta_{\text{N}_2\text{H}_4} = -0.40 - 0.059(\text{p}K_a) - E_{\text{appl}} \quad (3.2)$$

$$\eta_{\text{NH}_4^+} = +0.36 - 0.079(\text{p}K_a) - E_{\text{appl}} \quad (3.3)$$

$$\eta_{\text{N}_2\text{H}_4^+} = -0.15 - 0.074(\text{p}K_a) - E_{\text{appl}} \quad (3.4)$$

The first step in each N₂R mechanism is the reductive protonation of N₂ to form an “NNH” intermediate (Figure 3.1). This step is energetically challenging, even in the presence of a metal catalyst, and sets the required acid and reductant strength for several catalyst systems.^{25,26} Importantly, NH₃ and N₂H₄ are both possible products downstream of this limiting step. However, because NH₃ is the thermodynamic product, examination of eqns 3.1–4 reveals that N₂R selective for N₂H₄ with a given source of hydrogen atom equivalents operates at an intrinsically lower η than if it were selective for NH₃.^{20,27}

Restated, hydrazine as a product of N₂R makes more efficient use of the upfront energy⁶⁵ cost paid to activate N₂ toward any fixed-N product.

Our laboratory recently discovered that blue light irradiation of N₂R catalyzed by a tris(phosphino)borane iron complex (**Fe**⁺, see Figure 3.2 for structure), with decamethylcobaltocene (Cp*₂Co) as the reductant ($E^\circ(\text{Co}^{\text{III/II}}) = -1.9 \text{ V vs Fe}^{+/0}$ in MeCN)²⁸ and anilinium acids ($\text{p}K_a \leq 10.6$ in MeCN),²⁹ results in some selectivity for N₂H₄ (1:2.3 N₂H₄:NH₃).¹⁶ In the dark, this catalysis almost exclusively produces NH₃ (Figure 3.2, upper pathway).¹⁶ One rationalization for this observation is that the selectivity change arises from a photochemically generated excited state of a hydrazido(2-) intermediate **Fe**NNH₂* that features increased spin density at the proximal nitrogen (N_α) relative to its ground state, arising from the increased population of an Fe–N π antibonding orbital and poorer overlap in Fe–N π bonding orbitals. This manifests in the partial bending of the hydrazido ligand, which would give rise to higher corresponding reactivity of N_α via H⁺ or H[•] transfer, leading toward N₂H₄ generation. By contrast, the ground state of **Fe**NNH₂ is protonated by relatively strong acids at the distal nitrogen (N_β) to release NH₃.^{16,30}

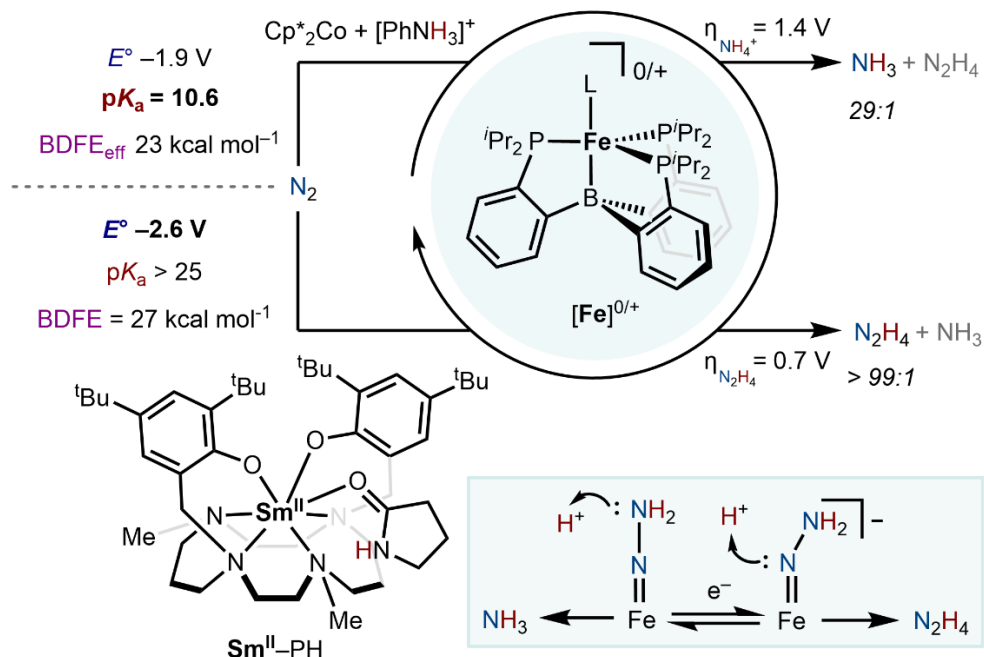


Figure 3.2: Selectivity of catalytic N_2R with **Fe** dependent on reagent thermodynamics.³¹

We wondered whether a comparatively low-overpotential N_2 -to- N_2H_4 catalytic process could be made highly selective using the same Fe catalyst via ground- rather than excited-state reactivity. Guiding our thinking, the singly reduced methyl analogue of FeNNH_2 , FeNNMe_2^- , exhibits a similar electronic structure to a low-lying excited state of FeNNH_2 .³² However, very strong reductants are necessary to access the anionic form ($E^\circ(\text{FeNNMe}_2^{0/-}) = -2.7 \text{ V}$ vs $\text{Fc}^{+/0}$ in THF). We therefore turned to the Sm-based reagent described in Chapter 2 comprised by a strongly reducing Sm^{II} complex (**Sm^{II}**) ligated by 2-pyrrolidinone (PH) as a weak proton donor (Figure 3.2).^{33,34} The thermochemical properties of **Sm^{II}**-PH map well onto the targeted Fe-catalyzed N_2 -to- N_2H_4 reduction. It should be a sufficiently strong reductant ($E^\circ(\text{Sm}^{\text{III/II}}\text{-PH}) = -2.6 \text{ V}$ vs $\text{Fc}^{+/0}$) to access FeNNH_2^- . It is also very weakly acidic; while the pK_a of the Sm^{II} state is unavailable, the pK_a of the oxidized cation [**Sm^{III}**-PH]⁺ is 25.4 in MeCN, which should strongly disfavor

NH₃ formation via N_β protonation from the **Fe**NNH₂ intermediate. Importantly, the N–H⁶⁷ bond dissociation free energy (BDFE_{N–H}) of **Sm**^{II}–PH is 27.2 kcal mol⁻¹, which is low enough to form, on thermodynamic grounds, the very weak N–H bonds in early N₂R intermediates.³⁵

Here, we leverage **Sm**^{II}–PH to achieve unprecedented catalytic selectivity (>99%) for N₂H₄ relative to NH₃ via this Fe-catalyst system (Figure 3.2). This represents a striking selectivity shift for a catalyst that is well known to be highly selective for NH₃. Our data point to competition between electron transfer (ET) vs proton transfer (PT) in the selectivity-determining branchpoint. Additionally, despite the very similar net hydrogen-atom donor strengths of **Sm**^{II}–PH and the Cp*₂Co/anilinium acid combinations we have previously reported with **Fe**,^{31,36} tailoring the reductant and acid characteristics of the reagents to the catalyst affords access to N₂H₄ as the kinetic product, resulting in a 700 mV decrease to the overpotential of the **Fe**-catalyzed N₂R process.

3.2 Results

The initial observation is as follows (Figure 3.3A): with **Fe**N₂ as the precatalyst, the reaction of **Sm**^{II} (120 equiv), PH (96 equiv), and N₂ (1 atm) in toluene at –78 °C for 16 h yields 16 ± 3 equiv of N₂H₄ per **Fe** (64% yield relative to PH) and a noncatalytic amount of NH₃ (0.76 ± 0.03 equiv, 2.4% yield, entry 1 in Table 3.1), with the oxidized, deprotonated **Sm**^{III}–pyrrolidinonate complex as the byproduct (91% yield, Figure 3.3B).³⁴ Conducting the reaction under ¹⁵N₂ produces ¹⁵NH₄⁺ and ¹⁵N₂H₅⁺ on acidic workup (Figure 3.3C), confirming N₂ as the N-atom source. No fixed-N products are observed in the absence of **Fe** (entry 2) or when N-methylpyrrolidinone (PMe) is used in place of PH (entry 3). **Sm**^{II}–PH and **Sm**^{II}–PMe are equally strong reductants,³⁴ thereby implicating PH as the

proton source in N_2R . Our group's previous reports of N_2R using **Fe**-based catalysts with ⁶⁸ high selectivity for NH_3 employed Et_2O as solvent.^{5,31} For direct comparison, substitution of **Sm^{II}-PH** for $Cp^*_2Co/[PhNH_3]OTf$ under the reported optimized conditions for the latter reagent cocktail (Et_2O solvent instead of toluene, **FeBAR₄^F** as precatalyst instead of **FeN₂**) gave N_2H_4 as the sole fixed-N product (6.1 ± 0.3 equiv, $25 \pm 1\%$ yield; entry 4), indicating that the observed selectivity inversion is not a solvent or precatalyst effect. The lower yield under these conditions is attributed to the low solubility of **Sm^{II}-PH** in Et_2O compared to toluene.

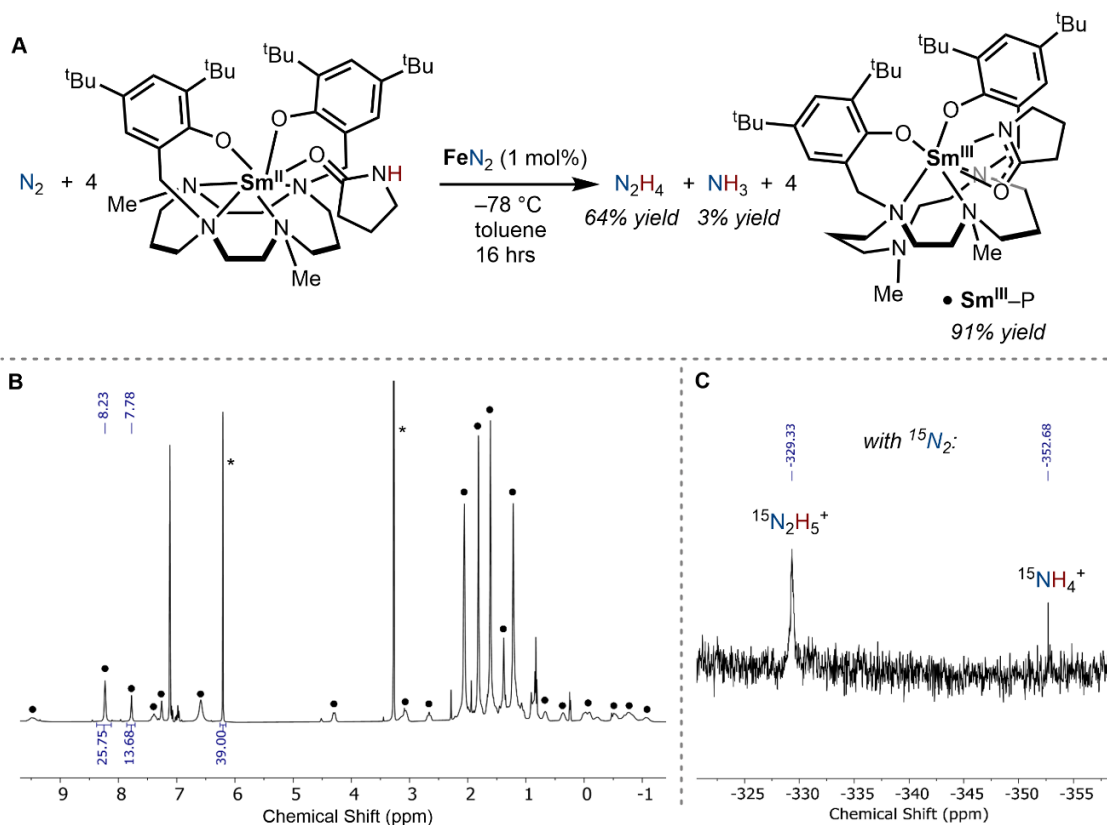
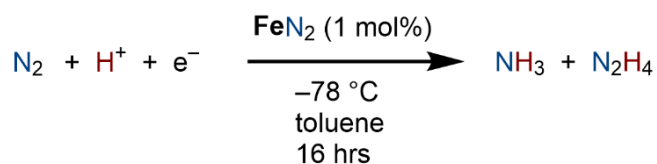


Figure 3.3: (A) **Fe**-catalyzed reduction of N_2 with **Sm^{II}-PH**. (B) 1H NMR (C_6D_6 , 400 MHz) spectrum of **Sm^{III}-P** as the byproduct of catalysis (*=1,3,5-trimethoxybenzene as internal standard). (C) $^{15}N\{^1H\}$ NMR (DMSO- d_6) spectrum of $^{15}NH_2^{15}NH_3Cl$ (329 ppm) and $^{15}NH_4Cl$ (353 ppm) obtained following acidic workup of the reaction under $^{15}N_2$.

Table 3.1: Summary of Fe-catalyzed N₂R data with Sm^{II}-based reductants.

Entry	H ⁺	e ⁻	NH ₃	N ₂ H ₄	% Yield (fixed N)
1	PH (96 equiv)	Sm ^{II} (120 equiv)	0.76 ± 0.03	16 ± 3	67 ± 11
2	PH (49 μmol) ^a	Sm ^{II} (61 μmol) ^a	-	-	< 1
3	none	Sm ^{II} -PMe (120 equiv)	< 0.1	< 0.3	< 1
4 ^b	PH (96 equiv)	Sm ^{II} (120 equiv)	< 0.1	6.1 ± 0.3	25 ± 1
5	PH (260 equiv)	Sm ^{II} (325 equiv)	< 0.1	37 ± 6	54 ± 9
6	PH (480 equiv)	Sm ^{II} (600 equiv)	< 0.1	46 ± 4	38 ± 3
7 ^c	PH (960 equiv)	Sm ^{II} (1200 equiv)	< 0.1	69	29
8	PH (96 equiv)	SmI ₂ (THF) ₂ (120 equiv)	< 0.1	< 0.3	< 1
9 ^d	PH (96 equiv)	SmI ₂ (THF) ₂ (120 equiv)	< 0.1	< 0.3	< 1
10 ^d	PH (96 equiv)	Sm ^{II} (120 equiv)	< 0.1	3.5 ± 0.3	14 ± 1
11	PH (96 equiv)	SmI ₂ (THF) ₂ (120 equiv) + HMPA (240 equiv)	0.4 ± 0.3	0.6 ± 0.4	4 ± 2
12	PH (96 equiv)	SmI ₂ (THF) ₂ (120 equiv) + HMPA (480 equiv)	< 0.1	3.1 ± 0.1	12.9 ± 0.2
13	CF ₃ PH (96 equiv)	Sm ^{II} (120 equiv)	1.8 ± 0.3	10.9 ± 0.2	51 ± 2
14	MeOH (96 equiv)	Sm ^{II} (120 equiv)	2.4 ± 0.6	6.3 ± 0.2	34 ± 1
15	[DBUH]OTf (96 equiv)	Sm ^{II} -PMe (120 equiv)	< 0.1	2.4 ± 1	10 ± 4
16	PH (96 equiv)	Sm ^{II} (96 equiv)	< 0.1	9.7 ± 0.1	40.2 ± 0.3
17	PH (96 equiv)	Sm ^{II} (120 equiv) + PMe (192 equiv)	0.3 ± 0.2	10.3 ± 0.2	44 ± 2

All values represent the average of two or more runs unless otherwise noted. ^aNo Fe. ^bEt₂O solvent; [Fe]BArF₄ as precatalyst. ^c72 h; single run. ^dTHF solvent.

Decreasing the loading of **FeN₂** to 0.4 mol% results in a higher N₂H₄ turnover (37⁷⁰ ± 6 equiv per **Fe**, entry 5) with a modest loss in fixed nitrogen efficiency (54% yield with respect to PH). No NH₃ is detected under the latter conditions. This result delineates a remarkable shift in selectivity for a catalyst known previously to generate almost entirely NH₃. It also represents the highest selectivity for N₂H₄ versus NH₃ yet reported with a molecular catalyst.^{12,13} Moreover, the yield and turnover number achieved with **Fe** and **Sm^{II}**–PH compare favorably with N₂H₄-selective N₂R using Cp*₂Co and Ph₂NH₂OTf and (depe)₂Fe as a catalyst, as reported by Ashley and coworkers (25 equiv of N₂H₄ and 38% yield at a comparable catalyst loading).¹² Higher turnover is established using even lower catalyst loadings (0.2 mol %, 46 ± 4 equiv N₂H₄ per Fe, entry 6); the fixed-N efficiency decreases further (38% with respect to PH).

Up to 69 equiv of N₂H₄ per Fe is obtained at 0.1 mol % **FeN₂** and a longer reaction time (72 h; entry 7). This turnover number for N₂H₄ is very similar to that of a highly active Fe catalyst supported by an anionic benzene-based PCP pincer ligand reported by Nishibayashi and coworkers (68 equiv N₂H₄ per Fe)¹⁵ but here with significantly higher N₂H₄ yield (up to 29% with **Fe** vs 4% with the Fe-pincer catalyst) and selectivity (NH₃ is instead the major fixed-N product with the Fe-pincer catalyst).

No N₂H₄ or NH₃ is obtained when the **Sm^{II}** complex is exchanged for SmI₂(THF)₂ (entry 8). The latter result could be due to the insolubility of SmI₂ in toluene; however, no fixed products are observed when SmI₂(THF)₂ is used as a soluble reductant in THF either (entry 9), whereas the **Sm^{II}** complex still provides a small but catalytic yield of N₂H₄ in THF (3.5 ± 0.3 equiv per Fe, entry 10). The Sm^{III/II} reduction potential of SmI₂(PH)(THF)_{*n*} is estimated to be ~1 V positive of **Sm^{II}**–PH,^{37,38} incompatible with not only the estimated

reduction potential of $\text{FeNNH}_2^{0/-}$ (~ -2.7 V vs $\text{Fc}^{+/0}$) but also the $\text{FeN}_2^{0/-}$ couple ($E^\circ =$ ⁷¹
 -2.2 V vs $\text{Fc}^{+/0}$).³⁹

To better understand the influence of $\text{Sm}^{\text{III/II}}$ reduction potential on catalysis, the high sensitivity of this parameter to the easily tunable Sm coordination sphere was exploited.^{38,40} Addition of 2 or 4 equiv of the strong Lewis base hexamethylphosphoramide (HMPA) to suspensions of $\text{SmI}_2(\text{THF})_2$ in toluene generates dark indigo or violet solutions, consistent with the coordination of HMPA to the Sm^{II} center. While solvent-dependent speciation limits quantitative estimation of reduction potentials for the reagents generated here in toluene, $E^\circ(\text{Sm}^{\text{III/II}})$ is expected to shift cathodically with increasing HMPA concentration as has been reported in THF.⁴¹ To crudely calibrate a relative scale of reducing capacity in toluene, **Fe** species were employed as chemical probes of the relative $E^\circ(\text{Sm}^{\text{III/II}})$. While **FeN₂** is unreactive toward $\text{SmI}_2(\text{THF})_2$, it is readily reduced to **FeN₂⁻** by $\text{SmI}_2(\text{THF})_2$ with both 2 and 4 equiv of HMPA in toluene, as judged by infrared (IR) and electron paramagnetic resonance (EPR) spectroscopy (Figure 3.4). The methylated hydrazido species **FeNNMe₂**, which is ~ 500 mV more difficult to reduce than **FeN₂** in THF,^{32,39} is reduced to **FeNNMe₂⁻** in toluene at -78°C by **Sm^{II}-PMe** and $\text{SmI}_2(\text{THF})_2$ mixed with 1 equiv of PMe and 4 equiv of HMPA but is not reduced when mixed with only 2 equiv of HMPA and 1 equiv of PMe. These data enable construction of a qualitative scale of the reduction potentials of these reagents (Figure 3.4).

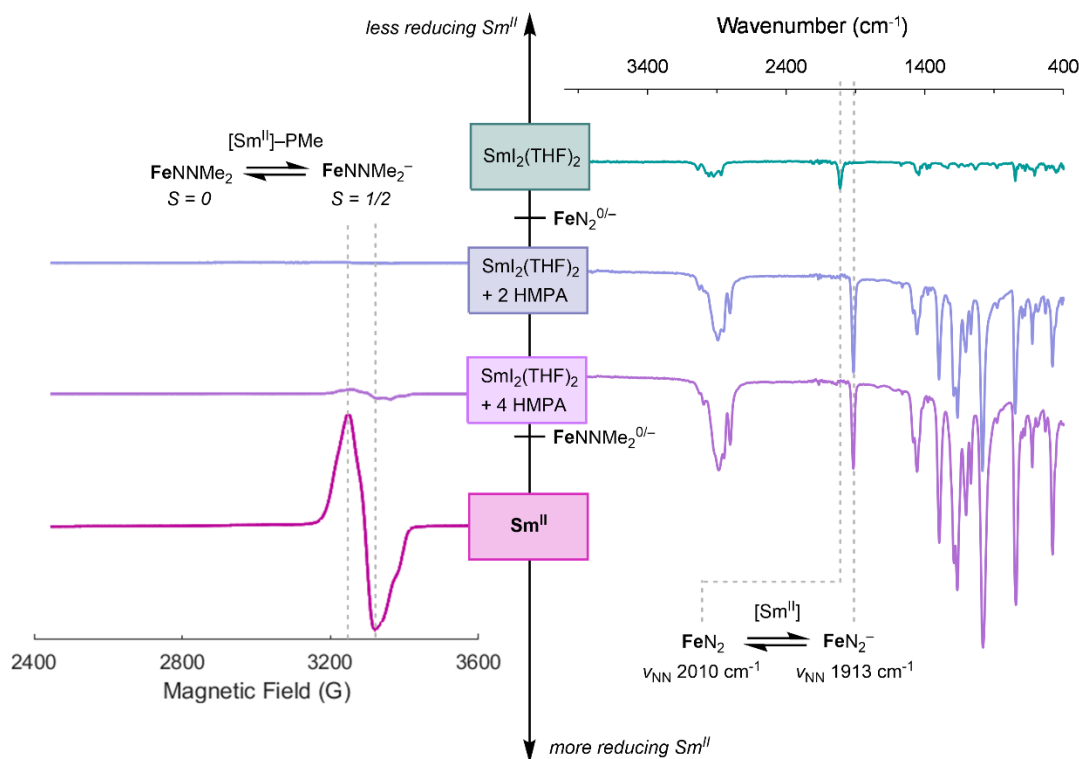


Figure 3.4: Relative reduction potentials of $\text{FeN}_2^{0/-}$, FeNNMe_2^- , and Sm^{II} reagents used in this study in toluene. Left: CW EPR spectra (toluene, 77K; MW power = 2 mW) following the reaction of FeNNMe_2 (2 mM) with 3 equiv of the indicated Sm^{II} reagent and 3 equiv of PME. Right: IR spectra (thin films deposited from room temperature toluene solutions) following the reaction of FeN_2 with 3 equiv of the indicated Sm^{II} reagent.

When combined with PH as the proton source, both $\text{SmI}_2(\text{HMPA})_n$ reductant cocktails are competent for N_2R with FeN_2 : with 2 equiv of HMPA, subcatalytic amounts of both NH_3 and N_2H_4 are obtained (entry 11 in Table 3.1, 0.4 ± 0.3 and 0.6 ± 0.4 equiv, respectively), whereas the stronger reductant generated with 4 equiv of HMPA drives N_2H_4 -selective catalytic N_2R (entry 12, 3.1 ± 0.1 equiv). We conclude that Sm^{II} reductants stronger than SmI_2 are necessary to achieve any N_2R with Fe in combination with the weak acid PH, while N_2H_4 selectivity turns on at a more negative $E^\circ(\text{Sm}^{\text{III/II}})$.

If competition between the rates of PT and ET to FeNNH₂ dictates N₂R selectivity,⁷³ it follows that increasing the acidity of the proton source should enhance the rate of protonation and turn on some degree of NH₃ production. In line with this hypothesis, when 5-(trifluoromethyl)pyrrolidinone (^{CF₃}PH) is used as a more acidic proton source, a significantly lower ratio of N₂H₄:NH₃ is obtained (6:1, entry 13). Exchanging PH for MeOH decreases the selectivity for N₂H₄ even further (6.3 ± 0.2 equiv per Fe, entry 14) and results in a small but catalytic amount of NH₃ (2.4 ± 0.6 equiv per Fe).

We have shown previously using the equilibrium in eqn 3.7 that the combination of MeOH with [Sm^{III}-NCMe]⁺ is 5.5 pK_a units more acidic than [Sm^{III}-PH]⁺ in MeCN.³⁴ Extension of this relationship to less coordinating solvents such as toluene, in which MeOH binds to the Sm center, is not straightforward. Still, decomposition of equilibrium 3.7 into component parts, including the coordination of MeCN to [Sm^{III}]⁺ (eqn 3.5), indicates that for donors weaker than MeCN, such as MeOH, the net acidity should decrease relative to the MeCN value. As a result, we anticipate that the decrease in pK_a between [Sm^{III}-PH]⁺ and [Sm^{III}-O(Me)H]⁺ is either similar, or more pronounced, in toluene compared to the difference measured in MeCN. Taken together, these data therefore point to an NH₃-selective protonation event.



In addition to serving as a strong reductant, Sm^{II}-PH is also a very strong net hydrogen atom donor. SmI₂ coordinated by polar protic ligands is known to react via concerted proton-electron transfer (CPET) in various cases.⁴²⁻⁴⁵ As discussed in Chapter 2, the reduction of styrenyl substrates by Sm^{II}-PH may proceed via either CPET or stepwise ET

74
followed by rapid PT.³⁴ CPET is kinetically favorable when at least two of the reaction components are colocalized (e.g., coordination of the proton source to the reductant) to decrease the molecularity of the reaction.^{46–48}

To evaluate whether the selectivity change observed in this **Fe**-mediated N₂R system results from more available CPET pathways using **Sm**^{II}–PH, we sought a thermodynamically equivalent acid/reductant pair that would be less prone to concerted reactivity. **Sm**^{II}–PMe was hence employed as an equally strong reductant as **Sm**^{II}–PH ($E^\circ(\text{Sm}^{\text{III/II}}\text{-PMe}) = -2.6 \text{ V vs Fc}^{+/0}$), and [DBUH]OTf was selected as a noncoordinating acid with a pK_a very similar to that of [**Sm**^{III}–PH]⁺ (DBU = 1,8-diazabicyclo[5.4.0]undec-7-ene, $pK_a = 24.3$ in MeCN).²⁹

Use of this reagent combination as the net hydrogen atom source in catalysis (Table 3.1, entry 15) yields N₂H₄ exclusively in 10% yield. This suggests that the overall 4H⁺/4e⁻ N₂-to-N₂H₄ reduction can proceed through stepwise electron and proton transfer steps, including the proposed key reduction of **Fe**NNH₂ to **Fe**NNH₂⁻. We therefore conclude that while contributing CPET steps cannot be discounted, a selective process for N₂H₄ formation does not require them and a series of stepwise ET/PT steps is catalytically viable.

To gain additional mechanistic insight, and to probe other possible factors contributing to selectivity for N₂H₄ using **Sm**^{II}, speciation during catalysis was investigated by freeze-quench spectroscopy. The ⁵⁷Fe Mössbauer spectrum of the reaction mixture freeze-quenched at 5 minutes (black trace in Figure 3.5A) is well-simulated as the singly reduced $S = 1/2$ [**Fe**N₂]⁻ complex (orange trace; δ 0.37 mm s⁻¹, ΔE_Q 1.03 mm s⁻¹, Γ_L/Γ_R 1.06/0.62 mm s⁻¹). As the reaction proceeds, the signal broadens to ultimately recapitulate the

spectrum obtained on reaction of FeN_2 with 1.6 equiv Sm^{II} in the absence of proton⁷⁵ source (magenta trace in Figure 3.5A).

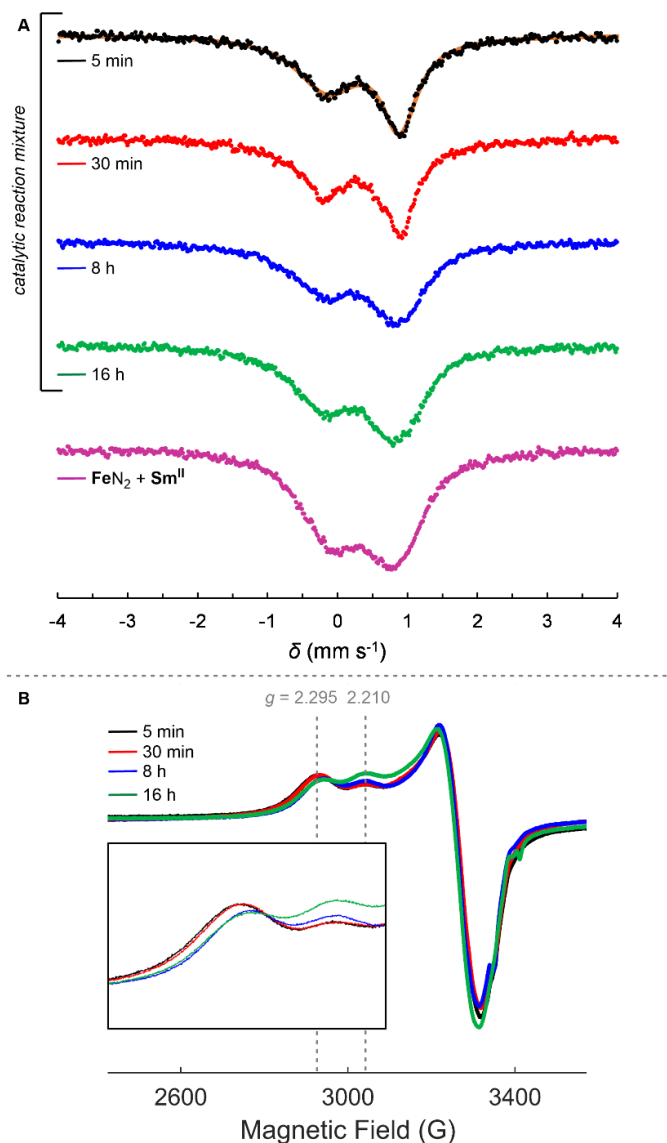


Figure 3.5: (A) Mössbauer spectra of the standard catalytic reaction mixture (toluene, 1 mM $^{57}\text{FeN}_2$, 32 equiv PH, 40 equiv Sm^{II}) freeze quenched after stirring at -78 °C for the indicated time compared to the products of reaction between $^{57}\text{FeN}_2$ and 1.6 equiv Sm^{II} in toluene at -78 °C for 5 minutes. All data were collected at 80 K. (B) CW X-band EPR spectra (77K, 2 mW) of the same catalytic mixture freeze-quenched after stirring at -78 °C for the indicated time.

frozen at the same time points corroborates this assignment and provides additional insight into speciation (Figure 3.5B). At 5 min, the EPR spectrum features two overlapping axial signals. The major signal, modeled with $g_3 = 2.295$, is assigned as FeN_2^- with $[\text{Sm}^{\text{III}}]^+$ as a noncoordinating counteranion by comparison to $[\text{FeN}_2][\text{Na}(12\text{-crown-}4)_2]$ ($g = [2.032\ 2.0482.304]$).³⁶ The second signal, with $g_3 = 2.210$, is assigned to a Sm^{III} -bound species $\text{FeN}_2^- \cdot \text{Sm}^{\text{III}}$ based on previous results, demonstrating that g_3 shifts to higher field in response to Na^+ binding to N_β in FeN_2^- ($g_3 = 2.23$).³⁹ The second signal increases in relative intensity over time in parallel with broadening of the Mössbauer spectrum.

Moreover, the reaction of FeN_2 with Sm^{II} in toluene at $-78\text{ }^\circ\text{C}$ yields the same two EPR signals but with a higher proportion of $\text{FeN}_2^- \cdot \text{Sm}^{\text{III}}$ than that in the catalytic reaction mixture containing PH (Figure 3.6A), suggesting that the broad Mössbauer spectrum obtained from the same reaction can be assigned as an unresolved mixture of $[\text{FeN}_2][\text{Sm}^{\text{III}}]$ and $\text{FeN}_2^- \cdot \text{Sm}^{\text{III}}$. Titration of PMe into this mixture results in a decrease in the Sm^{III} -bound signal and an increase in “free” FeN_2^- , indicating that PMe competes with FeN_2^- for binding to $[\text{Sm}^{\text{III}}]^+$ (Figure 3.6). The same shift in speciation is observed in thin-film IR spectra of residues obtained from room-temperature mixtures of FeN_2 , excess Sm^{II} , and varying amounts of PMe in toluene (Figure 3.6B). The bound form $\text{FeN}_2^- \cdot \text{Sm}^{\text{III}}$, present at low concentrations of PMe, has $\nu_{\text{NN}} = 1897\text{ cm}^{-1}$; displacement of the Fe complex from $[\text{Sm}^{\text{III}}]^+$ by addition of PMe results in conversion to $[\text{FeN}_2][\text{Sm}^{\text{III}}]$ with $\nu_{\text{NN}} = 1913\text{ cm}^{-1}$. Reduction of FeN_2 by $\text{SmI}_2(\text{THF})_2$ with 2 or 4 equiv of HMPA in toluene yields only “free” FeN_2^- (Figure 3.4 and Appendix B4).

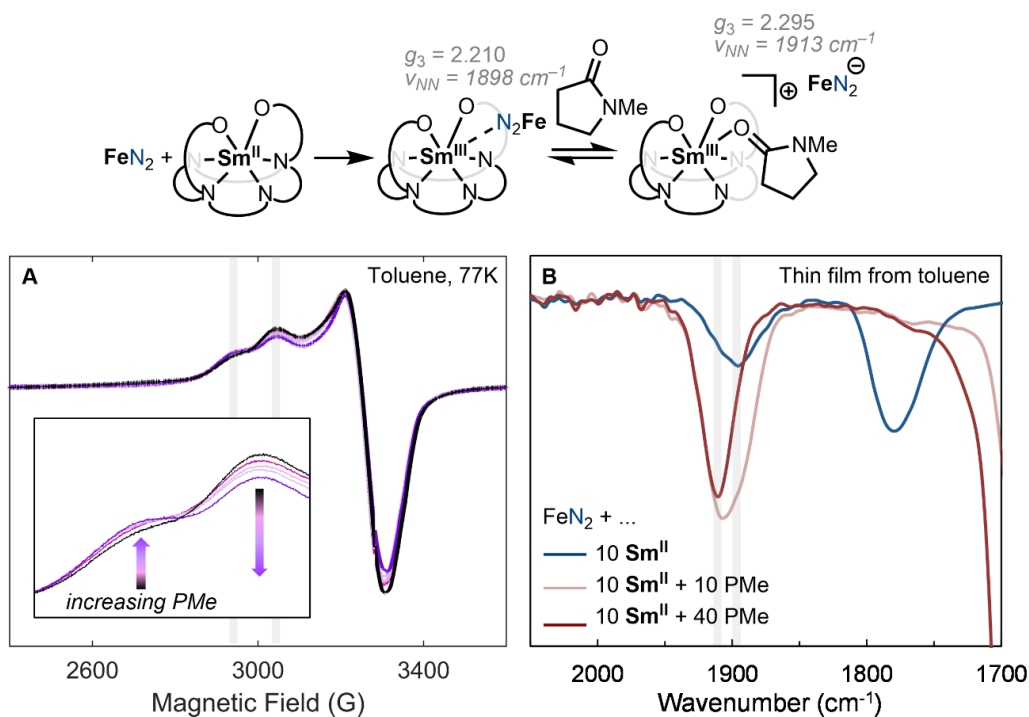


Figure 3.6: Displacement of $[\text{FeN}_2]^-$ from $[\text{Sm}^{\text{III}}]^+$ by PME evidenced by (A) CW X-band EPR spectra (77K, 2 mW) of FeN_2^- formed via addition of 1 equiv of Sm^{II} to FeN_2 (2 mM in toluene) in the presence of increasing concentrations of PME (0–16 equiv, black-purple traces) and (B) IR spectra (thin film deposited from toluene) of FeN_2^- formed via addition of 10 equiv Sm^{II} to FeN_2 in the presence of increasing concentrations of PME (0–24 equiv, blue-red traces).

Curiously, there is a correlation between conditions that favor FeN_2^- - Sm^{III} and higher yields of fixed-N products. EPR spectroscopy reveals almost exclusively $[\text{FeN}_2][\text{Sm}^{\text{III}}]$ in 2-MeTHF (Figure B7), indicating that this coordinating solvent disrupts the $\text{Fe}-\text{N}_2^-$ - Sm^{III} interaction; the fixed-N yield of catalysis decreases substantially when THF is used as the solvent instead of toluene (Table 3.1, entry 10). The yield is also lower when a lower ratio of $\text{Sm}^{\text{II}}:\text{PH}$ is used (compare entries 1 and 16) and when excess PME is added to the standard $\text{Sm}^{\text{II}}-\text{PH}$ reduction conditions (entry 17). Most strikingly, the ratio of free to Sm^{III} -bound FeN_2^- is higher during turnover than after catalysis is complete (Figure 3.5B).

This would be consistent with the bound form being more rapidly consumed in the⁷⁸ presence of excess **Sm^{II}**-PH, while after the reaction the spectrum more closely resembles the equilibrium distribution obtained with **Sm^{II}** in the absence of protons. Taken together, these data suggest that the **Sm^{III}**-bound species is more activated toward subsequent N₂R steps.

While further studies are of interest to more closely examine the nature of an **Fe**-N₂-**Sm^{III}** interaction and its effect on reactivity, our hypothesis is in accord with the “push-pull” model advanced for N₂ activation in nitrogenase in which the amount of electron density “pushed” into a coordinated N₂ ligand is enhanced by the “pull” of an exogenous Lewis acid.⁴⁹ A recent elegant study from Szymczak and coworkers demonstrates that coordination of Lewis acids (e.g., boranes, alkali metal cations) to Fe⁰-N₂ compounds simultaneously anodically shifts the Fe^{I/0} reduction potential of the complex and polarizes electron density in the Fe-N-N fragment toward N_β, facilitating N_β protonation.⁵⁰ Coordination of [**Sm^{III}**]⁺, a strong Lewis acid, may have similar consequences, with significant impacts on available reactivity pathways (Figure 3.7). For example, a Lewis acid-induced shift in reduction potential positive of the inaccessible value of the unactivated form ($E^\circ(\mathbf{FeN}_2^{-/2-}) = -3.1 \text{ V vs Fc}^{+/0}$, Figure B10) could enable a second reduction by **Sm^{II}**-PH ($E^\circ(\text{Sm}^{\text{III/II}}) = -2.6 \text{ V vs Fc}^{+/0}$). Alternatively, activation of **FeN₂⁻** toward N_β protonation could enable proton transfer from the weak acid [**Sm^{III}**-PH]⁺ ($pK_a = 25.4$ in MeCN).³⁴

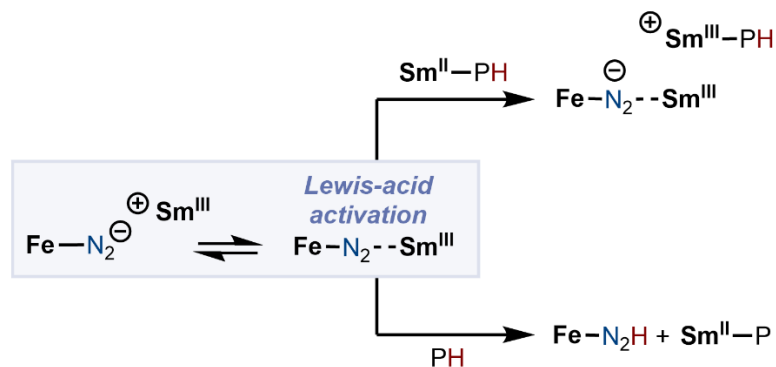


Figure 3.7: Possible pathways activated by $[\text{Sm}^{\text{III}}]^+$ coordination to FeN_2^- .

As the selectivity-determining state occurs after the turnover-limiting step in catalysis, the reactivity of proposed intermediates was evaluated to probe key N–H bond-forming steps. While our group has characterized FeNNH_2 via protonation of FeN_2^{2-} at low temperatures, this species is thermally very unstable and is not technically suited to synthetic reactivity studies.³⁰ We therefore employed its more stable and readily isolated analogue FeNNMe_2 to evaluate the viability of (dimethyl)hydrazine generation via N_α functionalization. Addition of FeNNMe_2 to 3 equiv $\text{Sm}^{\text{II}}-\text{PH}$ at $-78\text{ }^\circ\text{C}$ results in a color change over 5 min from the dark green of $\text{Sm}^{\text{II}}-\text{PH}$ to red. Me_2NNH_2 is observed in 25% yield among the basic, volatile products (Figure 3.8), indicating that the net transfer of two hydrogen atom equivalents to N_α in the neutral hydrazido(2–) species is facile with $\text{Sm}^{\text{II}}-\text{PH}$. FeN_2^- (as a mixture of free and Sm^{III} -bound), the resting state of catalysis, is observed as the major Fe-containing product by EPR spectroscopy along with a small amount of FeNNMe_2^- (Figure 3.8), indicating that reductive protonation of the hydrazido(2–) ligand generates a species which can (re)enter the catalytic cycle. Me_2NH is also generated in this reaction in 31% yield; as generation of hydrazine involves bending of the Fe–N–N bond to bring N_β and its substituents deeper into the inner coordination sphere,

hydrazine generation is expected to be less favorable from bulkier FeNNMe_2 than FeNNH_2 .

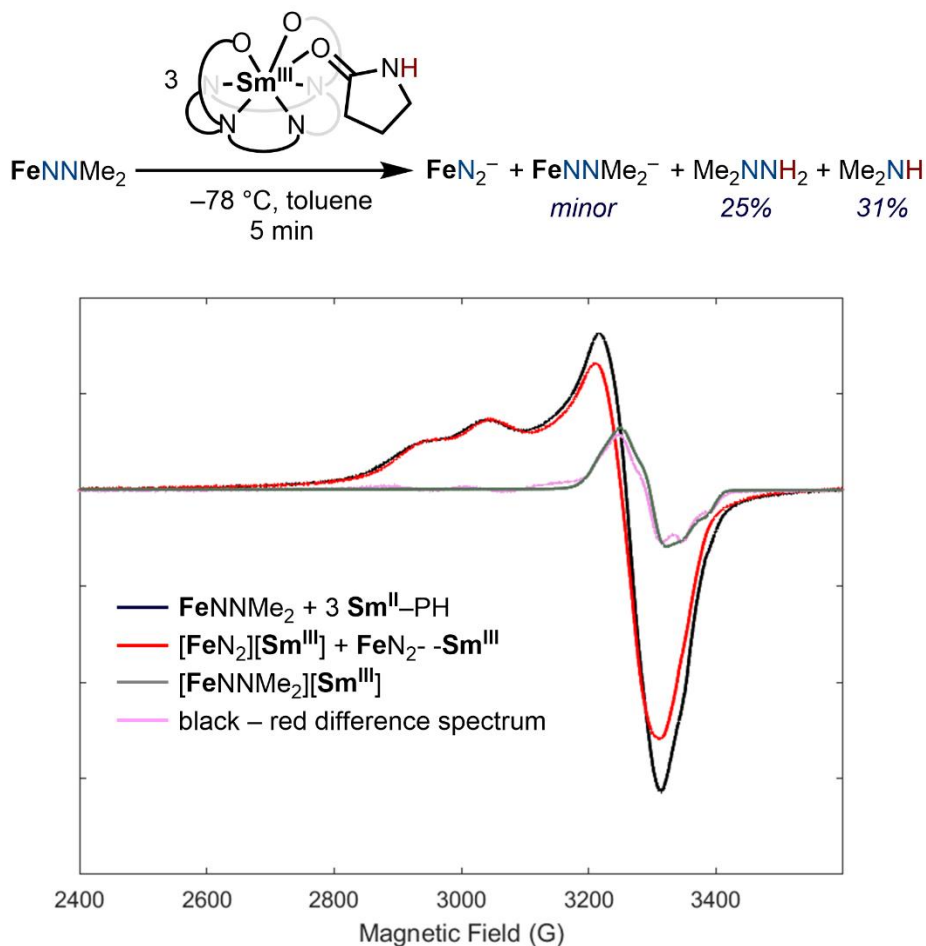


Figure 3.8: Products of reaction of FeNNMe_2 with 3 equiv $\text{Sm}^{\text{II}}\text{-PH}$. $S = \frac{1}{2}$ Fe products are assigned based on overlay of the CW EPR spectrum following the reaction (black) with that of a mixture of $\text{FeN}_2^- \text{-Sm}^{\text{III}}$ and $[\text{FeN}_2][\text{Sm}^{\text{III}}]$ obtained from the reaction of FeN_2 with 1 equiv $\text{Sm}^{\text{II}}\text{-PMe}$ (red, 62% intensity), the difference spectrum obtained from subtracting the red trace from the black trace (pink), and a spectrum of $[\text{FeNNMe}_2][\text{Sm}^{\text{III}}]$ obtained from the reaction of FeNNMe_2 with 3 equiv $\text{Sm}^{\text{II}}\text{-PMe}$ (gray, 15% intensity). All EPR spectra were collected at 2 mM Fe in toluene, 77K, 2 mW.

3.3 Discussion

Formation of the first very weak N–H bond is the most thermodynamically challenging step in the N₂R cycle with **Fe**, with a calculated BDFE_{N–H} for **FeNNH** of 31 kcal mol⁻¹.^{26,35} Observation of **FeN₂⁻** as the catalyst resting state in the system described herein is consistent with formation of the first N–H bond via addition of H⁺ (or H[•]) to this species as rate-contributing in N₂H₄ formation. Similarly, **FeN₂** and **FeN₂⁻** are observed as major components during catalytic turnover with Cp*₂Co and [Ph₂NH₂]OTf; formation of **FeNNH** is thus kinetically limiting in this N₂-to-NH₃ conversion system, which features a considerably weaker reductant paired with a much stronger acid.³⁶

While the individual electron- and proton-donating abilities of the two reagent pairs differ dramatically, the net hydrogen atom-donating abilities of **Sm^{II}–PH** and Cp*₂Co with anilinium acids are remarkably similar based on a comparison of their effective BDFE values (BDFE_{eff}). The BDFE_{eff} of the unassociated acid/reductant pairs can be evaluated using eqn 3.8.⁴⁸ The combination of Cp*₂Co with [PhNH₃]⁺, the weakest acid that is competent for N₂R with this reductant and **Fe** as the catalyst (pK_a = 10.6 in MeCN),^{29,31} has a BDFE_{eff} value of 23 kcal mol⁻¹, only 4 kcal mol⁻¹ lower than the BDFE_{N–H} of **Sm^{II}–PH** (27.2 kcal mol⁻¹ in MeCN).³⁴ Alternatively, Cp*₂Co can be protonated at the Cp* ring by strong anilinium acids to generate Cp*Co(C₅Me₅H)⁺, the BDFE_{C–H} of which has been bracketed as < 29 kcal mol⁻¹.⁵¹ Both acid/reductant systems are therefore operating near the limit at which the initial N–H bond formation (via either stepwise or concerted pathways) is thermodynamically favorable for **FeNNH**.

$$\text{BDFE}_{\text{eff}} = 23.06(E^\circ) + 1.37(\text{p}K_{\text{a}}) + 52.6 \text{ kcal mol}^{-1} \quad (3.8)$$

In both systems, attempts to employ reagent combinations with BDFE_{eff} above the limit imposed by **FeNNH** have generally proven unsuccessful. Acids weaker than PhNH₃⁺

are not competent for catalysis with Cp*₂Co.³¹ Similarly, while precise reduction⁸² potentials and pK_a values are unavailable for the SmI₂/HMPA/PH mixtures reported above, evidence suggests that the BDFE_{X-H} of [Sm^{II}-EH] reagents is most sensitive to E°(Sm^{III/II}),^{34,52} suggesting that the weaker Sm^{II} reductants that we find to be incompetent for N₂R with Fe and PH also have BDFE_{eff} values that are too high to access FeNNH at low temperatures.

As the milder SmI₂/HMPA_n reductants do not show appreciable binding to FeN₂⁻ following electron transfer (Appendix B4), this analysis of BDFE limits is not complicated by the effect of Lewis acid coordination. However, the proposed role of Sm coordination in the turnover-limiting step of the well-defined Sm^{II} system described here prompts us to comment on such interactions in the context of the recent emergence of SmI₂/ROH as highly effective net H• sources in N₂R with molecular catalysts.⁵³⁻⁵⁵ Sm coordination is predicted to increase BDFE_{N-H} for key M-N_xH_y intermediates; for example, the [Fe-N₂H-Sm^{III}]ⁿ⁺ species is expected to be more stable than the corresponding [Fe-N₂H]⁽ⁿ⁻¹⁾⁺,³⁵ enabling N-H bond formation that might otherwise be expected to be too uphill. In addition to this thermodynamic effect, coordination of both MN_xH_y intermediates and ROH to a coordinatively unsaturated Sm^{III} (or Sm^{II}) center should enhance the kinetics of proton (or alternatively H•) transfer.⁴³ While much remains to be learned about cooperative N₂ activation by low valent transition metals combined with Sm (or other high-coordinate Lewis acids), such interactions could be exploited to develop catalytic N₂R with more attractive reductants than SmI₂ or Sm^{II} (e.g., electrochemically-driven with Sm-based cocatalysts).

83
Despite its potent hydrogen atom donor strength, because the **Sm^{II}**–PH system is selective for N₂H₄, the net overpotential η determined using eqn 3.2, with values for the **Sm^{III/II}** reduction potential (–2.6 V) and the p*K*_a of [**Sm^{III}**–PH]⁺ (25.4), is only 700 mV.²⁰ This value is 600 mV lower than η for the NH₃-selective N₂R with Cp*₂Co (–1.9 V) and [PhNH₃]⁺ (p*K*_a = 10.6, eqn 3.1). Moreover, when protonation of NH₃ to NH₄⁺ occurs, operative under the more strongly acidic conditions (the p*K*_a of NH₄⁺ is 16.5 in MeCN), and is accounted for using eqn 3.3,²⁰ η is 1.4 V for the Cp*₂Co/PhNH₃⁺ system, double that of the Sm-based catalysis producing N₂H₄. This comparison underscores that while the MN_xH_y intermediate with the weakest N–H bond may dictate the input hydrogen atom donor strength necessary for catalysis, significantly more of the initial energy penalty is recovered when the system is tuned to favor N₂H₄ as the product of N₂R by controlling steps downstream of the rate-contributing formation of the earliest N–H bond.

The data described above, in the context of results from prior experimental and computational studies,⁵⁶ are consistent with the assignment of a critical role to the neutral hydrazido complex **FeNNH₂** as a common and selectivity-determining intermediate in catalytic N₂R to NH₃ and/or N₂H₄. As laid out using solid arrows in Figure 3.9, protonation of **FeNNH₂** (favored by the stronger acids historically employed with this catalyst) occurs at N_β followed by N–N bond cleavage to release 1 equiv of NH₃ and a terminal [**Fe≡N**]⁺.³⁰ Alternatively, reduction (favored by very strong reductants such as the **Sm^{II}** species employed in this study) induces bending of the Fe–N–N angle in **FeNNH₂[–]**, resulting in reactivity with H⁺ (or possibly H[•]) at N_α to ultimately evolve N₂H₄. As a third possibility, a low-lying excited state of **FeNNH₂**, accessed either thermally or by photoexcitation,¹⁶ reacts at N_α in a fashion similar to **FeNNH₂[–]**. This multifaceted reactivity presents several

methods to manipulate N_2R selectivity with the same catalyst by varying temperature, irradiation, acidity, and reductant strength. The latter two variables are demonstrated here to have the most pronounced effect on N_2H_4 vs NH_3 production: use of a 700 mV stronger reductant in concert with acids weaker by 10–15 pK_a units induces a complete inversion in selectivity to favor N_2H_4 .

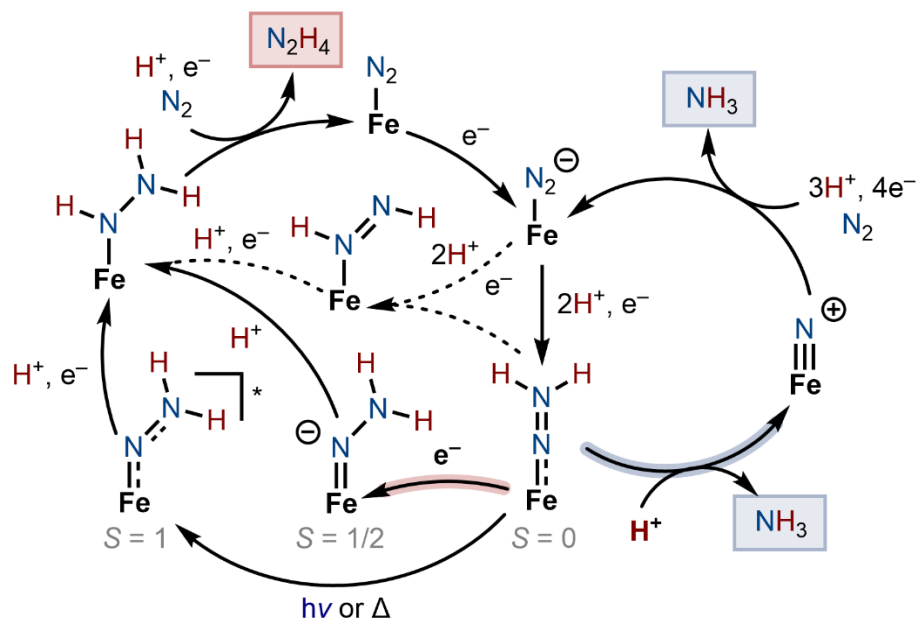


Figure 3.9: Proposed role of $FeNNH_2$ as selectivity branchpoint in Fe -catalyzed N_2R to NH_3 vs NH_3 .

An alternative explanation for the observed N_2H_4 selectivity is illustrated by the dashed arrows in Figure 3.9. While our group has demonstrated that N_β is the kinetic site of protonation of FeN_2^{2-} with strong acids to form $FeNNH_2$,³⁰ the neutral hydrazido(2-) and diazene isomers of Fe (i.e., $FeNNH_2$ vs $Fe(NHNH)$) have been calculated to have similar energies.⁵⁹ It is therefore worth considering that isomerization from $FeNNH_2$ to $Fe(NHNH)$, which might be outcompeted by N_β protonation and NH_3 formation under strongly acidic conditions, could be kinetically relevant with weaker acids and thus favor N_2H_4 generation. While we cannot rule out this pathway, the observation of Me_2NNH_2

85
from the reaction of FeNNMe_2 with $\text{Sm}^{\text{II}}\text{-PH}$ under catalytically relevant conditions provides evidence that a distal-to-alternating crossover mechanism from FeNNH_2 to an iron-hydrazido (1 $-$) species FeNHNH_2 is accessible. We deduce that a diazene intermediate $\text{Fe}(\text{NHNH})$ is not a prerequisite for N_2H_4 formation. Similarly, existing experimental¹⁶ and computational⁵⁶ studies conclude that NH_3 generation from later intermediates (e.g., $[\text{FeNHNH}_2]^{n+}$ or $[\text{FeNH}_2\text{NH}_2]^{n+}$) is unlikely to be kinetically competitive with N_2H_4 generation, supporting assignment of FeNNH_2 as the selectivity-determining intermediate.

Examination of early N_2R literature hints at a key role for MNNH_2 . Despite the field's common association of the limiting distal mechanism (which produces NH_3 as the sole fixed-N product) with Chatt, his group's pioneering studies of group VI metal N_2R intermediates also include some examples of N_2H_4 production.² Specifically, treatment of a series of tungsten hydrazido(2 $-$) complexes with H_2SO_4 resulted in mixtures of NH_3 and N_2H_4 , with N_2H_4 as the major fixed-N product in some cases (Figure 3.10).⁵⁷ In such reactions, the W center serves as the source of electrons. Notably, more reducing $\text{W}(\text{NNH}_2)$ complexes appear to favor N_2H_4 production at the expense of NH_3 . We show this by plotting the reported yields of N_2H_4 and NH_3 as a function of E° values of a series of $\text{W}(\text{NNH}_2)$ complexes of the same charge, yielding the negative correlations with N_2H_4 yield in Figure 3.10.⁵⁸ This trend mirrors the proposed role of $\text{FeNNH}_2^{0/-}$, suggesting that N_2R catalysts and conditions that access more reducing intermediates may generally exhibit higher selectivity for N_2H_4 .

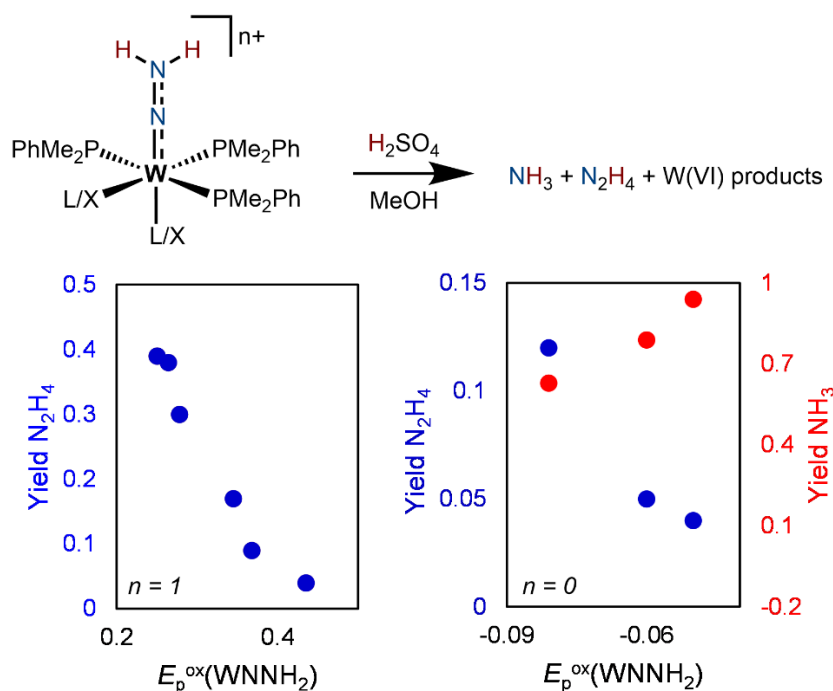


Figure 3.10: Relationship between reduction potential and N_2H_4 vs NH_3 yield upon protonation of a series of tungsten hydrazido(2⁻) complexes as reported by Chatt and coworkers.^{57,58}

3.4 Conclusions

Here, we render **Fe** an efficient and selective N_2 -to- N_2H_4 catalyst through introduction of **Sm^{II}**-PH as the net hydrogen atom donor. While this system operates at a very similar applied chemical driving force as we have previously achieved for N_2 -to- NH_3 conversion using this catalyst with weaker reductants and stronger acids, the conditions that are selective for N_2H_4 operate at a significantly lower net overpotential. On the basis of stoichiometric and catalytic reactivity, we attribute the switch in selectivity to an **FeNNH₂⁻** intermediate accessed by the very strong **Sm^{II}** reductant with proton- (and hydrogen atom-) accepting character at N_α . Meanwhile, the weakly acidic nature of Sm-bound PH disfavors the NH_3 -evolving protonation of **FeNNH₂**. This study demonstrates the utility of well-characterized thermochemical and electronic structural properties of both the catalyst and

reagents in understanding and designing multielectron, multiproton reactions such as⁸⁷
catalytic N₂R with finely tuned product selectivity.

REFERENCES

- (1) Chatt, Joseph.; Dilworth, J. R.; Richards, R. L. Recent advances in the chemistry of nitrogen fixation. *Chem. Rev.* **1978**, *78* (6), 589–625.
- (2) Chalkley, M. J.; Drover, M. W.; Peters, J. C. Catalytic N₂-to-NH₃ (or -N₂H₄) conversion by well-defined molecular coordination complexes. *Chem. Rev.* **2020**, *120* (12), 5582–5636.
- (3) Yandulov, D. V.; Schrock, R. R. Catalytic reduction of dinitrogen to ammonia at a single molybdenum center. *Science* **2003**, *301* (5629), 76–78.
- (4) Arashiba, K.; Miyake, Y.; Nishibayashi, Y. A molybdenum complex bearing PNP-type pincer ligands leads to the catalytic reduction of dinitrogen into ammonia. *Nat. Chem.* **2011**, *3* (2), 120–125.
- (5) Anderson, J. S.; Rittle, J.; Peters, J. C. Catalytic conversion of nitrogen to ammonia by an iron model complex. *Nature* **2013**, *501* (7465), 84–87.
- (6) Pickett, C. J. The Chatt cycle and the mechanism of enzymic reduction of molecular nitrogen. *JBIC J. Biol. Inorg. Chem.* **1996**, *1* (6), 601–606.
- (7) Barney, B. M.; Lukoyanov, D.; Yang, T.-C.; Dean, D. R.; Hoffman, B. M.; Seefeldt, L. C. A methyldiazene (HNNCH₃)-derived species bound to the nitrogenase active-site FeMo cofactor: Implications for mechanism. *Proc. Natl. Acad. Sci.* **2006**, *103* (46), 17113–17118.
- (8) Rittle, J.; Peters, J. C. An Fe-N₂ complex that generates hydrazine and ammonia via Fe=NNH₂: Demonstrating a hybrid distal-to-alternating pathway for N₂ reduction. *J. Am. Chem. Soc.* **2016**, *138* (12), 4243–4248.

- (9) Shilov, A.; Denisov, N.; Efimov, O.; Shuvalov, N.; Shuvalova, N.; Shilova, A. New nitrogenase model for reduction of molecular nitrogen in protonic media. *Nature* **1971**, *231* (5303), 460–461.
- (10) Bazhenova, T. A.; Shilov, A. E. Nitrogen fixation in solution. *Coord. Chem. Rev.* **1995**, *144*, 69–145.
- (11) Dilworth, M. J.; Eady, R. R. Hydrazine is a product of dinitrogen reduction by the vanadium-nitrogenase from *Azotobacter chroococcum*. *Biochem. J.* **1991**, *277* (2), 465–468.
- (12) Hill, P. J.; Doyle, L. R.; Crawford, A. D.; Myers, W. K.; Ashley, A. E. Selective catalytic reduction of N_2 to N_2H_4 by a simple Fe complex. *J. Am. Chem. Soc.* **2016**, *138* (41), 13521–13524.
- (13) Kuriyama, S.; Arashiba, K.; Nakajima, K.; Matsuo, Y.; Tanaka, H.; Ishii, K.; Yoshizawa, K.; Nishibayashi, Y. Catalytic transformation of dinitrogen into ammonia and hydrazine by iron-dinitrogen complexes bearing pincer ligand. *Nat. Commun.* **2016**, *7* (1), 12181.
- (14) Sekiguchi, Y.; Kuriyama, S.; Eizawa, A.; Arashiba, K.; Nakajima, K.; Nishibayashi, Y. Synthesis and reactivity of iron–dinitrogen complexes bearing anionic methyl- and phenyl-substituted pyrrole-based PNP-type pincer ligands toward catalytic nitrogen fixation. *Chem. Commun.* **2017**, *53* (88), 12040–12043.
- (15) Kuriyama, S.; Kato, T.; Tanaka, H.; Konomi, A.; Yoshizawa, K.; Nishibayashi, Y. Catalytic reduction of dinitrogen to ammonia and hydrazine using iron–dinitrogen complexes bearing anionic benzene-based PCP-type pincer ligands. *Bull. Chem. Soc. Jpn.* **2022**, *95* (4), 683–692.

- (16) Garrido-Barros, P.; Chalkley, M.; Peters, J. Light alters the NH₃ vs N₂H₄ product⁹⁰ profile in iron-catalyzed nitrogen reduction via dual reactivity from an iron hydrazido (Fe=NNH₂) intermediate. *Angew. Chem. Int. Ed.* **2023**, *62* (9).
- (17) Rees, N. V.; Compton, R. G. Carbon-free energy: a review of ammonia- and hydrazine-based electrochemical fuel cells. *Energy Environ. Sci.* **2011**, *4* (4), 1255–1260.
- (18) Evans, G. E.; Kordesch, K. V. Hydrazine-air fuel cells. *Science* **1967**, *158* (3805), 1148–1152.
- (19) Asazawa, K.; Yamada, K.; Tanaka, H.; Oka, A.; Taniguchi, M.; Kobayashi, T. A platinum-free zero-carbon-emission easy fuelling direct hydrazine fuel cell for vehicles. *Angew. Chem. Int. Ed.* **2007**, *46* (42), 8024–8027.
- (20) Lindley, B. M.; Appel, A. M.; Krogh-Jespersen, K.; Mayer, J. M.; Miller, A. J. M. Evaluating the thermodynamics of electrocatalytic N₂ reduction in acetonitrile. *ACS Energy Lett.* **2016**, *1* (4), 698–704.
- (21) Garrido-Barros, P.; Derosa, J.; Chalkley, M. J.; Peters, J. C. Tandem electrocatalytic N₂ fixation via proton-coupled electron transfer. *Nature* **2022**, *609* (7925), 71–76.
- (22) Johansen, C. M.; Boyd, E. A.; Peters, J. C. Catalytic transfer hydrogenation of N₂ to NH₃ via a photoredox catalysis strategy. *Sci. Adv.* **2022**, *8* (43), eade3510.
- (23) Ashida, Y.; Onozuka, Y.; Arashiba, K.; Konomi, A.; Tanaka, H.; Kuriyama, S.; Yamazaki, Y.; Yoshizawa, K.; Nishibayashi, Y. Catalytic nitrogen fixation using visible light energy. *Nat. Commun.* **2022**, *13* (1), 7263.
- (24) Hayashi, H. Hydrazine synthesis: Commercial routes, catalysis and intermediates. *Res. Chem. Intermed.* **1998**, *24* (2), 183–196.

- (25) Warren, J. J.; Tronic, T. A.; Mayer, J. M. Thermochemistry of proton-coupled⁹¹ electron transfer reagents and its implications. *Chem. Rev.* **2010**, *110* (12), 6961–7001.
- (26) Chalkley, M. J.; Peters, J. C. Relating N–H bond strengths to the overpotential for catalytic nitrogen fixation. *Eur. J. Inorg. Chem.* **2020**, *2020* (15–16), 1353–1357.
- (27) Catalysts which operate via initial cleavage of the N≡N bond represent an interesting exception.
- (28) Connelly, N. G.; Geiger, W. E. Chemical redox agents for organometallic chemistry. *Chem. Rev.* **1996**, *96* (2), 877–910.
- (29) Tshepelevitsh, S.; Kütt, A.; Lõkov, M.; Kaljurand, I.; Saame, J.; Heering, A.; Plieger, P. G.; Vianello, R.; Leito, I. On the basicity of organic bases in different media. *Eur. J. Org. Chem.* **2019**, *2019* (40), 6735–6748.
- (30) Thompson, N. B.; Green, M. T.; Peters, J. C. Nitrogen fixation via a terminal Fe(IV) nitride. *J. Am. Chem. Soc.* **2017**, *139* (43), 15312–15315.
- (31) Chalkley, M. J.; Del Castillo, T. J.; Matson, B. D.; Peters, J. C. Fe-mediated nitrogen fixation with a metallocene mediator: exploring pK_a effects and demonstrating electrocatalysis. *J. Am. Chem. Soc.* **2018**, *140* (19), 6122–6129.
- (32) Thompson, N. B.; Oyala, P. H.; Dong, H. T.; Chalkley, M. J.; Zhao, J.; Alp, E. E.; Hu, M.; Lehnert, N.; Peters, J. C. Electronic structures of an $[\text{Fe}(\text{NNR}_2)]^{+/0/-}$ redox series: Ligand noninnocence and implications for catalytic nitrogen fixation. *Inorg. Chem.* **2019**, *58* (5), 3535–3549.
- (33) Maria, L.; Soares, M.; C. Santos, I.; R. Sousa, V.; Mora, E.; Marçalo, J.; V. Luzyanin, K. A novel samarium(II) complex bearing a dianionic bis(phenolate)cyclam ligand:

synthesis, structure and electron-transfer reactions. *Dalton Trans.* **2016**, 45 (9),⁹² 3778–3790.

- (34) Boyd, E. A.; Peters, J. C. Sm(II)-mediated proton-coupled electron transfer: quantifying very weak N–H and O–H homolytic bond strengths and factors controlling them. *J. Am. Chem. Soc.* **2022**, 144 (46), 21337–21346.
- (35) Matson, B. D.; Peters, J. C. Fe-mediated HER vs N₂RR: Exploring factors that contribute to selectivity in P₃^EFe(N₂) (E = B, Si, C) catalyst model systems. *ACS Catal.* **2018**, 8 (2), 1448–1455.
- (36) Chalkley, M. J.; Del Castillo, T. J.; Matson, B. D.; Roddy, J. P.; Peters, J. C. Catalytic N₂-to-NH₃ conversion by Fe at lower driving force: A proposed role for metallocene-mediated PCET. *ACS Cent. Sci.* **2017**, 3 (3), 217–223.
- (37) Enemærke, R. J.; Daasbjerg, K.; Skrydstrup, T. Is samarium diiodide an inner- or outer-sphere electron donating agent? *Chem. Commun.* **1999**, 0 (4), 343–344.
- (38) Shabangi, M.; Sealy, J. M.; Fuchs, J. R.; Flowers, R. A. The effect of cosolvent on the reducing power of SmI₂ in tetrahydrofuran. *Tetrahedron Lett.* **1998**, 39 (25), 4429–4432.
- (39) Moret, M.-E.; Peters, J. C. Terminal iron dinitrogen and iron imide complexes supported by a tris(phosphino)borane ligand. *Angew. Chem. Int. Ed.* **2011**, 50, 2063–2067.
- (40) Shabangi, M.; Flowers, R. A. Electrochemical investigation of the reducing power of SmI₂ in THF and the effect of HMPA cosolvent. *Tetrahedron Lett.* **1997**, 38 (7), 1137–1140.

- (41) Enemærke, R. J.; Hertz, T.; Skrydstrup, T.; Daasbjerg, K. Evidence for ionic samarium(II) species in THF/HMPA solution and investigation of their electron-donating properties. *Chem. – Eur. J.* **2000**, *6* (20), 3747–3754.
- (42) Chciuk, T. V.; Flowers, R. A. Proton-coupled electron transfer in the reduction of arenes by SmI₂–water complexes. *J. Am. Chem. Soc.* **2015**, *137* (35), 11526–11531.
- (43) Chciuk, T. V.; Anderson, W. R.; Flowers, R. A. Proton-coupled electron transfer in the reduction of carbonyls by samarium diiodide–water complexes. *J. Am. Chem. Soc.* **2016**, *138* (28), 8738–8741.
- (44) Chciuk, T. V.; Li, A. M.; Vazquez-Lopez, A.; Anderson, W. R.; Flowers, R. A. Secondary amides as hydrogen atom transfer promoters for reactions of samarium diiodide. *Org. Lett.* **2017**, *19* (1), 290–293.
- (45) Kolmar, S. S.; Mayer, J. M. SmI₂(H₂O)_n reduction of electron rich enamines by proton-coupled electron transfer. *J. Am. Chem. Soc.* **2017**, *139* (31), 10687–10692.
- (46) Morton, C. M.; Zhu, Q.; Ripberger, H.; Troian-Gautier, L.; Toa, Z. S. D.; Knowles, R. R.; Alexanian, E. J. C–H alkylation via multisite-proton-coupled electron transfer of an aliphatic C–H bond. *J. Am. Chem. Soc.* **2019**, *141* (33), 13253–13260.
- (47) Chalkley, M. J.; Garrido-Barros, P.; Peters, J. C. A molecular mediator for reductive concerted proton-electron transfers via electrocatalysis. *Science* **2020**, *369* (6505), 850–854.
- (48) Agarwal, R. G.; Coste, S. C.; Groff, B. D.; Heuer, A. M.; Noh, H.; Parada, G. A.; Wise, C. F.; Nichols, E. M.; Warren, J. J.; Mayer, J. M. Free energies of proton-coupled electron transfer reagents and their applications. *Chem. Rev.* **2022**, *122* (1), 1–49.

- (49) Hoffman, B. M.; Lukoyanov, D.; Yang, Z.-Y.; Dean, D. R.; Seefeldt, L. C.⁹⁴
Mechanism of nitrogen fixation by nitrogenase: The next stage. *Chem. Rev.* **2014**, *114* (8), 4041–4062.
- (50) Geri, J. B.; Shanahan, J. P.; Szymczak, N. K. Testing the push–pull hypothesis: Lewis acid augmented N₂ activation at iron. *J. Am. Chem. Soc.* **2017**, *139* (16), 5952–5956.
- (51) Chalkley, M. J.; Oyala, P. H.; Peters, J. C. Cp* noninnocence leads to a remarkably weak C–H bond via metallocene protonation. *J. Am. Chem. Soc.* **2019**, *141* (11), 4721–4729.
- (52) Ramírez-Solís, A.; Bartulovich, C. O.; Chciuk, T. V.; Hernández-Cobos, J.; Saint-Martin, H.; Maron, L.; Anderson, W. R.; Li, A. M.; Flowers, R. A. Experimental and theoretical studies on the implications of halide-dependent aqueous solvation of Sm(II). *J. Am. Chem. Soc.* **2018**, *140* (48), 16731–16739.
- (53) Ashida, Y.; Arashiba, K.; Nakajima, K.; Nishibayashi, Y. Molybdenum-catalysed ammonia production with samarium diiodide and alcohols or water. *Nature* **2019**, *568* (7753), 536–540.
- (54) Ashida, Y.; Arashiba, K.; Tanaka, H.; Egi, A.; Nakajima, K.; Yoshizawa, K.; Nishibayashi, Y. Molybdenum-catalyzed ammonia formation using simple monodentate and bidentate phosphines as auxiliary ligands. *Inorg. Chem.* **2019**, *58* (14), 8927–8932.
- (55) Ashida, Y.; Mizushima, T.; Arashiba, K.; Egi, A.; Tanaka, H.; Yoshizawa, K.; Nishibayashi, Y. Catalytic production of ammonia from dinitrogen employing molybdenum complexes bearing N-heterocyclic carbene-based PCP-type pincer ligands. *Nat. Synth.* **2023**, 1–10.

- (56) Benedek, Z.; Papp, M.; Oláh, J.; Szilvási, T. Identifying the rate-limiting⁹⁵ elementary steps of nitrogen fixation with single-site Fe model complexes. *Inorg. Chem.* **2018**, *57* (14), 8499–8508.
- (57) Anderson, S. N.; Fakley, M. E.; Richards, R. L.; Chatt, J. Hydrazido(2–)-complexes as intermediates in the conversion of ligating dinitrogen into ammonia and hydrazine. *J. Chem. Soc. Dalton Trans.* **1981**, No. 9, 1973–1980.
- (58) Chatt, J.; J. Pearman, A.; L. Richards, R. Hydrazido(2–)-complexes of molybdenum and tungsten formed from dinitrogen complexes by protonation and ligand exchange. *J. Chem. Soc. Dalton Trans.* **1978**, 0 (12), 1766–1776.

REDUCTIVE SAMARIUM (ELECTRO)CATALYSIS ENABLED BY SAMARIUM(III)-ALKOXIDE PROTONOLYSIS

Reproduced in part with permission from Boyd, E.A.; Shin, C.; Charboneau, D. J.; Peters, J. C.; Reisman, S.E. *Science* 2024, 385, 847. doi: 10.1126/science.adp5777

4.1 Introduction

Sm^{II} species are very versatile, single-electron reductants. Since its introduction to synthesis by Kagan and colleagues in 1977,¹ SmI_2 in particular has become a privileged reagent.² The Ln coordination sphere is highly sensitive to Lewis basic additives, which modulate both the $\text{Sm}^{\text{III/II}}$ reduction potential and the steric profile of the reagent, enabling fine control of reactivity and stereoselectivity.^{3–5} This tunability is invaluable in natural product synthesis, in which stoichiometric Sm^{II} has been used to effect a variety of reductive transformations of carbonyl functional groups (see Figure 4.1 for a representative example).^{6–11} In contrast to alternative strong reductants, the compatibility of Sm^{II} species with Brønsted acids enables proton-coupled reduction reactions, including the conversion of N_2 to fixed-N products (Figure 4.1).^{12–15}

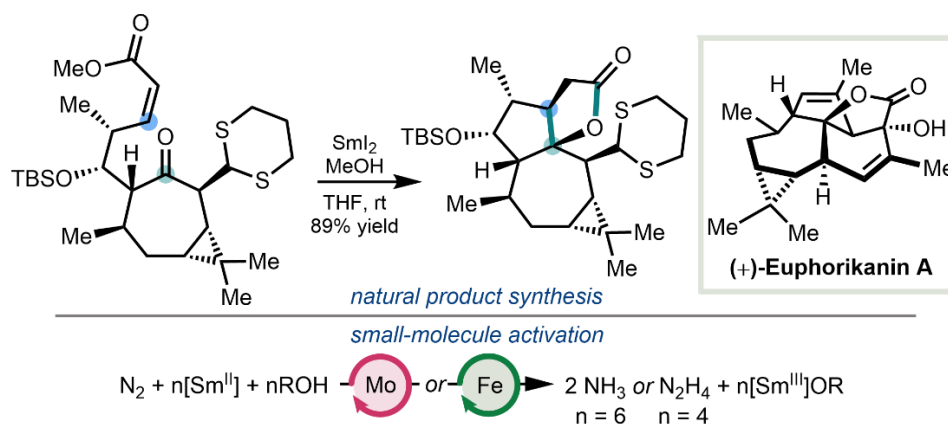


Figure 4.1: Utility of stoichiometric Sm^{II} reductants in diverse applications.^{6,13,15}

Despite the value and versatility of Sm^{II} reductants, they are predominantly⁹⁷ deployed (super)stoichiometrically. Additionally, SmI_2 typically must be used under dilute reaction conditions because the solubility of SmI_2 is $< 0.1 \text{ M}$ in tetrahydrofuran.¹⁶ Therefore, SmI_2 is not desirable for use as a reagent in large-scale settings or in the early stages of multistep synthesis. These limitations could be overcome by the development of a robust and generalizable strategy to use Sm^{II} in catalytic quantities.

The reactivity of Sm^{II} is typically driven by the high oxophilicity or azaphilicity that is characteristic of the f elements.¹⁷ For example, although electron transfer from SmX_2 to ketone substrates is disfavored based on the comparison of outer sphere reduction potentials (Figure 4.2, step i; $\text{X} = \text{halide}$, $\Delta E^\circ > 1 \text{ V}$ for $\text{X} = \text{I}$), the strong coulombic interaction between Sm^{III} and the resulting ketyl radical anion drives such reactions forward.¹⁸ However, this stabilizing interaction simultaneously presents the primary barrier to catalytic turnover.¹⁹ The cathodic reduction potentials of $\text{Sm}^{\text{III}}(\text{OR})_n$ species are prohibitively negative for desirable catalysis.^{20–22} Exchange of RO^- with X^- to generate more readily reduced SmX_3 species is an attractive approach for turnover (Figure 4.2, steps iii and iv), but mild, selective, and tunable methods for the cleavage of $\text{Sm}-\text{O}$ bonds remain elusive.

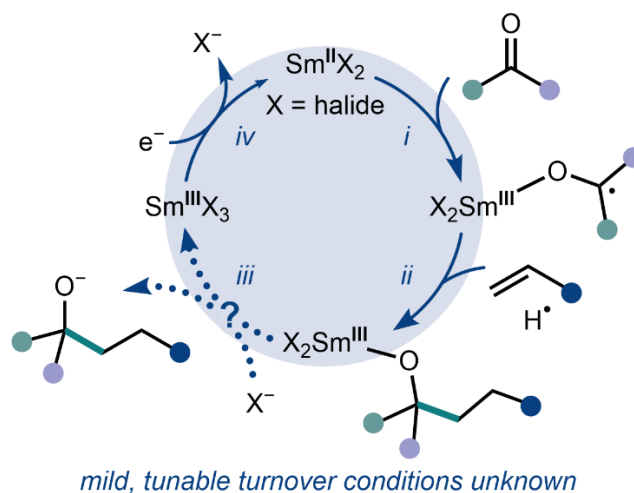


Figure 4.2: Targeted Sm^{II}-catalyzed cycle for ketyl-olefin coupling.

The few reports that have attempted to address the challenge of reductive Sm catalysis used halosilanes (R_3SiX) as oxophiles to cleave alkoxides from Sm^{III} (Figure 4.3A).^{23–26} Such methods have not been widely adopted, possibly because the reagents required for turnover have limited substrate compatibility. For instance, whereas relatively mild chlorosilane reagents are capable of cleaving alkoxides from Sm^{III} , as exemplified by a pinacol-coupling reaction reported by Greeves and coworkers (Figure 4.3A), chloride rapidly displaces iodide from the Sm coordination sphere (Figure 4.3B).^{25,27} $SmCl_3$ is more difficult to reduce than SmI_3 and therefore requires a strong terminal reductant such as Mg^0 . In what is likely the sole precedent of SmI_3/SmI_2 turnover (as opposed to $SmI_nCl_{3-n}/SmI_nCl_{2-n}$), Corey and Zheng avoided the problem of halide scrambling in their Sm-catalyzed cross-coupling of ketones and acrylates by using Me_3SiOTf as an oxophile in combination with LiI (Figure 4.3A); however, this required manual slow addition of Me_3SiOTf to mitigate parasitic consumption of the acrylate coupling partner.²³ As a final point, halosilanes are not compatible with the protic additives ubiquitous in Sm^{II} chemistry (Figure 4.2).

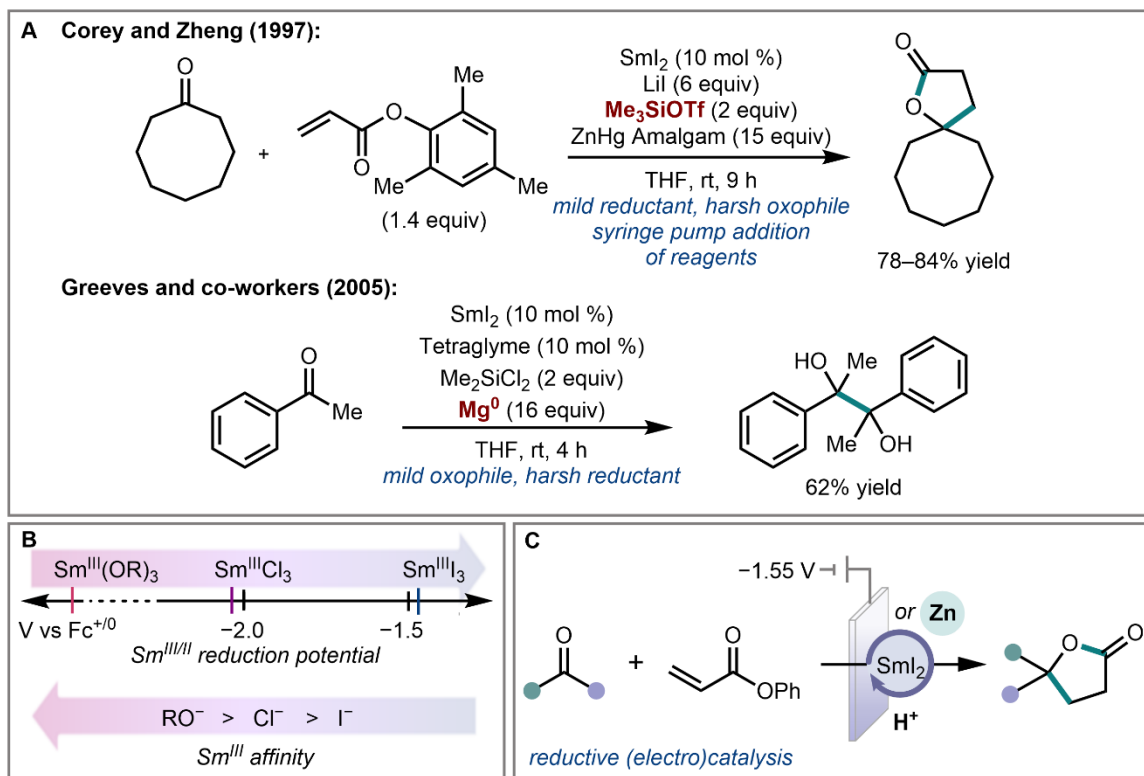


Figure 4.3: (A) Representative Sm catalysis precedents.^{23,25} (B) Inverse relationship between Sm^{III} -ligand affinity and reduction potential. (C) Sm-catalyzed reductive cross-coupling of ketones and acrylates under mild chemical and electrochemical conditions as described herein.

Considering the challenge of Sm^{III} -OR turnover, we recognized that protonation would be a tunable approach to Sm-alkoxide cleavage. Here, we demonstrate rapid and reversible protonolysis of alkoxide ligands from Sm^{III} through judicious pairings of cationic Brønsted acids and halide donors. This transformation was leveraged to achieve Sm-catalyzed reductive cross-coupling of ketones and acrylates using Zn^0 as a relatively mild source of reducing equivalents at the $\text{SmI}_3/\text{SmI}_2$ redox couple (Figure 4.3C). $\text{Sm}(\text{OTf})_3$ serves as a shelf-stable, commercially available Sm precursor, and the reactions can be conducted on a gram scale at 10-fold higher concentrations than is typically used when stoichiometric SmI_2 is used. The optimized conditions translate into a bona fide

electrocatalytic system, distinct from prior systems in which electrochemically driven ¹⁰⁰ Sm^{III/II} turnover has been difficult to firmly establish.²⁸⁻³¹ Finally, we provide a thermochemical analysis of the factors controlling the alkoxide protonolysis step as a basis for future developments in catalytic and electrocatalytic Sm chemistry.

4.2 Development of mild turnover conditions for reductive SmI₂ catalysis

We began our studies by using Sm(O^{*i*}Pr)₃ as a model of the Sm^{III}-alkoxide species generated under reductive coupling conditions with the goal of identifying a suitable proton donor and iodide source to generate redox-active SmI₃ and enable catalysis (Figure 4.4). We anticipated that successful conditions would meet the following requirements for alkoxide-iodide exchange at Sm^{III}: (i) the conjugate base of the acid should not outcompete coordination of I⁻ to Sm^{III}; (ii) the counterion should be chemically compatible with SmI₃/SmI₂ redox cycling,^{21,32} and (iii) the pK_a of the acid in MeCN should be <19, guided by the effective pK_a value of 19.9 for the cationic [Sm^{III}]⁺ complex with MeOH in MeCN³³ benchmarked in Chapter 2.

Thus, we investigated a panel of acids (baseH⁺) and iodide sources and identified lutidinium bis(trifluoromethylsulfonyl)imide (LutHNTf₂) as meeting these criteria, as demonstrated by cyclic voltammetry (CV). The strongly donating alkoxide ligands of Sm(O^{*i*}Pr)₃ render it redox inactive in the THF solvent window (Figure C14). However, after the addition of LutHNTf₂ (3.0 equiv; pK_a = 14.2 in MeCN)³⁴ and LiI (3 equiv) to Sm(O^{*i*}Pr)₃ in THF, a quasireversible wave centered at -1.44 V versus Fc⁺⁰ appeared in the CV (Figure 4.4A, magenta trace), suggestive of SmI₃ generation. To verify this assignment, SmI₃ was generated through ion exchange between Sm(OTf)₃ and LiI under identical electrochemical conditions. This mixture also featured a quasireversible reduction centered

at -1.47 V (Figure 4.4A, dashed blue trace). We attribute the small offset in potential to some degree of OTf^- association, as addition of LiOTf to the protonolysis mixture resulted in a 30 mV cathodic shift to recapitulate the wave observed following OTf^-/I^- exchange (Figure 4.4A, teal trace).

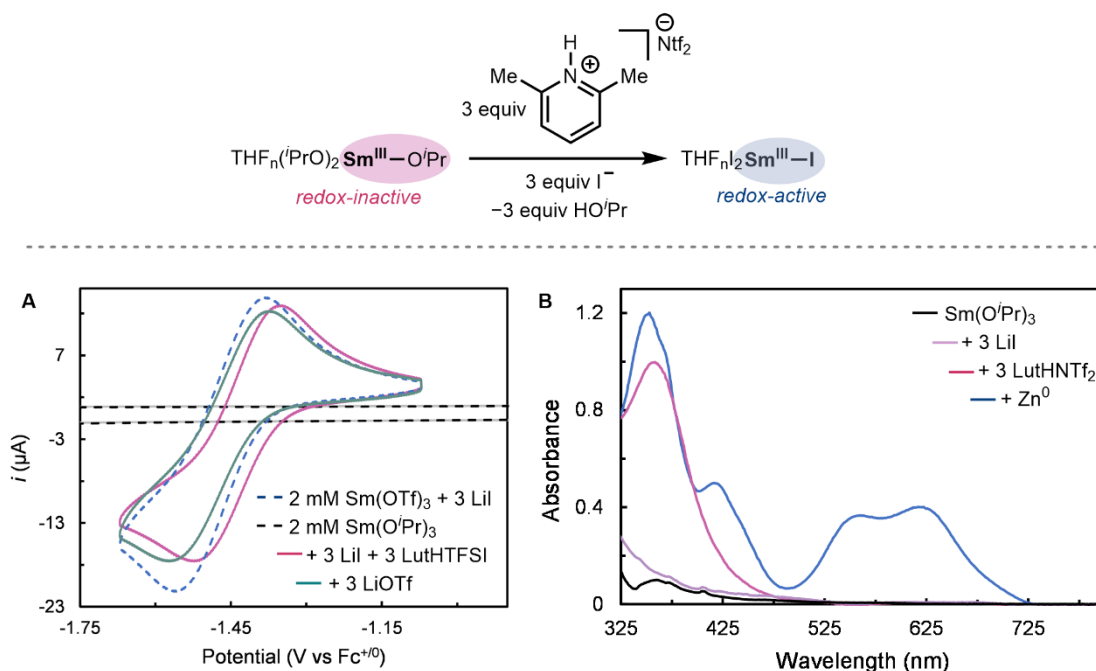


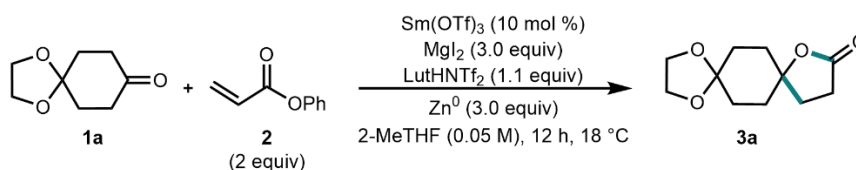
Figure 4.4: Proposed conversion of Sm-alkoxides to SmI_3 . (A) CVs of 2 mM $\text{Sm}(\text{O}^i\text{Pr})_3$ (black dashed trace) after the successive addition of 3 equiv each of LiI and LutHNTf_2 (magenta trace) and 3 equiv of LiOTf (green trace) overlaid with the CV of 2 mM $\text{Sm}(\text{OTf})_3$ after the addition of 3 equiv of LiI (dashed blue trace) at 100 mV s^{-1} on a glassy carbon working electrode in THF containing 0.1 M BMPipNTf_2 (where BMPip is 1-butyl-1-methylpiperidinium). (B) UV-vis spectra in THF of $\text{Sm}(\text{O}^i\text{Pr})_3$ (black, 5 mM total Sm) following the successive addition of 3 equiv of LiI (light purple, 5 mM total Sm), 3 equiv of LutHNTf_2 (magenta, 1 mM total Sm), and excess Zn^0 (blue, 1 mM total Sm).

A parallel spectrophotometric experiment confirmed the generation of SmI_3 from $\text{Sm}(\text{O}^i\text{Pr})_3$ through protonolysis-iodide substitution. Addition of 3 equiv of LutHNTf_2 to a

102
colorless solution of Sm(OⁱPr)₃ with 3 equiv of LiI in THF results in an instantaneous color change to yellow, consistent with SmI₃ generation (Figure 4.4B, magenta trace).²¹ Stirring this mixture over Zn⁰ powder for 30 minutes followed by filtration yields a blue solution with the characteristic absorption features of SmI₂ in THF at λ_{max} = 555 and 618 nm (Figure 4.4B, blue trace). An overall yield of SmI₂ of ca. 50% from Sm(OⁱPr)₃ by protonolysis followed by Zn⁰ reduction is obtained. Critically, the relatively mild acid LutHNTf₂ is compatible with Zn⁰ as a relatively mild reductant ($E^\circ(\text{Zn}^{2+}/\text{Zn}^0) = -1.58 \text{ V}$ vs Fc⁺⁰ in THF containing 0.2 M LiI), opening the door for selective delivery of reducing equivalents to intermediates of reductive Sm catalysis without a significant competing H₂ evolution reaction (HER).

Following identification of reagents for turnover of Sm^{III}-alkoxides, we explored the reductive coupling between 1,4-cyclohexanedione monoethyleneacetal (**1a**) and acrylates (R = ^tBu, CH₂CF₃, Ph) to give spirocyclic γ-lactone **3a** (Figure 4.5, entry 1).³⁵ Sm(OTf)₃ was used as an inexpensive, commercially available precatalyst. Although the CV studies used LiI as the iodide source, MgI₂ was found to be necessary for the synthetic transformation. When LiI or ⁿBu₄NI was used, the reactions did not change to the purple color indicative of SmI₂ in 2-methyltetrahydrofuran (2-MeTHF) (entry 2). After an initial evaluation of acrylates (R = ^tBu, CH₂CF₃, Ph; entries 3 and 4), phenyl acrylate was found to perform best, furnishing γ-lactone **3a** in quantitative yield under the optimal conditions [10 mol % Sm(OTf)₃, 3.0 equiv MgI₂, 1.1 equiv LutHNTf₂, 3.0 equiv Zn⁰ in 2-MeTHF (0.05 M) at 18°C]. No product was observed in the absence of Sm(OTf)₃ (entry 6), but lowering the MgI₂ loading decreased the yield slightly (entry 7). When Gd(OTf)₃ was used as a redox-inactive Lewis acid substitute for Sm(OTf)₃, no product was formed, supporting

Sm^{III/II} redox activity in catalysis (entry 8). Substituting Sm(OTf)₃ with Mg(OTf)₂ also did not furnish any product (entry 9). Zn⁰ was required for product formation (entry 10), whereas omission of LutHNTf₂ resulted in low yield (entry 11). Finally, 2-MeTHF was superior to THF as a solvent (entry 12). A practical advantage of the ability to use catalytic Sm for reductive transformations is that the reactions can be performed at substrate concentrations above the 0.1 M limit imposed by the solubility limit of SmI₂ in THF. Under these catalytic conditions, comparable yields of product **3a** can be formed at a 10-fold higher concentration (0.20 M **1a**; entries 13 and 14), which to the best of our knowledge is the highest concentration reported for a reductive Sm transformation.



Entry	Deviation from standard condition	Yield (%)
1	None	>99
2	Lil (6 equiv) or ⁿ Bu ₄ NI (6 equiv) instead of MgI ₂	0
3	^t Bu acrylate instead of Ph acrylate	88
4	2,2,2-TFE acrylate instead of Ph acrylate	88
5	5 mol % Sm(OTf) ₃	90
6	No Sm(OTf) ₃	0
7	2.0 equiv MgI ₂	91
8	Gd(OTf) ₃ instead of Sm(OTf) ₃	0
9	15 mol % Mg(OTf) ₂ instead of Sm(OTf) ₃	0
10	No Zn ⁰	0
11	No LutHNTf ₂	23
12	THF instead of 2-MeTHF	28
13	1.0 mmol 1a , 0.20 M	84
14	5.0 mmol 1a , 0.20 M	78

Figure 4.5: Reaction optimization and control experiments conducted at 0.05 mmol scale. Listed concentrations correspond to the ketone substrate **1a**. Yields for entries 1 to 12 were determined by ¹H nuclear magnetic resonance (¹H NMR) spectral integration using 1,3,5-trimethoxybenzene as an internal standard; entries 13 and 14 are isolated yields.

The scope of the above reaction is consistent with that of prior investigations³⁵ using¹⁰⁴ stoichiometric SmI₂. A variety of aliphatic and aromatic ketones performed well, giving the γ -lactone products in good to excellent yields (Figure 4.6). Common functional groups, such as silyl ethers (**3h**), esters (**3j**), aryl halides (**3n** to **3r**), sulfonates (**3w**), and boronate esters (**3x**), were compatible under the reaction conditions. Aryl ketones bearing strong electron-withdrawing substituents (**3aa**) resulted in lower yield due to competitive pinacol coupling. A cyclohexanone substrate bearing an α -tethered unactivated olefin exclusively formed the spirocyclic γ -lactone (**3i**, 3:1 dr) without any evidence of 5-*exo*-trig cyclization. The pharmaceutically relevant heterocyclic building blocks tetrahydrothiopyran (**3k**) and tetrahydropyran (**3l**) were produced in synthetically useful yields.

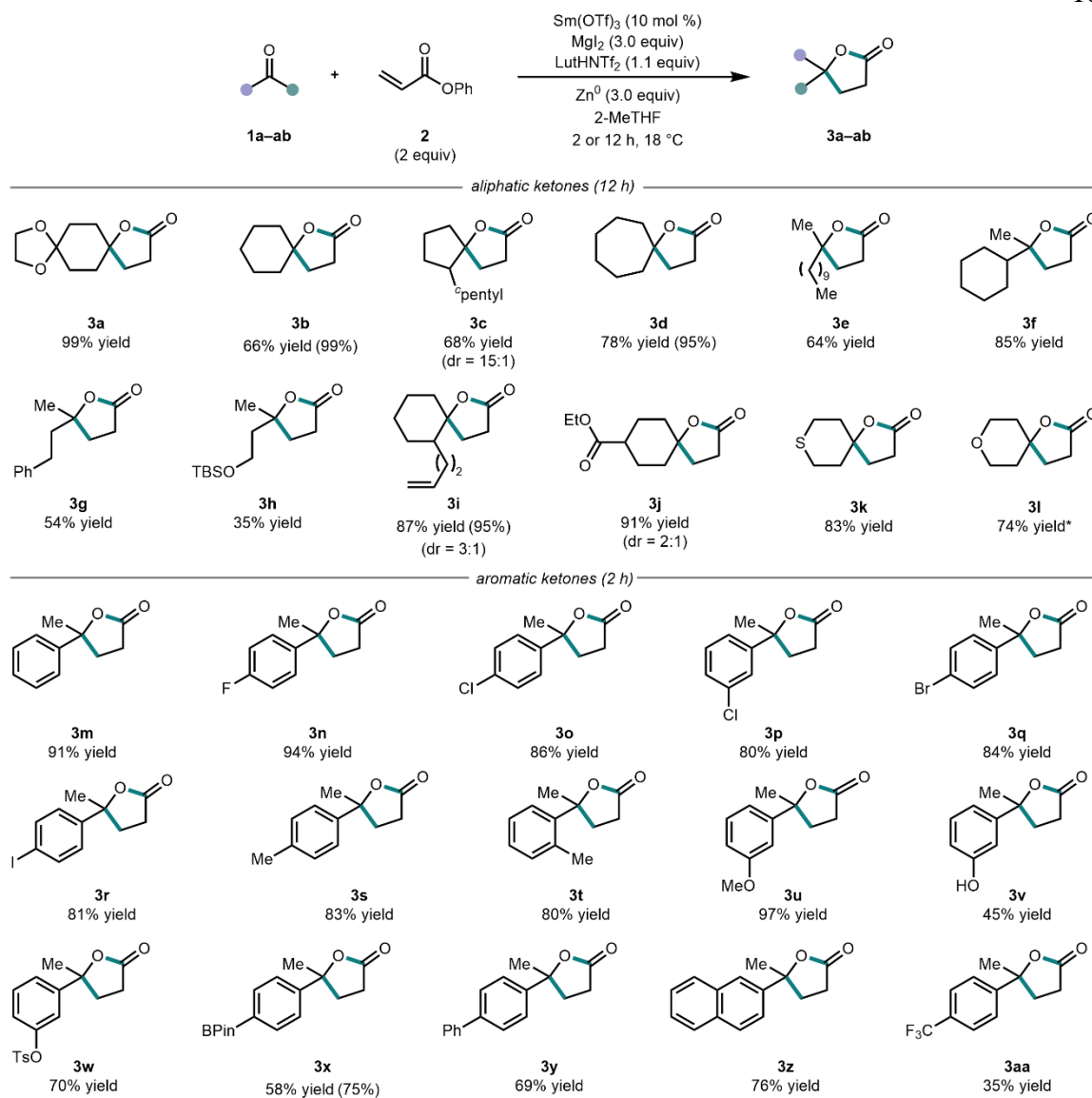


Figure 4.6: Substrate scope of Sm-catalyzed reactions. Reactions were conducted on a 0.3 mmol scale. Isolated yields are reported unless otherwise specified. Yields in parentheses were determined by ^1H NMR analysis using 1,3,5-trimethoxybenzene as an internal standard due to the volatility of the product or instability to silica gel. *3.3 equiv LutHNTf₂ was used.

In their recent total synthesis of (+)-euphorikanin A, Carreira and coworkers demonstrated that the diastereoselectivity of an intramolecular SmI₂-mediated lactonization is dictated by the *E/Z* geometry of the acrylate.⁶ To determine whether this is

also true under the catalytic conditions, an analogous pair of intramolecular reductive lactonizations were performed with *E*- and *Z*-**1ab** (Figure 4.7). Using stoichiometric conditions otherwise identical to those of Carreria et al., the *cis* product was favored using the *Z*-olefin, whereas the *trans* product was favored with the *E*-olefin. The inversion in diastereoselectivity was observed using the catalytic system, albeit with slightly diminished dr. The slight erosion in dr might result from competing Mg^{2+} ion coordination to the acrylate.

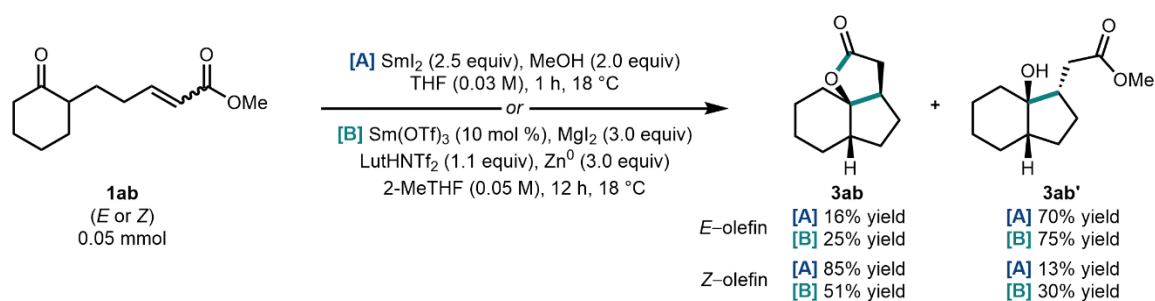


Figure 4.7: Diastereoselectivity of intramolecular Sm catalysis with *E*- and *Z*-**1ab**.

4.3 Demonstration of Electrocatalysis

Although Zn^0 is well suited to SmI_3/SmI_2 turnover, it is not suitable for generating Sm^{II} species with substantially more negative reduction potentials.³⁶ Electrochemical methods in which the applied potential can be matched to the $Sm^{III/II}$ reduction potential are thus appealing. However, Sm-mediated electrocatalysis is poorly developed. These reactions can suffer from competing reactivity mediated by the oxophile or metal cations generated at the sacrificial anodes; in some cases, the use of an Sm metal electrode was reported to be necessary.^{26,28–31} We sought to address these challenges by developing well-defined electrocatalysis using the Sm-alkoxide protonolysis strategy discussed above.

The CV of SmI₃ generated by combining Sm(OTf)₃ and MgI₂ in 2-MeTHF features¹⁰⁷ a quasi-reversible wave centered at -1.55 V (Figure 4.8, black traces). The CV of SmI₃ with ketone **1a**, acrylate **2**, and MgI₂ (Figure 4.8A, magenta trace) exhibits an irreversible wave that is double the current intensity of the 1e⁻ reduction of SmI₃. This response, which is also observed with the aromatic ketone substrate **1m** (Figure 4.8B, magenta trace), is consistent with net Sm-mediated 2e⁻ reductive coupling of the ketone and acrylate to yield a γ -alkoxy-enolate species (Figure 4.8, iii).

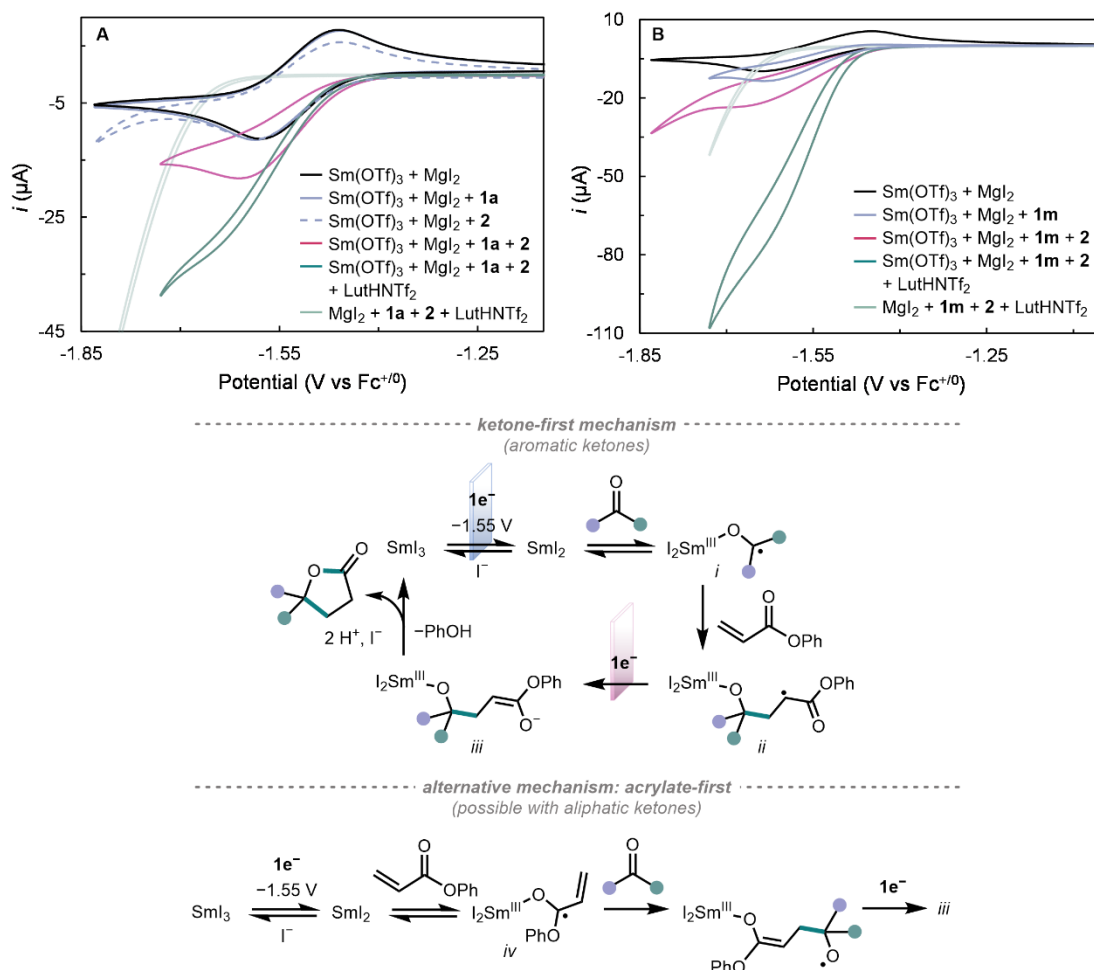


Figure 4.8: CVs of 2 mM Sm(OTf)₃ and MgI₂ (25 equiv, black traces) after the addition of either substrates **1a** or **1m** (10 equiv, solid light blue traces), **2** (20 equiv, dashed light blue trace), the combination of ketone and acrylate substrates (magenta traces), and the acid LutHNTf₂ (20 equiv, green trace) overlaid with the CVs of the substrates, acid, and MgI₂ in the absence of Sm (light green traces). All CVs were collected on a glassy carbon working electrode in 2-MeTHF containing 0.2 M BMPyNTf₂ (where BMPy is 1-butyl-1-methylpyrrolidinium) at 25 mV s⁻¹.

Further addition of LutHNTf₂ in the presence of both ketone and acrylate gave rise to S-shaped multielectron waves at the potential of SmI₃ reduction (Figure 4.8, green traces), indicative of electrocatalytic turnover. Control experiments confirmed that none of the

individual reaction components (see Appendix C3.1), nor their combination in the¹⁰⁹ absence of Sm (Figure 4.8, light green traces), were responsible for the current at -1.5 V. The higher current observed with **1m** compared to **1q** is indicative of a faster catalytic rate with the more easily reduced ketone.

An additional motivation for development of electrochemically driven Sm catalysis is to avoid generation of oxophilic metal cations as byproducts of metal powder reductants (e.g., Zn^{2+} , Mg^{2+}), as such species present in excess compete with Sm for binding of potential ancillary ligands, limiting straightforward extension to asymmetric Sm catalysis with chiral ligands. We thus investigated the use of $n\text{Bu}_4\text{NI}$ as an iodide source in place of MgI_2 . While SmI_3 is generated smoothly as evidenced by CV (Figure 4.9, black trace), in this case, addition of **1a** and **2** resulted in an irreversible wave with less enhancement in current relative to when MgI_2 was used (Figure 4.9, light blue trace, versus Figure 4.8A, magenta trace). The full $2e^-$ current was regained on titration of $\text{Mg}(\text{NTf}_2)_2$ (Figure 4.9, light blue-magenta traces), suggesting that the second electron transfer to the presumed radical intermediate (ii) at the electrode is facilitated by Mg^{2+} through formation of a magnesium-bound enolate (iii-Mg).³⁷ In most stoichiometric SmI_2 reductions, every electron transferred to substrate also generates an equivalent of Lewis acidic Sm^{III} ; with low concentrations of Sm, however, alternative Lewis acids may be necessary to activate and/or stabilize intermediates downstream of the initial Sm^{II} -mediated electron transfer.

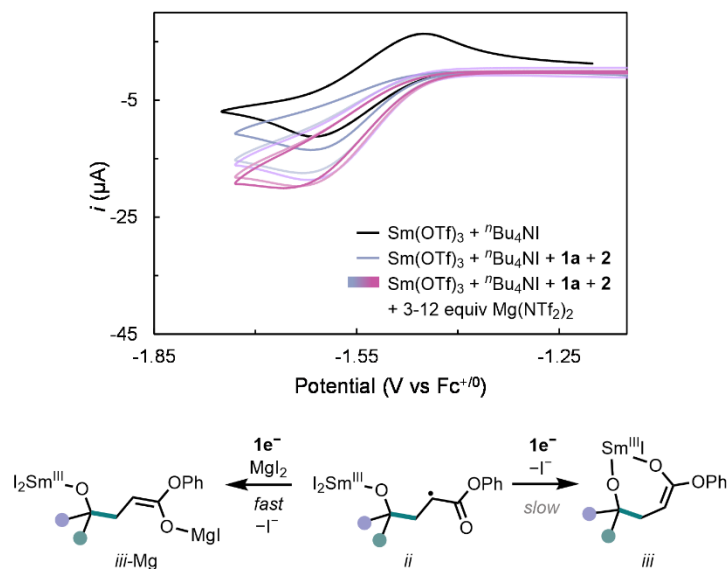
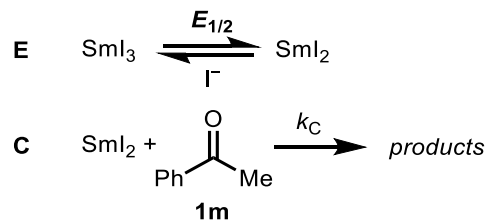


Figure 4.9: CVs of 2 mM Sm(OTf)₃ and ⁿBu₄NI (50 equiv, black trace) after the addition of the substrates **1a** and **2** (10 and 40 equiv, respectively, blue trace), followed by titration of Mg(NTf₂)₂ (light blue-magenta traces) in 2-MeTHF containing 0.2 M BMPyNTf₂ at 25 mV s⁻¹.

Substrate coupling could be initiated either by ketone reduction or acrylate reduction (Figure 4.8).³⁸ A “ketone-first” mechanism is likely operative with easily reduced aromatic ketones such as **1m**. At all sampled scan rates up to 100 mV s⁻¹, the CV of SmI₃ in the presence of excess acetophenone (**1m**) is fully irreversible and shifts positive with increasing [acetophenone] (Figure 4.10A). This response corresponds to an EC mechanism, where E is the electrochemical one-electron reduction of SmI₃ to SmI₂ and C is the irreversible chemical reaction of SmI₂ with **1m**. In the regime of pure kinetic control where no return anodic feature is observed, the evolution of the cathodic peak potential ($E_{p,c}$) as a function of the concentration of **1m** is described by eqn 4.2.³⁹



$$k_{obs} = k_C[\mathbf{1m}]^p \quad (4.1)$$

$$E_{p,c} = E_{1/2} - \frac{RT}{F}(0.78) + \frac{pRT}{2F} \ln \left(\frac{k_C[\mathbf{1m}]^{RT}}{Fv} \right) \quad (4.2)$$

Plots of $E_{p,c}$ vs $\log([\mathbf{1m}])$ collected at several different scan rates are linear with an average slope of $25 \pm 2 \text{ mV dec}^{-1}$ (Figure 4.10B), indicating that the chemical step C is first order in acetophenone ($p = 1$). Based on $E_{1/2} = -1.66 \text{ V vs Ag}^{+/0}$ measured for the SmI_3 redox wave measured immediately before titration with $\mathbf{1m}$ (black trace in Figure 10A), the intercepts of these plots provide an estimate of the rate constant k_C as $83 \pm 9 \text{ M}^{-1} \text{ s}^{-1}$ under these conditions.

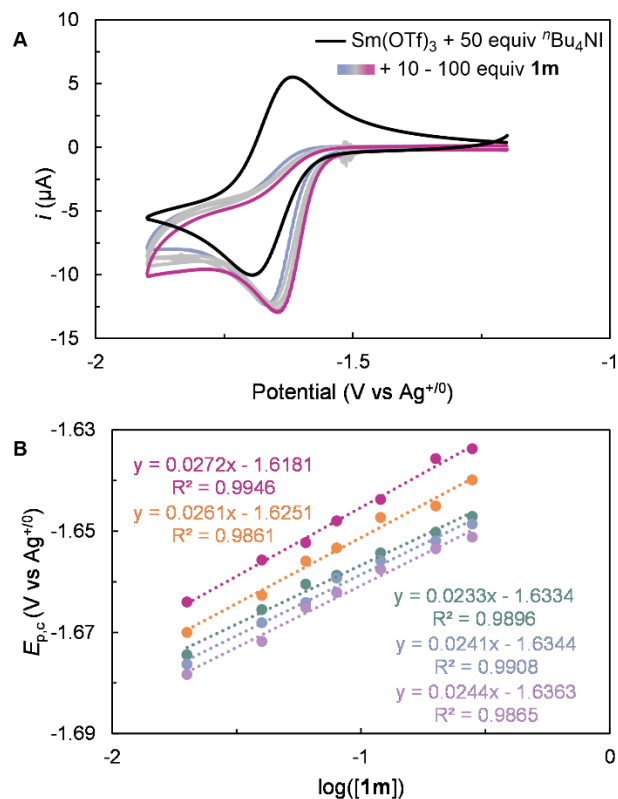


Figure 4.10: (A) CVs of $\text{Sm}(\text{OTf})_3$ (2 mM), $n\text{Bu}_4\text{NI}$ (50 mM), and acetophenone ($\mathbf{1m}$, 0-200 mM) in 2-MeTHF containing 0.2 M BMPyNTf_2 at 20 mV s^{-1} . (B) Plots of $E_{p,c}$ vs $\log([\mathbf{1m}])$ for CV data of $\text{Sm}(\text{OTf})_3$ (2 mM), $n\text{Bu}_4\text{NI}$ (50 mM), and acetophenone (20-280 mM) collected at 20 (magenta), 40 (orange), 60 (teal), 80 (blue), and 100 (purple) mV s^{-1} .

By contrast, the $\text{SmI}_3/\text{SmI}_2$ wave remained reversible in the presence of either (but not both) the aliphatic ketone $\mathbf{1a}$ or acrylate $\mathbf{2}$ (Figure 4.8A, solid and dashed light blue traces, respectively). These data indicate that the initial electron transfer step to form i or iv is slow and/or uphill with these substrates,³⁹ as is typical for the reduction of unactivated carbonyl substrates by SmI_2 .^{2,40} However, reduced and homocoupled products of both aliphatic ketones and acrylate $\mathbf{2}$ were observed when each substrate was subjected to the standard

Zn⁰-driven catalytic conditions in the absence of the respective cross-coupling partner,¹¹³ suggesting that SmI₂ is competent for reduction of both substrates (see Appendix C4.1).

Indeed, CVs of SmI₃ lost reversibility (Figure 4.11) at increased concentrations of **1a** and **2**. In this case, the CV wave shape corresponds to an EC mechanism in an intermediate kinetic regime with relatively slow k_C , necessitating simulations to extract kinetic parameters. First, the reversible CV of Sm(OTf)₃ in the presence of excess ⁿBu₄NI was simulated over a range of scan rates to estimate the electrochemical rate constant k_0 of the electron transfer step as $k_0 = 0.0075 \text{ cm s}^{-1}$. CVs were then simulated across a range of λ values to construct a working curve, where λ is a dimensionless parameter defined by eqn 4.3:

$$\lambda = \frac{RT}{F} \frac{k_{obs}}{v} \quad (4.3)$$

$$k_{obs} = k_C [\mathbf{1a}]^p \quad (4.4)$$

Experimental $i_{p,a}/i_{p,c}$ values collected at multiple scan rates at each [**1a**] were plotted vs $\log(\lambda/k_C)$ using varying values of p . The data collapses to a single curve with $p = 1$, indicating that the chemical step C is first-order in **1a**. The value of k_C was then varied in a plot of $i_{p,a}/i_{p,c}$ vs $\log(\lambda)$ until the experimental data overlaid with the simulated working curve (Figure 4.11A) to estimate a much slower bimolecular rate constant of $0.35 \text{ M}^{-1} \text{ s}^{-1}$ for the irreversible consumption of SmI₂ by the difficult-to-reduce ketone **1a**. The same analysis for the reaction of SmI₂ with the acrylate **2** under the electrochemical conditions indicates that the C step is second-order in **2** ($p = 2$, $k_C = 56 \text{ M}^{-2} \text{ s}^{-1}$; Figure 4.11B), suggesting that the observed kinetics are an aggregate of electron transfer and homocoupling rates. Without direct access to the relative rates of initial aliphatic ketone versus acrylate reduction, both “acrylate-first” and “ketone-first” mechanisms must be considered viable.

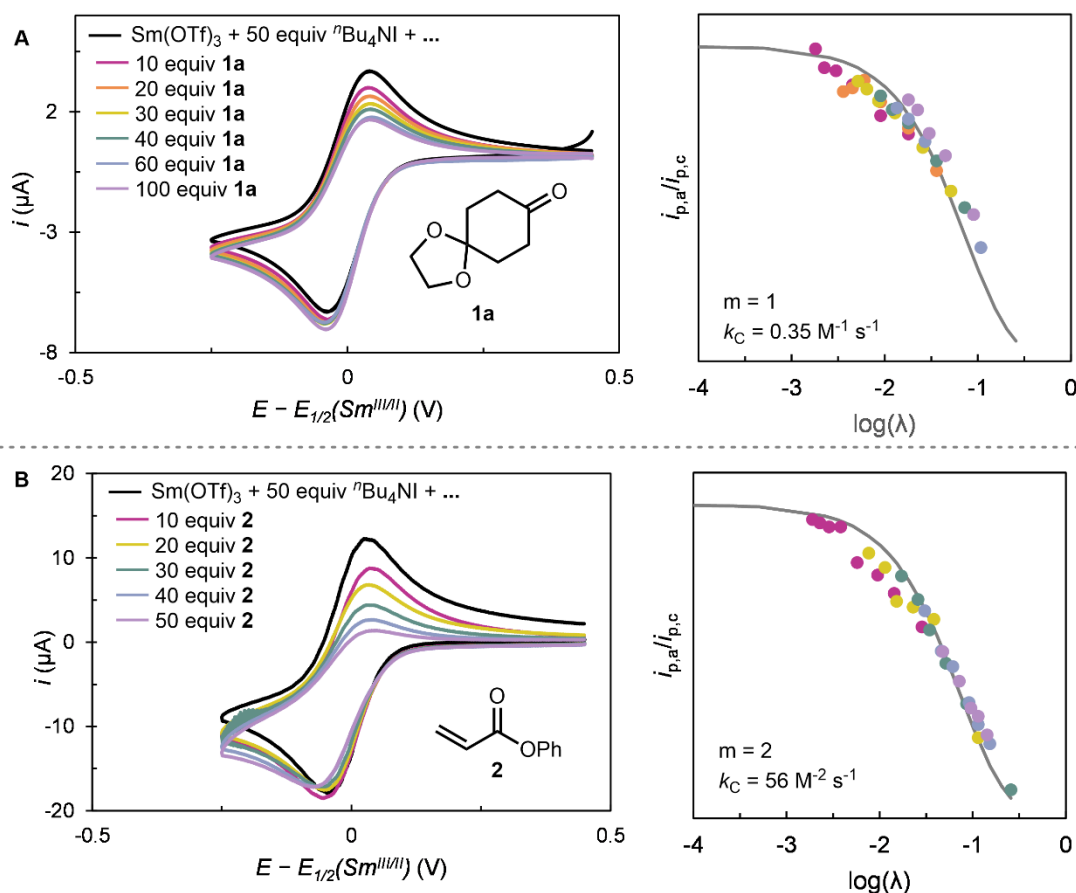


Figure 4.11: Left: CVs of $\text{Sm}(\text{OTf})_3$ (2 mM), $t\text{Bu}_4\text{NI}$ (50 mM), and **1a** or **2** in 2-MeTHF containing 0.2 M BMPyNTf₂ at 100 mV s⁻¹. Right: experimental $i_{p,a}/i_{p,c}$ values at varying scan rates at each substrate concentration plotted vs $\log(\lambda)$ using m and k_C values that result in a good fit with the simulated working curve (gray trace).

Having gained an understanding of the reduction events through electroanalytical studies, we investigated electrocatalytic formation of lactone **3a**. We used constant potential electrolysis (CPE) to avoid electrode-mediated HER with LutHNTf₂ (HER onsets at ~ -1.7 V under these conditions; Figure C9). Proton-coupled oxidation of Hantzsch ester (HEH₂) was selected as a well-behaved counter-reaction. CPE of ketone **1a** and acrylate **2** with $\text{Sm}(\text{OTf})_3$, LutHNTf₂, and MgI₂ at an applied potential of -1.55 V (carbon cloth

cathode; two-compartment cell) furnished the cross-coupled lactone **3a** in 75% yield at ¹¹⁵ 75% Faradaic efficiency (Figure 4.12). HE was produced quantitatively. Under the same conditions, phenyl-substituted lactone **3m** was prepared in 85% yield. With this more activated substrate, current attributable to ketone reduction was observed in the absence of Sm(OTf)₃ at -1.65 V; however, under these conditions, only the pinacol product **4m** was formed. This finding highlights the role of Sm in favoring lactone formation over possible competing processes.

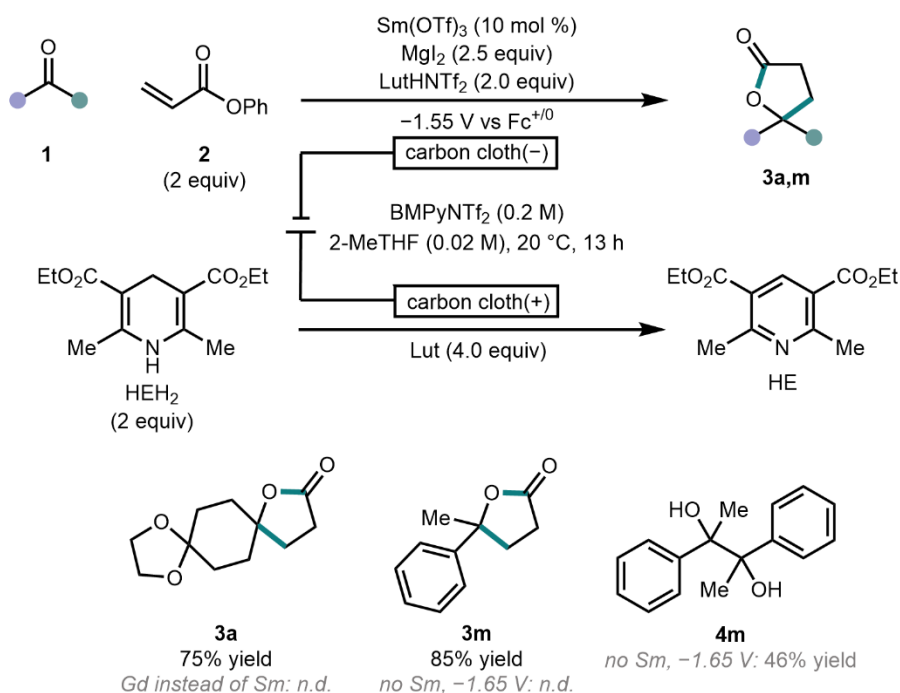


Figure 4.12: CPE conditions (0.1 mmol scale). Yields were determined by ¹H NMR analysis using 1,3,5-trimethoxybenzene as an internal standard.

4.4 Thermochemistry and Outlook

Finally, we investigated the factors influencing the key proton-transfer step in Sm^{III}-OR reactivation. The equilibrium of the Sm^{III} alkoxide protonolysis and ligand substitution can be decomposed into a thermochemical cycle of five components (Figure 4.13). Net protonolysis is favored by (i) a weaker affinity of the alkoxide for Sm^{III}, (ii) a higher p*K*_a

of the corresponding alcohol, (iii) a stronger Brønsted acid (baseH^+), (iv) a relatively ¹¹⁶ weak affinity of the halide for its corresponding counteranion M^+ , and (v) a stronger affinity of the halide for Sm^{III} . The last three components are readily decoupled through independent variation of the acid, the halide donor, and the identity of the halide, enabling rational control of the net alkoxide cleavage step.

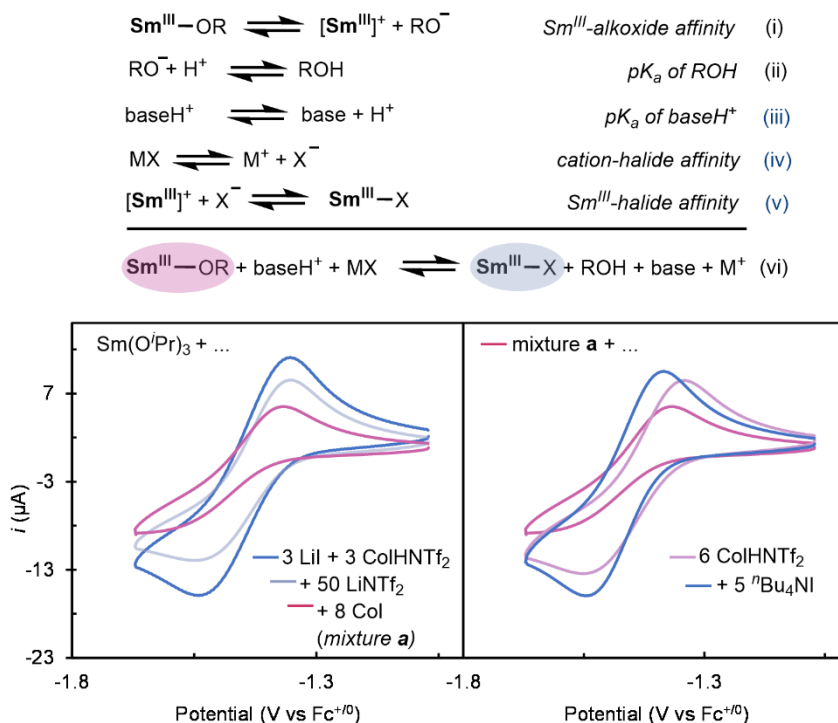


Figure 4.13: Thermochemical cycle describing $\text{Sm}^{\text{III}}-\text{OR}$ protonolysis and CVs demonstrating reversibility of $\text{Sm}(\text{O}^i\text{Pr})_3$ (2 mM) protonolysis and iodide substitution with ColHNTf_2 and LiI at 100 mV s^{-1} in THF containing 0.1 M BMPipNTf_2 .

Consistent with Le Chatelier's principle, the amount of redox-active SmI_3 after the reaction of $\text{Sm}(\text{O}^i\text{Pr})_3$ with LiI and ColHNTf_2 decreased with the addition of LiNTf_2 and col-lidine (as reflected in the CVs in Figure 4.13). The initial current intensity was restored by the addition of ColHNTf_2 and $^t\text{Bu}_4\text{NI}$. The influence of the pK_a of the acid (baseH^+) was demonstrated by using $^t\text{Bu}_4\text{NI}$ as the iodide source and collecting CV data with a panel

of acids spanning pK_a values of ~ 10 to 19 . The redox activity of the system, which¹¹⁷ reflects the position of the equilibrium between $\text{Sm}(\text{O}^i\text{Pr})_3$ and SmI_3 , decreased as the pK_a of the base H^+ increased (Figure 4.14). Addition of Mg cation [e.g., $\text{Mg}(\text{NTf}_2)_2$], which has a stronger affinity for I^- than does ${}^n\text{Bu}_4\text{N}^+$, shifted the equilibrium toward $\text{Sm}(\text{O}^i\text{Pr})_3$. As a result, stronger acids were required under these conditions to completely restore redox activity (Figure 4.14, compare the green versus red traces).

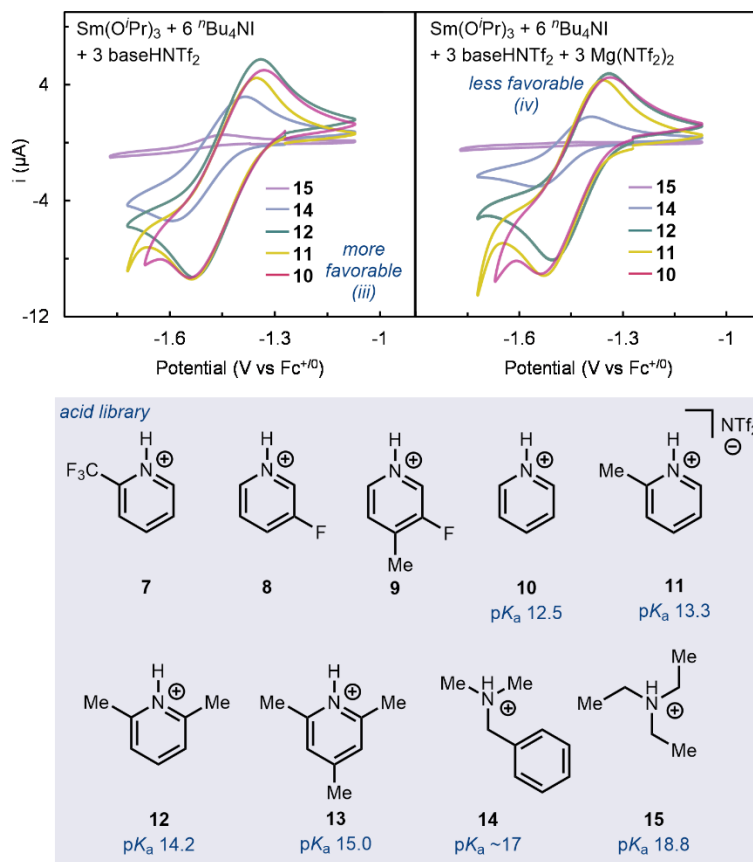


Figure 4.14: CVs demonstrating the sensitivity of net protonolysis and iodide substitution of $\text{Sm}(\text{O}^i\text{Pr})_3$ (2 mM) to the acid pK_a and availability of iodide at 25 mV s^{-1} in 2-MeTHF containing 0.1 M BMPipNTf₂.

This relationship points to the potential breadth of the parameter space accessible for optimization of Sm-catalyzed reactions involving different substrates, intermediates, and

desired products. As an illustrative example, depending on the acid and solvent used for¹¹⁸ the Sm-catalyzed coupling between **1m** and ^tBu-acrylate, different products were observed (Figure 4.15). The cross-coupled products **3m** and **5m** were favored with high- pK_a acids in solvents such as THF and 2-MeTHF. A pronounced selectivity for the lactone product **3m** over its acyclic counterpart **5m** was observed in 2-MeTHF. The pinacol and reduction products **4m** and **6m** were more prevalent with low- pK_a acids, particularly when strongly coordinating solvents such as acetonitrile or dimethoxyethane were used. This difference may be due to early protonolysis of the Sm^{III}-ketyl intermediate to release the neutral ketyl radical, which might rapidly dimerize or undergo reduction before productive addition to acrylate can occur.²⁷

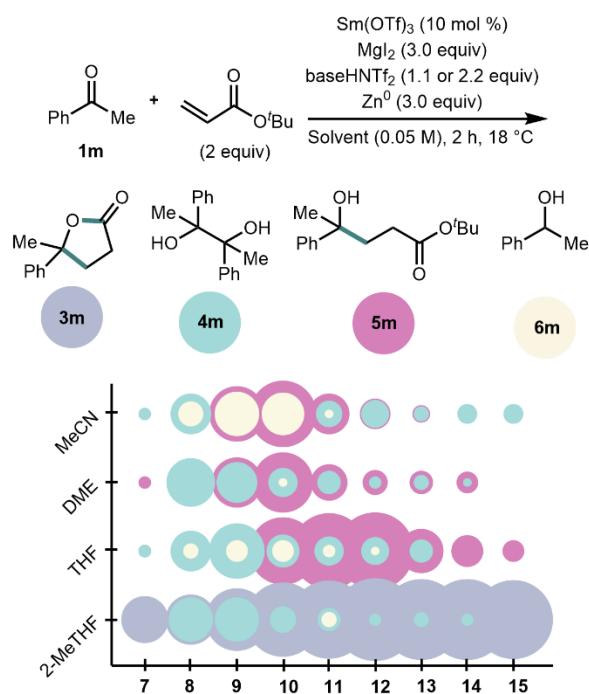


Figure 4.15: Product distribution of Sm-catalyzed reductive cross-coupling of acetophenone and ^tBu-acrylate as a function of dielectric strength and acid pK_a . Diameters of circles correlate to yield of each product determined by ¹H NMR analysis using 1,3,5-trimethoxybenzene as an internal standard.

The ability to tune the $\text{Sm}^{\text{III/II}}$ redox potential by using additives with SmI_2 is an enabling feature of this reagent. For example, the addition of Br^- generates the stronger reductant, SmBr_2 ,⁴¹ however, for redox cycling, an acid must be used that will protonate the Sm^{III} -alkoxide but will not undergo HER at the required potential for SmBr_3 reduction (-1.9 V). LutHNTf_2 is incompatible with such a strongly reducing potential. However, as the affinity of the incoming ligand for Sm^{III} increases, alkoxide cleavage becomes possible with a higher- pK_a acid. The weaker acid triethylammonium (**15**) met the needed criteria to enable redox cycling of SmBr_3 , giving rise to protonolysis of $\text{Sm}(\text{O}^i\text{Pr})_3$ in combination with LiBr to generate SmBr_3 at a potential positive of the acid's HER background (Figure 4.16, magenta trace). Similarly, the addition of the Lewis basic donor N-methylpyrrolidinone (PMe) resulted in a cathodic shift to the $\text{Sm}^{\text{III/II}}$ couple and enhanced alkoxide protonolysis with the intermediate acid $\text{BnMe}_2\text{NHNTf}_2$ (**14**; Figure 4.16, yellow trace).

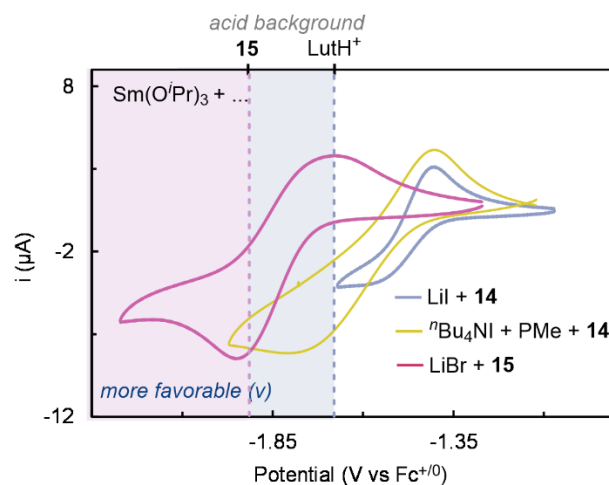


Figure 4.16: CVs demonstrating the sensitivity of net protonolysis and ligand substitution of $\text{Sm}(\text{O}^i\text{Pr})_3$ (2 mM) to the identity of the substituting ligand at 25 mV s^{-1} in THF containing 0.1 M BMPipNTf_2 . 3 equiv each of the iodide source and acid and 1 equiv of PMe are used.

These results lay the groundwork for a more generalized approach to reductive Sm¹²⁰ catalysis and electrocatalysis under different redox regimes. Catalyst design based on the incorporation of supporting ligands is of high interest, particularly with respect to developments in asymmetric Sm catalysis. Whereas the ligand environment influences the Sm^{III/II} reduction potential, the p*K*_a of the acid can enable rational optimization to favor a desired Sm-catalyzed coupling over competing HER. Successive proton and electron transfer to [Sm^{III}-OR] species is also ideal for the regeneration of [Sm^{II}-O(R)H] species, which can serve as potent net hydrogen atom donors. In sum, the straightforward Sm-O protonolysis strategy described herein is anticipated to enable diverse catalytic transformations, including the extension to other rare earth elements as catalysts.

REFERENCES

- (1) Girard, P.; Namy, J. L.; Kagan, H. B. Divalent lanthanide derivatives in organic synthesis. 1. Mild preparation of samarium iodide and ytterbium iodide and their use as reducing or coupling agents. *J. Am. Chem. Soc.* **1980**, *102* (8), 2693–2698.
- (2) Szostak, M.; Fazakerley, N. J.; Parmar, D.; Procter, D. J. Cross-coupling reactions using samarium(II) iodide. *Chem. Rev.* **2014**, *114* (11), 5959–6039.
- (3) Shabangi, M.; Flowers, R. A. Electrochemical investigation of the reducing power of SmI₂ in THF and the effect of HMPA cosolvent. *Tetrahedron Lett.* **1997**, *38* (7), 1137–1140.
- (4) Dahlén, A.; Nilsson, Å.; Hilmersson, G. Estimating the limiting reducing power of SmI₂/H₂O/amine and YbI₂/H₂O/amine by efficient reduction of unsaturated hydrocarbons. *J. Org. Chem.* **2006**, *71* (4), 1576–1580.
- (5) Szostak, M.; Spain, M.; Procter, D. J. Determination of the effective redox potentials of SmI₂, SmBr₂, SmCl₂, and their complexes with water by reduction of aromatic hydrocarbons. Reduction of anthracene and stilbene by samarium(II) iodide–water complex. *J. Org. Chem.* **2014**, *79* (6), 2522–2537.
- (6) Classen, M. J.; Böcker, M. N. A.; Roth, R.; Amberg, W. M.; Carreira, E. M. Enantioselective total synthesis of (+)-euphorikanin A. *J. Am. Chem. Soc.* **2021**, *143* (22), 8261–8265.
- (7) Edmonds, D. J.; Johnston, D.; Procter, D. J. Samarium(II)-iodide-mediated cyclizations in natural product synthesis. *Chem. Rev.* **2004**, *104* (7), 3371–3404.

- (8) Nicolaou, K. C.; Ellery, S. P.; Chen, J. S. Samarium diiodide mediated reactions in total synthesis. *Angew. Chem. Int. Ed.* **2009**, *48* (39), 7140–7165.
- (9) M. Heravi, M.; Nazari, A. Samarium(II) iodide-mediated reactions applied to natural product total synthesis. *RSC Adv.* **2022**, *12* (16), 9944–9994.
- (10) Sinast, M.; Zuccolo, M.; Wischnat, J.; Sube, T.; Hasnik, F.; Baro, A.; Dallavalle, S.; Laschat, S. Samarium iodide-promoted asymmetric Reformatsky reaction of 3-(2-haloacyl)-2-oxazolidinones with enals. *J. Org. Chem.* **2019**, *84* (16), 10050–10064.
- (11) Holzwarth, M.; Ludwig, J.; Bernz, A.; Claasen, B.; Majoul, A.; Reuter, J.; Zens, A.; Pawletta, B.; Bilitewski, U.; M. Weiss, I.; Laschat, S. Modulating chitin synthesis in marine algae with iminosugars obtained by SmI₂ and FeCl₃-mediated diastereoselective carbonyl ene reaction. *Org. Biomol. Chem.* **2022**, *20* (33), 6606–6618.
- (12) Boeckell, N. G.; Flowers, R. A. Coordination-induced bond weakening. *Chem. Rev.* **2022**, *122* (16), 13447–13477.
- (13) Ashida, Y.; Arashiba, K.; Nakajima, K.; Nishibayashi, Y. Molybdenum-catalysed ammonia production with samarium diiodide and alcohols or water. *Nature* **2019**, *568* (7753), 536–540.
- (14) Ashida, Y.; Mizushima, T.; Arashiba, K.; Egi, A.; Tanaka, H.; Yoshizawa, K.; Nishibayashi, Y. Catalytic production of ammonia from dinitrogen employing molybdenum complexes bearing N-heterocyclic carbene-based PCP-type pincer ligands. *Nat. Synth.* **2023**, 1–10.

- (15) Boyd, E. A.; Peters, J. C. Highly selective Fe-catalyzed nitrogen fixation to¹²³ hydrazine enabled by Sm(II) reagents with tailored redox potential and pK_a . *J. Am. Chem. Soc.* **2023**, *145* (27), 14784–14792.
- (16) Chopade, P. R.; Davis, T. A.; Prasad, E.; Flowers, R. A. Solvent-dependent diastereoselectivities in reductions of β -hydroxyketones by SmI₂. *Org. Lett.* **2004**, *6* (16), 2685–2688.
- (17) Maity, S.; Flowers, R. A.; Hoz, S. Aza versus oxophilicity of SmI₂: A break of a paradigm. *Chem. – Eur. J.* **2017**, *23* (67), 17070–17077.
- (18) Farran, H.; Hoz, S. Quantifying the electrostatic driving force behind SmI₂ reductions. *Org. Lett.* **2008**, *10* (21), 4875–4877.
- (19) Wedal, J. C.; Evans, W. J. A rare-earth metal retrospective to stimulate all fields. *J. Am. Chem. Soc.* **2021**, *143* (44), 18354–18367.
- (20) Halter, D. P.; Palumbo, C. T.; Ziller, J. W.; Gembicky, M.; Rheingold, A. L.; Evans, W. J.; Meyer, K. Electrocatalytic H₂O reduction with f-elements: mechanistic insight and overpotential tuning in a series of lanthanide complexes. *J. Am. Chem. Soc.* **2018**, *140* (7), 2587–2594.
- (21) Ware, S. D.; Zhang, W.; Charboneau, D. J.; Klein, C. K.; Reisman, S. E.; See, K. A. Electrochemical preparation of Sm(II) reagent facilitated by weakly coordinating anions. *Chem. – Eur. J.* **2023**, *29* (46), e202301045.
- (22) Andreu, R.; Pletcher, D. Ytterbium(II) as a mediator in organic electrosynthesis—possibilities and limitations. *Electrochimica Acta* **2003**, *48* (8), 1065–1071.
- (23) Corey, E. J.; Zheng, G. Z. Catalytic reactions of samarium (II) iodide. *Tetrahedron Lett.* **1997**, *38* (12), 2045–2048.

- (24) Nomura, R.; Matsuno, T.; Endo, T. Samarium iodide-catalyzed pinacol coupling of¹²⁴ carbonyl compounds. *J. Am. Chem. Soc.* **1996**, *118* (46), 11666–11667.
- (25) Aspinall, H. C.; Greeves, N.; Valla, C. Samarium diiodide-catalyzed diastereoselective pinacol couplings. *Org. Lett.* **2005**, *7* (10), 1919–1922.
- (26) Sun, L.; Sahloul, K.; Mellah, M. Use of electrochemistry to provide efficient SmI₂ catalytic system for coupling reactions. *ACS Catal.* **2013**, *3* (11), 2568–2573.
- (27) Maity, S.; Flowers, R. A. Mechanistic study and development of catalytic reactions of Sm(II). *J. Am. Chem. Soc.* **2019**, *141* (7), 3207–3216.
- (28) Hébri, H.; Duñach, E.; Heintz, M.; Troupel, M.; Périchon, J. Samarium-catalyzed electrosynthesis of 1,2-diketones by the direct reductive dimerization of aromatic esters: A novel coupling reaction. *Synlett* **1991**, *1991* (12), 901–902.
- (29) Hébri, H.; Duñach, E.; Périchon, J. Samarium-catalyzed electrochemical reduction of organic halides. *Synth. Commun.* **1991**, *21* (22), 2377–2382.
- (30) Espanet, B.; Duñach, E.; Périchon, J. SmCl₃-catalyzed electrochemical cleavage of allyl ethers. *Tetrahedron Lett.* **1992**, *33* (18), 2485–2488.
- (31) Hébri, H.; Duñach, E.; Périchon, J. SmCl₃-catalysed electrosynthesis of γ -butyrolactones from 3-chloroesters and carbonyl compounds. *J. Chem. Soc. Chem. Commun.* **1993**, No. 6, 499–500.
- (32) Arashiba, K.; Kanega, R.; Himeda, Y.; Nishibayashi, Y. Electrochemical reduction of samarium triiodide into samarium diiodide. *Chem. Lett.* **2020**, *49* (10), 1171–1173.
- (33) Boyd, E. A.; Peters, J. C. Sm(II)-mediated proton-coupled electron transfer: quantifying very weak N–H and O–H homolytic bond strengths and factors controlling them. *J. Am. Chem. Soc.* **2022**, *144* (46), 21337–21346.

- (34) Tshepelevitsh, S.; Kütt, A.; Lõkov, M.; Kaljurand, I.; Saame, J.; Heering, A.;¹²⁵
Plieger, P. G.; Vianello, R.; Leito, I. On the basicity of organic bases in different
media. *Eur. J. Org. Chem.* **2019**, *2019* (40), 6735–6748.
- (35) Fukuzawa, S.; Nakanishi, A.; Fujinami, T.; Sakai, S. Samarium(II) di-iodide induced
reductive coupling of α,β -unsaturated esters with carbonyl compounds leading to a
facile synthesis of γ -lactone. *J. Chem. Soc. Perkin I* **1988**, No. 7, 1669–1675.
- (36) Shabangi, M.; Sealy, J. M.; Fuchs, J. R.; Flowers, R. A. The effect of cosolvent on the
reducing power of SmI₂ in tetrahydrofuran. *Tetrahedron Lett.* **1998**, *39* (25), 4429–
4432.
- (37) Chen, Q.-C.; Kress, S.; Molinelli, R.; Wuttig, A. Interfacial tuning of electrocatalytic
Ag surfaces for fragment-based electrophile coupling. *Nat. Catal.* **2024**, 1–12.
- (38) Sono, M.; Hanamura, S.; Furumaki, M.; Murai, H.; Tori, M. First direct evidence of
radical intermediates in samarium diiodide induced cyclization by ESR spectra. *Org.*
Lett. **2011**, *13* (21), 5720–5723.
- (39) Savéant, J.-M. *Elements of Molecular and Biomolecular Electrochemistry*; John
Wiley & Sons, Inc: Hoboken, New Jersey, 2006.
- (40) Curran, D. P.; Fevig, T. L.; Jasperse, C. P.; Totleben, M. J. New mechanistic insights
into reductions of halides and radicals with samarium(II) iodide. *Synlett* **2002**, *1992*,
943–961.
- (41) Fuchs, J. R.; Mitchell, M. L.; Shabangi, M.; Flowers, R. A. The effect of lithium
bromide and lithium chloride on the reactivity of SmI₂ in THF. *Tetrahedron Lett.*
1997, *38* (47), 8157–8158.

PHOTODRIVEN SM(III)-TO-SM(II) REDUCTION FOR CATALYTIC APPLICATIONS

Reproduced in part with permission from Johansen, C. M.; Boyd, E.A.; Tarnopol, D.E.; Peters, J. C. *J. Am. Chem. Soc.* **2024**, *146*, 25456. doi: [10.1021/jacs.4c10053](https://doi.org/10.1021/jacs.4c10053)

5.1 Introduction

The versatility of $\text{SmI}_2(\text{THF})_n$ as a single-electron reductant can be attributed in part to its large and kinetically labile lanthanide coordination sphere, enabling recruitment of one or multiple substrates and additives to achieve selectivity in both organic synthesis and small-molecule reductions (Figure 5.1).¹⁻⁴ However, SmI_2 is employed stoichiometrically in all but a few select cases⁵⁻⁸ because its reactions typically terminate in the formation of highly stable Sm^{III} -alkoxide species. In most cases, catalytic regeneration of the Sm^{II} state requires abstraction of RO^- by a stoichiometric oxophile (EX) to generate a Sm^{III} species that can be reduced by a relatively mild reductant (Figure 5.1). The difficulty associated with this transformation has been cited as a motivation for the development of a variety of alternative photo- and electrochemically driven methods for ketyl radical generation.⁹⁻¹³ An ideal Sm^{II} turnover strategy should: (i) accommodate additives that shift $E^\circ(\text{Sm}^{\text{III/II}})$, (ii) use a terminal reductant that is not much stronger than the target Sm^{II} species to avoid background substrate reduction, and (iii) use a terminal oxophile that is not much more Lewis acidic than the target $[\text{Sm}^{\text{III}}]\text{X}$ species to avoid background substrate activation.

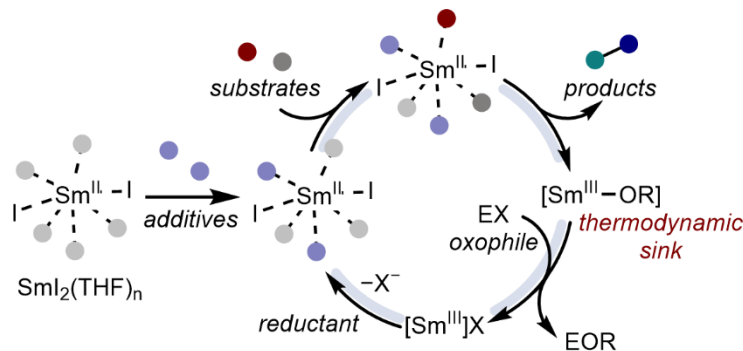


Figure 5.1: Generalized $\text{Sm}^{\text{III/II}}$ catalytic cycle.

Early strategies for reductive Sm catalysis relied on harsh combinations of halosilane oxophiles (R_3SiX) and low valent metals (Mg^0 for $\text{X} = \text{Cl}$; Zn^0 for $\text{X} = \text{I}$) or an applied electrochemical potential as the reductant; these conditions typically do not satisfy criteria (ii) and (iii).^{14–22} In the collaborative effort with the Reisman laboratory described in Chapter 4, we disclosed comparatively mild silane-free thermal and electrochemical conditions for catalytic turnover of SmI_2 in reductive coupling of ketones and acrylates through combination of cationic Brønsted acids with either Zn^0 or an applied potential of -1.55V vs $\text{Fc}^{+/0}$ ($\text{Fc}^{+/0}$ = ferrocenium/ferrocene; all potentials referenced to $\text{Fc}^{+/0}$).²³ However, ground-state turnover by PT/ET steps can suffer from competing HER, limiting access to catalysis with strongly reducing Sm^{II} intermediates (e.g., $\text{Sm}(\text{HMPA})_4^{2+}$; $E^\circ(\text{Sm}^{\text{III/II}}) -2.2\text{ V}$)²⁴ and motivating exploration of alternative strategies.

Given the growing interest in (metalla)photoredox catalysis,²⁵ photodriven strategies for $\text{LnI}^{\text{II/III}}$ catalysis remain surprisingly underexplored.^{26,27} In a strategy recently showcased by the groups of Borbas²⁸ and Nemoto,²⁹ photosensitizers are incorporated into the secondary coordination spheres of Ln^{III} complexes ($\text{Ln} = \text{Sm}, \text{Eu}$; Figure 5.2). Intramolecular oxidative quenching of the excited sensitizer by the Ln^{III} center produces a potent Ln^{II} reductant which can carry out a variety of transformations. While this and other

strategies show promise, the chelating ligand platforms used thus far in photodriven $\text{Ln}^{\text{III/II}}$ catalysis (cryptands, bidentate phosphine oxides) restrict the coordination sphere and/or shift $E^\circ(\text{Ln}^{\text{III/II}})$ to strongly negative potentials, belying direct translation to the rich stoichiometric chemistry of $\text{SmI}_2(\text{L})_n$ as an inner sphere reductant (L = solvent molecule, typically THF).

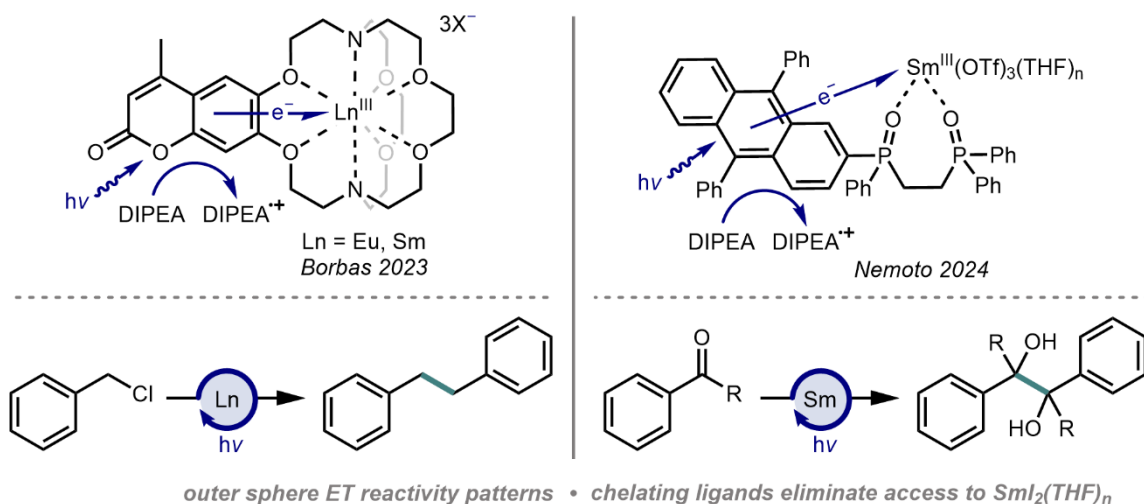


Figure 5.2: Antenna strategy for photodriven Ln^{II} catalysis.^{28,29}

Lewis acidic metal ions are commonly used to template substrates in photodriven reductive coupling reactions.^{10,30,31} Recently, in contrast to the use of photoredox catalysts, several Lewis acid-mediated photoreductions utilize the blue-light absorbing Hantzsch ester (HEH_2) as a photoreductant ($E(\text{HEH}_2^+/*\text{HEH}_2) = -2.5 \text{ V}$).^{32–35} Photoexcited HEH_2 ($*\text{HEH}_2$) carries out Cr^{III} reduction in a catalytic-in-Cr photodriven Nozaki–Hiyama–Kishi reaction.³⁶ Alternatively, HEH_2 acts as a photoreductant in a $\text{Gd}(\text{OTf})_3$ -mediated Giese addition of an N-hydroxyphthalimide (NHPI) ester-derived alkyl radical into α,β -unsaturated ketones or a lactone (Figure 5.3A).³⁷ In the latter study, an interaction between Gd and HEH_2 is observed, but Gd^{III} reduction to Gd^{II} is not accessible even by $*\text{HEH}_2$.²³

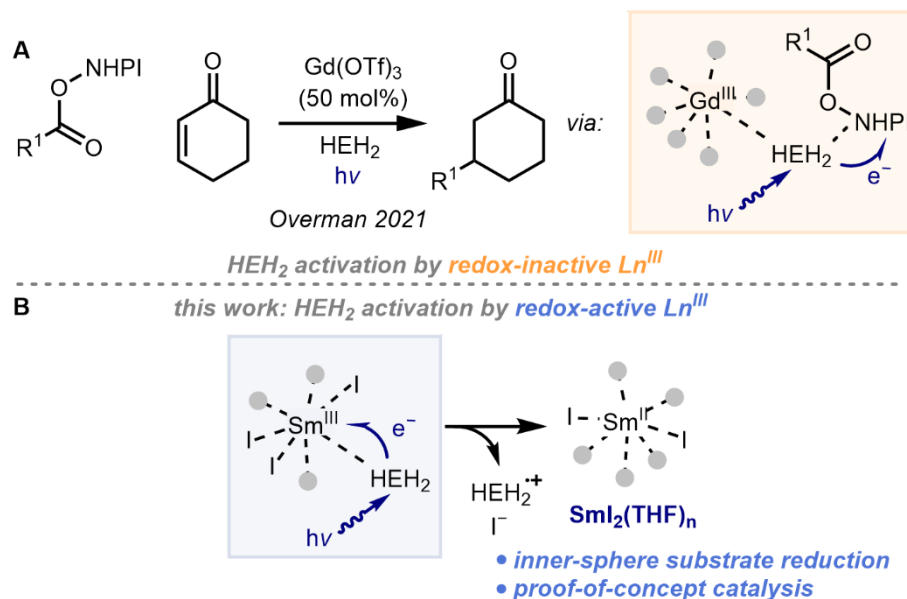


Figure 5.3: Activation of HEH₂ toward photoreduction by Gd^{III} (**A**)³⁷ or Sm^{III} (**B**, this work).

Based on these precedents we noted that *HEH₂ should be capable of reducing Sm^{III} species such as SmI₃ ($E^\circ(\text{SmI}_3/(\text{SmI}_2 + \text{I}^-)) = -1.58 \text{ V}$; Figure 5.3B). Because Sm and Gd are similar in size and oxophilicity, we envisioned that photo-excitation of HEH₂ bound to Sm^{III} could result in intramolecular oxidative quenching to produce Sm^{II} (Figure 5.3B). Crucially, however, a more dynamic Sm-chromophore interaction might allow access to coordinatively unsaturated SmI₂(L)_n species which could carry out inner-sphere reduction in a photodriven Sm-catalyzed cross-coupling reaction. Importantly, both HEH₂ and its 2H⁺/2e⁻ oxidized congener, HE, are weak bases and are therefore compatible with the acidic conditions necessary for recovery of inactive Sm^{III}-OR species by protonolysis.

5.2 Photoreduction of Sm^{III} species

Gratifyingly, HEH₂ proved competent as a photoreductant for Sm^{III}-to-Sm^{II} conversion. Monitoring the UV-visible absorption spectrum of a solution of SmI₃ (2 mM), HEH₂ (60 mM) and 2,6-lutidine base (Lut, 60 mM) following irradiation at 440 nm for 5

min in THF reveals the characteristic profile of blue $\text{SmI}_2(\text{THF})_n$ with λ_{max} at 555 and ¹³⁰618 nm (Figure 5.4, left panel). Extended irradiation (120 min) results in increasing SmI_2 buildup, with maximum yield $\sim 25\%$. Interestingly, in the absence of base this reaction does not proceed (Figure D14), likely due to rapid back-electron transfer (BET) between HEH_2^{*+} and SmI_2 . However, HEH_2^{*+} can be deprotonated in the presence of base, circumventing BET.

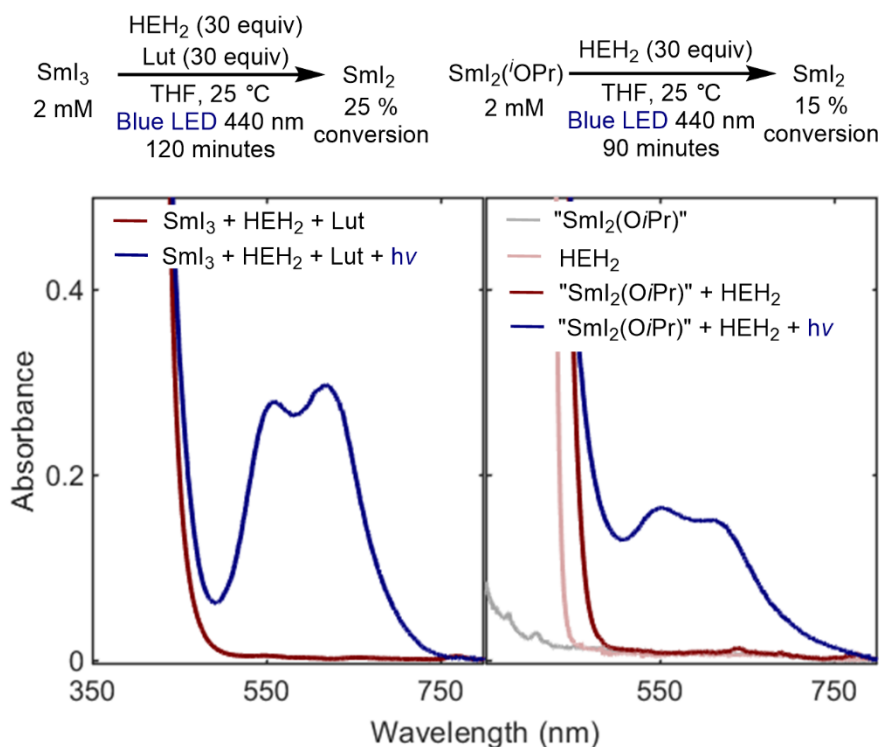


Figure 5.4: UV-vis spectra following photoreduction of SmI_3 (left) and $\text{SmI}_2(\text{O}^i\text{Pr})(\text{L})_n$ (right) by HEH_2 to form SmI_2 .

We next evaluated conditions for photogeneration of $\text{SmI}_2(\text{THF})_n$ from $\text{Sm}(\text{O}^i\text{Pr})_3$ as a model Sm^{III} -alkoxide. Irradiation of $\text{Sm}(\text{O}^i\text{Pr})_3$ (2 mM), tetra-*n*-heptylammoniumiodide ("Hep₄NI, 6 mM), and HEH_2 (60 mM) at 440 nm in THF shows no evidence of SmI_2 formation (Figure D15). However, upon the addition of only 1.5 equiv of the acid bis-trifluoromethylsulfonylimide (HNTf_2) to $\text{Sm}(\text{O}^i\text{Pr})_3$, $\text{SmI}_2(\text{THF})_n$ is generated upon

irradiation with ${}^n\text{Hep}_4\text{NI}$ and HEH_2 (Figure 5.4, right panel). Parallel CV studies¹³¹ demonstrate that no SmI_3 is generated from $\text{Sm}(\text{O}^i\text{Pr})_3$ at this acid loading (Figure 5.5, compare light and dark blue traces), and current attributable to Sm^{III} reduction (presumably of an intermediate mixture of solvated “ $\text{SmI}(\text{O}^i\text{Pr})_2$ ” and “ $\text{SmI}_2\text{O}^i\text{Pr}$ ”) does not onset until -2.3 V. In contrast to SmI_3 , no external base is needed, suggesting that the Sm-bound alkoxide might additionally serve the role of deprotonating HEH_2^{*+} to avoid BET. UV-vis studies reveal that addition of the colorless $\text{Sm}^{\text{III}}-\text{O}^i\text{Pr}$ species (gray trace in Figure 5.4, right panel) gives rise to a significantly red-shifted shoulder in the HEH_2 absorption profile (compare light and dark red traces in Figure 5.4, right panel), consistent with pre-association.

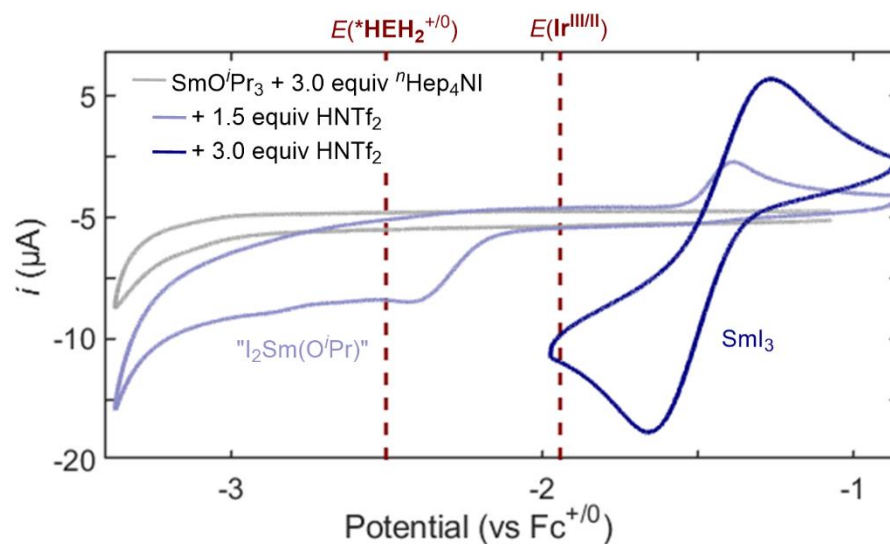


Figure 5.5: CVs of $\text{Sm}(\text{O}^i\text{Pr})_3$ (2 mM) in the presence of iodide and proton sources at 100 mV s^{-1} in THF containing 0.1 M BMPipNTf_2 .

The modest yields and rates of these reactions motivated the study of Sm^{III} reduction with a photoredox catalyst to overcome the low quantum yield and excited state lifetime (220 ps in MeCN)³⁸ of HEH_2 . We selected $[\text{Ir}(\text{dtbbpy})(\text{ppy})_2]^+$ ($[\text{Ir}^{\text{III}}]^+$)³⁹ as a

photosensitizer, which could undergo reductive quenching by a sacrificial electron donor¹³² to generate **Ir^{II}**. **Ir^{II}** is thermodynamically capable of reducing SmI₃ to SmI₂ ($E^\circ(\text{Ir}^{\text{III/II}}) = -1.94 \text{ V}$, Figure 5.5 and Figure D29). Irradiating SmI₃ or SmI₂O^{*i*}Pr (2 mM) with **[Ir^{III}]**PF₆ (0.2 mM), HEH₂ (60 mM) as sacrificial reductant, and Lut (60 mM) rapidly generates SmI₂ (80% or 30% conversion in 2 min, Figure 5.6). Again, the weak base Lut enhances the process (Figure D16).

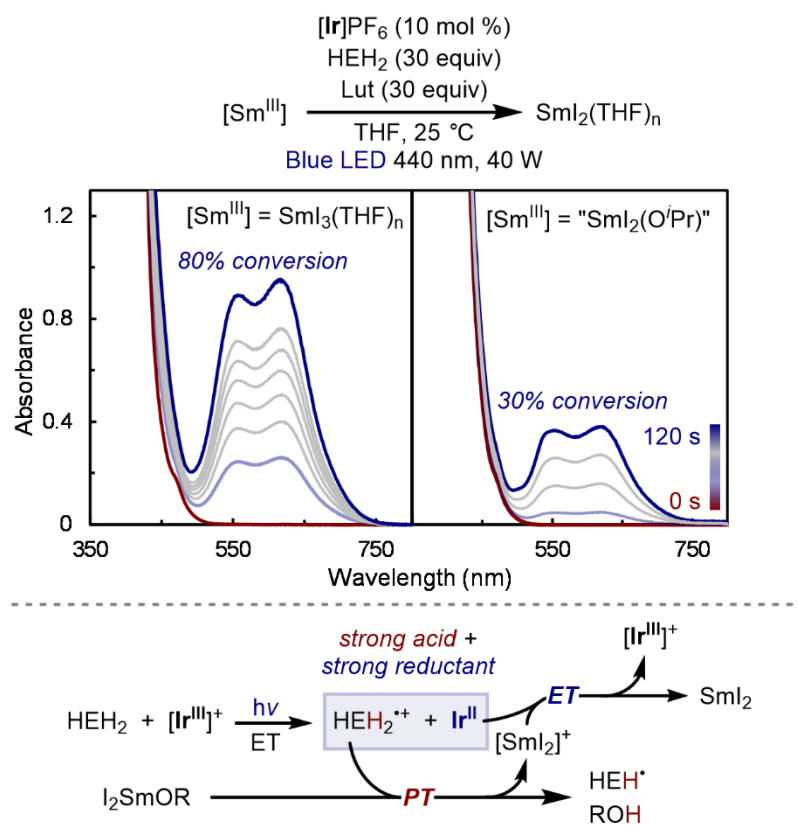


Figure 5.6: UV-vis spectra following photoreductions of Sm^{III} species with **[Ir]**PF₆ photocatalyst and rationale for photoinduced net PCET from HEH₂ to [Sm^{III}–OR] species.

The accelerated reduction of SmI₂O^{*i*}Pr is curious, as electron transfer from **Ir^{II}** to this Sm^{III} species is uphill by 400 mV (Figure 5.5). A rationale for these observations is provided in Figure 5.6: reductive quenching of **[Ir^{III}]⁺** by HEH₂ generates not only the

strong reductant **Ir^{II}**, but also the strong acid $\text{HEH}_2^{*\dagger}$ ($\text{p}K_{\text{a}} -1$ in MeCN),^{40,41} the¹³³ combination of which can carry out net proton-coupled electron transfer to $\text{Sm}^{\text{III}}\text{-O}^i\text{Pr}$. Proton transfer from $\text{HEH}_2^{*\dagger}$ to a $\text{Sm}^{\text{III}}\text{-O}^i\text{Pr}$ species, likely via proton relay mediated by Lut, liberates $^i\text{PrOH}$ and $[\text{SmI}_2]^+$. Analogous net proton-coupled electron transfer to Ti^{IV} -alkoxide species to generate Ti^{III} has been proposed in photodriven Ti redox catalysis.⁴² The latter can then be reduced to SmI_2 by **Ir^{II}**.

Development of Sm-catalysis leveraging diverse ligand coordination to modulate reactivity is an attractive goal. Exploration of Sm^{II} generation in the presence of potential coligands was carried out pursuant to these interests. Satisfyingly, Sm^{II} species are readily photogenerated from SmI_3 by $[\text{Ir}^{\text{III}}]^+$ and quencher (HEH_2 or Et_3N) in the presence of several protic additives (e.g., ethylene glycol, Figures D17-18),^{3,43-45} including a chiral aminediol (Figure 5.7A, Figure D19) that has been utilized in several enantioselective SmI_2 -mediated transformations.⁴⁶⁻⁴⁸

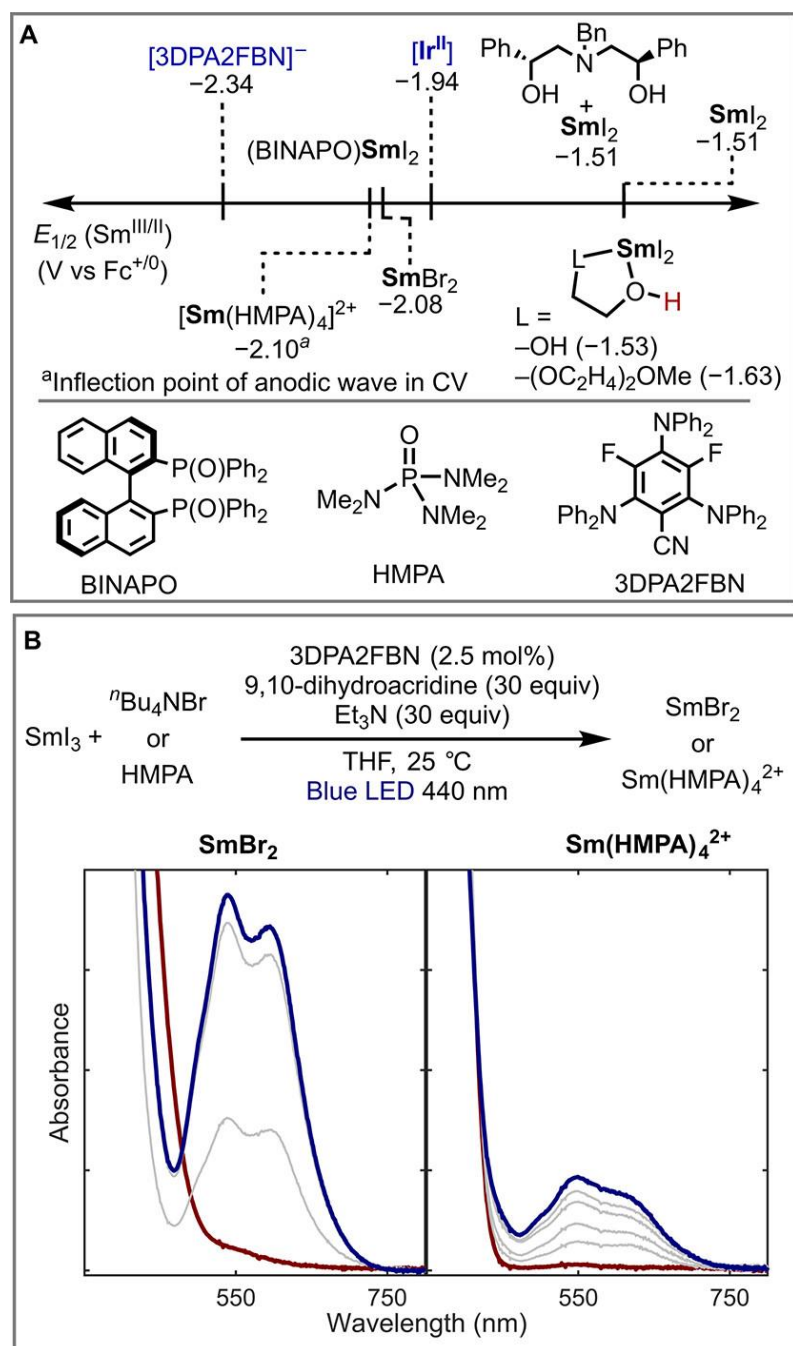


Figure 5.7: (A) Sm^{II} species generated in the presence of various ligands by a photoredox approach. See Appendix D4 for relevant electrochemical data. (B) UV-vis spectra following photogeneration of SmBr_2 and $\text{Sm}(\text{HMPA})_4^{2+}$.

The reduction potential and reactivity of Sm^{II} is highly sensitive to coordination of Lewis-basic additives (HMPA , Br^- ; Figure 5.7A).⁴⁹ While $[\text{Ir}^{\text{II}}]$ is insufficiently reducing

to access such species, the more reducing photocatalyst 3DPA2FBN (Figure 5.7A),⁵⁰135 when paired with the more reducing quencher 9,10-dihydroacridine and Et₃N as base, mediates generation of both SmBr₂ and Sm(HMPA)₄²⁺ (Figure 5.7B). 3DPA2FBN also facilitates Sm^{III} reduction and binding to the chiral BINAPO ligand (Figures 5.7A and D29).⁵¹ A clear Sm^{III/II} couple cannot be assigned from the CV of a 1:1 mixture of SmI₃:BINAPO, which contains multiple features consistent with a complex speciation. However, these redox events appear negative of -2 V (Figure D36), consistent with the necessity of the more reducing photocatalyst for photogeneration of the Sm^{II} state.

Access to Sm(HMPA)₄²⁺, which is ubiquitous in the stoichiometric reactivity of Sm^{II}, is of particular note. Ground-state Sm catalyst turnover by reductive protonation (as described in Chapters 2 and 4) relies on selecting an acid with weakly coordinating conjugate base whose pK_a is low enough that protonolysis of relevant Sm^{III}-alkoxide species to generate reducible [Sm^{III}]X species is exergonic (pK_a < 13 in THF for X = I), but high enough to avoid a rapid competing hydrogen evolution reaction (HER) with the stoichiometric reductant. In the case of the deeply cathodic Sm^{III/II} reduction potential imposed by HMPA, candidate baseH⁺ meeting these criteria have not been identified. Photochemical generation of transient strong H⁺/e⁻ equivalents offers a means to kinetically favor their delivery to desired intermediates,¹² mitigating the background HER which dominates under bulk reducing conditions.

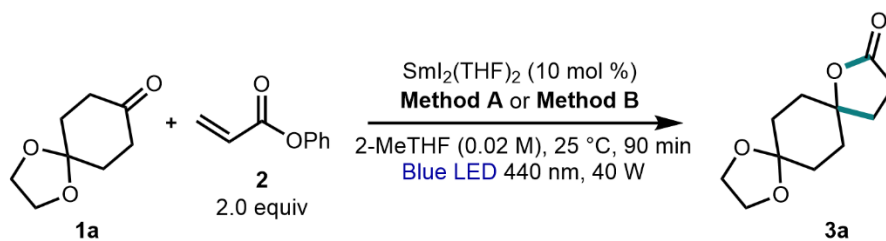
5.3 Proof-of-concept Photodriven Sm Catalysis

Having established two different photochemical approaches to Sm^{II} generation, we targeted intermolecular ketone-acrylate coupling as a model reaction to benchmark photodriven Sm-catalysis (Table 5.1). This reaction is representative of the qualities that

set SmI₂ apart as a stoichiometric reductant. Inner-sphere electron transfer to one or both¹³⁶ of the carbonyl substrates is obligatory based on comparison of outer-sphere reduction potentials.²³ Importantly, a Sm-alkoxide is generated as the byproduct of lactonization, enabling evaluation of the ability of a set of conditions to overcome this critical barrier to generalizable Sm catalysis.

Irradiation of ketone **1a** (0.04 mmol), phenyl acrylate **2** (2 equiv), and SmI₂(THF)₂ (10 mol %) in the presence of HEH₂ (4.0 equiv) in 2-MeTHF (0.02 M) at 440 nm for 90 min yields lactone **3a** in 76% yield (Table 5.1, entry 1, method A). Addition of the photoredox catalyst ([Ir]PF₆, 1 mol %) with pyridine (2 equiv) results in an increase in yield to 89% (entry 1, method B). Light and Sm were required for catalytic formation of **2** by either method (entries 3 and 4). Sm(OTf)₃ is a competent precatalyst with 50 mol % MgI₂ included as an iodide source (entry 4). Substitution of Gd(OTf)₃ for Sm(OTf)₃ results in trace product formation, supporting a key role for Sm^{II} in catalysis (entry 5).

Table 5.1: Photodriven Sm-catalyzed coupling of ketones and phenyl acrylate to form lactone products.



Method A: HEH_2 (4 equiv)

Method B: HEH_2 (4 equiv), $[\text{Ir}]\text{PF}_6$ (1 mol%), pyridine (2 equiv)

Entry	Deviation from standard condition	Yield (%)	
		Method A	Method B
1	None	76	89
2	No irradiation	4	4
3	No Sm	0	0
4	10 mol % $\text{Sm}(\text{OTf})_3$ / 50 mol % MgI_2 instead of SmI_2	60	85
5	10 mol % $\text{Gd}(\text{OTf})_3$ / 50 mol % MgI_2 instead of SmI_2	0	6
6	2 equiv pyridine added	72	-
7	No pyridine	-	82
8	2 equiv Et_3N added (A) / instead of pyridine (B)	5	15
9	5,6-dihydrophenanthridine instead of HEH_2	0	77
10	15 min	29	60
11	Ethyl acrylate instead of 2	31	58

Entry	12	13	14	15 ^a
Product				
Method A:	32%	>95%	77%	43%
Method B:	77%	90%	49%	29%

Yields were determined by ^1H NMR analysis with 1,3,5-trimethoxybenzene as internal standard.

^a*tert*-butyl acrylate used as coupling partner; lactonization only observed on acidic workup.

Both methods are competent in the presence/absence of pyridine (entries 1, 6, and 7), but yields are greatly diminished in the presence of a stronger base (Et_3N , entry 8). This suggests that the dynamics of Sm-alkoxide protonation play an important role in turnover.²³ Interestingly, the use of a dihydropyridine without carbonyl groups, 5,6-dihydrophenan-

thridine, only shows product formation with $[\mathbf{Ir}]^+$ (entry 9). In the absence of \mathbf{Ir} , the¹³⁸ specific interaction between Sm and HEH_2 appears to be required. The Ir-catalyzed reaction is also faster, achieving 60% conversion in 15 min, compared to 29% by method A (entry 10).

Methods A and B were tested against alternative coupling partners to assess their relative efficacies. When using less activated substrate pairs (aliphatic ketones and alkyl acrylates, entries 1, 11, and 12), method B is favored, perhaps because these slower cross-couplings require rapid Sm^{III} -to- Sm^{II} conversion. Method A is preferred when using aryl ketones (entries 13–15), as method B gives considerable pinacol-coupled side-products (Table D1). With method A, selective inner-sphere photogeneration of Sm^{II} by Sm^{III} - HEH_2 may favor Sm^{II} -mediated cross-coupling, while with method B background \mathbf{Ir} -mediated substrate reduction to homocoupled products can dominate.

A proposed mechanism for this photodriven lactonization reaction (by method A) is presented in Figure 5.8. The mechanism can be divided into two parts, a photoreduction side in which Sm^{III} is reduced to Sm^{II} , and a SmI_2 cross-coupling side where the organic substrates are coupled. Starting from $\text{SmI}_2(\text{OPh})$, association with HEH_2 (as demonstrated in Figure 5.4) followed by excitation to $^*\text{HEH}_2$ allows for the proton and electron transfer required to generate SmI_2 , with PhOH and HEH^{\bullet} as additional products. Subsequently, SmI_2 couples the acrylate and ketone to form a radical intermediate. As in the (electro)chemically-driven conditions for this transformation described in Chapter 4, substrate coupling could be initiated either by ketone or acrylate reduction, leading to either an α -ester radical or an alkoxy radical intermediate, respectively, following addition to the corresponding coupling partner.^{52,53} In the case of difficult-to-reduce ketone substrates

such as **1a**, neither pathway can be reliably ruled out. HEH^\bullet is capable of reducing either of the possible radical intermediates as a potent H atom donor, although alternative schemes for delivery of the second reducing equivalent can be envisioned (Figure D38). Following reduction and lactonization, **3a** is formed along with $\text{SmI}_2(\text{OPh})$. With $[\text{Ir}]^+$, a similar mechanism is proposed, differing only in the regeneration of Sm^{II} from Sm^{III} -alkoxides as depicted in Figure 5.6 (see Figure D39 for full scheme).

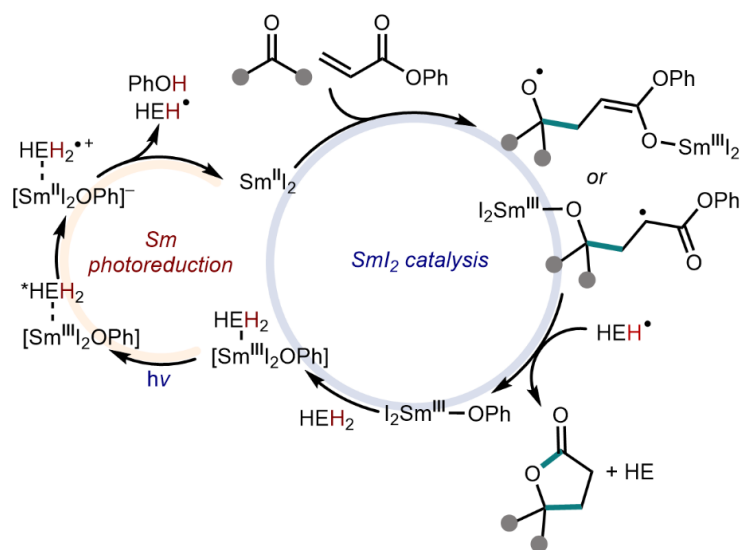


Figure 5.8: Proposed mechanism of Sm cross-coupling under Ir-free conditions (method A).

In summary, we have demonstrated photodriven generation of $\text{SmI}_2(\text{THF})_2$ from Sm^{III} precursors using both a photoreductant and a photoredox catalyst. These conditions translate to proof-of-concept photodriven reductive Sm-catalyzed ketone-acrylate coupling. Distinct from reported methods, photodriven Sm-catalysis occurs in the absence of competing Lewis-acidic metal additives and byproducts (e.g., Mg^{2+} and Zn^{2+} salts),^{14–18,21,23} which may be of utility in development of Sm-catalysis with ligands. These findings are anticipated to facilitate applications of Sm-catalysis beyond the types of thermally driven transformations studied thus far.

REFERENCES

- (1) Girard, P.; Namy, J. L.; Kagan, H. B. Divalent lanthanide derivatives in organic synthesis. 1. Mild preparation of samarium iodide and ytterbium iodide and their use as reducing or coupling agents. *J. Am. Chem. Soc.* **1980**, *102* (8), 2693–2698.
- (2) Szostak, M.; Fazakerley, N. J.; Parmar, D.; Procter, D. J. Cross-coupling reactions using samarium(II) iodide. *Chem. Rev.* **2014**, *114* (11), 5959–6039.
- (3) Ashida, Y.; Arashiba, K.; Nakajima, K.; Nishibayashi, Y. Molybdenum-catalysed ammonia production with samarium diiodide and alcohols or water. *Nature* **2019**, *568* (7753), 536–540.
- (4) Lee, C. C.; Hu, Y.; Ribbe, M. W. Catalytic reduction of CN⁻, CO, and CO₂ by nitrogenase cofactors in lanthanide-driven reactions. *Angew. Chem.-Int. Ed.* **2015**, *54* (4), 1219–1222.
- (5) Huang, H.-M.; McDouall, J. J. W.; Procter, D. J. SmI₂-catalysed cyclization cascades by radical relay. *Nat. Catal.* **2019**, *2* (3), 211–218.
- (6) Agasti, S.; Beattie, N. A.; McDouall, J. J. W.; Procter, D. J. SmI₂-catalyzed intermolecular coupling of cyclopropyl ketones and alkynes: A link between ketone conformation and reactivity. *J. Am. Chem. Soc.* **2021**.
- (7) Agasti, S.; Beltran, F.; Pye, E.; Kaltsoyannis, N.; Crisenza, G. E. M.; Procter, D. J. A catalytic alkene insertion approach to bicyclo[2.1.1]hexane bioisosteres. *Nat. Chem.* **2023**, *15* (4), 535–541.
- (8) Mansell, J. I.; Yu, S.; Li, M.; Pye, E.; Yin, C.; Beltran, F.; Rossi-Ashton, J. A.; Romano, C.; Kaltsoyannis, N.; Procter, D. J. Alkyl cyclopropyl ketones in catalytic

- formal [3 + 2] cycloadditions: The role of SmI₂ catalyst stabilization. *J. Am. Chem. Soc.* **2024**, *146* (18), 12799–12807.
- (9) Edgecomb, J. M.; Alektiar, S. N.; Cowper, N. G. W.; Sowin, J. A.; Wickens, Z. K. Ketyl radical coupling enabled by polycyclic aromatic hydrocarbon electrophotocatalysts. *J. Am. Chem. Soc.* **2023**, *145* (37), 20169–20175.
- (10) Lee, K. N.; Lei, Z.; Ngai, M.-Y. β -selective reductive coupling of alkenylpyridines with aldehydes and imines via synergistic Lewis acid/photoredox catalysis. *J. Am. Chem. Soc.* **2017**, *139* (14), 5003–5006.
- (11) Derosa, J.; Garrido-Barros, P.; Peters, J. C. Electrocatalytic ketyl-olefin cyclization at a favorable applied bias enabled by a concerted proton–electron transfer mediator. *Inorg. Chem.* **2022**, *61* (17), 6672–6678.
- (12) Tarantino, K. T.; Liu, P.; Knowles, R. R. Catalytic ketyl-olefin cyclizations enabled by proton-coupled electron transfer. *J. Am. Chem. Soc.* **2013**, *135* (27), 10022–10025.
- (13) Seo, H.; Jamison, T. F. Catalytic generation and use of ketyl radical from unactivated aliphatic carbonyl compounds. *Org. Lett.* **2019**, *21* (24), 10159–10163.
- (14) Corey, E. J.; Zheng, G. Z. Catalytic reactions of samarium (II) iodide. *Tetrahedron Lett.* **1997**, *38* (12), 2045–2048.
- (15) Nomura, R.; Matsuno, T.; Endo, T. Samarium iodide-catalyzed pinacol coupling of carbonyl compounds. *J. Am. Chem. Soc.* **1996**, *118* (46), 11666–11667.
- (16) Aspinall, H. C.; Greeves, N.; Valla, C. Samarium diiodide-catalyzed diastereoselective pinacol couplings. *Org. Lett.* **2005**, *7* (10), 1919–1922.
- (17) Sun, L.; Sahloul, K.; Mellah, M. Use of electrochemistry to provide efficient SmI₂ catalytic system for coupling reactions. *ACS Catal.* **2013**, *3* (11), 2568–2573.

- (18) Maity, S.; Flowers, R. A. Mechanistic study and development of catalytic reactions of Sm(II). *J. Am. Chem. Soc.* **2019**, *141* (7), 3207–3216.
- (19) Hébri, H.; Duñach, E.; Heintz, M.; Troupel, M.; Périchon, J. Samarium-catalyzed electrosynthesis of 1,2-diketones by the direct reductive dimerization of aromatic esters: A novel coupling reaction. *Synlett* **1991**, *1991* (12), 901–902.
- (20) Hebri, H.; Duñach, E.; Périchon, J. SmCl₃-catalysed electrosynthesis of γ -butyrolactones from 3-chloroesters and carbonyl compounds. *J. Chem. Soc. Chem. Commun.* **1993**, No. 6, 499–500.
- (21) Hebri, H.; Duñach, E.; Périchon, J. Samarium-catalyzed electrochemical reduction of organic halides. *Synth. Commun.* **1991**, *21* (22), 2377–2382.
- (22) Espanet, B.; Duñach, E.; Périchon, J. SmCl₃-catalyzed electrochemical cleavage of allyl ethers. *Tetrahedron Lett.* **1992**, *33* (18), 2485–2488.
- (23) Boyd, E. A.; Shin, C.; Charboneau, D. J.; Peters, J. C.; Reisman, S. E. Reductive samarium (electro)catalysis enabled by Sm^{III}-alkoxide protonolysis. *Science* **2024**, *385* (6711), 847–853.
- (24) Enemærke, R. J.; Hertz, T.; Skrydstrup, T.; Daasbjerg, K. Evidence for ionic samarium(II) species in THF/HMPA solution and investigation of their electron-donating properties. *Chem. – Eur. J.* **2000**, *6* (20), 3747–3754.
- (25) Chan, A. Y.; Perry, I. B.; Bissonnette, N. B.; Buksh, B. F.; Edwards, G. A.; Frye, L. I.; Garry, O. L.; Lavagnino, M. N.; Li, B. X.; Liang, Y.; Mao, E.; Millet, A.; Oakley, J. V.; Reed, N. L.; Sakai, H. A.; Seath, C. P.; MacMillan, D. W. C. Metallaphotoredox: The merger of photoredox and transition metal catalysis. *Chem. Rev.* **2022**, *122* (2), 1485–1542.

- (26) Meyer, A. U.; Slanina, T.; Heckel, A.; König, B. Lanthanide ions coupled with photoinduced electron transfer generate strong reduction potentials from visible light. *Chem. – Eur. J.* **2017**, *23* (33), 7900–7904.
- (27) Jenks, T. C.; Bailey, M. D.; Hovey, J. L.; Fernando, S.; Basnayake, G.; Cross, M. E.; Li, W.; Allen, M. J. First use of a divalent lanthanide for visible-light-promoted photoredox catalysis. *Chem. Sci.* **2018**, *9* (5), 1273–1278.
- (28) Tomar, M.; Bhimpuria, R.; Kocsi, D.; Thapper, A.; Borbas, K. E. Photocatalytic generation of divalent lanthanide reducing agents. *J. Am. Chem. Soc.* **2023**, *145* (41), 22555–22562.
- (29) Kuribara, T.; Kaneki, A.; Matsuda, Y.; Nemoto, T. Visible-light-antenna ligand-enabled samarium-catalyzed reductive transformations. *J. Am. Chem. Soc.* **2024**.
- (30) Yoon, T. P. Photochemical stereocontrol using tandem photoredox–chiral Lewis acid catalysis. *Acc. Chem. Res.* **2016**, *49* (10), 2307–2315.
- (31) Huang, X.; Luo, S.; Burghaus, O.; Webster, R. D.; Harms, K.; Meggers, E. Combining the catalytic enantioselective reaction of visible-light-generated radicals with a by-product utilization system. *Chem. Sci.* **2017**, *8* (10), 7126–7131.
- (32) Jung, J.; Kim, J.; Park, G.; You, Y.; Cho, E. J. Selective debromination and α -hydroxylation of α -bromo ketones using Hantzsch esters as photoreductants. *Adv. Synth. Catal.* **2016**, *358* (1), 74–80.
- (33) Ohnishi, Y.; Kagami, M.; Ohno, A. Reduction by a model of NAD(P)H. Photoactivation of NADH and its model compounds toward the reduction of olefines. *Chem. Lett.* **1975**, *4* (2), 125–128.

- (34) Johansen, C. M.; Boyd, E. A.; Peters, J. C. Catalytic transfer hydrogenation of N₂¹⁴⁴ to NH₃ via a photoredox catalysis strategy. *Sci. Adv.* **2022**, *8* (43), eade3510.
- (35) Ji, C.-L.; Han, J.; Li, T.; Zhao, C.-G.; Zhu, C.; Xie, J. Photoinduced gold-catalyzed divergent dechloroalkylation of gem-dichloroalkanes. *Nat. Catal.* **2022**, *5* (12), 1098–1109.
- (36) Liu, Y.; Lin, S.; Zhang, D.; Song, B.; Jin, Y.; Hao, E.; Shi, L. Photochemical Nozaki–Hiyama–Kishi coupling enabled by excited Hantzsch ester. *Org. Lett.* **2022**, *24* (18), 3331–3336.
- (37) Pitre, S. P.; Allred, T. K.; Overman, L. E. Lewis acid activation of fragment-coupling reactions of tertiary carbon radicals promoted by visible-light irradiation of EDA complexes. *Org. Lett.* **2021**, *23* (3), 1103–1106.
- (38) Deng, G.; Xu, H.-J.; Chen, D.-W. Mechanism of photoreduction of diethyl benzylidene malonates by NAD(P)H model and comparison with thermal reaction. *J. Chem. Soc. Perkin Trans. 2* **1990**, No. 7, 1133–1137.
- (39) Slinker, J. D.; Gorodetsky, A. A.; Lowry, M. S.; Wang, J.; Parker, S.; Rohl, R.; Bernhard, S.; Malliaras, G. G. Efficient yellow electroluminescence from a single layer of a cyclometalated iridium complex. *J. Am. Chem. Soc.* **2004**, *126* (9), 2763–2767.
- (40) Shen, G.-B.; Fu, Y.-H.; Zhu, X.-Q. Thermodynamic network cards of Hantzsch Ester, benzothiazoline, and dihydrophenanthridine releasing two hydrogen atoms or ions on 20 elementary steps. *J. Org. Chem.* **2020**, *85* (19), 12535–12543.
- (41) Schmittel, M.; Burghart, A. Understanding reactivity patterns of radical cations. *Angew. Chem. Int. Ed. Engl.* **1997**, *36* (23), 2550–2589.

- (42) Gualandi, A.; Calogero, F.; Mazzarini, M.; Guazzi, S.; Fermi, A.; Bergamini, G.;¹⁴⁵
Cozzi, P. G. Cp₂TiCl₂-catalyzed photoredox allylation of aldehydes with visible light.
ACS Catal. **2020**, *10* (6), 3857–3863.
- (43) Chciuk, T. V.; Flowers, R. A. Proton-coupled electron transfer in the reduction of
arenes by SmI₂–water complexes. *J. Am. Chem. Soc.* **2015**, *137* (35), 11526–11531.
- (44) Kolmar, S. S.; Mayer, J. M. SmI₂(H₂O)_n reduction of electron rich enamines by
proton-coupled electron transfer. *J. Am. Chem. Soc.* **2017**, *139* (31), 10687–10692.
- (45) Boeckell, N. G.; Bartulovich, C. O.; Maity, S.; Flowers, R. A. I. Accessing unusual
reactivity through chelation-promoted bond weakening. *Inorg. Chem.* **2023**, *62* (12),
5040–5045.
- (46) Kern, N.; Plesniak, M. P.; McDouall, J. J. W.; Procter, D. J. Enantioselective
cyclizations and cyclization cascades of samarium ketyl radicals. *Nat. Chem.* **2017**, *9*
(12), 1198–1204.
- (47) Evans, D. A.; Nelson, S. G.; Gagne, M. R.; Muci, A. R. A chiral samarium-based
catalyst for the asymmetric Meerwein-Ponndorf-Verley reduction. *J. Am. Chem. Soc.*
1993, *115* (21), 9800–9801.
- (48) Wang, Y.; Zhang, W.-Y.; Yu, Z.-L.; Zheng, C.; You, S.-L. SmI₂-mediated
enantioselective reductive dearomatization of non-activated arenes. *Nat. Synth.* **2022**,
1 (5), 401–406.
- (49) Miller, R. S.; Sealy, J. M.; Shabangi, M.; Kuhlman, M. L.; Fuchs, J. R.; Flowers, R.
A. Reactions of SmI₂ with alkyl halides and ketones: Inner-sphere vs outer-sphere
electron transfer in reactions of Sm(II) reductants. *J. Am. Chem. Soc.* **2000**, *122* (32),
7718–7722.

- (50) Speckmeier, E.; Fischer, T. G.; Zeitler, K. A toolbox approach To construct broadly¹⁴⁶ applicable metal-free catalysts for photoredox chemistry: Deliberate tuning of redox potentials and importance of halogens in donor–acceptor cyanoarenes. *J. Am. Chem. Soc.* **2018**, *140* (45), 15353–15365.
- (51) Mikami, K.; Yamaoka, M. Chiral ligand control in enantioselective reduction of ketones by SmI₂ for ketyl radical addition to olefins. *Tetrahedron Lett.* **1998**, *39* (25), 4501–4504.
- (52) Hansen, A. M.; Lindsay, K. B.; Sudhadevi Antharjanam, P. K.; Karaffa, J.; Daasbjerg, K.; Flowers, R. A.; Skrydstrup, T. Mechanistic evidence for intermolecular radical carbonyl additions promoted by samarium diiodide. *J. Am. Chem. Soc.* **2006**, *128* (30), 9616–9617.
- (53) Sono, M.; Hanamura, S.; Furumaki, M.; Murai, H.; Tori, M. First direct evidence of radical intermediates in samarium diiodide induced cyclization by ESR spectra. *Org. Lett.* **2011**, *13* (21), 5720–5723.

SAMARIUM AS AN ELECTRON-TRANSFER MEDIATOR IN ELECTROCATALYTIC NITROGEN REDUCTION TO AMMONIA

Reproduced in part with permission from [Boyd, E.A.; Jung, H.; Peters, J. C. *J. Am. Chem. Soc.* **2025**, *147*, 4695. doi: \[10.1021/jacs.4c14845\]\(https://doi.org/10.1021/jacs.4c14845\)](#)

6.1 Introduction

Ammonia synthesis by catalytic nitrogen reduction (N_2R) using renewably sourced electricity is being explored to decrease the CO_2 emissions associated with the industrial Haber-Bosch process as currently implemented.^{1,2} Direct electrochemical N_2R (eN_2R) coupled to water oxidation could ultimately be economically competitive with the Haber-Bosch process in some scenarios, but available technologies are severely limited.² Although eN_2R under aqueous conditions has been reported with a surprisingly broad range of heterogeneous electrocatalysts, validation of N_2 as the N atom source in these systems remains a subject of debate.³ Nonaqueous Li-mediated N_2R (Figure 6.1A) can operate at remarkable Faradaic efficiency (F.E., 99%) at elevated pressure,⁴ but the high overpotential (η) required to reduce Li^+ to Li^0 , as well as uncertainties surrounding the involvement of electrolyte degradation products, represent significant obstacles to implementation. Building on early demonstrations of electrolytic and electrocatalytic N_2R with well-defined molecular complexes by our laboratory and others,⁵⁻⁷ our lab recently reported comparatively low-overpotential eN_2R with homogeneous catalysts. However, these systems, which employ both direct electrolysis⁸ and proton-coupled redox-mediated strategies (Figure 6.1B),⁹ operate at modest F.E. (<55%) by comparison to Li-mediated

N_2R . An $e\text{N}_2\text{R}$ system approaching aspirational efficiency metrics ($\eta < 0.60$ V, F.E. > 95%) remains elusive.²

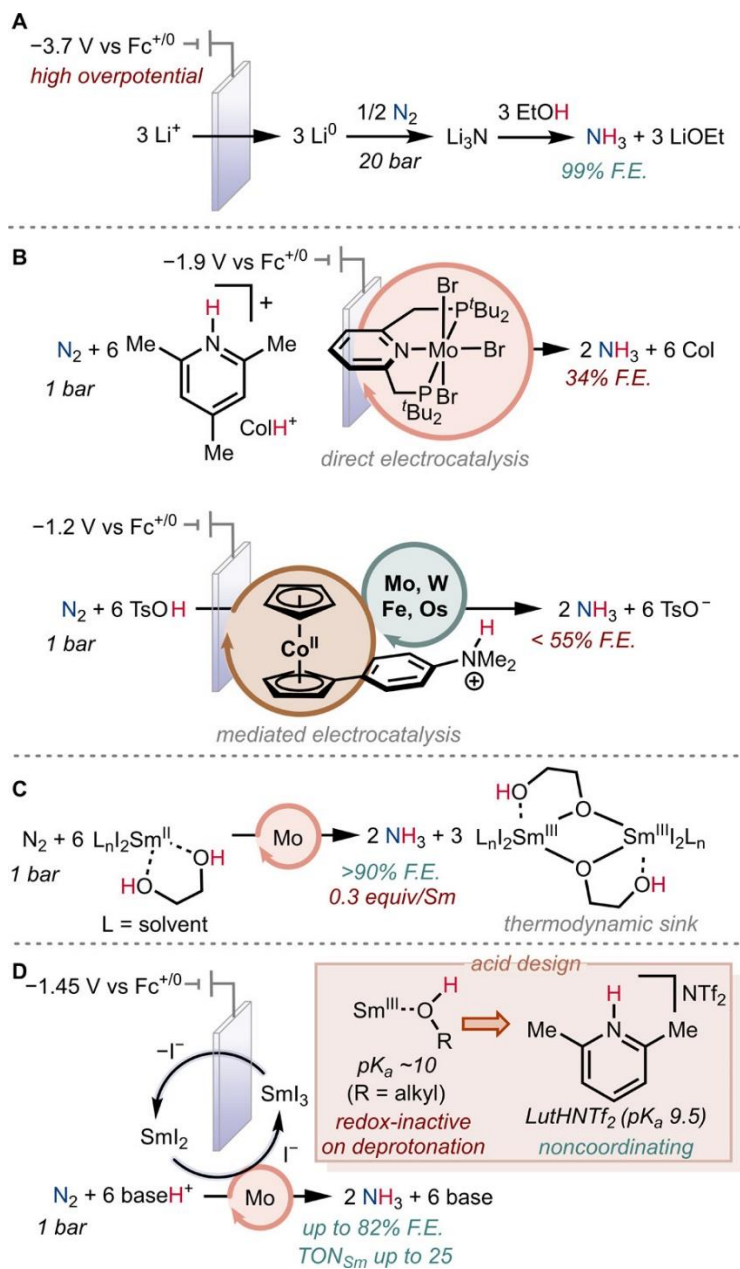


Figure 6.1: (A) Li-mediated $e\text{N}_2\text{R}$.⁴ (B) Low-overpotential $e\text{N}_2\text{R}$ with well-defined homogeneous catalysts.^{8,9} (C) Mo-catalyzed N_2R using stoichiometric SmI_2 as the reductant.¹⁰ (D) This work: tandem Sm/Mo-catalyzed $e\text{N}_2\text{R}$.

Sm^{II} reagents have emerged as particularly selective stoichiometric reductants in ¹⁴⁹ N₂R.^{10,11} With Mo catalysts supported by pincer-type ligands (e.g., PNPMoBr₃, Figure 6.1B), Nishibayashi and co-workers used SmI₂ in combination with ethylene glycol or water as proton sources to achieve a very high yield in the conversion of N₂ to NH₃ (>95% with respect to SmI₂ as the limiting reagent, Figure 6.1C). The SmI₂/ROH pairs are compatible with a range of Mo-based precatalysts,^{12–14} and tuning the Sm^{III/II} reduction potential enables Sm^{II}-driven Fe-mediated catalysis to selectively produce N₂H₄.¹⁵ However, even in the most efficient of these catalytic reactions,^{16,17} at most 0.3 equiv of NH₃ is produced per Sm equivalent. To address this limitation, in this chapter we describe an *e*N₂R system in which selective Sm^{II} reductants are catalytically regenerated from oxidized Sm^{III} byproducts under applied potential (Figure 6.1D).

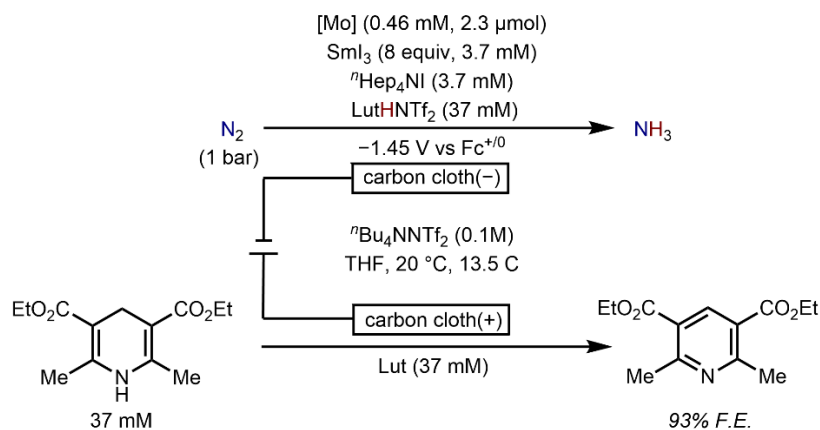
Chapter 4 details development of conditions for electrocatalytic turnover of SmI₂ in the overall 2H⁺/2e⁻ reductive coupling of ketones and acrylates.¹⁸ In this system, the selection of a terminal acid (2,6-dimethylpyridinium (LutH⁺); p*K*_a 9.5 in THF)¹⁹ whose conjugate base does not inhibit Sm^{III} reduction at mild applied potentials is critical for turnover of Sm^{III}-alkoxide intermediates. While application of the same strategy for turnover of the spent Sm^{III} products from reported Mo-catalyzed N₂R might seem plausible, the oxidized Sm^{III} species that result when water or ethylene glycol is paired with SmI₂ (insoluble samarium oxide and multimeric “I₂Sm^{III}(O(CH₂)₂OH)” species stabilized by the chelate effect, respectively) are particularly ill-suited to turnover (Figure 6.1C).¹⁰

We recognized that the formation of Sm^{III}-alkoxides is not obligatory in the overall *e*N₂R (Figure 6.1D). Coordinating O–H-based proton sources ([I₂Sm^{II}–O(R)H]) dominate the literature applications of stoichiometric SmI₂ in N₂R, with concerted proton-coupled

electron transfer (PCET) reactivity generally proposed to play a role based on analogy¹⁵⁰ to the PCET mechanism operative in reduction of select unsaturated hydrocarbons by SmI₂/EH reagents.^{10,20–22} However, net PCET from Sm^{II}–O(R)H to MoN_xH_y intermediates could instead occur by an asynchronous electron transfer (ET)/proton transfer (PT) process, as is observed in reduction of aliphatic ketones and aldehydes by SmI₂/H₂O (and as we propose in the Fe-catalyzed N₂R system described in Chapter 3).²³ Initial uphill ET would generate a [Sm^{III}–O(R)H] intermediate in which the Lewis-acidic Sm center acidifies the O–H bond (pK_a < 11 in THF for Sm^{III} = SmI₃ and R = alkyl), enabling subsequent PT. Based on such a scenario, we posited that tandem electrocatalysis might be enabled by replacing high-affinity proton donors with LutHNTf₂ (NTf₂ = bis-(trifluoromethanesulfonimide)), the latter being thermodynamically capable of carrying out the key PT steps without interfering with electrochemical Sm^{III/II} cycling.

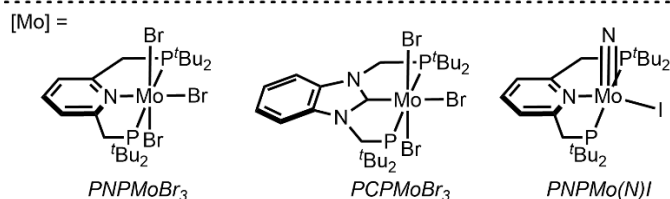
6.2 Results and Discussion

Controlled potential electrolysis (CPE) of SmI₃ (3.7 mM),²⁴ PNPMoBr₃ (0.46 mM), ⁿHep₄NI (3.7 mM), and LutHNTf₂ (37 mM) at –1.45 V vs Fc⁺⁰ in THF (0.1 M ⁿBu₄NNTf₂) in a divided cell yields 16.9 equiv of NH₃ per Mo (2.1 equiv per Sm) with 82% F.E. (Table 6.1, entry 1; dihydrogen (H₂) is produced with 20% F.E.). The Hantzsch ester (HEH₂) is oxidized by 2H⁺/2e[–] in the presence of Lut at the anode to generate the pyridine HE with 93% F.E. (Figure E.7). Both Mo and an applied potential are required for NH₃ generation (entry 2). Under ¹⁵N₂, labeled ¹⁵NH₄⁺ is observed exclusively following acidic workup (see Appendix E2-3 for controls establishing N₂ as N-atom source).

Table 6.1. Summary of electrocatalytic N₂R data mediated by Mo and Sm.

Entry	Variation	equiv NH ₃ /Mo	F.E. (%)	e ⁻ /Sm
<i>[Mo] = PNP₂MoBr₃</i>				
1	None	16.9 ± 0.3 ^a	82 ± 2	6.3 ± 0.1
2 ^b	No Mo or no E _{app} or no N ₂ ^c	0	0	0
3 ^b	No Sm	0.5	20	-
4 ^b	GdI ₃ instead of SmI ₃	2.0	27	-
5 ^b	CoHNTf ₂ (pK _a 10.4)	0.9	35	1.0
6	+ 1 equiv H ₂ O per Sm / 3.8 C	2.4	42	0.8
7	+ 1 equiv tetraglyme per Sm	9.5	47	3.6
8	+ 1 equiv MeOH per Sm / 15.2 C	18.8	82	7.0
9	no acid / 0.8 C	0.9	75	0.3
10	240 equiv LutHNTf ₂ ^d / 40.5 C	33.0	55	12.4
<i>[Mo] = PCP₂MoBr₃</i> (0.23 mM, 1.2 μmol)				
11	None	32.5	80	6.1
12	No Sm / 9 C	1.2	4	-
13	0.5 μmol Mo	55 ± 2 ^a	60 ± 2	4.4 ± 0.2
14	320 equiv LutHNTf ₂ ^e / 27 C	67.2	83	12.6
<i>[Mo] = PNP₂Mo(N)I</i>				
15	None	16.7	82	6.3
16 ^f	No Sm	1.3	33	-
17	2 equiv Sm / 10.5 C	12.5	75	19.0
18	1 equiv Sm / 7 C	8.4	79	25
19	No Sm, -1.65 V vs Fc ^{+/0}	5.7	28	-

^aAverage of 2 or more runs; ^b9 h instead of 13.5 C; ^c1 bar argon; ^dAdded in 3 portions; ^eAdded in 2 portions; ^f6 h instead of 13.5 C.



152

In the absence of Sm, little charge passes (entry 3, 0.5 equiv per Mo). Use of GdI_3 as a redox-inactive substitute for SmI_3 results in a small increase in yield above this background (entry 4, 2.0 equiv per Mo, 27% F.E.).⁸ While this result indicates that strong Lewis-acid activation increases the N_2R activity of the Mo catalyst at moderate E_{app} (consistent with our group's previous observation of Li^+ as a key activator in unmediated $e\text{N}_2\text{R}$ with PNP Mo at -1.9 V),⁸ the significant enhancement with Sm in both yield and selectivity suggests that $\text{Ln}^{\text{III/II}}$ redox-mediation has a more pronounced benefit in $e\text{N}_2\text{R}$.

As hypothesized, LutH^+ is a privileged proton source both in terms of $\text{p}K_{\text{a}}$ and affinity for Sm^{III} following deprotonation. With the slightly weaker but structurally analogous acid ColHNTf_2 ($\text{ColH}^+ = 2,4,6\text{-trimethylpyridinium}$; $\text{p}K_{\text{a}} 10.4$ in THF), only 5.3 C pass, resulting in generation of 2.8 equiv of NH_3 per Mo (entry 5, 35% F.E.). Addition of H_2O (1 equiv per Sm) to SmI_3 results in only a 25 mV cathodic shift to $E_{1/2}(\text{Sm}^{\text{III/II}})$ (Figure E.9). However, CPE under the standard conditions with addition of H_2O shows rapid decay of the current over the first 2 C (corresponding to 1 reducing equivalent per Sm), consistent with conversion of redox-active $[\text{SmI}_3(\text{OH}_2)]$ to redox-inactive and poorly basic $[\text{Sm}^{\text{III}}\text{-OH}]$ or $[\text{Sm}^{\text{III}}_2\text{O}]$ sinks following consumption of $1e^-$ and 1H^+ per Sm. Curiously, in addition to inhibiting Sm turnover, H_2O decreases the $e\text{N}_2\text{R}$ selectivity (42% F.E. for NH_3 , entry 6). Tetraglyme as an aprotic but strongly coordinating additive has a similar effect (1 equiv per Sm, entry 7; 47% F.E.). Addition of weakly coordinating MeOH has no impact on the selectivity (entry 8, 82% F.E.). It also does not interfere with turnover, likely because LutH^+ is sufficiently acidic to liberate the monodentate alkoxide MeO^- from $\text{Sm}^{\text{III}}\text{I}_2\text{OMe}$ by protonolysis.

In the absence of LutHNTf₂, only 0.8 C passes before the current density becomes negligible. The CV of the cathode solution following this electrolysis features a partially reversible SmI₃ reduction wave at -1.45 V and a new reversible wave at -1.03 V (Figure 6.2A). The latter is assigned as the Mo^{V/IV} couple of PNPMo(N)I (Figure 6.2B, red trace), which is generated on treatment of PNPMoBr₃ with SmI₂ (Figure 6.2C).¹⁰ In both cases, the current intensity of the Mo^{V/IV} couple is consistent with ca. 80% yield of the nitride species by comparison to the CV of an authentic sample of PNPMo(N)I at the same concentration and scan rate. The stoichiometric amount of NH₃ detected from the acid-free electrolysis (0.9 equiv per Mo, entry 9) is attributed to decomposition of PNPMo(N)I on workup.

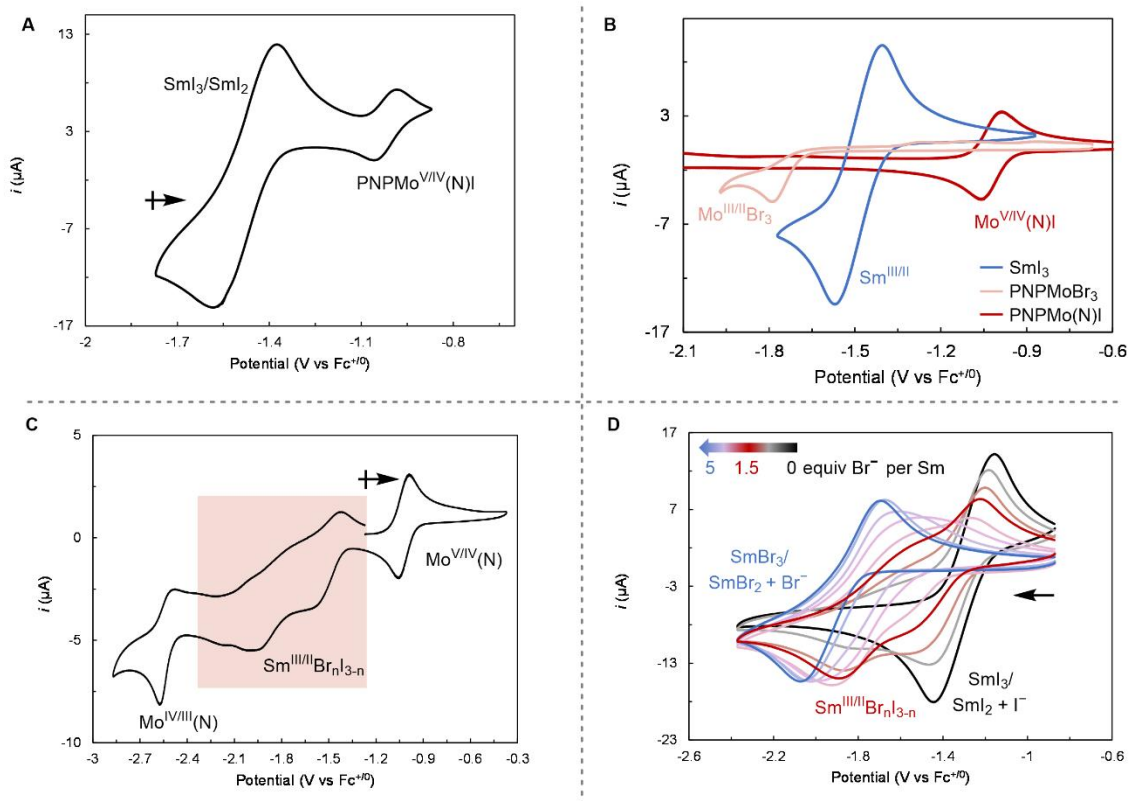
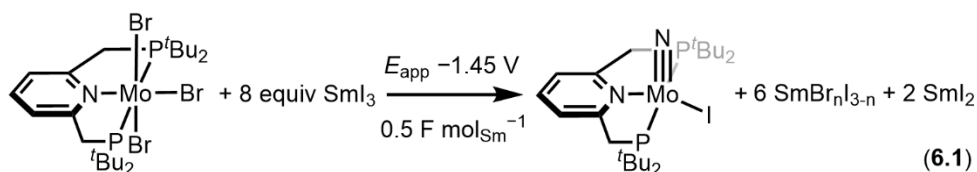


Figure 6.2: CVs of (A) the cathode solution following exhaustive electrolysis of SmI_3 (3.7 mM) with PNPMoBr_3 (0.46 mM) at -1.45 V at 25 mV s^{-1} ; (B) SmI_3 (2 mM, blue trace), PNPMoBr_3 (0.5 mM, pink trace), and PNPMo(N)I (0.5 mM, red trace) at 25 mV s^{-1} ; (C) the reaction mixture of SmI_2 (0.92 mM) and PNPMoBr_3 (0.5 equiv) at 25 mV s^{-1} ; (D) SmI_3 (2 mM) following addition of ${}^t\text{Bu}_4\text{NBr}$ (0-5 equiv) at 100 mV s^{-1} . All CVs are collected in 0.1 M ${}^t\text{Bu}_4\text{NNTf}_2$ /4 mM ${}^t\text{Hep}_4\text{NI}$ in THF with a glassy carbon disk working electrode, $\text{Ag}^{+/0}$ pseudoreference electrode, and Pt wire counter electrode.

This transformation releases 3 equiv of Br^- per Mo into the reaction mixture, resulting in formation of $\text{SmBr}_n\text{I}_{(3-n)}$ byproducts due to the higher affinity of Sm for Br^- than I^- . Indeed, the CV of the reaction mixture of SmI_2 with PNPMoBr_3 (0.5 equiv; 1.5 equiv Br^- per Sm; Figure 6.2D) contains broad $\text{Sm}^{\text{III/II}}$ features spanning -1.4 to -2.1 V that match the features observed in the CV of SmI_3 in the presence of 1.5 equiv ${}^t\text{Bu}_4\text{NBr}$ under the

same conditions (Figure 6.2C). Formation of Sm–Br bonds presumably facilitates the SmI_3 -mediated reduction of PNPMoBr_3 at -1.45 V, when direct reduction of PNPMoBr_3 at the electrode does not onset until -1.7 V (Figure 6.2B, peach trace). Indeed, the observation that only 0.5 reducing equivalents are passed per Sm (eqn 6.1) before the current decays to baseline suggests that some halide exchange to form redox-inactive $\text{SmBr}_n\text{I}_{(3-n)}$ species occurs by $[\text{Mo}^{\text{III}}-\text{Br}]/[\text{Sm}^{\text{III}}-\text{I}]$ anion methathesis prior to electrolysis.



Over the first 1.3 C of electrolysis under the standard conditions with LutHNTf_2 at -1.45 V, the same new $\text{Mo}^{\text{V/IV}}$ couple grows in while the intensity of the $\text{Sm}^{\text{III/II}}$ wave decreases (Figure 6.3A), consistent with activation of PNPMoBr_3 to form the on-path species $\text{PNPMo(N)I}^{25,26}$ with concomitant loss of active SmI_3 cocatalyst to $\text{SmBr}_n\text{I}_{(3-n)}$ species that are redox-inactive at -1.45 V. Meanwhile, NH_3 generation displays a brief induction period for the first 0.2 C as PNPMo(N)I grows in (Figure 6.3A inset) before increasing linearly with the charge passed (Figure E.6), indicating constant Faradaic efficiency over time.

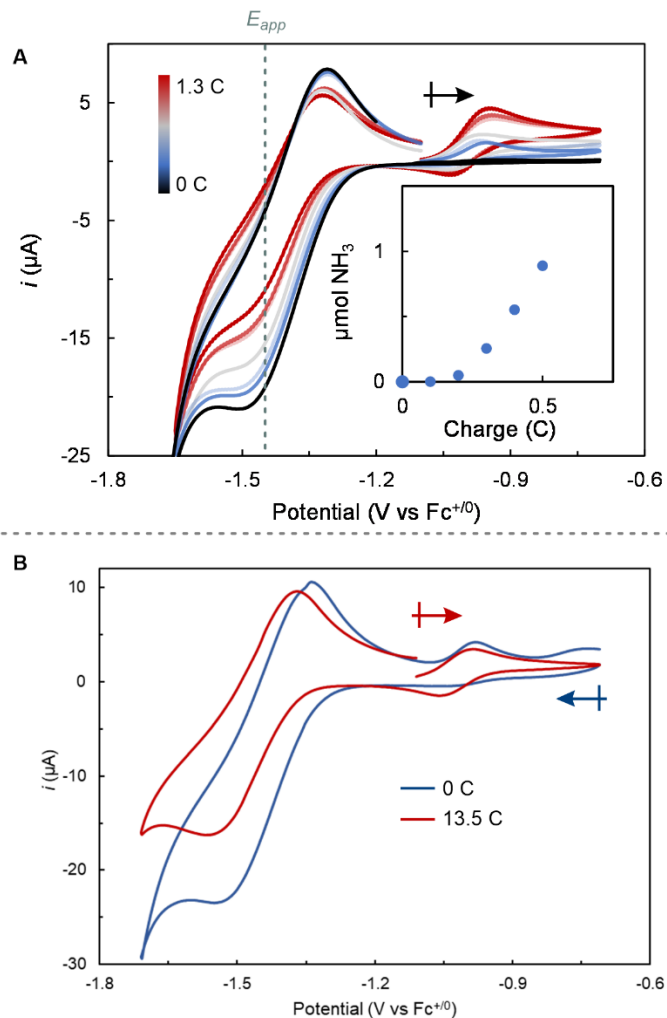


Figure 6.3: (A) CVs of the cathode solution under the standard electrocatalytic conditions with PNPMoBr₃ recorded after passage of 0-1.3 C; inset: NH₃ production as a function of charge passed. (B) CVs of the cathode solution before and after exhaustive electrolysis at 25 mV s⁻¹. In all cases the first scan is shown initiated at the indicated potential.

The CV of the cathode solution after passage of 13.5 C (corresponding to 60 reducing equivalents per Mo) shows that both PNPMo(N)I and SmI₃ are present with minimal catalyst degradation (Figure 6.3). Accordingly, the eN₂R remains efficient following the addition of further portions of LutHNTf₂ and continued electrolysis at -1.45 V. Up to 33

equiv of NH_3 per Mo (12.4 e^- per Sm, entry 10) is produced following two successive¹⁵⁷ additions of acid (80 equiv per Mo each), with an overall F.E. of 55%.

A >80% F.E. for N_2R is also attained with the N-heterocyclic carbene-based Mo catalyst PCPMoBr_3 under Sm-mediated electrocatalytic conditions (entries 11–14). As has been observed by Nishibayashi and co-workers with other reductant/acid combinations,^{11,27} this catalyst remains robust at low loadings, enabling a higher Mo turnover number (up to 67 equiv NH_3 per Mo, entry 12).

PNPMo(N)I performs analogously to PNPMoBr_3 under the standard conditions with Sm (Table 6.1, entry 15; 16.7 equiv/Mo, 82% F.E., 6.3 e^- per Sm). In the absence of Sm at -1.45V , little charge passes and a subcatalytic amount of NH_3 is produced at only 33% F.E. (entry 16), indicating that Sm increases the rate and selectivity of $e\text{N}_2\text{R}$ beyond precatalyst activation.

The Sm turnover number was next evaluated using the bromide-free catalyst PNPMo(N)I , with which none of the initial SmI_3 loading is deactivated as $\text{SmBr}_n\text{I}_{(3-n)}$.²⁸ Decreasing the Sm concentration by a factor of 4 (1 mM) results in the generation of 6.3 equiv of NH_3 per Sm at 75% F.E. (entry 17), representing a 19-fold increase in the number of electrons transferred per Sm equivalent compared to conditions under which SmI_2 is the terminal reductant. At 0.5 mM SmI_3 , 8.4 equiv of NH_3 is produced per Sm (~ 25 electrons per Sm) with 79% F.E. (entry 18), but only 7.0 C pass before the current density becomes negligible. No features attributable to SmI_3 reduction are present in the CV following electrolysis (Figure E.11), indicating that catalyst deactivation pathways are competitive with $e\text{N}_2\text{R}$ at a very low Sm loading.

Reductive protonation of Mo^{IV} -nitride species to form Mo^{III} -imides is typically the most thermodynamically challenging $1\text{H}^+/1\text{e}^-$ step in N_2R with Mo-pincer complexes,¹¹ prompting us to probe activation modes of $\text{PNPMo}(\text{N})\text{I}$ as the bulk Mo resting state under Sm-mediated electrocatalytic conditions. $\text{PNPMo}(\text{N})\text{I}$ undergoes reversible oxidation with $E_{1/2}(\text{Mo}^{\text{V/IV}}) = -1.03$ V (Figure 6.4A, black trace). The open circuit potential shifts from -1.1 V to -0.5 V following addition of 0.5 equiv I_2 but the potential and intensity of the CV wave is unchanged (Figure 6.4A, red trace), demonstrating clean conversion to generate the Mo^{V} -nitride. The position of the wave is insensitive to $[\text{}^n\text{Hep}_4\text{NI}]$ (Figure 6.4B), indicating that the $\text{Mo}^{\text{V/IV}}$ couple is not coupled to iodide association/dissociation and the Mo^{V} complex is best formulated as the cation $\text{PNPMo}(\text{N})\text{I}^+$ under the electrochemical conditions. This species was found to be more stable in the presence of acid than the Mo^{IV} -nitride (which was prone to oxidation on the timescale of a detailed electroanalytical experiment), and thus further studies were conducted with in situ-generated $\text{PNPMo}(\text{N})\text{I}^+$ as the bulk Mo analyte.

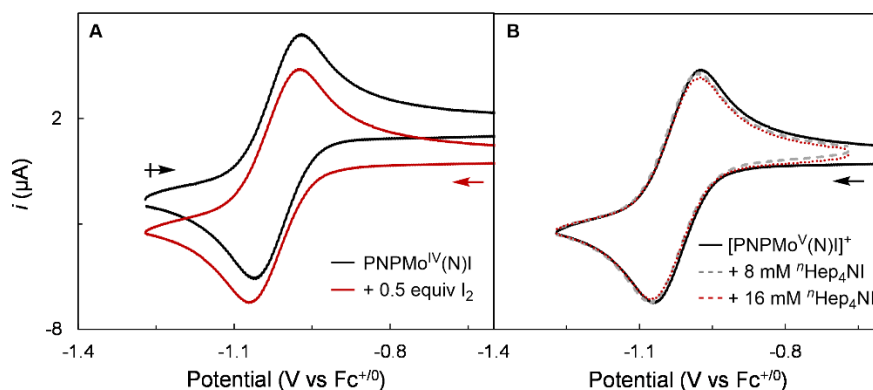


Figure 6.4. CVs of (A) $\text{PNPMo}(\text{N})\text{I}$ (0.46 mM, black trace) following addition of 0.5 equiv I_2 (red trace) and (B) in situ-generated $[\text{PNPMo}^{\text{V}}(\text{N})\text{I}]^+$ (0.46 mM, black trace) in the presence of increasing $[\text{}^n\text{Hep}_4\text{NI}]$ (8-16 mM, gray and red dashed

traces) at 100 mV s^{-1} ($0.1 \text{ M } ^n\text{Bu}_4\text{NNTf}_2$ in THF, glassy carbon disk working electrode, $\text{Ag}^{+/0}$ pseudoreference electrode, Pt wire counter electrode).

Addition of LutHNTf_2 to PNPMo(N)I^+ results in an overall anodic shift to the MoV/IV couple and broadening of the anodic wave (Figure 6.5A, upper dataset). This behavior is reversed by addition of the conjugate base Lut (Figure 6.5A, lower dataset). With the stronger acid PicHNTf_2 ($\text{p}K_a$ 8.6 in THF), the positive shift to the cathodic wave is more pronounced (Figure 6.5B, upper dataset). Additionally, the anodic wave splits into multiple features with $E_{p,a}$ ca. -0.8 , -0.6 , and -0.5 V (Figure 6.5C); the most negative feature becomes relatively less intense at high scan rate. Addition of Pic (2 mM) results in collapse of the anodic features back to a single wave, and further titration of Pic leads to a cathodic shift to the redox couple (Figure 6.5B, lower dataset).

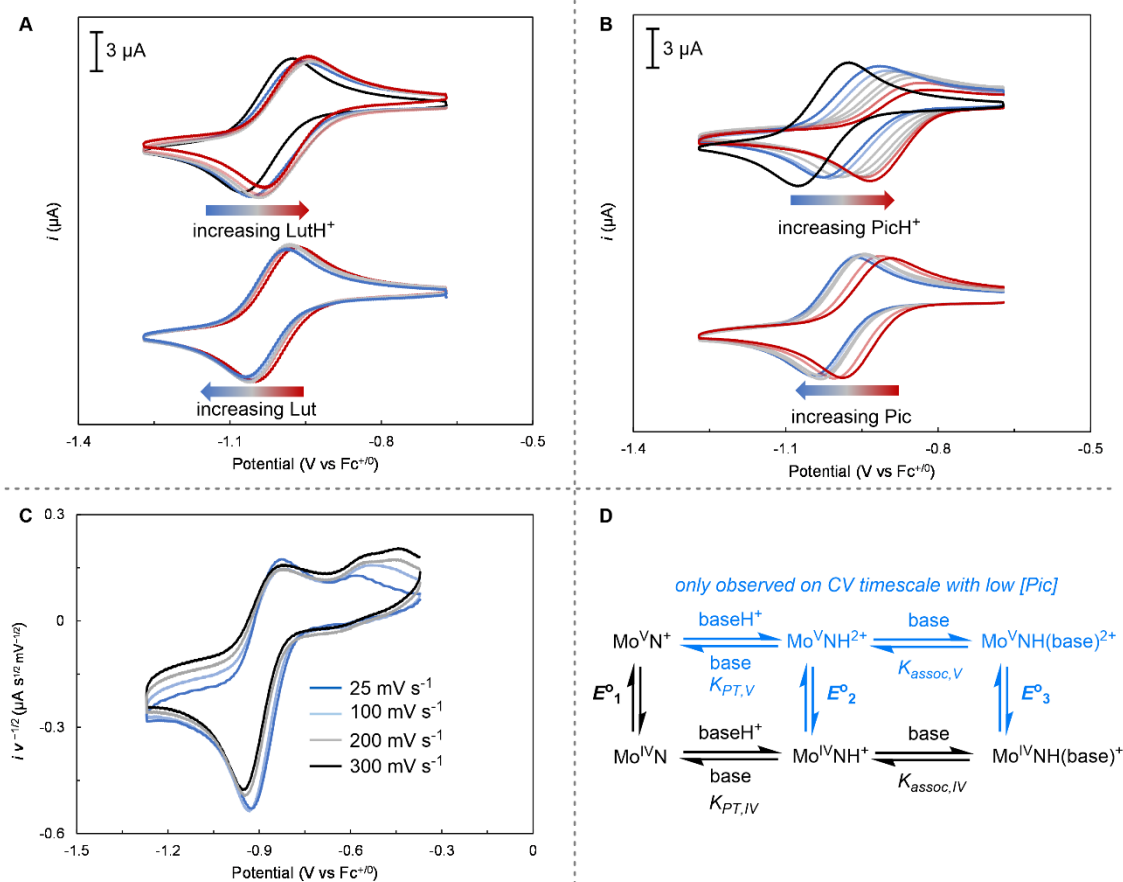


Figure 6.5: CVs of in situ-generated $[\text{PNPMo}^{\text{V}}(\text{N})\text{I}]^+$ (0.46 mM, black trace) following successive addition of (A) 4–80 mM of LutHNTf_2 and 2–80 mM Lut or (B) 2–64 mM PicHNTf_2 and 2–64 mM Pic at 100 mV s^{-1} ; (C) 64 mM PicHNTf_2 at varying scan rates (0.1 M $n\text{-Bu}_4\text{NNTf}_2$ in THF, glassy carbon disk working electrode, $\text{Ag}^{+/0}$ pseudoreference electrode, Pt wire counter electrode); and (D) Square scheme describing PT and ET steps at the $\text{PNPMo}^{\text{V/IV}}(\text{N})\text{I}$ redox couple.

In sum, these observations are qualitatively consistent with the scheme in Figure 6.5D.

The cathodic sweep comprises an EC mechanism (where E and C represent electrochemical and chemical steps, respectively; bottom left corner of the square scheme), in which reduction of $\text{Mo}^{\text{V}}\text{N}^+$ generates the more basic $\text{Mo}^{\text{IV}}(\text{N})$ complex. Rapid and reversible PT from baseH^+ generates an equilibrium mixture of $\text{Mo}^{\text{IV}}(\text{N})$ and $\text{Mo}^{\text{IV}}(\text{NH})^+$

(we formulate the latter as a cation due to the insensitivity of the CV in the presence of¹⁶¹ excess LutH⁺ to the concentration of I⁻; see Figure E.16). The anodic sweep contains the reverse CE process: deprotonation of Mo^{IV}(NH)⁺ by the conjugate base generates Mo^{IV}(N), which undergoes oxidation at ca. -0.9 V.

The CV response observed with PicHNTf₂ in the absence of added Pic represents a special case. In the presence of a low concentration of the weak base, the reverse deprotonation step is slow, and so a second EC process is also observed in which Mo^{IV}NH⁺ is oxidized at more positive potentials followed by rapid deprotonation to regenerate Mo^VN. Nishibayashi and coworkers have observed that protonation of PNPMo(N)Cl by pyridinium triflate results in binding of the conjugate base pyridine to the imide complex.²⁵ We therefore tentatively assign the multiple new peaks observed at fast scan rates on the anodic sweep as a combination of EC and CE pathways for the overall conversion of an equilibrium mixture of Mo^{IV}(NH)⁺ and Mo^{IV}(NH)(Pic)⁺ back to Mo^V(N)⁺.

For both buffer systems, with both acid and base present in excess, the overall Mo^{V/IV} interconversion appears as a single reversible couple, indicating that coupled chemical steps (bottom pathway of Figure 6.5D) are fast on the CV timescale. The anodic displacement of the observed $E_{1/2}$ from $E^\circ(\text{Mo}^{\text{V/IV}}(\text{N}))$ (-1.03 V vs Fc⁺⁰) is a measure of the pseudo-first order equilibrium constant for the reversible reaction of Mo^{IV}N with baseH⁺ according to eqn 6.2, derived below for the case where the reaction provides a mixture of free and base-coordinated imide complexes.²⁹ Plotting $E_{1/2}(\text{Mo}^{\text{V/IV}})$ at varying [baseH⁺]:[base] (holding [baseH⁺] constant) according to eqn 6.2 yields linear relationships (Figure 6.6). The slopes provide estimates of $K_{\text{PT,IV}}$ as 0.029 ± 0.001 and 0.75 ± 0.02 for the LutH⁺:Lut and PicH⁺:Pic buffer systems, respectively. The larger equilibrium constant

with the stronger acid supports assignment of the chemical step in the square scheme to a proton transfer. Based on the model in Figure 6.5D, the intercepts of these plots (1.8 ± 0.4 and 0.9 ± 0.1 for PicH⁺:Pic and LutH⁺:Lut, respectively) provide estimates of the affinity of each base for the imide complex. Consistent with our interpretation, a larger intercept is observed for the more sterically accessible base Pic. For Lut, the intercept is within error of unity, suggesting that the flanking methyl groups hinder coordination following proton transfer.

$$\exp\left(\frac{F}{RT}(E_{1/2} - E^0_1)\right) = K_{PT,IV} \frac{[baseH^+]}{[base]} + K_{PT,IV}K_{assoc,IV}[baseH^+] + 1 \quad (6.2)$$

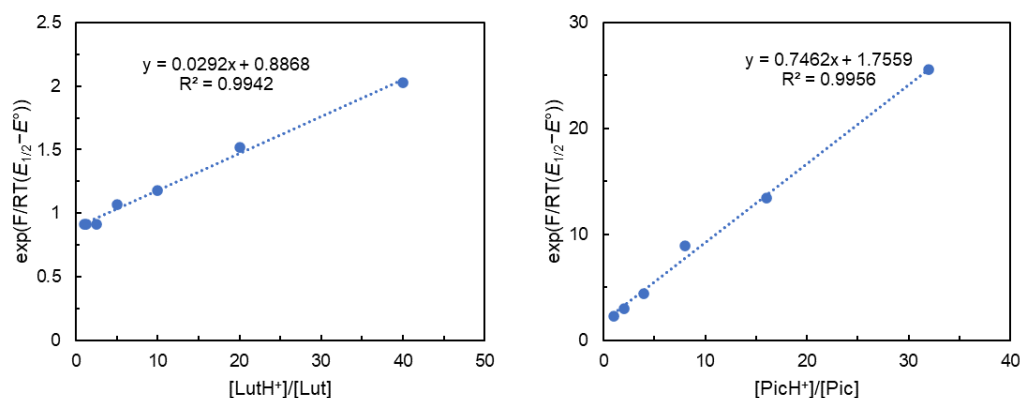


Figure 6.6: Plots of the measured $\text{Mo}^{V/IV} E_{1/2}$ values as a function of the $[\text{baseH}^+]:[\text{base}]$ ratio according to eqn 6.2.

We conclude that PNP $\text{Mo}(\text{N})\text{I}$ exists in an equilibrium mixture with PNP $\text{Mo}(\text{NH})\text{I}^+$ under the standard electrocatalytic conditions. Reduction of PNP $\text{Mo}(\text{N})\text{I}$ requires a strongly cathodic applied potential ($E_{p,c} = -2.60$ V; Figure 6.2C). However, the addition of 80 equiv of LutHNTf₂ gives rise to an irreversible wave just positive of background reduction of LutH⁺, assigned to reduction of [PNP $\text{Mo}(\text{NH})\text{I}^+$] (Figure 6.7). Electrolysis of this mixture at -1.65 V increases the charge passed and the ammonia yield (Table 1, entry

17; 5.7 equiv per Mo) relative to the Sm-free reaction at -1.45 V, but the F.E. remains low (28%; 25% F.E. for H_2).¹⁶³

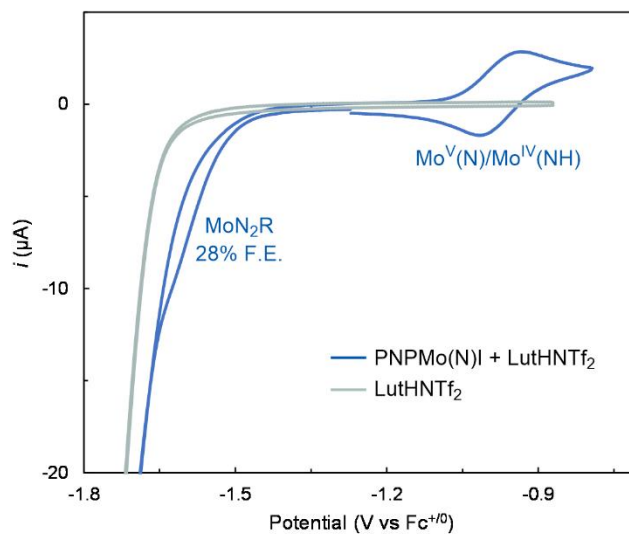


Figure 6.7: CV of PNPMo(N)I (0.46 mM) in the presence of LutHNTf₂ (80 equiv, blue trace) overlaid with the LutHNTf₂ background at 100 mV s⁻¹ (0.1 M ⁿBu₄NNTf₂ in THF, glassy carbon disk working electrode, Ag⁺⁰ pseudoreference electrode, Pt wire counter electrode).

As illustrated in Figure 6.8A, we conclude that reduction of PNPMo(N)I by $1H^+/1e^-$ equivalent toward ammonia generation is kinetically feasible with the combination of LutH⁺ and $E_{app} < -1.6$ V.^{8,11} However, the rate of background reduction of LutH⁺ at the electrode is competitive at these potentials,³⁰⁻³² leading to low F.E. Addition of Sm as a redox mediator enhances the rate of N₂R at a more anodic potential with minimal competing acid reduction, presumably by accelerating a limiting ET step in the N₂R cycle such as reduction of PNPMo(NH)I⁺.

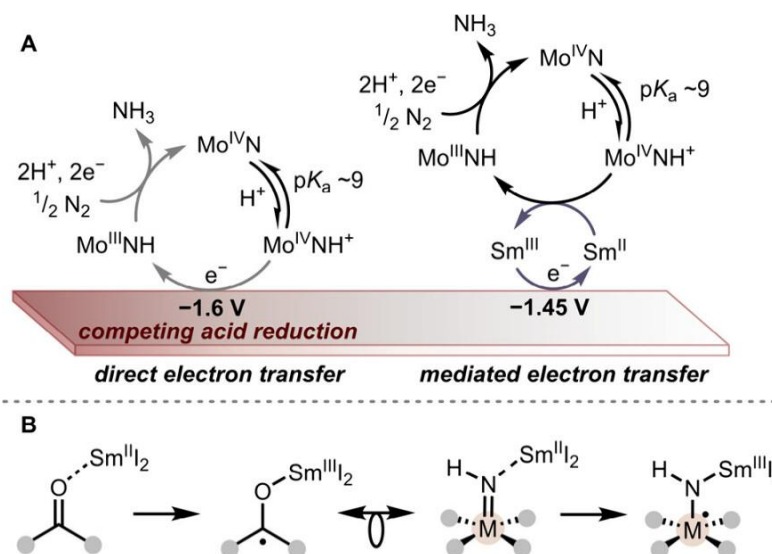


Figure 6.8: (A) Proposed role of Sm^{III/II} redox in mediation of selective Mo-catalyzed N₂R. (B) Analogy between reduction of a carbonyl and a metal-imide complex by SmI₂.

The behavior of SmI₂ in this system mirrors its catalytic role in the electrochemical reduction of carbonyl substrates.¹⁸ ET from SmI₂ to ketones occurs by an inner-sphere mechanism comprising coordination of the substrate to Sm^{II} followed by electron transfer to form a Sm^{III}-ketyl radical species (Figure 6.8B),³³ providing a substantial additional driving force to enable reductions that would be uphill by >1 V via an outer-sphere pathway.³⁴ An analogous inner-sphere process driven by the azaphilicity of Sm^{III} may be operable here (Figure 6.8B).^{15,35–39}

The Sm-mediated tandem catalysis described here operates at the lowest overpotential and highest Faradaic efficiency reported to date for a nonaqueous *e*N₂R system at atmospheric pressure (Figure 6.9).^{4,7–9,40} While the yield rate (~1 nmol of NH₃ cm⁻² s⁻¹) is substantially lower than that of LiN₂R (20 nmol of NH₃ cm⁻² s⁻¹ at 1 bar N₂ with 2 M LiNTf₂), when normalized by the concentration of the ET mediator, the yield rate per [Sm] is higher than that per [Li] (~250 nmol of NH₃ M_{Sm}⁻¹ cm⁻² s⁻¹ vs 10 nmol of NH₃ M_{Li}⁻¹

cm⁻² s⁻¹). Electrolysis at higher [Sm] is hampered by the relatively low solubility of¹⁶⁵ SmI₃ in THF, calling for future electrolyte design. Additionally, strategies to replace HEH₂ with H₂ or H₂O as the terminal reductant are warranted.

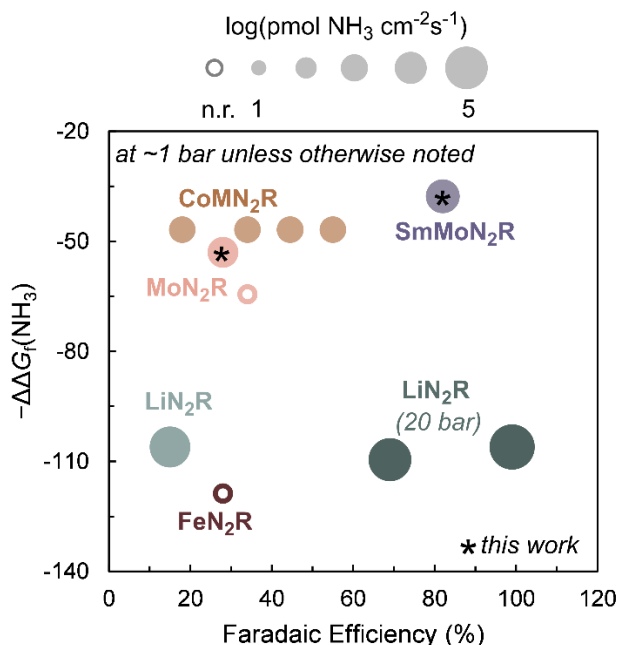


Figure 6.9: Comparison of the overpotential, Faradaic efficiency, and yield rate of the Sm- and Mo-mediated $e\text{N}_2\text{R}$ reported here with representative nonaqueous $e\text{N}_2\text{R}$ systems from the literature. Note: While Sm-mediated versus unmediated N_2R by the Mo-catalyst featured herein can be directly compared, conditions vary among the other examples in the plot, and it hence serves as a qualitative guide.

To conclude, the use of LutH^+ as a low-affinity proton source enables electrochemical turnover of SmI_2 in Mo-catalyzed N_2R . Sm catalyzes the reaction at a milder applied potential and higher F.E. (82% F.E. for NH_3) than unmediated Mo N_2R electrocatalysis, which is limited by competing acid reduction. Additionally, the efficacy of the Sm-mediated $e\text{N}_2\text{R}$ system, which operates in the absence of a coordinating alcohol, demonstrates that concerted PCET from a $\text{Sm}^{\text{II}}\text{-O(R)H}$ adduct is not necessary for selective Sm-mediated N–H bond formation.

REFERENCES

- (1) MacFarlane, D. R.; Cherepanov, P. V.; Choi, J.; Suryanto, B. H. R.; Hodgetts, R. Y.; Bakker, J. M.; Vallana, F. M. F.; Simonov, A. N. A roadmap to the ammonia economy. *Joule* **2020**, *4* (6), 1186–1205.
- (2) Hochman, G.; Goldman, A. S.; Felder, F. A.; Mayer, J. M.; Miller, A. J. M.; Holland, P. L.; Goldman, L. A.; Manocha, P.; Song, Z.; Aleti, S. Potential economic feasibility of direct electrochemical nitrogen reduction as a route to ammonia. *ACS Sustain. Chem. Eng.* **2020**, *8* (24), 8938–8948.
- (3) Choi, J.; Suryanto, B. H. R.; Wang, D.; Du, H.-L.; Hodgetts, R. Y.; Ferrero Vallana, F. M.; MacFarlane, D. R.; Simonov, A. N. Identification and elimination of false positives in electrochemical nitrogen reduction studies. *Nat. Commun.* **2020**, *11* (1), 5546.
- (4) Du, H.-L.; Chatti, M.; Hodgetts, R. Y.; Cherepanov, P. V.; Nguyen, C. K.; Matuszek, K.; MacFarlane, D. R.; Simonov, A. N. Electroreduction of nitrogen with almost 100% current-to-ammonia efficiency. *Nature* **2022**, *609* (7928), 722–727.
- (5) Pickett, C. J.; Talarmin, J. Electrosynthesis of ammonia. *Nature* **1985**, *317* (6038), 652–653.
- (6) Del Castillo, T. J.; Thompson, N. B.; Peters, J. C. A synthetic single-site Fe nitrogenase: high turnover, freeze-quench ^{57}Fe Mössbauer data, and a hydride resting state. *J. Am. Chem. Soc.* **2016**, *138* (16), 5341–5350.

- (7) Chalkley, M. J.; Del Castillo, T. J.; Matson, B. D.; Peters, J. C. Fe-mediated¹⁶⁷ nitrogen fixation with a metallocene mediator: exploring pK_a effects and demonstrating electrocatalysis. *J. Am. Chem. Soc.* **2018**, *140* (19), 6122–6129.
- (8) Ibrahim, A. F.; Garrido-Barros, P.; Peters, J. C. Electrocatalytic nitrogen reduction on a molybdenum complex bearing a PNP pincer ligand. *ACS Catal.* **2023**, *13* (1), 72–78.
- (9) Garrido-Barros, P.; Derosa, J.; Chalkley, M. J.; Peters, J. C. Tandem electrocatalytic N_2 fixation via proton-coupled electron transfer. *Nature* **2022**, *609* (7925), 71–76.
- (10) Ashida, Y.; Arashiba, K.; Nakajima, K.; Nishibayashi, Y. Molybdenum-catalysed ammonia production with samarium diiodide and alcohols or water. *Nature* **2019**, *568* (7753), 536–540.
- (11) Ashida, Y.; Mizushima, T.; Arashiba, K.; Egi, A.; Tanaka, H.; Yoshizawa, K.; Nishibayashi, Y. Catalytic production of ammonia from dinitrogen employing molybdenum complexes bearing N-heterocyclic carbene-based PCP-type pincer ligands. *Nat. Synth.* **2023**, 1–10.
- (12) Hegg, A. S.; Mercado, B. Q.; Miller, A. J. M.; Holland, P. L. Catalytic reduction of dinitrogen to ammonia using molybdenum porphyrin complexes. *Faraday Discuss.* **2023**, *243* (0), 429–449.
- (13) Ashida, Y.; Arashiba, K.; Tanaka, H.; Egi, A.; Nakajima, K.; Yoshizawa, K.; Nishibayashi, Y. Molybdenum-catalyzed ammonia formation using simple monodentate and bidentate phosphines as auxiliary ligands. *Inorg. Chem.* **2019**, *58* (14), 8927–8932.

- (14) Bruch, Q. J.; Connor, G. P.; Chen, C.-H.; Holland, P. L.; Mayer, J. M.; Hasanayn, F.; Miller, A. J. M. Dinitrogen reduction to ammonium at rhenium utilizing light and proton-coupled electron transfer. *J. Am. Chem. Soc.* **2019**, *141* (51), 20198–20208.
- (15) Boyd, E. A.; Peters, J. C. Highly selective Fe-catalyzed nitrogen fixation to hydrazine enabled by Sm(II) reagents with tailored redox potential and pK_a . *J. Am. Chem. Soc.* **2023**, *145* (27), 14784–14792.
- (16) Arashiba, K.; Kanega, R.; Himeda, Y.; Nishibayashi, Y. Electrochemical reduction of samarium triiodide into samarium diiodide. *Chem. Lett.* **2020**, *49* (10), 1171–1173.
- (17) Arashiba, K.; Kanega, R.; Himeda, Y.; Nishibayashi, Y. Catalytic ammonia formation with electrochemically reduced samarium diiodide from samarium triiodide and water from dinitrogen. *Chem. Lett.* **2021**, *50* (7), 1356–1358.
- (18) Boyd, E. A.; Shin, C.; Charboneau, D. J.; Peters, J. C.; Reisman, S. E. Reductive samarium (electro)catalysis enabled by Sm^{III}-alkoxide protonolysis. *Science* **2024**, *385* (6711), 847–853.
- (19) Garrido, G.; Koort, E.; Ràfols, C.; Bosch, E.; Rodima, T.; Leito, I.; Rosés, M. Acid–base equilibria in nonpolar media. Absolute pK_a scale of bases in tetrahydrofuran. *J. Org. Chem.* **2006**, *71* (24), 9062–9067.
- (20) Chciuk, T. V.; Flowers, R. A. Proton-coupled electron transfer in the reduction of arenes by SmI₂–water complexes. *J. Am. Chem. Soc.* **2015**, *137* (35), 11526–11531.
- (21) Kolmar, S. S.; Mayer, J. M. SmI₂(H₂O)_n reduction of electron rich enamines by proton-coupled electron transfer. *J. Am. Chem. Soc.* **2017**, *139* (31), 10687–10692.
- (22) Boeckell, N. G.; Flowers, R. A. Coordination-induced bond weakening. *Chem. Rev.* **2022**, *122* (16), 13447–13477.

- (23) Chciuk, T. V.; Anderson, W. R.; Flowers, R. A. Proton-coupled electron transfer in the reduction of carbonyls by samarium diiodide–water complexes. *J. Am. Chem. Soc.* **2016**, *138* (28), 8738–8741.
- (24) Anhydrous, homogeneous solutions of $\text{SmI}_3(\text{THF})_n$ are in all cases prepared in situ by addition of 0.5 equiv of I_2 to a solution of $\text{SmI}_2(\text{THF})_n$.
- (25) Tanaka, H.; Arashiba, K.; Kuriyama, S.; Sasada, A.; Nakajima, K.; Yoshizawa, K.; Nishibayashi, Y. Unique behaviour of dinitrogen-bridged dimolybdenum complexes bearing pincer ligand towards catalytic formation of ammonia. *Nat. Commun.* **2014**, *5* (1), 3737.
- (26) Arashiba, K.; Eizawa, A.; Tanaka, H.; Nakajima, K.; Yoshizawa, K.; Nishibayashi, Y. Catalytic nitrogen fixation via direct cleavage of nitrogen–nitrogen triple bond of molecular dinitrogen under ambient reaction conditions. *Bull. Chem. Soc. Jpn.* **2017**, *90* (10), 1111–1118.
- (27) Eizawa, A.; Arashiba, K.; Tanaka, H.; Kuriyama, S.; Matsuo, Y.; Nakajima, K.; Yoshizawa, K.; Nishibayashi, Y. Remarkable catalytic activity of dinitrogen-bridged dimolybdenum complexes bearing NHC-based PCP-pincer ligands toward nitrogen fixation. *Nat. Commun.* **2017**, *8* (1), 14874.
- (28) Miller, R. S.; Sealy, J. M.; Shabangi, M.; Kuhlman, M. L.; Fuchs, J. R.; Flowers, R. A. Reactions of SmI_2 with alkyl halides and ketones: Inner-sphere vs outer-sphere electron transfer in reactions of Sm(II) reductants. *J. Am. Chem. Soc.* **2000**, *122* (32), 7718–7722.
- (29) Savéant, J.-M. *Elements of Molecular and Biomolecular Electrochemistry*; John Wiley & Sons, Inc: Hoboken, New Jersey, 2006.

- (30) Raghavan, R.; Iwamoto, R. T. Chemical-electrochemical method for the¹⁷⁰ determination of the positions of coupling in the dimeric one-electron reduction products of ring-substituted 1-alkylpyridinium ions. *J. Electroanal. Chem. Interfacial Electrochem.* **1979**, *102* (1), 85–92.
- (31) Munisamy, T.; R. Schrock, R. An electrochemical investigation of intermediates and processes involved in the catalytic reduction of dinitrogen by [HIPTN₃N]Mo (HIPTN₃N = (3,5-(2,4,6-i-Pr₃C₆H₂)₂C₆H₃NCH₂CH₂)₃N). *Dalton Trans.* **2012**, *41* (1), 130–137.
- (32) McCarthy, B. D.; Martin, D. J.; Rountree, E. S.; Ullman, A. C.; Dempsey, J. L. Electrochemical reduction of Brønsted acids by glassy carbon in acetonitrile—implications for electrocatalytic hydrogen evolution. *Inorg. Chem.* **2014**, *53* (16), 8350–8361.
- (33) Enemærke, R. J.; Daasbjerg, K.; Skrydstrup, T. Is samarium diiodide an inner- or outer-sphere electron donating agent? *Chem. Commun.* **1999**, *0* (4), 343–344.
- (34) Farran, H.; Hoz, S. Quantifying the electrostatic driving force behind SmI₂ reductions. *Org. Lett.* **2008**, *10* (21), 4875–4877.
- (35) Evans, W. J.; Ulibarri, T. A.; Ziller, J. W. Isolation and x-ray crystal structure of the first dinitrogen complex of an f-element metal, [(C₅Me₅)₂Sm]₂N₂. *J. Am. Chem. Soc.* **1988**, *110* (20), 6877–6879.
- (36) Evans, W. J.; Kociok-Koehn, G.; Leong, V. S.; Ziller, J. W. Reactivity of hydrazines with organometallic samarium complexes and the x-ray crystal structures of (C₅Me₅)₂Sm(η²-PhNHNPh)(THF), (C₅Me₅)₂Sm(NHPh)(THF), and [(C₅Me₅)₂Sm]₂(μ-η²:η²-HNNH). *Inorg. Chem.* **1992**, *31* (17), 3592–3600.

- (37) Glassman, T. E.; Liu, A. H.; Schrock, R. R. Bimetallic hydrazido(3- and 4-) and¹⁷¹ nitrido complexes of tungsten containing the $W(\eta^5-C_5Me_5)Me_3$ core. *Inorg. Chem.* **1991**, *30* (25), 4723–4732.
- (38) Jori, N.; Moreno, J. J.; Shivaraam, R. A. K.; Rajeshkumar, T.; Scopelliti, R.; Maron, L.; Campos, J.; Mazzanti, M. Iron promoted end-on dinitrogen-bridging in heterobimetallic complexes of uranium and lanthanides. *Chem. Sci.* **2024**, *15* (18), 6842–6852.
- (39) Maity, S.; Flowers, R. A.; Hoz, S. Aza versus oxophilicity of SmI_2 : A break of a paradigm. *Chem. – Eur. J.* **2017**, *23* (67), 17070–17077.
- (40) Suryanto, B. H. R.; Matuszek, K.; Choi, J.; Hodgetts, R. Y.; Du, H.-L.; Bakker, J. M.; Kang, C. S. M.; Cherepanov, P. V.; Simonov, A. N.; MacFarlane, D. R. Nitrogen reduction to ammonia at high efficiency and rates based on a phosphonium proton shuttle. *Science* **2021**, *372* (6547), 1187–1191.

SUPPLEMENTARY INFORMATION FOR CHAPTER 2

Reproduced with permission from Boyd, E.A.; Peters, J. C. *J. Am. Chem. Soc.* **2022**, *144*, 21337. doi: 10.1021/jacs.2c09580

A1 Experimental Part**A1.1 General Considerations**

All manipulations were carried out using standard Schlenk or glovebox techniques under an N₂ atmosphere. Unless otherwise noted, solvents were deoxygenated and dried by thoroughly sparging with N₂ gas followed by passage through an activated alumina column in the solvent purification system by SG Water, USA LLC. Non-halogenated solvents were tested with a standard purple solution of sodium benzophenone ketyl in tetrahydrofuran to confirm effective oxygen and moisture removal. All reagents were purchased from commercial vendors and used without further purification unless otherwise stated. MeOH was stirred over 3 Å molecular sieves under N₂ for one week, vacuum transferred into a Schlenk flask, and stored sealed in a glovebox. 1,8-diazabicyclo[5.4.0]undec-7-ene (DBU) was distilled from CaH₂ and stored in a glovebox. *N*-methylpyrrolidinone, pyrrolidinone, and 1,1-diphenylethylene were degassed and passed over a pipet filter of activated alumina. ⁿBu₄NPF₆ was recrystallized from hot EtOH three times and then dried under vacuum at 100°C for >12 hours before use as electrolyte. (^tBu₂ArO)₂Me₂cyclam)Sm was synthesized via reported literature procedures.^{1,2} 2-pyrrolidinone was deuterated by stirring in CD₃OD for 30 min followed by removal of solvent *in vacuo* (75% deuteration measured by ¹H NMR).

A1.2 Nuclear Magnetic Resonance Spectroscopy

Deuterated solvents were purchased from Cambridge Isotope Laboratories, Inc. C_6D_6 was degassed, stirred over NaK, and passed over activated alumina before use. CD_3CN was degassed and passed over activated alumina 5 times immediately before use with moisture-sensitive compounds. 1H and ^{13}C chemical shifts are reported in ppm relative to tetramethylsilane, using residual solvent resonances as internal standards. ^{31}P chemical shifts are reported in ppm relative to 85% aqueous H_3PO_4 .

A1.3 X-ray Crystallography

X-ray diffraction (XRD) studies were carried out at the Beckman Institute Crystallography Facility on a Bruker Kappa Apex II diffractometer (Mo $K\alpha$ radiation, $\lambda = 0.71073$). All crystals were mounted on a glass fiber loop under Paratone N oil. Structures were solved using SHELXS or SHELXT and refined against F^2 on all data by full-matrix least squares with SHELXL.³ All of the solutions were performed in the Olex2 program.⁴ All hydrogen atoms were placed in calculated positions. Nonhydrogen atoms were refined anisotropically.

A1.4 Electrochemistry

Electrochemical measurements were carried out in an N_2 -filled glovebox in a 20 mL scintillation vial fitted with a septum cap containing punched-out holes for insertion of electrodes. A CD instruments 600B electrochemical analyzer was used for data collection. A freshly-polished glassy carbon electrode was used as the working electrode. A silver wire immersed in a 5 mM solution of AgOTf in electrolyte separated from the working solution by a frit was used as pseudoreference and a platinum wire was used as the auxiliary electrode. All reported potentials are referenced to the ferrocene couple, Cp_2Fe^+/Cp_2Fe

measured at the end of each electrochemical experiment. Electrochemistry solvents were¹⁷⁴
passed over a pipet filter of activated alumina immediately before use.

A2 Synthetic Procedures

A2.1 Synthesis of $[(\text{tBu}_2\text{ArO})_2\text{Me}_2\text{cyclam})\text{Sm}^{\text{III}}(\text{THF})]\text{PF}_6$ ($[\text{Sm}^{\text{III}}]\text{PF}_6$)

Analogous to the reported synthesis of $[\text{Sm}^{\text{III}}]\text{BPh}_4$,² a solution of TlPF_6 (43 mg, 0.123 mmol) in THF (~1 mL) was added dropwise to a dark green solution of Sm^{II} (100 mg, 0.123 mmol) in THF (~2 mL). The solution immediately lightened and dark gray Tl metal precipitated. The reaction mixture was filtered to remove Tl^0 and concentrated to ~0.5 mL. Addition of pentane (~10 mL) led to precipitation of the title compound as a pale yellow solid, which was isolated by filtration (93 mg, 79% yield). ^1H NMR (400 MHz, CD_3CN) δ 9.05 (s, 2H, Ar-H), 7.96 (s, 2H, Ar-H), 5.75 (br), 4.39 (br), 1.92 (s, 18H, $-\text{C}(\text{CH}_3)_3$), 1.33 (s, 18H, $-\text{C}(\text{CH}_3)_3$), 0.70 (br), -1.69 (br), -3.15 (br) ppm. ^{19}F NMR (376 MHz, CD_3CN) δ -73.8 (d, $^1J_{\text{F,P}} = 706.2$ Hz) ppm. $^{31}\text{P}\{^1\text{H}\}$ NMR (162 MHz, CD_3CN) δ -147.7 (h, $^1J_{\text{P,F}} = 706.2$ Hz) ppm. Peaks corresponding to ~1 equiv free THF (3.64 (m, 2H) and 1.80 (m, 2H) ppm) are observed in the ^1H NMR in CD_3CN of this material, indicating that MeCN fully displaces THF in this solvent. Anal. Calcd for $\text{C}_{46}\text{H}_{78}\text{N}_4\text{O}_3\text{SmPF}_6$: C 53.62; H 7.63; N 5.44. Found C 53.22; H 7.61; N 5.64.

A2.2 Synthesis of $[(\text{tBu}_2\text{ArO})_2\text{Me}_2\text{cyclam})\text{Sm}^{\text{III}}(\kappa^2\text{-pyrrolidinonate})$ ($\text{Sm}^{\text{III}}\text{-P}$)

All solvents used in synthesis, isolation, and characterization of $\text{Sm}^{\text{III}}\text{-P}$ were stirred over NaK for >12 hours and passed over activated alumina immediately before use. $[\text{Sm}^{\text{III}}]\text{PF}_6$ (50 mg, 0.052 mmol) was dissolved in THF (~1 mL) and transferred to a 20 mL scintillation vial containing KH (10.5 mg, 0.26 mmol) and equipped with a stir bar. A ~1 mL THF solution of 2-pyrrolidinone (4.4 mg, 0.052 mmol) was added at room temperature and stirred for 30 min, resulting in evolution of H_2 and a color change from pale yellow to colorless. Solvent was removed *in vacuo* and the resulting colorless residue was extracted

with pentane (~3 mL) and passed over filter paper. Removal of solvent yielded the title¹⁷⁶ compound as a white powder (33 mg, 71% yield). Alternatively, **Sm^{III}-P** could be prepared with a persistent 5% ligand impurity as follows: **Sm^{II}** (50 mg, 0.061 mmol) was dissolved in C₆H₆ (~1 mL) in a 20 mL scintillation vial equipped with a stir bar. A ~1 mL C₆H₆ solution containing 2-pyrrolidinone (5.3 mg, 0.062 mmol) and excess styrene (100 μL) was added, resulting in a color change from brown to dark green to colorless over ~30 seconds. Solvent was removed by lyophilization and the resulting colorless residue was extracted with pentane (~3 mL) and passed over filter paper. Slow evaporation of the filtrate in a sealed vessel containing HMDSO yielded colorless square crystals suitable for X-ray diffraction. The supernatant was decanted and the crystals were washed with pentane and ~1 mL C₆H₆ to yield the title compound with a 5% protonated ligand impurity (27 mg, 59% yield). ¹H NMR (400 MHz, C₆D₆) δ 9.5 (br, 1H), 8.28 (s, 2H, Ar-*H*) 7.83 (s, 1H, Ar-*H*), 7.44 (t, 1H), 7.31 (s, 1H, Ar-*H*), 6.63 (br, 3H), 4.35 (br d, *J* = 11.8 Hz), 3.25 – 3.01 (br m), 2.71 (br t, *J* = 12.3 Hz, 1H), 2.11 (s, 10H, -C(CH₃)₃ + 1H), 1.87 (s, 9H, -C(CH₃)₃), 1.66 (s, 10H, -C(CH₃)₃ + 1H), 1.43 (s, 3H), 1.27 (s, 9H, -C(CH₃)₃), 1.12 (br), 0.91 (br), 0.72 (br), 0.41 (br), 0.02 (br), -0.05 (br), -0.19 (br), -0.49 (br), -0.72 (br), -1.03 (br), -1.77 (br), -2.34 (br) ppm. ¹³C{¹H} NMR (126 MHz, C₆D₆) δ 189.1, 172.9, 162.6, 136.9, 136.7, 135.6, 134.9, 129.4, 126.7, 125.0, 124.4, 124.3, 74.4, 62.5, 61.8, 61.1, 59.0, 57.0, 55.7 (br), 53.6, 53.1 (br), 52.8 (br), 51.4, 47.3, 44.1, 37.0, 35.7, 35.1, 34.7, 32.7, 32.5, 31.0, 30.4, 29.8, 22.8, 21.8, 18.7 ppm (one aryl resonance masked by C₆D₆ residual). Anal. Calcd for C₄₆H₇₆N₅O₃Sm: C 61.56; H 8.54; N 7.80. Found C 61.69; H 8.72; N 7.48.

A2.3 Synthesis of $[(t\text{Bu}^2\text{ArO})_2\text{Me}_2\text{cyclam})\text{Sm}^{\text{III}}\text{-OMe}] (\text{Sm}^{\text{III}}\text{-OMe})$

All solvents used in synthesis, isolation, and characterization of $\text{Sm}^{\text{III}}\text{-OMe}$ were stirred over NaK for >12 hours and passed over activated alumina immediately before use. $[\text{Sm}^{\text{III}}]\text{PF}_6$ (50 mg, 0.052 mmol) was dissolved in THF (~1 mL) and transferred to a 20 mL scintillation vial containing KH (10.5 mg, 0.26 mmol) and equipped with a stir bar. 80 μL of a 620 mM solution of MeOH in THF (0.050 mmol) was added at room temperature and stirred for 30 min, resulting in evolution of H_2 and a color change from pale yellow to colorless. Solvent was removed *in vacuo* and the resulting colorless residue was extracted with pentane (~3 mL) and passed over filter paper. Removal of solvent yielded the title compound as a white powder (38 mg, 86% yield). Single crystals suitable for X-ray diffraction were obtained by slow evaporation of a pentane solution of the residue remaining after removing solvent from the ^1H NMR sample used to quantify products of the reaction of $\text{Sm}^{\text{II}}\text{-MeOH}$ with *trans*-stilbene (procedure B, Figure A13). ^1H NMR (400 MHz, C_6D_6) δ 10.48 (br), 9.75 (br), 9.12 (s, 1H, Ar-*H*), 9.00 (s, 1H, Ar-*H*), 7.75 (s, 2H, Ar-*H*), 6.52 (br), 5.92 (br), 4.58 (br), 2.95 (br), 2.05 (s, 9H, $-\text{C}(\text{CH}_3)_3$), 2.03 (s, 9H, $-\text{C}(\text{CH}_3)_3$), -0.16 (br), -0.70 (s with br shoulder, 18H, $-\text{C}(\text{CH}_3)_3$), -0.97 (br) ppm. ^1H NMR (400 MHz, CD_3CN) δ 8.63 (s, 1H, Ar-*H*), 8.58 (s, 1H, Ar-*H*), 7.22 (s, 1H, Ar-*H*), 7.16 (s, 1H, Ar-*H*), 6.07 (br), 2.94 (br), 1.72 (s, 9H, $-\text{C}(\text{CH}_3)_3$), 1.69 (s, 9H, $-\text{C}(\text{CH}_3)_3$), -0.66 (br, 9H, $-\text{C}(\text{CH}_3)_3$), -0.89 (s, 9H, $-\text{C}(\text{CH}_3)_3$) ppm. $^{13}\text{C}\{^1\text{H}\}$ NMR (126 MHz, C_6D_6) δ 129.1, 124.5, 62.3 (br), 35.1, 34.2, 32.92, 32.88, 28.9 (br), 18.1 (br) ppm. Anal. Calcd for $\text{C}_{43}\text{H}_{73}\text{N}_4\text{O}_3\text{Sm}$: C 61.16; H 8.71; N 6.63. Found C 61.38; H 8.84; N 6.90.

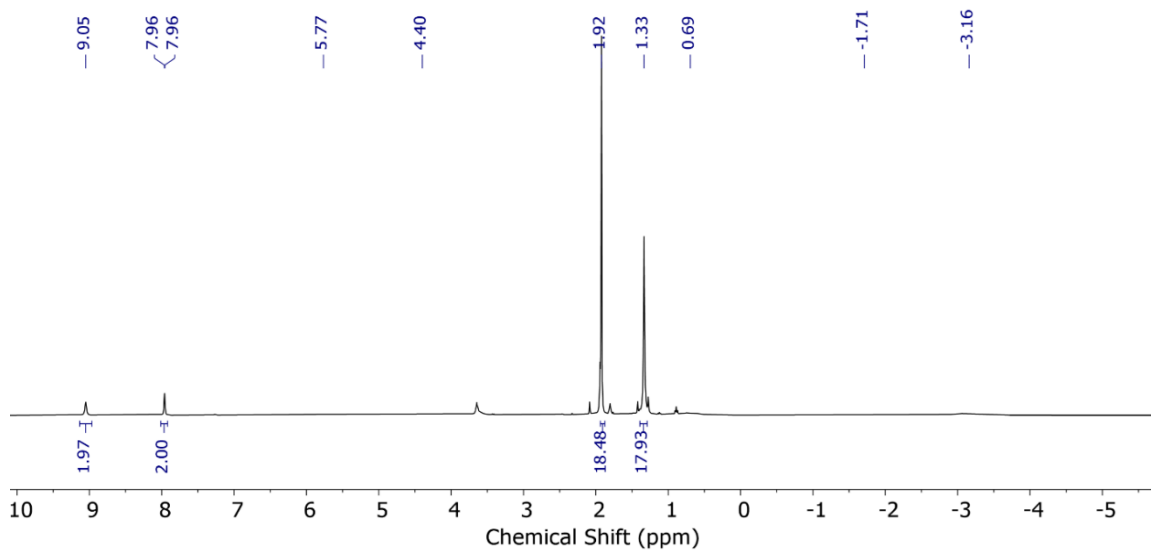
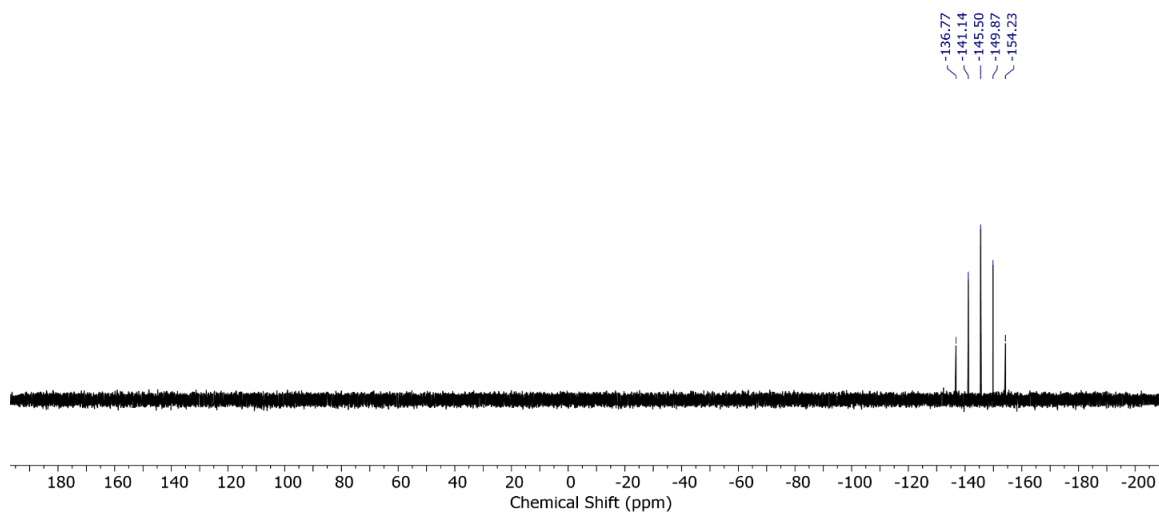
A2.4 General Procedure for the Synthesis of PF₆⁻ Salts of Protonated Bases

Adapted from the reported preparation of ⁱPr₂NH₂PF₆.⁵ The base (~3 mmol) was dissolved in DCM (~5 mL) in a vial equipped with a stirbar. 1 equiv of NH₄PF₆ was dissolved in ~1 mL DCM and added dropwise to the base. After stirring at room temperature for 1 hour, the reaction mixture was filtered over celite and solvent was removed under reduced pressure. The resulting white solids were brought into the glovebox, dissolved in THF, and passed over activated alumina. The solution was concentrated to ~1 mL and layered with Et₂O. Cooling to -35°C yielded white crystals that were subsequently dried under vacuum. Yields greater than 90% were obtained for all bases. ¹H NMR spectra of acids prepared by this route match literature values in reported solvents;^{6,7} shifts in CD₃CN are listed below.

Diisopropylammonium hexafluorophosphate: ¹H NMR (CD₃CN, 400 MHz): δ 6.26 (br, 1H), 3.46 (h, *J* = 6.5 Hz, 2H), 1.28 (d, *J* = 6.5 Hz, 6H) ppm.

Quinuclidinium ([quinH]⁺) hexafluorophosphate:⁶ ¹H NMR (CD₃CN, 400 MHz): δ 3.26-3.19 (m, 6H), 2.10 (h, *J* = 3.3 Hz, 1H), 1.91-1.85 (m, 6H) ppm.

[DBUH]⁺ hexafluorophosphate:⁷ ¹H NMR (CD₃CN, 400 MHz): δ 7.44 (br, 1H), 3.56-3.50 (m, 2H), 3.46 (t, *J* = 6.0 Hz, 2H), 3.27 (td, *J* = 6.0, 2.9 Hz, 2H), 2.63-2.53 (m, 2H), 1.97 (p, *J* = 6.0 Hz, overlapping solvent residual), 1.81-1.57 (m, 6H) ppm.

A3.1 Characterization of $[\text{Sm}^{\text{III}}]\text{PF}_6$, $\text{Sm}^{\text{III}}\text{-P}$, and $\text{Sm}^{\text{III}}\text{-OMe}$ Figure A1. ^1H NMR of $[\text{Sm}^{\text{III}}]\text{PF}_6$ in CD_3CN (400 MHz).Figure A2. ^{31}P NMR of $[\text{Sm}^{\text{III}}]\text{PF}_6$ in CD_3CN (162 MHz).

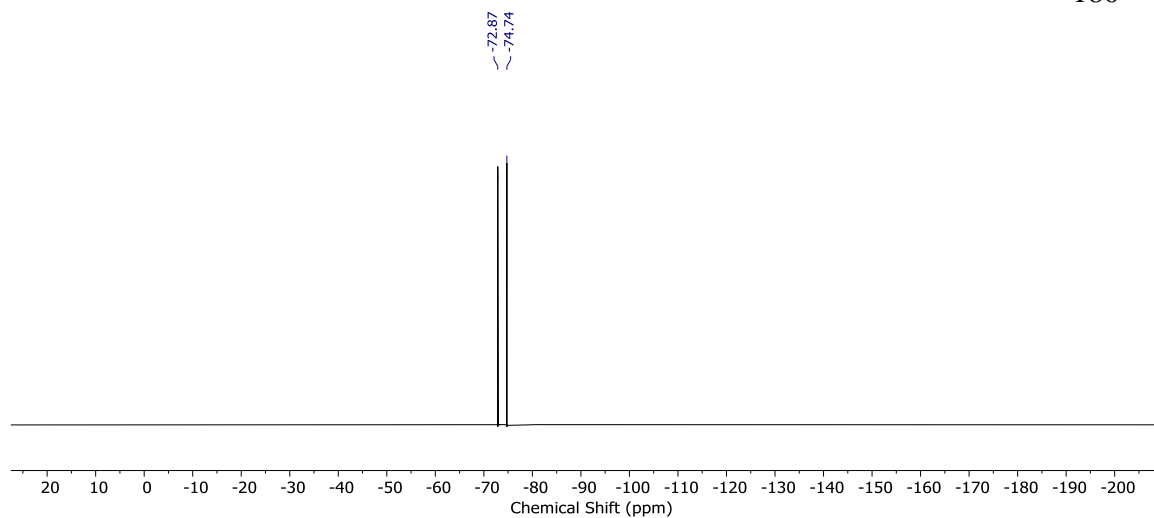


Figure A3. ^{19}F NMR of $[\text{Sm}^{\text{III}}]\text{PF}_6$ in CD_3CN (376 MHz).

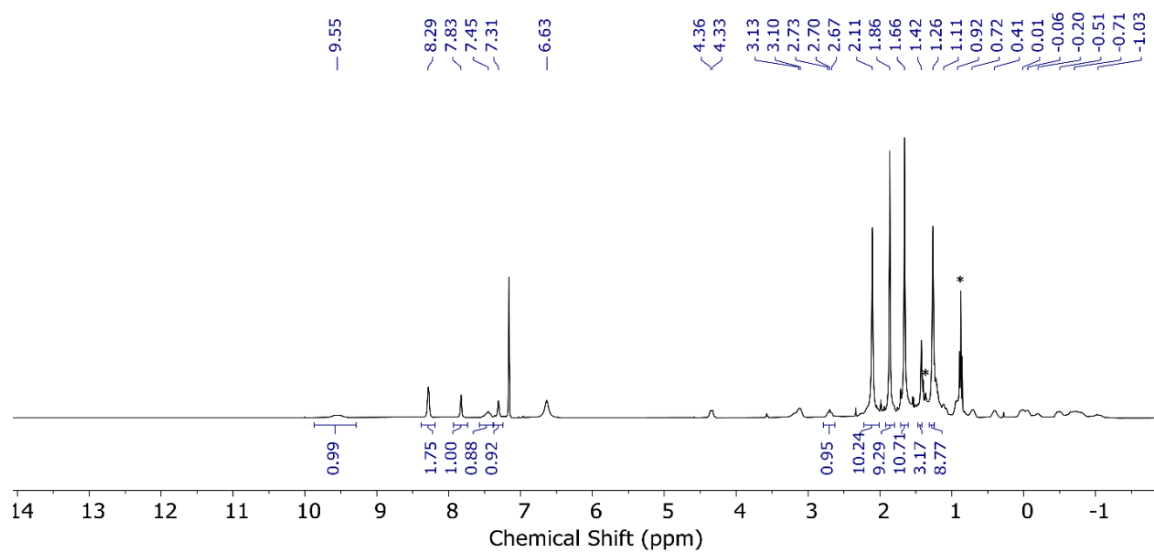


Figure A4. ^1H NMR of $\text{Sm}^{\text{III}}\text{-P}$ in C_6D_6 (400 MHz, * = pentane).

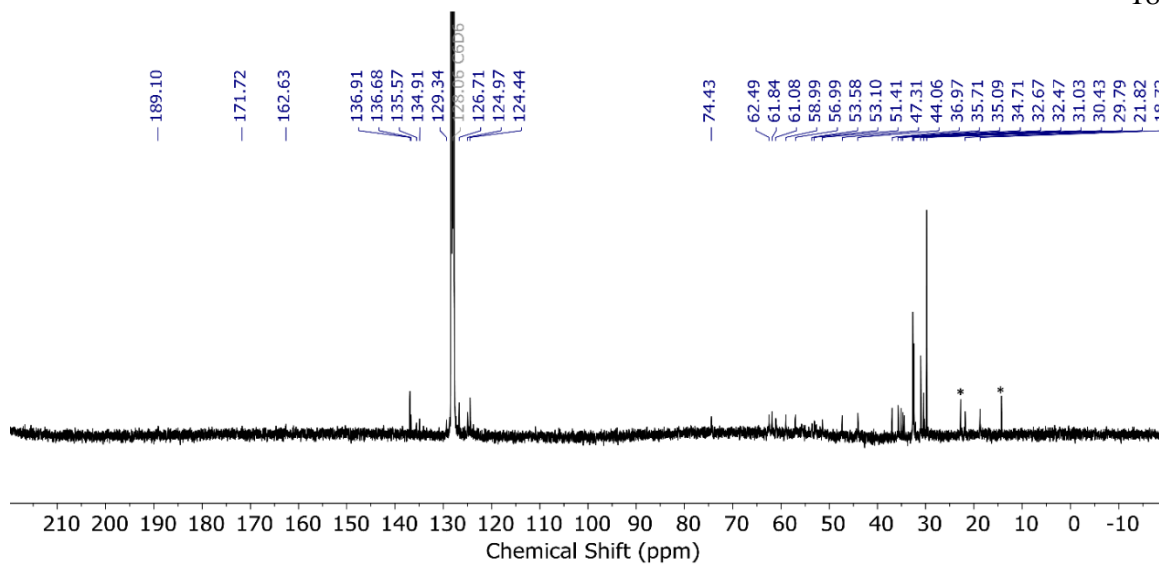


Figure A5. $^{13}\text{C}\{^1\text{H}\}$ NMR of $\text{Sm}^{\text{III}}\text{-P}$ in C_6D_6 (126 MHz, * = pentane).

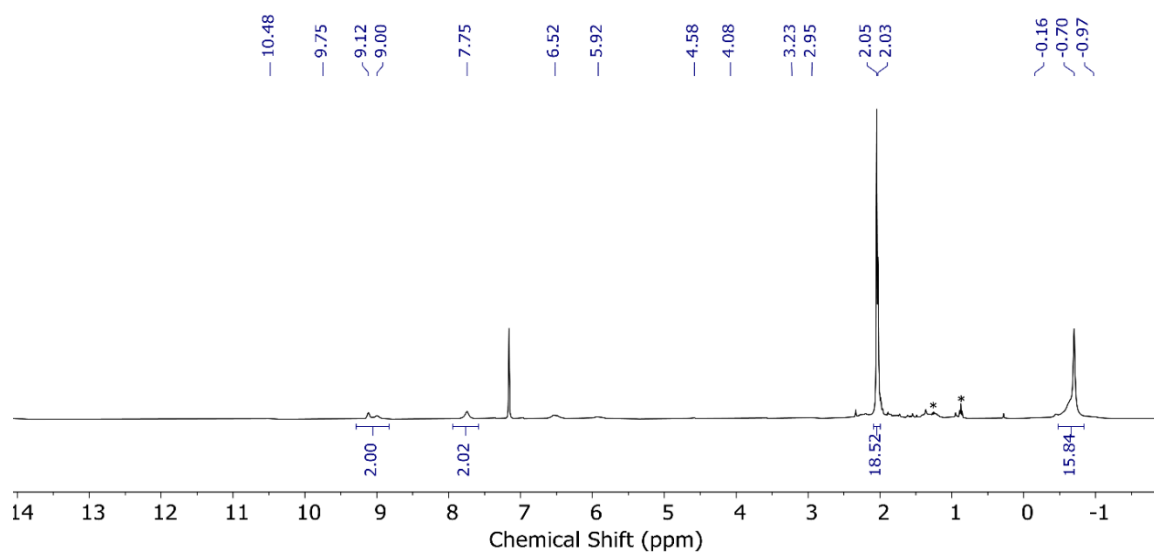


Figure A6. ^1H NMR of $\text{Sm}^{\text{III}}\text{-OMe}$ in C_6D_6 (400 MHz, * = pentane).

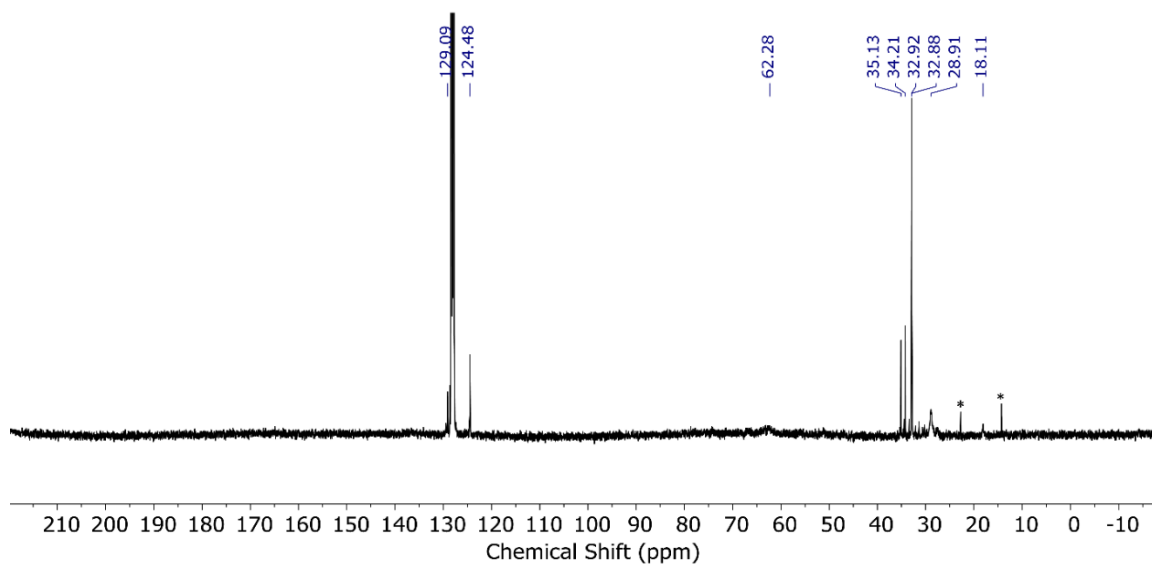


Figure A7. $^{13}\text{C}\{^1\text{H}\}$ NMR of $\text{Sm}^{\text{III}}\text{-OMe}$ in C_6D_6 (126 MHz, * = pentane).

A3.2 H₂ Evolution from Sm^{II}-PH and Sm^{II}-MeOH

A3.2.1 Procedure

In an N₂-filled glovebox, **Sm^{II}** (20 mg, 0.025 mmol) and bibenzyl (~3 mg) were dissolved in C₆D₆ and transferred to a J. Young NMR tube. The ¹H NMR was recorded to precisely determine the initial ratio of **Sm^{II}** to the internal standard. The tube was brought back into the glovebox and 1 equiv PH or MeOH were added (20 μL of a 612 mM stock solution) and the color of the solution changed from dark brown to dark green. The reaction was monitored by ¹H NMR at various time points.

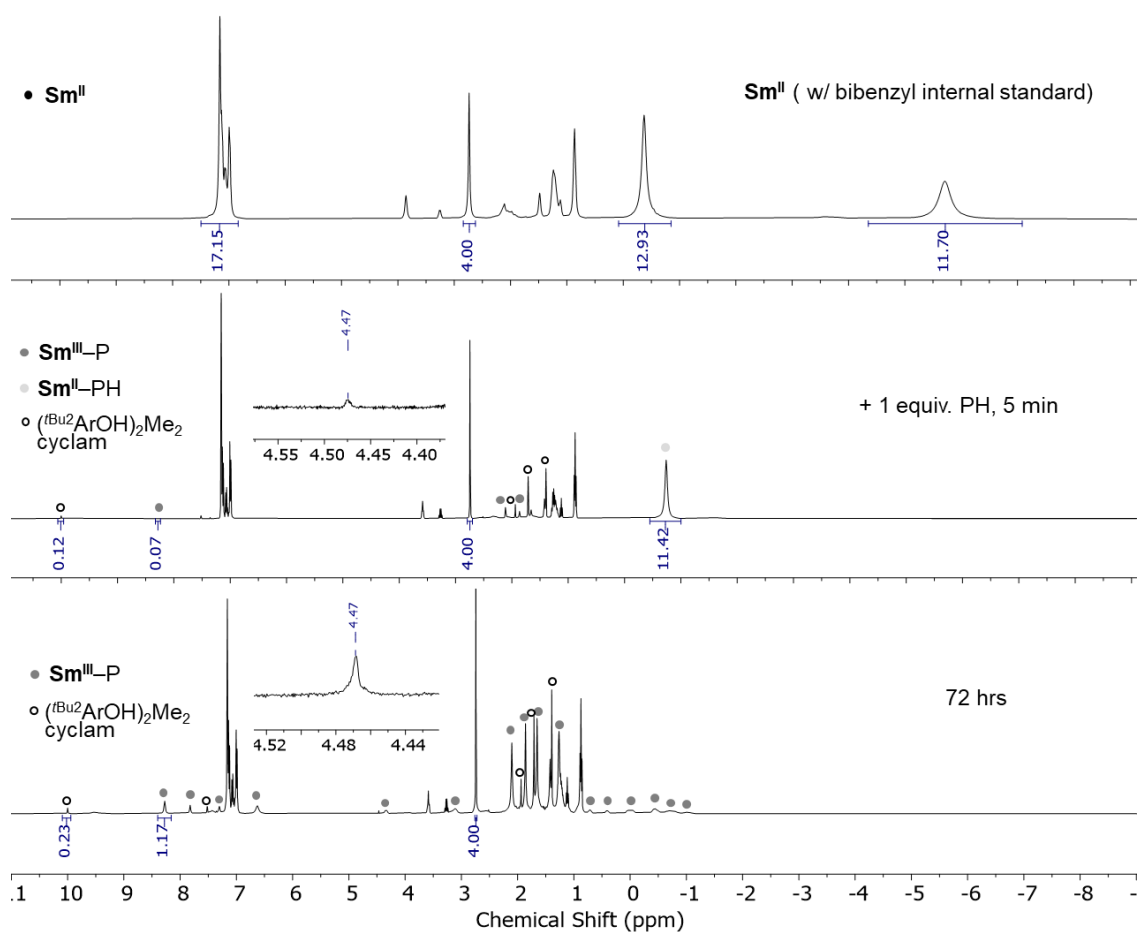


Figure A8. ^1H NMR in C_6D_6 (400 MHz, r.t.) following the reaction of Sm^{II} with 1 equiv. 2-pyrrolidinone (PH) in a J. Young NMR tube. The upper spectrum contains Sm^{II} integrated vs. bibenzyl as an internal standard. The middle spectrum is 5 min. after addition of PH, showing some conversion to $\text{Sm}^{\text{III}}\text{-P}$, free protonated ligand, and a species assigned as $\text{Sm}^{\text{II}}\text{-PH}$. The lower spectrum is 72 hours after addition, showing conversion to $\text{Sm}^{\text{III}}\text{-P}$ (8%) and free protonated ligand (16%). Insets show peak corresponding to H_2 .

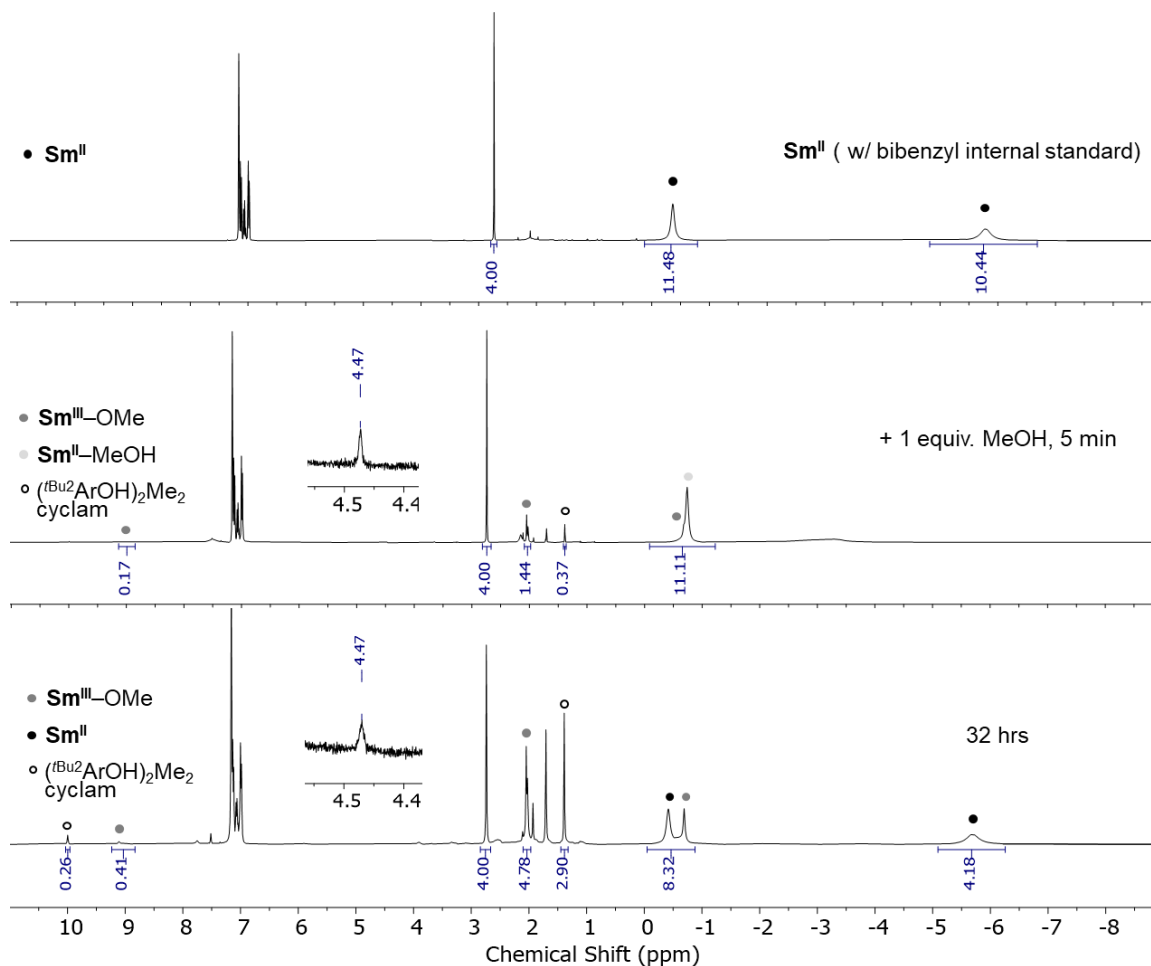


Figure A9. ^1H NMR in C_6D_6 (400 MHz, r.t.) following the reaction of Sm^{II} with 1 equiv. MeOH in a J. Young NMR tube. The upper spectrum contains Sm^{II} integrated vs. bibenzyl as an internal standard. The middle spectrum is 5 min. after addition of MeOH, showing some conversion to $\text{Sm}^{\text{III}}\text{-OMe}$, free protonated ligand, and a species assigned as $\text{Sm}^{\text{II}}\text{-MeOH}$. The lower spectrum is 32 hours after addition, showing recovery of 38% of Sm^{II} and conversion to $\text{Sm}^{\text{III}}\text{-OMe}$ (42%) and free protonated ligand (25%). Insets show peak corresponding to H_2 .

A3.3 Reactions of Sm^{II} -EH with Styrenyl Substrates

A3.3.1 Procedure A with Sm^{II} -PH

In an N_2 -filled glovebox, Sm^{II} (30 mg, 0.037 mmol) was dissolved in 1 mL THF in a scintillation vial equipped with a stirbar. PH (3.2 mg, 0.037 mmol) and substrate (0.019 mmol) were dissolved in 1 mL THF and added dropwise at room temperature to Sm^{II} with stirring. The reaction was stirred for 5 min, brought out of the box, and quenched with 1 M $\text{HCl}_{(\text{aq})}$ (10 mL). The mixture was extracted with Et_2O (3 x 5 mL). The organic layer was dried over Na_2SO_4 and solvent was removed *in vacuo*. The remaining residue was dissolved in 0.7 mL of CDCl_3 containing 10 mM 1,3,5-trimethoxybenzene. Conversion to the hydrogenated products was determined by integration of the ^1H NMR benzyl resonance relative to the Ar-H protons of the internal standard.

A3.3.2 Procedure B with Sm^{II} -MeOH

In an N_2 -filled glovebox, Sm^{II} (30 mg, 0.037 mmol) was dissolved in 1 mL THF in a scintillation vial equipped with a stirbar. MeOH (20 μL of a 1.85 M stock solution, 0.037 mmol) and substrate (0.019 mmol) were dissolved in 1 mL THF and added dropwise at room temperature to Sm^{II} with stirring. The reaction was stirred for 5 min and the solvent was removed *in vacuo*. A known mass of 1,3,5-trimethoxybenzene (~4 mg) was added to the remaining residue and the mixture was taken up in C_6D_6 . Conversion to hydrogenated products as well as Sm^{III} -OMe and free ligand was determined by integration relative to the Ar-H protons of the internal standard.

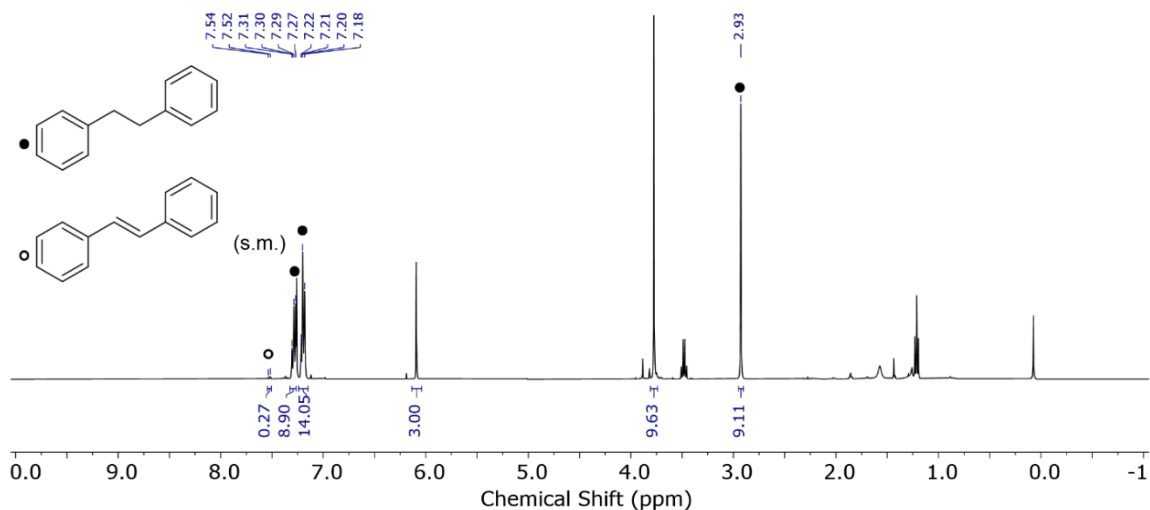


Figure A10. ^1H NMR in CDCl_3 (400 MHz, r.t.) showing organic products of the reaction of $\text{Sm}^{\text{II}}\text{-PH}$ with 0.5 equiv. *trans*-stilbene by procedure A. The yield of bibenzyl was determined as 92.6% based on integration to internal 1,3,5-trimethoxybenzene standard. 2.6% of the starting material was also recovered.

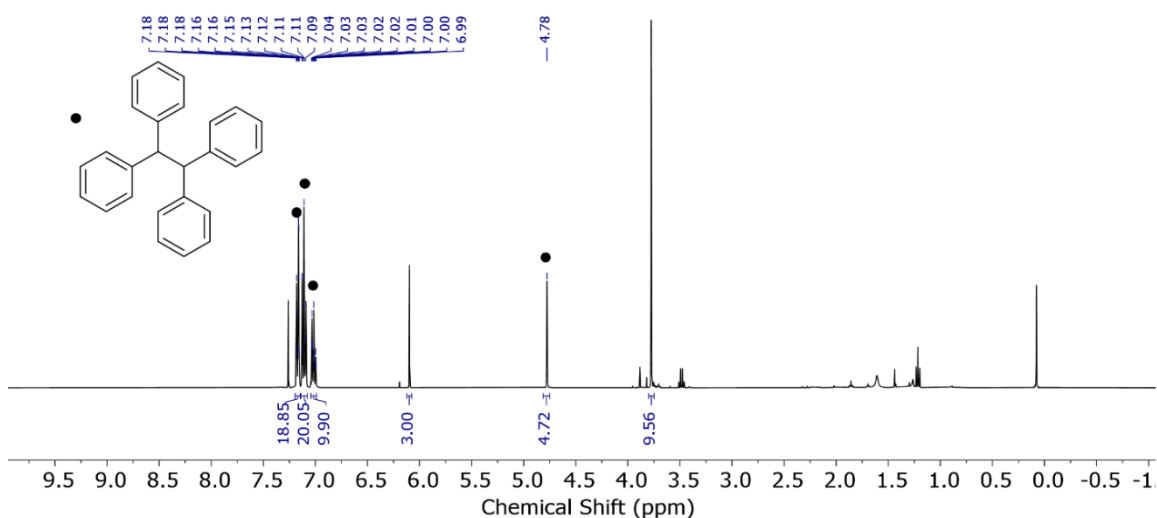


Figure A11. ^1H NMR in CDCl_3 (400 MHz, r.t.) showing organic products of the reaction of $\text{Sm}^{\text{II}}\text{-PH}$ with 0.5 equiv. tetraphenylethylene by procedure A. The yield of 1,1,2,2-tetraphenylethane was determined as 90.8% based on integration to internal 1,3,5-trimethoxybenzene standard.

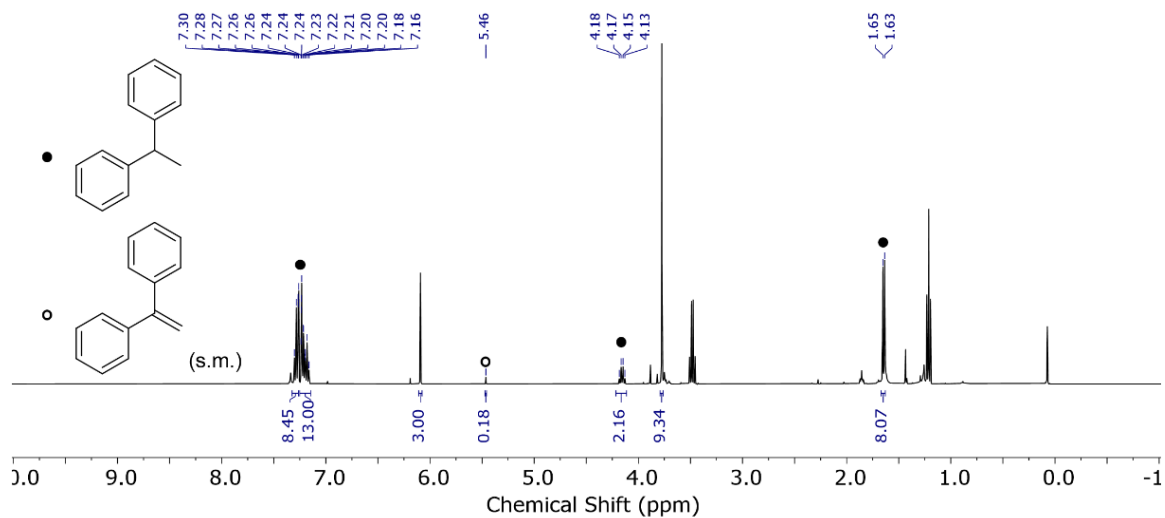


Figure A12. ^1H NMR in CDCl_3 (400 MHz, r.t.) showing organic products of the reaction of $\text{Sm}^{\text{II}}\text{-PH}$ with 0.5 equiv. 1,1-diphenylethylene by procedure A. The yield of 1,1-diphenylethane was determined as 83.1% based on integration to internal 1,3,5-trimethoxybenzene standard. 3.5% of the starting material was also recovered.

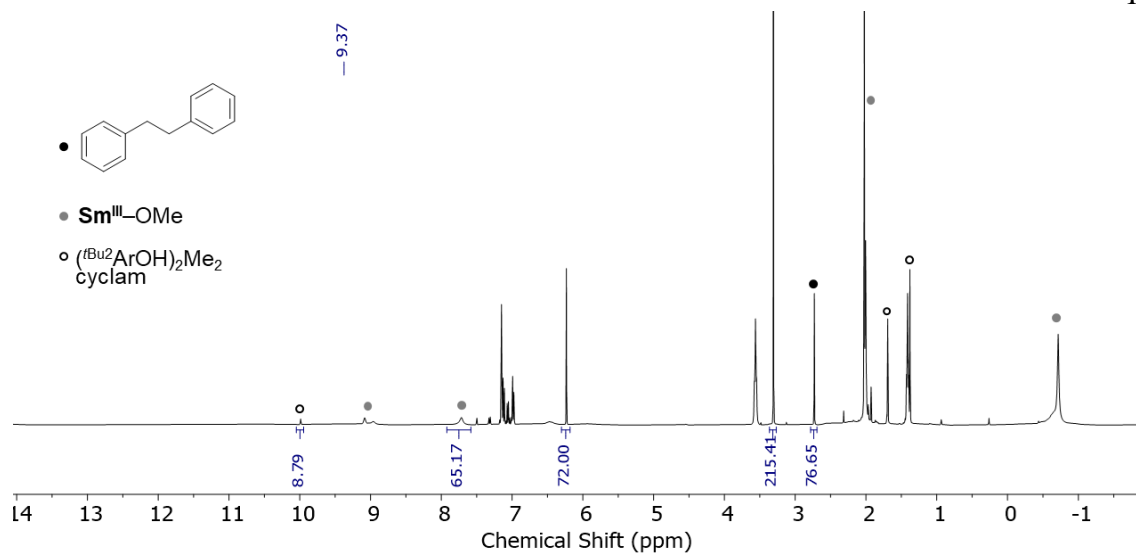


Figure A13. ^1H NMR in C_6D_6 (400 MHz, r.t.) showing products of the reaction of $\text{Sm}^{\text{II}}\text{-MeOH}$ with 0.5 equiv. *trans*-stilbene by procedure B. Percent conversion to bibenzyl (>99%), $\text{Sm}^{\text{III}}\text{-OMe}$ (88%), and free ligand (11%) were determined based on integration to internal 1,3,5-trimethoxybenzene standard.

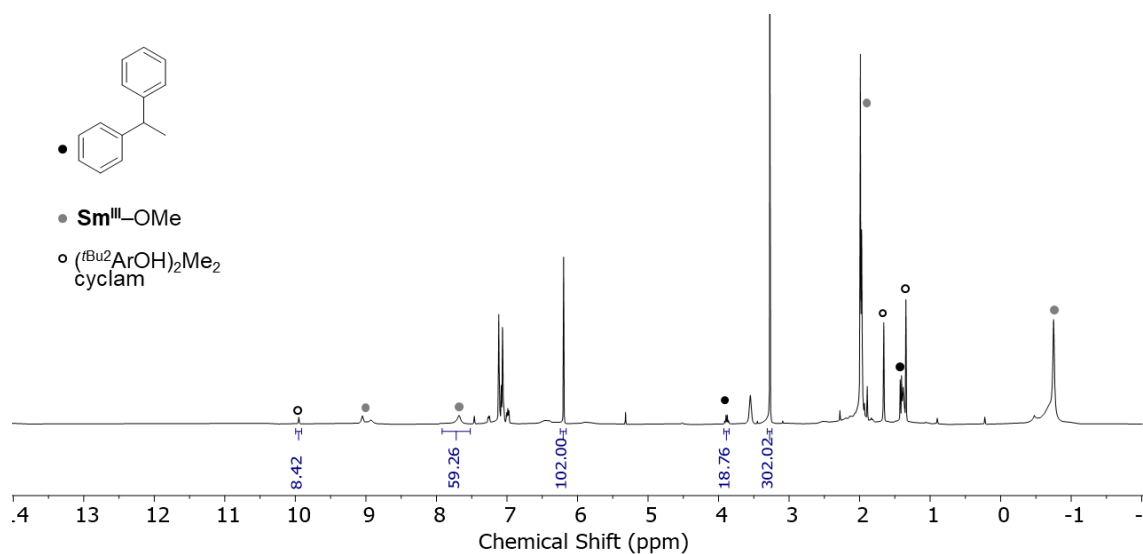


Figure A14. ^1H NMR in C_6D_6 (400 MHz, r.t.) showing products of the reaction of $\text{Sm}^{\text{II}}\text{-MeOH}$ with 0.5 equiv. 1,1-diphenylethylene by procedure B. Percent conversion to 1,1-diphenylethane (>99%), $\text{Sm}^{\text{III}}\text{-OMe}$ (80%), and free ligand (11%) were determined based on integration to internal 1,3,5-trimethoxybenzene standard.

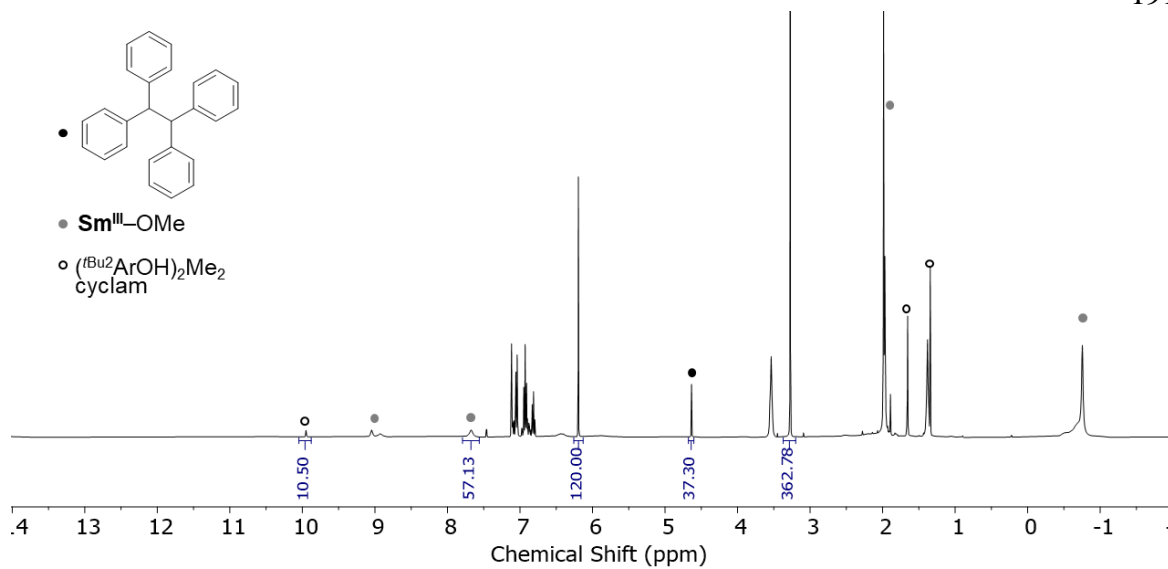


Figure A15. ^1H NMR in C_6D_6 (400 MHz, r.t.) showing products of the reaction of $\text{Sm}^{\text{II}}\text{-MeOH}$ with 0.5 equiv. 1,1,2,2-tetraphenylethylene by procedure B. Percent conversion to 1,1,2,2-tetraphenylethane (>99%), $\text{Sm}^{\text{III}}\text{-OMe}$ (77%), and free ligand (14%) were determined based on integration to internal 1,3,5-trimethoxybenzene standard.

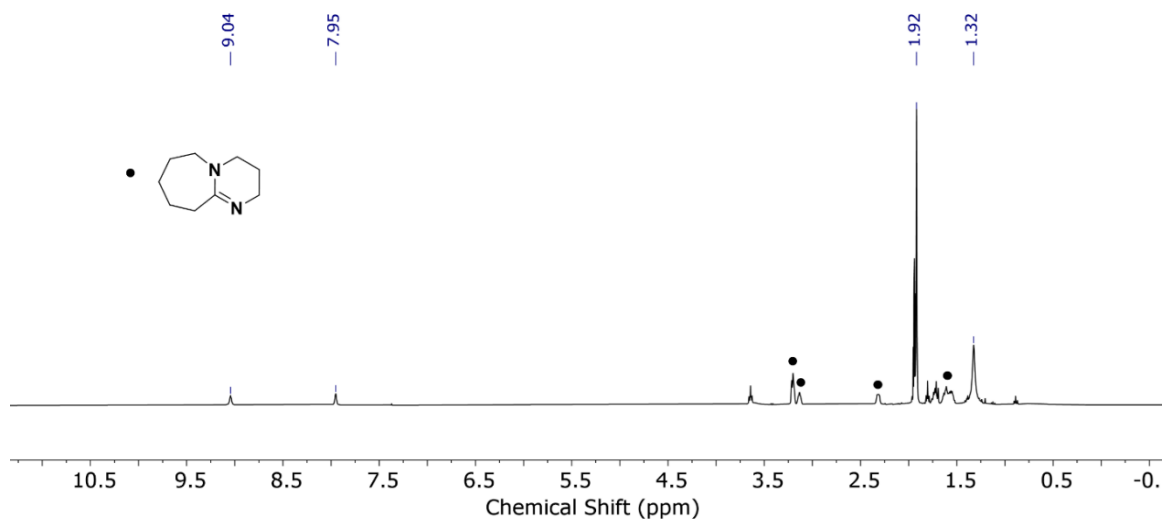
A3.4 NMR Spectra of $[\text{Sm}^{\text{III}}]\text{PF}_6$ with PMe and Bases

Figure A16. ^1H NMR in CD_3CN (400 MHz, r.t.) of $[\text{Sm}^{\text{III}}]\text{PF}_6$ in the presence of 1 equiv. DBU. Peaks corresponding to $[\text{Sm}^{\text{III}}]\text{PF}_6$ are picked and are unshifted from those of pure $[\text{Sm}^{\text{III}}]\text{PF}_6$.

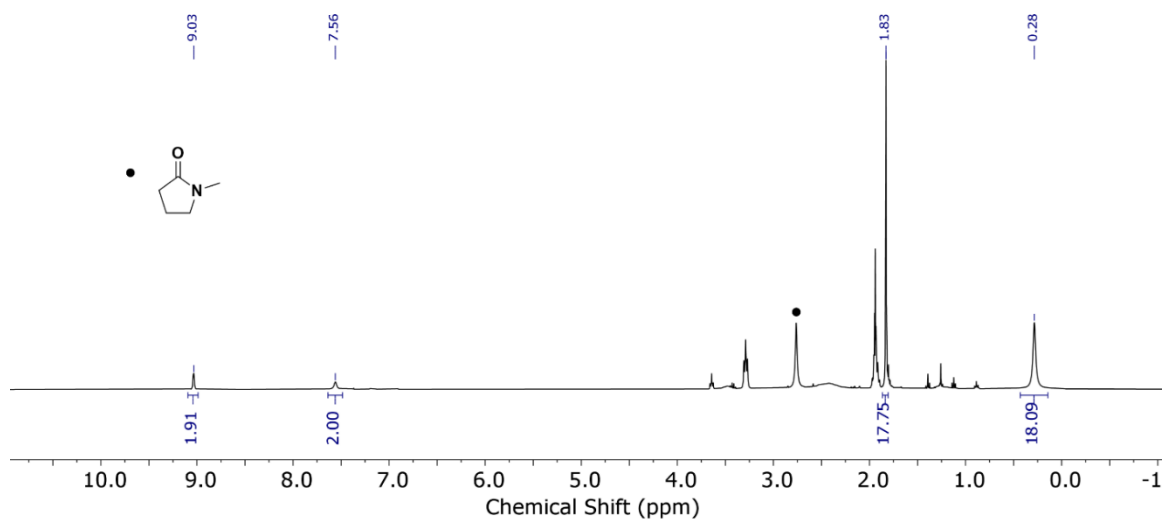


Figure A17. ^1H NMR in CD_3CN (400 MHz, r.t.) of $[\text{Sm}^{\text{III}}]\text{PF}_6$ in the presence of 3 equiv. *N*-methylpyrrolidinone (PMe). Peaks assigned to a $[\text{Sm}^{\text{III}}\text{-PMe}]\text{PF}_6$ adduct are picked and integrated.

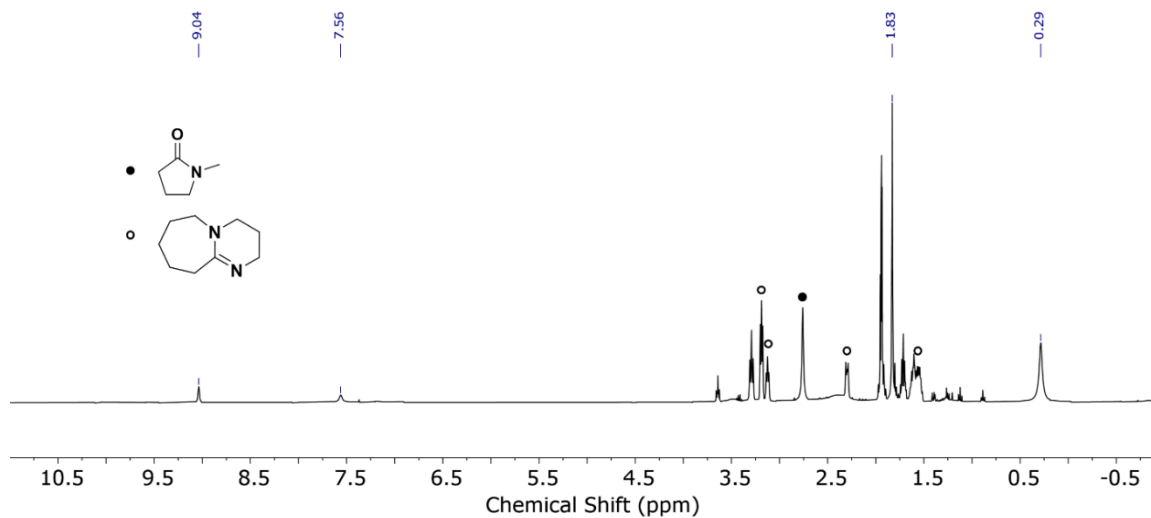


Figure A18. ¹H NMR in CD₃CN (400 MHz, r.t.) of [Sm^{III}]PF₆ in the presence of 3 equiv. *N*-methylpyrrolidinone (PMe) and 2 equiv. DBU. Peaks assigned to a [Sm^{III}-PMe]PF₆ adduct are unshifted from those in Figure A17.

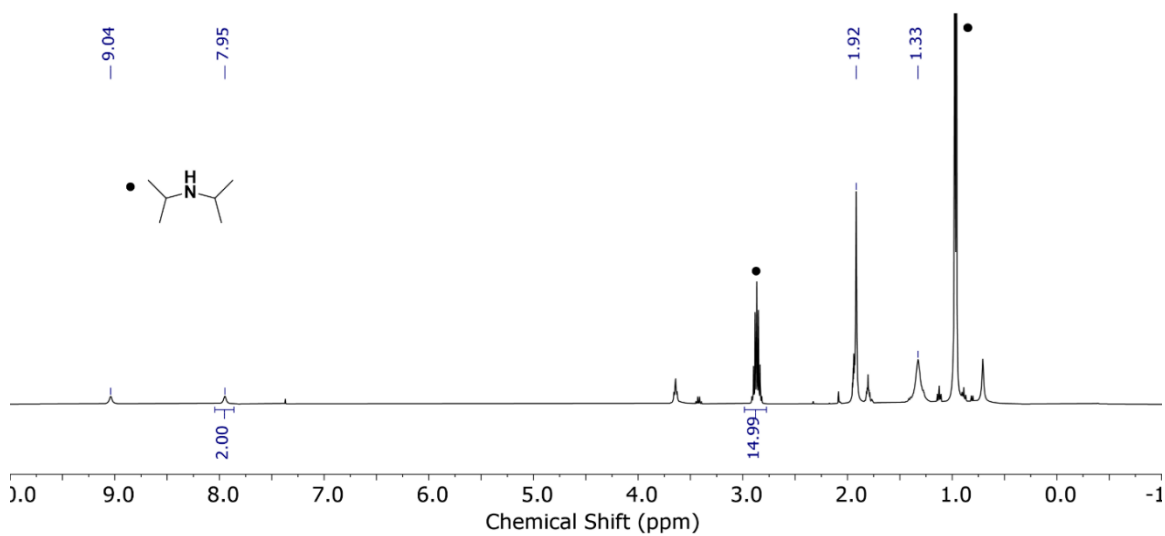


Figure A19. ¹H NMR in CD₃CN (400 MHz, r.t.) of [Sm^{III}]PF₆ in the presence of 7.5 equiv. *i*-Pr₂NH. Peaks corresponding to [Sm^{III}]PF₆ are picked and are unshifted from those of pure [Sm^{III}]PF₆.

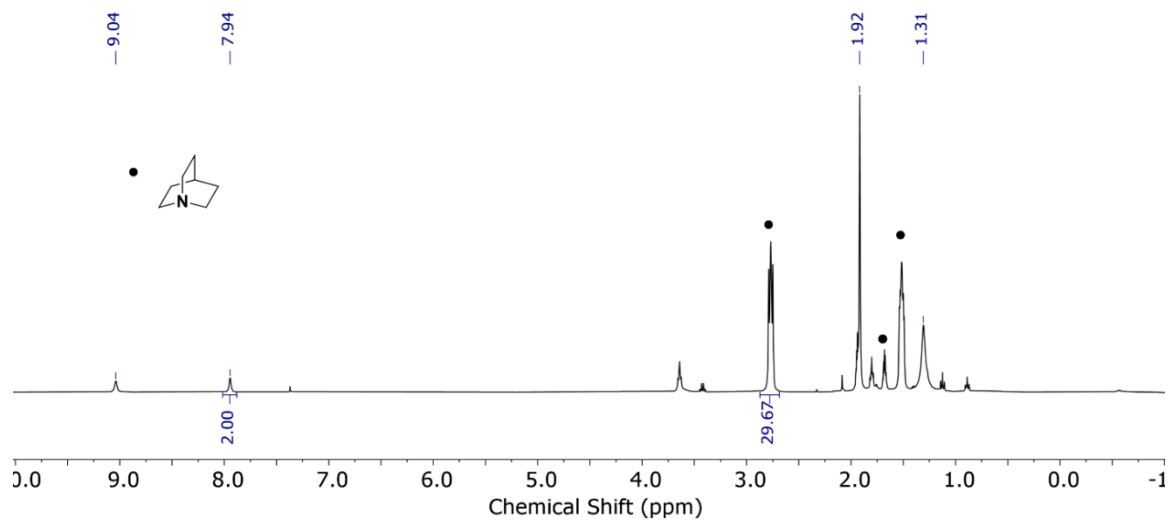


Figure A20. ^1H NMR in CD_3CN (400 MHz, r.t.) of $[\text{Sm}^{\text{III}}]\text{PF}_6$ in the presence of 5 equiv. quinuclidine (quin). Peaks corresponding to $[\text{Sm}^{\text{III}}]\text{PF}_6$ are picked and are unshifted from those of pure $[\text{Sm}^{\text{III}}]\text{PF}_6$.

A3.5 DOSY

Table A1: DOSY measured diffusion coefficients, D , and estimated hydrodynamic radii, r_H , of the **Sm** complexes. The similarity of $r_{H(\text{exp})}$ determined for all compounds, as well as the similarity of the measured values to theoretical values estimated from structural data, suggests that all species are monomeric in benzene solution.

Species	D_{Fc^*} ($10^{-6} \text{ cm}^2 \text{ s}^{-1}$)	D ($10^{-6} \text{ cm}^2 \text{ s}^{-1}$)	$r_{H(\text{exp})}^a$ (Å)	$r_{H(\text{theo})}^b$ (Å)
Fc*				4.08 ⁸
Sm^{II} -PH	14.7	8.75	6.85	-
Sm^{II} -MeOH	15.4	8.56	7.34	-
Sm^{III} -P	15.4	8.26	7.61	7.40
Sm^{III} -OMe	15.1	8.17	7.54	7.10

^aEstimated by taking the ratio of the measured diffusion coefficient to that of Fc*: ($r_{H(\text{theo}, \text{Fc}^*)}(D_{\text{Fc}^*}/D) = r_{H(\text{exp})}$). ^bAverage of the half lengths of the principle axes of a homogeneous ellipsoid used to approximate the complex, estimated from the crystal structure.

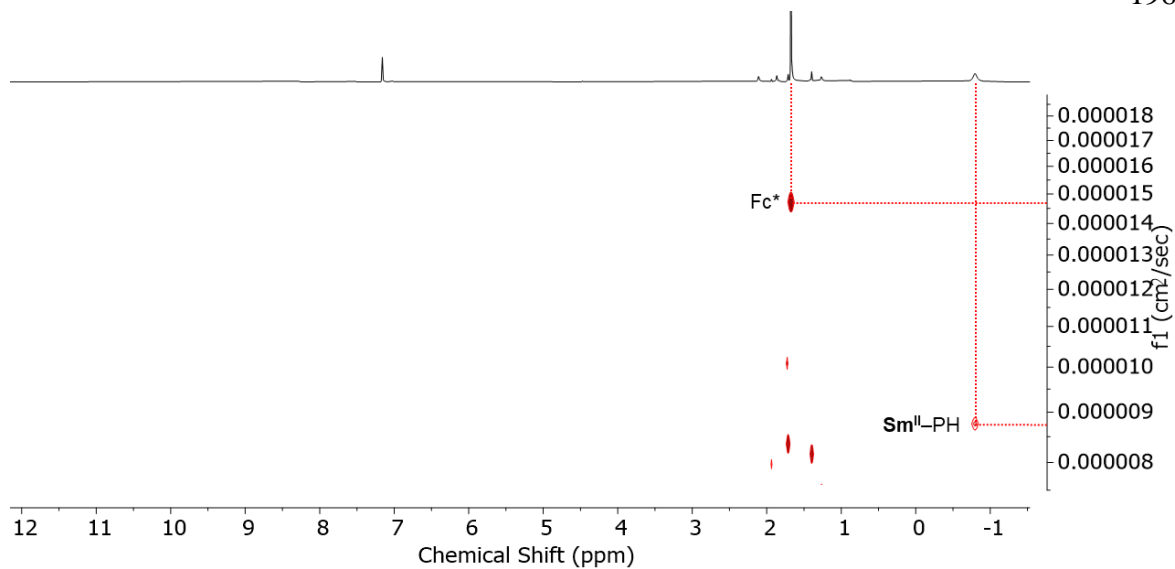


Figure A21. ¹H DOSY in C₆D₆ (400 MHz, r.t., $\delta = 4.0$ ms, $\Delta = 150$ ms) of **Sm^{II}-PH** (20 mM) and decamethylferrocene (**Fc***, 20 mM) recorded 15 min after PH addition (some **Sm^{III}-P** and free ligand are evolved in this time).

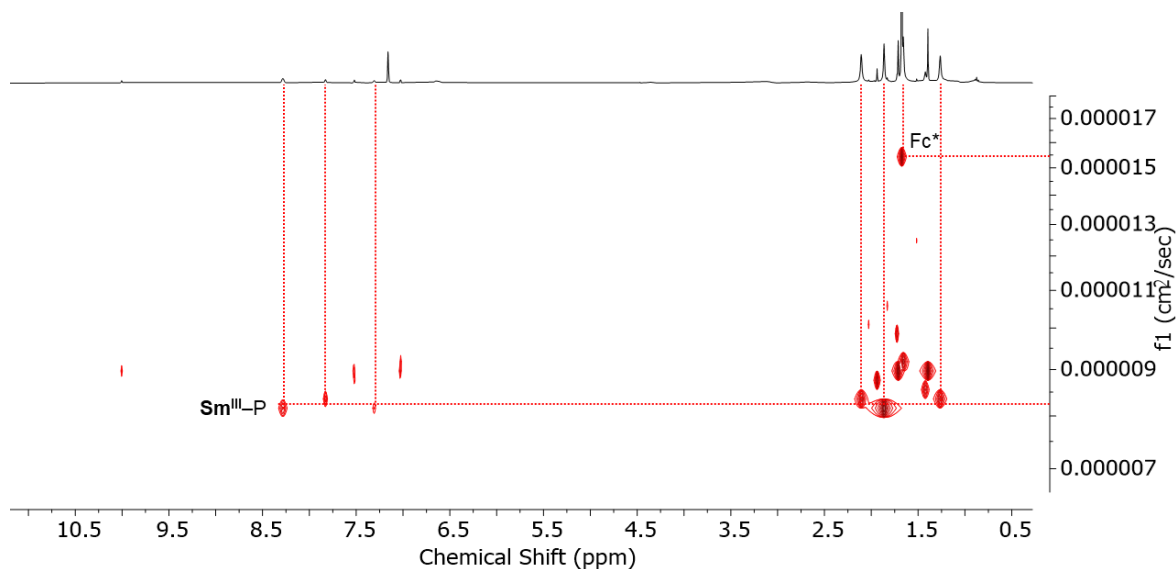


Figure A22. ¹H DOSY in C₆D₆ (400 MHz, r.t., $\delta = 4.0$ ms, $\Delta = 150$ ms) of **Sm^{III}-P** (generated from **Sm^{II}-PH** by H₂ evolution procedure in A3.2.1, 20 mM) and decamethylferrocene (**Fc***, 20 mM).

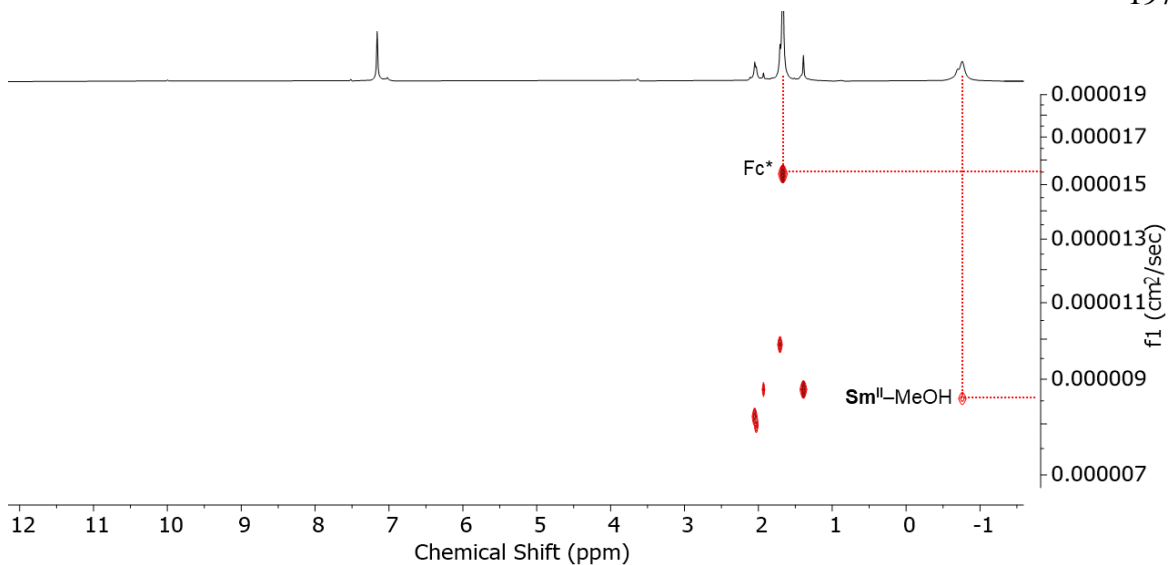


Figure A23. ^1H DOSY in C_6D_6 (400 MHz, r.t., $\delta = 4.0$ ms, $\Delta = 150$ ms) of $\text{Sm}^{\text{II}}\text{-MeOH}$ (20 mM) and decamethylferrocene (Fc^* , 20 mM) recorded 15 min after MeOH addition (some $\text{Sm}^{\text{III}}\text{-OMe}$ and free ligand are evolved in this time).

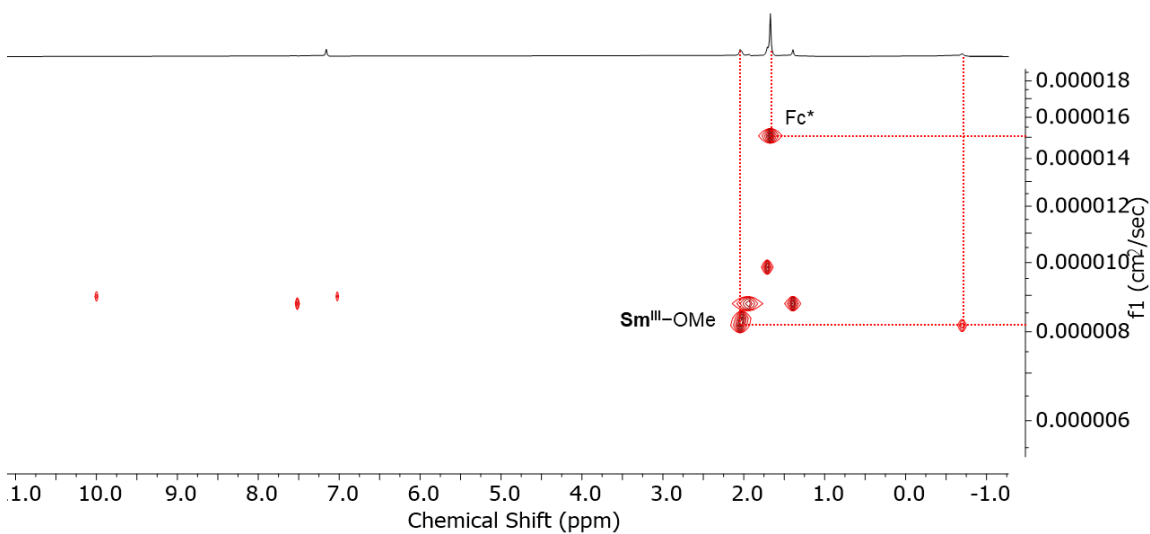


Figure A24. ^1H DOSY in C_6D_6 (400 MHz, r.t., $\delta = 4.0$ ms, $\Delta = 150$ ms) of $\text{Sm}^{\text{III}}\text{-OMe}$ (generated from $\text{Sm}^{\text{II}}\text{-MeOH}$ by H_2 evolution procedure in A3.2.1, 20 mM) and decamethylferrocene (Fc^* , 20 mM).

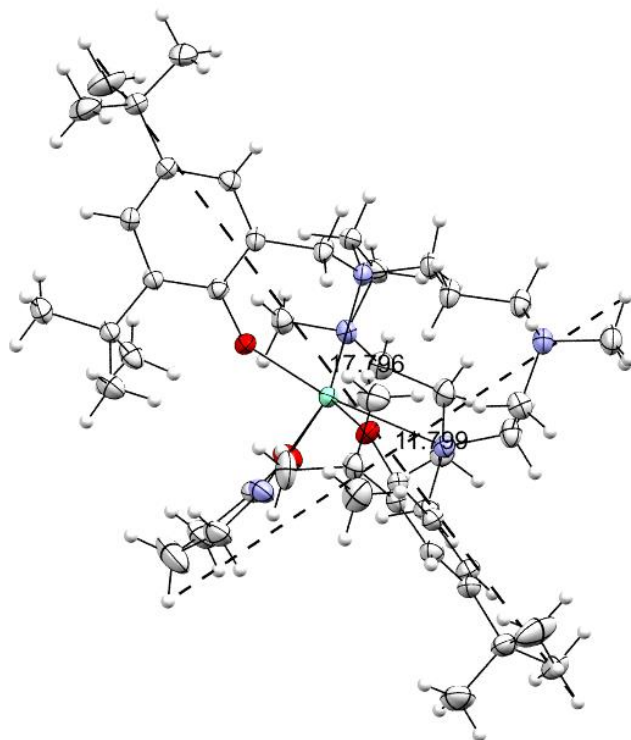


Figure A25. Points used to estimate $r_{H(\text{theo})}$ for **Sm^{III}-P**.

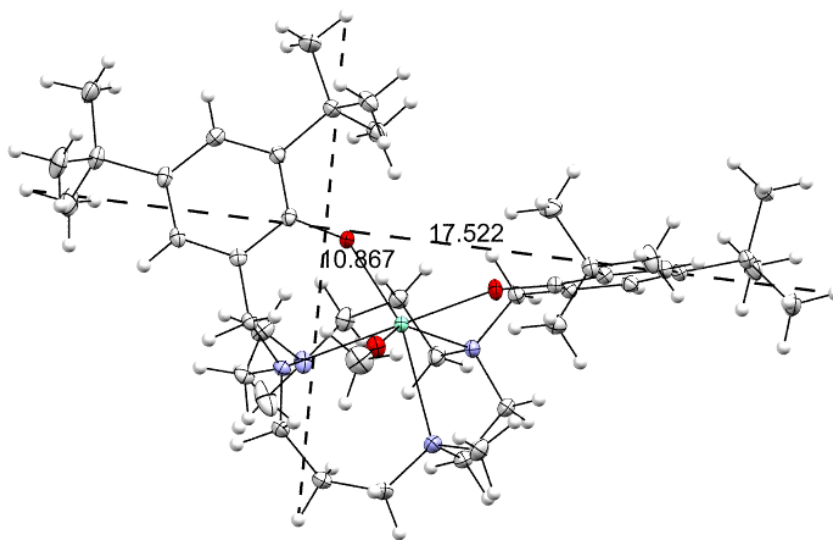


Figure A26. Points used to estimate $r_{H(\text{theo})}$ for **Sm^{III}-OMe**.

A4 X-Ray Crystallography

Cambridge Crystallographic Data Centre 2195229-2195230 contains the supplementary crystallographic data for this paper:

http://www.ccdc.cam.ac.uk/data_request/cif

Table A2. Crystallographic data for complexes **Sm^{III}-P** and **Sm^{III}-OMe**.

Compound	Sm^{III}-P	Sm^{III}-OMe
Empirical formula	C ₄₉ H ₇₉ N ₅ O ₃ Sm	C ₄₃ H ₇₃ N ₄ O ₃ Sm
Formula weight	936.52	844.40
Temperature (K)	200.0	100.0
Crystal system	monoclinic	triclinic
Space group	P2 ₁ /c	P-1
a (Å)	10.7625(3)	8.9047(9)
b (Å)	23.5936(6)	14.4085(14)
c (Å)	19.1334(5)	17.4572(17)
α (°)	90	83.097(3)
β (°)	90.3450(10)	85.076(3)
γ (°)	90	79.771(3)
Volume (Å ³)	4858.4(2)	2183.5(4)
Z	4	2
ρ _{calc} (g cm ⁻³)	1.280	1.284
μ (mm ⁻¹)	1.252	1.385
F ₀₀₀	1976.0	890.0
Crystal size (mm ³)	0.15 × 0.15 × 0.1	0.2 × 0.2 × 0.2
Wavelength (Å)	0.71073	0.71073
Reflections Collected	65582	57805
Independent Reflections	11152	10022
Data/Restraints/Parameters	11152/0/537	10022/0/475
GOOF	1.073	1.104
R(F) (I > 2σ(I))	R ₁ = 0.0215, wR ₂ = 0.0498	R ₁ = 0.0158, wR ₂ = 0.0401
wR(F ²) (all)	R ₁ = 0.0252, wR ₂ = 0.0511	R ₁ = 0.0164, wR ₂ = 0.0403

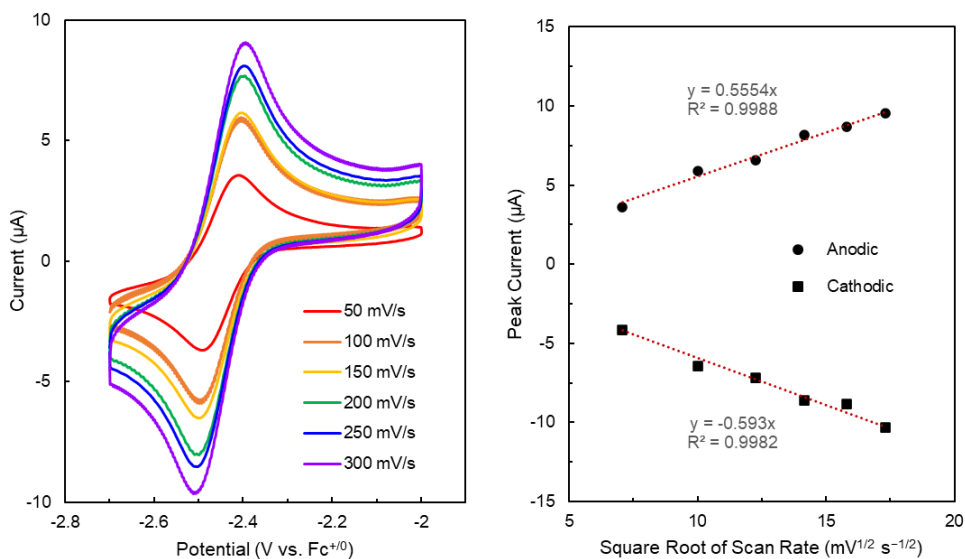


Figure A27. Left: CVs of 1 mM Sm^{II} in DME (0.2 M nBu₄NPF₆) on glassy carbon with variable scan rate. The scans began at -2.7 V vs. Fc⁺⁰ and swept positive. Right: Plot of peak current versus the square root of the scan rate for the anodic and cathodic waves. The points are fit with a straight line forced through the origin.

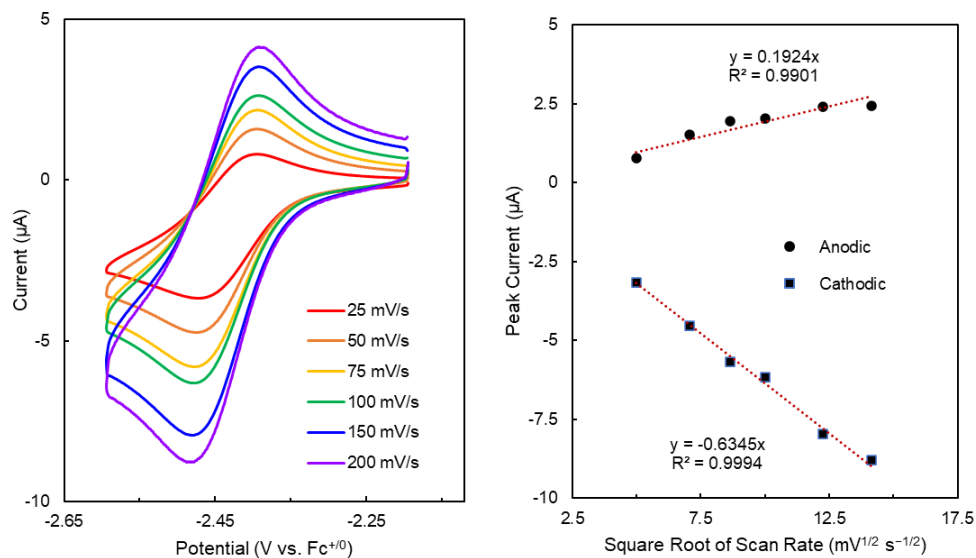


Figure A28. Left: CVs of 1 mM [Sm^{III}]PF₆ in DME (0.2 M ⁿBu₄NPF₆) on glassy carbon with variable scan rate. The scans began at -2.2 V vs. Fc⁺⁰ and swept negative. Right: Plot of peak current versus the square root of the scan rate for the anodic and cathodic waves. The points are fit with a straight line forced through the origin.

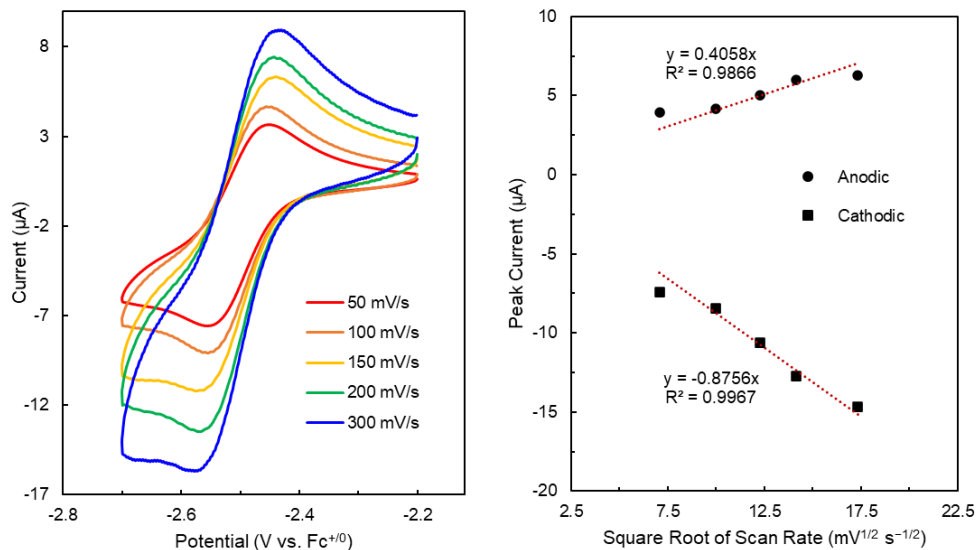


Figure A29. Left: CVs of 1 mM [Sm^{III}]PF₆ in CH₃CN (0.1 M nBu₄NPF₆) on glassy carbon with variable scan rate. The scans began at -2.2 V vs. Fc⁺⁰ and swept negative. Right: Plot of peak current versus the square root of the scan rate for the anodic and cathodic waves. The points are fit with a straight line forced through the origin.

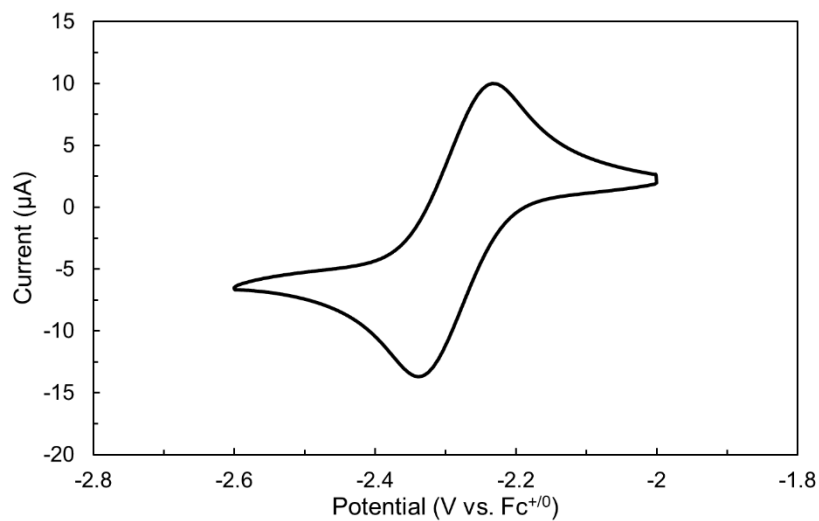


Figure A30. CV in DME (0.2 M nBu₄NPF₆) on glassy carbon of 1 mM benzophenone at 100 mV s⁻¹. The scans began at ca. -2 V vs. Fc⁺⁰ and swept negative.

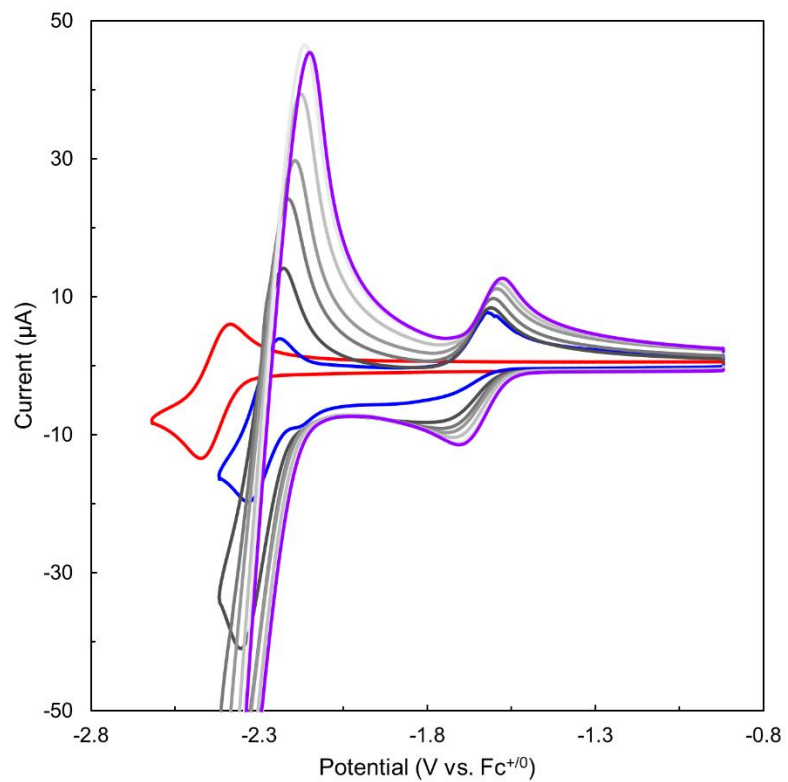
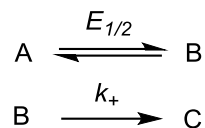


Figure A31. CVs in DME (0.2 M $t\text{Bu}_4\text{NPF}_6$) on glassy carbon of 1 mM $[\text{Sm}^{\text{III}}]\text{PF}_6$ (red trace) with 1-10 mM benzophenone (blue-purple traces) at 100 mV s^{-1} . The scans began at ca. $-0.9 \text{ V vs. Fc}^{+/0}$ and swept negative.

A5.1 Determination of k_{PCET}

For a simple EC mechanism such as electrochemical reduction of $[\text{Sm}^{\text{III}}\text{-PH}]\text{PF}_6$ to $\text{Sm}^{\text{II}}\text{-PH}$ followed by reaction with DPE, the peak potential shifts according to the following equation:⁹



$$E_p = E_{1/2} - \frac{RT}{F}(0.78) + \frac{RT}{2F} \ln \left(\frac{k_+ RT}{Fv} \right) \quad (\text{A1})$$

k_+ can therefore be estimated from the evolution of the cathodic peak potential as a function of scan rate (Figure A33, left). The cathodic peak potentials were corrected for solution resistance by the following procedure: the CV of ferrocene was recorded in the electrolyte of interest (0.2 M $n\text{Bu}_4\text{NPF}_6$ in DME) at 25, 50, 75, 100, 150, and 200 mV s^{-1} . The peak-to-peak separation (ΔE_p) and anodic and cathodic peak currents ($i_{p,a}$ and $i_{p,c}$) of the $\text{Fe}^{\text{III/II}}$ couple were measured for each CV. The following equation was used to estimate the solution resistance for each CV, using the assumption that ferrocene should show a peak-to-peak separation of 59 mV in the absence of solution resistance R_u :

$$R_u = \frac{(\Delta E_p - 0.059 \text{ V})}{|i_{p,a}| - |i_{p,c}|} \quad (\text{A2})$$

The average R_u across the sampled scan rates was 1800 Ω . This value was not found to vary significantly with added organic substrates. All measured peak potentials with associated current values were therefore corrected by ΔE given by:

$$\Delta E = i(1800\Omega) \quad (\text{A3})$$

Using a pseudo-first order excess of DPE, the plot of k_+ vs. $[\text{DPE}]$ (Figure A33, right) is linear, indicating that the reaction is first order in substrate. The slope of this plot is therefore k_{PCET} :

$$\text{rate} = k_+[Sm] \quad (\text{A4})$$

$$k_+ = k_{PCET}[DPE] \quad (\text{A5})$$

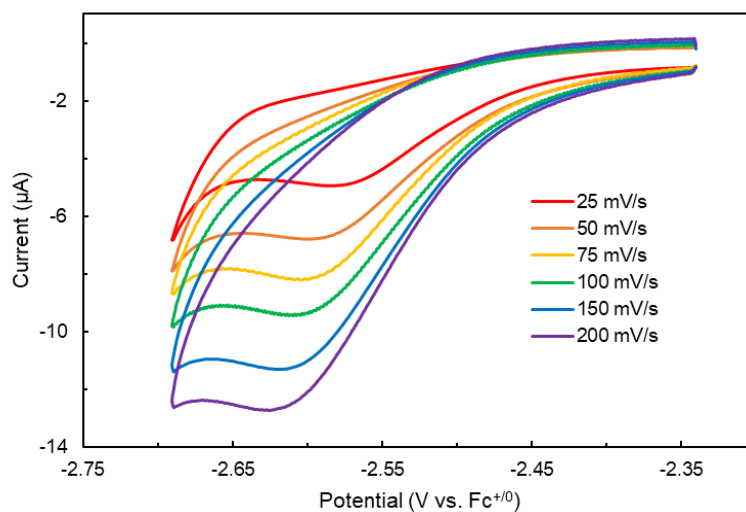


Figure A32. CVs in DME (0.2 M $n\text{Bu}_4\text{NPF}_6$) on glassy carbon of 1 mM $[\text{Sm}^{\text{III}}]\text{PF}_6$ with 30 equiv. PH and 80 equiv. DPE at varying scan rate. The scans began at ca. -2.35 V vs. $\text{Fc}^{+/0}$ and swept negative.

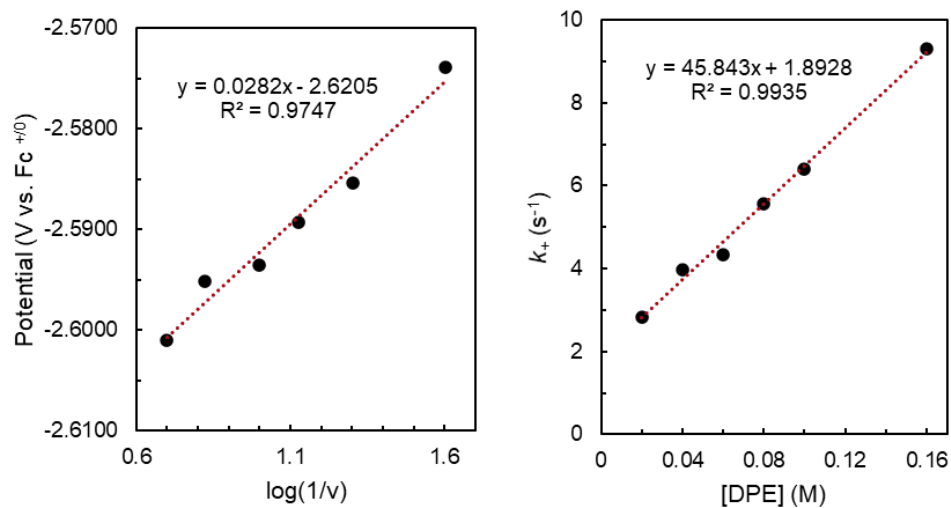


Figure A33. Left: linear plot of peak cathodic potential vs. the logarithm of the scan rate for the data in Figure A32. Right: Plot of k_+ determined from the intercepts of plots of the type on the left using eqn A1 vs. the concentration of DPE. The slope of the linear fit of this data is k_{PCET} .

A6 Equilibrium Measurements

A6.1.1 Procedure for K_{assoc} Determination

The association constant K_{assoc} for the binding of PH to $[\text{Sm}^{\text{III}}]\text{PF}_6$ was determined in CD_3CN using ^1H NMR spectroscopy at room temperature on a 400 MHz spectrometer (Tables A3-4 and Figures A43-45). CD_3CN was passed 5 times over activated alumina before use. $[\text{Sm}^{\text{III}}]\text{PF}_6$ was dissolved in CD_3CN (0.7 mL) and added to a J. Young NMR tube along with 16 mM 1,3,5-trimethoxybenzene as an internal standard. An initial NMR was taken to verify purity and then aliquots of PH were added to the tube from a stock solution (250 mM) which also contained 16 mM 1,3,5-trimethoxybenzene. The total concentration of Sm complexes was determined for each addition by integration of the aryl resonance relative to the Ar-H protons of the internal standard. The relative concentrations of the bound/unbound species were determined from the observed chemical shifts relative to the shifts of pure $[\text{Sm}^{\text{III}}-\text{NCMe}]\text{PF}_6$ and $[\text{Sm}^{\text{III}}-\text{PH}]\text{PF}_6$ using eqn A6. The latter values were taken as the shifts obtained from saturating a solution of $[\text{Sm}^{\text{III}}-\text{NCMe}]\text{PF}_6$ with PH (Figure A40, no peak shifts were observed with >3 equiv. PH).

$$f(\text{Sm}^{\text{III}} - \text{NCMe}) = \frac{\delta - \delta_{\text{Sm}^{\text{III}}-\text{PH}}}{\delta_{\text{Sm}^{\text{III}}-\text{NCMe}} - \delta_{\text{Sm}^{\text{III}}-\text{PH}}} \quad (\text{A6})$$

The fraction of $[\text{Sm}^{\text{III}}-\text{NCMe}]\text{PF}_6$ was determined for each ^1H environment and then averaged. This average was used to determine the absolute concentrations of each Sm species and PH using eqns 7-9:

$$[Sm^{III} - NCMe] = f(Sm^{III} - NCMe) \times [Sm]_{tot} \quad (\mathbf{A7})$$

$$[Sm^{III} - PH] = [Sm]_{tot} - [Sm^{III} - NCMe] \quad (\mathbf{A8})$$

$$[PH] = [PH]_{tot} - [Sm^{III} - PH] \quad (\mathbf{A9})$$

The association constant was then determined using eqn A10.

$$K_{assoc} = \frac{[Sm^{III} - PH]}{[Sm^{III} - NCMe][PH]} \quad (\mathbf{A10})$$

A6.1.2 Procedure for p*K*_a Determinations

Experiments for the p*K*_a determination of [**Sm**^{III}-PH]PF₆ were performed in CD₃CN using ¹H NMR spectroscopy at room temperature (Tables A5-15 and Figures A46-48). In a standard experiment [**Sm**^{III}]PF₆ and 3 equiv. PH were dissolved in CD₃CN and added to a J-Young NMR tube along with 1,3,5-trimethoxybenzene as an internal standard. An initial NMR was taken to verify purity and then aliquots of DBU were added to the tube from a stock solution (333 mM). The relative concentrations of the protonated/deprotonated species ([**Sm**^{III}-PH]PF₆/**Sm**^{III}-P, [DBUH]PF₆/DBU) were determined from the chemical shifts of each peak relative to the shifts of the fully protonated or fully deprotonated forms using eqns A11 and 12.

$$f(\text{Sm}^{\text{III}} - \text{PH}) = \frac{\delta - \delta_{\text{Sm}^{\text{III}}-\text{P}}}{\delta_{\text{Sm}^{\text{III}}-\text{PH}} - \delta_{\text{Sm}^{\text{III}}-\text{P}}} \quad (\text{A11})$$

$$f(\text{DBUH}^+) = \frac{\delta - \delta_{\text{DBU}}}{\delta_{\text{DBUH}^+} - \delta_{\text{DBU}}} \quad (\text{A12})$$

The fractions of [**Sm**^{III}-PH]PF₆ and [DBUH]PF₆ were determined for each ¹H environment and then averaged. The total concentration of Sm was normalized as 1 for each addition. The relative integral of the 2H resonance at ~2.3 ppm was used to determine the total relative concentration of [DBUH]PF₆/DBU. Relative concentrations of the individual components [**Sm**^{III}-PH]PF₆, **Sm**^{III}-P, [DBUH]PF₆, and DBU were determined using eqns A13-16 and the averaged fractions of protonated species:

$$[\text{Sm}^{\text{III}} - \text{PH}] = f(\text{Sm}^{\text{III}} - \text{PH}) \quad (\text{A13})$$

$$[\text{Sm}^{\text{III}} - \text{P}] = 1 - [\text{Sm}^{\text{III}} - \text{PH}] \quad (\text{A14})$$

$$[\text{DBUH}^+] = f(\text{DBUH}^+) \times [\text{DBUH}^+/\text{DBU}]_{\text{tot}} \quad (\text{A15})$$

$$[\text{DBU}] = [\text{DBUH}^+/\text{DBU}]_{\text{tot}} - [\text{DBUH}^+] \quad (\text{A16})$$

The equilibrium constant for the proton transfer reaction was then determined using eqn A17.

$$K_{eq} = \frac{[DBUH^+][Sm^{III}-P]}{[Sm^{III}-PH][DBU]} \quad (\text{A17})$$

The pK_a of DBU in MeCN (24.3) was then used to determine the pK_a of $[Sm^{III}-PH]PF_6$ from K_{eq} .

The effective pK_a of $[Sm^{III}-NCMe]PF_6$ and MeOH in CH_3CN was determined similarly (Tables A16-26 and Figures A49-51), but the absolute concentrations of species must be used rather than relative concentrations because of the form of the equilibrium constant. In a standard experiment $[Sm^{III}]PF_6$ and 2 equiv. MeOH were dissolved in 0.7 mL CD_3CN and added to a J-Young NMR tube along with 1,3,5-trimethoxybenzene (21 mM) as an internal standard. An initial NMR was taken to verify purity and then aliquots of base (quin or iPr_2NH) were added to the tube from a stock solution (250 mM). The total concentrations of Sm, MeOH (either in the form of free MeOH or Sm-bound OMe^-), and acid/base were determined for each addition by integration of the Sm^{III} aryl resonance, the MeOH methyl resonance (which shifts and broadens as $Sm^{III}-OMe$ is generated), and the acid/base resonances relative to the Ar-H protons of the internal standard. The relative concentrations of the protonated/deprotonated species ($[Sm^{III}-NCMe]PF_6 + MeOH/Sm^{III}-OMe$, $[amineH]PF_6/amine$) were determined from the chemical shifts of each peak relative to the shifts of the fully protonated or fully deprotonated forms using eqns A18 and A19.

$$f(Sm^{III} - NCMe) = \frac{\delta - \delta_{Sm^{III}-OMe}}{\delta_{Sm^{III}-NCMe} - \delta_{Sm^{III}-OMe}} \quad (\text{A18})$$

$$f(amineH^+) = \frac{\delta - \delta_{amine}}{\delta_{amineH^+} - \delta_{amine}} \quad (\text{A19})$$

The fractions of [**Sm^{III}**-NCMe]PF₆ and [amineH]PF₆ were determined for each ¹H²¹⁰ environment and then averaged. Absolute concentrations of the individual components [**Sm^{III}**-NCMe]PF₆, **Sm^{III}**-OMe, MeOH, [amineH]PF₆, and amine were determined using eqns A20-24:

$$[Sm^{III} - NCMe] = f(Sm^{III} - NCMe) \times [Sm]_{tot} \quad (\text{A20})$$

$$[Sm^{III} - OMe] = [Sm]_{tot} - [Sm^{III} - NCMe] \quad (\text{A21})$$

$$[MeOH] = [MeOH]_{tot} - [Sm^{III} - OMe] \quad (\text{A22})$$

$$[amineH^+] = f(amineH^+) \times [amineH^+/amine]_{tot} \quad (\text{A23})$$

$$[amine] = [amineH^+/amine]_{tot} - [amineH^+] \quad (\text{A24})$$

The equilibrium constant for the proton transfer reaction was then determined using eqn A25.

$$K_{eq} = \frac{[amineH^+][Sm^{III}-OMe]}{[Sm^{III}-NCMe][amine][MeOH]} \quad (\text{A25})$$

The pK_a's of quin and ⁱPr₂NH in MeCN (18.8 and 19.7) were then used to determine the effective pK_a of [**Sm^{III}**-NCMe]PF₆ and MeOH from K_{eq}.

A6.2 Tabulated Shifts and Determination of K_{assoc} and $\text{p}K_{\text{a}}$'s

Table A3: ^1H NMR shifts of pure compounds used in the K_{assoc} determination for $[\text{Sm}^{\text{III}}\text{-PH}]\text{PF}_6$ in CD_3CN .

Compound	$[\text{Sm}^{\text{III}}\text{-PH}]\text{PF}_6$	$[\text{Sm}^{\text{III}}\text{-NCMe}]\text{PF}_6$
Shift 1	7.69	7.96
Shift 2	1.87	1.92
Shift 3	0.37	1.33

Table A4: ^1H NMR data for the Sm complex during three separate titration experiments of $[\text{Sm}^{\text{III}}\text{-NCMe}]\text{PF}_6$ in 0.7 mL CD_3CN with aliquots of 250 mM PH (Figure A43-45). All chemical shifts are in ppm. In parentheses is the fraction of $[\text{Sm}^{\text{III}}\text{-NCMe}]\text{PF}_6$ ($f(\text{Sm}^{\text{III}}\text{-NCMe})$) in the total Sm loading indicated by that chemical shift. The integral of the 2H $[\text{Sm}^{\text{III}}]$ aryl resonance relative to the 16 mM 1,3,5-trimethoxybenzene internal standard is listed.

Volume	Shift 1	Shift 2	Shift 3	Average $f(\text{Sm}^{\text{III}}\text{-NCMe})$	Std. Dev.	Sm Integral	K_{assoc}
20 μL	7.822 (0.50)	1.897 (0.53)	0.881 (0.53)	0.52	0.02	23.41	0.7×10^{-3}
40 μL	7.721 (0.12)	1.878 (0.14)	0.51 (0.15)	0.14	0.01	22.67	1.7×10^{-3}
60 μL	7.698 (0.04)	1.873 (0.04)	0.41 (0.04)	0.042	0.002	21.29	2.4×10^{-3}
20 μL	7.808 (0.45)	1.894 (0.47)	0.827 (0.48)	0.46	0.02	22.80	1.4×10^{-3}
40 μL	7.715 (0.10)	1.877 (0.12)	0.486 (0.12)	0.11	0.01	22.59	2.2×10^{-3}
60 μL	7.695 (0.03)	1.873 (0.04)	0.410 (0.04)	0.036	0.008	19.28	2.6×10^{-3}
20 μL	7.828 (0.52)	1.898 (0.55)	0.898 (0.55)	0.54	0.02	23.92	0.6×10^{-3}
40 μL	7.724 (0.14)	1.879 (0.16)	0.521 (0.16)	0.15	0.01	23.41	1.5×10^{-3}
60 μL	7.698 (0.04)	1.874 (0.05)	0.417 (0.05)	0.046	0.006	22.08	2.2×10^{-3}

Final K_{assoc} is 1700 ± 700 .

Table A5: ^1H NMR shifts of pure compounds used in the $\text{p}K_{\text{a}}$ determination for $[\text{Sm}^{\text{III}}\text{-PH}]\text{PF}_6$ in CD_3CN .

Compound	DBU	[DBUH] PF_6	$[\text{Sm}^{\text{III}}\text{-PH}]\text{PF}_6$	$\text{Sm}^{\text{III}}\text{-P}^a$
Shift 1	2.28	2.57	7.69	
Shift 2	1.70	1.97	1.87	1.82, 1.74
Shift 3			0.38	-0.45, -0.94

^a $\text{Sm}^{\text{III}}\text{-P}$ displays lower solution symmetry than $[\text{Sm}^{\text{III}}\text{-PH}]\text{PF}_6$, leading to splitting of equivalent resonances in the aryl groups of the cation into two environments in the deprotonated form. The average of the two split shifts was used as $\delta_{\text{Sm}(\text{III})\text{-P}}$ in eqn A11.

Table A6: ^1H NMR data for the Sm complex during a titration of $[\text{Sm}^{\text{III}}\text{-PH}]\text{PF}_6$ with DBU. All chemical shifts are in ppm. In parentheses is the fraction of $[\text{Sm}^{\text{III}}\text{-PH}]\text{PF}_6$ in the total Sm loading indicated by that chemical shift.

Volume	Shift 2	Shift 3	Average	Std. Dev.
20 μL	1.86 (0.89)	0.28 (0.91)	0.90	0.01
40 μL	1.89 (0.89)	0.22 (0.85)	0.87	0.03
80 μL	1.85 (0.78)	0.12 (0.76)	0.77	0.01
160 μL	1.84 (0.67)	-0.01 (0.64)	0.65	0.02

Table A7: ^1H NMR data for the amidine/amidinium during a titration of $[\text{Sm}^{\text{III}}\text{-PH}]\text{PF}_6$ with DBU. All chemical shifts are in ppm. Shifts that are unidentifiable at a given loading due to overlap with other components are omitted. In parentheses is the fraction of $[\text{DBUH}]\text{PF}_6$ in the total amidine/amidinium loading indicated by that chemical shift.

Volume	Shift 1	Shift 2	Average	Std. Dev.	Relative Integral
20 μL	2.37 (0.31)		0.31	N/A	0.53
40 μL	2.34 (0.21)	1.75 (0.19)	0.20	0.02	1.15
120 μL	2.32 (0.14)	1.73 (0.11)	0.12	0.02	2.57
160 μL	2.31 (0.10)	1.72 (0.07)	0.09	0.02	4.66

Table A8: Equilibrium constants derived from data in Table A6 and Table A7.

Volume	K_{eq}
20 μL	0.05
40 μL	0.04
80 μL	0.04
160 μL	0.05

Table A9: ^1H NMR data for the Sm complex during a second titration of $[\text{Sm}^{\text{III}}\text{-PH}]\text{PF}_6$ with DBU. All chemical shifts are in ppm. In parentheses is the fraction of $[\text{Sm}^{\text{III}}\text{-PH}]\text{PF}_6$ in the total Sm loading indicated by that chemical shift.

Volume	Shift 2	Shift 3	Average	Std. Dev.
40 μL	1.85 (0.78)	0.21 (0.84)	0.81	0.05
60 μL	1.85 (0.78)	0.17 (0.80)	0.79	0.02
80 μL	1.84 (0.67)	0.12 (0.76)	0.71	0.06
100 μL	1.84 (0.67)	0.09 (0.73)	0.70	0.04

Table A10: ^1H NMR data for the amidine/amidinium during a second titration of $[\text{Sm}^{\text{III}}\text{-PH}]\text{PF}_6$ with DBU. All chemical shifts are in ppm. Shifts that are unidentifiable at a given loading due to overlap with other components are omitted. In parentheses is the fraction of $[\text{DBUH}]\text{PF}_6$ in the total amidine/amidinium loading indicated by that chemical shift.

Volume	Shift 1	Shift 2	Average	Std. Dev.	Relative Integral
40 μL	2.39 (0.38)		0.38	N/A	1.20
60 μL	2.36 (0.28)	1.77 (0.26)	0.27	0.01	2.78
80 μL	2.35 (0.24)	1.75 (0.19)	0.21	0.04	4.00
100 μL	2.34 (0.21)	1.75 (0.19)	0.20	0.02	6.14

Table A11: Equilibrium constants derived from data in Table A9 and Table A10.

Volume	K_{eq}
40 μL	0.14
60 μL	0.10
80 μL	0.11
100 μL	0.11

Table A12: ^1H NMR data for the Sm complex during a third titration of $[\text{Sm}^{\text{III}}\text{-PH}]\text{PF}_6$ with DBU. All chemical shifts are in ppm. In parentheses is the fraction of $[\text{Sm}^{\text{III}}\text{-PH}]\text{PF}_6$ in the total Sm loading indicated by that chemical shift.

Volume	Shift 2	Shift 3	Average	Std. Dev.
40 μL	1.85 (0.78)	0.23 (0.86)	0.82	0.06
80 μL	1.85 (0.78)	0.15 (0.79)	0.78	0.01
100 μL	1.84 (0.67)	0.11 (0.75)	0.71	0.06
120 μL	1.84 (0.67)	0.08 (0.72)	0.69	0.04

Table A13: ^1H NMR data for the amidine/amidinium during a third titration of $[\text{Sm}^{\text{III}}\text{-PH}]\text{PF}_6$ with DBU. All chemical shifts are in ppm. Shifts that are unidentifiable at a given loading due to overlap with other components are omitted. In parentheses is the fraction of $[\text{DBUH}]\text{PF}_6$ in the total amidine/amidinium loading indicated by that chemical shift.

Volume	Shift 1	Shift 2	Average	Std. Dev.	Relative Integral
40 μL	2.40 (0.41)		0.41	N/A	1.92
80 μL	2.35 (0.24)	1.76 (0.22)	0.23	0.01	3.62
100 μL	2.34 (0.21)	1.75 (0.19)	0.20	0.02	4.56
120 μL	2.33 (0.17)	1.74 (0.15)	0.16	0.02	5.88

Table A14: Equilibrium constants derived from data in Table A12 and Table A13. 216

Volume	K_{eq}
40 μL	0.16
80 μL	0.08
100 μL	0.10
120 μL	0.08

Table A15: Final equilibrium constants from Table A8, A11, and A14.

Base	K_{eq}	Std. Dev.	$\text{p}K_{\text{a}}$
DBU (1)	0.05	0.007	25.6 ± 0.1
DBU (2)	0.11	0.02	25.2 ± 0.1
DBU (3)	0.11	0.03	25.3 ± 0.2

Final $\text{p}K_{\text{a}}$ is 25.4 ± 0.2 .

Table A16: ^1H NMR shifts of pure compounds used in the $\text{p}K_{\text{a,eff}}$ determination for $[\text{Sm}^{\text{III}}\text{-NCMe}]\text{PF}_6$ and MeOH in CD_3CN .

Compound	$^i\text{Pr}_2\text{NH}$	$[\text{}^i\text{Pr}_2\text{NH}_2]\text{PF}_6$	quin	$[\text{quinH}]\text{PF}_6$	$[\text{Sm}^{\text{III}}\text{-NCMe}]\text{PF}_6 + \text{MeOH}$	$\text{Sm}^{\text{III}}\text{-OMe}^a$
Shift 1	2.85	3.47	2.76	3.23	9.05	8.63, 8.58
Shift 2	0.96	1.28	1.67	2.10	7.96	7.22, 7.16
Shift 3			1.50	1.88	1.92	1.72, 1.69
Shift 4					1.33	-0.66, -0.89

^a $\text{Sm}^{\text{III}}\text{-OMe}$ displays lower solution symmetry than $[\text{Sm}^{\text{III}}\text{-NCMe}]\text{PF}_6$, leading to splitting of equivalent resonances in the aryl groups of the cation into two environments in the deprotonated form. The average of the two split shifts was used as $\delta_{\text{Sm(III)-OMe}}$ in eqn A18.

Table A17: ^1H NMR data for the Sm complex during a titration of $[\text{Sm}^{\text{III}}\text{-NCMe}]\text{PF}_6$ and MeOH with $^i\text{Pr}_2\text{NH}_2$. All chemical shifts are in ppm. In parentheses is the fraction of $[\text{Sm}^{\text{III}}\text{-NCMe}]\text{PF}_6$ in the total Sm loading indicated by that chemical shift. The total concentrations of Sm determined through integration to the internal trimethoxybenzene standard are given.

Volume	Shift 1	Shift 2	Shift 3	Shift 4	Average	Std. Dev.	$[\text{Sm}]_{\text{tot}}$ (mM)
20 μL	9.04 (0.98)	7.95 (0.99)	1.92 (1.0)	1.41 (0.99)	0.99	0.009	13.2
40 μL	9.04 (0.98)	7.94 (0.97)	1.92 (1.0)	1.30 (0.99)	0.98	0.01	12.4
80 μL	9.03 (0.96)	7.93 (0.96)	1.91 (0.95)	1.28 (0.98)	0.96	0.01	11.7
160 μL	9.03 (0.96)	7.92 (0.95)	1.91 (0.95)	1.25 (0.96)	0.95	0.006	10.5

Table A18: ^1H NMR data for the amine/ammonium during a titration of $[\text{Sm}^{\text{III}}\text{-NCMe}]\text{PF}_6$ and MeOH with $^i\text{Pr}_2\text{NH}_2$. All chemical shifts are in ppm. In parentheses is the fraction of $[^i\text{Pr}_2\text{NH}_2]\text{PF}_6$ in the total amine/ammonium loading indicated by that chemical shift. The total concentration of the amine/ammonium determined through integration to the internal trimethoxybenzene standard is given.

Volume	Shift 1	Shift 2	Average	Std. Dev.	$[\text{B}] + [\text{BH}^+]$ (mM)
20 μL	2.92 (0.11)	1.00 (0.11)	0.11	0.002	10.5
40 μL	2.89 (0.06)	0.99 (0.08)	0.07	0.01	20.6
80 μL	2.88 (0.05)	0.98 (0.05)	0.05	0.001	40.3
160 μL	2.87 (0.03)	0.97 (0.03)	0.03	0.0007	69.3

Table A19: Equilibrium constants derived from data in Table A17 and Table A18.

Volume	K_{eq}
20 μ L	0.062
40 μ L	0.054
80 μ L	0.095
160 μ L	0.082

Table A20: ^1H NMR data for the Sm complex during a titration of $[\text{Sm}^{\text{III}}\text{-NCMe}]\text{PF}_6$ and MeOH with quin. All chemical shifts are in ppm. In parentheses is the fraction of $[\text{Sm}^{\text{III}}\text{-NCMe}]\text{PF}_6$ in the total Sm loading indicated by that chemical shift. The total concentrations of Sm determined through integration to the internal trimethoxybenzene standard are given.

Volume	Shift 1	Shift 2	Shift 3	Shift 4	Average	Std. Dev.	$[\text{Sm}]_{\text{tot}}$ (mM)
20 μ L	9.03 (0.96)	7.93 (0.96)	1.91 (0.95)	1.27 (0.97)	0.96	0.008	14.1
40 μ L	9.02 (0.93)	7.91 (0.94)	1.91 (0.95)	1.20 (0.94)	0.94	0.009	13.1
80 μ L	9.00 (0.89)	7.87 (0.88)	1.90 (0.91)	1.12 (0.90)	0.89	0.01	12.2
160 μ L	8.97 (0.82)	7.82 (0.82)	1.88 (0.81)	1.01 (0.85)	0.83	0.02	10.9

Table A21: ^1H NMR data for the amine/ammonium during a titration of $[\text{Sm}^{\text{III}}\text{-NCMe}]\text{PF}_6$ and MeOH with quin. All chemical shifts are in ppm. In parentheses is the fraction of $[\text{quinH}]\text{PF}_6$ in the total amine/ammonium loading indicated by that chemical shift. The total concentration of the amine/ammonium determined through integration to the internal trimethoxybenzene standard is given.

Volume	Shift 1	Shift 2	Shift 3	Average	Std. Dev.	[B] + [BH ⁺] (mM)
20 μL	2.86 (0.21)		1.58 (0.21)	0.21	0.002	7.7
40 μL	2.82 (0.13)	1.73 (0.14)	1.56 (0.16)	0.14	0.01	15.4
80 μL	2.80 (0.09)	1.71 (0.09)	1.54 (0.11)	0.09	0.01	25.5
160 μL	2.79 (0.06)	1.70 (0.07)	1.52 (0.05)	0.06	0.009	48.0

Table A22: Equilibrium constants derived from data in Table A20 and Table A21.

Volume	K_{eq}
20 μL	0.50
40 μL	0.49
80 μL	0.62
160 μL	0.81

Table A23: ^1H NMR data for the Sm complex during a titration of $[\text{Sm}^{\text{III}}\text{-NCMe}]\text{PF}_6$ and MeOH with quin. All chemical shifts are in ppm. In parentheses is the fraction of $[\text{Sm}^{\text{III}}\text{-NCMe}]\text{PF}_6$ in the total Sm loading indicated by that chemical shift. The total concentrations of Sm determined through integration to the internal trimethoxybenzene standard are given.

Volume	Shift 1	Shift 2	Shift 3	Shift 4	Average	Std. Dev.	$[\text{Sm}]_{\text{tot}}$ (mM)
20 μL	9.03 (0.96)	7.93 (0.96)	1.91 (0.95)	1.26 (0.97)	0.96	0.006	13.1
40 μL	9.02 (0.93)	7.90 (0.92)	1.91 (0.95)	1.20 (0.94)	0.94	0.01	12.4
80 μL	8.99 (0.87)	7.87 (0.88)	1.89 (0.86)	1.11 (0.90)	0.88	0.02	12.0
160 μL	8.96 (0.80)	7.81 (0.81)	1.88 (0.81)	0.98 (0.83)	0.81	0.02	10.8

Table A24: ^1H NMR data for the amine/ammonium during a titration of $[\text{Sm}^{\text{III}}\text{-NCMe}]\text{PF}_6$ and MeOH with quin. All chemical shifts are in ppm. In parentheses is the fraction of $[\text{quinH}]\text{PF}_6$ in the total amine/ammonium loading indicated by that chemical shift. The total concentration of the amine/ammonium determined through integration to the internal trimethoxybenzene standard is given.

Volume	Shift 1	Shift 2	Shift 3	Average	Std. Dev.	$[\text{B}] + [\text{BH}^+]$ (mM)
20 μL	2.87 (0.23)		1.59 (0.24)	0.24	0.002	7.0
40 μL	2.83 (0.15)	1.74 (0.17)	1.56 (0.16)	0.16	0.007	16.7
80 μL	2.80 (0.09)	1.71 (0.09)	1.54 (0.11)	0.09	0.01	27.4
160 μL	2.79 (0.06)	1.70 (0.07)	1.53 (0.08)	0.07	0.007	52.1

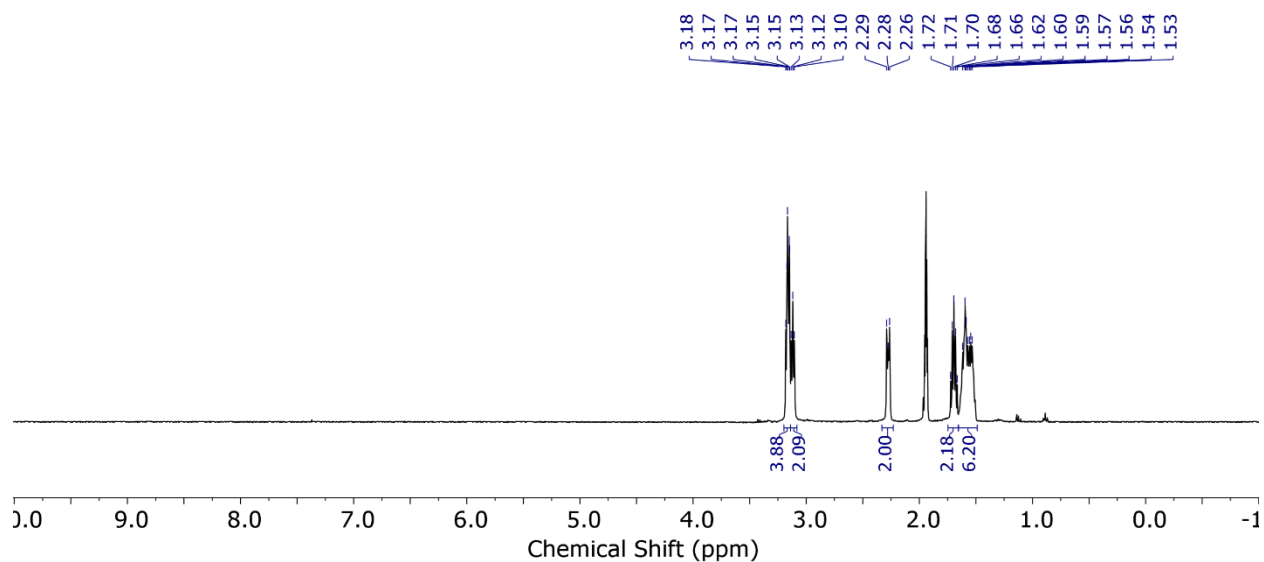
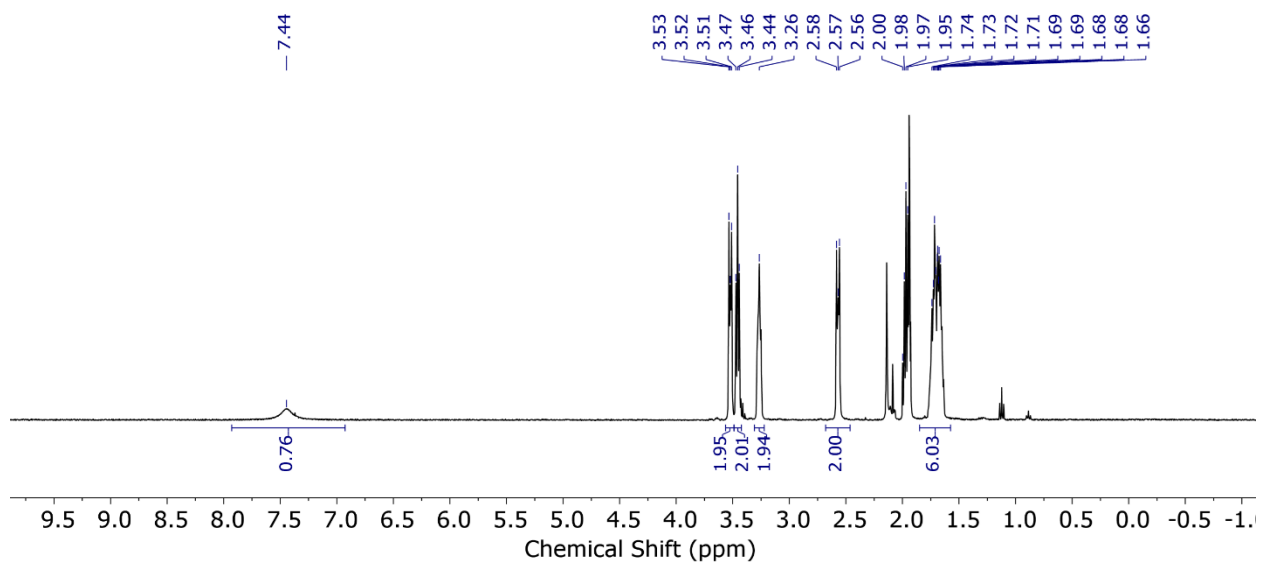
Table A25: Equilibrium constants derived from data in Table A23 and Table A24.

Volume	K_{eq}
20 μL	0.54
40 μL	0.54
80 μL	0.69
160 μL	0.94

Table A26: Final equilibrium constants from Table A19, A22, and A25.

Base	K_{eq}	Std. Dev.	$\text{p}K_{\text{a,eff}}$
$i\text{Pr}_2\text{NH}_2$	0.07	0.02	19.9 ± 0.4
quin (1)	0.6	0.2	19.9 ± 0.3
quin (2)	0.7	0.2	19.9 ± 0.4

Final $\text{p}K_{\text{a,eff}}$ is 19.9 ± 0.2 .

A6.3 ^1H NMR Spectra of Pure Compounds used in Equilibrium MeasurementsFigure A34. ^1H NMR in CD_3CN (400 MHz, r.t.) of DBU.Figure A35. ^1H NMR in CD_3CN (400 MHz, r.t.) of $[\text{DBUH}]\text{PF}_6$.

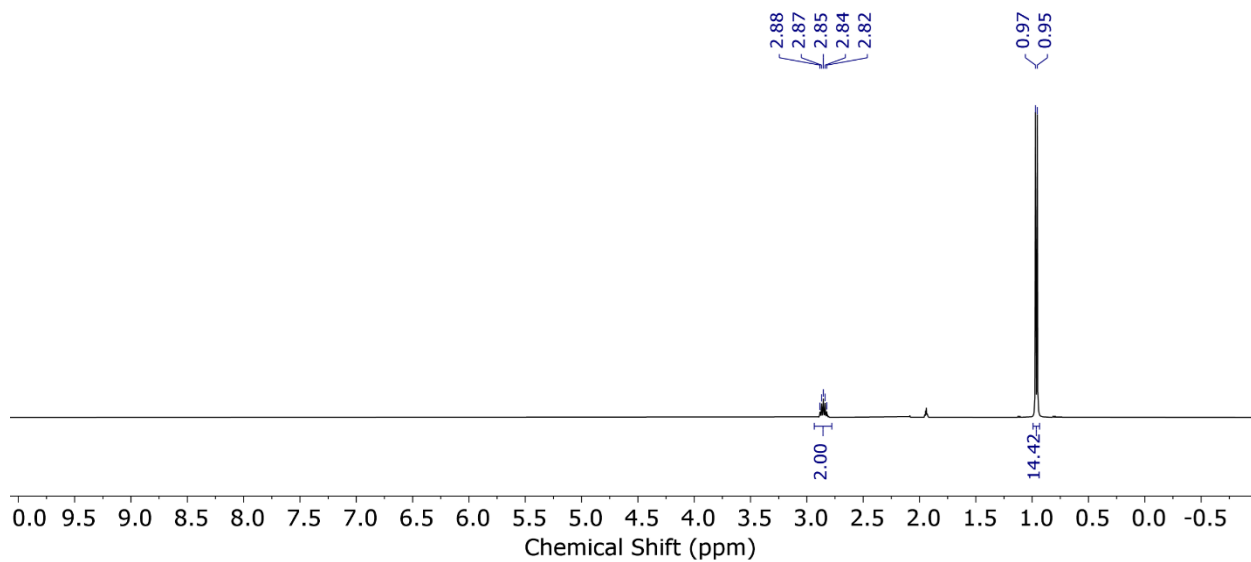


Figure A36. ^1H NMR in CD_3CN (400 MHz, r.t.) of $i\text{Pr}_2\text{NH}$.

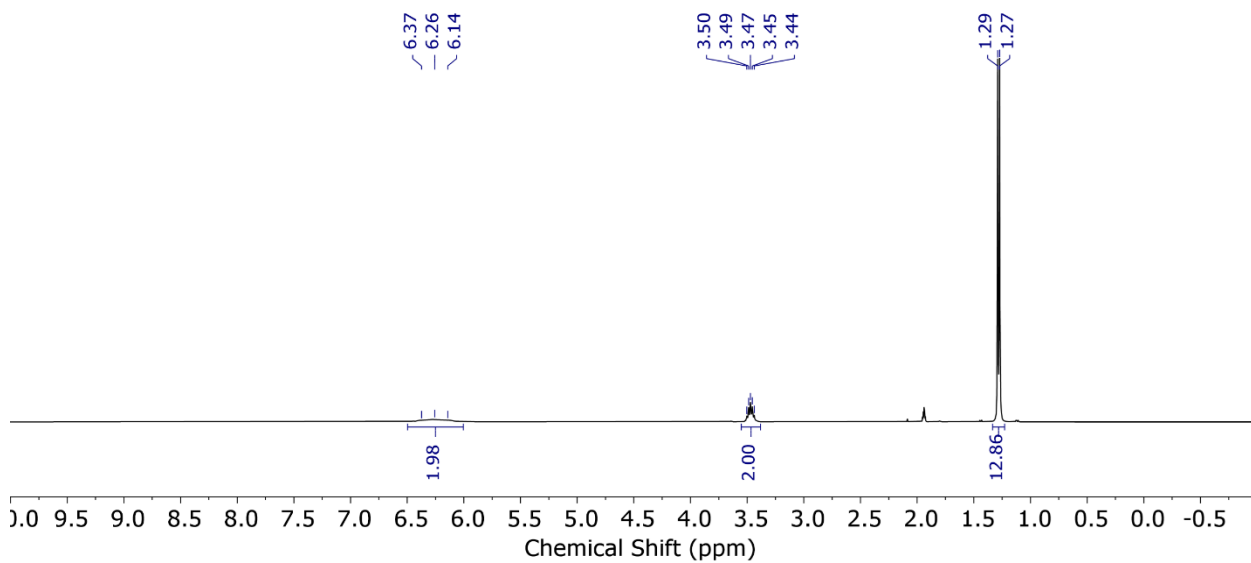


Figure A37. ^1H NMR in CD_3CN (400 MHz, r.t.) of $[i\text{Pr}_2\text{NH}]\text{PF}_6$.

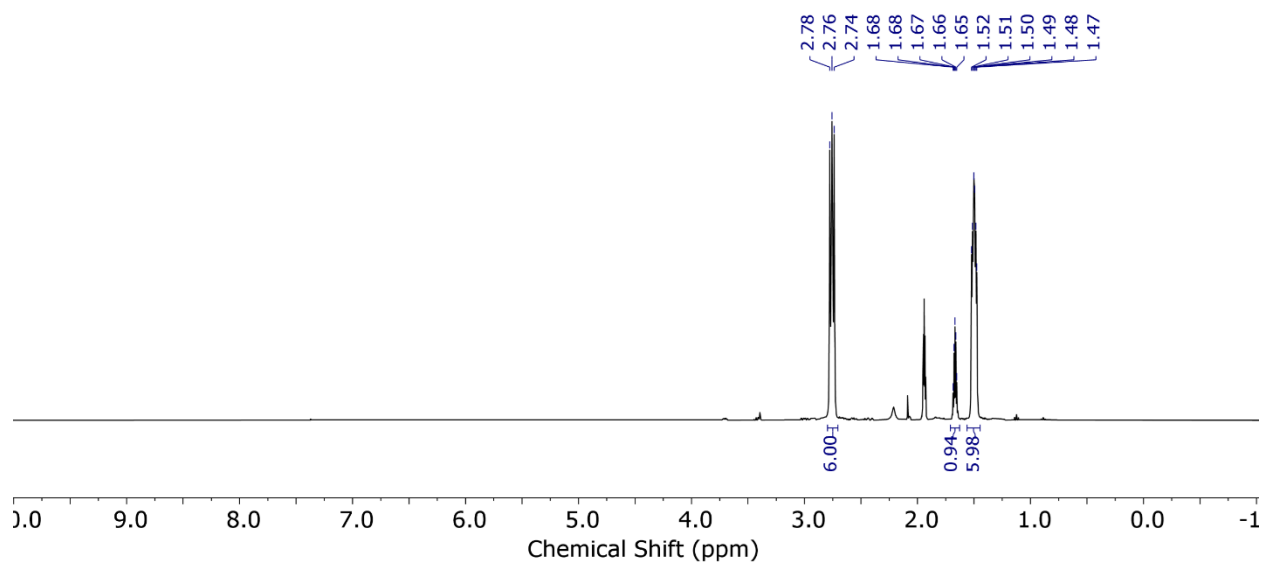


Figure A38. ¹H NMR in CD₃CN (400 MHz, r.t.) of quin.

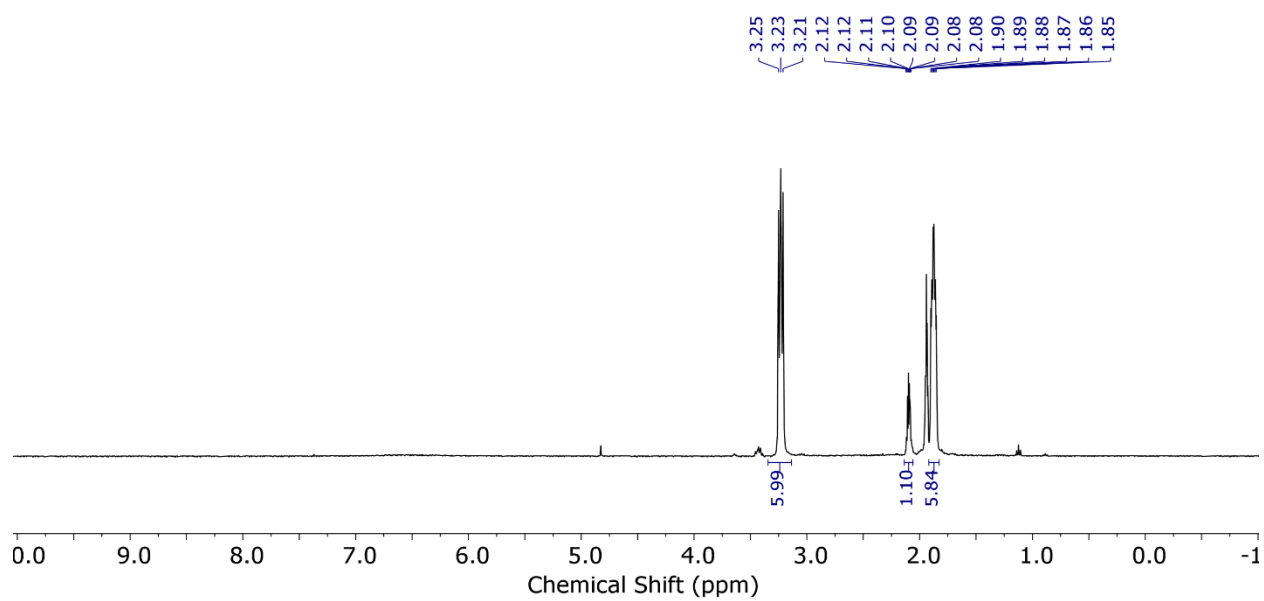


Figure A39. ¹H NMR in CD₃CN (400 MHz, r.t.) of [quinH]PF₆.

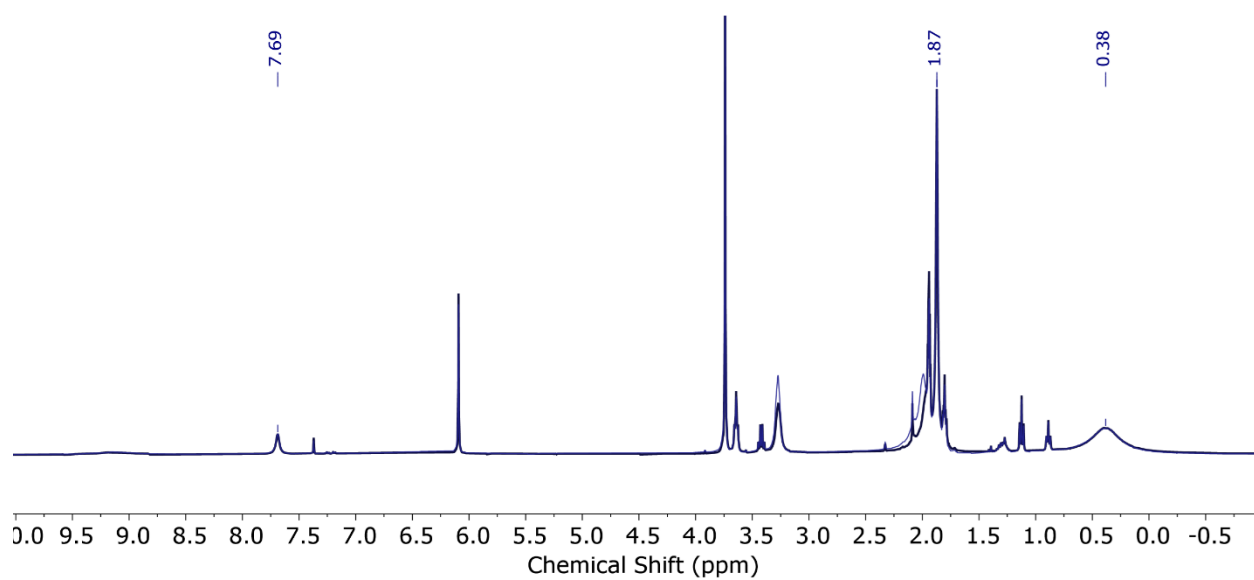


Figure A40. Superimposed ¹H NMR in CD₃CN (400 MHz, r.t.) of [Sm^{III}-NCMe]PF₆ in the presence of 3 equiv. (dark blue) and 4 equiv. (light blue) PH. Picked peaks are assigned to [Sm^{III}-PH]PF₆. 1,3,5-trimethoxybenzene is present as an internal standard.

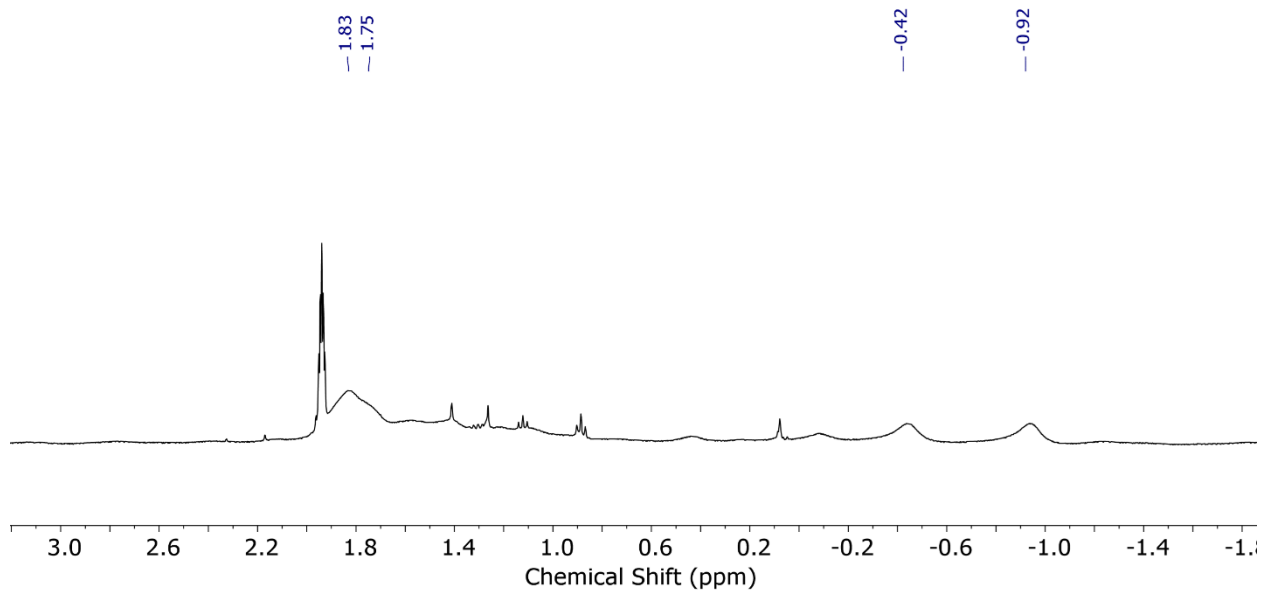


Figure A41. Aliphatic region of ^1H NMR of $\text{Sm}^{\text{III}}\text{-P}$ in CD_3CN (400 MHz) with resonances corresponding to *t*Bu groups picked. $\text{Sm}^{\text{III}}\text{-P}$ is not sufficiently soluble in MeCN to readily identify any other resonances.

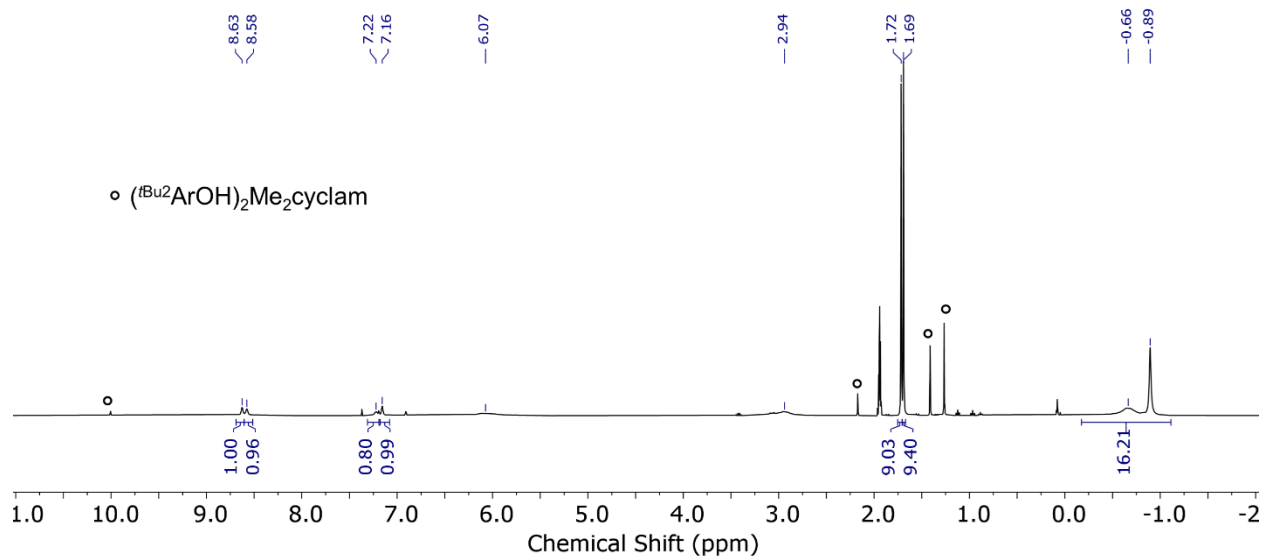


Figure A42. ^1H NMR of $\text{Sm}^{\text{III}}\text{-OMe}$ in CD_3CN (400 MHz). Peaks corresponding to protonated ligand impurity (10%) are marked.

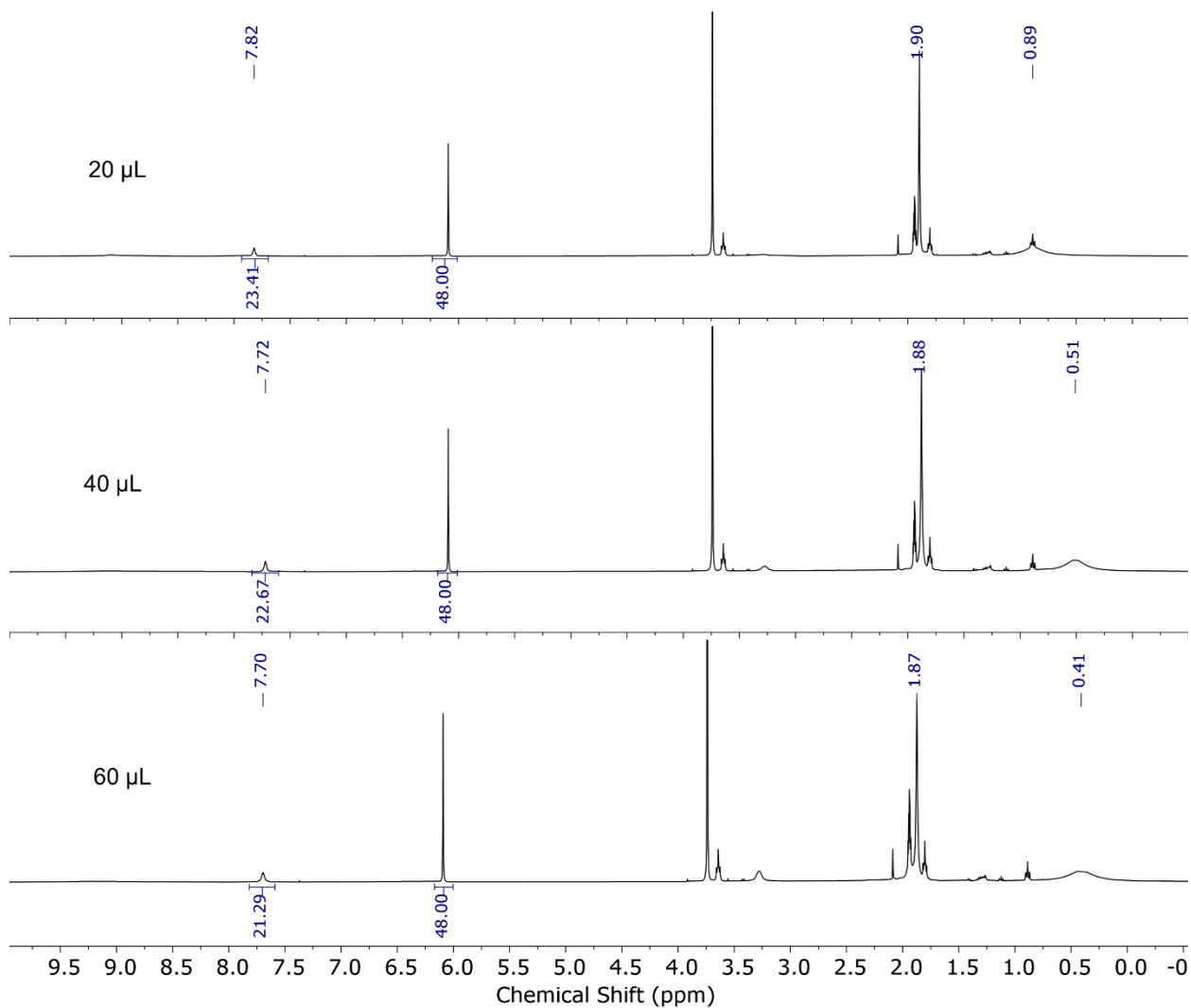


Figure A43. ^1H NMR in CD_3CN (400 MHz, r.t.) of a set of titration experiments of $[\text{Sm}^{\text{III}}\text{-NCMe}]\text{PF}_6$ with PH and 1,3,5-trimethoxybenzene (16 mM) as an internal standard. Spectra are labeled with the total volume of a 250 mM PH stock solution added to the reaction mixture.

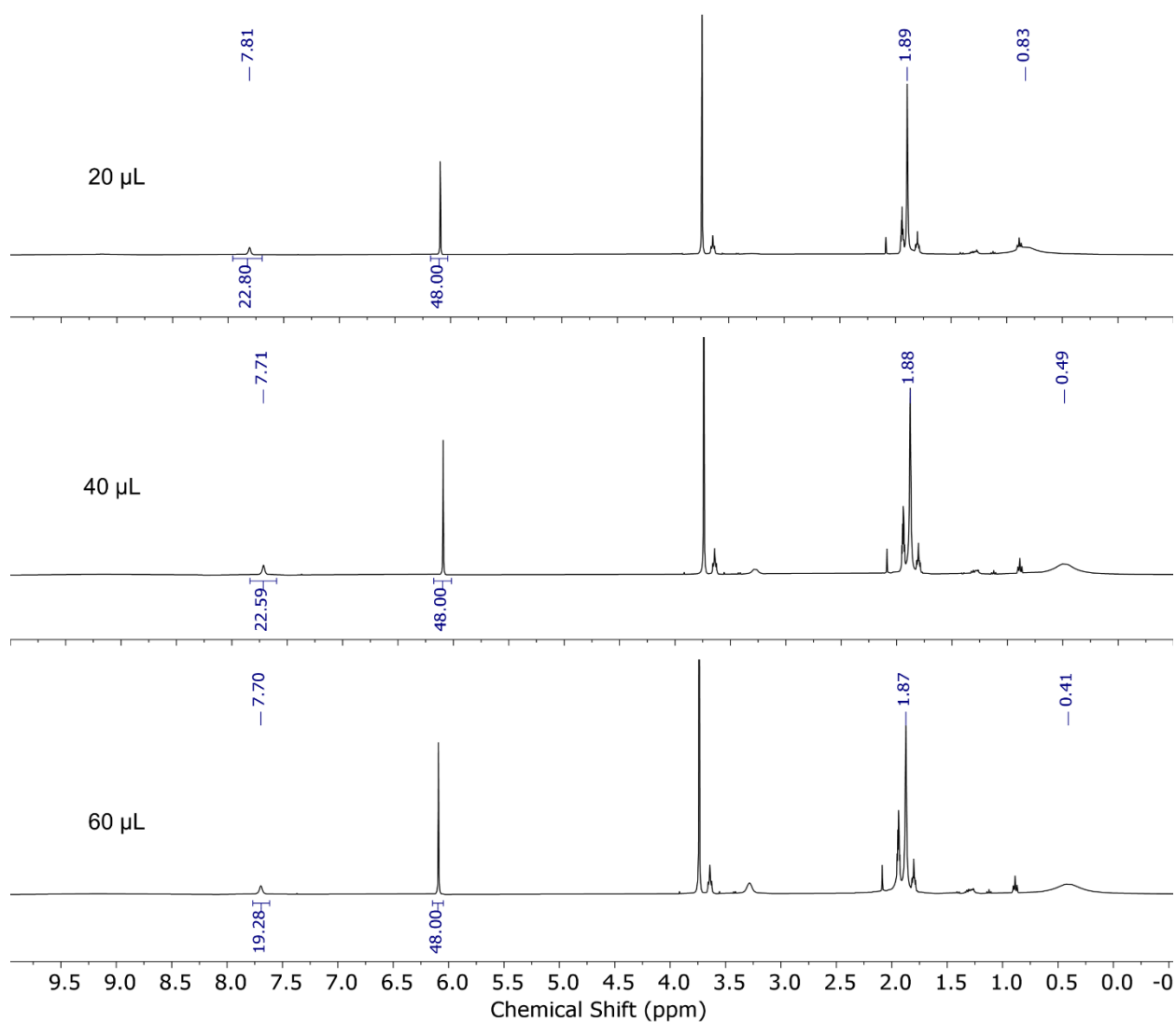


Figure A44. ^1H NMR in CD_3CN (400 MHz, r.t.) of a second set of titration experiments of $[\text{Sm}^{\text{III}}\text{-NCMe}]\text{PF}_6$ with PH and 1,3,5-trimethoxybenzene (16 mM) as an internal standard. Spectra are labeled with the total volume of a 250 mM PH stock solution added to the reaction mixture.

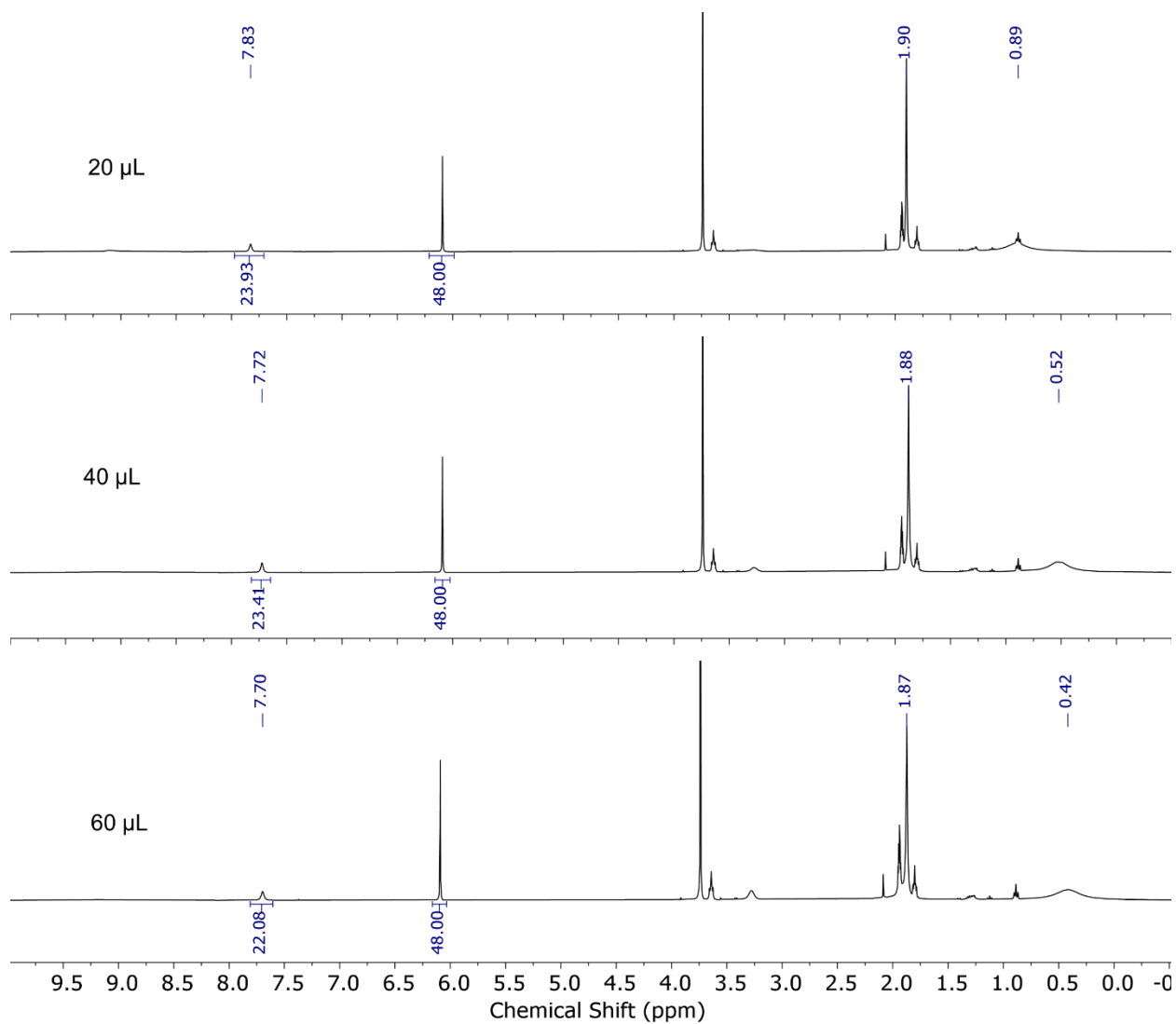


Figure A45. ^1H NMR in CD_3CN (400 MHz, r.t.) of a third set of titration experiments of $[\text{Sm}^{\text{III}}\text{-NCMe}]\text{PF}_6$ with PH and 1,3,5-trimethoxybenzene (16 mM) as an internal standard. Spectra are labeled with the total volume of a 250 mM PH stock solution added to the reaction mixture.

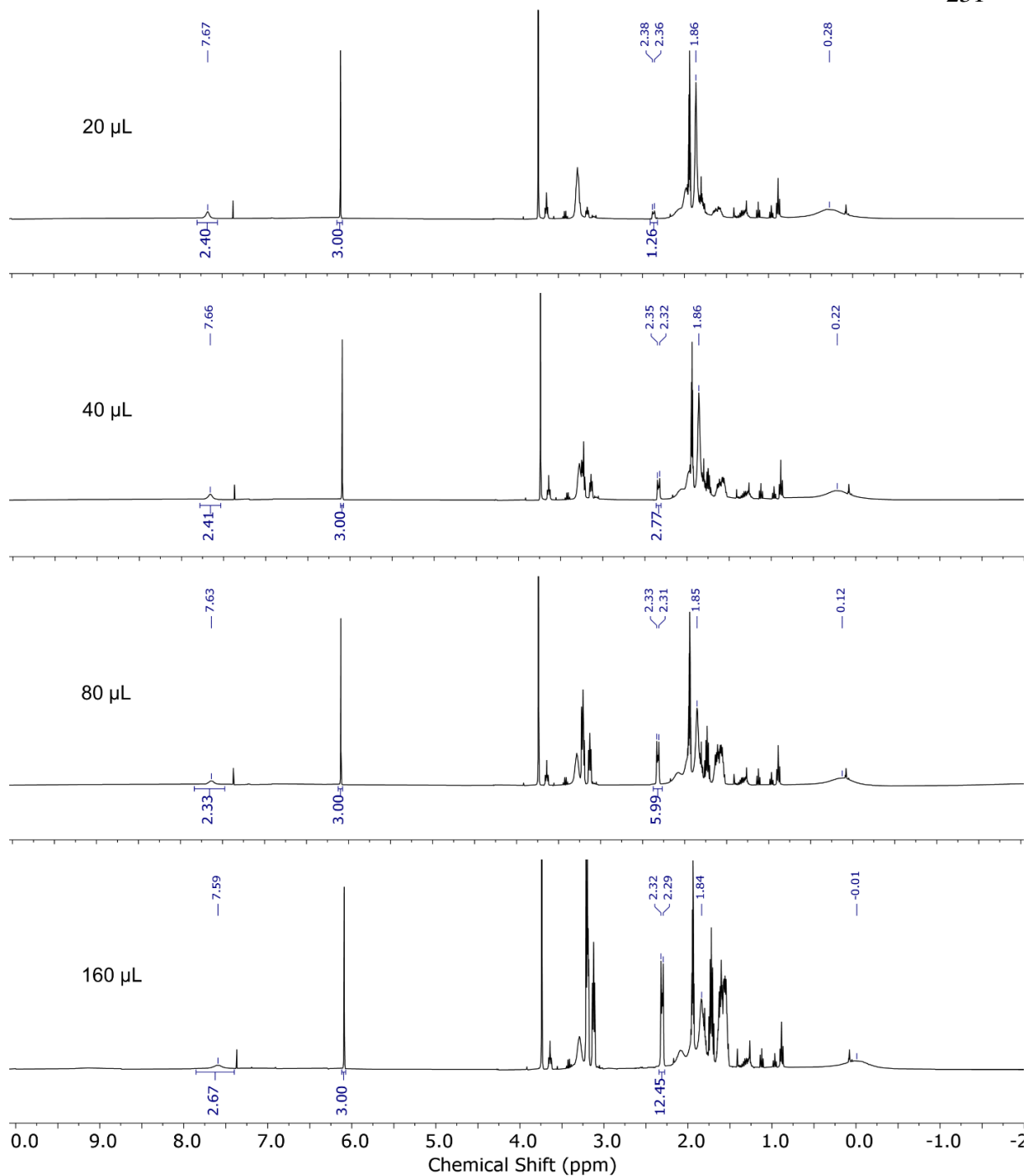


Figure A46. ^1H NMR in CD_3CN (400 MHz, r.t.) of titration experiments of $[\text{Sm}^{\text{III}}\text{-PH}]\text{PF}_6$ (0.010 mmol) with DBU and 1,3,5-trimethoxybenzene as an internal standard. Spectra are labeled with the total volume of a 333 mM DBU stock solution added to the reaction mixture.

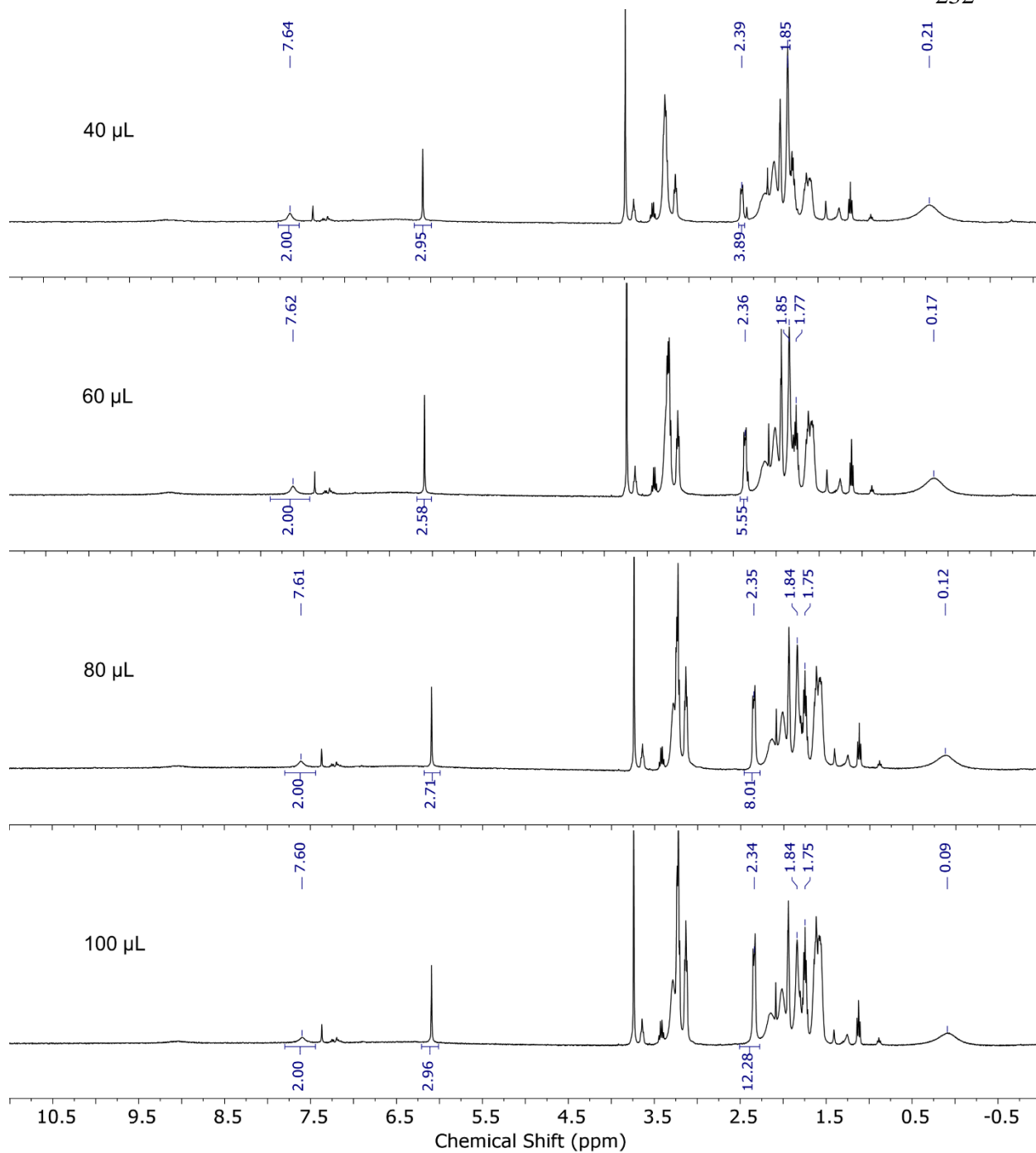


Figure A47. ^1H NMR in CD_3CN (400 MHz, r.t.) of a second set of titration experiments of $[\text{Sm}^{\text{III}}\text{-PH}]\text{PF}_6$ (0.010 mmol) with DBU and 1,3,5-trimethoxybenzene as an internal standard. Spectra are labeled with the total volume of a 500 mM DBU stock solution added to the reaction mixture.

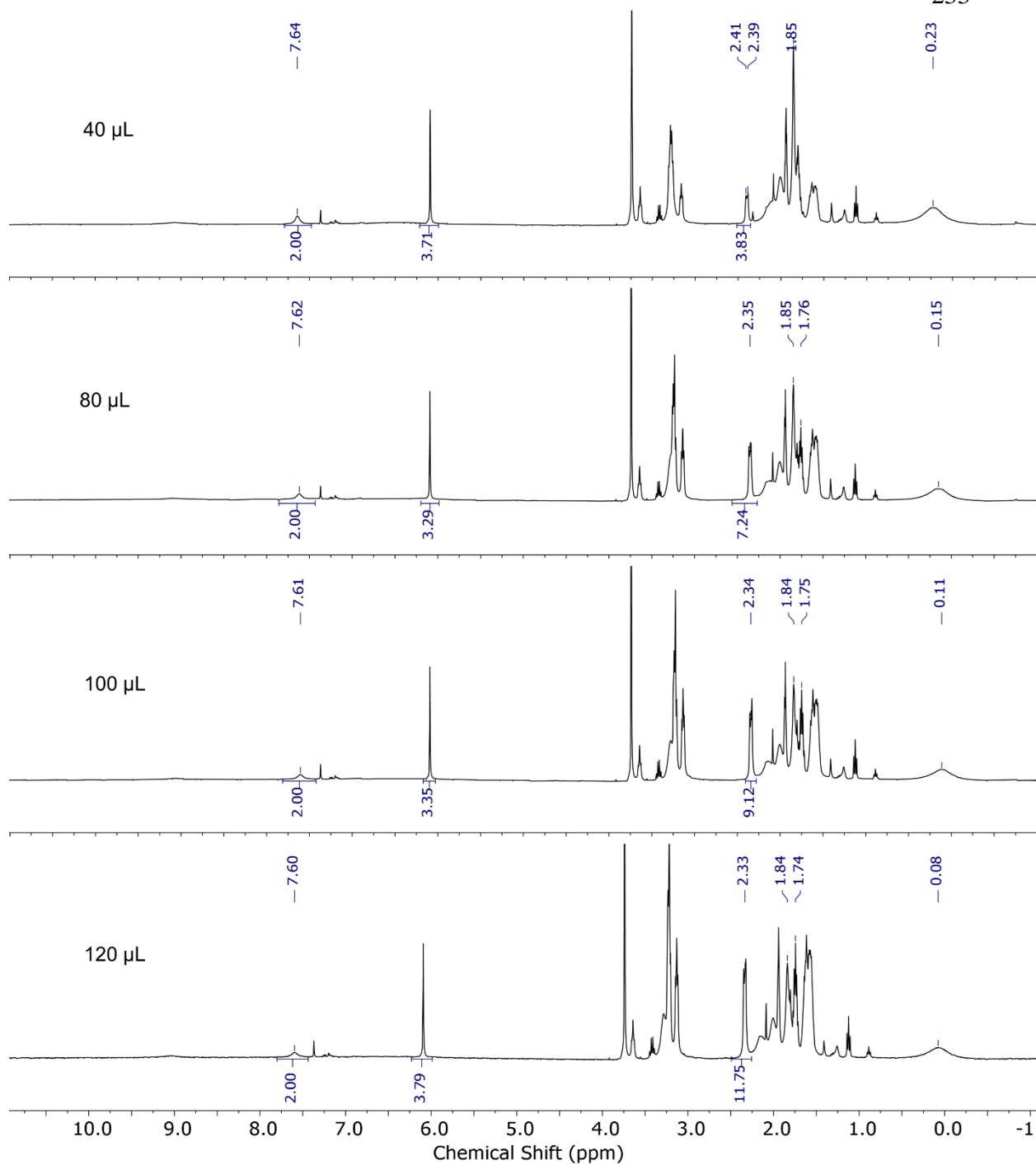


Figure A48. ^1H NMR in CD_3CN (400 MHz, r.t.) of a third set of titration experiments of $[\text{Sm}^{\text{III}}\text{-PH}]\text{PF}_6$ (0.013 mmol) with DBU and 1,3,5-trimethoxybenzene as an internal standard. Spectra are labeled with the total volume of a 500 mM DBU stock solution added to the reaction mixture.

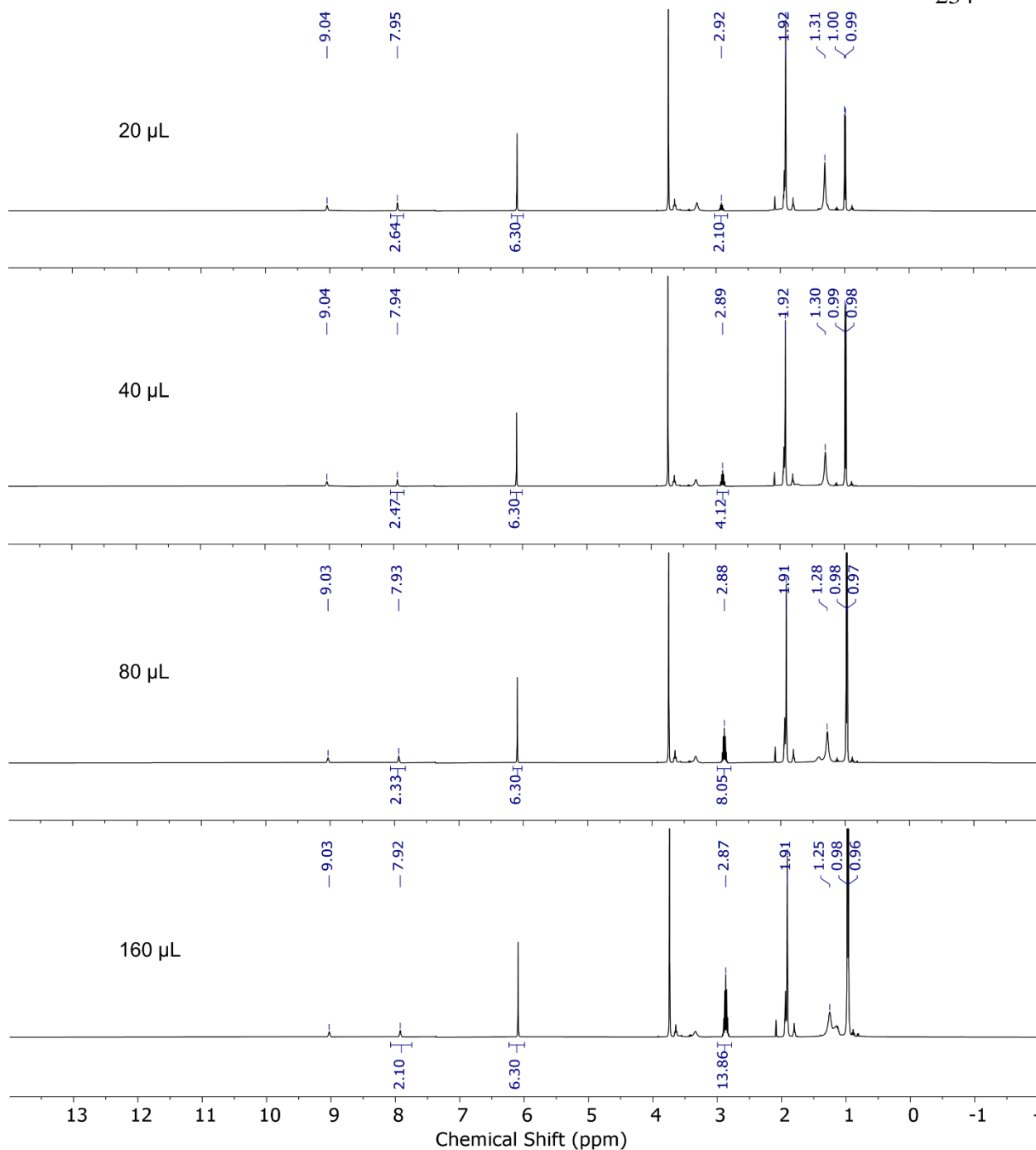


Figure A49. ^1H NMR in CD_3CN (400 MHz, r.t.) of titration experiments of $[\text{Sm}^{\text{III}}\text{-NCMe}]\text{PF}_6$ and MeOH with $i\text{Pr}_2\text{NH}$ and 1,3,5-trimethoxybenzene (21 mM) as an internal standard. Spectra are labeled with the total volume of a 250 mM $i\text{Pr}_2\text{NH}$ stock solution added to the reaction mixture.

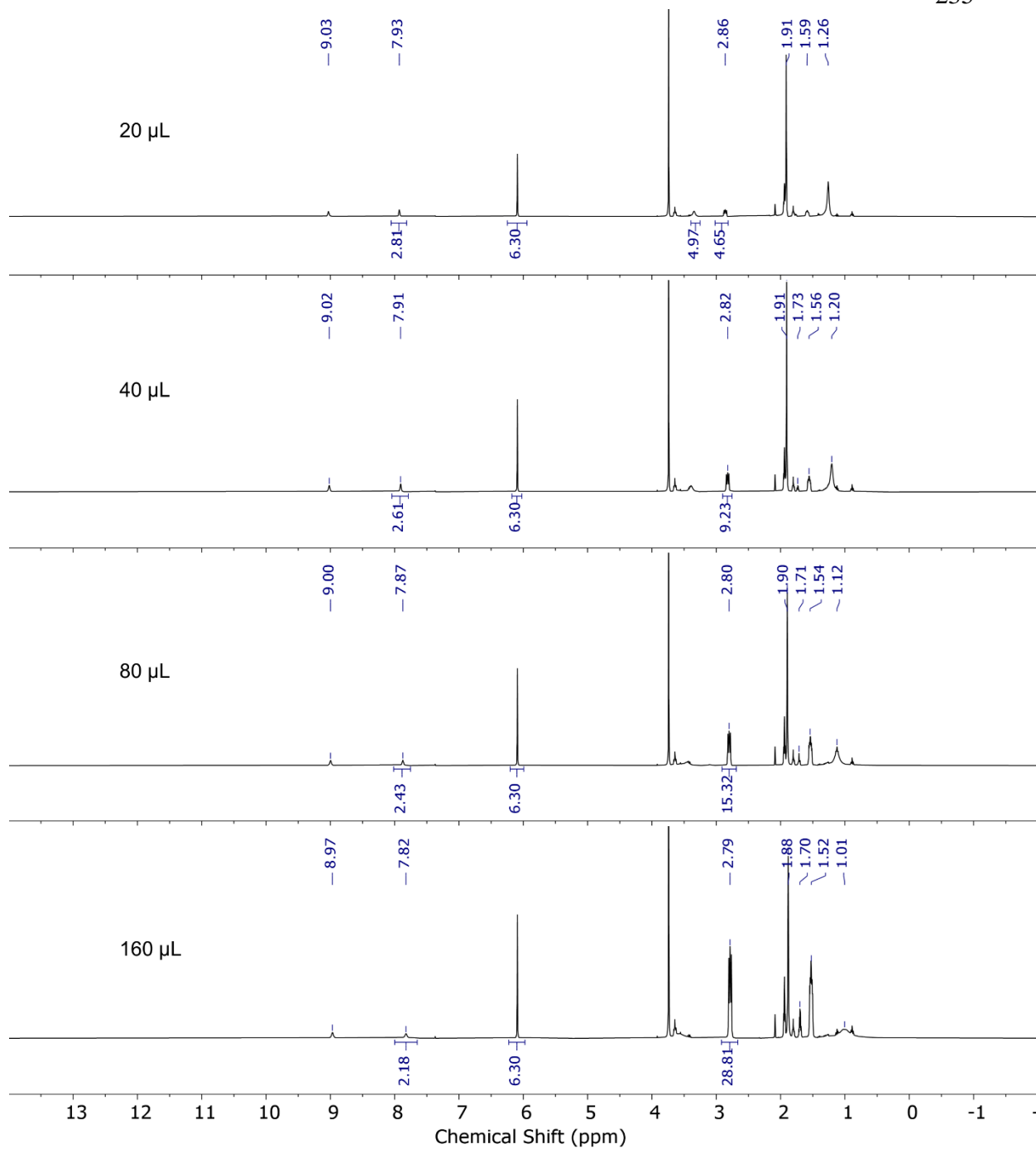


Figure A50. ^1H NMR in CD_3CN (400 MHz, r.t.) of titration experiments of $[\text{Sm}^{\text{III}}\text{-NCMe}]\text{PF}_6$ and MeOH with quin and 1,3,5-trimethoxybenzene (21 mM) as an internal standard. Spectra are labeled with the total volume of a 250 mM quin stock solution added to the reaction mixture.

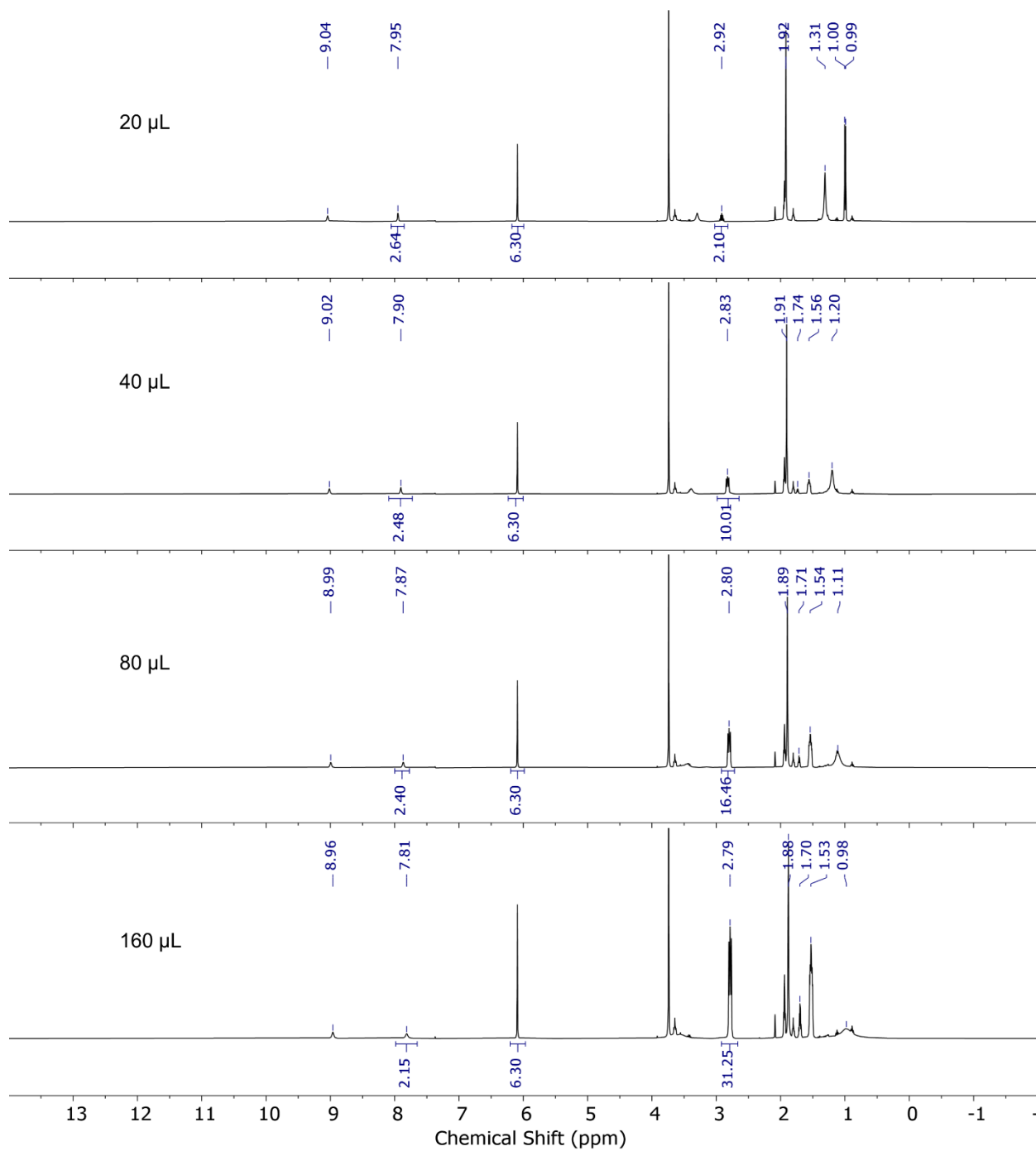
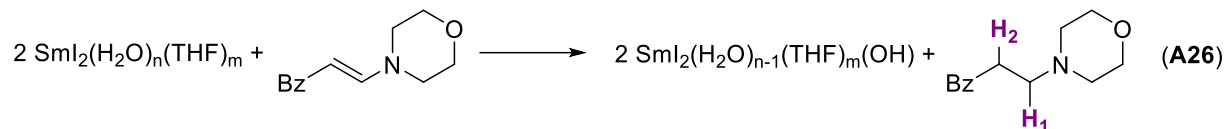


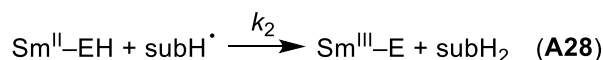
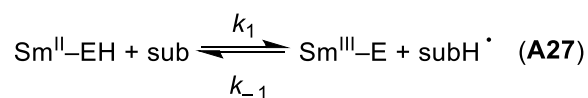
Figure A51. ^1H NMR in CD_3CN (400 MHz, r.t.) of a second set of titration experiments of $[\text{Sm}^{\text{III}}\text{-NCMe}]\text{PF}_6$ and MeOH with quin and 1,3,5-trimethoxybenzene (21 mM) as an internal standard. Spectra are labeled with the total volume of a 250 mM quin stock solution added to the reaction mixture.

A7 Bracketing of BDFE_{O-H} for SmI₂(H₂O)_n(THF)_m based on Kinetic Analysis

Eqn A26 shows the balanced reaction of SmI₂(H₂O)_n(THF)_m with enamine substrate reported by Mayer and coworkers.¹⁰



Eqn A26 is proposed to go through an initial concerted proton-coupled electron transfer (CPET) at the H₁ position followed by transfer of a second hydrogen atom equivalent. This mechanism is summarized in eqn A27 and A28.



From the absence of deuterium incorporation into H₁,¹⁰ it is unlikely that eqn A27 establishes a rapid pre-equilibrium. The steady-state approximation is therefore used to derive the rate law for this mechanism:

$$\frac{d[\text{subH}_2]}{dt} = \frac{k_1 k_2 [\text{sub}] [\text{Sm}^{\text{II}}\text{-EH}]^2}{k_{-1} [\text{Sm}^{\text{III}}\text{-E}] + k_2 [\text{Sm}^{\text{II}}\text{-EH}]} \quad (\text{A29})$$

Eqn A29 simplifies to eqn A30 when $k_{-1}[\text{Sm}^{\text{III}}\text{-E}] \ll k_2[\text{Sm}^{\text{II}}\text{-EH}]$.

$$\frac{d[\text{subH}_2]}{dt} = k_1 [\text{sub}] [\text{Sm}^{\text{II}}\text{-EH}] \quad (\text{A30})$$

Eqn A30 was rearranged and integrated as follows, with $x = [\text{subH}_2]$.

$$\int_0^x \frac{dx}{[\text{Sm}^{\text{II}}\text{-EH}] [\text{sub}]} = \int_0^t k_1 dt \quad (\text{A31})$$

From the stoichiometry of reaction 1, production of one mole of x requires consumption of one mole of substrate and two moles of Sm^{II}-EH. So, at time t :

$$[\text{sub}] = [\text{sub}]_0 - x \quad (\text{A32})$$

$$[Sm^{II} - EH] = [Sm^{II} - EH]_0 - 2x \quad (\text{A33})$$

Insertion of eqn A32 and A33 into A31 followed by rearrangement to eqn A35 and evaluation yields the integrated rate law eqn A36.

$$\int_0^x \frac{dx}{([Sm^{II} - EH]_0 - 2x)([sub]_0 - x)} = \int_0^t k_1 dt \quad (\text{A34})$$

$$\frac{1}{[sub]_0 - \frac{1}{2}[Sm^{II} - EH]_0} \int_0^x \frac{dx}{[Sm^{II} - EH]_0 - 2x} + \frac{1}{[Sm^{II} - EH]_0 - 2[sub]_0} \int_0^x \frac{dx}{[sub]_0 - x} = \int_0^t k_1 dt \quad (\text{A35})$$

$$\frac{1}{[Sm^{II} - EH]_0 - 2[sub]_0} \left(\ln \left(\frac{[sub]_0([Sm^{II} - EH]_0 - 2x)}{[Sm^{II} - EH]_0([sub]_0 - x)} \right) \right) = k_1 t \quad (\text{A36})$$

We envision two possible scenarios in which the condition $k_{-1}[Sm^{III} - E] \ll k_2[Sm^{II} - EH]$ is met and eqn A36 applies:

Scenario 1: $k_2 > k_{-1}$ such that the condition holds even at the end of the reaction, when $[Sm^{II} - EH] < [Sm^{III} - E]$.

Scenario 2: The $Sm^{III} - E$ products of eqn A27 are typically reported to precipitate, i.e., $[Sm^{III} - E] \approx 0$.

Mayer and coworkers report that the reduction of enamine substrates by $SmI_2(THF)_n(H_2O)_m$ is complete in 10 minutes at room temperature with $[sub]_0 = 0.024$ M. H_2O is present at 3.6 M in this reaction, which falls into the concentration window in which CPET reactions of SmI_2/H_2O are reported to be zero-order in water.¹¹ For the purpose of this analysis we therefore assume that the Sm^{II} centers are saturated by H_2O such that $[Sm^{II} - EH]_0 = [Sm^{II}]_0 = 0.072$ M. Taking 10 minutes as four half-lives (e.g., at $t = 10$ minutes, $x = 0.94 * [sub]_0 = 0.0225$ M), eqn A36 can be solved for $k_1 = 0.12 \text{ M}^{-1}\text{s}^{-1}$.

For the initial PCET step, the ratio of forward and backward rate constants k_1/k_{-1} can be expressed in terms of the free energy change of this step:

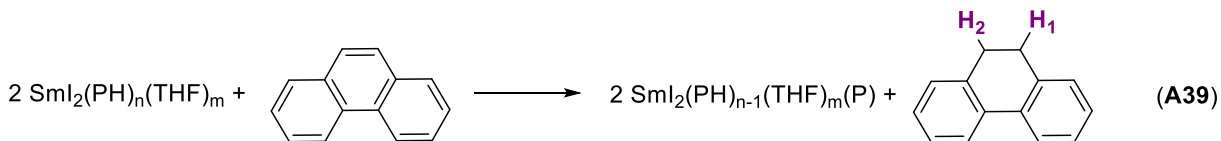
$$\Delta G^\circ_1 = BDFE_{Sm^{II} - OH_2} - BDFE_{CH,1} = \Delta BDFE \quad (\text{A37})$$

$$\frac{k_1}{k_{-1}} = K_1 = e^{\frac{-\Delta BDFE}{RT}} \quad (\text{A38})$$

Scenario 1: In this scenario, k_2 is assumed to be diffusion-limited and k_{-1} must be bounded such that $k_{-1}[\text{Sm}^{\text{III}}\text{-E}] \ll k_2[\text{Sm}^{\text{II}}\text{-EH}]$ at all points in the reaction. Assuming $\text{Sm}^{\text{III}}\text{-E}$ remains soluble and monomeric, when the reaction is complete $[\text{Sm}^{\text{III}}\text{-E}] = 0.048$ M and remaining $[\text{Sm}^{\text{II}}\text{-EH}] = 0.024$ M. Using $k_2 \leq 10^9 \text{ M}^{-1}\text{s}^{-1}$ (i.e., diffusion-limited), k_{-1} is bounded as $\leq 5 \times 10^6 \text{ M}^{-1}\text{s}^{-1}$. Substitution into eqn A38 (with $T = 298$ K) gives $\Delta BDFE$ as $\leq 10.4 \text{ kcal mol}^{-1}$. Given $BDFE_{\text{CH},1} = 31 \text{ kcal mol}^{-1}$ for the enamine substrate, the $BDFE_{\text{O-H}}$ of $\text{SmI}_2(\text{THF})_n(\text{H}_2\text{O})_m$ can be bracketed as $\leq 41.4 \text{ kcal mol}^{-1}$.

Scenario 2: In this scenario, the only requirement is that k_{-1} is bounded to a physically realistic value. Using $k_1 = 0.12 \text{ M}^{-1}\text{s}^{-1}$, $k_{-1} \leq 10^9 \text{ M}^{-1}\text{s}^{-1}$ (i.e., diffusion-limited), and $T = 298$ K, eqn A38 can be solved for an upper limit on $\Delta BDFE$ as $\leq 13.5 \text{ kcal mol}^{-1}$. Given $BDFE_{\text{CH},1} = 31 \text{ kcal mol}^{-1}$ for the enamine substrate, the $BDFE_{\text{O-H}}$ of $\text{SmI}_2(\text{THF})_n(\text{H}_2\text{O})_m$ can be bracketed as $\leq 44.5 \text{ kcal mol}^{-1}$.

The same analysis was carried out for the reaction in eqn A39:¹²



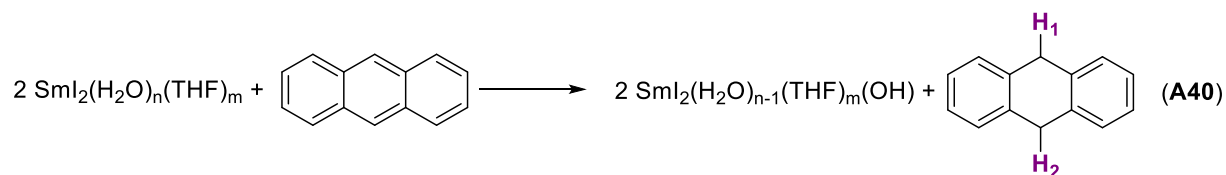
Flowers and coworkers report this reaction to be 26% complete after running overnight at room temperature with $[\text{sub}]_0 = 0.04$ M and $[\text{Sm}^{\text{II}}\text{-EH}]_0 = [\text{Sm}^{\text{II}}]_0 = 0.1$ M.¹² Taking 13 hours as “overnight”, eqn A36 can be evaluated for $x = 0.26 * [\text{sub}]_0 = 0.01$ M to solve for $k_1 = 7.3 \times 10^{-5} \text{ M}^{-1}\text{s}^{-1}$.

Scenario 1: In this scenario, k_2 is assumed to be diffusion-limited and k_{-1} must be bounded such that $k_{-1}[\text{Sm}^{\text{III}}\text{-E}] \ll k_2[\text{Sm}^{\text{II}}\text{-EH}]$ at all points in the reaction. Assuming $\text{Sm}^{\text{III}}\text{-E}$ remains soluble and monomeric, when the reaction is stopped $[\text{Sm}^{\text{III}}\text{-E}] = 0.02$ M

and remaining $[\text{Sm}^{\text{II}}\text{-EH}] = 0.08 \text{ M}$. Using $k_2 \leq 10^9 \text{ M}^{-1}\text{s}^{-1}$ (i.e., diffusion-limited), k_{-1} is²⁴⁰ bounded as $\leq 4 \times 10^7 \text{ M}^{-1}\text{s}^{-1}$. Substitution into eqn A38 (with $T = 298 \text{ K}$) gives ΔBDFE as $\leq 16 \text{ kcal mol}^{-1}$. Given $\text{BDFE}_{\text{CH},1} = 25.3 \text{ kcal mol}^{-1}$ for phenanthrene, the $\text{BDFE}_{\text{N-H}}$ of $\text{SmI}_2(\text{THF})_n(\text{PH})_m$ can be bracketed as $\leq 41.3 \text{ kcal mol}^{-1}$.

Scenario 2: $\Delta\text{BDFE} \leq 17.9 \text{ kcal mol}^{-1}$. Given $\text{BDFE}_{\text{CH},1} = 25.3 \text{ kcal mol}^{-1}$ for phenanthrene, the $\text{BDFE}_{\text{N-H}}$ of $\text{SmI}_2(\text{THF})_n(\text{PH})_m$ can be bracketed as $\leq 43.2 \text{ kcal mol}^{-1}$.

Finally, Eqn A40 shows the balanced reaction of $\text{SmI}_2(\text{H}_2\text{O})_n(\text{THF})_m$ with ²⁴¹anthracene reported by Flowers and coworkers.¹¹



The reported pseudo-first order rate constant k_{obs} at $[\text{sub}]_0 = 0.1 \text{ M}$ and $[\text{Sm}^{\text{II}}]_0 = 0.01 \text{ M}$ for this reaction with $[\text{H}_2\text{O}]$ sufficiently high that the reaction is zero-order in water is 0.15 s^{-1} .¹¹ In this concentration regime, k_{obs} is defined as follows:

$$k_{\text{obs}} = k_1[\text{sub}]$$

k_1 is therefore $1.5 \text{ M}^{-1} \text{ s}^{-1}$.

Scenario 1: Undefined (in this case SmI_2 is not used in excess).

Scenario 2: $\Delta\text{BDFE} \leq 12 \text{ kcal mol}^{-1}$. Given $\text{BDFE}_{\text{CH},1} = 38.5 \text{ kcal mol}^{-1}$ for anthracene, the $\text{BDFE}_{\text{O-H}}$ of $\text{SmI}_2(\text{THF})_n(\text{H}_2\text{O})_m$ can be bracketed as $\leq 50.5 \text{ kcal mol}^{-1}$.

REFERENCES

- (1) Maria, L.; Santos, I. C.; Alves, L. G.; Marçalo, J.; Martins, A. M. Rare earth metal complexes anchored on a new dianionic bis(phenolate)dimethylaminecyclam ligand. *J. Organomet. Chem.* **2013**, *728*, 57–67.
- (2) Maria, L.; Soares, M.; C. Santos, I.; R. Sousa, V.; Mora, E.; Marçalo, J.; V. Luzyanin, K. A novel samarium(II) complex bearing a dianionic bis(phenolate)cyclam ligand: synthesis, structure and electron-transfer reactions. *Dalton Trans.* **2016**, *45* (9), 3778–3790.
- (3) Sheldrick, G. M. A short history of SHELX. *Acta Crystallogr. A* **2008**, *64* (1), 112–122.
- (4) Dolomanov, O. V.; Bourhis, L. J.; Gildea, R. J.; Howard, J. A. K.; Puschmann, H. OLEX2: a complete structure solution, refinement and analysis program. *J. Appl. Crystallogr.* **2009**, *42*, 339.
- (5) Bolton, S. L.; Schuehler, D. E.; Niu, X.; Gopal, L.; Sponsler, M. B. Olefin metathesis for metal incorporation: Preparation of conjugated ruthenium-containing complexes and polymers. *J. Organomet. Chem.* **2006**, *691* (24), 5298–5306.
- (6) Lan, X.; Wang, X.; Zhang, D. X.; Mu, T.; Lan, X. Z. Cation and anion transfer in quinuclidinium hexafluorophosphate plastic crystal: Role of constituent ions and the crystalline structure. *J. Phys. Chem. C* **2021**, *125* (38), 21169–21178.
- (7) Atifi, A.; Boyce, D. W.; DiMeglio, J. L.; Rosenthal, J. Directing the outcome of CO₂ reduction at bismuth cathodes using varied ionic liquid promoters. *ACS Catal.* **2018**, *8* (4), 2857–2863.

- (8) Casey, K. C.; Brown, A. M.; Robinson, J. R. Yttrium and lanthanum bis(phosphine-oxide)methanides: structurally diverse, dynamic, and reactive. *Inorg. Chem. Front.* **2021**, 8 (6), 1539–1552.
- (9) Savéant, J.-M. *Elements of Molecular and Biomolecular Electrochemistry*; John Wiley & Sons, Inc: Hoboken, New Jersey, 2006.
- (10) Kolmar, S. S.; Mayer, J. M. $\text{SmI}_2(\text{H}_2\text{O})_n$ reduction of electron rich enamines by proton-coupled electron transfer. *J. Am. Chem. Soc.* **2017**, 139 (31), 10687–10692.
- (11) Chciuk, T. V.; Flowers, R. A. Proton-coupled electron transfer in the reduction of arenes by SmI_2 –water complexes. *J. Am. Chem. Soc.* **2015**, 137 (35), 11526–11531.
- (12) Chciuk, T. V.; Li, A. M.; Vazquez-Lopez, A.; Anderson, W. R.; Flowers, R. A. Secondary amides as hydrogen atom transfer promoters for reactions of samarium diiodide. *Org. Lett.* **2017**, 19 (1), 290–293.

SUPPLEMENTARY INFORMATION FOR CHAPTER 3

Reproduced in part with permission from Boyd, E.A.; Peters, J. C. *J. Am. Chem. Soc.* **2023**, *145*, 14784. doi: 10.1021/jacs.3c03352

B1 Experimental Part**B1.1 General Considerations**

All manipulations were carried out using standard Schlenk or glovebox techniques under an N₂ atmosphere. Unless otherwise noted, solvents were deoxygenated and dried by thoroughly sparging with N₂ gas followed by passage through an activated alumina column in the solvent purification system by SG Water, USA LLC. Non-halogenated solvents were tested with a standard purple solution of sodium benzophenone ketyl in tetrahydrofuran to confirm effective oxygen and moisture removal. All reagents were purchased from commercial vendors and used without further purification unless otherwise stated. 2-methyltetrahydrofuran (2-MeTHF) was degassed and stored over 4 Å molecular sieves and then stirred over NaK and passed over activated alumina immediately before use. MeOH was stirred over 3 Å molecular sieves under N₂ for one week, vacuum transferred into a Schlenk flask, and stored sealed in a glovebox. *N*-methylpyrrolidone (PMe), 2-pyrrolidone (PH), hexamethylphosphoramide (HMPA), and diisopropylamine (ⁱPr₂NH) were degassed and passed over a pipet filter of activated alumina. 5-(trifluoromethyl)pyrrolidone was dried by dissolving in Et₂O and passing over a pipet filter of activated alumina. ⁿBu₄NPF₆ was recrystallized from hot EtOH three times and then dried under vacuum at 100°C for >12 hours before use as electrolyte. ¹⁵N₂ (99%) was obtained from Cambridge Isotope Laboratories, Inc. 2-pyrrolidone was deuterated by

stirring in CD₃OD for 30 minutes followed by removal of solvent *in vacuo* (75%²⁴⁵ deuteration measured by ¹H NMR). Me₂NNH₃Cl was generated by treatment of Me₂NNH₂ with excess of a solution of HCl in Et₂O at -78°C followed by removal of solvent *in vacuo*. (^tBu₂ArO)₂Me₂cyclam)Sm (Sm^{II}),^{1,2} [Sm^{III}]PF₆,^{2,3} SmI₂(THF)₂,⁴ P₃^BFeN₂ (FeN₂),⁵ FeBAr^F₄,⁶ FeNNMe₂,⁷ and [DBUH]OTf⁸ were synthesized via reported literature procedures.

B1.2 Nuclear Magnetic Resonance (NMR) Spectroscopy

Deuterated solvents were purchased from Cambridge Isotope Laboratories, Inc. C₆D₆ was degassed, stirred over NaK, and passed over activated alumina before use. CD₃CN was degassed and passed over a pipet filter of activated alumina five times immediately before use. ¹H chemical shifts are reported in ppm relative to tetramethylsilane, using residual solvent resonances as internal standards.⁹ ¹⁵N chemical shifts are referenced to CH₃NO₂ following the recommended scale based on ratios of absolute frequencies (Ξ).¹⁰

B1.3 Electron Paramagnetic Resonance (EPR) Spectroscopy

X-band EPR spectra were obtained on a Bruker EMX spectrometer. Samples were collected at a power of 2 mW with modulation amplitudes of 2.00 G, and modulation frequencies of 100.00 kHz. EPR spectra were modeled using the easyspin program.¹¹

B1.4 ⁵⁷Fe Mössbauer Spectroscopy

Mössbauer spectra were recorded on a spectrometer from SEE Co. (Edina, MN) operating in the constant acceleration mode in a transmission geometry. The samples were kept in an SVT-400 cryostat from Janis (Wilmington, MA). The quoted isomer shifts are relative to the centroid of the spectrum of a metallic foil of α-Fe at room temperature. Data

analysis was performed using version 4 of the program WMOSS (www.wmoss.org) and²⁴⁶ quadrupole doublets were fit to Lorentzian lineshapes.

B1.5 Infrared (IR) Spectroscopy

IR measurements were obtained as thin films formed by evaporation of solutions using a Bruker Alpha Platinum ATR spectrometer with OPUS software.

B1.6 Electrochemistry

Electrochemical measurements were carried out in an N₂-filled glovebox in a 20 mL scintillation vial fitted with a septum cap containing punched-out holes for insertion of electrodes. A CD instruments 600B electrochemical analyzer was used for data collection. A glassy carbon disk (3 mm diameter) was used as the working electrode. It was freshly polished with 1, 0.3, and 0.05 μm alumina powder water slurries and rinsed with water and acetone before use. A silver wire immersed in a 5 mM solution of AgOTf in electrolyte separated from the working solution by a frit was used as pseudoreference and a platinum wire was used as the auxiliary electrode. Cyclic voltammograms (CVs) are plotted using IUPAC convention. For all measurements IR compensation was applied accounting for 85% of the total resistance. All reported potentials are referenced to the ferrocene couple, Cp₂Fe⁺/Cp₂Fe measured at the end of each electrochemical experiment. Electrochemistry solvents were passed over a pipet filter of activated alumina immediately before use.

B2 Hydrazine and Ammonia Generation Details

B2.1 Standard N₂H₄/NH₃ Generation Reaction Procedure

All solvents are stirred with Na/K for ≥ 2 hours and filtered over activated alumina prior to use. In a nitrogen-filled glovebox, a long tube with a female 24/40 joint at the top is charged with the Sm^{II} reductant as a solid (and HMPA as a liquid in reactions with this additive). The tube is then sealed at room temperature with a septum that is secured with copper wire. The tube is chilled in a glovebox cold well immersed in a dry ice/acetone bath and allowed to equilibrate for 10 minutes. To the chilled tube is added 1 mL of a room temperature solution of the acid and/or P_{Me} via syringe. The contents of the tube are stirred and warmed for five minutes to dissolve the reductant. The tube is again chilled at -78°C for 10 minutes. A 1 mM solution of the Fe precatalyst is similarly chilled. A 0.5 mL aliquot of this solution (0.5 μmol) is added to the tube via syringe and the mixture is allowed to stir and warm to room temperature overnight (≥ 12 h). In the case of lower catalyst loadings, smaller volumes of the 1 mM Fe solution are added to the tube along with additional chilled solvent to achieve the desired Fe loading and a total reaction volume of 1.5 mL. The tube is then brought out of the glovebox and analyzed for NH₃ and N₂H₄.

For the catalytic run conducted under ¹⁵N₂, the standard procedure is modified as follows: after premixing **Sm^{II}** (50 mg, 60 μmol) and PH (4.2 mg, 48 μmol) in 1 mL toluene as described above in a Schlenk tube, an additional 0.5 mL of toluene is added. The reaction mixture is then degassed (three freeze-pump-thaw cycles, thawing only to -78°C). The degassed reaction mixture is frozen in a liquid nitrogen-cooled cold well under vacuum. The tube is opened and 50 μL of a 10 mM solution of P₃^BFeN₂ (0.5 μmol) is added along

the wall of the tube. The tube is allowed to equilibrate at 77K for 5 minutes and²⁴⁸ evacuated. It is then warmed to -78°C , backfilled with $^{15}\text{N}_2$, and allowed to stir at -78°C for 24 hours.

B2.2 Ammonia and Hydrazine Quantification

Reaction mixtures are cooled to 77 K and allowed to freeze. HCl (3 mL of a 2.0 M solution in Et_2O , 6 mmol) is added to the frozen tube via syringe over 1-2 minutes and allowed to freeze. The septum on the tube is then exchanged for a Schlenk tube adapter and the headspace of the tube is evacuated. After sealing the tube, it is then allowed to warm to room temperature and stirred at room temperature for at least 10 minutes. Solvent is removed *in vacuo*, and the solids are extracted with 1 M HCl(aq) and filtered to give a total solution volume of 10 mL. From this solution, a 200 μL aliquot is analyzed for the presence of NH_3 (present as NH_4Cl) by the indophenol method.¹² Quantification was performed with UV-vis spectroscopy by analyzing the absorbance at 635 nm using a calibration curve.¹³ A further 200 μL aliquot of this solution was analyzed for the presence of N_2H_4 (present as $\text{N}_2\text{H}_5\text{Cl}$) by a standard colorimetric method.¹⁴ Quantification was performed with UV-vis spectroscopy by analyzing the absorbance at 458 nm using a calibration curve.¹⁵ For the catalytic run conducted under $^{15}\text{N}_2$, the solid residue remaining after quenching with HCl in Et_2O was extracted into $\text{DMSO}-d_6$ and analyzed by $^{15}\text{N}\{^1\text{H}\}$ NMR spectroscopy.

The presence of HMPA in catalytic reaction mixtures was found to interfere with the indophenol method for ammonia quantification. An alternative procedure was therefore employed to quantify ammonia from reactions with HMPA. A Schlenk tube is charged with HCl (3 mL of a 2.0 M solution in Et_2O , 6 mmol) to serve as a collection flask. The

volatiles of the reaction mixture are vacuum transferred at RT into this collection flask.

After completion of the vacuum transfer, the collection flask is sealed and warmed to RT. Solvent is removed *in vacuo*, and the remaining residue is dissolved in 0.7 mL of DMSO-*d*₆ containing 1,3,5-trimethoxybenzene as an internal standard. The ¹H NMR signal observed for NH₄⁺ is then integrated against the two peaks of trimethoxybenzene to quantify the ammonium present.

B2.3 Me₂NNH₂/Me₂NH Generation and Quantification Procedure

All solvents are stirred with Na/K for ≥ 2 hours and filtered over activated alumina prior to use. In a nitrogen-filled glovebox, a Schlenk tube is charged with the Sm^{II} reductant as a solid (15.3 mg, 19 μ mol). The tube is chilled in a glovebox cold well immersed in a dry ice/acetone bath and allowed to equilibrate for 10 minutes. To the chilled tube is added 1 mL of a room temperature solution of PH in toluene (15 mM, 15 μ mol) via syringe. The contents of the tube are stirred and warmed for five minutes to dissolve the reductant. The tube is again chilled at -78°C for 10 minutes. A 10 mM solution of FeNNMe₂ is similarly chilled. A 0.5 mL aliquot of this solution (5 μ mol) is added, the tube is sealed, and the mixture is allowed to stir for 5 minutes, at which point Sm^{II}-PH is fully consumed as judged by the disappearance of its dark green color. The tube is then frozen in liquid nitrogen. A solution of NaO^tBu in MeOH (1 mL of a 0.2 M solution, 0.2 mmol) is added along the walls of the tube. The tube is resealed and the headspace is evacuated. The mixture is allowed to warm and stir at room temperature for 20 minutes. A second Schlenk tube is charged with HCl (3 mL of a 2.0 M solution in Et₂O, 6 mmol) to serve as a collection flask. The volatiles of the quenched reaction mixture are vacuum transferred at RT into this collection flask. After completion of the vacuum transfer, the collection flask is sealed and

warmed to RT. Solvent is removed *in vacuo*, and the remaining residue is dissolved in²⁵⁰ 0.6 mL of CD₃OD containing 1,3,5-trimethoxybenzene as an internal standard. The ¹H NMR signals observed for the methyl protons of Me₂NH₂⁺ (2.70 ppm) and Me₂NNH₃⁺ (2.91 ppm) are then integrated against the methyl peak of trimethoxybenzene to quantify their production.

B3 NMR Spectroscopy

B3.1 Procedure for Quantification of Sm-containing Byproducts of Catalysis

The procedure for catalytic N_2H_4 generation (S2.1) is followed to carry out the reaction of Sm^{II} (50 mg, 0.061 mmol), PH (1 mL of a 48 mM solution in toluene, 0.048 mmol), and FeN_2 (0.5 mL of a 1 mM solution in toluene, 0.5 μmol) with N_2 (1 atm) at -78°C in a glovebox cold well. Instead of analyzing fixed-N products, the volatiles of the reaction mixture are removed *in vacuo*. The remaining residue is extracted with 3 \sim 1 mL portions of pentane and filtered over celite to a total solution volume of 3.3 mL. A 1 mL aliquot of this solution is transferred to a vial containing 2.2 mg (0.013 mmol) of 1,3,5-trimethoxybenzene as an internal standard and solvent is removed *in vacuo*. The residue is taken up in C_6D_6 and analyzed by ^1H NMR.

B3.1 Procedure for NMR Titrations

CD_3CN was passed 5 times over activated alumina before use. An NMR signature for $[\text{Sm}^{\text{III}} - \text{CF}_3\text{PH}]\text{PF}_6$ was first obtained as follows:³ $[\text{Sm}^{\text{III}}]\text{PF}_6$ was dissolved in 0.7 mL of a 7.5 mM CD_3CN solution of 1,3,5-trimethoxybenzene (tmb) as an internal standard and added to a J. Young NMR tube. An initial NMR was taken to verify purity and then aliquots of CF_3PH were added to the tube from a stock solution (535 mM) which also contained 7.5 mM tmb until resonances corresponding to the aryl and ^tBu protons of the Sm complex no longer shifted with increasing $[\text{CF}_3\text{PH}]$, indicating saturation.

To bracket the acidity of $[\text{Sm}^{\text{III}} - \text{CF}_3\text{PH}]\text{PF}_6$, aliquots of $^i\text{Pr}_2\text{NH}$ were added to the tube from a stock solution (1.1 M) which also contained 7.5 mM tmb.

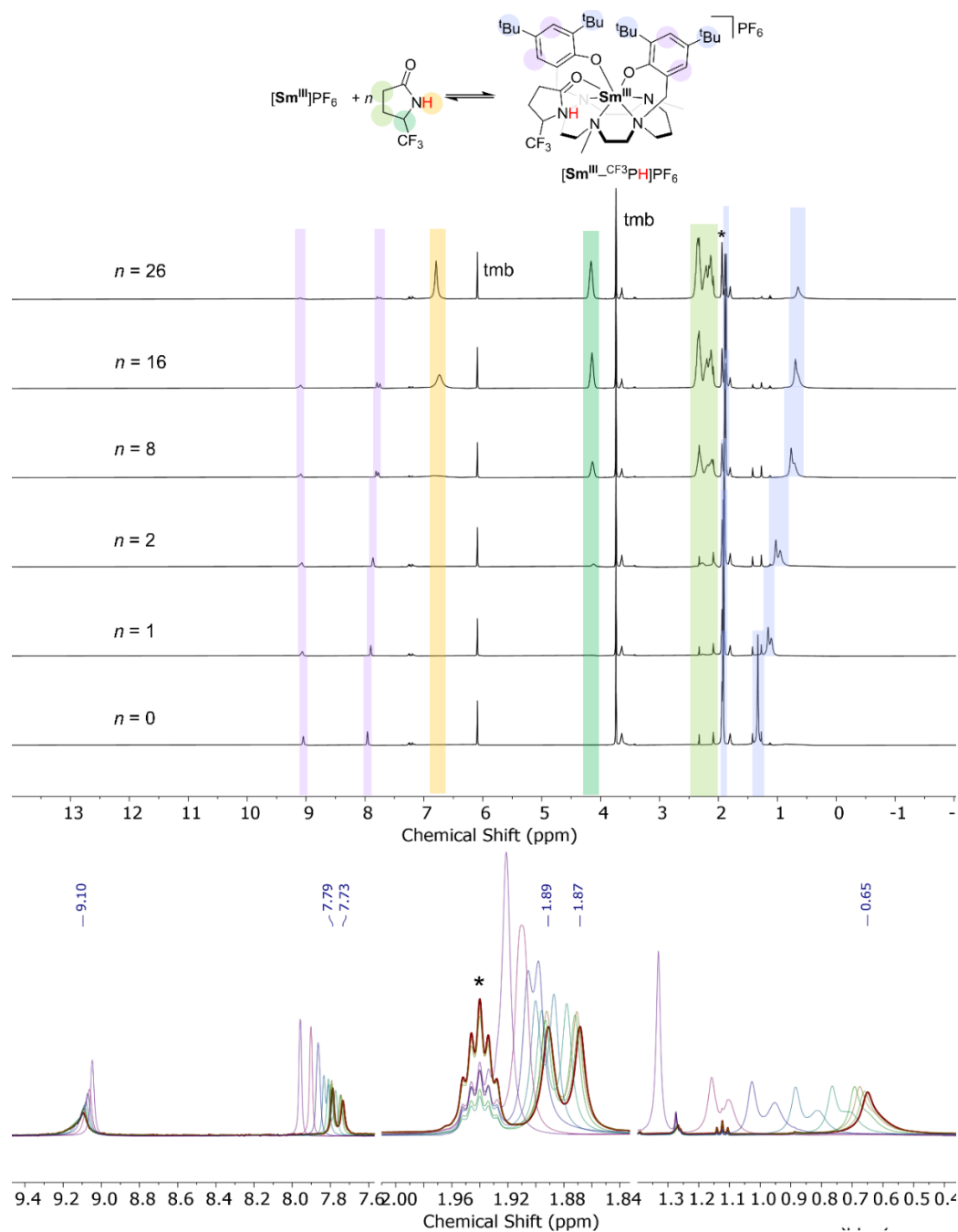


Figure B1. ^1H NMR (CD_3CN , 400 MHz) spectra of $[\text{Sm}^{\text{III}}]\text{PF}_6$ (8.5 mM) with varying amounts of CF_3PH (1-26 equiv). Select regions of the overlaid spectra (lower panel) show the shift in the aryl and tBu peaks of the Sm complex with increasing CF_3PH ; the final picked peaks are assigned to a C_1 -symmetric $[\text{Sm}^{\text{III}}\text{-CF}_3\text{PH}]\text{PF}_6$ adduct. * = CD_3CN solvent residual

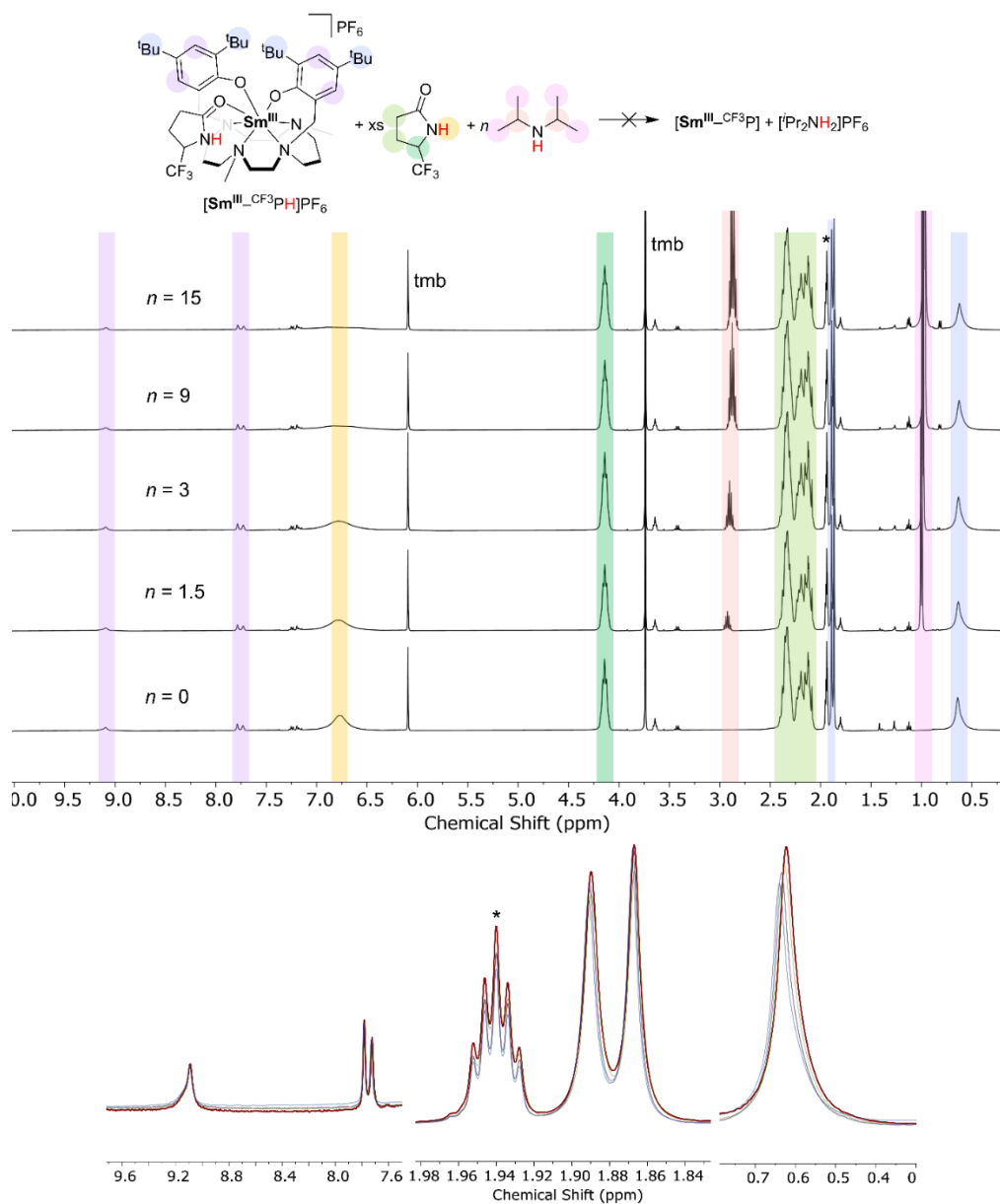


Figure B2. ^1H NMR (CD_3CN , 400 MHz) spectra of $[\text{Sm}^{\text{III}}\text{-CF}_3\text{PH}]\text{PF}_6$ (8.5 mM, formed *in situ* by addition of 26 equiv CF_3PH to $[\text{Sm}^{\text{III}}]\text{PF}_6$) with varying amounts of $t\text{Pr}_2\text{NH}$ (1.5-15 equiv). Select regions of the overlaid spectra (lower panel) show that the aryl and $t\text{Bu}$ resonances are essentially unperturbed by addition of the base ($\text{p}K_{\text{a}} = 18.8$ in MeCN), consistent with a conservative lower bound of > 20 for the $\text{p}K_{\text{a}}$ of $[\text{Sm}^{\text{III}}\text{-CF}_3\text{PH}]\text{PF}_6$ in CH_3CN . * = CD_3CN solvent residual

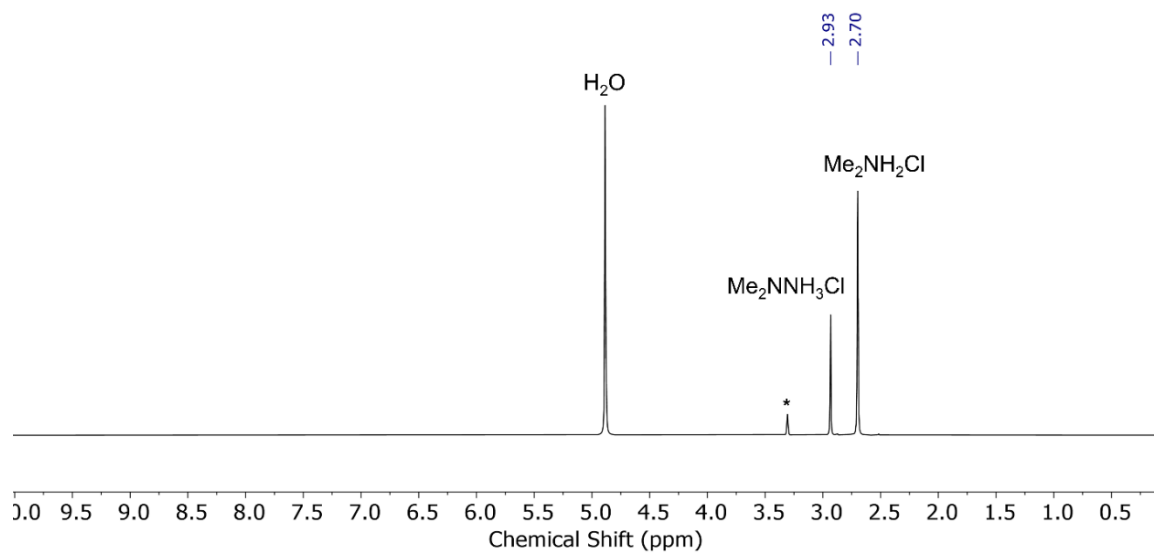


Figure B3. ^1H NMR (CD_3OD , 400 MHz) spectrum of $\text{Me}_2\text{NNH}_3\text{Cl}$ and $\text{Me}_2\text{NH}_2\text{Cl}$. * = CD_3OD solvent residual

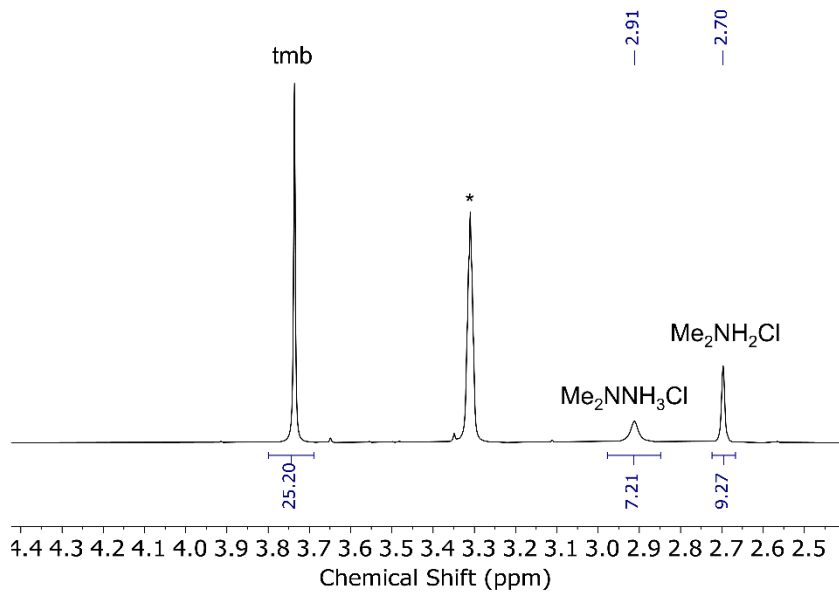


Figure B4. ^1H NMR (CD_3OD , 400 MHz) spectrum of $\text{Me}_2\text{NNH}_3\text{Cl}$ and $\text{Me}_2\text{NH}_2\text{Cl}$ (2.70 ppm) generated from the reaction of $\text{P}_3^{\text{B}}\text{FeNNMe}_2$, Sm^{II} (3 equiv), and PH (3 equiv) in toluene at -78°C . The methyl resonances of the products are integrated relative to the methyl resonance of 1,3,5-trimethoxybenzene as an internal standard (4.7 mM) to determine yields of 25% and 30%, respectively. * = CD_3OD solvent residual

B4 EPR Spectroscopy

B4.1 General Procedure for Preparation of Freeze-quench EPR Samples of Catalytic Reaction Mixtures

The procedure for catalytic N_2H_4 generation (S2.1) is followed to carry out the reaction of Sm^{II} (50 mg, 0.061 mmol), PH (1 mL of a 48 mM solution in toluene, 0.048 mmol), and FeN_2 (0.5 mL of a 3 mM solution in toluene, 1.5 μmol) with N_2 (1 atm) at -78°C in a glovebox cold well. A timer is set to zero as soon as the precatalyst is added to the reaction. At the desired time, the septum is removed from the flask and a pipet which has been chilled at -78°C is used to transfer a ~ 0.2 mL aliquot of the reaction mixture into a similarly chilled EPR tube. The EPR sample is then frozen in $\text{N}_{2(l)}$. The sample is quickly transferred out of the glovebox and put into $\text{N}_{2(l)}$ before it can warm.

B4.1 General Procedure for Preparation of EPR Samples of the Reaction of Fe Complexes with Sm^{II} Reductants

All manipulations are carried out inside of a nitrogen-filled glovebox, and all samples are prepared with a final $[\text{Fe}]$ of 2 mM. For experiments using Sm^{II} , 0.5 mL of a 4.2 or 12.6 mM solution of Sm^{II} (2.1 or 6.3 μmol) is transferred to a scintillation vial with a stirbar and cooled to -78°C in a glovebox cold well. Aliquots of a stock solution of PMe or PH are then added to achieve the desired ratio of $\text{Sm}^{\text{II}}:\text{PMe}/\text{H}$. For experiments using 10 equiv $\text{SmI}_2(\text{THF})_2$ per Fe, the reductant (11 mg, 20 μmol) is weighed in a scintillation vial. A stir bar, 0.5 mL of solvent, and the desired amount of HMPA is added and the mixture is stirred at r.t. until homogeneous. It is then cooled to -78°C in a glovebox cold well. A similarly cooled solution of the Fe complex (0.5 mL of a 4 mM solution, 2 μmol) is then added. The mixture is allowed to stir for ~ 5 min and then an aliquot is transferred to a chilled EPR tube

using a chilled pipet. The sample is then frozen in $N_{2(l)}$, quickly transferred out of the ²⁵⁷
glovebox, and put into $N_{2(l)}$ before it can warm.

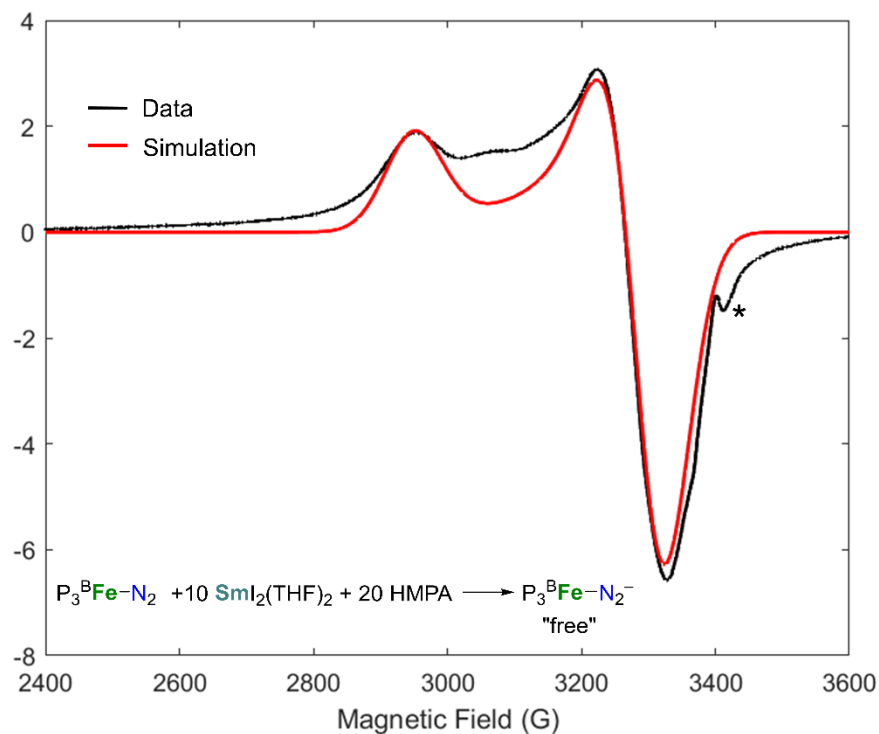


Figure B5. CW X-band EPR spectrum (toluene, 77K; MW frequency = 9.43 GHz; MW power = 2 mW) following the reaction of FeN_2 (2 mM) with 10 equiv $\text{SmI}_2(\text{THF})_2$ and 20 equiv HMPA. The simulated spectrum ($g = [2.285 \ 2.052 \ 2.032]$) is consistent with “free” FeN_2^- as the dominant reduced species.¹⁷ A small amount of a second, unidentified species is generated in this reaction (*).

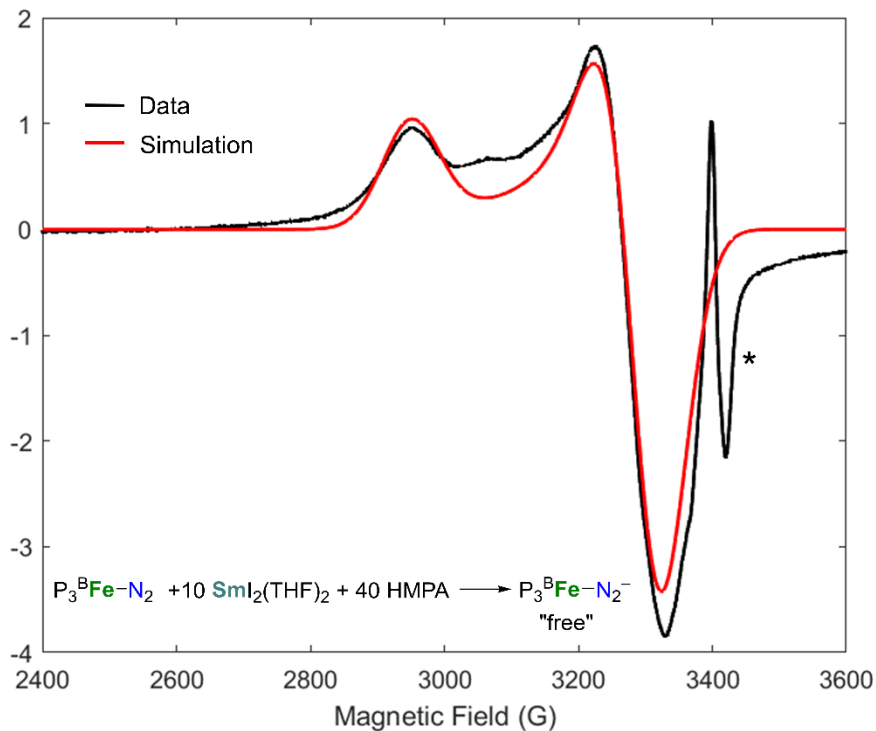


Figure B6. CW X-band EPR spectrum (toluene, 77K; MW frequency = 9.43 GHz; MW power = 2 mW) following the reaction of FeN_2 (2 mM) with 10 equiv $\text{SmI}_2(\text{THF})_2$ and 40 equiv HMPA. The simulated spectrum ($g = [2.285 \ 2.052 \ 2.032]$) is consistent with “free” FeN_2^- as the dominant reduced species.¹⁷ A larger amount of a second, unidentified species (*) is generated in this reaction than in the reaction with 20 equiv HMPA. Only one N_2 stretch is observed by IR in the products of these reactions, suggesting that the unidentified species is not an $[\text{FeN}_2]$ complex.

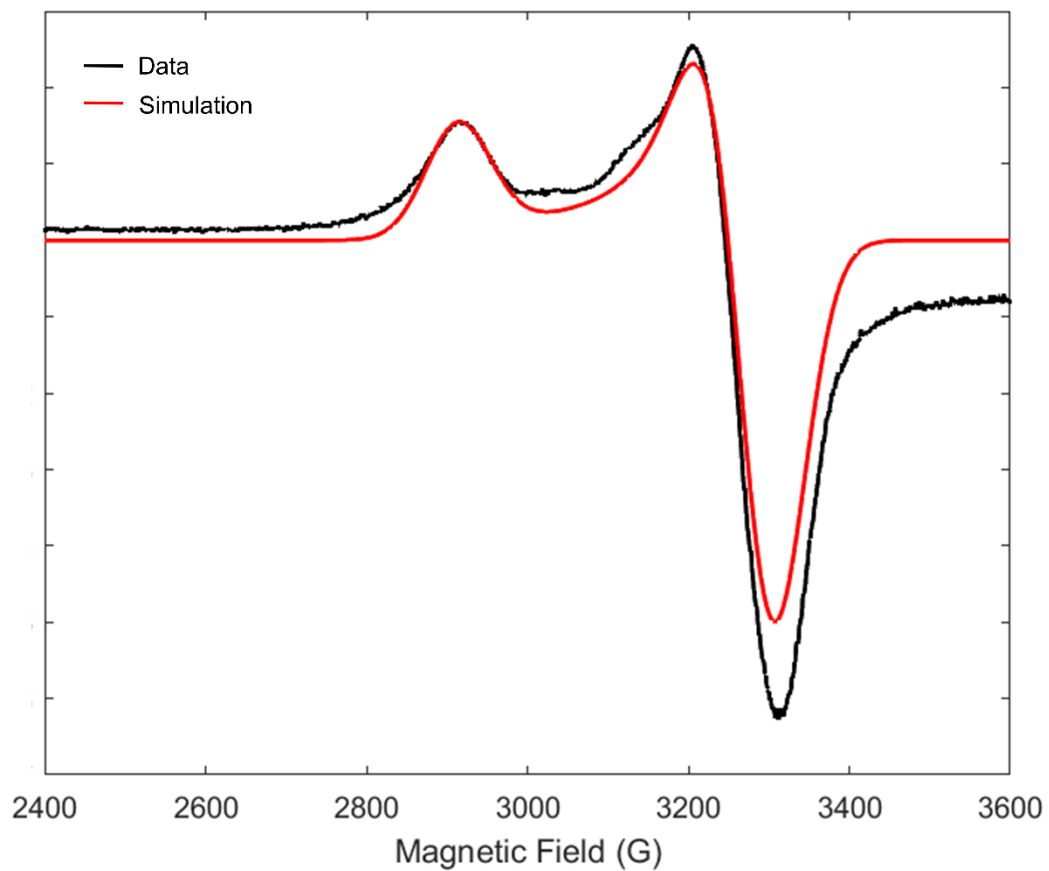


Figure B7. CW EPR spectrum (2-MeTHF, 77K) following the reaction of FeN_2 (2 mM) with 1 equiv Sm^{II} . The simulated spectrum ($g = [2.297 \ 2.053 \ 2.023]$) is consistent with “free” FeN_2^- as the dominant reduced species in coordinating solvent.¹⁷

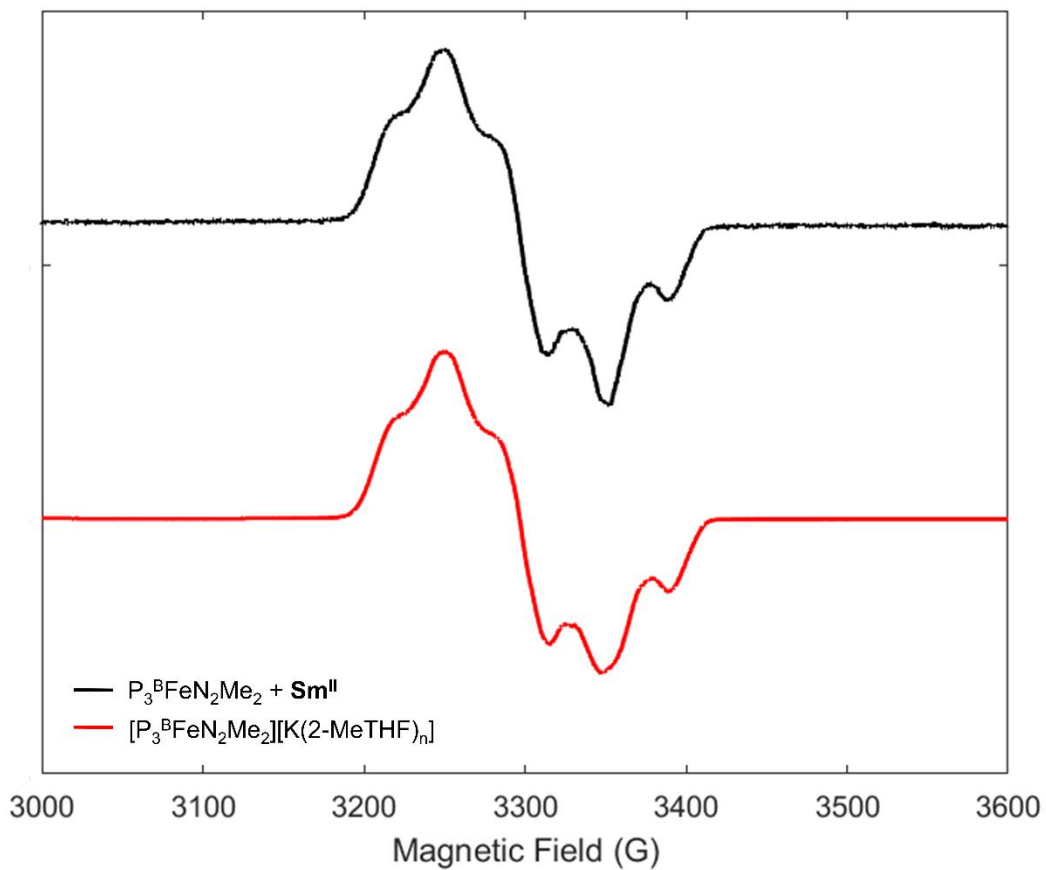


Figure B8. CW EPR spectrum (2-MeTHF, 77K, MW frequency = 9.43 GHz; MW power = 2 mW) following the reaction of FeN_2Me_2 (2 mM) with 1 equiv Sm^{II} (black). The observed spectrum is consistent with the reported spectrum of $[FeN_2Me_2][K(2-MeTHF)_n]$ in 2-MeTHF (red).

B5.1 General Procedure for Preparation of Freeze-quench Mössbauer Samples of Catalytic Reaction Mixtures

The procedure for catalytic N_2H_4 generation (S2.1) is followed to carry out the reaction of Sm^{II} (50 mg, 0.061 mmol), PH (1 mL of a 48 mM solution in toluene, 0.048 mmol), and $^{57}\text{FeN}_2$ (0.5 mL of a 3 mM solution in toluene, 15 μmol) at -78°C in a glovebox cold well. A timer is set to zero as soon as the precatalyst is added to the reaction. At the desired time, the septum is removed from the flask and a pipet which has been chilled at -78°C is used to transfer the reaction mixture into a similarly chilled Delrin cup. The sample in the cup is then frozen in $\text{N}_{2(l)}$. The sample is quickly transferred out of the glovebox and put into $\text{N}_{2(l)}$ before it can warm and is then mounted in the cryostat.

B5.2 Procedure for Preparation of Mössbauer Sample of the Reaction of FeN_2 with Sm^{II}

All manipulations are carried out inside of a nitrogen-filled glovebox. A solution of $^{57}\text{FeN}_2$ (1 mg, 1.5 μmol) in 0.5 mL toluene in a vial with a stir bar and a solution of Sm^{II} (2 mg, 2.5 μmol) in 1 mL toluene are cooled at -78°C in a glovebox cold well. The Sm^{II} solution is added to the $^{57}\text{FeN}_2$ and the mixture is stirred for 5 minutes. It is then transferred to a precooled Delrin cup. The sample in the cup is then frozen in $\text{N}_{2(l)}$. The sample is quickly transferred out of the glovebox and put into $\text{N}_{2(l)}$ before it can warm and is then mounted in the cryostat.

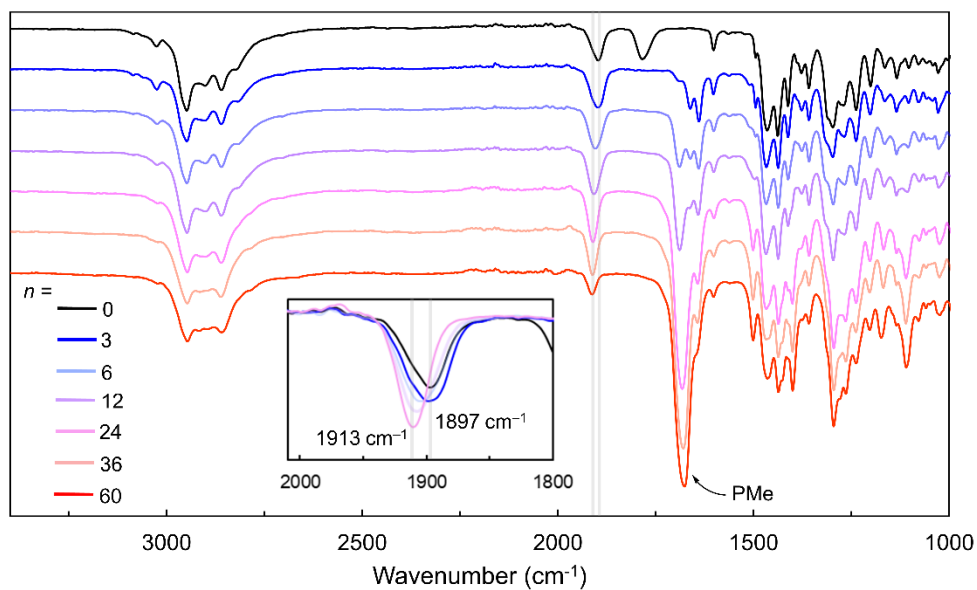


Figure B9. Full IR spectra (thin films deposited from room temperature toluene solutions) of the reaction of FeN_2 with 3 equiv Sm^{II} and n equiv PMe. The inset highlights the shift in ν_{NN} from 1897 to 1913 cm^{-1} between $\text{FeN}_2\text{-Sm}^{\text{III}}$ (dominant at low n) and $[\text{FeN}_2][\text{Sm}^{\text{III}}]$ (dominant at low n).

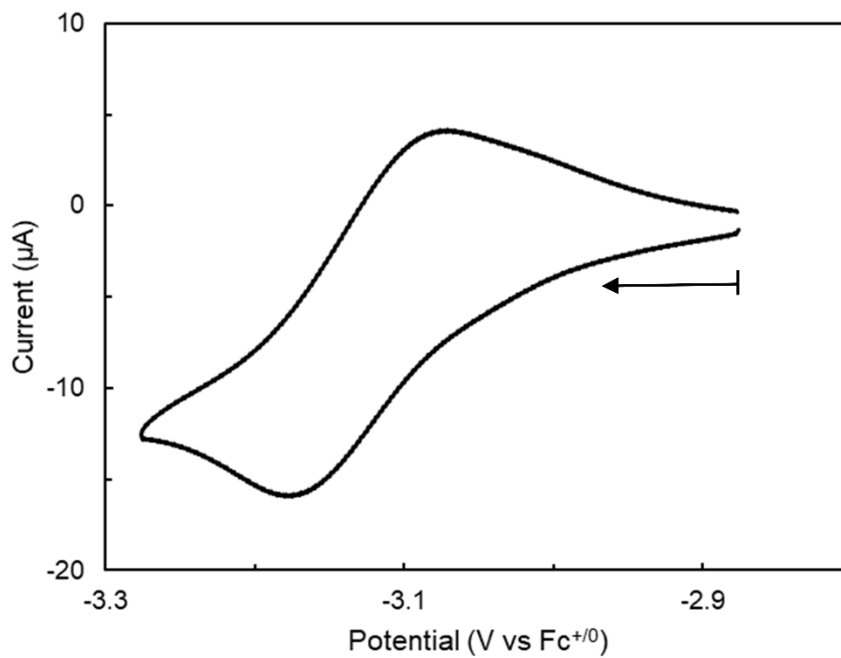


Figure B10. CV of FeN_2 (1 mM) in DME (0.2 M $t\text{Bu}_4\text{NPF}_6$) in a window showing the FeN_2^{-2-} couple at -3.1 V vs $\text{Fc}^{+/0}$. The scan began at -2.85 V vs $\text{Fc}^{+/0}$ and swept negative (100 mV s^{-1}).

B8 H/D Isotope Effect**Table B1.** Catalysis with variable acid (0.5 $\mu\text{mol FeN}_2$, toluene, -78°C , 12 h)

Entry	Acid (equiv)	Reductant (equiv)	equiv NH_3 (%)	equiv N_2H_4 (%)	Total Fixed-N % Yield
1	PH (96)	Sm^{II} (120)	0.76 ± 0.03 (2.4 ± 0.1)	16 ± 3 (64 ± 11)	67 ± 11
2	MeOH (96)	Sm^{II} (120)	2.4 ± 0.6 (8 ± 2)	6.3 ± 0.2 (26.1 ± 0.6)	34 ± 1
3	PD (96)	Sm^{II} (120)	1.0 ± 0.2 (3.1 ± 0.6)	12.1 ± 0.5 (50 ± 2)	53 ± 3
4	CD_3OD (96)	Sm^{II} (120)	5.7 ± 0.1 (17.8 ± 0.3)	7.7 ± 0.5 (32 ± 2)	50 ± 2

B8.1 Discussion of Isotope Effect

Deuteration of the acid sources in the catalytic reactions reveals an H/D isotope effect on the selectivity of the N_2R . The $\text{N}_2\text{H}_4:\text{NH}_3$ ratio with PH ($(21 \pm 4):1$ at 96 equiv acid loading) drops to $(12 \pm 2.5):1$ with PD. Similarly, the $\text{N}_2\text{H}_4:\text{NH}_3$ ratio with MeOH ($(2.6 \pm 0.7):1$) drops to $(1.4 \pm 0.1):1$ with CD_3OD . These data suggest that while stronger acids favor the NH_3 -evolving pathway, the N_2H_4 -evolving pathway has a higher primary H/D isotope effect than the NH_3 pathway. We note that this observation has many possible reasonable interpretations. As just one example, a plausible N_2H_4 -evolving pathway is given by A in Figure B11, which comprises preequilibrium ET to FeNNH_2 to form $[\text{FeNNH}_2][\text{Sm}^{\text{III}}\text{-EH}]$ followed by irreversible PT to N_α . This path might be expected to have a larger isotope effect (equivalent to the KIE of the PT step) than the NH_3 -evolving pathway shown in B, which comprises preequilibrium PT to N_β of FeNNH_2 , followed by N–N bond cleavage (the isotope effect would be equivalent to the EIE of the preequilibrium PT step). It is worth noting that these results bear similarity to observations in oxygen

reduction literature: stronger acids promote O–O bond cleavage in $\text{Fe}^{\text{III}}\text{-O-OH}^{266}$ complexes via protonation of O_β to form H_2O , and a small inverse H/D isotope effect has been observed for this reaction.¹⁶

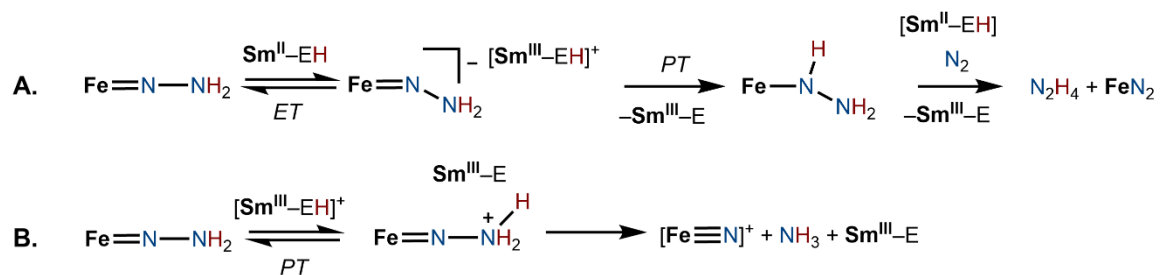


Figure B11: Possible pathways consistent with observed H/D isotope effect on N_2H_4 vs NH_3 selectivity.

REFERENCES

- (1) Maria, L.; Santos, I. C.; Alves, L. G.; Marçalo, J.; Martins, A. M. Rare earth metal complexes anchored on a new dianionic bis(phenolate)dimethylaminecyclam ligand. *J. Organomet. Chem.* **2013**, *728*, 57–67.
- (2) Maria, L.; Soares, M.; C. Santos, I.; R. Sousa, V.; Mora, E.; Marçalo, J.; V. Luzyanin, K. A novel samarium(II) complex bearing a dianionic bis(phenolate)cyclam ligand: synthesis, structure and electron-transfer reactions. *Dalton Trans.* **2016**, *45* (9), 3778–3790.
- (3) Sheldrick, G. M. A short history of SHELX. *Acta Crystallogr. A* **2008**, *64* (1), 112–122.
- (4) Dolomanov, O. V.; Bourhis, L. J.; Gildea, R. J.; Howard, J. A. K.; Puschmann, H. *OLEX2*: a complete structure solution, refinement and analysis program. *J. Appl. Crystallogr.* **2009**, *42*, 339.
- (5) Bolton, S. L.; Schuehler, D. E.; Niu, X.; Gopal, L.; Sponsler, M. B. Olefin metathesis for metal incorporation: Preparation of conjugated ruthenium-containing complexes and polymers. *J. Organomet. Chem.* **2006**, *691* (24), 5298–5306.
- (6) Lan, X.; Wang, X.; Zhang, D. X.; Mu, T.; Lan, X. Z. Cation and anion transfer in quinuclidinium hexafluorophosphate plastic crystal: Role of constituent ions and the crystalline structure. *J. Phys. Chem. C* **2021**, *125* (38), 21169–21178.
- (7) Atifi, A.; Boyce, D. W.; DiMeglio, J. L.; Rosenthal, J. Directing the outcome of CO₂ reduction at bismuth cathodes using varied ionic liquid promoters. *ACS Catal.* **2018**, *8* (4), 2857–2863.

- (8) Casey, K. C.; Brown, A. M.; Robinson, J. R. Yttrium and lanthanum bis(phosphine-oxide)methanides: structurally diverse, dynamic, and reactive. *Inorg. Chem. Front.* **2021**, 8 (6), 1539–1552.
- (9) Savéant, J.-M. *Elements of Molecular and Biomolecular Electrochemistry*; John Wiley & Sons, Inc: Hoboken, New Jersey, 2006.
- (10) Kolmar, S. S.; Mayer, J. M. $\text{SmI}_2(\text{H}_2\text{O})_n$ reduction of electron rich enamines by proton-coupled electron transfer. *J. Am. Chem. Soc.* **2017**, 139 (31), 10687–10692.
- (11) Chciuk, T. V.; Flowers, R. A. Proton-coupled electron transfer in the reduction of arenes by SmI_2 –water complexes. *J. Am. Chem. Soc.* **2015**, 137 (35), 11526–11531.
- (12) Chciuk, T. V.; Li, A. M.; Vazquez-Lopez, A.; Anderson, W. R.; Flowers, R. A. Secondary amides as hydrogen atom transfer promoters for reactions of samarium diiodide. *Org. Lett.* **2017**, 19 (1), 290–293.

SUPPLEMENTARY INFORMATION FOR CHAPTER 4

Reproduced in part with permission from [Boyd, E.A.](#); Shin, C.; Charboneau, D. J.; Peters, J. C.; Reisman, S.E. *Science* **2024**, 385, 847. doi: 10.1126/science.adp5777

C1 Experimental Part**C1.1 General Considerations**

All manipulations were carried out using standard Schlenk or glovebox techniques under an N₂ atmosphere. Unless otherwise noted, solvents were deoxygenated and dried by thoroughly sparging with N₂ gas followed by passage through an activated alumina column in the solvent purification system by SG Water, USA LLC. 2-MeTHF purchased as anhydrous grade from Millipore Sigma and stored in N₂-filled glovebox. Samarium(III) trifluoromethanesulfonate [Sm(OTf)₃], samarium(III) isopropoxide [Sm(OⁱPr)₃], and magnesium iodide were purchased from Sigma–Aldrich. Zinc powder was purchased from Strem Chemicals. Bis(trifluoromethane)sulfonimide (HNTf₂), 1-Butyl-1-methylpyrrolidinium bis(trifluoromethane)sulfonimide (BMPyNTf₂), and 1-Butyl-1-methylpiperidinium (BMPipNTf₂) were purchased from TCI chemicals. Unless otherwise stated, all reagents were used as received. **1h**,¹ **1i**,² **1w**,³ and **1ab**⁴ were synthesized by reported literature procedures. Full characterization data of all organic products is available at doi: 10.1126/science.adp5777.

C1.2 Nuclear Magnetic Resonance (NMR) Spectroscopy

Deuterated solvents were purchased from Cambridge Isotope Laboratories, Inc. ¹H chemical shifts are reported in ppm relative to tetramethylsilane, using residual solvent resonances as internal standards.⁵

C1.3 Electrochemistry

All electrochemical experiments were conducted using a CH instruments 600B electrochemical analyzer. A nonaqueous Ag^{+0} reference electrode (BASi) consisting of a silver wire immersed in 5 mM AgOTf in DME containing 0.2 M $n\text{Bu}_4\text{NPF}_6$ separated from the working solution by a CoralPor® frit was used for all experiments. All reported potentials are referenced to the ferrocenium/ferrocene (Fc^{+0}) couple used as an external standard. All CVs were carried out in an N_2 -filled glovebox in a 20 mL scintillation vial fitted with a septum cap containing punched-out holes for insertion of electrodes. A glassy carbon disk (3 mm diameter) was used as the working electrode for all CVs. It was freshly polished with 1, 0.3, and 0.05 μm alumina powder water slurries, rinsed with water and acetone, and dried before use. A platinum wire was used as the auxiliary electrode for CVs. CVs are plotted using IUPAC convention. Unless otherwise noted, IR compensation was applied accounting for 85% of the total resistance.

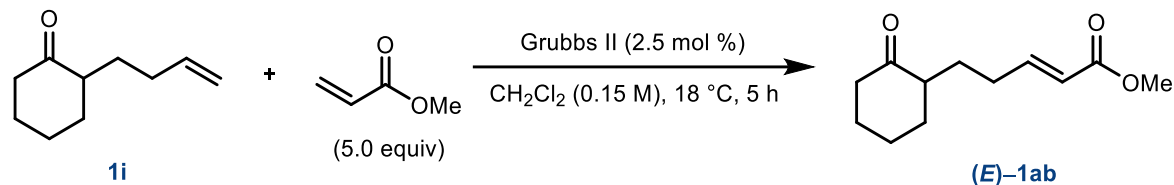
C1.4 UV-Visible Absorption Spectroscopy

UV-visible absorption spectra were collected on a Cary 50 spectrophotometer using a 1 cm quartz cell sealed with a Teflon stopcock.

C2 Synthetic Procedures

C2.1 Synthesis of substrates and reagents

Synthesis of methyl (E)-5-(2-oxocyclohexyl)pent-2-enoate ((E)-1ab)



To a N₂-filled 20 mL scintillation vial charged with Grubbs 2nd generation catalyst (25.5 mg, 0.030 mmol, 0.025 equiv) was added a solution of 2-(but-3-en-1-yl)cyclohexan-1-one (0.183 g, 1.2 mmol, 1.0 equiv) and methyl acrylate (0.517 g, 6.0 mmol, 5.0 equiv) in CH₂Cl₂ (8 mL). The vial was capped with a septum and stirred for 5 h with a N₂ balloon placed on top. Upon completion, saturated NH₄Cl (10 mL) was added to the reaction mixture and extracted with CH₂Cl₂ (3 x 10 mL). The combined organic layer was dried with MgSO₄ and concentrated under reduced pressure. The resulting crude residue was purified via flash chromatography over silica gel (5% → 20% gradient EtOAc/Hexane) to give (**E**)-**1ab** as colorless oil (187 mg, 74% yield).

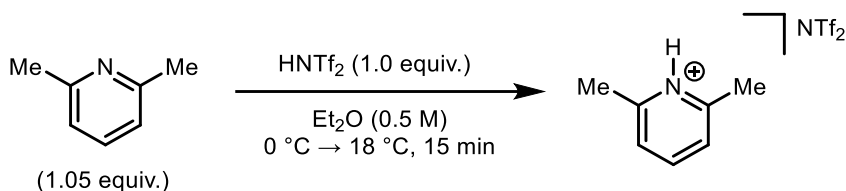
Preparation of SmI₂ solutions

Prior to setup, finely ground samarium metal was prepared from Sm ingot purchased from Sigma Aldrich. Diiodoethane was dissolved in Et₂O and washed with saturated solution of Na₂S₂O₃. The organic layer was concentrated and dried under vacuum for at least 2 h to obtain white powder.

To an oven-dried N₂-filled Schlenk flask charged with finely ground samarium metal (0.211 g, 1.40 mmol, 1.75 equiv) was added dry, deoxygenated solvent (THF or 2-MeTHF, 8 mL), followed by diiodoethane (0.225 g, 0.80 mmol, 1.0 equiv). The reaction was stirred

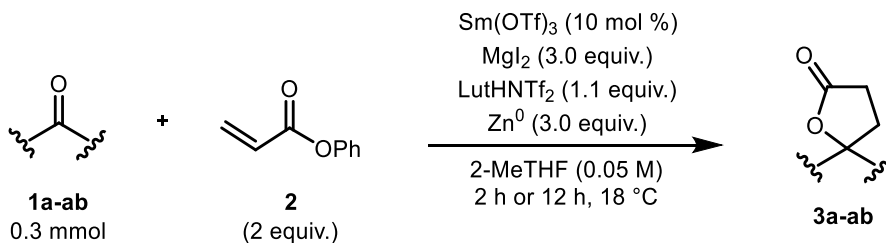
for at least 6 h at room temperature to obtain deep blue (THF) or purple (2-MeTHF)²⁷² solution. The solution was settled for at least 5 min prior to use.

General procedure for synthesis of base HNTf_2



The base was passed through neutral alumina prior to reaction unless a new, colorless batch was used. To a 50 mL round-bottom flask charged with a magnetic stir bar were added bis(trifluoromethane)sulfonimide (5.05 g, 18.0 mmol, 1.0 equiv) and Et_2O (30 mL) to give a biphasic mixture. The reaction was cooled to $0\text{ }^\circ\text{C}$ using ice bath, and a solution of 2,6-lutidine (2.12 g, 19.8 mmol, 1.1 equiv) in Et_2O (6 mL) was added dropwise over 3 min. Ice bath was removed, and the reaction was allowed to stir for 15 min. The reaction still stayed a biphasic mixture. The top organic layer was decanted off, and the remaining bottom layer was washed with hexane (3 x 25 mL) and concentrated under reduced pressure to give colorless ionic liquid as a crude product. The ionic liquid was dried under vacuum for at least 12 h. Crystallization was induced either by cooling the product to $-30\text{ }^\circ\text{C}$ for 5 min or by spatula to give LutHNTf_2 as white solid (6.97 g, 94% yield).

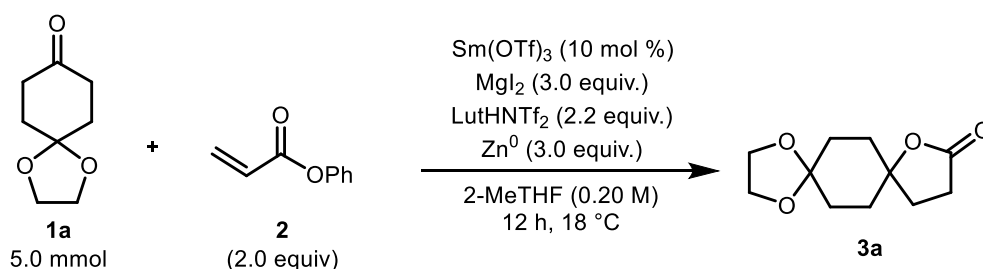
C2.2 General procedure for Sm-catalyzed reaction with Zn^0



To a 20 mL scintillation vial charged with a magnetic stir bar and a mixture of samarium(III) trifluoromethanesulfonate (17.9 mg, 0.030 mmol, 0.10 equiv), magnesium iodide (250 mg, 0.90 mmol, 3.0 equiv), zinc powder (58.8 mg, 0.90 mmol, 3.0 equiv),

LutHNTf₂ (128 mg, 0.33 mmol, 1.1 equiv) and ketone substrate (*if solid*, 0.30 mmol, 1.0²⁷⁴ equiv) were added 2-MeTHF (6 mL), ketone substrate (*if liquid*, 0.30 mmol, 1.0 equiv) and phenyl acrylate (88.9 mg, 0.60 mmol, 2.0 equiv) in a sequential order. The reaction mixture was then stirred at room temperature for 2 h (*if aromatic ketones*) or 12 h (*if aliphatic ketones*). Upon completion, the reaction mixture was diluted with CH₂Cl₂ (20 mL) and saturated NH₄Cl (20 mL). The mixture was then extracted with CH₂Cl₂ (3 x 20 mL). The combined organic layer was dried with Na₂SO₄, concentrated under reduced pressure and purified by flash column chromatography using silica gel (*specific conditions specified with characterization data*) to give final product.

C2.3 General procedure for mmol scale reaction at 0.20 M



The reaction was setup under N₂-filled atmosphere. To a 50-mL round-bottom flask charged with a mixture of samarium(III) trifluoromethanesulfonate (0.299 g, 0.50 mmol, 0.10 equiv) and magnesium iodide (4.17 g, 15.0 mmol, 3.0 equiv) was added 2-MeTHF (25 mL, 0.20 M). The reaction mixture was heated at 40 °C until all solids are dissolved. Once it's cooled to room temperature, zinc powder (0.981 g, 15.0 mmol, 3.0 equiv), 1,4-cyclohexanedione monoethylene acetal **1a** (0.781 g, 5.0 mmol, 1.0 equiv), phenyl acrylate (1.48 g, 10.0 mmol, 2.0 equiv) and LutHNTf₂ (4.27 g, 11.0 mmol, 2.2 equiv) were added in a sequential order. The reaction was then stirred for 12 h. Upon completion, the reaction mixture was quenched with air until the solution turns yellow, followed by the addition of

CH₂Cl₂ (100 mL) and saturated NH₄Cl (100 mL). The reaction mixture was extracted²⁷⁵ with CH₂Cl₂ (3 x 100 mL). The combined organic layer was dried with Na₂SO₄ and concentrated under reduced pressure. The resulting crude residue was purified by flash column chromatography over silica gel (10% → 40% gradient EtOAc/Hexane) to give **3a** as white solid (0.821 g, 77% yield).

C2.4 General procedure for stoichiometric reactions

To a N₂-filled 1-dram vial charged with a solution of substrate (0.05 mmol, 1 equiv) and methanol (3.2 mg, 0.10 mmol, 2.0 equiv) in THF (0.5 mL) was added SmI₂ solution (1.25 mL, 0.10 M, 2.5 equiv). After 1 h of stirring, CH₂Cl₂ (3 mL) and saturated NH₄Cl (3 mL) was added. The reaction was then extracted with CH₂Cl₂ (3 x 3 mL), dried with Na₂SO₄ and concentrated under reduced pressure. The resulting crude residue was purified by flash column chromatography over silica gel (*specific column condition specified with characterization data*) to give final product.

C2.5 General procedure for controlled potential electrolysis

CPE experiments were carried out in a gas-tight two compartment cell (**Fig. S15**) assembled in an N₂-filled glovebox. Plain carbon cloth (AvCarb) was cut to 1 cm x 4 cm pieces. The Zn counter electrode was polished with a stainless-steel sponge and washed repeatedly with water and acetone. The glassy carbon plate electrode was polished with 1, 0.3, and 0.05 μm alumina powder water slurries, and rinsed with water and acetone. All electrodes were dried in a vacuum oven for > 6 hours before use.

In a typical experiment, a solution of BMPyNTf₂ (0.2 M) in 2-MeTHF was prepared and dried by passing over a column of activated alumina. Sm(OTf)₃ (6.0 mg, 0.01 mmol, 0.1 equiv), MgI₂ (69.0 mg, 0.25 mmol, 2.5 equiv), the ketone substrate (*if solid*, 0.10 mmol, 1.0 equiv), and LutHNTf₂ (77.7 mg, 0.20 mmol, 2.0 equiv) were dissolved in 5 mL of the electrolyte solution and added to the working compartment of the cell. HEH₂ (51.0 mg, 0.20 mmol, 2 equiv) was dissolved in 5 mL of the electrolyte solution and added to the counter compartment. The ketone substrate (*if liquid*, 0.10 mmol, 1.0 equiv) and phenyl acrylate (27.5 μL, 0.20 mmol, 2.0 equiv) were added to the working solution. Lutidine (46

μL , 0.40 mmol, 4 equiv) was added to the counter solution. The cell was fitted with the ²⁷⁷ working electrode and reference electrode in the working compartment and the counter electrode in the counter compartment. A fixed potential was applied (-1.55 V vs $\text{Fc}^{+/0}$ unless otherwise noted) and the solutions were stirred throughout the experiment (~ 200 rpm). After the desired reaction time or until charge corresponding to full $2e^-$ conversion of the starting material to product had passed (19.5 C), the solutions in both compartments were combined, diluted with Et_2O (100 mL), and passed over a plug of silica. Following solvent removal *in vacuo*, a crude quantitative ^1H NMR (*q*NMR) was taken with 1,3,5-trimethoxybenzene as internal standard and analyzed.

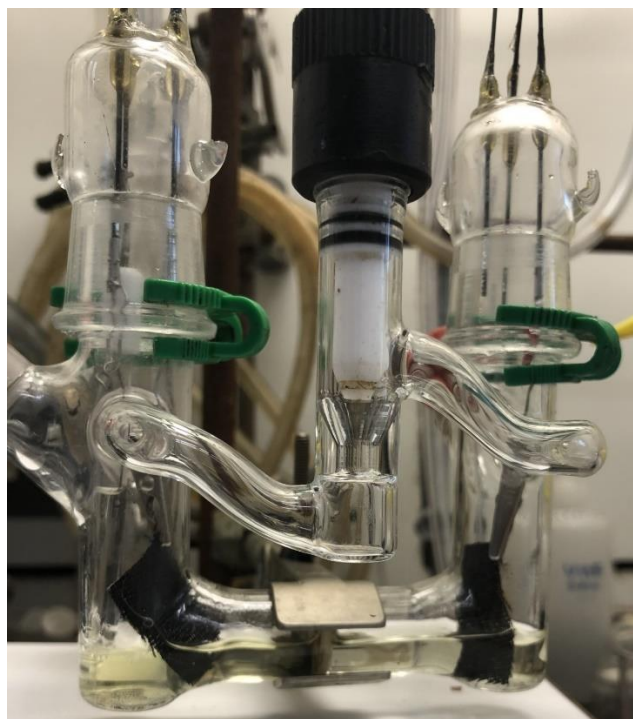
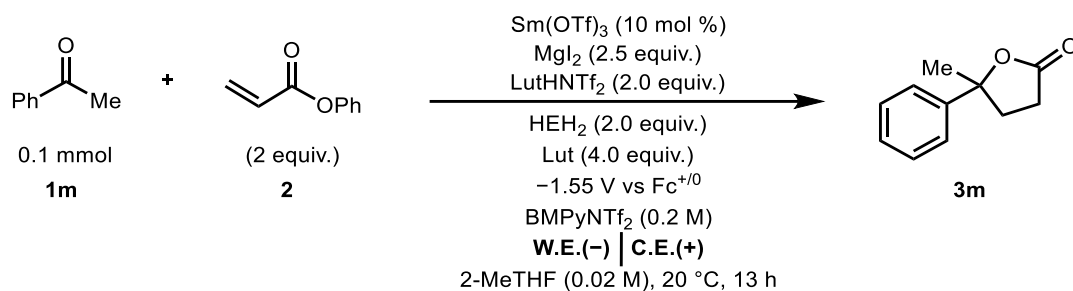
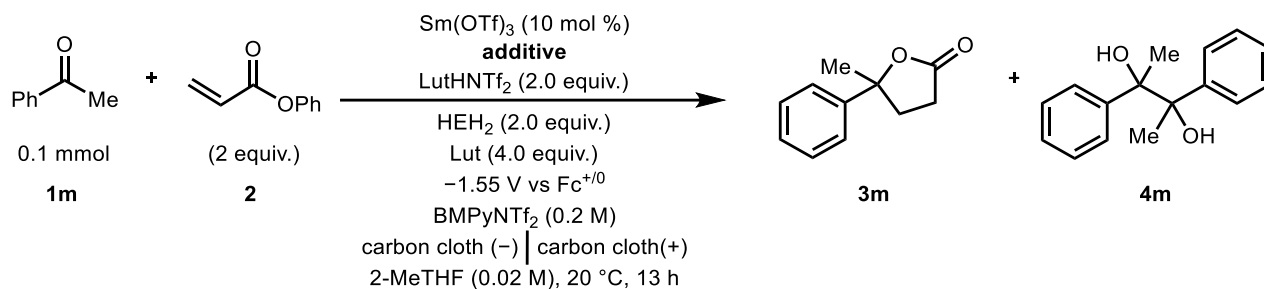


Figure C1: Photograph of the two-compartment cell employed in CPE experiments.

Table C1: Selected electrode screening data toward optimized CPE conditions.Yields determined by *q*NMR using 1,3,5-trimethoxybenzene as internal standard.

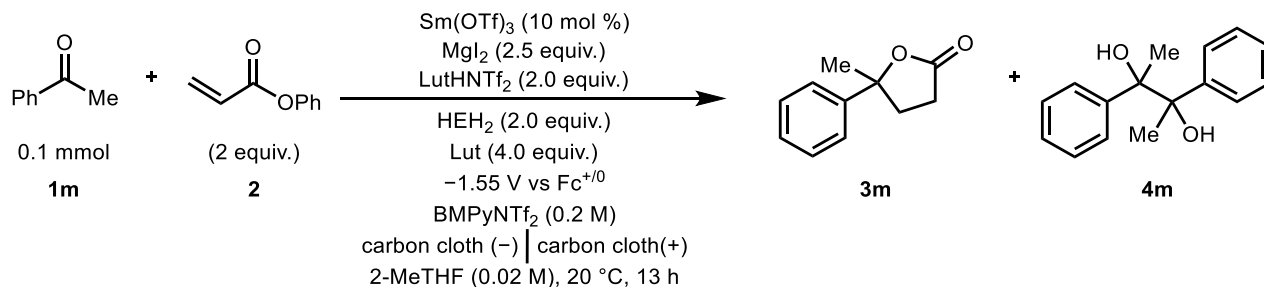
Entry	Cathode	Anode	3m (F.E.) (%)	Recovered s.m. (%)
1	Glassy carbon	Zn plate*	53 (78)	46
2	Carbon cloth	Zn plate*	62 (74)	25
3	Carbon cloth	RVC	73 (74)	12
4	Carbon cloth	Carbon cloth	85 (71)	7

*HEH₂ and 2,6-lutidine omitted.

Table C2: Selected additive screening data toward optimized CPE conditions.Yields determined by *q*NMR using 1,3,5-trimethoxybenzene as internal standard.

Entry	Additive (equiv)	3m (F.E.) (%)	4m (F.E.) (%)	Recovered s.m. (%)
1	^t Bu ₄ NI (5.0)	9 (23)	11 (14)	73
2	MgI ₂ (1.8)	63 (70)	6 (4)	19
3	MgI ₂ (3.0)	72 (73)	9 (5)	15
4	^t Bu ₄ NI (5.0) and Mg(NTf ₂) ₂ (2.5)	85 (84)	n.d.	6

Table C3: Control experiments probing role of electrochemically-driven Sm^{III/II} redox in CPE. Yields determined by *q*NMR using 1,3,5-trimethoxybenzene as internal standard.



Entry	Variation	3m (F.E.) (%)	4m (F.E.) (%)	Recovered s.m. (%)
1	no Sm	4 (17)	11 (22)	79
2	no electricity	0	0	70
3	no Sm, -1.65 V	n.d.	46 (14)	17
4	Gd instead of Sm	29 (36)	14 (8)	38

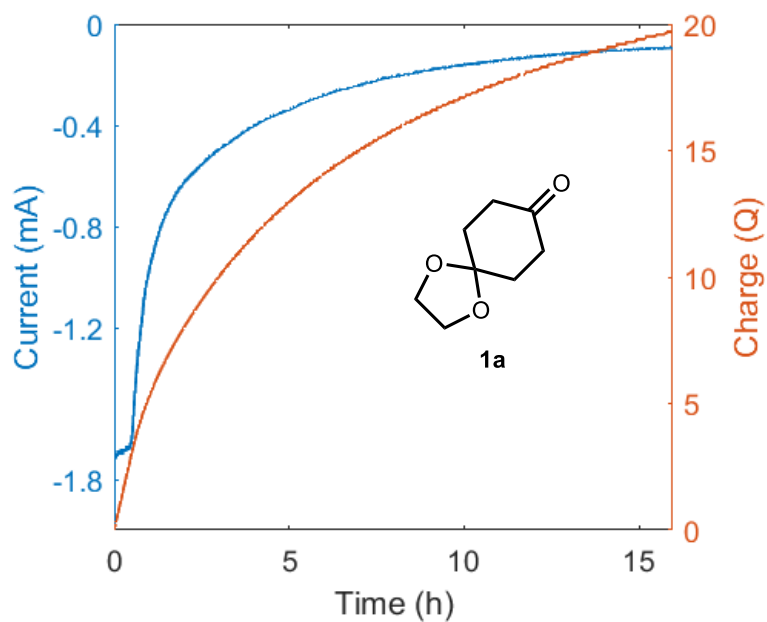


Figure C2: CPE of **1a** under the standard conditions.

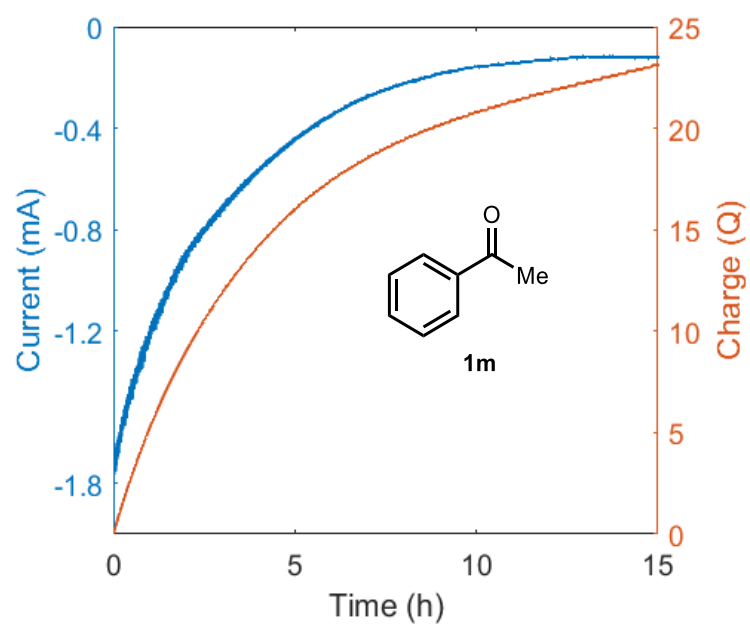


Figure C3: CPE of **1m** under the standard conditions.

C3.1 CVs relevant to electrocatalysis

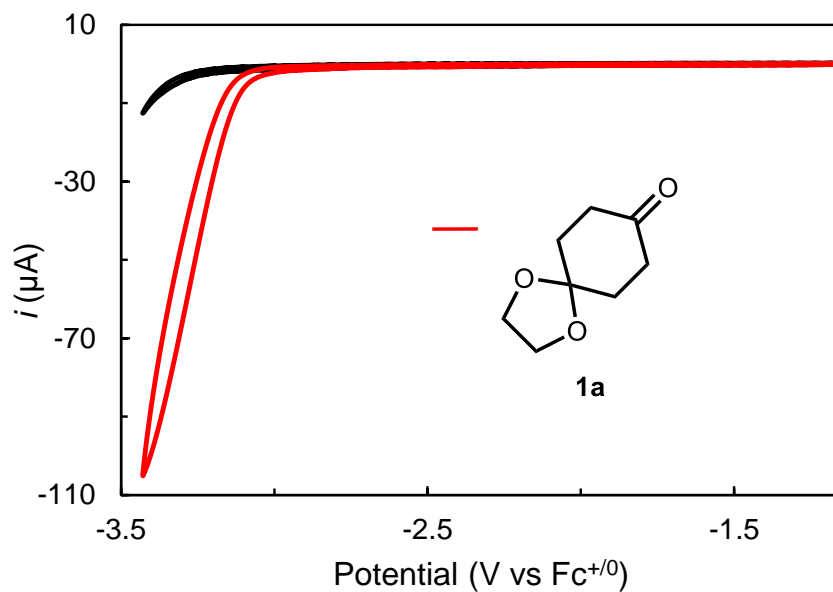


Figure C4: CV of **1a** (20 mM) in 2-MeTHF containing 0.2 M B MPyNTf_2 at 25 mV s^{-1} (red) overlaid with the electrolyte background (black).

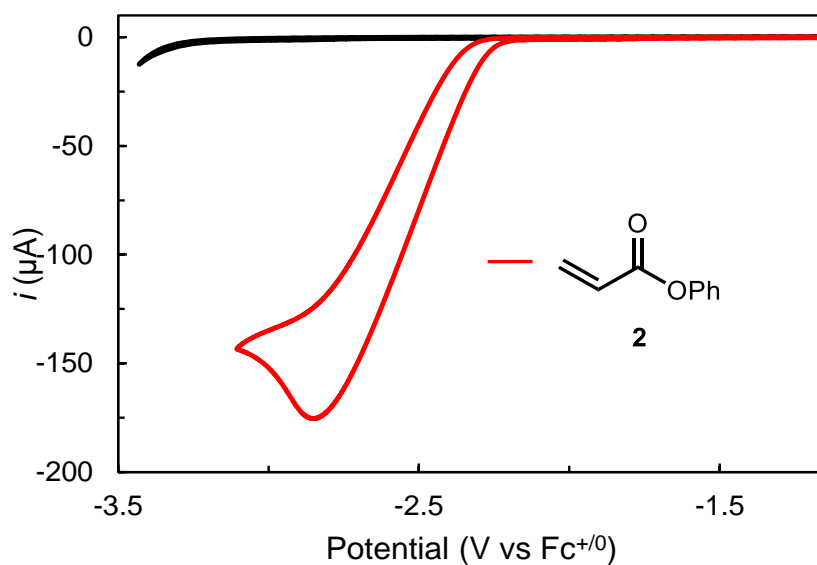


Figure C5: CV of phenyl acrylate (**2**, 40 mM) in 2-MeTHF containing 0.2 M BMPyNTf₂ at 25 mV s⁻¹ overlaid with the electrolyte background (black).

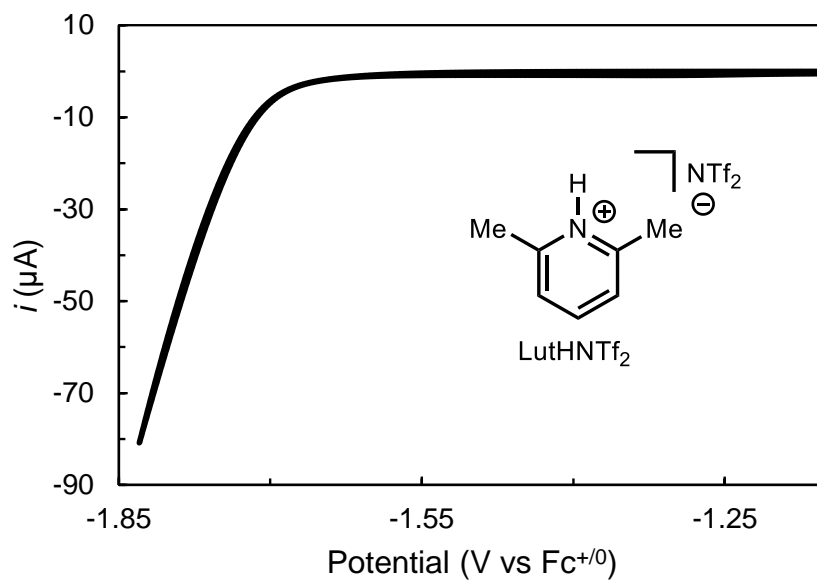


Figure C6: CV of LutHNTf₂ (40 mM) in 2-MeTHF containing 0.2 M BMPyNTf₂ at 25 mV s⁻¹.

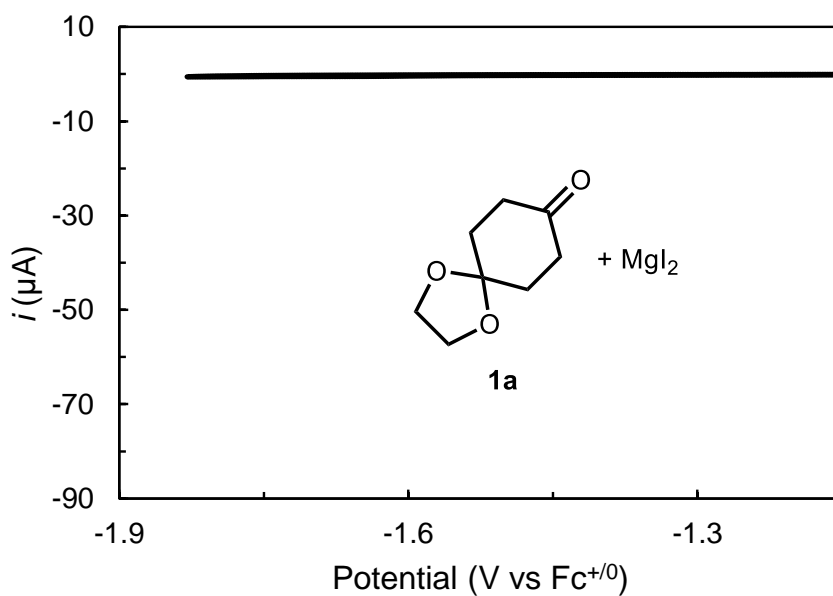


Figure C7: CV of **1a** (20 mM) and MgI_2 (50 mM) in 2-MeTHF containing 0.2 M BMPyNTf_2 at 25 mV s^{-1} .

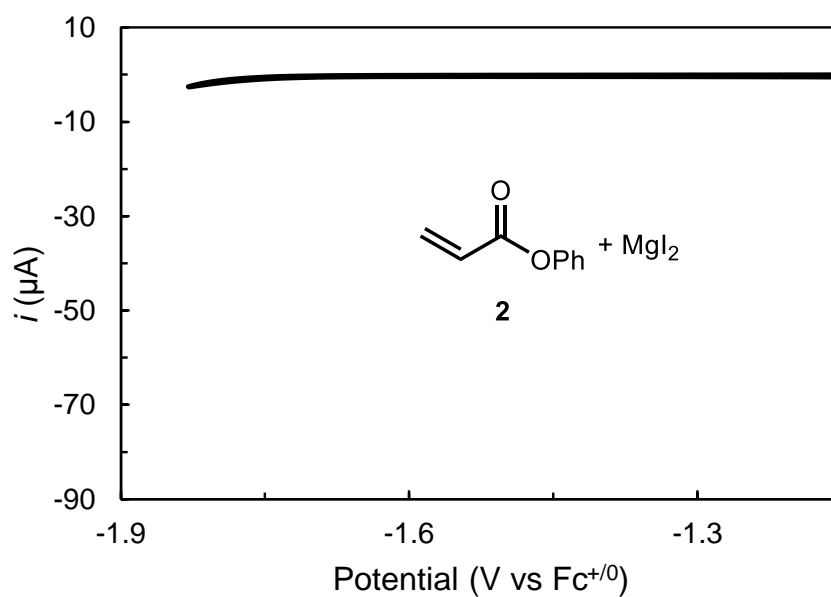


Figure C8: CV of **2** (40 mM) and MgI_2 (50 mM) in 2-MeTHF containing 0.2 M BMPyNTf_2 at 25 mV s^{-1} .

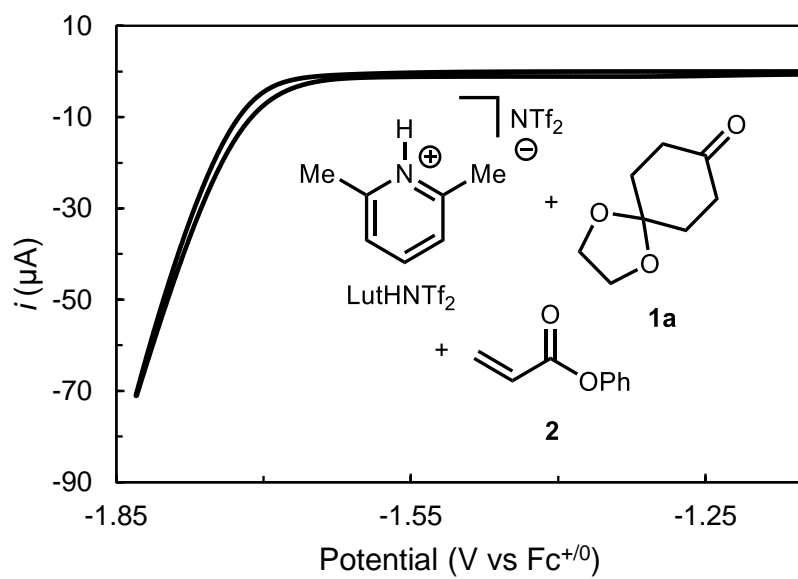


Figure C9: CV of **1a** (20 mM), **2** (40 mM), and LutHNTf₂ (40 mM) in 2-MeTHF containing 0.2 M BMPyNTf₂ at 25 mV s⁻¹.

C3.2 CV simulation details

Simulations were performed using a Matlab script for CVs following a simple EC mechanism.⁶

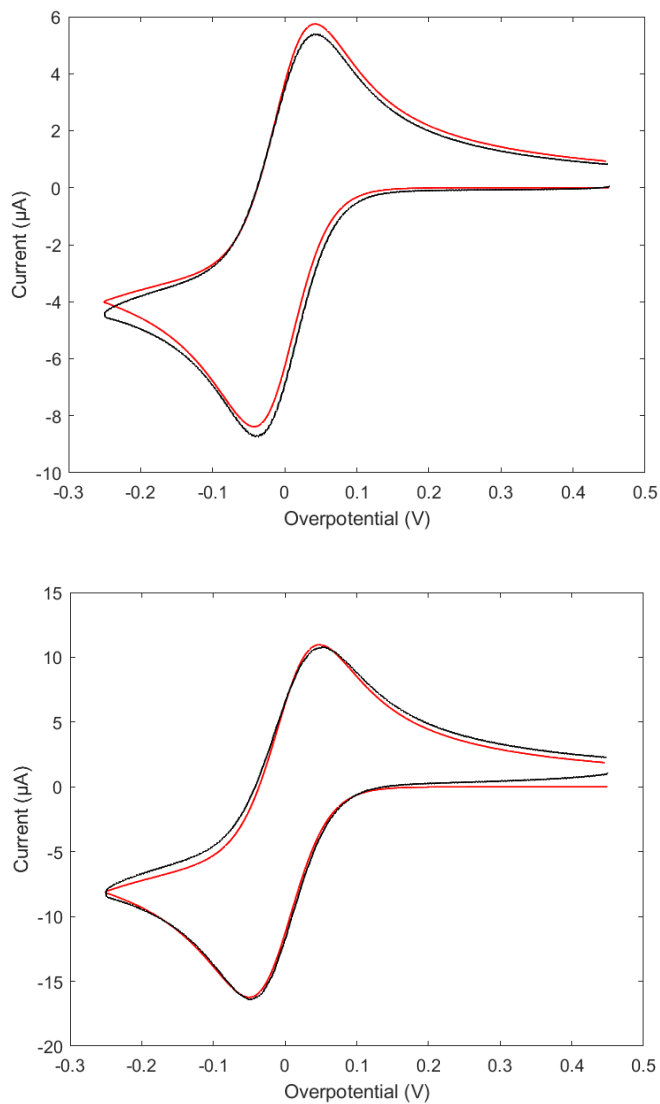


Figure C10: Representative simulations (red) overlaid with experimental CVs (black) of $\text{Sm}(\text{OTf})_3$ (2 mM) and $n\text{Bu}_4\text{NI}$ (50 mM) in 2-MeTHF containing 0.2 M BMPyNTf_2 at 20 and 80 mV s^{-1} (top and bottom panels, respectively). The data is well-modeled across a range of scan rates with the electrochemical rate constant k_0 set as 0.0075 cm s^{-1} .

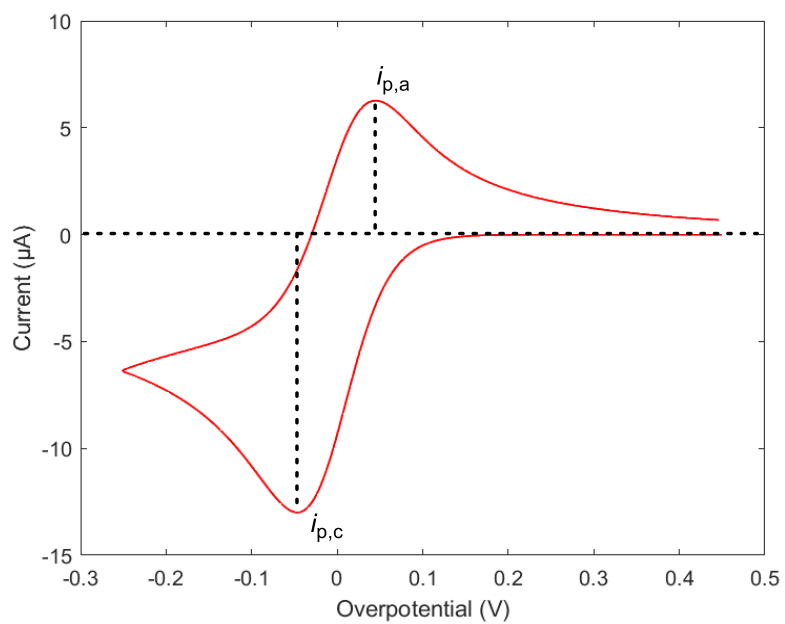


Figure C11: Representative simulation of an EC wave with $k_0 = 0.0075 \text{ cm s}^{-1}$, $k_{\text{obs}} = 0.05 \text{ s}^{-1}$, and $\nu = 50 \text{ mV s}^{-1}$ used to extract theoretical current ratios.

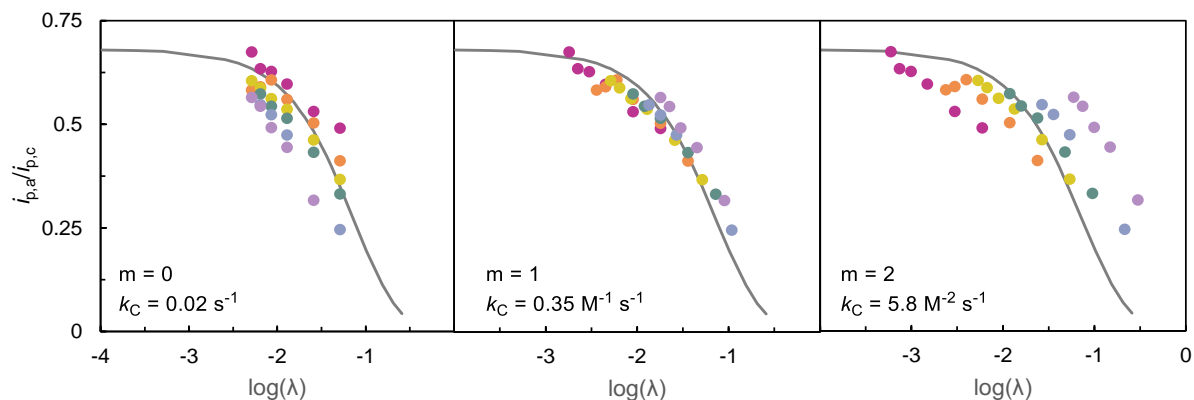


Figure C12: Experimental $i_{p,a}/i_{p,c}$ values collected from CVs at varying scan rates of $\text{Sm}(\text{OTf})_3$ (2 mM), ${}^n\text{Bu}_4\text{NI}$ (50 mM), and the aliphatic ketone **1a** at 20 mM (magenta), 40 mM (orange), 60 mM (yellow), 80 mM (teal), 120 mM (blue), and 200 mM (purple) plotted vs $\log(\lambda)$ using k_C values that provide the best fit with the simulated working curve (gray trace). Left: zero-order in **1a** ($p = 0$); Middle: first-order in **1a** ($p = 1$); Right: second-order in **1a** ($p = 2$).

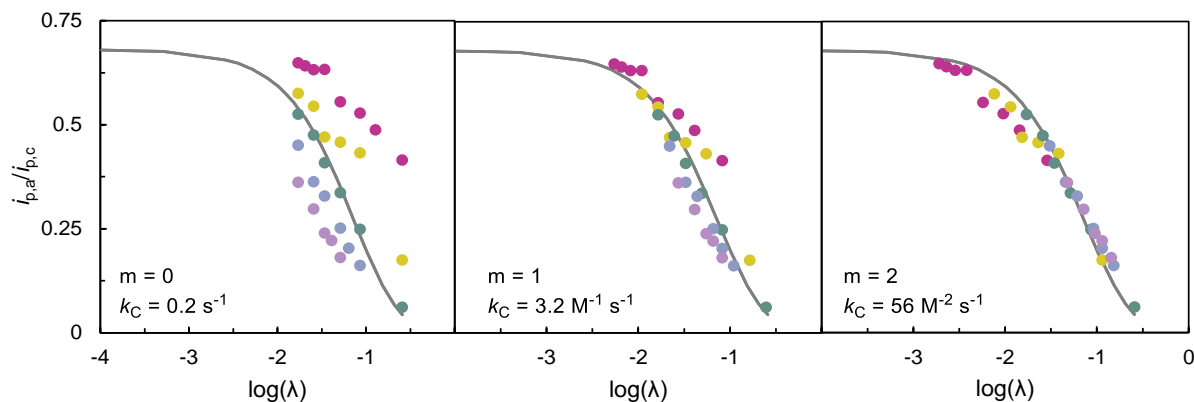


Figure C13: Experimental $i_{p,a}/i_{p,c}$ values collected from CVs at varying scan rates of $\text{Sm}(\text{OTf})_3$ (2 mM), ${}^n\text{Bu}_4\text{NI}$ (50 mM), and phenyl acrylate (**2**) at 20 mM (magenta), 40 mM (yellow), 60 mM (teal), 80 mM (blue), and 100 mM (purple) plotted vs $\log(\lambda)$ using k_C values that provide the best fit with the simulated working curve (gray trace). Left: zero-order in **2** ($p = 0$); Middle: first-order in **2** ($p = 1$); Right: second-order in **2** ($p = 2$).

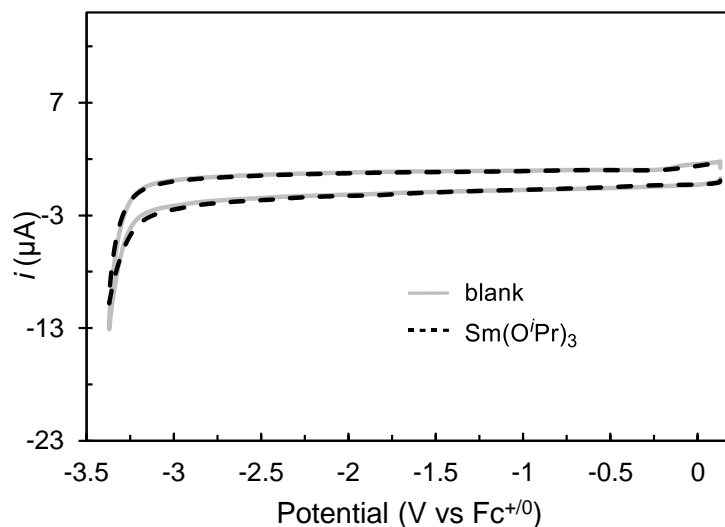


Figure C14: CV of $\text{Sm}(\text{O}^i\text{Pr})_3$ (2 mM) in THF containing 0.1 M BMPipNTf₂ at 100 mV s⁻¹ (dashed black) overlaid with the electrolyte background (gray).

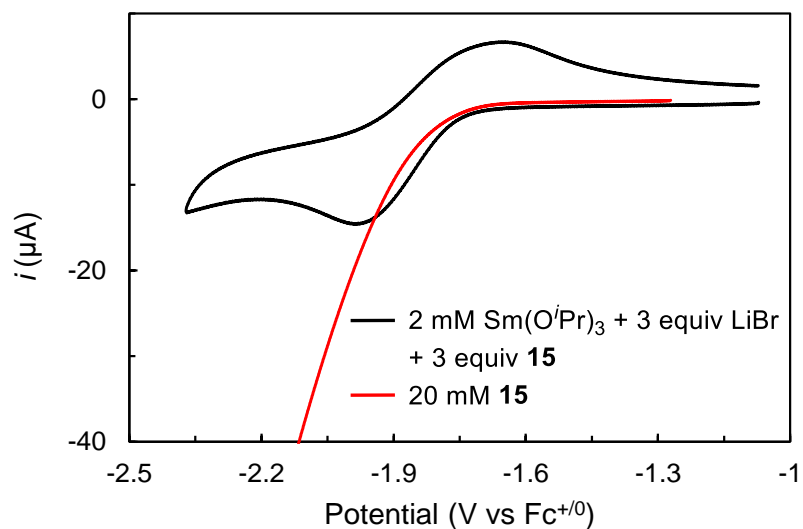


Figure C15: CV of $\text{Sm}(\text{O}^i\text{Pr})_3$ (2 mM), Et₃NHNTf₂ (**15**, 6 mM), and LiBr (6 mM) (black) overlaid with the CV of **15** (20 mM, red) in THF containing 0.1 M BMPipNTf₂ at 100 mV s⁻¹.

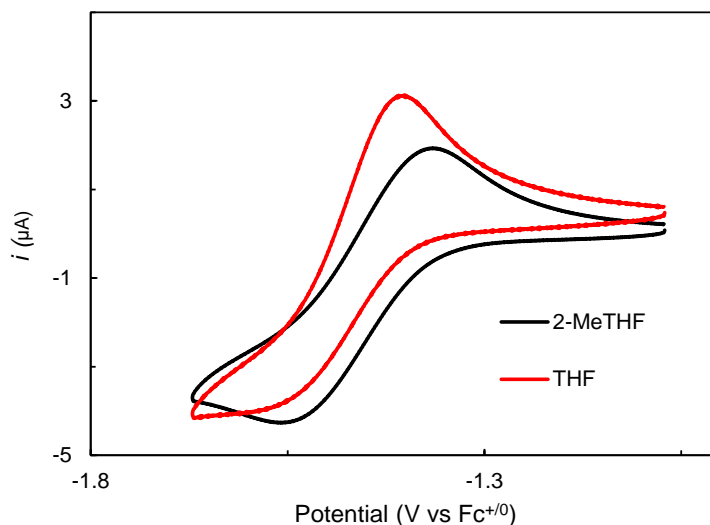


Figure C16: CV of $\text{Sm}(\text{O}^i\text{Pr})_3$ (2 mM), LiI (6 mM), and $\text{BnMe}_2\text{NHNTf}_2$ (**14**, 6 mM) at 25 mV s^{-1} in THF (**red**) or 2-MeTHF (**black**) containing 0.1 M BMPipNTf_2 .

Different wave shapes are observed in the CVs of SmI_3 generated by protonolysis with **14** and LiI in THF and 2-MeTHF (Figure C16). In THF, a plateau is observed on the cathodic sweep coupled to a peak on the return sweep. In 2-MeTHF, a typical quasireversible couple is observed with peak-shaped waves on both the cathodic and anodic sweeps. The reversible protonolysis of redox-inactive $\text{Sm}(\text{O}^i\text{Pr})_3$ to generate redox-active SmI_3 comprises a CE mechanism (C indicates a chemical step, E indicates an electrochemical step). The solvent-dependent wave shapes are characteristic of different regimes in the zone diagram for a CE process describing the equilibrium position of the C step, the rate of the equilibrium in the C step, and the scan rate.⁷ At a fixed scan rate of 25 mV s^{-1} , the 2-MeTHF wave shape maps to a regime in which the equilibrium process is both relatively slow and unfavorable, while the THF wave shape corresponds to a similarly unfavorable, but *faster*, equilibrium protonolysis step. While detailed study of the

mechanism underlying net protonolysis/halide substitution is warranted, this observation²⁹¹
suggests that the more coordinating solvent enhances the rate of protonolysis.

C4 Additional Sm catalysis products

C4.1 Homocoupled products

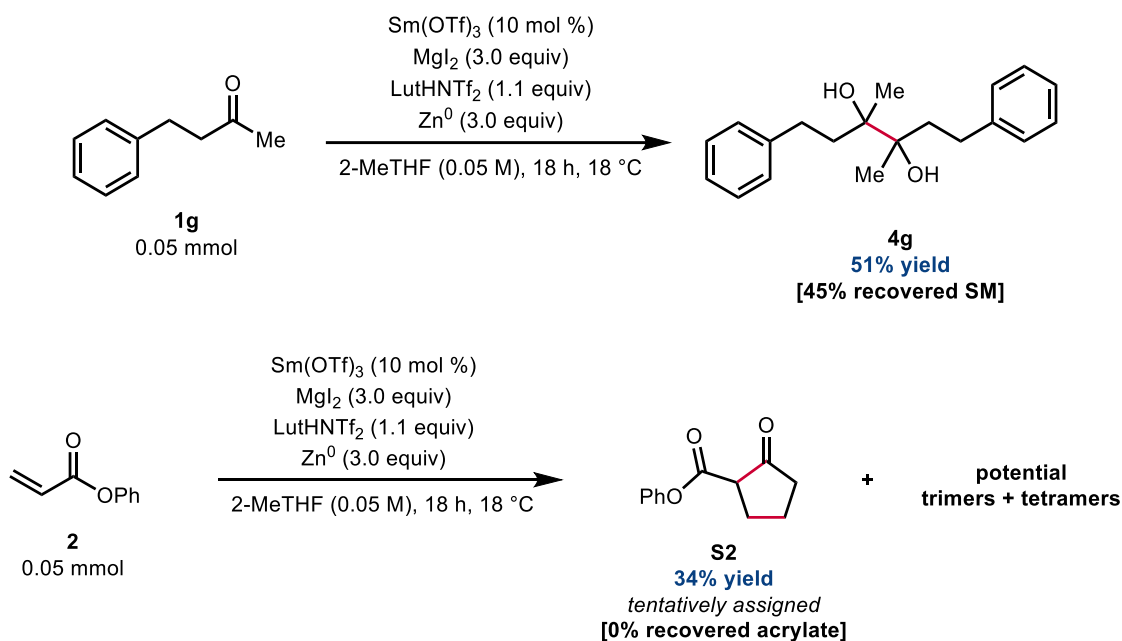


Figure C17: Dimerization study of aliphatic ketone (top) and phenyl acrylate (bottom) under standard condition. All yields are determined based on ¹H NMR analysis with 1,3,5-trimethoxybenzene as an internal standard. NMR data of **4g** matches the data reported by See and coworkers.⁸

C4.2 Solvent-acidity study

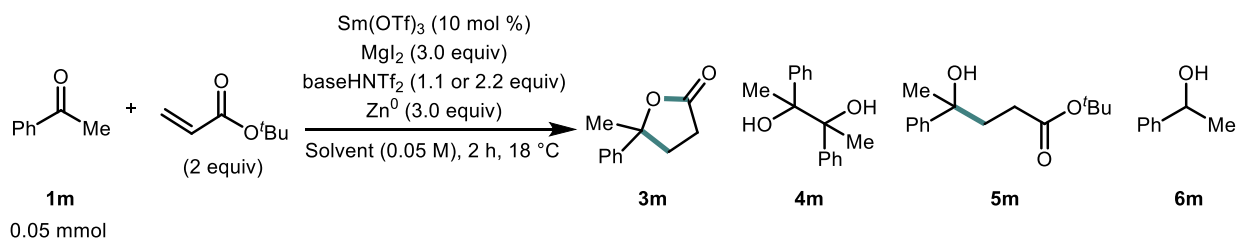


Table C4: Product distribution with 2-MeTHF as a solvent (1.1 equiv baseHNTf₂).

baseHNTf ₂	3m	5m	4m	3m	Total
7	28	0	0	0	28
8	32	0	25	0	57
9	50	0	25	0	75
10	70	0	9	0	79
11	78	0	7	3	88
12	87	0	2	0	89
13	83	0	3	0	86
14	83	0	2	0	85
15	79	0	0	0	79

Table C5. Product distribution with THF as a solvent (2.2 equiv baseHNTf₂).

baseHNTf ₂	3m	5m	4m	3m	Total
7	0	2	2	0	4
8	0	6	21	3	30
9	0	26	39	6	71
10	0	58	14	6	78
11	0	73	11	2	86
12	0	76	10	1	87
13	0	25	7	0	32
14	0	13	0	0	13
15	0	6	0	0	6

Table C6: Product distribution with MeCN as a solvent (2.2 equiv baseHNTf₂).

baseHNTf₂	3m	5m	4m	3m	Total
7	0	1	2	0	3
8	0	19	21	8	48
9	0	39	25	25	89
10	0	56	18	23	97
11	0	21	9	1	31
12	0	12	10	0	22
13	0	4	3	0	7
14	0	4	5	0	9
15	0	3	5	0	8

Table C7: Product distribution with DME as a solvent (2.2 equiv baseHNTf₂).

baseHNTf₂	3m	5m	4m	3m	Total
7	0	2	0	0	2
8	0	10	30	3	43
9	0	32	21	1	54
10	0	46	11	0	57
11	0	17	7	0	24
12	0	8	2	0	10
13	0	7	3	0	10
14	0	6	1	0	7
15	0	6	1	0	7

REFERENCES

- (1) Tu, J.; Ripa, R. A.; Kelley, S. P.; Harmata, M. Intramolecular (4+3) cycloadditions of oxidopyridinium ions: Towards Daphnicyclidin A. *Chem. – Eur. J.* **2022**, *28* (41), e202200370.
- (2) Maity, S.; Flowers, R. A. Mechanistic study and development of catalytic reactions of Sm(II). *J. Am. Chem. Soc.* **2019**, *141* (7), 3207–3216.
- (3) Lei, X.; Jalla, A.; Shama, M. A. A.; Stafford, J. M.; Cao, B. Chromatography-free and eco-friendly synthesis of aryl tosylates and mesylates. *Synthesis* **2015**, *47*, 2578–2585.
- (4) Still, W. C.; Gennari, C. Direct synthesis of Z-unsaturated esters. A useful modification of the horner-emmons olefination. *Tetrahedron Lett.* **1983**, *24* (41), 4405–4408.
- (5) Fulmer, G. R.; Miller, A. J. M.; Sherden, N. H.; Gottlieb, H. E.; Nudelman, A.; Stoltz, B. M.; Bercaw, J. E.; Goldberg, K. I. NMR chemical shifts of trace impurities: common laboratory solvents, organics, and gases in deuterated solvents relevant to the organometallic chemist. *Organometallics* **2010**, *29* (9), 2176–2179.
- (6) Attia, P. Cyclic voltammetry simulator, 2024.
- (7) Savéant, J.-M. *Elements of Molecular and Biomolecular Electrochemistry*; John Wiley & Sons, Inc: Hoboken, New Jersey, 2006.
- (8) Ware, S. D.; Zhang, W.; Charboneau, D. J.; Klein, C. K.; Reisman, S. E.; See, K. A. Electrochemical preparation of Sm(II) reagent facilitated by weakly coordinating anions. *Chem. – Eur. J.* **2023**, *29* (46), e202301045.

SUPPLEMENTARY INFORMATION FOR CHAPTER 5

Reproduced in part with permission from Johansen, C. M.; Boyd, E.A.; Tarnopol, D.E.; Peters, J. C. *J. Am. Chem. Soc.* **2024**, *146*, 25456. doi: [10.1021/jacs.4c10053](https://doi.org/10.1021/jacs.4c10053)

D1 Experimental Part**D1.1 General Considerations**

All manipulations were carried out using standard Schlenk or glovebox techniques under an N₂ atmosphere. Solvents were deoxygenated and dried by thoroughly sparging with N₂ followed by passage through an activated alumina column in a solvent purification system by SG Water, USA LLC. Nonhalogenated solvents were tested with sodium benzophenone ketyl in tetrahydrofuran (THF) to confirm the absence of oxygen and water. Deuterated solvents were purchased from Cambridge Isotope Laboratories, Inc.

Phenyl acrylate was purchased from Ambeed, degassed, and used without further purification. Cyclohexanedione monoethylene ketal (**1a**) was purchased from TCI and used without further purification. All bases (DBU, Et₃N, pyridine, 2,6-lutidine) were purchased from Sigma Aldrich and distilled prior to use. Sm(OTf)₃, Gd(OTf)₃, and MgI₂ were purchased from Sigma–Aldrich. Ir(ppy)₂(dtbbpy)[PF₆] was purchased from Strem and used without further purification. 3DPA2FBN (2,4,6-tris(diphenylamino)-3,5-difluorobenzonitrile) was purchased from Ambeed and used without further purification. 9,10-dihydroacridine was purchased from Combi-blocks and purified by sublimation prior to use. Hexamethylphosphoramide, ethylene glycol, and 2-(2-(2-methoxyethoxy)ethoxy)ethan-1-ol were purchased from Sigma Aldrich and degassed. Tetraheptylammonium iodide was purchased from TCI and dried at 100°C under dynamic

vacuum for 16 hours. Tetrabutylammonium bromide was acquired from Strem and then²⁹⁷ dried by heating to 85°C for 48 hours under dynamic vacuum using P₂O₅ as a desiccant. 1-Butyl-1-methylpiperidinium (BMPipNTf₂) was purchased from TCI chemicals and used without further purification.

SmI₂(THF)₂,¹ phenH₂,² BINAPO,³ aminodiol (L*),⁴ and LutHNTf₂⁵ were synthesized following literature procedures.

HEH₂⁶ was synthesized following literature procedure and then dried by heating to 80 °C for 24 hours under dynamic vacuum using P₂O₅ as a desiccant.

The 2-MeTHF used was dried extensively prior to use in ketyl-olefin coupling experiments. Inhibitor-free solvent was refluxed over CaH₂ for 24 hours (under N₂ atmosphere) and distilled into a Strauss flask. This flask was brought into the glovebox, where NaK was added, and the solvent was stirred for 24 hours. The solvent was then vacuum transferred into a fresh Strauss flask and stored over activated sieves.

D1.2 Nuclear Magnetic Resonance (NMR) Spectroscopy

Deuterated solvents were purchased from Cambridge Isotope Laboratories, Inc. ¹H chemical shifts are reported in ppm relative to tetramethylsilane, using residual solvent resonances as internal standards.⁷

D1.3 Electrochemistry

All electrochemical experiments were conducted using a CH instruments 600B electrochemical analyzer. A nonaqueous Ag^{+ / 0} reference electrode (BASi) consisting of a silver wire immersed in 5 mM AgOTf in DME containing 0.2 M ⁿBu₄NPF₆ separated from the working solution by a CoralPor® frit was used for all experiments. All reported

potentials are referenced to the ferrocenium/ferrocene ($\text{Fc}^{+/0}$) couple used as an external²⁹⁸ standard. All CVs were carried out in an N_2 -filled glovebox in a 20 mL scintillation vial fitted with a septum cap containing punched-out holes for insertion of electrodes. A glassy carbon disk (3 mm diameter) was used as the working electrode for all CVs. It was freshly polished with 1, 0.3, and 0.05 μm alumina powder water slurries, rinsed with water and acetone, and dried before use. A platinum wire was used as the auxiliary electrode for CVs. CVs are plotted using IUPAC convention. Unless otherwise noted, IR compensation was applied, accounting for 85% of the total resistance.

D1.4 UV-Visible Absorption Spectroscopy

UV-visible absorption spectra were collected on a Cary 50 spectrophotometer using a 1 cm quartz cell sealed with a Teflon stopcock. All samples had a blank sample background subtraction applied. Temperature regulation for UV-Vis measurements was carried out with a Unisoku cryostat.

D2 Catalytic ketone-olefin coupling reactions

D2.1 Standard procedure in the absence of Ir-photocatalyst

In the glovebox, HEH_2 (40.4 mg, 160 μmol) was added as a solid to a Schlenk flask. 2-MeTHF (0.5 mL) was added to the flask. A freshly prepared stock solution of $\text{SmI}_2(\text{THF})_2$ in 2-MeTHF (2.2 mg per mL, 4 mM) was added to the flask (1 mL added). A stock solution of the remaining organics: ketone (12.6 mg per mL; 80 mM), phenyl acrylate (22 μL per mL; 160 mM), and when noted base was prepared, and 0.5 mL was added to the reaction flask. The color of SmI_2 (purple) rapidly changes to yellow upon the addition of the organic reagents. The reaction flask is sealed and brought out of the glovebox, where it is irradiated by two H160 PR Kessil™ 440 nm Blue LED lamps for 90 minutes in a water bath in a reflective dewar. The reaction was continuously stirred (1200 rpm). The temperature of the water bath was monitored and did not exceed 25 °C during the reaction. A picture of the setup is shown in Figure D1.

Following completion of the reaction, the flask was opened to air, and 2 mL Et_2O was added. The contents of the flask were filtered through a silica plug into a vial containing a known amount of 1,3,5-trimethoxybenzene (TMB; ~7 mg). The reaction flask was washed with additional Et_2O (2x1 mL), and the washes were passed through the silica plug into the vial. The solvent was removed *in vacuo* and the products were taken up in CDCl_3 and analyzed by ^1H NMR integrating against the TMB standard.

The lactone products (e.g., **3a**; 1,4,9-trioxadispiro[4.2.48.25]tetradecan-10-one) is detected by ^1H NMR with features matching literature spectra.⁵

D2.2 Standard procedure with an Ir-photocatalyst

In the glovebox, Ir(ppy)₂(dtbbpy)[PF₆] (0.36 mg, 0.4 μmol) was dissolved in THF and added to a Schlenk flask, and the solvent was removed *in vacuo*, depositing a thin film. Following this HEH₂, SmI₂(THF)₂ and organics were added as described in **D2.1**.



Figure D1: Typical setup for catalytic experiments. Lights are turned off for clarity.

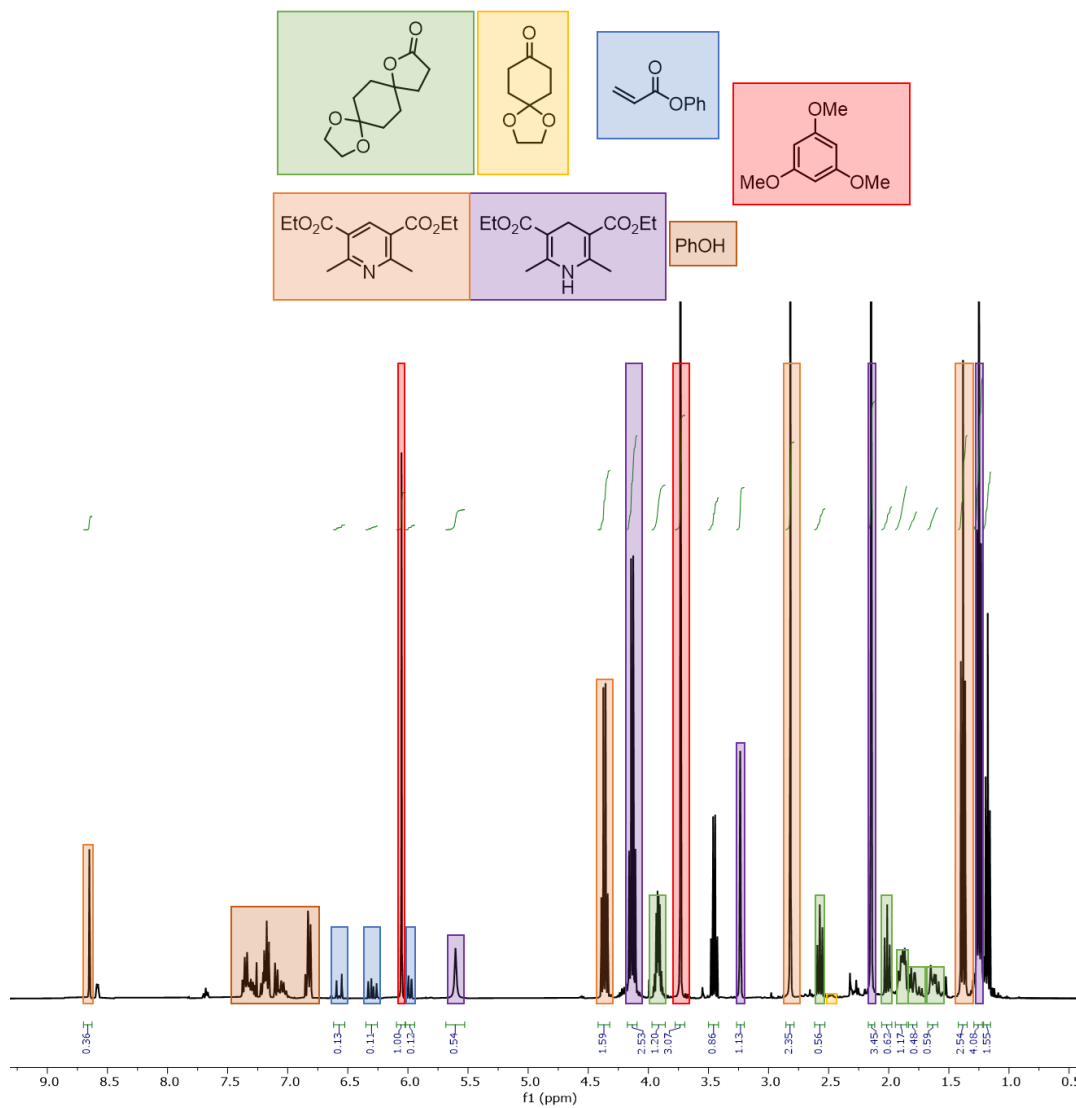


Figure D2: ¹H NMR (400 MHz, CDCl₃) of a typical crude reaction mixture reacting **1a** with phenyl acrylate to produce **3a** by method B with key products/starting materials highlighted as indicated.

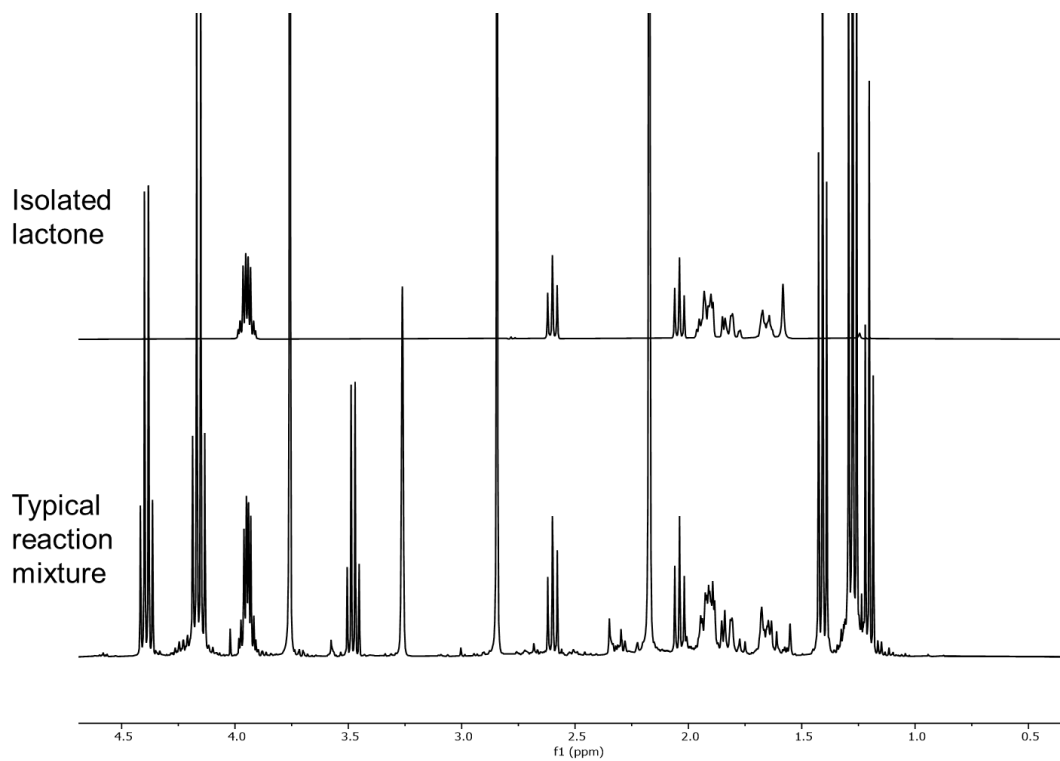


Figure D3: Comparison of ¹H NMR of typical reaction spectra with authentic lactone product.⁵ ¹H NMR (400 MHz, CDCl₃): δ 4.00 – 3.90 (m, 4H), 2.60 (t, *J* = 8.5 Hz, 2H), 2.04 (t, *J* = 8.5 Hz, 2H), 1.97 – 1.88 (m, 4H), 1.82 (ddd, *J* = 17.5, 10.9, 4.0 Hz, 2H), 1.70 – 1.62 (m, 2H).

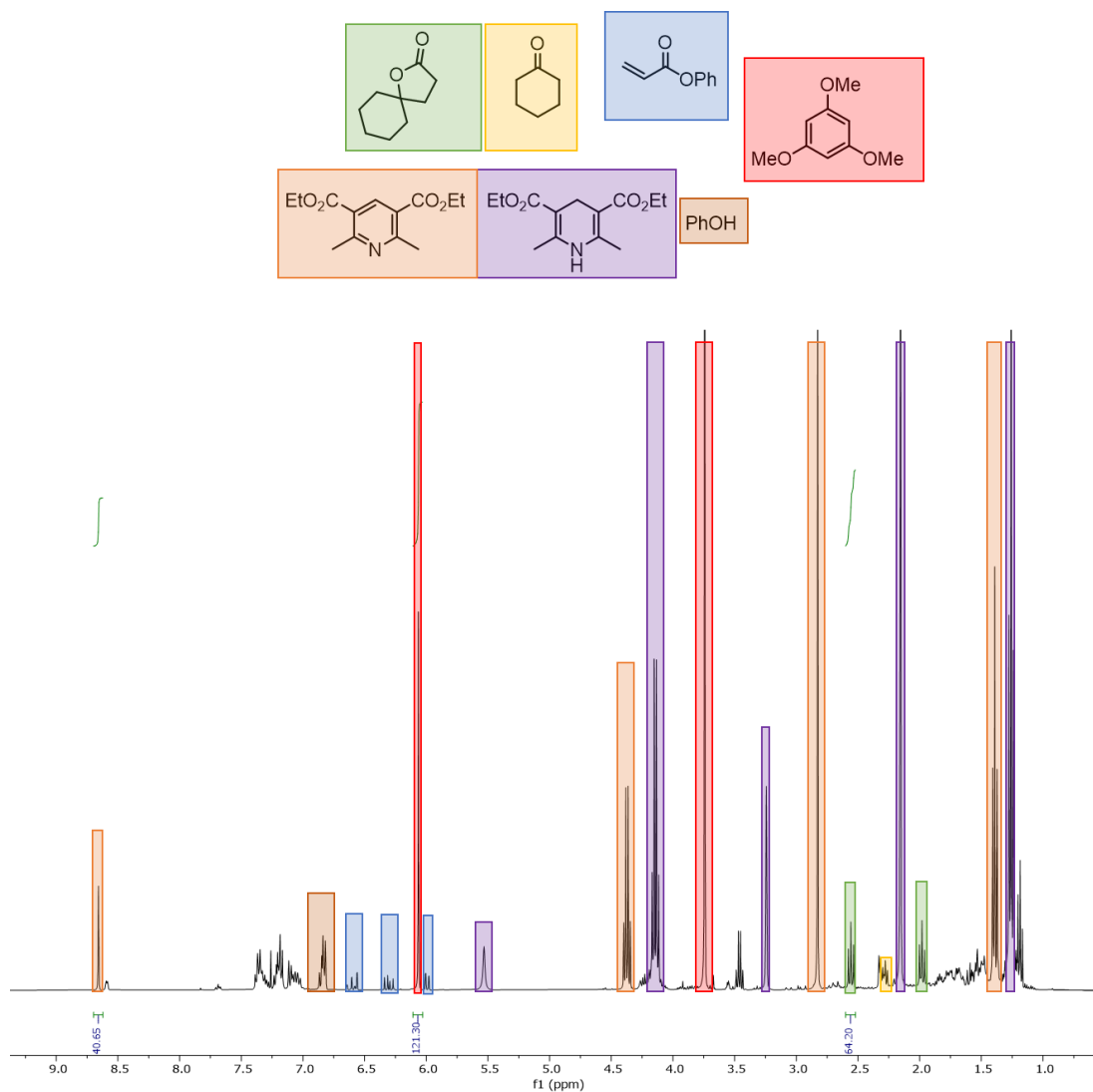


Figure D4: ^1H NMR (400 MHz, CDCl_3) of a typical crude reaction mixture reacting **1b** with phenyl acrylate to produce **3b** by method B with key products/starting materials highlighted as indicated.

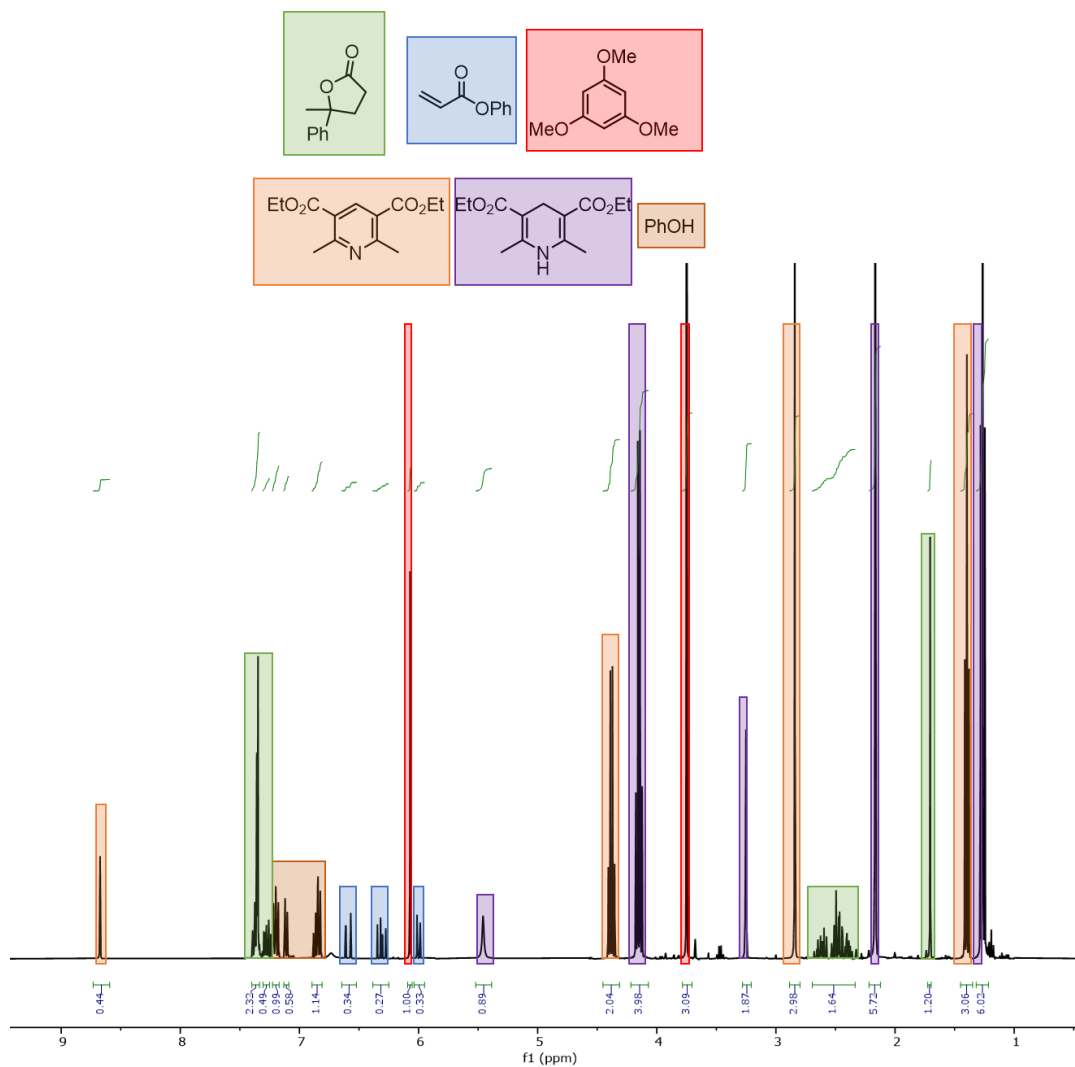


Figure D5: ^1H NMR (400 MHz, CDCl_3) of a typical crude reaction mixture reacting **1m** with phenyl acrylate to produce **3m** by method A with key products/starting materials highlighted as indicated.

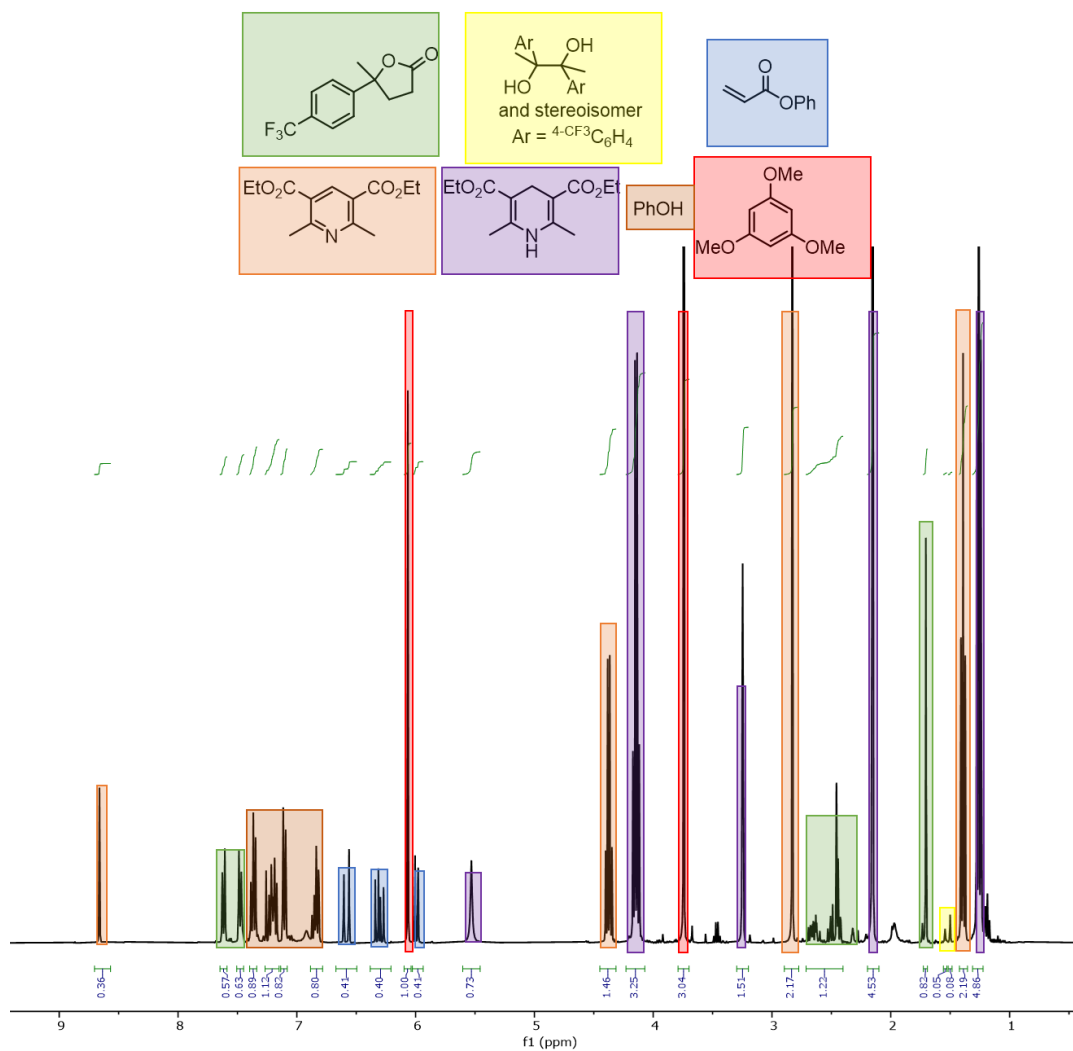


Figure D6: ¹H NMR (400 MHz, CDCl₃) of a typical crude reaction mixture reacting **1aa** with phenyl acrylate to produce **3aa** and **4aa** by method A with key products/starting materials highlighted as indicated.

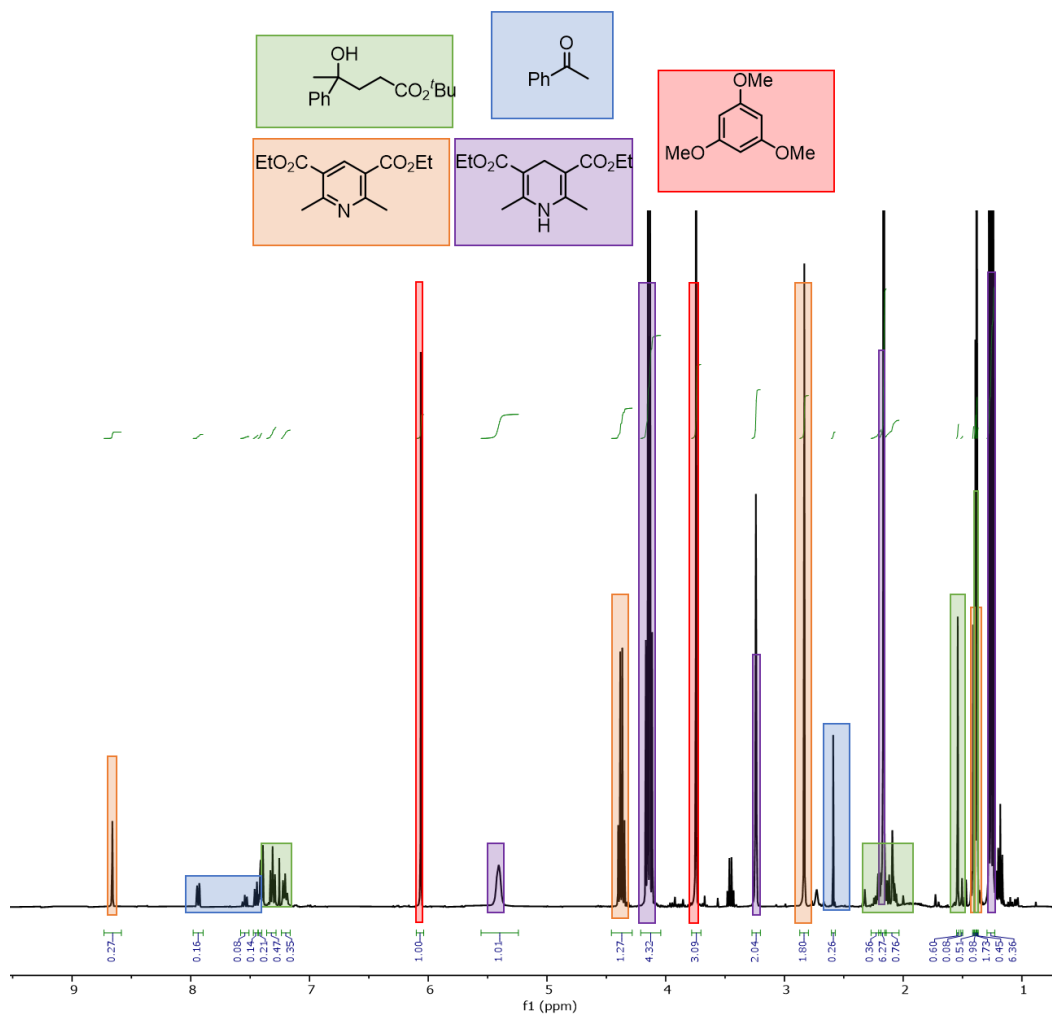
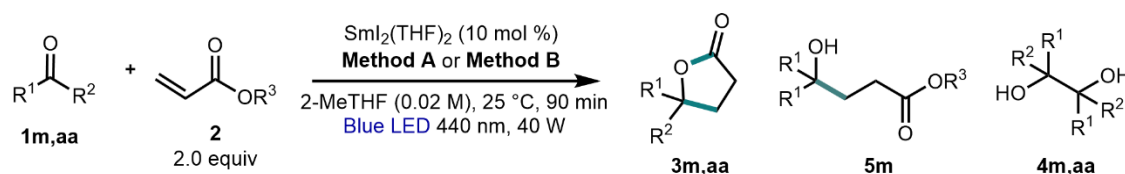


Figure D7: ¹H NMR (400 MHz, CDCl₃) of a typical crude reaction mixture reacting **1m** with *tert*-butyl acrylate to produce **5m** by method A with key products/starting materials highlighted as indicated.

Table D1: Yields for cross- vs homocoupled products in selected aryl ketone cross-coupling reactions.



Method A: HEH₂ (4 equiv)

Method B: HEH₂ (4 equiv), [Ir]PF₆ (1 mol%), pyridine (2 equiv)

Entry	Coupling partners	% yield cross-coupled product		% yield 4m,aa (meso:dr)	
		Method A	Method B	Method A	Method B
1	1m , R ³ = Ph	3m ; >95	3m ; 90	n.d.	8 (1:1)
2	1aa , R ³ = Ph	3aa ; 77	3aa ; 49	16 (0.6:1)	50 (0.8:1)
3	1m , R ³ = ^t Bu	5m ; 43	5m ; 29	4 (0.4:1)	45 (0.7:1)
4	1aa , R ³ = Ph; <i>no Sm</i>	n.d.	n.d.	15 (1:1)	100 (1:1)

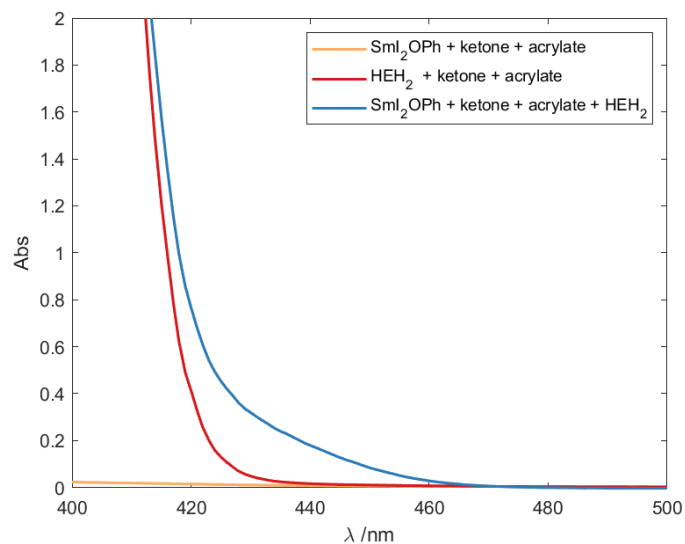
D3.1 Evidence for Sm^{III}-dihydropyridine interaction

Figure D8: UV-vis traces following the reaction of SmI₂ (2 mM) + ketone **1a** (20 mM) + acrylate **2** (40 mM) (yellow trace, *in situ* forms colorless Sm^{III}I₂(OPh)); HEH₂ (80 mM) + **1a** (20 mM) + **2** (40 mM) (red trace); and SmI₂ (2 mM) + HEH₂ (80 mM) + **1a** (20 mM) + **2** (40 mM) (blue trace) in 2-MeTHF.

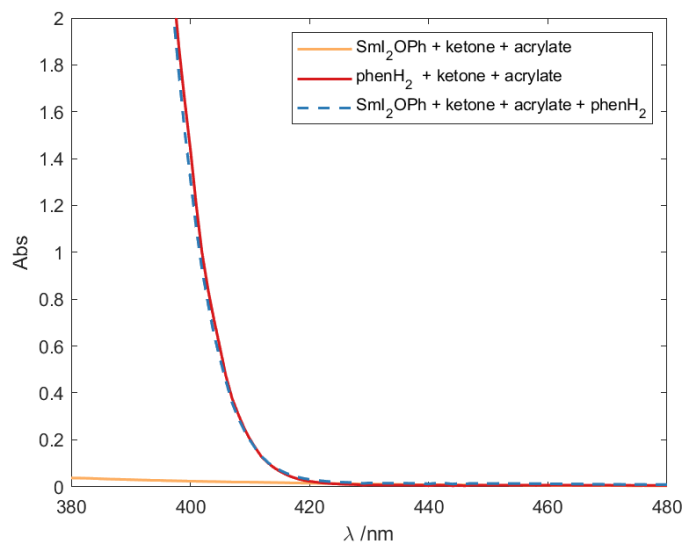


Figure D9: UV-vis traces following the reaction of SmI₂ (2 mM) + **1a** (20 mM) + **2** (40 mM) (yellow trace, *in situ* forms colorless Sm^{III}I₂(OPh)); phenH₂ (80 mM) + **1a** (20 mM) + **2** (40 mM) (red trace); and SmI₂ (2 mM) + **1a** (20 mM) + **2** (40 mM) + phenH₂ (80 mM) (blue dashed trace) in 2-MeTHF.

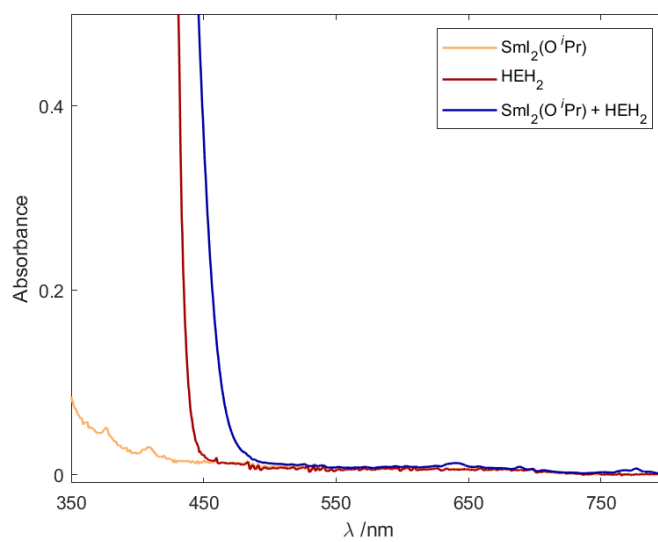


Figure D10: UV-vis traces of Sm(OⁱPr)₃ (2 mM), ⁿHep₄NI (6 mM), and HNTf₂ (3 mM) (yellow trace, *in situ* forms colorless Sm^{III}I₂(OⁱPr)); HEH₂ (60 mM) (red trace); and Sm(OⁱPr)₃ (2 mM), ⁿHep₄NI (6 mM), HNTf₂ (3 mM), and HEH₂ (60 mM) (blue trace) in THF.

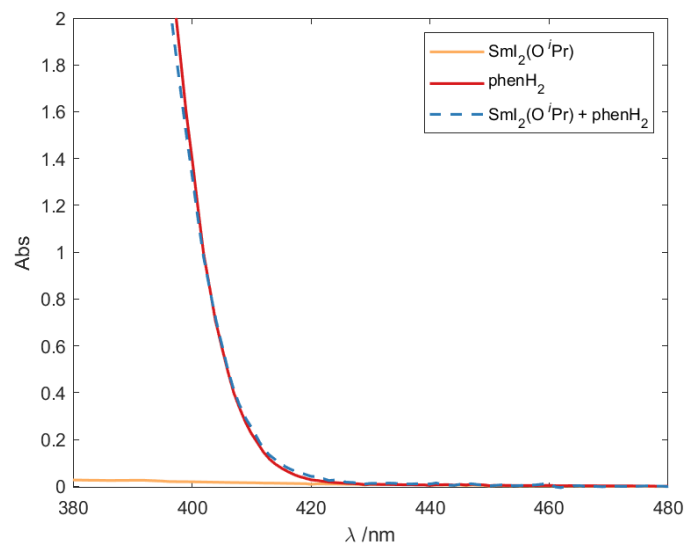


Figure D11: UV-vis traces of $\text{Sm}(\text{O}^i\text{Pr})_3$ (2 mM), $^n\text{Hep}_4\text{NI}$ (6 mM), LutHNTf_2 (3 mM) (yellow trace, *in situ* forms colorless $\text{Sm}^{\text{III}}\text{I}_2(\text{O}^i\text{Pr})$); phenH_2 (60 mM) (red trace); and $\text{Sm}(\text{O}^i\text{Pr})_3$ (2 mM), $^n\text{Hep}_4\text{NI}$ (6 mM), LutHNTf_2 (3 mM), and phenH_2 (60 mM) (dashed blue trace) in THF.

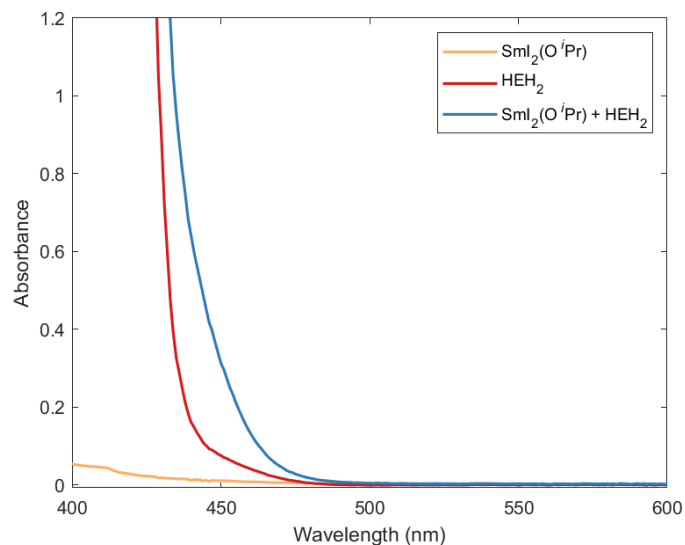


Figure D12: UV-vis traces of $\text{Sm}(\text{O}^i\text{Pr})_3$ (2 mM), ${}^n\text{Hep}_4\text{NI}$ (6 mM), LutHNTf_2 (3 mM) (yellow trace, *in situ* forms colorless $\text{Sm}^{\text{III}}\text{I}_2(\text{O}^i\text{Pr})$); HEH_2 (60 mM) (red trace); and $\text{Sm}(\text{O}^i\text{Pr})_3$ (2 mM), ${}^n\text{Hep}_4\text{NI}$ (6 mM), LutHNTf_2 (3 mM), and HEH_2 (60 mM) (blue trace) in THF.

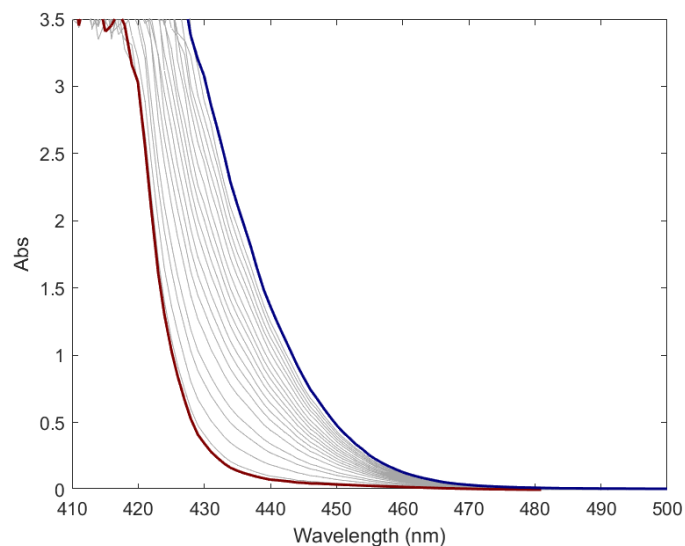


Figure D13: Titration of $\text{Sm}(\text{OTf})_3$ (0 to 5 mM, from red to blue trace) into a solution of HEH_2 (100 mM) in THF.

D3.2 Sm^{II} photogeneration experiments

D3.2.1 General procedure for Sm^{II} photogeneration experiments

A fresh 5 mM stock solution of SmI₂ in THF is prepared immediately before use. SmI₃ is prepared by titrating this 5 mM THF solution of SmI₂ with I₂ until the characteristic blue color of SmI₂ disappears.

An aliquot of the resulting SmI₃ solution (1 mL, 0.005 mmol) is added to a vial (1 mL) containing reductant (0.15 mmol, 30 equiv) and an additional 1 mL of THF, and this solution is transferred to a 1 cm path-length cuvette. 100 uL of a stock solution of photocatalyst is added to the cuvette, followed by base (0.15 mmol, 30 equiv), an additional 0.5 mL THF and any alternative ligands (e.g. ^tBu₄NBr, BINAPO) as indicated.

D3.2.2 General procedure for Sm^{II}(HMPA)₄ photogeneration experiments

For the Sm^{II}(HMPA)₂⁺ generation, 4 equiv HMPA was added to the initial SmI₂ solution prior to oxidation by I₂. The rest of the procedure was identical following **D3.2.1**.

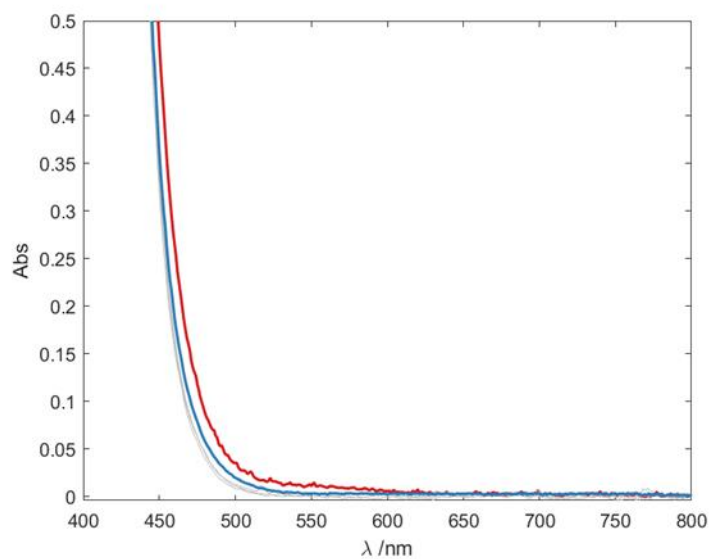


Figure D14: Attempted photogeneration of SmI₂ from a THF solution of SmI₃ (2 mM) and HEH₂ (60 mM) on irradiation with H160-440 nm; t = 0 (red trace); t = 60 min (blue trace).

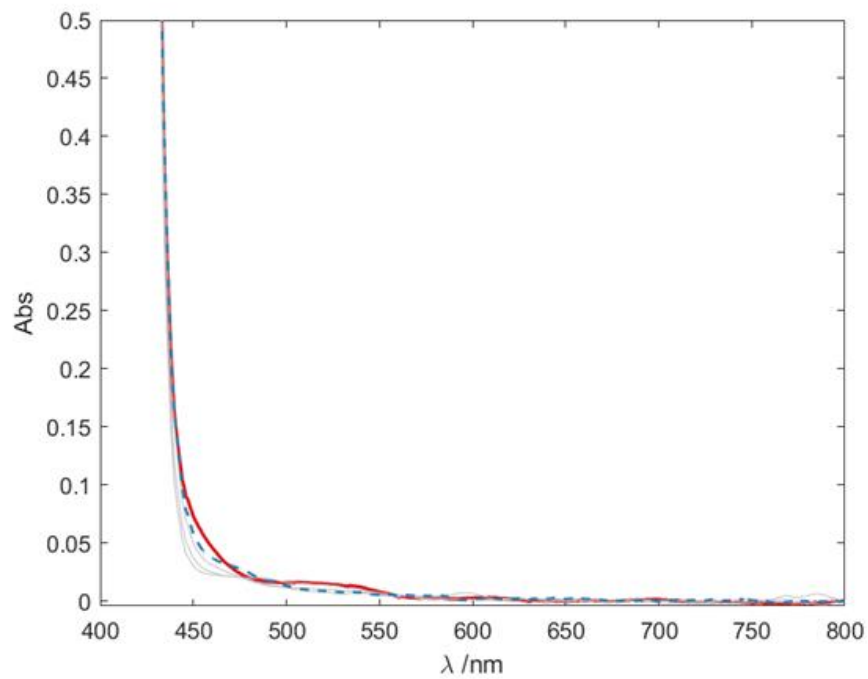


Figure D15: Attempted photogeneration of SmI₂ from a THF solution of Sm(OⁱPr)₃ (2 mM), nHep₄NI (6 mM), and HEH₂ (60 mM) on irradiation with H160-440 nm LED; t = 0 (red trace); t = 40 min (blue dashed trace).

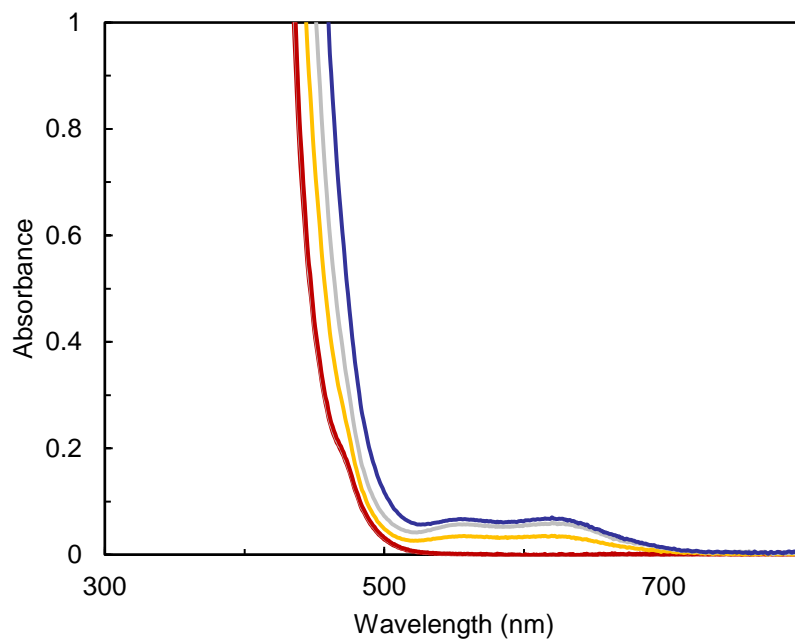


Figure D16: Photogeneration of SmI_2 from a THF solution of SmI_3 (2 mM) and HEH_2 (60 mM) with $[\text{Ir}]\text{PF}_6$ (0.2 mM) in the absence of base on irradiation with H160-440 nm LED over $t = 2$ min (red trace), $t = 6$ min (yellow trace), to $t = 16$ min (dark blue trace). Maximum intensity suggests $<10\%$ conversion to SmI_2 over prolonged irradiation.

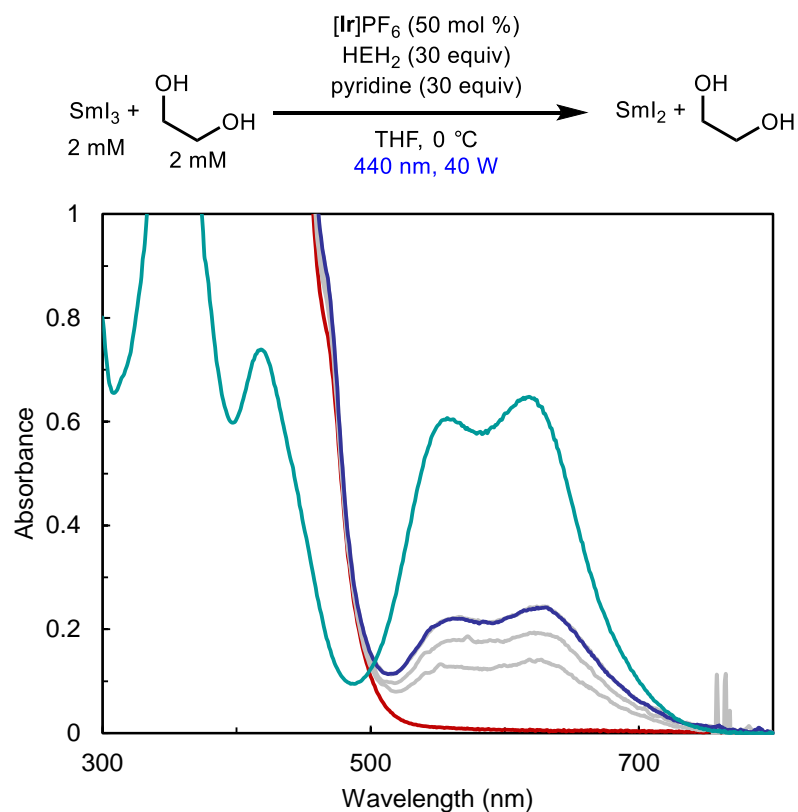


Figure D17: Photogeneration of SmI_2 in the presence of ethylene glycol (2mM) from a THF solution of SmI_3 (2 mM), HEH_2 (60 mM), and pyridine (60 mM) with $[\text{Ir}]\text{PF}_6$ (1 mM) on irradiation with H160-440 nm LED over $t = 0$ (red trace) to $t = 2$ min (dark blue trace) overlaid with the spectrum of SmI_2 (1 mM) in the presence of ethylene glycol (1 mM) in THF (teal trace). Maximum intensity suggests ~15% steady state population of Sm^{II} under irradiation.

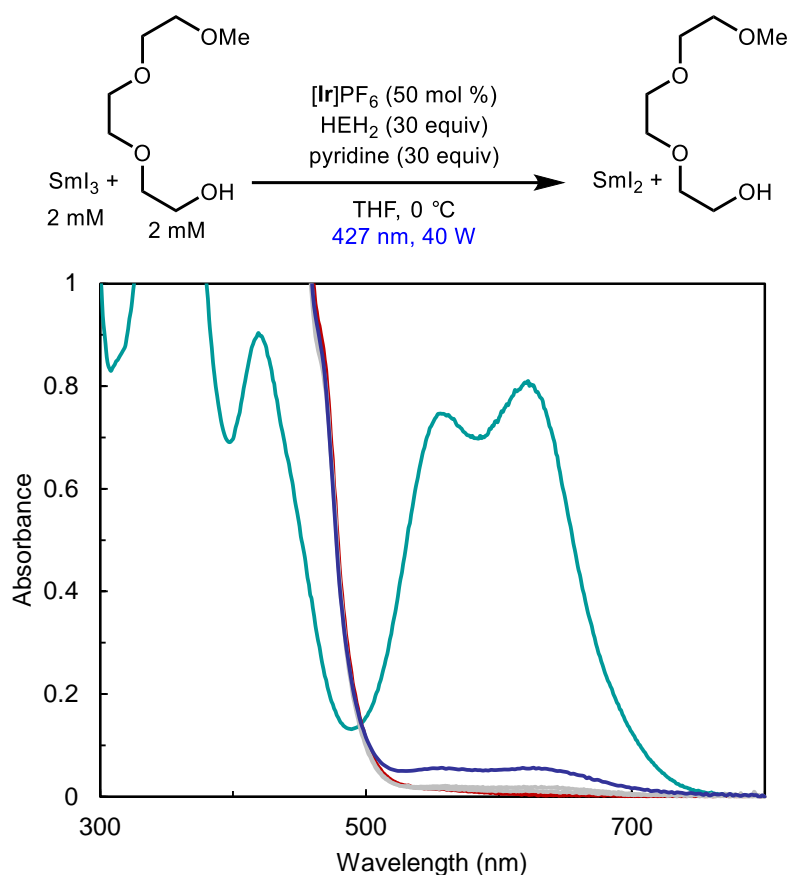


Figure D18: Photogeneration of SmI_2 in the presence of $\text{MeO}((\text{CH}_2)_2\text{O})_3\text{H}$ (2mM) from a THF solution of SmI_3 (2 mM), HEH_2 (60 mM), and pyridine (60 mM) with $[\text{Ir}]\text{PF}_6$ (1 mM) on irradiation with H160-427 nm LED over $t = 0$ (red trace) to $t = 30$ min (dark blue trace) overlaid with the spectrum of SmI_2 (1 mM) in the presence of $\text{MeO}((\text{CH}_2)_2\text{O})_3\text{H}$ (1 mM) in THF (teal trace). Maximum intensity suggests ~5% steady state population of Sm^{II} under irradiation.

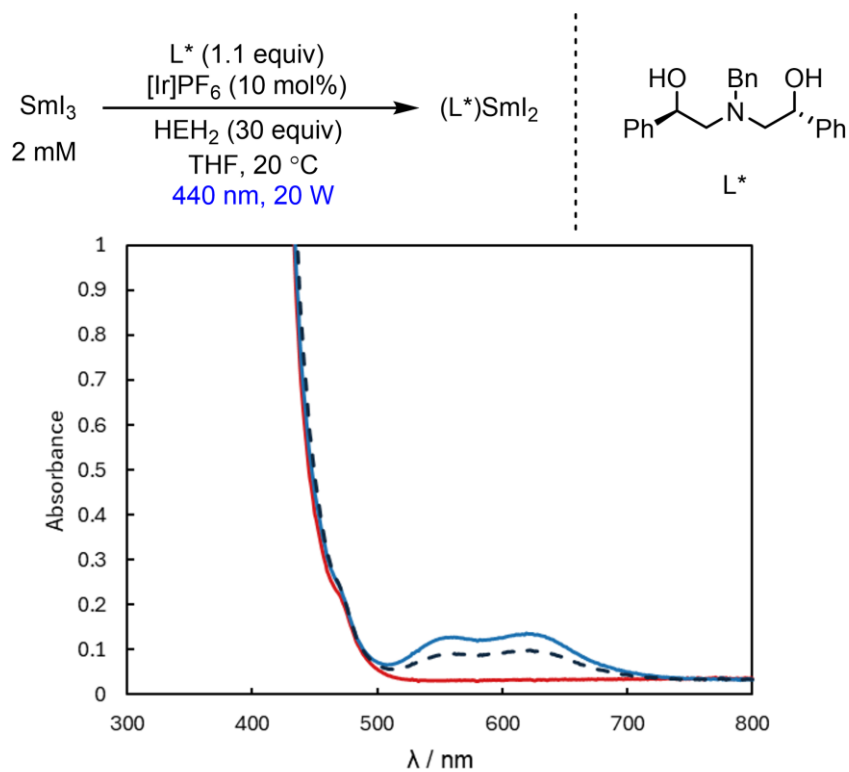


Figure D19: Photogeneration and decay of SmI_2 from THF solution of SmI_3 (2 mM), L^* (2.2 mM), $[\text{Ir}]\text{PF}_6$ (0.2 mM), HEH_2 (60 mM) on irradiation with H160-440 nm LED; $t = 0$ (red); $t = 1$ min (blue trace); $t = 60$ min (dashed). Maximum intensity suggests about 10% conversion to Sm^{II} .

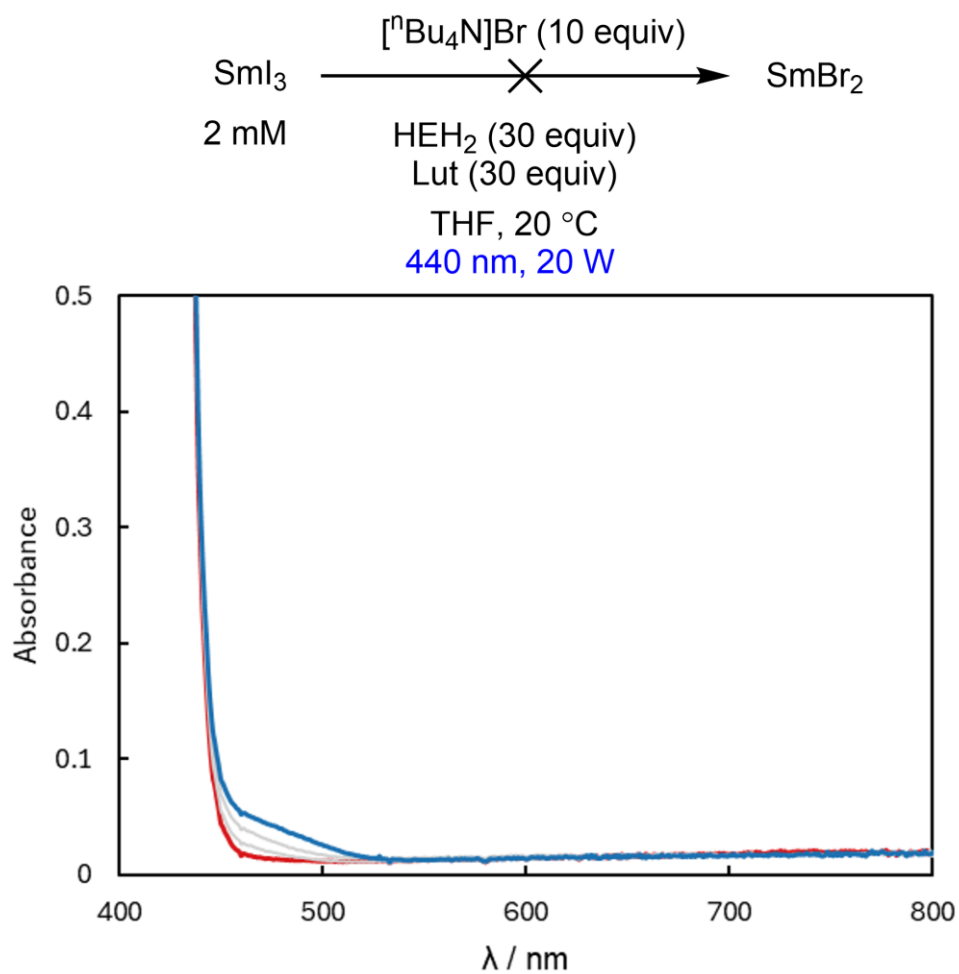


Figure D20: Attempted photogeneration of SmBr_2 from a THF solution of SmI_3 (2 mM), nBu_4NBr (20 mM), HEH_2 (60 mM), and Lut (60 mM) on irradiation with H160-440 nm LED; t = 0 (red trace); t = 60 min (blue trace).

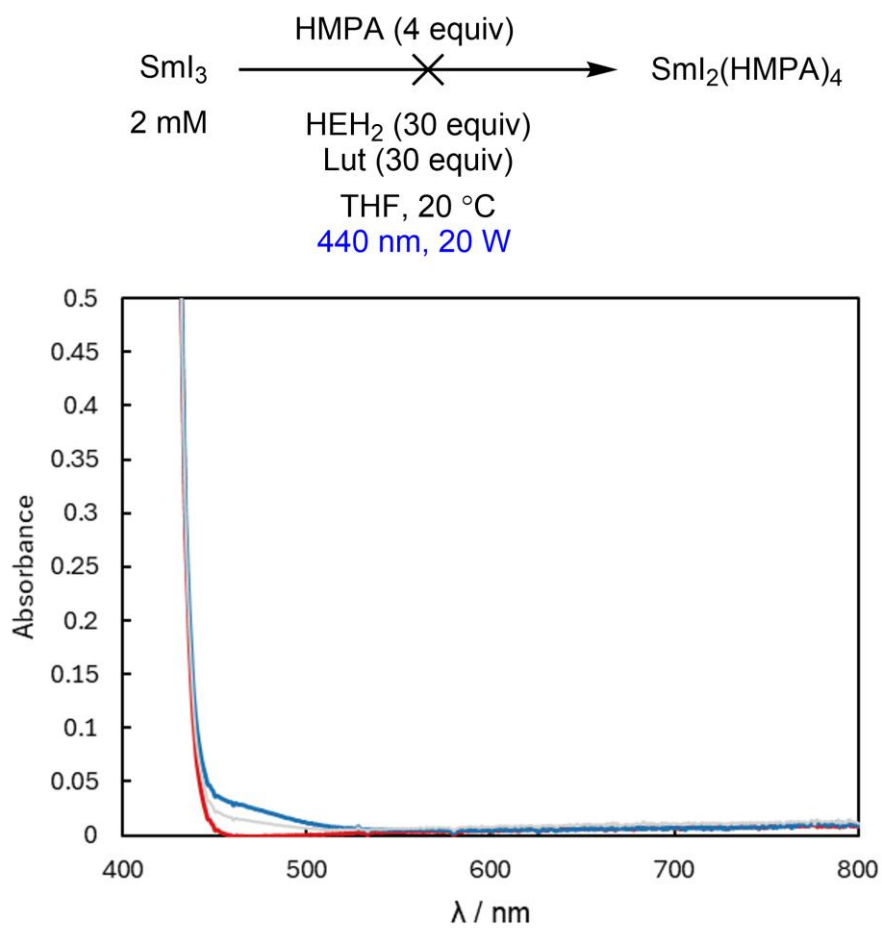


Figure D21: Attempted photogeneration of $\text{Sm}(\text{HMPA})_4^{2+}$ from a THF solution of SmI_3 (2 mM), HMPA (8 mM), HEH₂ (60 mM) and Lut (60 mM) on irradiation with H160-440 nm LED; t = 0 (red trace); t = 60 min (blue trace).

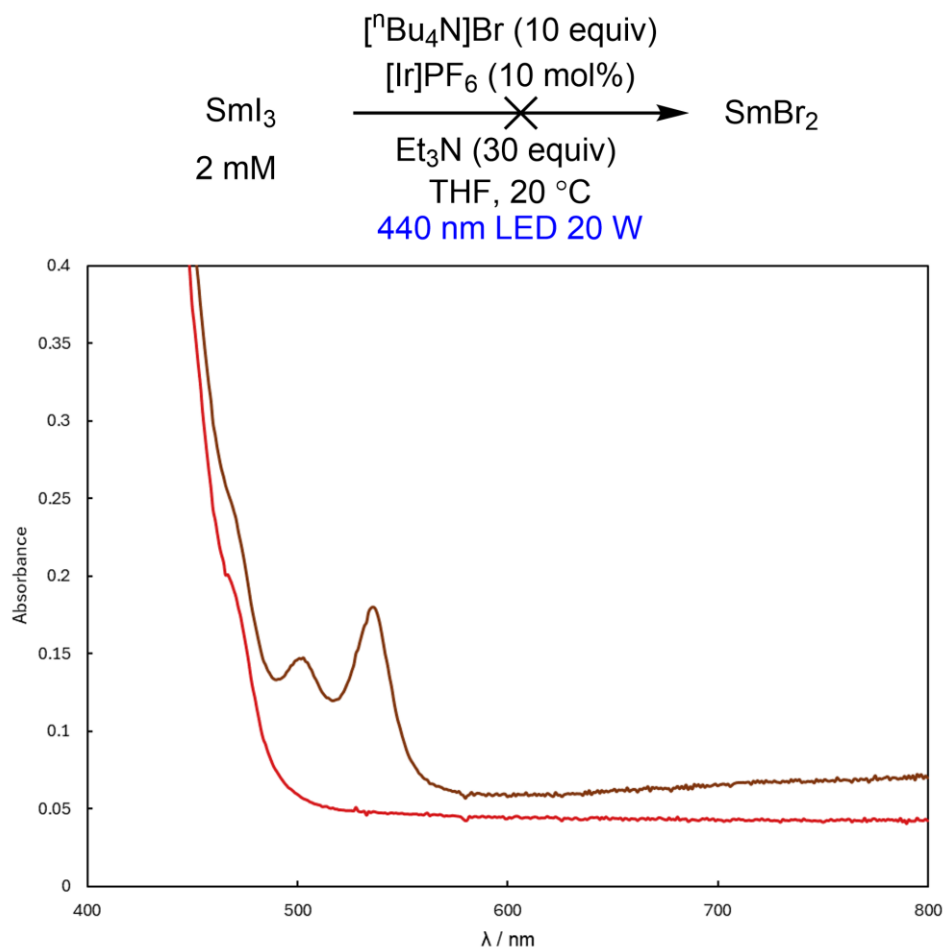


Figure D22: Attempted photogeneration of SmBr_2 from a THF solution of SmI_3 (2 mM), nBu_4NBr (20 mM), $[\text{Ir}(\text{ppy})_2(\text{dtbbpy})]\text{PF}_6$ (0.2 mM), and Et_3N (60 mM) on irradiation with H160-440 nm LED; $t = 0$ (red trace); $t = 20$ min (brown trace) shows formation of $[\text{Ir}^{\text{II}}(\text{ppy})_2(\text{dtbbpy})]$.⁸

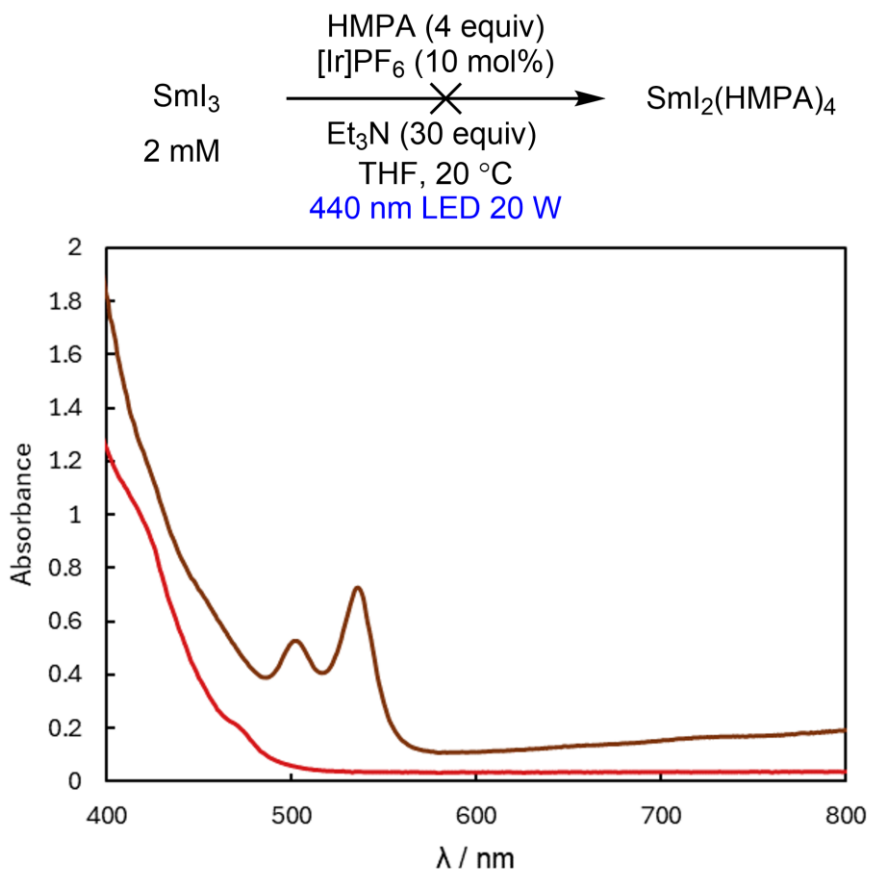


Figure D23: Attempted photogeneration of $\text{Sm}(\text{HMPA})_4^{2+}$ from a THF solution of SmI_3 (2 mM), HMPA (8 mM), $[\text{Ir}(\text{ppy})_2(\text{dtbbpy})]\text{PF}_6$ (0.2 mM), and Et_3N (60 mM) on irradiation with H160-440 nm LED; $t = 0$ (red trace); $t = 20$ min (brown trace) shows formation of $[\text{Ir}^{\text{II}}(\text{ppy})_2(\text{dtbbpy})]$.⁸

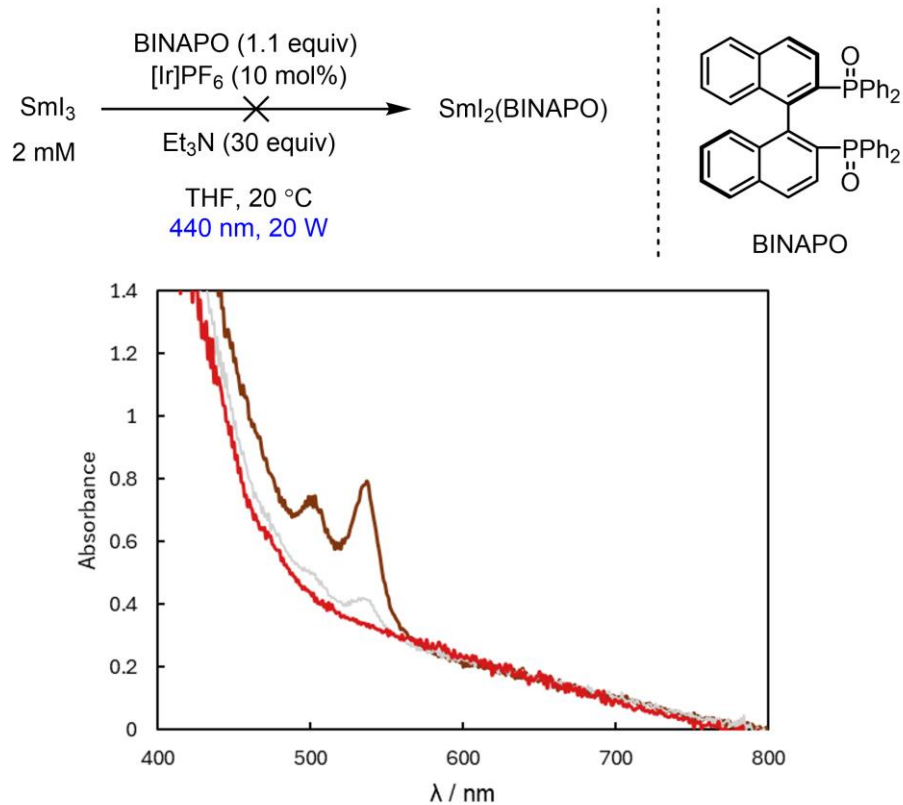


Figure D24: Attempted photogeneration of $\text{Sm}(\text{BINAPO})\text{I}_2$ from a THF solution of SmI_3 (2 mM), BINAPO (2.2 mM), $[\text{Ir}(\text{ppy})_2(\text{dtbbpy})]\text{PF}_6$ (0.2 mM), and Et_3N (60 mM) on irradiation with H160-440 nm LED; $t = 0$ (red trace); $t = 20$ min (brown trace) shows formation of $[\text{Ir}^{\text{II}}(\text{ppy})_2(\text{dtbbpy})]$.⁸ Note: white solids precipitate from the solution, leading to poor transmission.

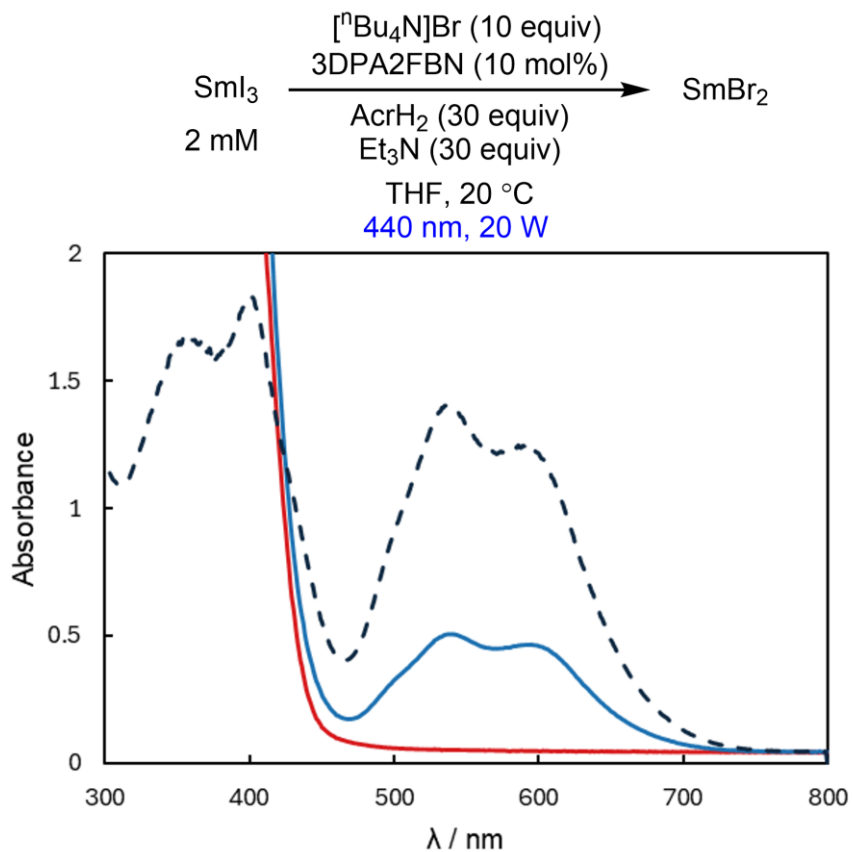


Figure D25: Photogeneration of SmBr_2 from THF solution of SmI_3 (2 mM), nBu_4NBr (20 mM), 3DPA2FBN (0.2 mM), AcrH_2 (60 mM), and Et_3N (60 mM) on irradiation with H160-440 nm LED; $t = 0$ (red trace); $t = 1$ min (blue trace) overlaid with spectrum of 2 mM SmBr_2 (dashed trace). Maximum intensity suggests about 40% conversion to SmBr_2 .

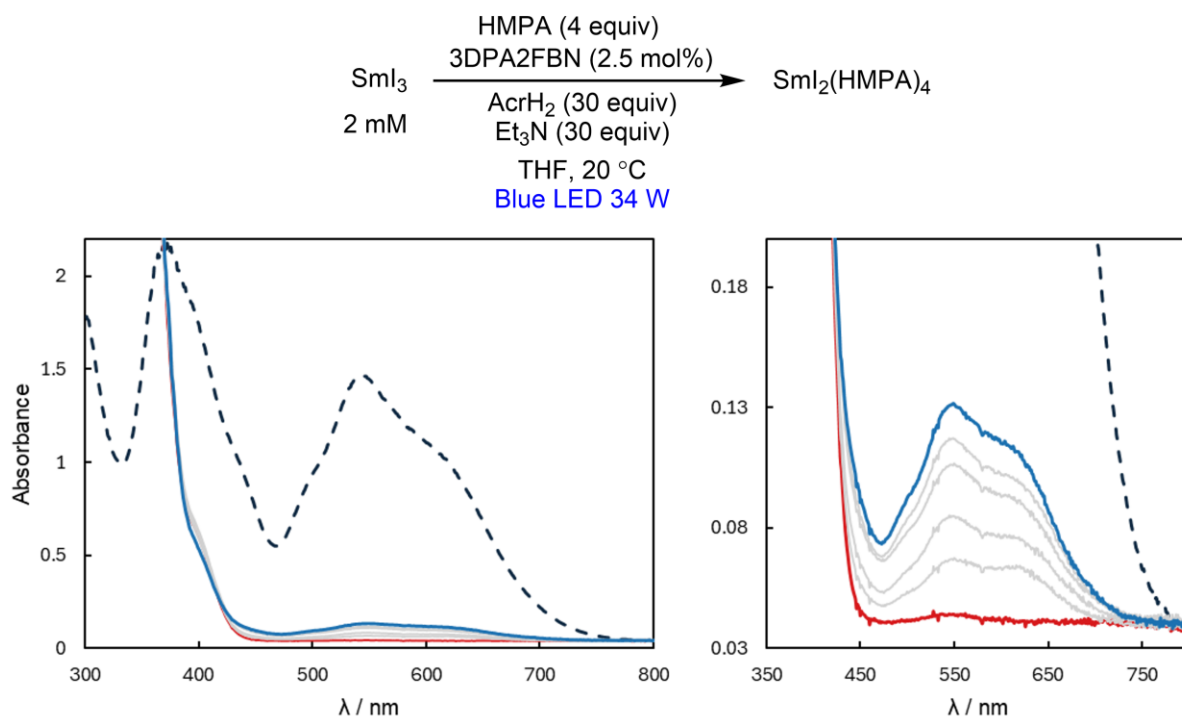


Figure D26: Photogeneration of $\text{SmI}_2(\text{HMPA})_4$ from THF solution of SmI_3 (2 mM), HMPA (8 mM), 3DPA2FBN (0.05 mM), AcrH_2 (60 mM), and Et_3N (60 mM) on irradiation with H150-Blue LED; $t = 0$ (red); $t = 60$ min (blue). Right most plot shows magnified region of relevant Sm(II) absorbance. Maximum intensity suggests about 10% conversion to $\text{Sm}(\text{HMPA})_4\text{I}_2$.

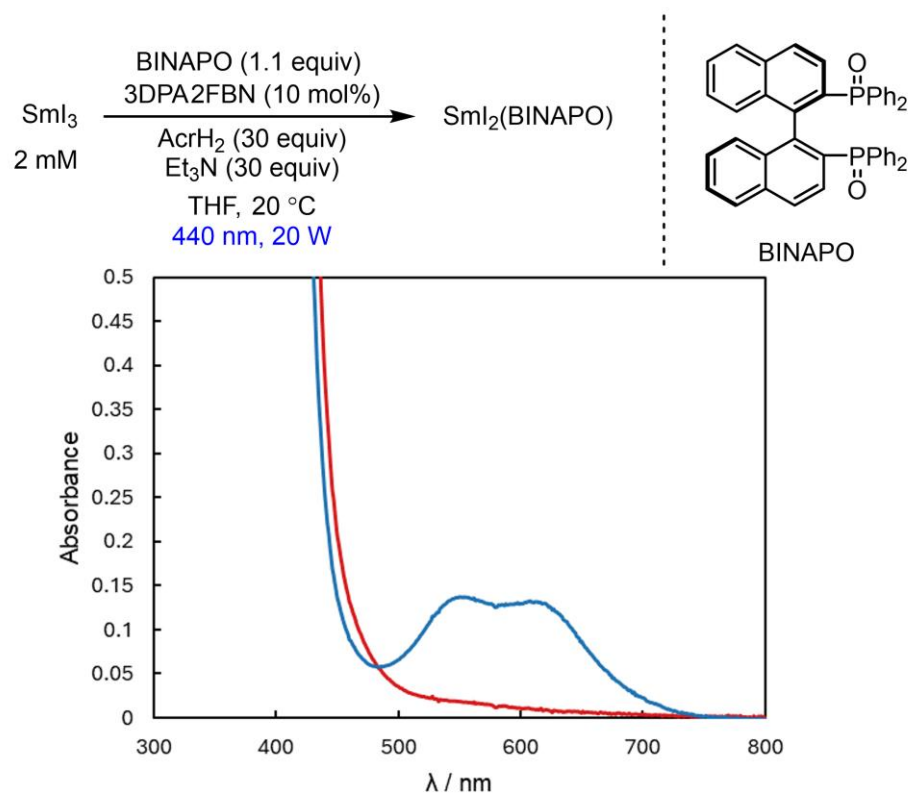


Figure D27: Photogeneration of $\text{Sm}(\text{BINAPO})\text{I}_2$ from THF solution of SmI_3 (2 mM), BINAPO (2.3 mM), 3DPA2FBN (0.2 mM), AcrH_2 (60 mM), and Et_3N (60 mM) on irradiation with H160-440 nm LED; $t = 0$ (red); $t = 2$ min (blue). Maximum intensity suggests about 10% conversion to $\text{Sm}(\text{BINAPO})\text{I}_2$.

D4 Electrochemistry

The solution-phase speciation of SmX_n is ill-defined and highly dependent on the concentration of both Sm and potential ligands. As a result, rigorous definition of $\text{Sm}^{\text{III/II}}$ redox potentials for discrete species is nontrivial. Cyclic voltammetry of SmI_3 in THF is illustrative of this issue. As shown in Figure 28, the observed $E_{1/2}$ of the reversible $\text{Sm}^{\text{III/II}}$ couple of $\text{SmI}_3(\text{THF})_n$ (using a tetraalkylammonium triflimide salt as a relatively innocent supporting electrolyte) shifts negative by 59 mV per decade increase in $^n\text{Hep}_4\text{NI}$ concentration. This behavior is consistent with reversible dissociation of Γ^- upon reduction, with the position of the wave described by the Nernst eqn **D1**:

$$E_{1/2} = E^\circ - \frac{RT}{F} \ln ([\Gamma^-]) \quad (\mathbf{D1})$$

The standard potential $E^\circ(\text{SmI}_3/\text{SmI}_2 + \Gamma^-)$, which can be extrapolated from the intercept of a plot of $E_{1/2}$ vs $-\log[\Gamma^-]$ as -1.58 V vs $\text{Fc}^{+/0}$, is therefore only equivalent to the $E_{1/2}$ observed by CV if $[\Gamma^-] = 1$ M.

Despite this challenge, knowledge of the electrochemical properties of Sm species in the presence of various additives is useful in guiding selection of appropriate photoreductants and photoredox catalysts for Sm^{III} reduction. For the purpose of this study, we have collected CV data under a unified set of conditions, using concentrations of Sm and additives relevant to the UV-Vis studies of Sm^{II} generation. It should be emphasized, however, that the observed reduction potentials in these specific cocktails must not be treated as diagnostic standard reduction potentials for discrete $\text{Sm}^{\text{II}}\text{L}_n$ species.

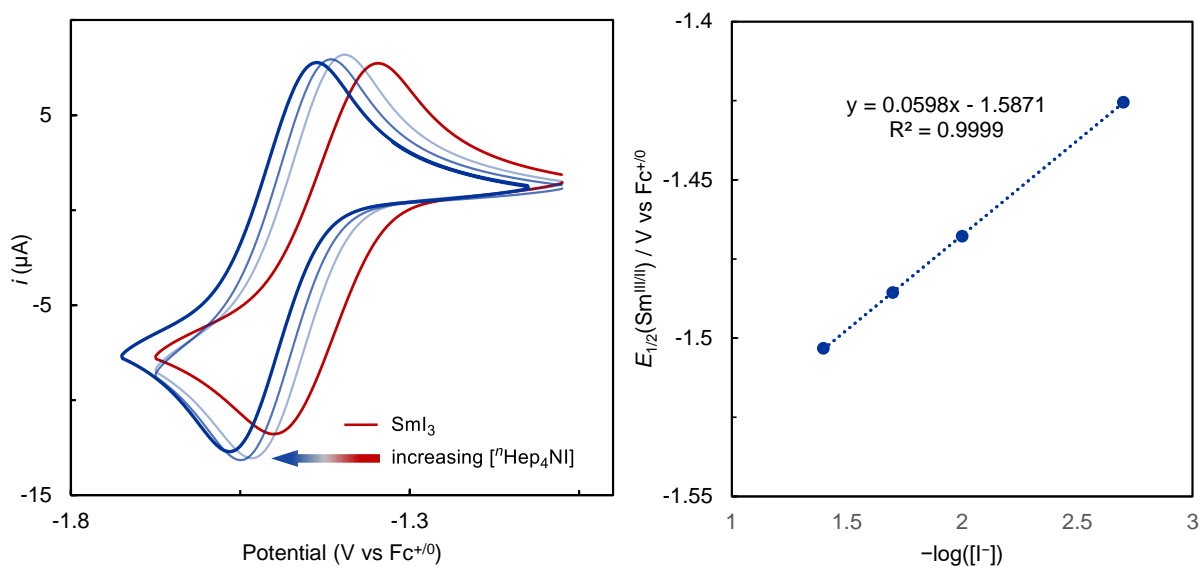


Figure D28: Left: CVs of SmI_3 (2 mM) in the presence of 0-40 mM $n\text{Hep}_4\text{NI}$ (red-dark blue traces) in THF containing 0.1 M BMPipNTf_2 at 25 mV s^{-1} . Right: plot of $E_{1/2}$ values from each CV vs $-\log([\text{I}^-])$.

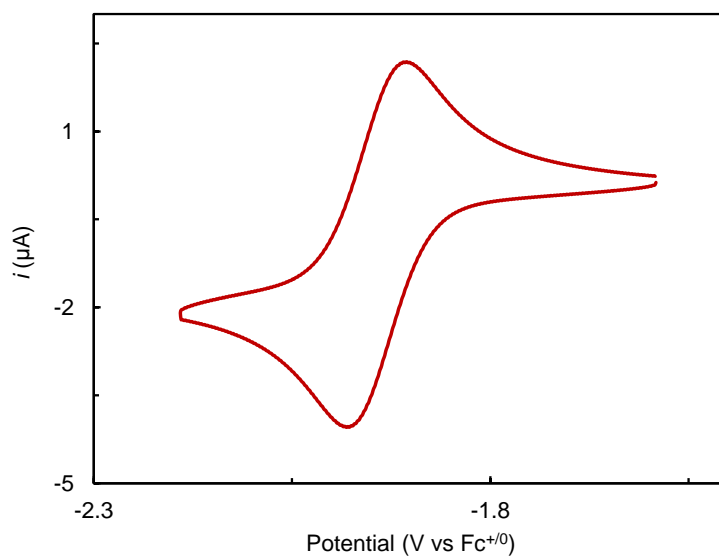


Figure D29: CV of $[\text{Ir}]\text{PF}_6$ (0.5 mM) in THF containing 0.1 M BMPipNTf_2 at 25 mV s^{-1} .

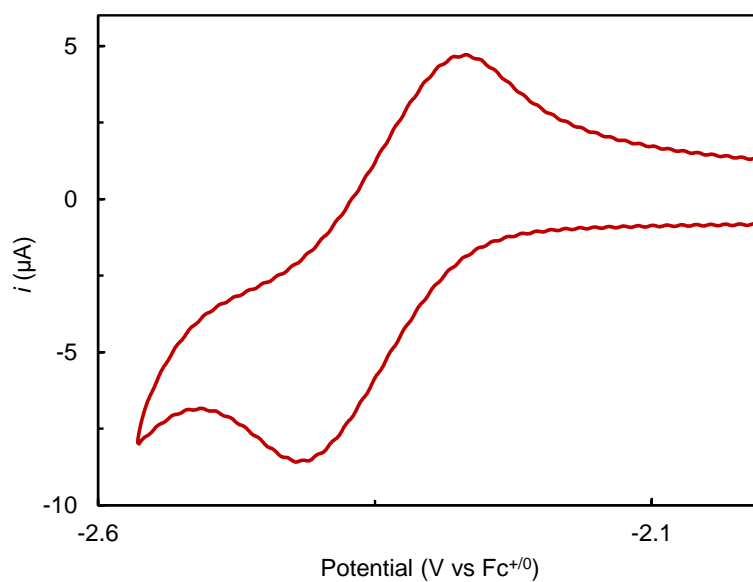


Figure D30: CV of 3DPA2FBN (1 mM) in THF containing 0.1 M BMPipNTf₂ at 100 mV s⁻¹.

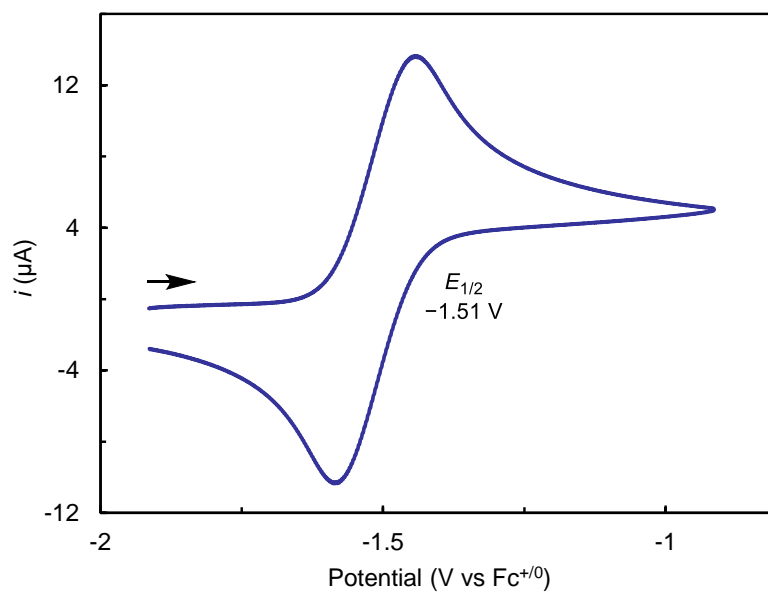


Figure D31: CV of SmI₂ (2 mM) and ⁿHep₄NI (10 mM) in THF containing 0.1 M BMPipNTf₂ at 25 mV s⁻¹.

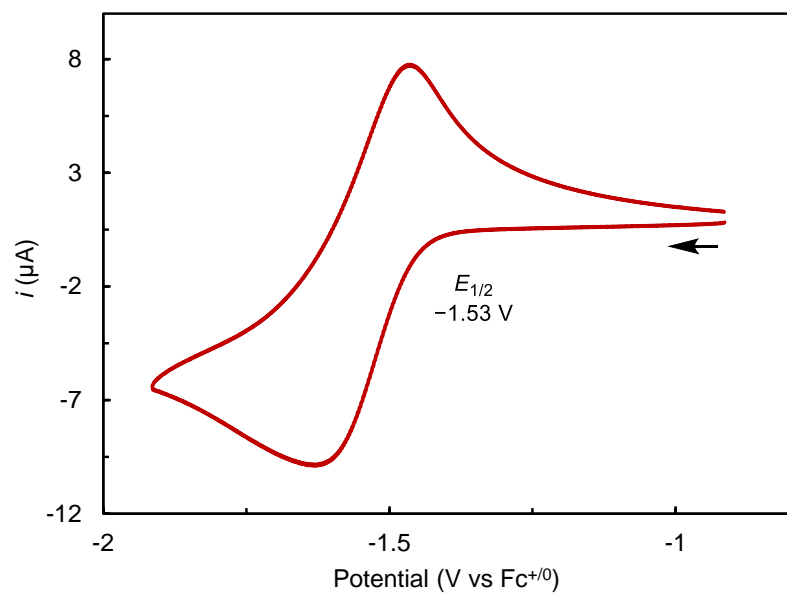


Figure D32: CV of SmI_3 (2 mM), $n\text{Hep}_4\text{NI}$ (10 mM), and ethylene glycol (2 mM) in THF containing 0.1 M BMPipNTf_2 at 25 mV s^{-1} .

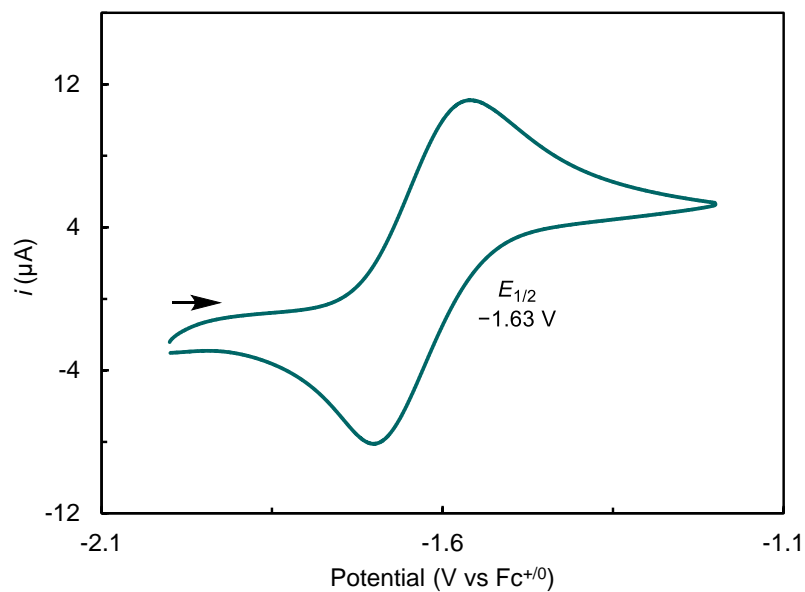


Figure D33: CV of SmI_2 (2 mM), $n\text{Hep}_4\text{NI}$ (10 mM), and $\text{MeO}((\text{CH}_2)_2\text{O})_3\text{H}$ (2 mM) in THF containing 0.1 M BMPipNTf_2 at 25 mV s^{-1} .

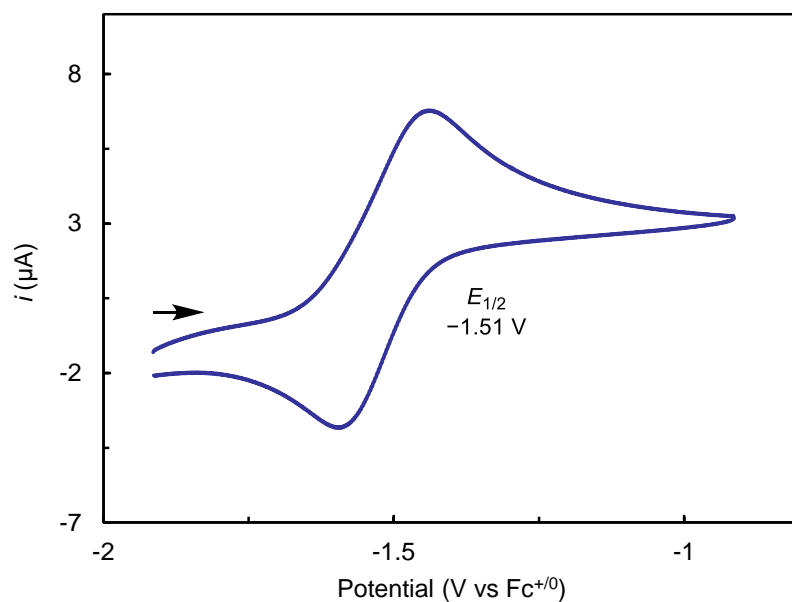


Figure D34: CV of SmI_2 (2 mM), $^n\text{Hep}_4\text{NI}$ (10 mM), and 3-aza-3-benzyl-1(R),5(R)-dihydroxy-1,5-diphenylpentane (2 mM) in THF containing 0.1 M BMPipNTf_2 at 25 mV s^{-1} .

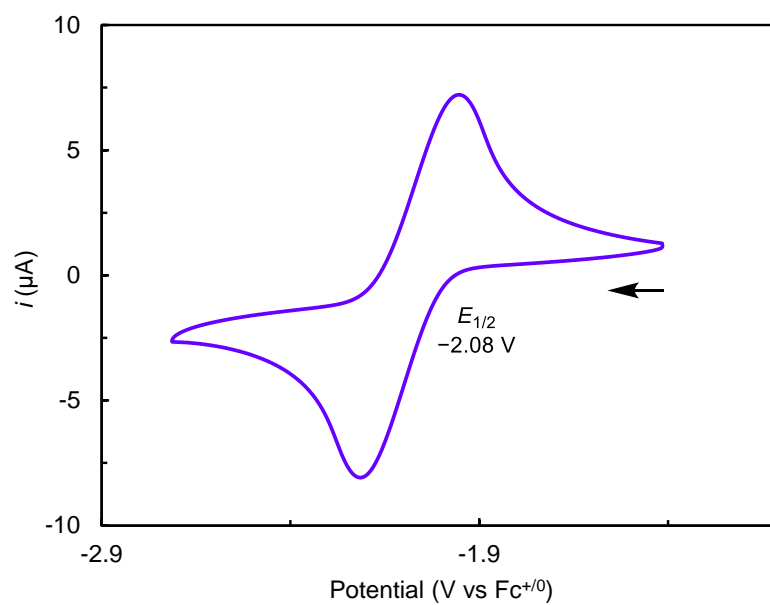


Figure D35: CV of SmI_3 (2 mM) and ${}^t\text{Bu}_4\text{NBr}$ (20 mM) in THF containing 0.1 M BMPipNTf_2 at 25 mV s^{-1} .

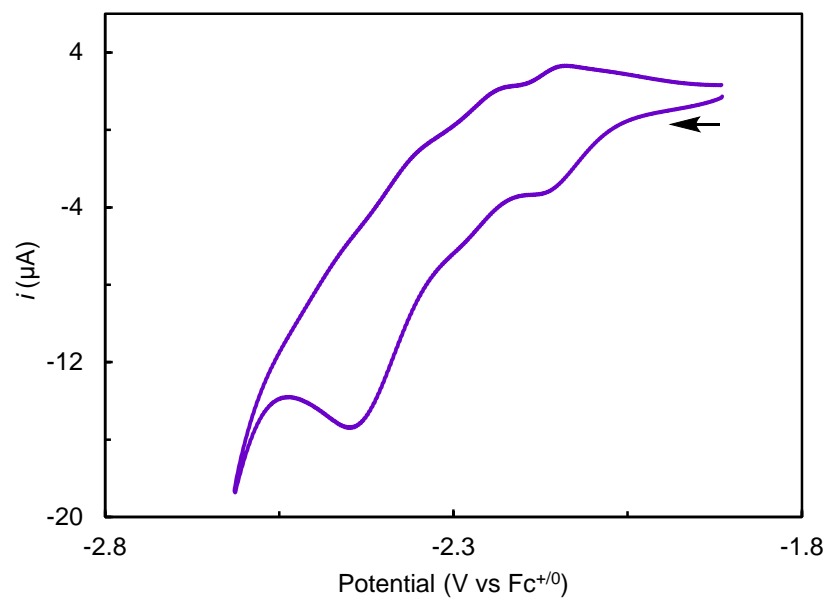


Figure D36: CV of SmI_2 (2 mM), ${}^t\text{Hep}_4\text{NI}$ (10 mM), and BINAPO (2 mM) in THF containing 0.1 M BMPipNTf_2 at 25 mV s^{-1} .

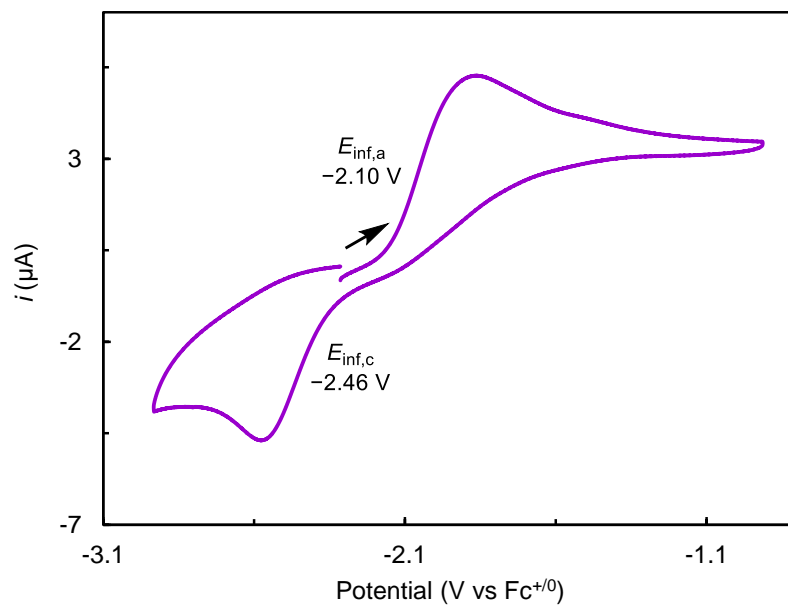
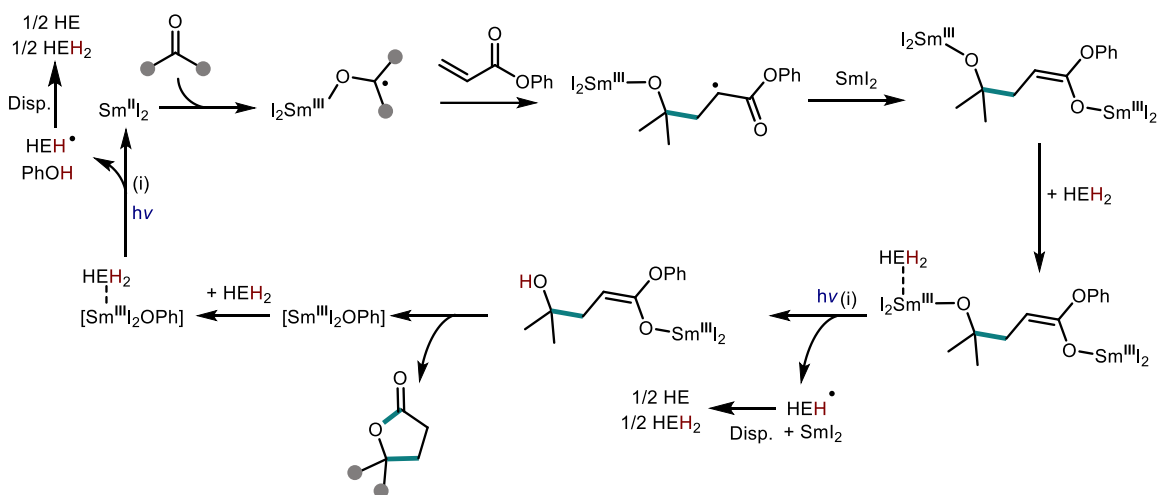


Figure D37: CV of SmI₂ (2 mM) and HMPA (8 mM) in THF containing 0.1 M BMPipNTf₂ at 25 mV s⁻¹. 334

D5 Additional mechanistic schemes



For clarity combined HEH_2 activation, Sm^{III} reduction and alkoxide protonation are labelled (i) and combined in a single step. A proposed sequence of steps is presented below, although other schemes (e.g. PT before dissociation) might be possible

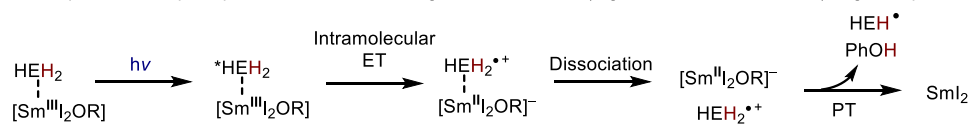


Figure D38: An alternative scheme for catalytic ketone-acrylate coupling reaction where HEH^\bullet does not terminate radical and instead two equivalents of SmI_2 are required per reduction.

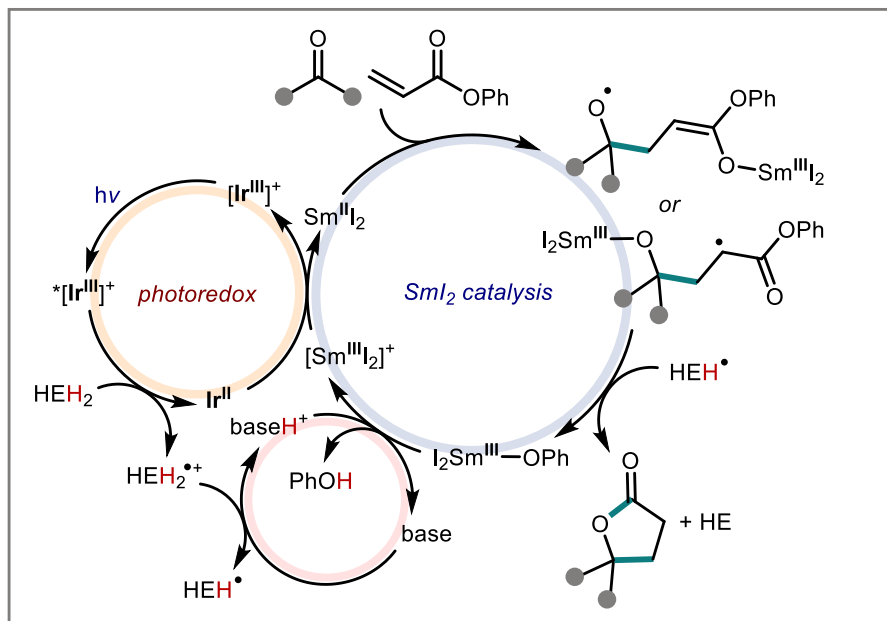


Figure D39: Proposed scheme for catalytic ketone-acrylate coupling reaction with [Ir]⁺.

REFERENCES

- (1) Watson, P. L.; Tulip, T. H.; Williams, I. Defluorination of perfluoroolefins by divalent lanthanoid reagents: activating carbon-fluorine bonds. *Organometallics* **1990**, *9* (7), 1999–2009.
- (2) Matesic, L.; Locke, J. M.; Vine, K. L.; Ranson, M.; Bremner, J. B.; Skropeta, D. Synthesis and anti-leukaemic activity of pyrrolo[3,2,1-hi]indole-1,2-diones, pyrrolo[3,2,1-ij]quinoline-1,2-diones and other polycyclic isatin derivatives. *Tetrahedron* **2012**, *68* (34), 6810–6819.
- (3) Seki, T.; McEleney, K.; Crudden, C. M. Enantioselective catalysis with a chiral, phosphane-containing PMO material. *Chem. Commun.* **2012**, *48* (51), 6369–6371.
- (4) Evans, D. A.; Nelson, S. G.; Gagne, M. R.; Muci, A. R. A chiral samarium-based catalyst for the asymmetric Meerwein-Ponndorf-Verley reduction. *J. Am. Chem. Soc.* **1993**, *115* (21), 9800–9801.
- (5) Boyd, E. A.; Shin, C.; Charboneau, D. J.; Peters, J. C.; Reisman, S. E. Reductive samarium (electro)catalysis enabled by Sm^{III}-alkoxide protonolysis. *Science* **2024**, *385* (6711), 847–853.
- (6) Norcross, B. E.; Clement, G.; Weinstein, M. The Hantzsch pyridine synthesis: A factorial design experiment for the introductory organic laboratory. *J. Chem. Educ.* **1969**, *46* (10), 694–695.
- (7) Fulmer, G. R.; Miller, A. J. M.; Sherden, N. H.; Gottlieb, H. E.; Nudelman, A.; Stoltz, B. M.; Bercaw, J. E.; Goldberg, K. I. NMR chemical shifts of trace impurities:

common laboratory solvents, organics, and gases in deuterated solvents relevant to³³⁸
the organometallic chemist. *Organometallics* **2010**, *29* (9), 2176–2179.

- (8) Baek, Y.; Reinhold, A.; Tian, L.; Jeffrey, P. D.; Scholes, G. D.; Knowles, R. R. Singly reduced iridium chromophores: Synthesis, characterization, and photochemistry. *J. Am. Chem. Soc.* **2023**, *145* (23), 12499–12508.

SUPPLEMENTARY INFORMATION FOR CHAPTER 6

Reproduced in part with permission from [Boyd, E.A.](#); Jung, H.; Peters, J. C. *J. Am. Chem. Soc.* **2025**, *147*, 4695. doi: [10.1021/jacs.4c14845](https://doi.org/10.1021/jacs.4c14845)

E1 Experimental Part**E1.1 General Considerations**

All manipulations were carried out using standard Schlenk or glovebox techniques under an N₂ atmosphere. Unless otherwise noted, solvents were deoxygenated and dried by thoroughly sparging with N₂ gas followed by passage through an activated alumina column in the solvent purification system by SG Water, USA LLC. Non-halogenated solvents were tested with a standard purple solution of sodium benzophenone ketyl in tetrahydrofuran to confirm effective oxygen and moisture removal. All reagents were purchased from commercial vendors and used without further purification unless otherwise stated. ⁿBu₄NNTf₂ was prepared by ion exchange of LiNTf₂ and ⁿBu₄NBr following a literature procedure,¹ recrystallized from hot EtOH, and then dried under vacuum at 100°C for >12 hours before use as electrolyte. ⁿHep₄NI was dried under vacuum at 100°C for >12 hours before use. Lutidine was distilled from CaH₂ and stored over activated molecular sieves. SmI₂(THF)₂,² PNPMoBr₃,³ PNPMo(N)I,^{3,4} PCPMoBr₃,⁵ LutHNTf₂,⁶ and HEH₂⁷ were synthesized by reported literature procedures.

E1.2 Nuclear Magnetic Resonance (NMR) Spectroscopy

Deuterated solvents were purchased from Cambridge Isotope Laboratories, Inc. ¹H chemical shifts are reported in ppm relative to tetramethylsilane, using residual solvent resonances as internal standards.⁸

E1.3 Electrochemistry

All electrochemical experiments were conducted using a CH instruments 600B electrochemical analyzer. A nonaqueous Ag^{+0} reference electrode (BASi) consisting of a silver wire immersed in 5 mM AgOTf in DME containing 0.2 M tBu_4NPF_6 separated from the working solution by a CoralPor® frit was used for all experiments. All reported potentials are referenced to the ferrocenium/ferrocene (Fc^{+0}) couple used as an external standard. All CVs were carried out in an N_2 -filled glovebox in a 20 mL scintillation vial fitted with a septum cap containing punched-out holes for insertion of electrodes. A glassy carbon disk (3 mm diameter) was used as the working electrode for all CVs. It was freshly polished with 1, 0.3, and 0.05 μm alumina powder water slurries, rinsed with water and acetone, and dried before use. A platinum wire was used as the auxiliary electrode for CVs. CVs are plotted using IUPAC convention. Unless otherwise noted, IR compensation was applied accounting for 85% of the total resistance.

E1.4 UV-Visible Absorption Spectroscopy

UV-Vis absorption spectra were collected on a Cary 50 spectrophotometer using a 1 cm quartz cuvette.

E1.5 Gas Chromatography

H_2 was quantified on an Agilent 7890A gas chromatograph (HP-PLOT U, 30 m, 0.32 mm ID; 30 °C isothermal; nitrogen carrier gas) using a thermal conductivity detector. A 1 mL manual injection was used and integration area was converted to percent H_2 composition by use of a calibration obtained from injection of H_2 solutions in N_2 of known concentration.

E2 Ammonia Generation Details

E2.1 Standard Electrochemical NH₃ Generation Reaction Procedure

All controlled potential electrolysis (CPE) experiments were carried out in a two-compartment cell separated by a fine glass frit (e.g., Figure E.1) in an N₂-filled glovebox. In a standard experiment, a solution of SmI₂(THF)₂ (5 mL, 3.7 mM, 19 μmol) in THF containing 0.1 M ⁿBu₄NNTf₂ is titrated with a concentrated solution of I₂ in THF until the blue color is consumed. ⁿHep₄NI (10.2 mg, 19 μmol), PNPMoBr₃ (100 μL of a 23 mM stock solution, 2.3 μmol), and LutHNTf₂ (71.4 mg, 0.19 mmol) are then added and the solution is transferred to the working compartment of the cell. A separate 5 mL solution of HEH₂ (51.4 mg, 0.20 mmol) and Lut (23 μL, 0.20 mmol) in THF containing 0.1 M ⁿBu₄NNTf₂ is prepared and transferred to the counter compartment of the cell. The cell is fitted with the working electrode (plain carbon cloth, AvCarb) and reference electrode in the working compartment and the counter electrode (carbon cloth) in the counter compartment. A fixed potential is applied (−1.45 V vs Fc⁺⁰ unless otherwise noted) and the solutions are stirred (~600 rpm) for the desired reaction time or until charge corresponding to 3e[−] / 4H⁺ has passed (13.5 C for the standard acid loading).



Figure E1: Two-compartment cell used for CPE experiments.

E2.2 Electrochemical $^{15}\text{NH}_3$ Generation Reaction Procedure under $^{15}\text{N}_2$

The two-compartment cell shown in Figure E.1 is assembled in a $^{14}\text{N}_2$ -filled glovebox using the standard procedure in S2.1. The cell is then passed out of the glovebox and both compartments are sparged with argon for 15 min. The working compartment is then sparged with $^{15}\text{N}_2$ (Cambridge Isotopes, 99%) for 5 min. All sparging gases are first passed through a trap containing a saturated THF solution of SmI_2 as a scrubber. A fixed potential is then applied (-1.45 V vs $\text{Fc}^{+/0}$ unless otherwise noted) and the solutions are stirred (~ 600 rpm) until the desired amount of charge has passed.

It was found that the Sm catalyst is deactivated much more rapidly under these conditions than under the standard conditions, likely due to a higher content of poisons (e.g., O_2 , H_2O) in the sparging gases than in the catalyst-purified glovebox atmosphere.

However, similar yields of $^{14}\text{NH}_3$ and $^{15}\text{NH}_3$ are obtained with the corresponding N_2 ³⁴⁴ isotopologue following the same series of manipulations (Figure E.4), supporting assignment of N_2 as the N-atom source in the electrochemically produced ammonia.

E2.3 Ammonia Quantification

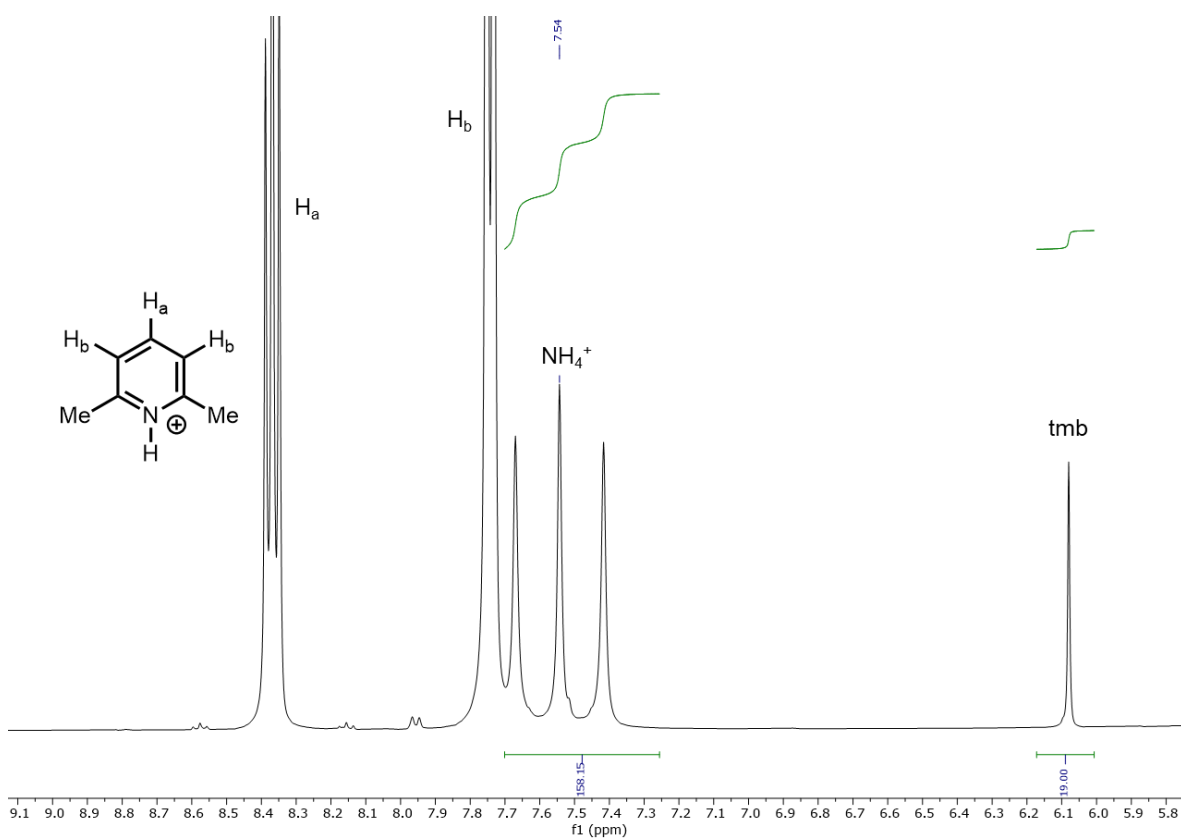
The contents of both compartments of the cell are transferred to a Schlenk tube. The cell is rinsed with 3 x 1 mL portions of THF and the rinses are added to the Schlenk tube. The tube is sealed, brought out of the glovebox, and frozen in liquid nitrogen. The tube is briefly opened and NaO^tBu (2 mL of a 0.25 M solution in MeOH, 0.5 mmol) is added down the walls of the flask. The tube is resealed and allowed to equilibrate in liquid nitrogen for 10 min. While frozen, the headspace of the flask is removed and the tube is resealed. The mixture is then allowed to warm and stir at room temperature for 15 min. A second Schlenk tube is charged with HCl (3 mL of a 2.0 M solution in Et₂O, 6 mmol) to serve as a collection flask. The volatiles of the reaction mixture are vacuum transferred at room temperature into this collection flask. After completion of the vacuum transfer, the collection flask is sealed and warmed to RT. Solvent is removed *in vacuo*, and the remaining residue is dissolved in 0.7 mL of DMSO-*d*₆ containing 1,3,5-trimethoxybenzene (9 mM) as an internal standard. The ¹H NMR signal observed for NH₄⁺ is then integrated against the aryl protons of trimethoxybenzene to quantify the ammonium present.

Alternatively, a 100 μL aliquot of the cathode solution is diluted first with 5.00 mL of an aqueous solution of phenol (5.0 g per 500 mL) and sodium nitroprusside (25.0 mg per 500 mL) followed by 5.00 mL of an alkaline hypochlorite solution (2.5 g of sodium hydroxide and 4.2 mL of sodium hypochlorite per 500 mL).⁹ At the same time, a 100 μL solution of 0.1 M ⁿBu₄NNTf₂ in THF is subjected to the same conditions. After

development for 45 min, the UV-visible absorption at 635 nm of the reaction mixture³⁴⁵ sample is recorded. The absorption of the background sample prepared with electrolyte is recorded and subtracted from this value. The corrected absorption value is used to quantify the yield of NH₃ using a calibration curve. Good agreement is obtained between the indophenol and ¹H NMR spectroscopy quantification methods (Table E1).

Table E1: Individual eN_2R experiments under the standard conditions.

Entry	Quantification method	Charge (C)	yield NH_3 (μmol)	equiv NH_3 per Mo	F.E.
A	1H NMR	13.5	39.5	17.2	83
B	1H NMR	14.0	38.2	16.6	79
C	1H NMR	13.5	38.5	16.7	82
D	Indophenol ^a	10.8	31.3	17.0	84
Average				16.9 ± 0.3	82 ± 2

^a4.0 mL cathode and anode volumes**Figure E2:** 1H NMR (d_6 -DMSO, 400 MHz) spectrum of the basic, volatile products of eN_2R under the standard conditions. Integration of the 4H signal of $^{14}NH_4Cl$ at 7.54 ppm versus the 3H aryl peak of 1,3,5-trimethoxybenzene (9 mM, 6.3 μmol) as an internal standard provides the NH_3 yield (39 μmol , 17 equiv per Mo, 83% F.E.).

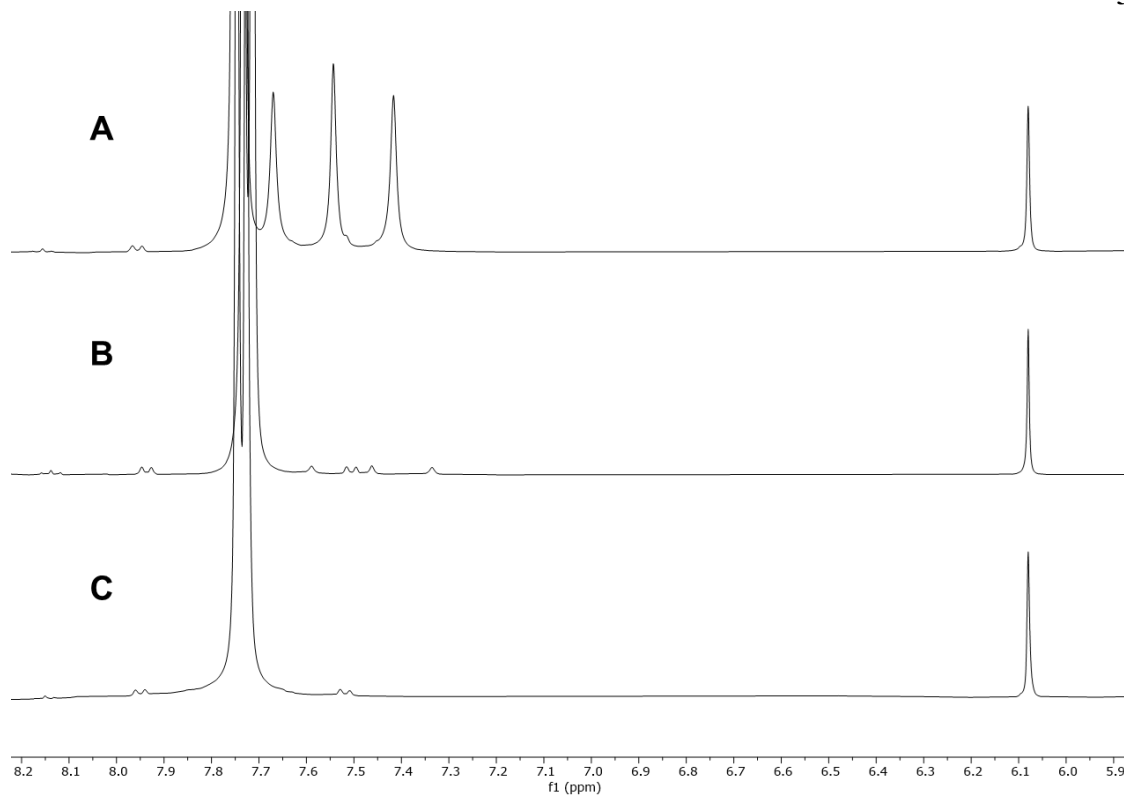


Figure E3: ^1H NMR (d_6 -DMSO, 400 MHz) spectrum of the basic, volatile products of $e\text{N}_2\text{R}$ under (A) the standard conditions; (B) the standard conditions in the absence of Sm; and (C) the standard conditions in the absence of Mo. The spectrum intensities are normalized to 1,3,5-trimethoxybenzene present at the same concentration (9 mM, 6.3 μmol) in each sample as an internal standard.

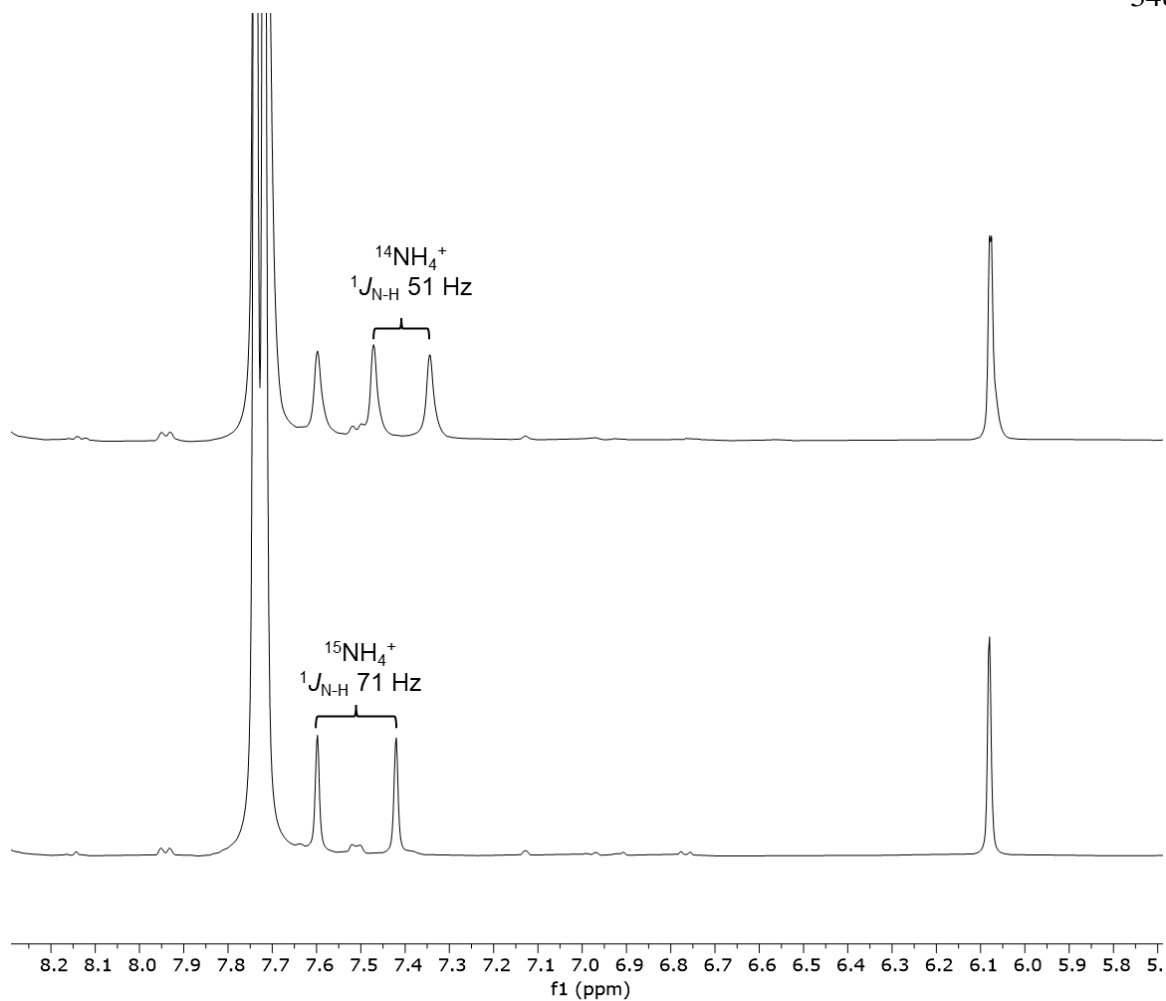


Figure E4: ^1H NMR (d_6 -DMSO, 400 MHz) spectrum of the basic, volatile products of $e\text{N}_2\text{R}$ under $^{14}\text{N}_2$ (top) or $^{15}\text{N}_2$ (bottom) as described in S2.2. The spectrum intensities are normalized to 1,3,5-trimethoxybenzene present at the same concentration (9 mM, 6.3 μmol) in each sample as an internal standard.

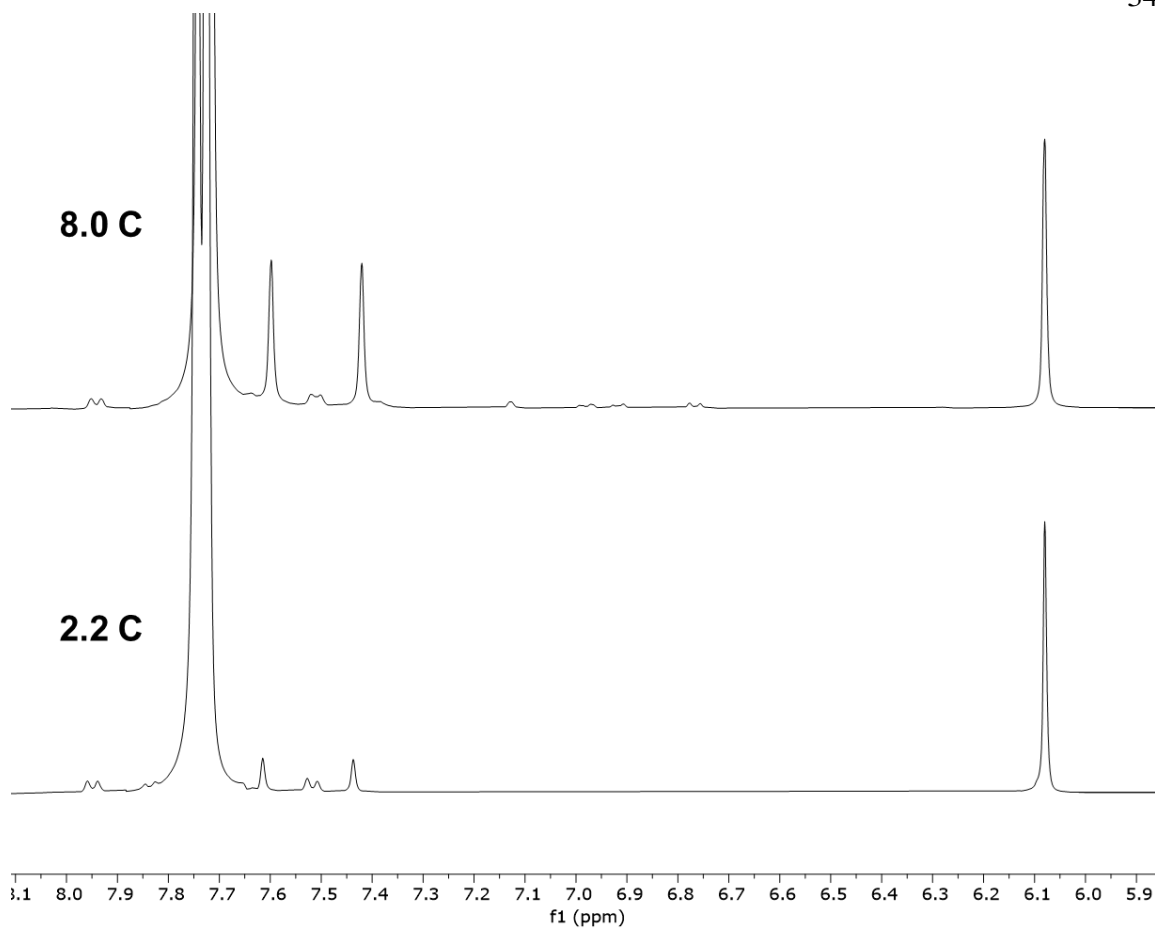


Figure E5: ^1H NMR (d_6 -DMSO, 400 MHz) spectrum of the basic, volatile products of $e\text{N}_2\text{R}$ under $^{15}\text{N}_2$ stopped after passage of 2.2 or 8.0 C, demonstrating that the produced $^{15}\text{NH}_4^+$ is coming from the electrocatalytic process. The spectrum intensities are normalized to 1,3,5-trimethoxybenzene present at the same concentration (9 mM, 6.3 μmol) in each sample as an internal standard.

Table E2: Results of electrolysis under the standard conditions under 1 atm argon instead of N_2 .

Entry	Charge (C)	yield NH_3 (μmol)	equiv NH_3 per Mo	F.E. NH_3 (%)	F.E. H_2 (%)
1	6.4	0	0	0	58
2 ^a	4.0	0	0	0	63

^aNo Sm

E2.4 Reaction Progress of eN_2R

Procedure: The cell is assembled under the standard conditions described in S2.1. To track ammonia generation, 100 μL of the cathode solution is removed by syringe through the septum of the working compartment after passage of the desired amounts of charge and analyzed by the indophenol method. A 100 μL portion of 0.1 M $n\text{Bu}_4\text{NNTf}_2$ is added to the cathode solution to maintain a constant volume in each compartment of the cell.

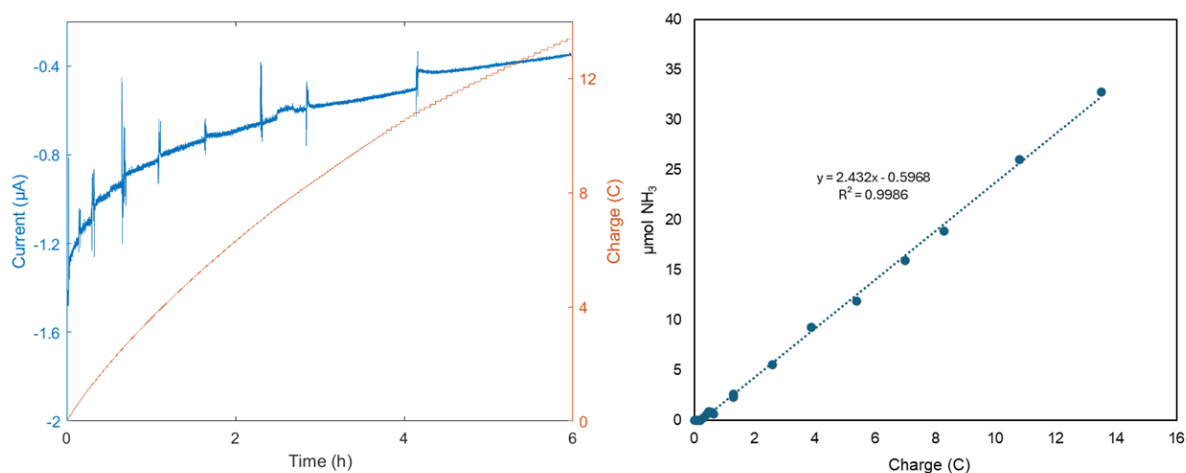


Figure E6: Left: CPE under the standard eN_2R conditions with removal of 100 μL aliquots from the cathode solution at various time points; Right: Plot of the total yield of NH_3 vs charge passed. These data demonstrate that the ammonia measured at the end of the electrolysis is produced electrochemically with a constant F.E.

E2.5 Organic Product Quantification

Procedure: The eN_2R was conducted as described in S2.1. Following passage of 10.8 C, the contents of the anode compartment were transferred to a vial and solvent was removed *in vacuo*. The residue was extracted into Et₂O (3 x 3 mL) and passed over a plug of silica. After removing solvent, the remaining solids were taken up in CDCl₃ containing a known amount of 1,3,5-trimethoxybenzene and analyzed by ¹H NMR spectroscopy.

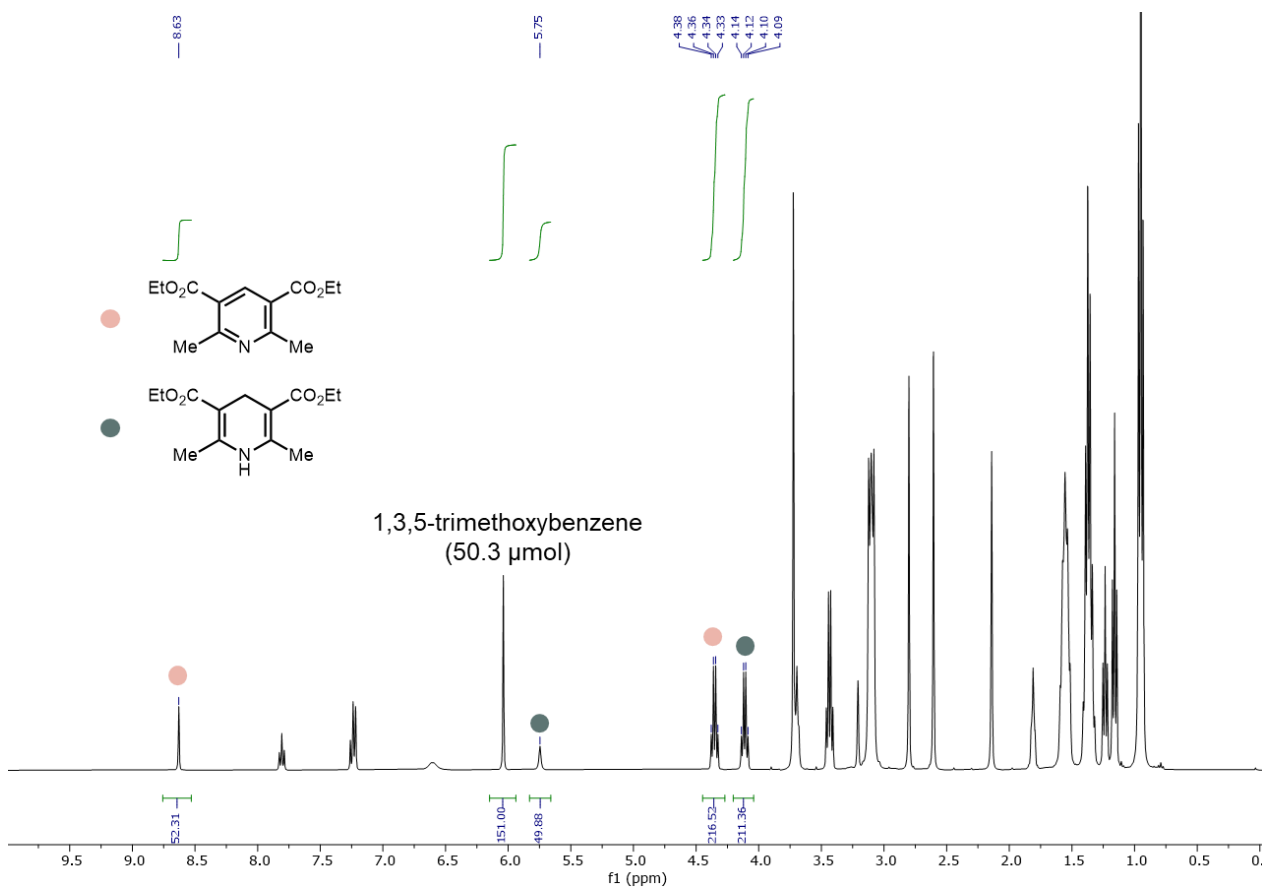


Figure E7: ¹H NMR (CDCl₃, 400 MHz) spectrum of the organic species extracted from the anode compartment following passage of 10.8 C of charge under the standard eN_2R conditions. Integration to the internal standard 1,3,5-trimethoxybenzene indicates that the $2H^+ / 2e^-$ oxidation of HEH₂ to form HE proceeds with 93% F.E.

E2.6 Selected CPE Traces

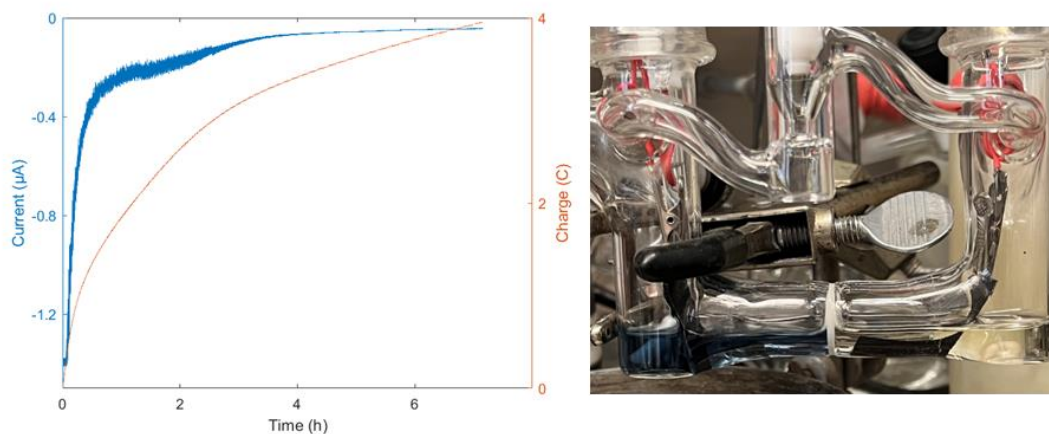


Figure E8: Left: CPE under the standard eN_2R conditions in the absence of $PNPMoBr_3$. Right: Photograph of the eN_2R cell during electrolysis in the absence of $PNPMoBr_3$. The characteristic dark blue color of the cathode solution indicates that $SmI_2(THF)_2$ is generated under these conditions and builds up without the Mo cocatalyst.

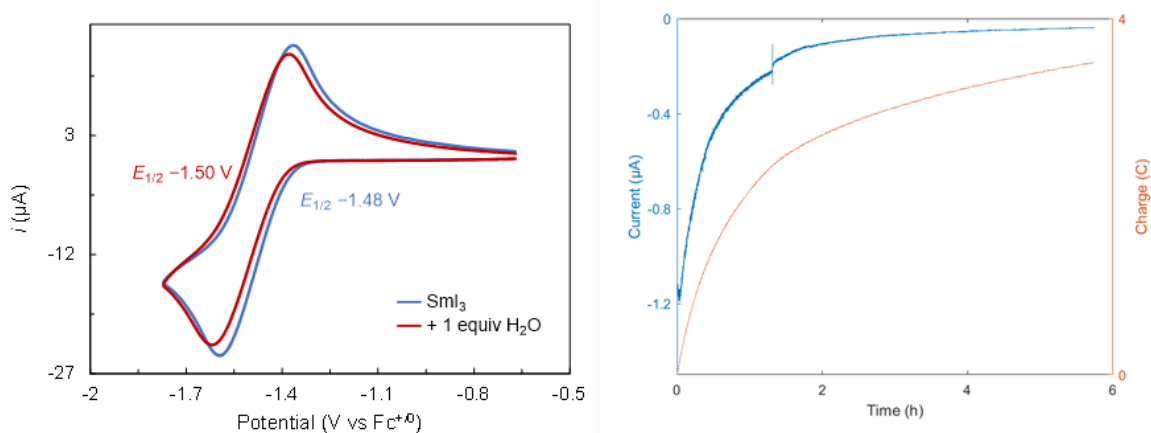


Figure E9: Left: CV of SmI_3 (3.7 mM, blue trace) following the addition of 1 equiv H_2O (3.7 mM, red trace) at 25 mV s^{-1} (0.1 M $n\text{-Bu}_4\text{NNTf}_2$ /3.7 mM $n\text{-Hep}_4\text{NI}$ in THF, glassy carbon disk working electrode, $Ag^{+/0}$ pseudoreference electrode, Pt wire counter electrode). Right: CPE under the standard eN_2R conditions in the presence of 1 equiv H_2O per Sm.

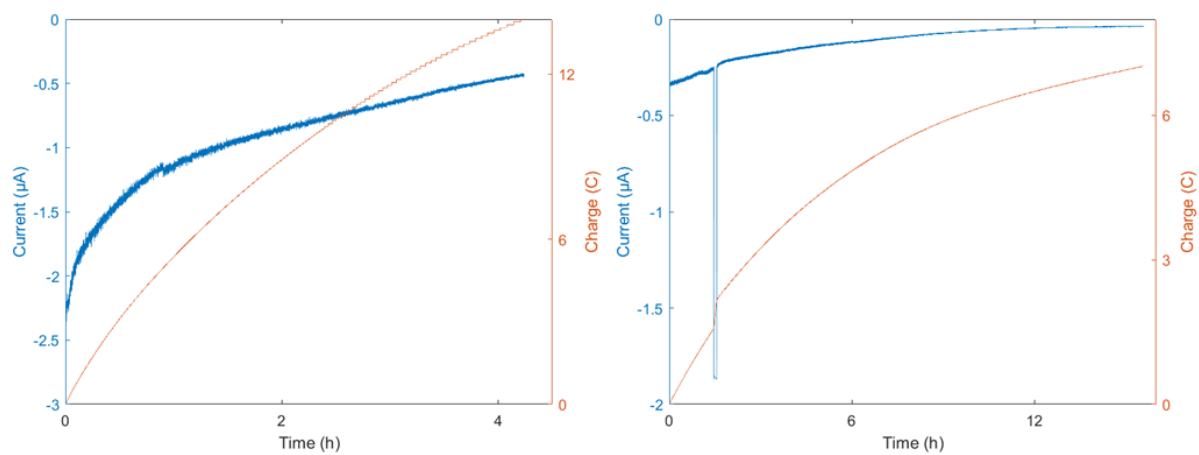


Figure E10: CPE under the standard eN_2R conditions using PNPMo(N)I (0.46 mM) and SmI_3 as catalysts at Sm loadings of 3.7 mM (left) and 0.46 mM (right).

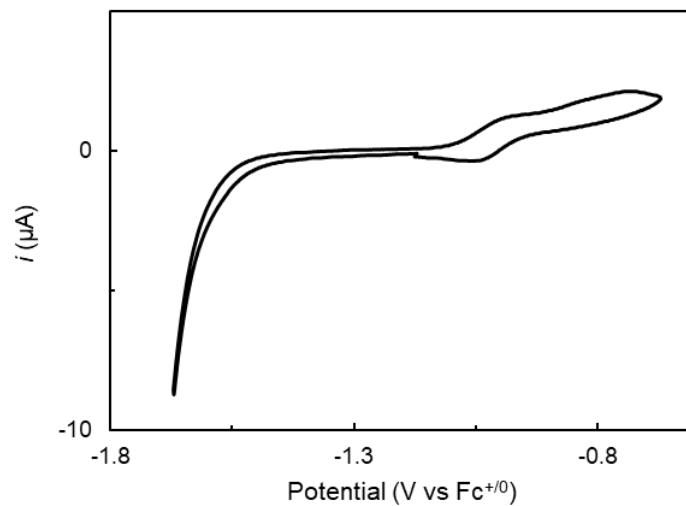


Figure E11: CV of the cathode solution after passage of 7.0 C using PNPMoNI (0.46 mM) and SmI₃ (0.46 mM) as catalysts under otherwise standard *e*N₂R conditions. The absence of a quasireversible couple at -1.45 V indicates that the redox-active Sm species is deactivated at low [Sm].

E3 NO_x Quantification

NO_x impurities in the gas supplies were quantified by their conversion to NO₂⁻ and NO₃⁻ in basic media and quantification of the former by the Griess method using the following color development solutions.¹⁰

Solution A: 0.1 g sulfanilamide was dissolved in 1.0 mL 32 wt.% HCl, followed by dilution with deionized water to a total volume of 10.0 mL.

Solution B: 10.0 mg of *N*-1-naphthylethylenediamine dihydrochloride was dissolved in 10 mL of deionized water.

Specifically, an electrochemical cell under ¹⁴N₂ or ¹⁵N₂ atmosphere from the same source as employed in the N₂RR experiments was filled with 5 mL of 0.1 M KOH aqueous solution and allowed to stir for 2h. Any gas-phase NO_x impurity is assumed to be quantitatively converted into NO₂⁻ or NO₃⁻ in this basic solution. A 200 μL sample of the trap solution was diluted with 300 μL 0.1 M KOH followed by addition of 500 μL 0.1 M HCl, 25 μL of the sulfanilamide solution A, and 25 μL of the *N*-1-naphthylethylenediamine dihydrochloride solution B. The mixture was allowed to incubate for 20 min at room temperature. It was then diluted with 3.0 mL of water and the UV-Vis absorption at 538 nm was recorded. The sample was then treated with 50 μL of a solution of vanadium(III) chloride (VCl₃) in 6 M HCl (0.02 wt.%) and incubated at 60 °C for 25 min to convert NO₃⁻ to NO₂⁻. The resulting solution was brought to room temperature and any increase in the absorption at 538 nm was recorded. Comparison to calibration curves indicates that the NO_x content in the gas supplies is <0.3% of the moles of NH₃ produced under the standard conditions.¹¹

Similarly, the NO_x content in the electrolyte was quantified by subjecting a 200 μL aliquot of 0.1 M ¹⁸Bu₄NNTf₂ in THF to the color development procedure described above.

The concentration of $\text{NO}_2^- + \text{NO}_3^-$ in the electrolyte is $<0.3\%$ of the concentration of ³⁵⁶ NH_3 produced under the standard conditions.

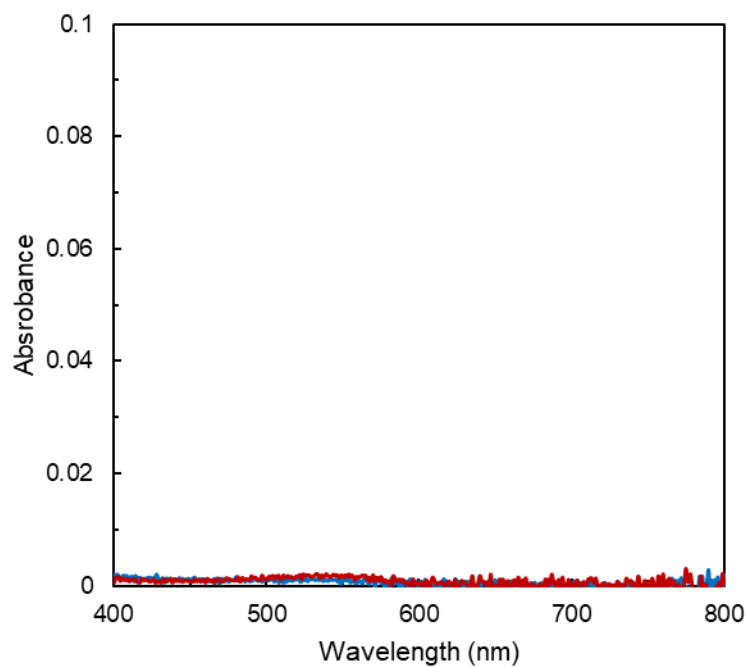


Figure E12: UV-Vis spectra for the Griess analysis of a 0.1 M KOH solution exposed to the atmosphere of the $^{14}\text{N}_2$ -filled glovebox used for CPE experiments before (red trace) and after (blue trace) treatment with VCl_3 . The total content of $\text{NO}_2^- + \text{NO}_3^-$ is $<0.04 \mu\text{mol}$.

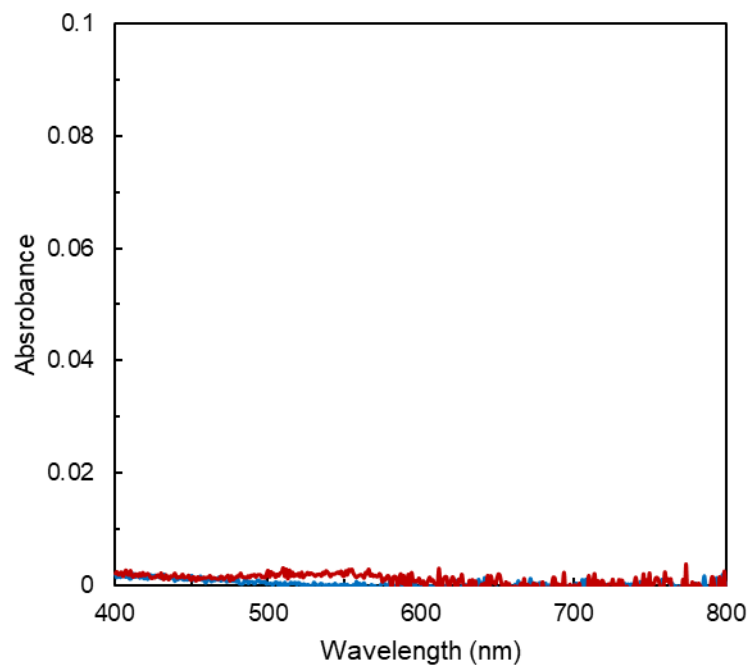


Figure E13: UV-Vis spectra for the Griess analysis of a 0.1 M KOH solution exposed to $^{15}\text{N}_2$ passed through a saturated solution of SmI_2 in THF before (red trace) and after (blue trace) treatment with VCl_3 . The total content of $\text{NO}_2^- + \text{NO}_3^-$ is $<0.1 \mu\text{mol}$.

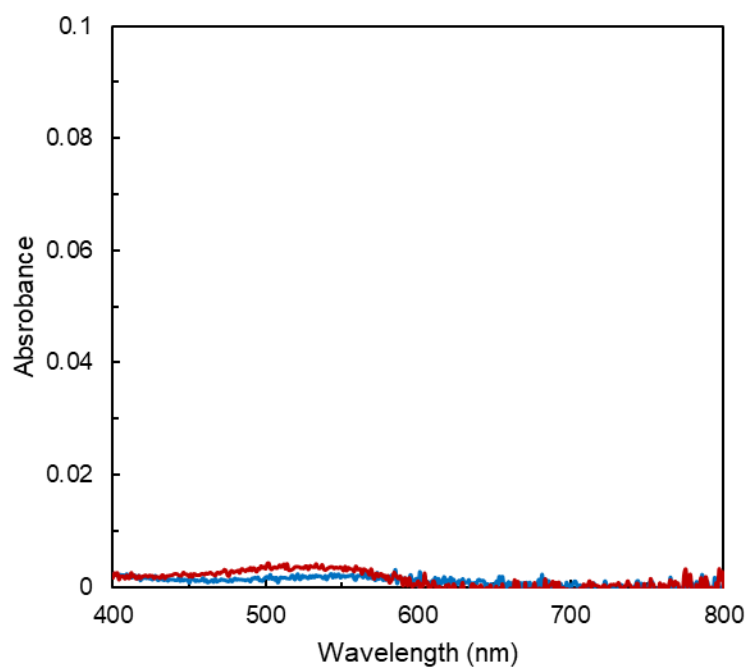


Figure E14: UV-Vis spectra for the Griess analysis of a 0.1 M solution of ³⁵⁸
"Bu₄NNTf₂ in THF before (red trace) and after (blue trace) treatment with VCl₃.
The total content of NO₂⁻ + NO₃⁻ is <0.1 μmol.

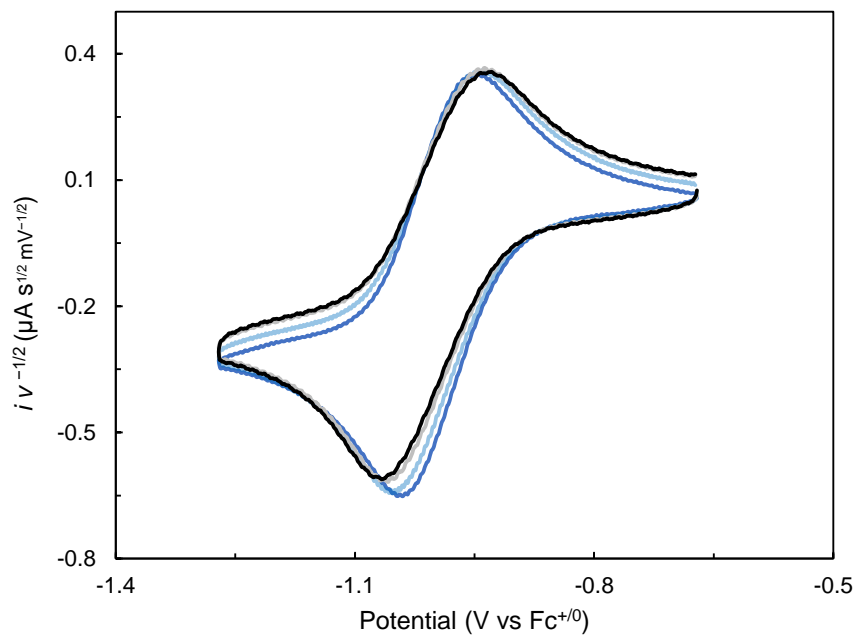


Figure E15: Scan rate-normalized CVs of in situ-generated $[\text{PNPMo}^{\text{V}}(\text{N})\text{I}]^+$ (0.46 mM) in the presence of 8 mM LutHNTf₂ at 25-300 mV s^{-1} (blue-black traces; 0.1 M $n\text{-Bu}_4\text{NNTf}_2$ /16 mM $n\text{-Hept}_4\text{NI}$ in THF, glassy carbon disk working electrode, $\text{Ag}^{+/0}$ pseudoreference electrode, Pt wire counter electrode).

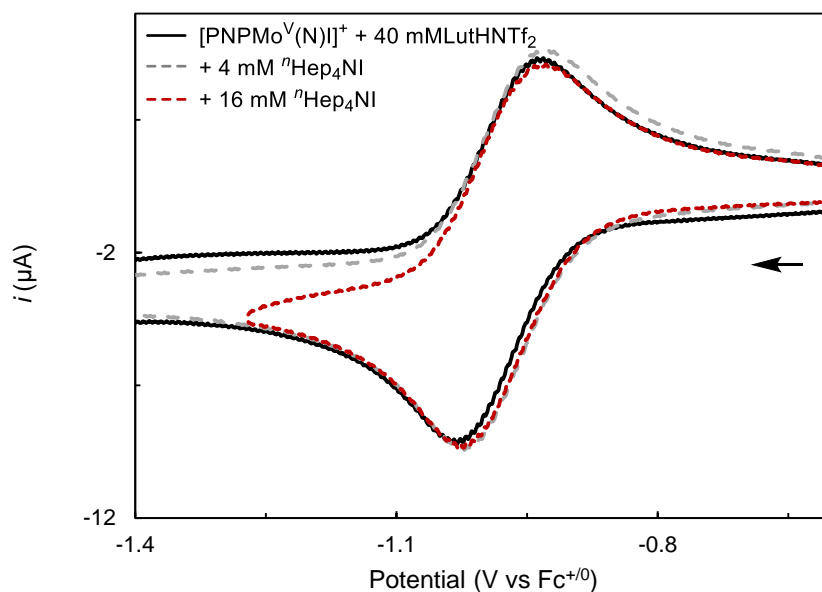


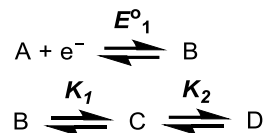
Figure E16: CVs of in situ-generated $[\text{PNPMo}^{\text{V}}(\text{N})\text{I}]^+$ (0.46 mM, black trace) in the presence of LutHNTf₂ (40 mM) following addition of $n\text{Hep}_4\text{NI}$ (4-16 mM, gray and red dashed traces) at 100 mV s^{-1} (0.1 M $n\text{Bu}_4\text{NNTf}_2$ in THF, glassy carbon disk working electrode, $\text{Ag}^{+/\text{0}}$ pseudoreference electrode, Pt wire counter electrode). The $\text{Mo}^{\text{V}/\text{IV}}$ couple remains insensitive to $[\text{I}^-]$ in the presence of acid, indicating that the proton-coupled redox event is not coupled to iodide association/dissociation.

E4.1 Derivation of Eqn 6.2

The one-electron reduction of a species A to form B obeys the Nernst eqn E.2. When the electron transfer is followed by equilibration to a mixture of species C and D, the Nernst equation has the following form:

$$E = E^\circ_1 - \frac{RT}{F} \ln \left(\frac{[\text{B}]}{[\text{A}]} \right) \quad (\text{E.1})$$

$$E = E^{\circ'} - \frac{RT}{F} \ln \left(\frac{[\text{B}] + [\text{C}] + [\text{D}]}{[\text{A}]} \right) \quad (\text{E.2})$$



Subtraction of eqn E.2 from eqn E.1 yields eqn E.3:

$$E^{\circ'} = E^\circ_1 + \frac{RT}{F} \ln \left(1 + \frac{[C]}{[B]} + \frac{[D]}{[B]} \right) \quad (\text{E.3})$$

The concentrations of species C and D can be expressed in terms of [B] through relation to the first order equilibrium constants K_1 and K_2 as follows:

$$K_1 = \frac{[C]}{[B]} \quad K_2 = \frac{[D]}{[C]}$$

$$[C] = K_1[B] \quad [D] = K_1K_2[B]$$

Substitution of these relations into eqn E.3 yields eqn E.4:

$$E_{1/2} = E^{\circ'} = E^\circ_1 + \frac{RT}{F} \ln (1 + K_1 + K_1K_2) \quad (\text{E.4})$$

For the proton-coupled reduction of $[\text{Mo}^{\text{V}}(\text{N})]^+$ (species A) to a mixture of $\text{Mo}^{\text{IV}}(\text{N})$ (species B), $[\text{Mo}^{\text{IV}}(\text{NH})]^+$ (species C), and $[\text{Mo}^{\text{IV}}(\text{NH})(\text{base})]^+$ (species D), the equilibrium constants for proton transfer and conjugate base coordination have the following forms:

$$K_{PT,IV} = \frac{[\text{Mo}^{\text{IV}}(\text{NH})^+][\text{base}]}{[\text{Mo}^{\text{IV}}(\text{N})][\text{baseH}^+]} \quad K_{assoc,IV} = \frac{[\text{Mo}^{\text{IV}}(\text{NH})\text{base}^+]}{[\text{Mo}^{\text{IV}}(\text{NH})^+][\text{base}]}$$

At high $[\text{baseH}^+]$ and $[\text{base}]$ relative to $[\text{Mo}]$, the pseudo-first order equilibrium constants are defined as:

$$K_1 = K_{PT,IV} \frac{[\text{baseH}^+]}{[\text{base}]} \quad K_2 = K_{assoc,IV}[\text{base}]$$

Substitution of these relations into eqn E.4 yields eqn E.5, which can be rearranged to eqn 6.2.

$$E_{1/2} = E^\circ_1 + \frac{RT}{F} \ln \left(1 + K_{PT,IV} \frac{[\text{baseH}^+]}{[\text{base}]} + K_{PT,IV}K_{assoc,IV}[\text{baseH}^+] \right) \quad (\text{E.5})$$

E5 Estimation of N₂R Driving Force

Comparison of overpotential across representative nonaqueous *e*N₂R systems is complicated by the lack of robust thermodynamic constants available in the ethereal solvents that are typically employed.¹² To minimize over-approximations, we rely here on effective bond-dissociation free energy values as a proxy for driving force which are *relatively* insensitive to changes in media according to eqn E.6. Comparison of this value to the BDFE of H₂ enables benchmarking to the driving force of N₂R with H₂ (eqn E.7).¹³

$$BDFE_{eff} = 23.06 * E_{app} + 1.37 * pK_a + C_G \text{ (E.6)}$$

$$\Delta\Delta G_{f(NH_3)} = 3 * (BDFE(H_2)/2 - BDFE_{eff}) \text{ (E.7)}$$

For systems where the pK_a of the employed acid is reliably estimated in THF, this value is used along with the C_G constant for THF (59.8 kcal mol⁻¹).¹⁴ For systems where the pK_a of the employed acid is not known in THF, the reduction potential of the redox mediator in MeCN is combined with the pK_a of the employed acid in MeCN along with the C_G constant for MeCN (52.6 kcal mol⁻¹). For LiNRR, the bulk of the driving force comes from the applied potential; we therefore estimate an upper bound on the BDFE_{eff} of the combination of this potential with a conservative upper bound on the pK_a of the very weak acids used in these systems as <40 in THF.

Table E3: Estimation of overpotential $\Delta\Delta G_{f(\text{NH}_3)}$ for representative $e\text{N}_2\text{R}$ systems. 364

Entry	Proton source	pK_a (solvent)	E_{app} (V vs $\text{Fc}^{+/0}$)	BDFE_{eff}	$\Delta\Delta G_{f(\text{NH}_3)}$
Sm/PNPMo	LutH ⁺	9.5 (THF) ¹⁵	-1.45	39.4	39
PNPMo	LutH ⁺	9.5 (THF) ¹⁵	-1.65	34.8	53
PNPMo ¹⁶	CoIH ⁺	10.4 (THF) ¹⁵	-1.89	30.5	65
Fe ¹⁷	Ph ₂ NH ₂ ⁺	6.0 (MeCN) ¹⁸	-2.1	12.4	119
Co ^N /P ₄ W ¹¹	TsOH	8.5 (MeCN) ¹⁹	-1.25	35.4	47
Co ^N /P ₄ Mo ¹¹	TsOH	8.5 (MeCN)	-1.25	35.4	47
Co ^N /PNPMo ¹¹	TsOH	8.5 (MeCN)	-1.25	35.4	47
Co/Fe ¹¹	TsOH	8.5 (MeCN)	-1.25	35.4	47
2 M LiNTf ₂ ²⁰	EtOH	< 40 (THF)	-4.3	<20	>100
0.2 M LiBF ₄ ¹⁰	R ₃ P(CH ₂)R	< 40 (THF)	-4.25	<20	>100

REFERENCES

- (1) Izumiya, R.; Atobe, M.; Shida, N. Electrochemically triggered hole-catalytic benzylic substitution reaction at a polymer chain containing β -O-4 linkage. *Bull. Chem. Soc. Jpn.* **2023**, *96* (4), 353–358.
- (2) Watson, P. L.; Tulip, T. H.; Williams, I. Defluorination of perfluoroolefins by divalent lanthanoid reagents: activating carbon-fluorine bonds. *Organometallics* **1990**, *9* (7), 1999–2009.
- (3) Arashiba, K.; Eizawa, A.; Tanaka, H.; Nakajima, K.; Yoshizawa, K.; Nishibayashi, Y. Catalytic nitrogen fixation via direct cleavage of nitrogen–nitrogen triple bond of molecular dinitrogen under ambient reaction conditions. *Bull. Chem. Soc. Jpn.* **2017**, *90* (10), 1111–1118.
- (4) Ashida, Y.; Arashiba, K.; Nakajima, K.; Nishibayashi, Y. Molybdenum-catalysed ammonia production with samarium diiodide and alcohols or water. *Nature* **2019**, *568* (7753), 536–540.
- (5) Eizawa, A.; Arashiba, K.; Egi, A.; Tanaka, H.; Nakajima, K.; Yoshizawa, K.; Nishibayashi, Y. Catalytic reactivity of molybdenum–trihalide complexes bearing PCP-type pincer ligands. *Chem. – Asian J.* **2019**, *14* (12), 2091–2096.
- (6) Boyd, E. A.; Shin, C.; Charboneau, D. J.; Peters, J. C.; Reisman, S. E. Reductive samarium (electro)catalysis enabled by Sm^{III} -alkoxide protonolysis. *Science* **2024**, *385* (6711), 847–853.

- (7) Norcross, B. E.; Clement, G.; Weinstein, M. The Hantzsch pyridine synthesis: A³⁶⁶ factorial design experiment for the introductory organic laboratory. *J. Chem. Educ.* **1969**, *46* (10), 694–695.
- (8) Fulmer, G. R.; Miller, A. J. M.; Sherden, N. H.; Gottlieb, H. E.; Nudelman, A.; Stoltz, B. M.; Bercaw, J. E.; Goldberg, K. I. NMR chemical shifts of trace impurities: common laboratory solvents, organics, and gases in deuterated solvents relevant to the organometallic chemist. *Organometallics* **2010**, *29* (9), 2176–2179.
- (9) Weatherburn, M. W. Phenol-hypochlorite reaction for determination of ammonia. *Anal Chem* **1967**, *39* (8), 971–974.
- (10) Suryanto, B. H. R.; Matuszek, K.; Choi, J.; Hodgetts, R. Y.; Du, H.-L.; Bakker, J. M.; Kang, C. S. M.; Cherepanov, P. V.; Simonov, A. N.; MacFarlane, D. R. Nitrogen reduction to ammonia at high efficiency and rates based on a phosphonium proton shuttle. *Science* **2021**, *372* (6547), 1187–1191.
- (11) Garrido-Barros, P.; Derosa, J.; Chalkley, M. J.; Peters, J. C. Tandem electrocatalytic N₂ fixation via proton-coupled electron transfer. *Nature* **2022**, *609* (7925), 71–76.
- (12) Lindley, B. M.; Appel, A. M.; Krogh-Jespersen, K.; Mayer, J. M.; Miller, A. J. M. Evaluating the thermodynamics of electrocatalytic N₂ reduction in acetonitrile. *ACS Energy Lett.* **2016**, *1* (4), 698–704.
- (13) Chalkley, M. J.; Drover, M. W.; Peters, J. C. Catalytic N₂-to-NH₃ (or -N₂H₄) conversion by well-defined molecular coordination complexes. *Chem. Rev.* **2020**, *120* (12), 5582–5636.
- (14) Wise, C. F.; Agarwal, R. G.; Mayer, J. M. Determining proton-coupled standard potentials and X–H bond dissociation free energies in nonaqueous solvents using

open-circuit potential measurements. *J. Am. Chem. Soc.* **2020**, *142* (24), 10681–³⁶⁷10691.

- (15) Garrido, G.; Koort, E.; Ràfols, C.; Bosch, E.; Rodima, T.; Leito, I.; Rosés, M. Acid–base equilibria in nonpolar media. Absolute pK_a scale of bases in tetrahydrofuran. *J. Org. Chem.* **2006**, *71* (24), 9062–9067.
- (16) Ibrahim, A. F.; Garrido-Barros, P.; Peters, J. C. Electrocatalytic nitrogen reduction on a molybdenum complex bearing a PNP pincer ligand. *ACS Catal.* **2023**, *13* (1), 72–78.
- (17) Chalkley, M. J.; Del Castillo, T. J.; Matson, B. D.; Peters, J. C. Fe-mediated nitrogen fixation with a metallocene mediator: Exploring pK_a effects and demonstrating electrocatalysis. *J. Am. Chem. Soc.* **2018**, *140* (19), 6122–6129.
- (18) Tshepelevitsh, S.; Kütt, A.; Lõkov, M.; Kaljurand, I.; Saame, J.; Heering, A.; Plieger, P. G.; Vianello, R.; Leito, I. On the basicity of organic bases in different media. *Eur. J. Org. Chem.* **2019**, *2019* (40), 6735–6748.
- (19) Kütt, A.; Tshepelevitsh, S.; Saame, J.; Lõkov, M.; Kaljurand, I.; Selberg, S.; Leito, I. Strengths of acids in acetonitrile. *Eur. J. Org. Chem.* **2021**, *2021* (9), 1407–1419.
- (20) Du, H.-L.; Chatti, M.; Hodgetts, R. Y.; Cherepanov, P. V.; Nguyen, C. K.; Matuszek, K.; MacFarlane, D. R.; Simonov, A. N. Electroreduction of nitrogen with almost 100% current-to-ammonia efficiency. *Nature* **2022**, *609* (7928), 722–727.